PL-TR-94-2217
Environmental Research Papers, No. 1157

AD-A284 667

PROCEEDINGS OF THE 16TH ANNUAL SEISMIC RESEARCH SYMPOSIUM, 7-9 SEPTEMBER 1994

DTIC
ELECTE
SEP 06 1994
S G D

Editors:

John J. Cipar
James F. Lewkowicz
Jeanne M. McPhetres

94-28897

8 August 1994

APPROVED FOR PUBLIC RELEASE; DISTRIBUTION UNLIMITED

DTIC QUALITY INSPECTED 5

PHILLIPS LABORATORY
Directorate of Geophysics
AIR FORCE MATERIEL COMMAND
HANSCOM AIR FORCE BASE, MA 01731-3010

94 9 08 093

"This technical report has been reviewed and is approved for publication."

JOHN J. CIPAR
Task Scientist
Earth Sciences Division

JAMES F. LEWKOWICZ
Director
Earth Sciences Division

This report has been reviewed by the ESC Public Affairs Office (PA) and is releasable to the National Technical Information Service (NTIS).

Qualified requestors may obtain additional copies from the Defense Technical Information Center. All others should apply to the National Technical Information Service.

If your address has changed, or if you wish to be removed from the mailing list, or if the addressee is no longer employed by your organization, please notify PL/IM, 29 Randolph Road, Hanscom AFB, MA 01731-3010. This will assist us in maintaining a current mailing list.

Do not return copies of this report unless contractual obligations or notices on a specific document requires that it be returned.

REPORT DOCUMENTATION PAGE

Form Approved
OMB No. 0704-0188

Public reporting burden for this collection of information is estimated to average 1 hour per response, including the time for reviewing instructions, searching existing data sources, gathering and maintaining the data needed, and completing and reviewing the collection of information. Send comments regarding this burden estimate or any other aspect of this collection of information, including suggestions for reducing this burden, to Washington Headquarters Services, Directorate for Information Operations and Reports, 1215 Jefferson Davis Highway, Suite 1204, Arlington, VA 22202-4302, and to the Office of Management and Budget, Paperwork Reduction Project (0704-0188), Washington, DC 20503.

1. AGENCY USE ONLY (Leave blank)	2. REPORT DATE	3. REPORT TYPE AND DATES COVERED
	8 August 1994	Scientific, Final

4. TITLE AND SUBTITLE
Proceedings of the 16th Annual Seismic Research Symposium, 7-9 September 1994

5. FUNDING NUMBERS
PE 61102F
PR 2309
TA G2
WU 10

6. AUTHOR(S)
John J. Cipar
Editors: James F. Lewkowicz
Jeanne M. McPhetres

7. PERFORMING ORGANIZATION NAME(S) AND ADDRESS(ES)
Phillips Laboratory /GPE
29 Randolph Road
Hanscom AFB, MA 01731-3010

8. PERFORMING ORGANIZATION REPORT NUMBER
PL-TR-94-2217
ERP, No.1157

9. SPONSORING/MONITORING AGENCY NAME(S) AND ADDRESS(ES)
AFOSR/NM
110 Duncan Avenue, Suite B115
Bolling AFB, DC 20332-0001

10. SPONSORING/MONITORING AGENCY REPORT NUMBER

11. SUPPLEMENTARY NOTES
This research was supported by AFOSR under PE 61102F, by PL under PE 62101F and by ARPA under PE 62301E.

12a. DISTRIBUTION/AVAILABILITY STATEMENT
Approved for Public Release; distribution unlimited

12b. DISTRIBUTION CODE

13. ABSTRACT *(Maximum 200 words)*

These Proceedings contain papers presented at the Sixteenth Annual Seismic Research Symposium held 7-9 September 1994, in Thornwood, New York. This Symposium represents the combined annual review for the seismic verification research programs funded by the Air Force Phillips Laboratory, PL/GPE and the Air Force Office of Scientific Research, AFOSR/NM. The scientific objectives of the research programs are to improve the Air Force's capability to seismically detect, locate, identify, and characterize underground nuclear explosions. The purpose of these Symposia, organized annually by GPE, is to provide the sponsoring agency an opportunity to review research, particularly contractor research, accomplished during the preceding year and to outline areas of investigation for the coming year. For the researchers, it provides a forum for the exchange of scientific information to help achieve program goals, and an opportunity to meet PL and AFOSR staff to discuss results and future plans. In addition, the Symposium and the technical

14. SUBJECT TERMS
underground nuclear explosions, discrimination, regional seismology, earthquake sources, structure of the crust and upper mantle

15. NUMBER OF PAGES
422

16. PRICE CODE

17. SECURITY CLASSIFICATION OF REPORT	18. SECURITY CLASSIFICATION OF THIS PAGE	19. SECURITY CLASSIFICATION OF ABSTRACT	20. LIMITATION OF ABSTRACT
UNCLASSIFIED	UNCLASSIFIED	UNCLASSIFIED	UL

presentations serve as an important avenue for technology transition to the Air Force user. The papers include studies of the identification and characterization of seismic explosion sources (discrimination), the acquisition and processing of seismic data including data from the Commonwealth of Independent States, regional seismic wave propagation from both an empirical and theoretical viewpoint, and determination of crustal and upper mantle structure in selected regions of the globe, theoretical and empirical models for the physics of earthquake and explosion sources.

TABLE OF CONTENTS

PAGE

Ahrens, Thomas J.; **Anderson**, William W.
Shock-Induced Damage and Radiation of Seismic Energy from Confined Explosions 1

Aki, Keiiti; **Chen**, Xiaofei; **Jin**, Anshu
Study on the Discrimination of Explosions and Earthquakes at Regional Distance by Using Coda Q^{-1} Method 5

Alexander, Shelton S.; **Hsu**, Roy C.; **Gupta**, Indra N.; **Salzberg**, David H.
Development of Discriminants and Improved Locations for Regional Events in Iran 13

Anderson, David P.; **Stump**, Brian W.
Utilization of Near-Source Video and Ground Motion in the Assessment of Seismic Source Functions from Mining Explosions 20

Baker, G. Eli; **Cormier**, Vernon; **Minster**, J. Bernard
Effects on Pn, Pg, and Lg Amplitudes of Nuclear Explosion Waveforms Recorded in Southern California 27

Barker, T. G.; **McLaughlin**, K. L.; **Stevens**, J. L.
Network Identification Capability Evaluation (NICE) of Regional Networks 34

Baumgardt, Douglas R.; **Der**, Zoltan
Performance and Portability of Regional Seismic Waveform Discriminants in Different Tectonic Regions 41

Bennett, T. J.; **Barker**, B. W.; **Murphy**, J. R.
Identification of Rockbursts, Earthquakes, Chemical Blasts and Small Nuclear Explosions at Regional Distances 49

Blackman, Donna K.; **Orcutt**, John A.
Seismoacoustic Studies of the Norwegian Sea 56

Cormier, Vernon F.; **Anderson**, Tom; **Baker**, G. Eli
Ray Synthesis of Regional Seismograms 60

Dainty, Anton M.; **Kushnir**, Alexander F.
Enhancing Surface Wave Signals Using the Undistorting Group Filter 64

Availability Codes

Dist	Avail and / or Special
A-1	

PAGE

Drake, Lawrence A.; **Ramos**, Estela Minaya
Seismic Wave Propagation in South America 71

Ekström, Göran; **Dziewonski**, Adam M.; **Su**, Wei-jia; **Smith**, Gideon P.
Elastic and Anelastic Structure Beneath Eurasia 78

Fielding, Eric; **Barazangi**, Muawia; **Isacks**, Bryan; **Seber**, Dogan
A Network-Accessible Geological and Geophysical Database for Eurasia, North Africa, and the Middle East: Digital Database Development for the Middle East and North Africa 85

Fisk, Mark D.; **Gray**, Henry L.; **McCartor**, Gary D.
Preliminary Assessment of Seismic CTBT/NPT Monitoring Capability 92

Frohlich, Cliff; **Zhao**, Lian-She
Location of Regional Seismic Events Using Single-Station Broadband Data 99

Gao, Liping; **Richards**, Paul G.
Studies of Earthquakes on and Near the Lop Nor, China, Nuclear Test Site 106

Gibson, R. L.; **Toksöz**, M. N.; **Dong**, W.
Radiation from Seismic Sources in Cylindrical Cavities 113

Goff, John A.; **Holliger**, Klaus; **Levander**, Alan
Modal Fields: A New Method for Characterization of Random Seismic Velocity Heterogeneity 120

Gray, H. L.; **Woodward**, W. A.; **McCartor**, G. D.; **Fisk**, M.D.
A Hypothesis-Testing Approach to Discriminant Analysis with Mixed Categorical and Continuous Variables when Data are Missing 124

Hansen, Roger, A.; **Harvey**, Danny J.
High Frequency 3-Component Waveform Inversion for Source and Structural Parameters 131

Harkrider, D. G.; **Ben-Menahem**, A.
Theoretical Rayleigh and Love Waves from Explosions in Non-Spherical Cavities and from Tectonic Release in Compressive Stress Fields 138

Hedlin, Michael A. H.; **Minster**, J. Bernard; **Vernon**, Frank L.; **Orcutt**, John A.
Imaging Prominent Crustal Scatterers and Constraining Source Depth Using the Piñon Flat Broad-band 3-Component Array 145

PAGE

Herrin, Eugene; **Burlacu**, Valeriu; **Gray**, Henry L.; **Swanson**, Jack
Golden, Paul; **Myers**, Billie
Research in Regional Event Discrimination Using Ms:m_b and Autoregressive Modeling of Lg Waves 152

Herrmann, R. B.; **Hutchenson**, K. D.
Quantification of Small Sources 159

Husebye, Eystein S.; **Mendi**, C. Deniz; **Ruud**, Bent O.
Near Real Time Seismic Magnitude and Moment Measurements 164

Jih, R.-S.
Numerical Modeling of Crustal Phase Propagation in Irregular Waveguides 173

Johnson, Lane R.; **McEvilly**, T. V.
Near-Source Observations of the NPE 182

Jordan, Thomas H.; **Gaherty**, James B.
Polarization Anisotropy and Small-Scale Structure of the Continental Upper Mantle 189

Keers, H.; **Vogfjörd**, K.; **Nolet**, G.; **Phinney**, R.
The Character of Lg-Waves from a Mode and Ray Point of View 196

Kennett, B. L. N.
The Exploitation of Regional and Teleseismic Waveforms 203

Kim, Won-Young; **Richards**, Paul G.; **Khalturin**, Vitaly I.;
Rautian, Tatyana G.
Borovoye, Kazakhstan, (BRVK) Seismic Data Analysis 210

Langston, Charles A.;
Anatomy of Regional Phases and Source Characterization of the Soviet Joint Verification Experiment, Underground Nuclear Explosion 217

Lay, Thorne; **Zhang**, Tianrun
Calibration of Regional Wave Discriminants in Diverse Geological Environments: Topographic Correlations 224

Li, Y.; **Rodi**, W.; **Toksöz**, M. N.
Seismic Source Characterization with Empirical Green's Function and Relative Location Techniques 231

Mangino, Stephen; **Priestley**, Keith
Seismic Studies of the Caspian Basin and Surrounding Regions 238

PAGE

Miller, Kate C.; **Keller**, G. Randy
Studies of Lithospheric Structure in Southwestern North America Part II: Lithospheric Structure of the Sierra Nevada: 1993 Field Observations of the NPE and the Southern Sierra Nevada Continental Dynamics Project 245

Montana, Carlos; **Keller**, G. Randy; **Miller**, Kate; **Whitelaw**, Julia
Studies of Lithospheric Structure in Southwestern North America Part III: Lithospheric Profiles in the Nevada Test Site Region: The DELTA FORCE Experiment 252

Morozova, Elena A.; **Morozov**, Igor B.; **Smithson**, Scott B.; **Shatzman**, James; **Solodilov**, Leonid N.
Studies of P_n, S_n and L_g Wave Propagation Across Major Crustal Studies using PNEs 255

Murphy, J. R.; **Kitov**, I. O.; **Stevens**, J. L.; **Sultanov**, D. D.
Analyses of the Seismic Characteristics of U.S. and Russian Cavity Decoupled Explosions 262

Nyffenegger, Paul A.; **Zhao**, Lian-She; **Frohlich**, Cliff
Investigation of Non-Double-Couple Earthquake Sources 269

Orrey, Jeffrey; **Archambeau**, Charles
A Generalized Pseudospectral Method and its Application to Regional 3-D Seismic Wavefield Synthesis 275

Park, Jeffrey; **Yu**, Yang; **Su**; Liqiang; **Lilly**, Jonathan; **Fischer**, Robert
The Effects of Anisotropy on Regional Seismic Wave Propagation 284

Pavlis, Gary L.; **Mahdi**, Hanan; **Vernon**, Frank L.
Surface Wave Propagation in Central Asia: Observations of Scattering and Multipathing with the Kyrgyz Broadband Array 291

Roberts, Donald G.; **Keller**, G. Randy
Studies of Lithospheric Structure in Southwestern North America Part I: Lithospheric Structure of West-Central New Mexico Determined from the Minor Uncle Test at White Sands Missile Range 298

Rodgers, Arthur; **Hearn**, Thomas; **Ni**, James
Uppermost Mantle Structure in Southern Eurasia from Pn Tomography and Sn Attenuation 304

Ruud, B. O.; **Husebye**, E. S.
2D Finite Difference Modeling of Scismic Wave Propagation in Complex Crust – Upper Mantle Media 310

PAGE

Sammis, Charles G.
Modeling the Damage Regime in Nonlinear Explosion Source Simulations 317

Sykes, Lynn R.
Dealing with Decoupled Nuclear Explosions Under a Comprehensive Test Ban Treaty 324

Teng, Yu-Chiung; **Kuo**, John T.
The Effect of Sediments on Attenuation, Scattering, and Blockage of Lg Wave Propagation 331

Vogfjord, Kristin S.; **Nyblade**, Andrew A.; **Langston**, Charles A.
Regional Wave Propagation in Central and Southern Africa 338

Wagner, Gregory S.; **Owens**, Thomas J.
Waveform Estimates from Multi-Channel Seismic Data 345

Wallace, Terry C.; **Beck**, Susan L.
Characterization of Broadband, Regional Distance Seismograms in Eurasia and Other Regions of Potential Underground Testing: Path Effects in South America 352

Wallace, Terry C.; **Beck**, Susan L.
Discrimination at Regional Distances: Seismic Characterization of South America and Korea 359

Woods, Bradley B.; **Saikia**, Chandan K.
A Comparison of Regional Explosion and Earthquake Waveforms in North America and Eurasia with Application to Event Discrimination 364

Woods, Bradley B.; **Helmberger**, Donald V.
Regional Seismic Discriminants using Wavetrain Energy Ratios 372

Wu, Ru-Shan; **Lay**, Thorne
Modeling Elastic Wave Propagation in 3D Heterogeneous Media by Elastic Complex-Screen (ECS) Method 379

Xie, Jiakang; **Cong**, Lianli; **Ni**, Jiang Chuan; **Mitchell**, B. J.
Source Scaling and Depth Determination from Lg Spectra 386

Zhang, J.
Polarization Characteristics of Seismic Waves from the May 21, 1992 Lop Nor Nuclear Explosion Using IRIS/GSN Broadband Data 393

PAGE

Zhao, Lian-She; **Frohlich**, Cliff
Crustal and Upper Mantle Velocity Structure Beneath Seismic Stations from Modeling Teleseismic Waveforms 400

Zhu, L.; **Helmberger**, D. V.
Regional Earthquake Waveform Modeling on the Tibetan Plateau 407

SHOCK-INDUCED DAMAGE AND RADIATION OF SEISMIC ENERGY FROM CONFINED EXPLOSIONS

Thomas J. Ahrens and William W. Anderson

Seismological Laboratory
California Institute of Technology
Pasadena, California 91125

Contract No. F49620-92-J-0402

OBJECTIVE

For media ranging from nonporous granite to 25% porous limestone, ~60% to 98% of the energy released by a confined underground explosion is deposited near the source and not radiated as far-field seismic energy. The decay of the anelastic stress wave controls the radiated seismic energy which can be detected by regional and global seismic arrays. Our recent stress wave calculations employing compression and release data yield the energy deposition and resultant stress wave decay rates and demonstrate that the peak stress, P, is a function of radius, r, given by $P \sim r^{-a}$ where a varies from 1.4 to 2.3 in going from granite to porous limestone. Even considering hysteresis in the shock-release path, wavecode models of actual explosions do not accurately account for the reduced displacement potentials observed in the elastic shock regime unless the medium in which the explosion occurs is assumed to have been significantly weakened by the shock wave from the source. Damage produced in the rock by passage of the shock wave accounts for this effect. The present effort is directed at understanding the mechanisms of shock-induced weakening in different types of rock and obtaining quantitative models of the amount of weakening produced by varying shock stresses.

RESEARCH ACCOMPLISHED

The phenomenon of shock induced weakening and resultant shock wave decay is being studied by quantifying the damage beneath craters in rocks which have been subjected to a quasi-spherically diverging and decaying stress wave in the laboratory. Experiments with San Marcos gabbro and Bedford

limestone have been performed in which these rocks have been subjected to decaying compressional and tensional stress waves in the 10 to 1000 MPa stress range.

The damage in the rocks was quantified by sectioning the rock and measuring the P-wave velocity deficits and visible crack densities as a function of distance from the crater. The P-wave velocity deficits give a direct measure of the reduction in the strength of the rock (which we measured separately and correlated with the theory of Ashby and Sammis [1990]). Figures 1 and 2 show contours of mean P-wave velocity (taken as the algebraic mean of the velocities measured in 3 orthogonal directions) in cross-sections through the center of the crater. In both samples, the contours are roughly concentric about a spheroid centered on the effective depth of burst (usually near the crater floor), except at low stresses where preexisting variability in the rock is still detectable and near free surfaces where reflection of rarefaction waves complicates the stress history.

In Bedford limestone, the P-wave velocity of undamaged rock is 3.9 km/s, while velocities in shocked rock vary from ~1.6 km/s for a shock stress of 900 MPa to ~3.9 km/s for a shock stress of 200 MPa. The velocity deficit corresponds to the damage parameter, D, defined by

$$D = 1 - (Vp/Vpo)^2 \qquad (1)$$

where Vp is the P-wave velocity of the shocked rock and Vpo is the P-wave velocity of the undamaged rock. D can to first order be taken as the fractional reduction in the effective elastic moduli of the medium. The observed velocity deficits in the limestone correspond to values of D ranging from ~0 for a 200 MPa shock stress to ~.83 for a shock stress of 900 MPa. In gabbro, the undamaged rock P-wave velocity is 6.4 km/s, while shocked rock shows mean velocities ranging from ~4.0 km/s (D ~ .61) to ~6.4 km/s (D ~ 0) for shock stresses ranging from ~6.4 GPa to ~1.4 GPa. In both rock types, decay of the "elastic" wave is considerably faster than would be expected from geometrical considerations alone.

CONCLUSIONS AND RECOMMENDATIONS

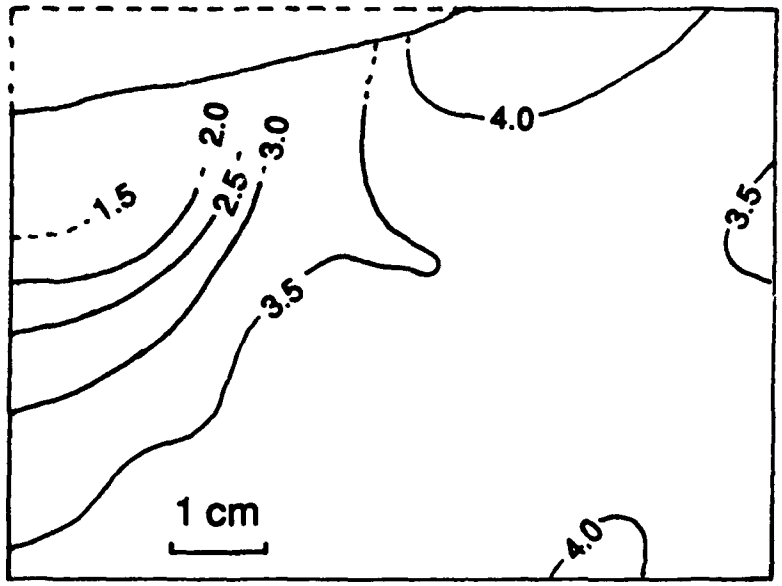


Figure 1. Contours of average P-wave velocity in cratered Bedford limestone. The velocities are given in km/s. Because the impact geometry was axisymmetric, only one half of the sample cross section through the center of the crater is shown.

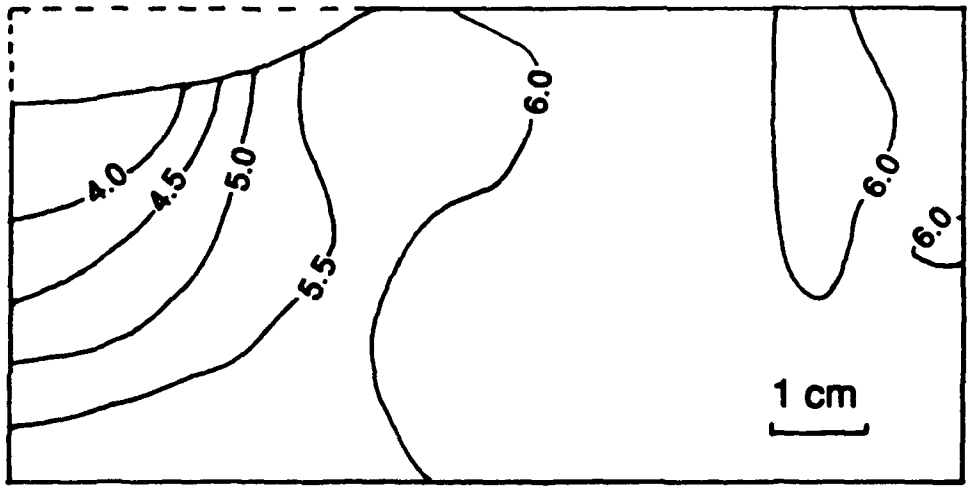


Figure 2. Contours of average P-wave velocity in cratered San Marcos gabbro. Units and comments for Figure 1 apply to this figure.

The observed decay of the quasi-elastic shock in the present study, as well as observations from other studies on confined laboratory-scale explosions in rock, shows the importance of shock-induced weakening in robbing the advancing shock front of energy. Simple consideration of consequences of the weakening process shows that the stress wave is weakened both by doing work to damage the rock and by being dispersed as the elastic moduli of the rock change (with attendant change in the trailing edge of the stress pulse). The data obtained thus far suggest that, for the isotropic to weakly anisotropic rocks studied, the reduction in the effective elastic moduli is approximately described by

$$D \sim P^3 \qquad (2)$$

where P is the amplitude of the stress wave.

The present results are confined to the previously sparsely studied finite amplitude anelastic regime which is treated by most studies as elastic or nearly elastic because the anelasticity is a result of mechanical failure and fracture formation rather than plastic yielding and has thus far been difficult to treat quantitatively in wavecode calculations. Present efforts are being directed toward studying these effects in previously unstudied rock types, e.g., sedimentary rocks such as shale and sandstone and highly anisotropic rocks such as shale and slate, as well as conducting measurements of Q^{-1} in shock-damaged rocks by directly measuring attentuation of elastic waves in the damaged rocks.

Reference

Ashby, M. F., and C. G. Sammis, The damage mechanics of brittle solids in compression, Pure Appl. Geophys., 113, 489-521, 1990.

STUDY ON THE DISCRIMINATION OF EXPLOSIONS AND EARTHQUAKES AT REGIONAL DISTANCE BY USING CODA Q^{-1} METHOD

Keiiti Aki, Xiaofei Chen and Anshu Jin
Department of Geological Sciences, University of
Southern California, Los Angeles, CA90089-740

Contract Number: F49620-93-1-0016

OBJECTIVE

The objective of this study is to discriminate the explosions and earthquakes at regional distance by using the coda wave method. In an earlier study, Su and Aki (1991) found a significant difference in coda attenuation, Q_c^{-1}, for quarry blasts and earthquakes for lower frequencies of 1.5 and 3 Hz for lapse time less than 30 seconds (see Fig. 1), and they suggested that such a significant difference in Q_c^{-1} may be attributed to the seismic surface wave's contributions. To interpret the observed seismic coda waves we need to consider the seismic surface wave scattering processes. Wu (1985) and Zeng et al. (1991, 1993) have shown that the energy transfer theory can successfully describe the seismic body waves scattering processes in a random scattering and absorption full-space medium. In this report, we shall first develop the energy transfer theory for surface wave and body wave to study their scattering and coupling processes. Then, using this theory we shall explain the discrimination of quarry blasts and earthquakes at local distance (about 30 to 40 km) observed by Su and Aki (1991). By fitting our synthetic coda attenuation curves with the observed data, we will obtain the scattering and coupling coefficients. Finally, with the derived scattering and coupling coefficients, we shall simulate the surface wave and body wave's energy transfer processes at regional distance, and investigate the possibility of discrimination of explosions and earthquakes at regional distance by using the coda Q^{-1} method.

RESEARCH ACCOMPLISHED

1. Energy transfer theory for S and Rayleigh waves' scattering processes

In the last report, we have considered only the scattering processes of surface waves, and neglected the body waves' conversions. In this report we shall consider the coupling effect of body waves with surface waves. For simplicity, we consider only the

coupling process between the S wave and Rayleigh wave. The energy transfer equation described such an coupled scattering process can be written as follows,

$$E^R(x,\omega) = G^R(x,x_s)e^{-\eta^R|r-r_s|}\varepsilon_o^R(x,\omega) \qquad (1a)$$

$$+ \int_V G^R(x,x')e^{-\eta^R|r-r'|}\{\eta_s^{RR}E^R(x',\omega) + \eta_s^{SR}E^S(x',\omega)\}dV(x')$$

$$E^S(x,\omega) = G^S(x,x_s)e^{-\eta^S|r-r_s|}\varepsilon_o^S(x,\omega) \qquad (1b)$$

$$+ \int_V G^S(x,x')e^{-\eta^S|x-x'|}\{\eta_s^{RS}E^R(x',\omega) + \eta_s^{SS}E^S(x',\omega)\}dV(x') \ .$$

Where,

$E^S(x,\omega)$: seismic energy carried by S wave per unit volume at x;

η^R : total attenuation coefficient for Rayleigh wave, $\eta^R = \eta_i^R + \eta_s^{RR} + \eta_s^{SR}$;

η_s^{RR}: Rayleigh to Rayleigh waves scattering coefficient;

η_s^{SR} : S to Rayleigh waves scattering coefficient;

η^S : total attenuation coefficient for S wave, $\eta^S = \eta_i^S + \eta_s^{RS} + \eta_s^{SS}$;

η_i^S : absorption coefficient for S wave;

η_s^{RS} : Rayleigh to S waves scattering coefficient;

η_s^{SS} : S to S waves scattering coefficient;

$\varepsilon_0^S(x_s,\omega)$: total S wave energy rate radiated from source divided by the velocity of S wave;

$G^S(x,x')$: the geometrical spreading function for S wave.

As shown in the last report that the above equations can be solved by using Fourier transform method. Solving these coupled equations, we can obtain the solution of energy transfer processes of S and Rayleigh waves. The time-history of total scattering energy can be determined by introducing proper time-delay phase factors to these coupled equations.

2. Application to the Discrimination of Earthquakes and Quarry Blasts at Local Distance

In an earlier study, Su and Aki (1991) found a significant difference in coda attenuation, Q_c^{-1}, for quarry blasts and earthquakes for lower frequency of 1.5Hz and 3.0Hz for lapse time less than 30 seconds as shown in Figure 1. As we have shown in the last

report that this discrimination can be qualitatively interpreted by our energy transfer theory of S and Rayleigh waves (Chen and Aki, 1993). In this study we shall quantitatively interpret the Su and Aki's observation, and determine the corresponding attenuation coefficients and the coupling coefficients by fitting our synthetic attenuation curves with the observed ones. We here consider only the S wave coda attenuation, Q_c^{-1}, that mainly includes the S to S waves scattering as well as Rayleigh to S waves scattering. For simplicity, we neglect the S to Rayleigh conversions, thus the only coupling coefficient needs to be determined is η_s^{ss}. As reported in the last report that the discrimination between the earthquakes and quarry blasts can be attributed to the contributions of Rayleigh wave, namely, the me re of coda attenuation of the quarry blasts contains significant Rayleigh wave's conve because of the shallow focal depth (about 0 km), while the coda attenuation of the earthquakes contains little Rayleigh waves conversions because of the deeper focal depth (about 5 km). Based on this results we shall, first, determine the S wave's intrinsic and scattering coefficients, i.e., η_i^s and η_s^{ss}, by matching our synthetic S wave's attenuation with the observed earthquake's coda attenuation, Q_c^{-1}. At this stage, we let $\eta_s^{sr}=0$. Having the coefficients of η_i^s and η_s^{ss}, we then can determine the coefficients of η_s^{sr}, η_s^{rr} and η_i^r by fitting our synthetic attenuation curves with the observed quarry blasts coda attenuation, Q_c^{-1}.

After more than 20 trials, we found the attenuation coefficients for the best matching with the observed data are given in Table 1. And the corresponding coda attenuation curves are shown in Figure 2. These attenuation curves are calculated using the same method as described in Su and Aki's study (1991) from our theoretical scattered S wave energy envelope. Our results indicate that the coupled scattering coefficients, η_s^{sr}, which describes the scattering conversion from Rayleigh wave to S wave, are strongly depends on frequency in the following way: for frequency lower than 3Hz, $\eta_s^{sr}=0.005$ $(km)^{-1}$; while for frequency greater than 6Hz $\eta_s^{sr}<0.00005$ km^{-1}. Therefore, there may exist a critical frequency between 3Hz and 6Hz beyond which the Rayleigh wave conversions are negligible, while below which the Rayleigh wave conversions to S wave are significant.

3.Discussion on the discrimination of earthquakes and explosions at regional distance

Having the theoretical studies on the discrimination of earthquakes and quarry blasts at local distance, we can discuss the possibility of the discrimination of earthquakes and explosions at regional distance using the method of coda attenuation, Q_c^{-1}. In the

following discussion we assume that the intrinsic and scattering attenuation coefficients of S and Rayleigh waves, and the coupled scattering coefficients obtained in the above study is still valid for the events at regional distance. Using those derived coefficients we calculated the synthetic coda attenuation curves for earthquakes and explosions at regional distances as shown in Figure 3. Here, we assume the hypocenter is 600 km, and the focal depth is 10 km for earthquakes and 0.01 km for explosions. As shown in Figure 3, our theoretical simulations show that the Rayleigh wave conversion to scattered S wave at regional distance is much more significant than that at local distance, because the Rayleigh wave has a weaker geometrical spreading factor that S wave. For lower frequency (e.g., f=3Hz or 1.5Hz), the synthetic result predicts a strong increase in coda attenuation that starts just after the Rayleigh wave's arrival and last about 50 seconds. For higher frequency (e.g., f=6Hz or 12Hz), a similar increase is also predicted by our synthetic result, although it is not as strong as the one for lower frequencies. It should be pointed out that this increase amount in the coda attenuation for lower frequency is an upper-limit, the actual predicted increase in coda attenuation should be in the range between nothing and this amount, because the value of coupled scattering coefficient η_s^m is given in the range of 0 to 0.00005 km^{-1}. Our preliminary study on the data of Chinese Digital Seismic Network shows a similar result for high frequency case as predicted (we shall report this result later), therefore the coda attenuation method is a promising method, at least for high frequency cases, to discriminate the earthquakes and explosions at regional distance.

SUMMARY

To date, we have developed the energy transfer theory for Rayleigh and S wave's propagation in a random scattering and attenuation medium, and successfully applied it to interpret the Su and Aki's observed discrimination of earthquakes and the quarry blasts at local distance (1991). Our study indicates that the Rayleigh waves' scatterings become important for the events with shallower focal depth, for instance, the quarry blasts and nuclear explosions. By fitting our theoretical attenuation curves with the observed ones by Su and Aki (1991) at local distance, we have obtained the S and Rayleigh waves' intrinsic and scattering coefficients, and the coupled scattering coefficient of Rayleigh with S waves. By assuming these coefficients are still valid for the events at regional distance, we have discussed the problem of discrimination between the earthquakes and explosions at regional distance. Our theoretical study shows that the Rayleigh wave's contributions become more significant for shallower events (e.g., explosions), while for deeper events (e.g., earthquakes) the Rayleigh wave's contributions are still negligible. According to our theoretical study and the preliminary study on the data of CDSN, the discrimination of earthquakes

and explosions at regional distance is possible by using the coda attenuation method, if the corresponding coda attenuation can be measured from the actual seismic data.

REFERENCES

Aki, K. and P. G. Richards (1980). *Quantitative Seismology: Theory and Methods*, W. H. Freeman, San Francisco.

Su, F. , K. Aki, and N. N. Biswas (1991). Discriminating quarry blasts from earthquakes using coda waves, *Bull. Seism. Soc. Am.*, **81**, 161-178.

Wu, R. S. (1985). Multiple scattering and energy transfer of seismic waves--seperation of scattering effect from intrinsic attenuation, I. Theoretical modeling, *Geophys. J. R. Astr. Soc.*, **82**, 57-80.

Zeng, Y. H., F. Su, and K. Aki (1991). Scattering wave energy propagation in a random isotropic scattering medium, 1. Theory, *J. Geophys. Res.*, **96**, 607-620.

Table 1. Inverted intrinsic, scattering & coupling coefficients

frequency (Hz)	η_i^s (km^{-1})	η_s^{ss} (km^{-1})	η_i^p (km^{-1})	η_s^{pp} (km^{-1})	η_s^{ps} (km^{-1})
1.5	0.01	0.017	0.07	0.05	0.005
3.0	0.02	0.007	0.07	0.05	0.005
6.0	0.025	0.01	0.07	0.05	.00005
12.0	0.028	0.012	0.07	0.05	.00005

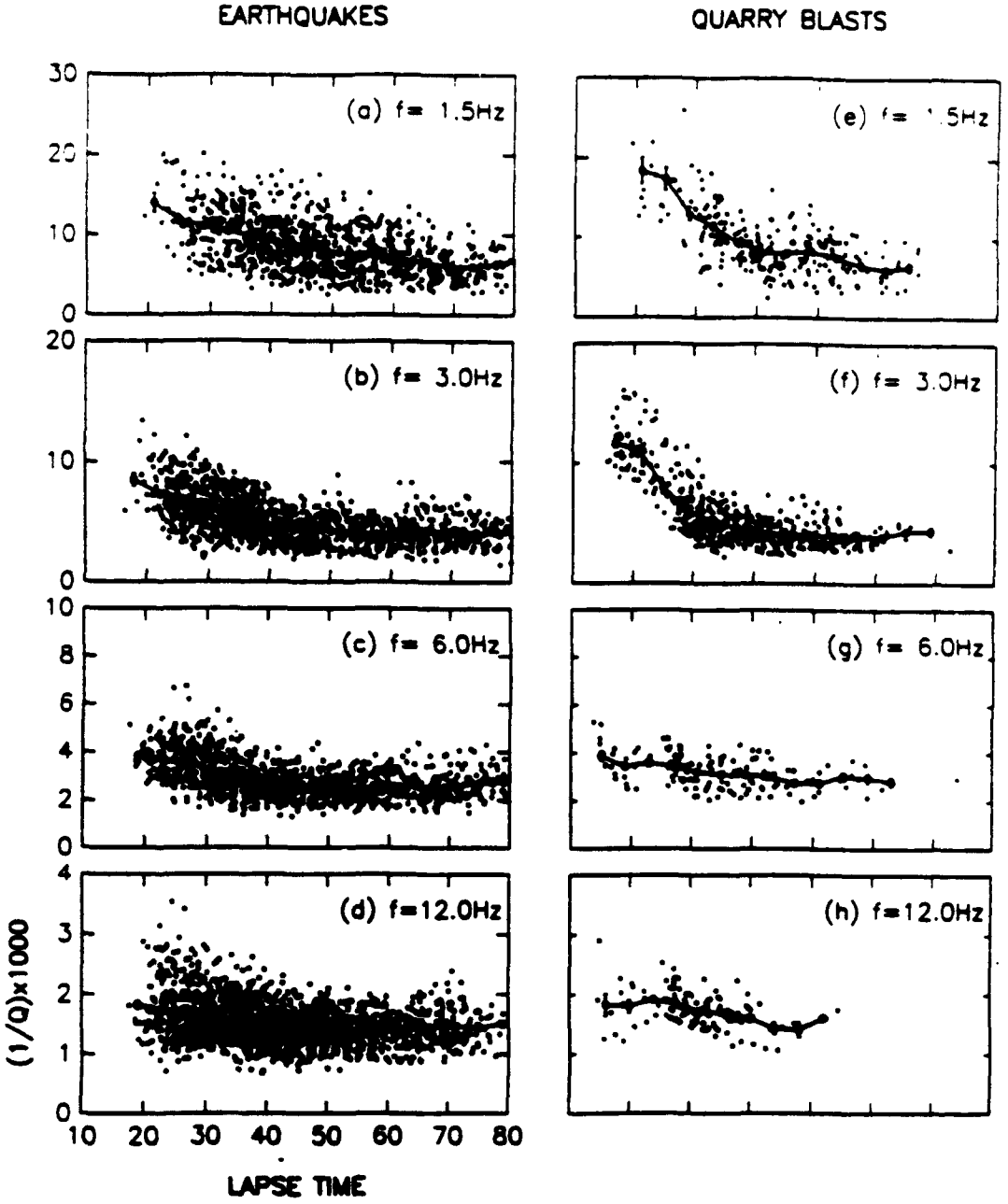


Figure 1. Coda Q^{-1} vs. lapse time obtained using the local earthquakes and quarry blasts in the south central Mojave Desert area. each open circle on the plot represents one measurement for a particular seismogram on a time window of 34 sec for frequency 1.5 Hz, 25Hz for 3 Hz, and 20sec for 6Hz and 12Hz. The solid line connects the mean points (solid circles) calculated by averaging the individual measurements in each 8 sec time interval with 4 sec overlapping at the adjacent mean points. The standard error of the mean is also shown for each mean point (from Su and Aki, 1991).

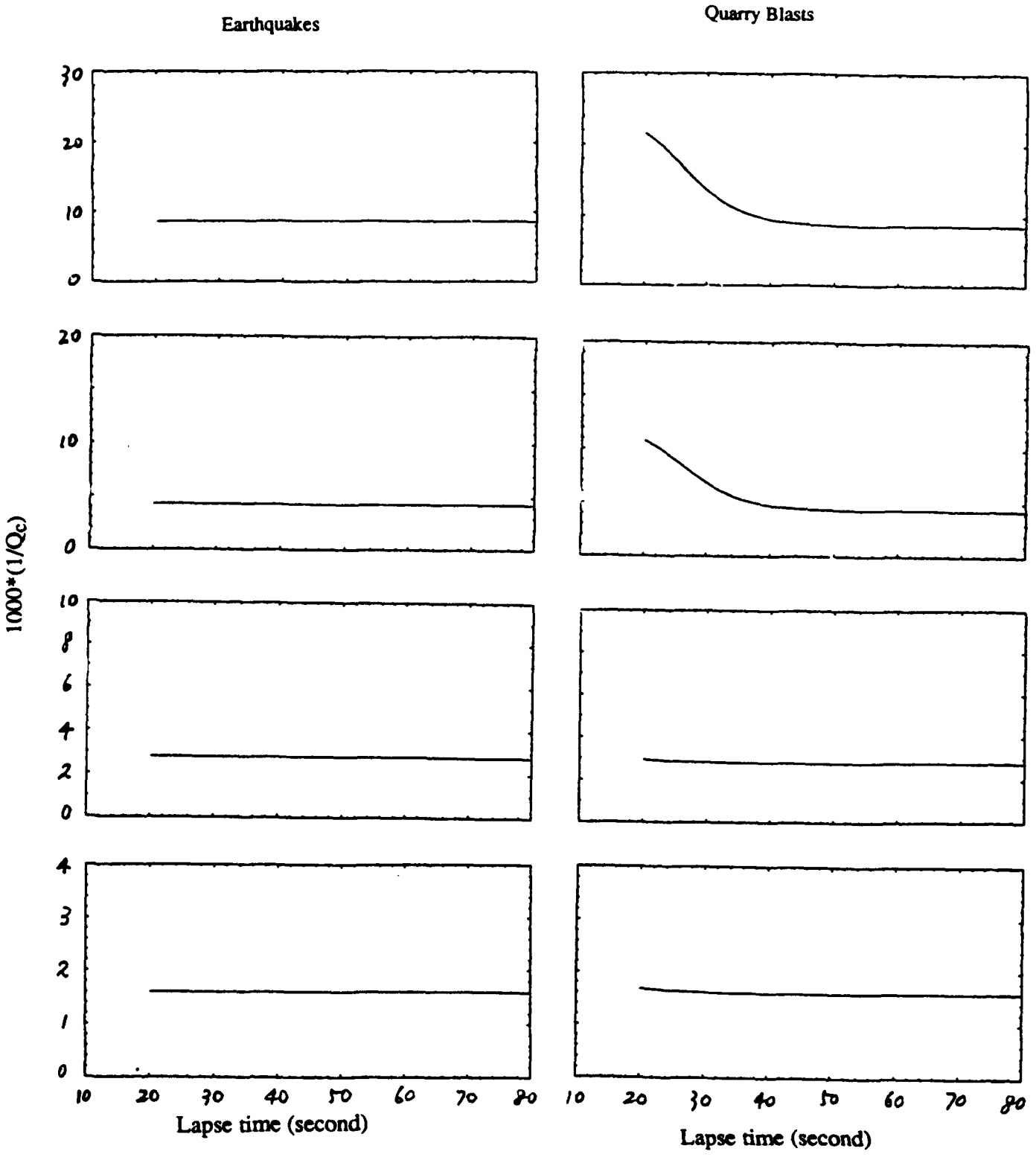


Figure 2. The synthetic coda attenuation curves obtained by solving the energy transfer equations of S and Rayleigh waves, i.e., equations (1a) and (1b). The results correspond to the best fitting coefficients listed in Table 1.

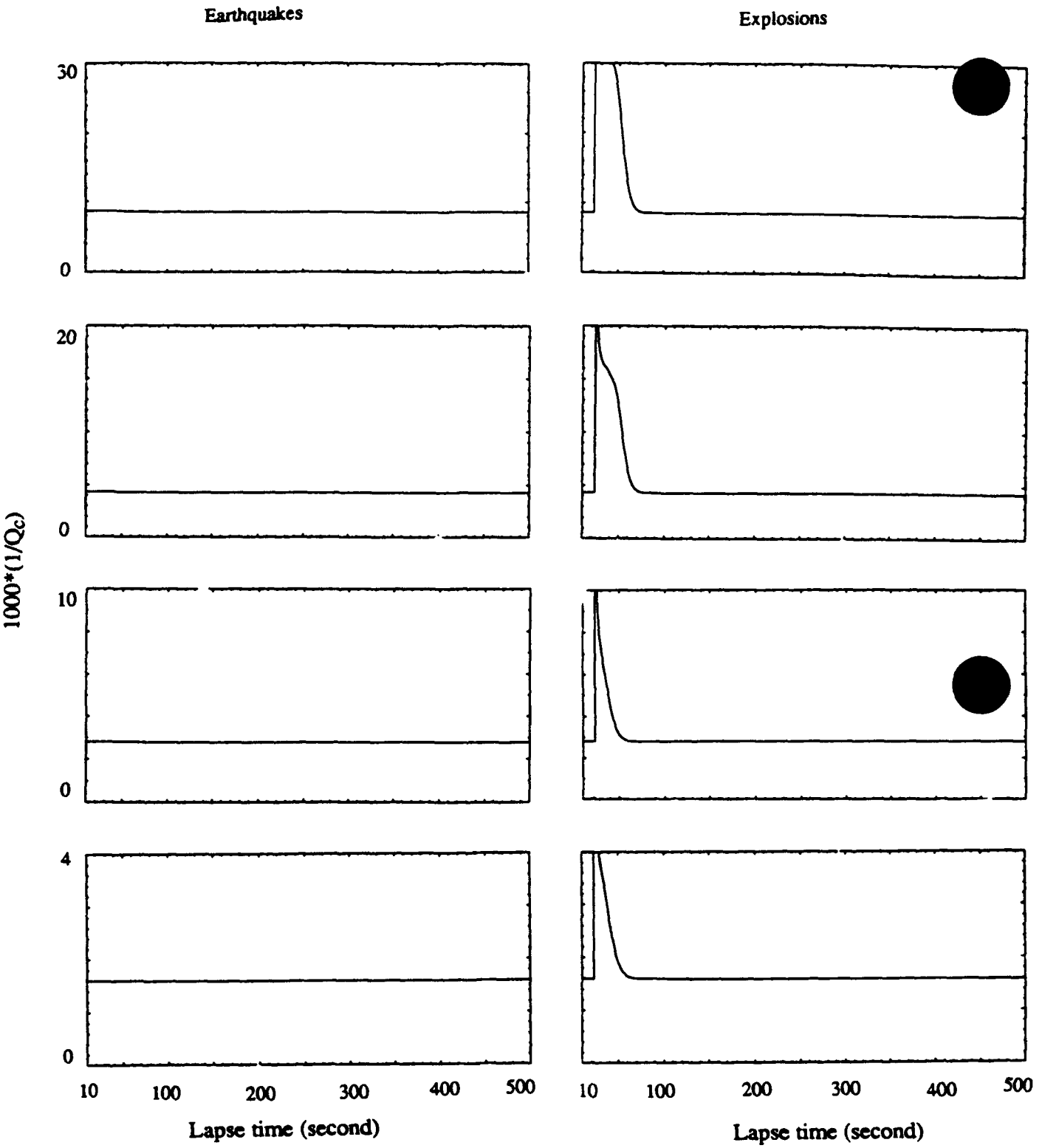


Figure 3. The synthetic coda attenuation curves for the events at regional distance. These results are calculated by assuming the derived various attenuation coefficients and coupling coefficients are still valid in this case.

DEVELOPMENT OF DISCRIMINANTS AND IMPROVED LOCATIONS FOR REGIONAL EVENTS IN IRAN

Shelton S. Alexander and Roy C. Hsu (Penn State University)
Indra N. Gupta and David H. Salzberg (Multimax Inc.)

Grant No. F49620-94-1-0179

Objective

The principal objective of this study is to develop regional discriminants such as Lg/Pn, Lg/Pg, Ms (or moment) vs mb, and Rg for Iran. Related objectives are to obtain improved event locations using well-constrained or known reference evnts; to develop signal processing approaches appropriate for near-real-time automated event identification; and to derive empirical Green's functions that can be used to simulate signals from underground nuclear explosions in Iran.

Research Accomplished

The early phases of the investigation have been devoted to determining the number of Iranian events that are well-recorded at the in-country SRO station MAIO and the ILPA array and analyzing an initial subset of events. Several hundred regional events were recorded during the intervals of operation of these stations and a significant number were large enough to be recorded at two or more regional stations outside Iran (e.g. ANTO (Turkey) and KAAO (Afghanistan)) allowing improved epicentral locations to be determined. We have obtained maps showing the location of various types of mining activity and the distribution of past seismicity throughout Iran; locations of events with respect to mining areas and tectonically active areas help in the identification of regional events. Using recordings of multiple events spanning regional distances ranging from less than 100 km to about 1000 km the dependence of various discriminants on propagation distance and path in Iran can be determined. Transformation of the signals into frequency vs velocity or frequency vs slowness seismic images facilitates the comparison of events at different distances and allows pattern recognition or trained neural network approaches to be used for discrimination, in addition to the relative excitation of selected regional phases.

Regional phases Pn, Lg, and Rg from a number of Iranian events recorded digitally at Mashhed (MAIO) have been examined thus far. One data set (Table 1) consists of 13 events at epicentral distances varying from about 90 to 280 km. These events show a significant variation in the relative excitation of regional phases. Three of these events have explosion-like characteristics, based on experience with regional discriminants in other source regions, and they are located in areas of known mining activity. Seventeen known aftershocks of a Ms 7.4 Iranian earthquake all exhibit generally similar relative excitation of regional phases. Spectral characteristics of the observed regional phases Pn, Lg, and Rg are determined by bandpass filtering, spectral ratios, and waveform modeling, as well as frequency vs velocity seismic images. Presented below are selected illustrative examples from the events listed in Table 1; the event locations

are shown in Figure 1.

Table 1.

List of 13 Events Within 2.5 Degrees of Mashed, Iran (MAIO)

No.	DATE	ORIGIN TIME (UT)	LAT (deg)	LON (deg)	DEPTH* (km)	Mb**	DIST (deg)	AZ (deg)
1	07/16/76	13:43:16.7	37.510	59.004	53.0	-1.00	1.270	161.8
2	11/07/76	04:00:50.3	33.864	59.233	5.6	5.60	2.440	5.0
3	11/07/76	07:59:54.3	33.863	59.215	0.0	-1.00	2.442	5.3
4	02/23/77	05:11:49.8	35.604	58.198	33.0	-1.00	1.261	56.2
5	03/19/77	03:29:05.5	33.819	59.360	3.2	-1.00	2.478	2.5
6	03/25/77	01:38:38.0	35.779	56.648	33.0	-1.00	2.365	76.5
7	03/25/77	17:44:21.9	37.237	59.083	35.6	-1.00	0.992	160.4
8	05/21/77	14:00:52.5	37.252	56.656	33.0	-1.00	2.469	111.8
9	06/04/77	21:28:12.5	35.527	58.115	33.0	-1.00	1.360	55.0
10	07/28/77	03:20:38.6	35.263	57.641	33.0	-1.00	1.828	55.0
11	11/10/77	13:52:33.1	34.108	59.444	6.2	4.60	2.187	1.1
12	12/16/77	17:55:14.7	37.026	59.879	33.0	-1.00	0.788	203.2
13	03/20/78	23:25:23.3	37.318	57.804	33.0	4.10	1.695	126.3

* Depth of 33.0 km is arbitrarily assigned when depth is not determined.
** Magnitudes listed as -1 are undetermined.

Figure 2 shows raw and bandpass-filtered seismograms of two events (4 and 9 in Table 1) which are inferred to be mining blasts. They are located in an area of mining activity and relatively low seismicity (Figure 1), have small Lg/P ratios at high frequencies, and have prominent Rg indicating shallow focal depth. Figure 2 also shows the frequency vs velocity images (un-normalized and normalized frequency by frequency) for these two events. These images exhibit low Lg/P excitation at the higher frequencies and the second event also shows evidence of frequency modulation indicative of ripple firing.

Figure 3 shows raw and bandpass-filtered seismograms for two events (1 and 13 in Table 1), which are inferred to be earthquakes, because they are located in an area of no mining activity (Figure 1) and have large Lg/P excitation at all frequencies relative to those in Figure 2. Also the magnitude of event 13 (mb = 4.1) is probably too large to be a mining blast. Figure 3 also shows the corresponding frequency vs velocity images for these two events.

Figure 4 shows raw and bandpass-filtered seismograms for event 10 which is located in a region of mining activity (Figure 1) and may be an explosion. This event has a high-frequency Lg/P ratio of about one, which is somewhat larger than is typical for explosions, but the P-wave spectrum of this event shows evidence of scalloping (Figure 4b) indicative of a ripple-fired explosion.

Figure 5 shows synthetic signals for (a) a CLVD source simulating a

shallow explosion and (b) a thrust earthquake at a depth of 10 km. The distance is 145 km and the Iranian crustal structure model II determined by Berberian (GIRAS, 68, 1982, p504) is used for these calculations. Note the general resemblance of the CLVD explosion synthetics in Figure 5a to the actual observed signals for events 4 and 9 shown in Figure 2 and the resemblance of the earthquake synthetics in Figure 5b to the events in Figure 3 (especially event no. 1) further supporting the conclusion that events 4 and 9 are explosions and events 1 and 13 are earthquakes.

Work in progress includes a continuing effort to develop a ground-truth data base of known earthquakes and known (or simulated) explosions, based on available publications, satellite images and other information, sufficient to obtain reliable regional discriminants; analysis of numerous additional events from different parts of Iran recorded at MAIO and ILPA; generation of synthetic regional seismograms for earthquake and explosion sources at different focal depths in crustal structure models for Iran, using existing wavenumber integration codes; and the application of trained neural networks developed for other source regions to Iranian events. Seismograms from closely clustered events will be stacked at each observing station to obtain an empirical Green's function for each source-receiver path and then convolved with the appropriate nuclear explosion source function to simulate the expected nuclear explosion signatures at each receiver.

Conclusions and Recommendations

Preliminary results from the analysis of Iranian events recorded at regional distances indicate that the regional discriminants similar to those that are effective for other source regions can be used for identification of Iranian earthquakes and explosions. However, the distance dependence of some of the regional discriminants and magnitude thresholds for their use are likely to be different from other regions that are less tectonically active.

For at least some parts of Iran Rg is well-recorded for shallow events, which provides a very useful depth discriminant. Additional work on long-period fundamental mode surface wave excitation and propagation is needed to determine the threshold above which the Ms vs mb discriminant can be used to identify Iranian events.

Because earthquakes and/or mining explosions occur throughout most parts of Iran, it should be possible to develop empirical Green's functions for any particular area of interest. This will enable simulations of signals from underground nuclear explosions at any desired source location to be generated and used to refine regional discriminants.

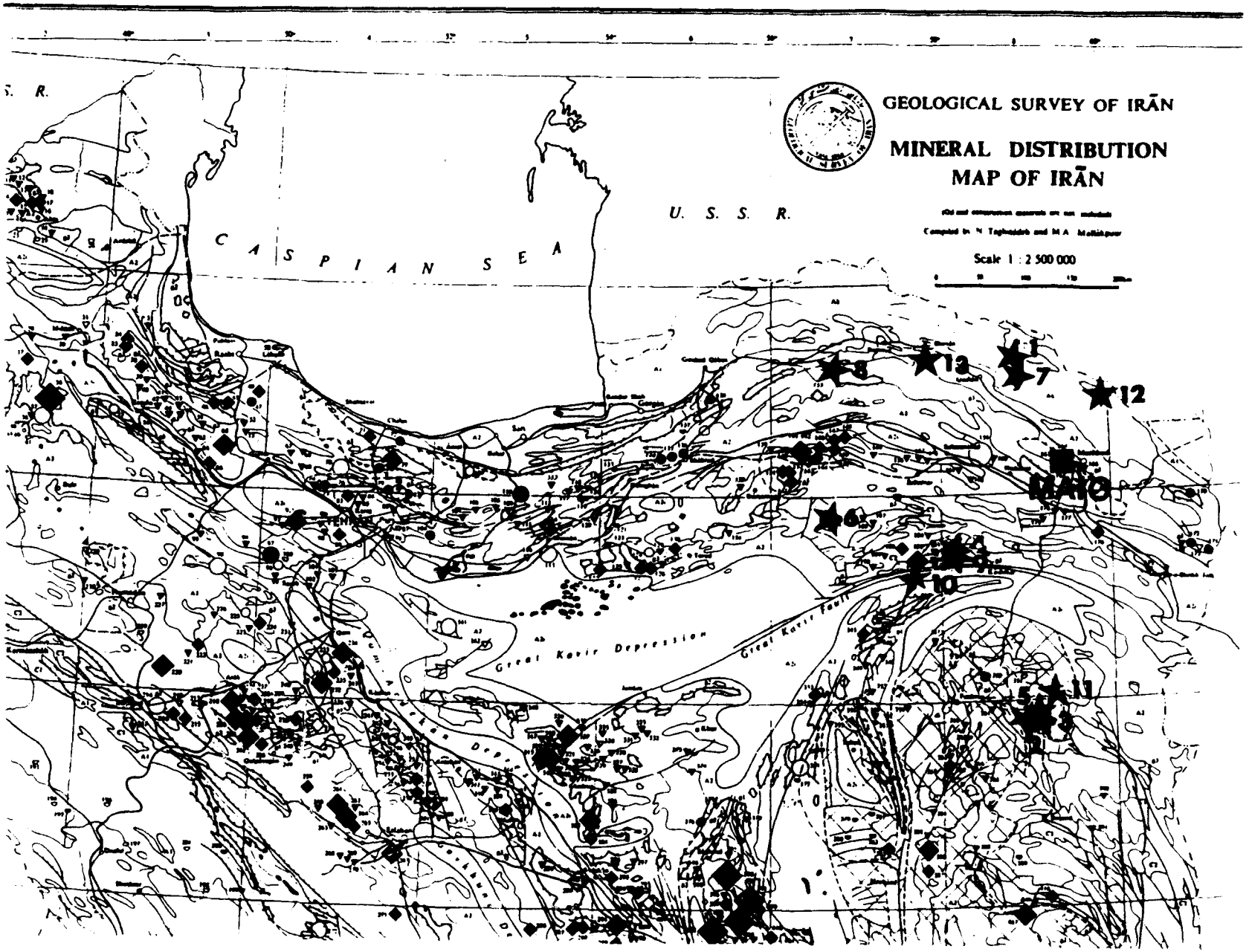


Fig. 1. Map showing locations of events listed in Table 1 (stars) superimposed on mining sites in north (indicated by diamonds, circles and triangles); SRO station Mashed (MAIO) is shown by the soli are.

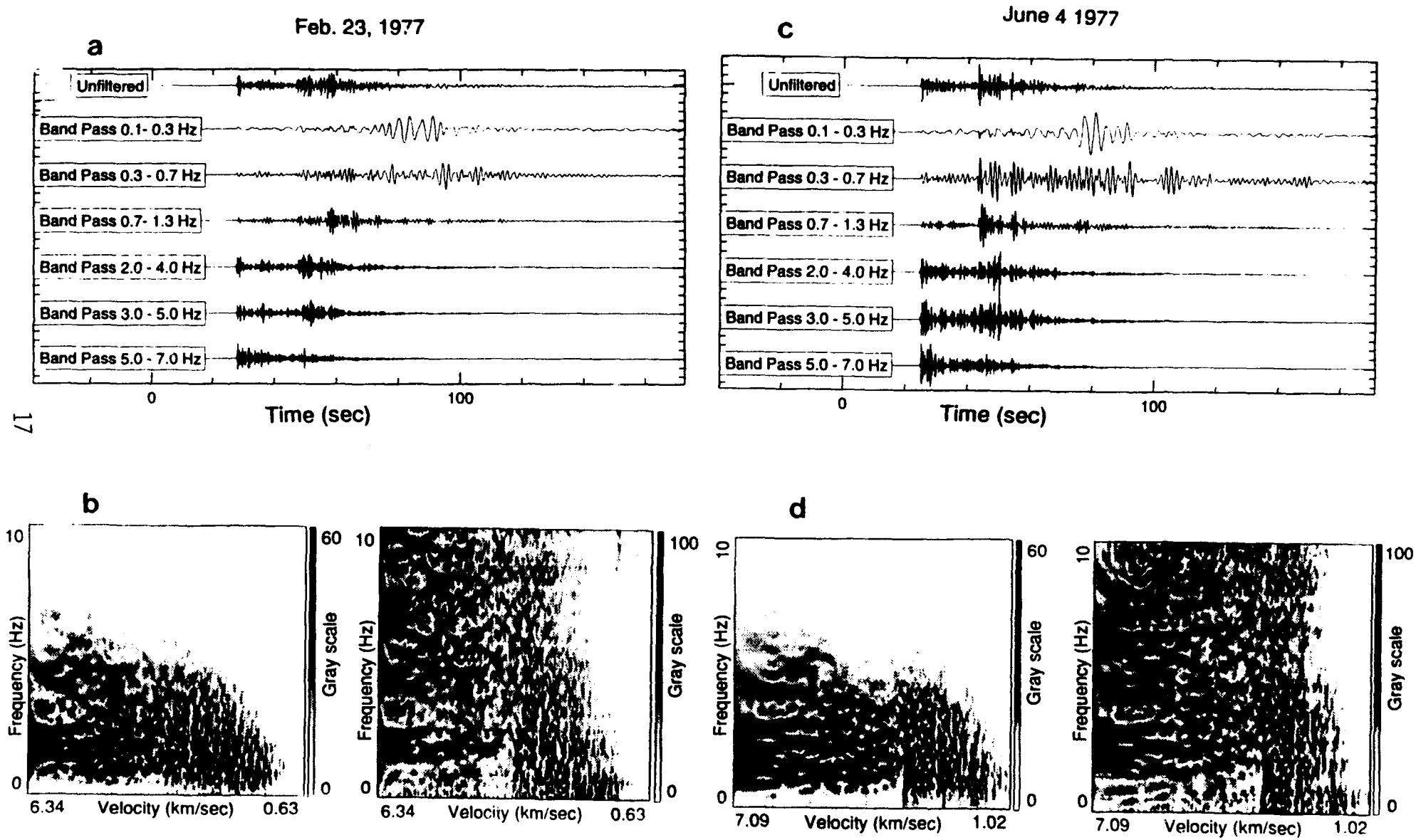


Figure 2. (a) Raw and bandpass-filtered seismograms for event 4 in Table 1; (b) Un-normalized frequency vs velocity image of event 4 (left) and the corresponding image normalized at each frequency (right); (c) Raw and bandpass-filtered seismograms for event 9 in Table 1; (d) Un-normalized frequency vs velocity image of event 9 (left) and the corresponding image normalized at each frequency (right).

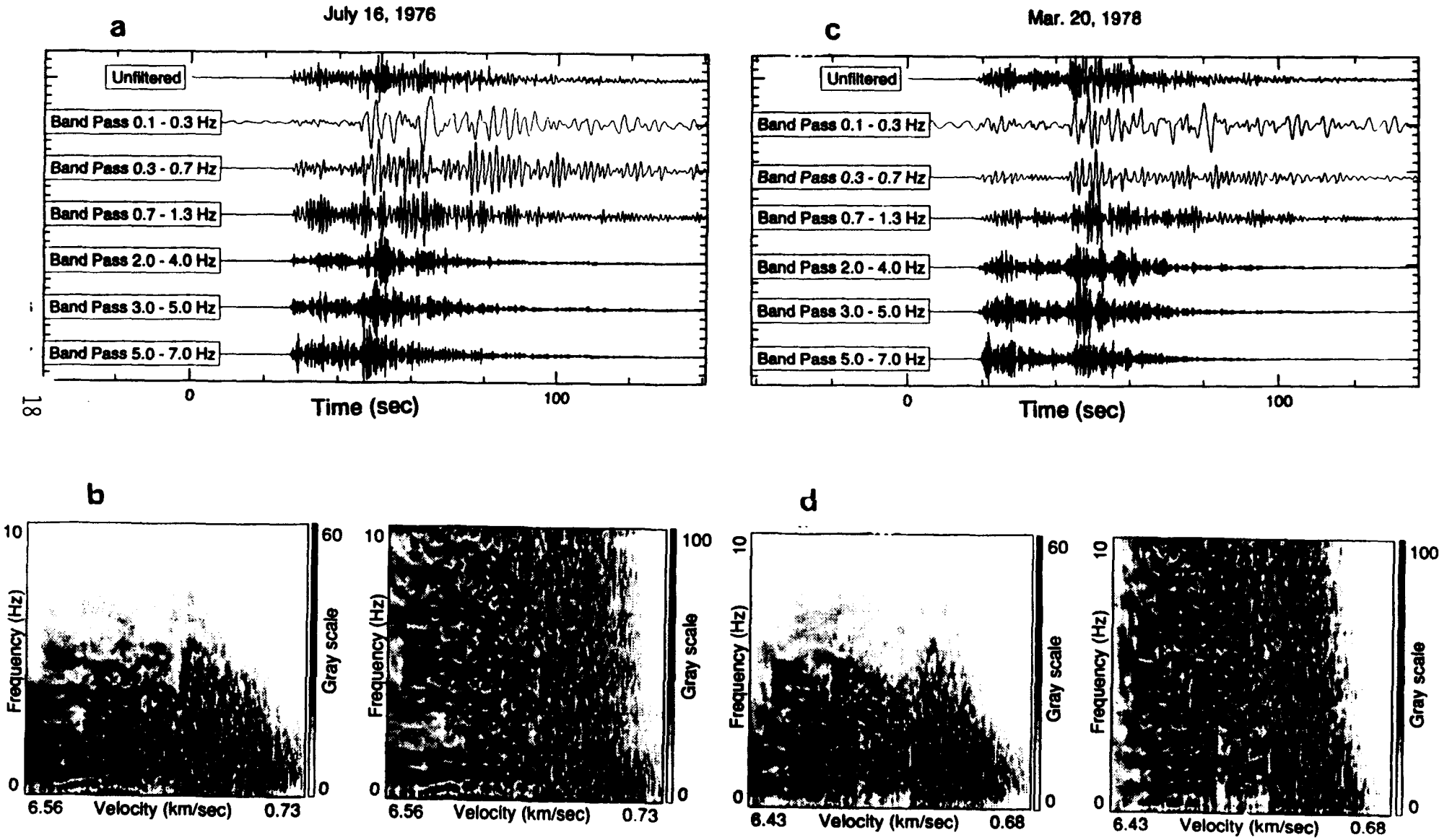
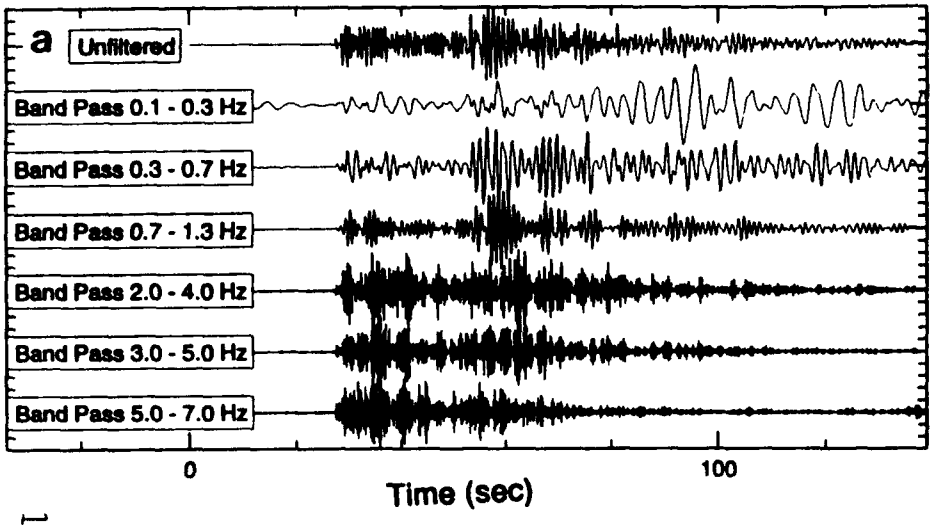


Figure 3. (a) Raw and bandpass-filtered seismograms for event 1 in Table 1; (b) Un-normalized frequency vs velocity image of event 1 (left) and the corresponding image normalized at each frequency (right); (c) Raw and bandpass-filtered seismograms for event 13 in Table 1; (d) Un-normalized frequency vs velocity image of event 13 and the corresponding image normalized at each frequency (right).



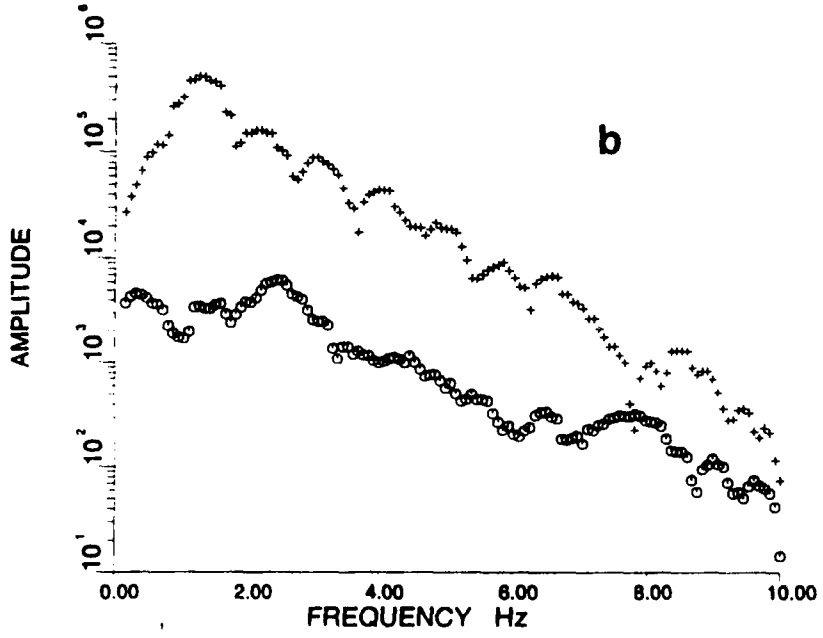
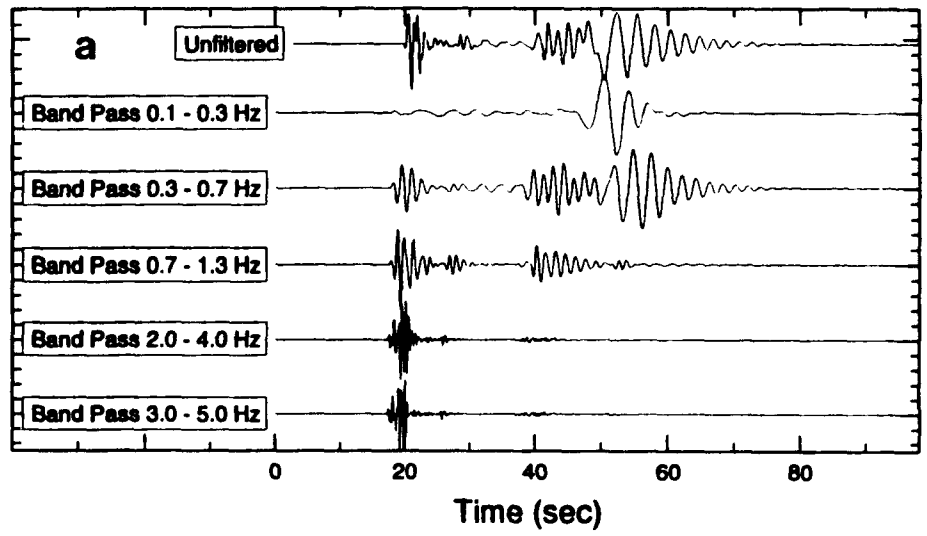


Figure 4. (a) Raw and bandpass-filtered seismograms for event 10 in Table 1: (b) P-wave and noise spectra of event 10 showing signal scalloping.



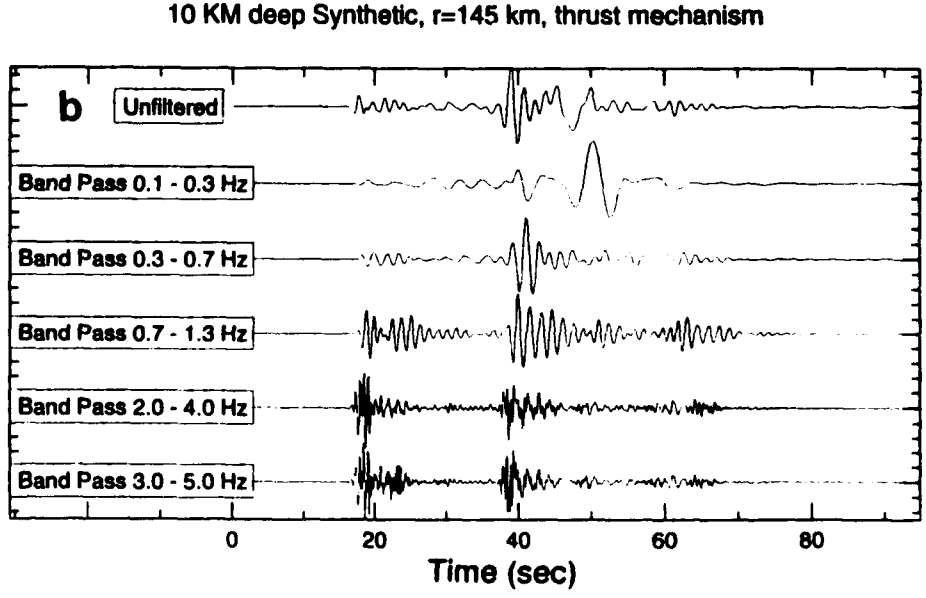


Figure 5. (a) Synthetic signals for a CLVD source simulating an underground nuclear explosion in Iran; (b) synthetic signals for a thrust earthquake at 10 km depth.

UTILIZATION OF NEAR-SOURCE VIDEO AND GROUND MOTION IN THE ASSESSMENT OF SEISMIC SOURCE FUNCTIONS FROM MINING EXPLOSIONS

David P. Anderson
Southern Methodist University
Department of Geological Sciences
Dallas, TX 75275

Brian W. Stump
Southern Methodist University
Los Alamos National Laboratory
EES-3, MS-C335
Los Alamos, NM 87545

AFOSR Grant F49620-93-1-0146

OBJECTIVE: Identification of seismic events detected under a Comprehensive Test Ban Treaty requires a clear physical understanding of the different types of seismic sources including mining explosions, rock bursts, mine collapse and small, shallow earthquakes. Constraint of the operative physical processes in the source region and linkage to the generation of seismic waveforms with particular emphasis on regional seismograms is needed. In order to properly address the multi-dimensional aspect of data sets designed to constrain these sources, we are investigating a number of modern visualization tools that have only recently become available with new, high-speed graphical computers that can utilize relatively large data sets. The results of this study will provide a basis for identifying important physical processes in the source region that contribute to regional seismograms.

RESEARCH ACCOMPLISHMENTS: Mining explosions have been identified as a possible source of seismic signals that at small magnitude might have to be discriminated from a nuclear explosion, possibly tested in a clandestine environment. Many mining explosions occur each year as documented by Richards *et al.*, 1992. The coupling as well as the source characterization of these events must be investigated in order to assess the possible impact they might have on a monitoring system. The source characterization studies are directly linked to attempts to discriminate events based upon the relative excitation of different regional phases and the spectral content of the signals. One of the most discussed discriminants has been spectral scalloping of the signals resulting from either the delay times between the individual charges in the mining explosion or the total duration of the shot. The literature contains many studies that attribute this possible discriminant to one of these mechanisms with no consensus on the cause (Baumgardt and Ziegler, 1988; Hedlin *et al.*, 1989; Hedlin *et al.*, 1990; Smith, 1989; Chapman *et al.*, 1992). None of these studies made any direct observations of the blasts that could confirm or deny the

conclusions of the analysis of the regional data. In some cases, official blasting records from the mines were available for comparison but as Stump *et al.*, 1994 point out these records sometimes are in disagreement with actual blasting practices. In addition to spectral differences, a number of authors have investigated the generation of regional P, S and surface waves by mining explosions and have suggested the use of the relative excitation of these phases. Modeling to accompany these studies has attempted to quantify the relative importance of the directly coupled energy from the explosions, vertical and horizontal spall, the rubblization process and the three dimensional structure of the mine itself on the resulting regional waveforms (Barker and McLaughlin, 1992; McLaughlin *et al.*, 1993).

Following the work of Reamer *et al.*, 1992, this paper reports on efforts to document physical processes in the near-source region of mining explosions for the purposes of unambiguously constraining the important characteristics of mining explosions that generate seismic waves. Studies such as this in conjunction with regional observations from the same events provide the mechanism for placing regional discriminants on a firm physical foundation that can then be extrapolated to new environments or locations. The recent Non-Proliferation Experiment (Denny and Zucca, 1994) illustrates one such controlled experiment in which a combination of near-source and regional measurements were used to explore the similarities and differences of chemical and nuclear explosions.

Mining explosions are designed for a variety of purposes including the fragmentation and movement of materials. The blast design is dependent on the particular application intended and the material properties of the rock. The range of mining applications from hard rock quarrying to coal exposure to mineral recovery leads to a great variety of blasting practices. A common component of many of the sources is that they are detonated at or near the earth's surface and thus can be recorded by camera or video. Although our primary interest is in the seismic waveforms these blasts generate, the visual observations of the blasts provide important constraints that can be applied to the physical interpretation of the seismic source function. In particular, high speed images can provide information on detonation times of individual charges, the timing and amount of mass movement during the blasting processes and in some instances evidence of wave propagation away from the source. All of these characteristics can be valuable in interpreting the equivalent seismic source function for a set of mine explosions and quantifying the relative importance of the different processes. This report documents an attempt to take standard Hi-8 video of mine blasts, recover digital images from them and combine them with ground motion records for interpretation. The steps in the data acquisition, processing, display and interpretation will be outlined. Two applications, the first a single cylindrical charge at standard burden distances and a small, four-by-four, ripple-fired explosion will be used to illustrate the techniques.

The blasts were all recorded on a Sony TR101 Hi-8 video camera at 30 frames/s and a 1/10000 shutter speed. The camera was deployed approximately 100 m from the single cylindrical charge parallel with the free face in front of the charge. During the ripple-fired explosion, the camera was deployed approximately 250 m behind and above the explosion. In each deployment, there was a near-by ground motion sensor for correlation with the video. The ground motion data was acquired with a 16-bit

Refraction Technology Data Acquisition System, Terra Technology accelerometers and Sprengnether S-6000 2 Hz seismometers. The focus of this discussion will be on the video acquisition and processing as the ground motion data was processed in standard ways.

The raw video images were transferred to a Sony CVR 5000 laser disk using the Silicon Graphics Inc. (SGI) Galileo Card for time-base correction, a process which takes a few seconds. 150 frames (i.e., 30 fps * 5 sec) of the video were digitized outside of real-time from the laser disk and transferred to hard disk using the SGI Galileo Video card. This process produces YUV format color images each 640x486 pixels for a total size of 150 MBytes. The files are converted from YUV to RGB format and written as Run Length Encoded (RLE) files using the Utah Raster Toolkit conversion utility (URT tools are available free from the ftp anonymous login cs.utah.edu). At this point each individual frame of the image consist of two interlaced fields sampled 1/60 sec apart. Figure 1 illustrates one of the interlaced frames from the single, cylindrical explosion. The fuzzy nature of the image is due to the rapid speed at which the material is moving and the interlacing of two fields sampled 1/60 sec apart to produce a single video frame.



Figure 1: Raw, interlaced video frame from the single cylindrical explosion. The frame follows the detonation of the explosive by 500 msec.

The frames are next de-interlaced and interpolated into one even and one odd field which represent two instances in time separated by 0.01667 sec. Additional contrast and image enhancement is performed on the de-interlaced images using RLE public domain utilities. The marked improvement in the image quality after these steps is illustrated in Figure 2.



Figure 2: De-interlaced and image enhancement of the even field from the frame displayed in Figure 1.

Although not obvious in the single frames and fields displayed in this paper, the camera moves as the P wave arrives at the recording site. This motion degrades the interpretation of the blast and so a simple correction scheme called de-jittering was devised. The location of a stationary distant point or points is noted in each frame and then the field is corrected to this location to remove camera motion. The resulting corrections for all the frames in the video are combined to produce a representation of the camera motion in the plane of the picture. The individual frames are then combined and animated on the SGI to produce a digital record of the blast at 0.01667 sec resolution. *An animated representation of these images will be available for review at the meeting.*

The final step of the process is to combine the digital video images with the digital ground motions so that one can begin to investigate the relationships between the ground motion and the source processes as recorded by the camera. The ground motions are superimposed on the bottom of the video frame along with a vertical cursor that indicates the location in time of the waveform relative to the image currently being viewed. Time correlation between the video images and the ground motion records is made with the P arrival record. The composite animation are next reconverted to RGB format and sequenced one frame at a time back onto the laser disk. The laser disk can then be used to play the animation at speeds from 30 frames per second (1/2 real time after de-interlacing) to a single frame stop motion. We have found that the ability to interact with the animation at various speeds has been one of most important visualization tools. An example of one frame from the composite is given in Figure 3.

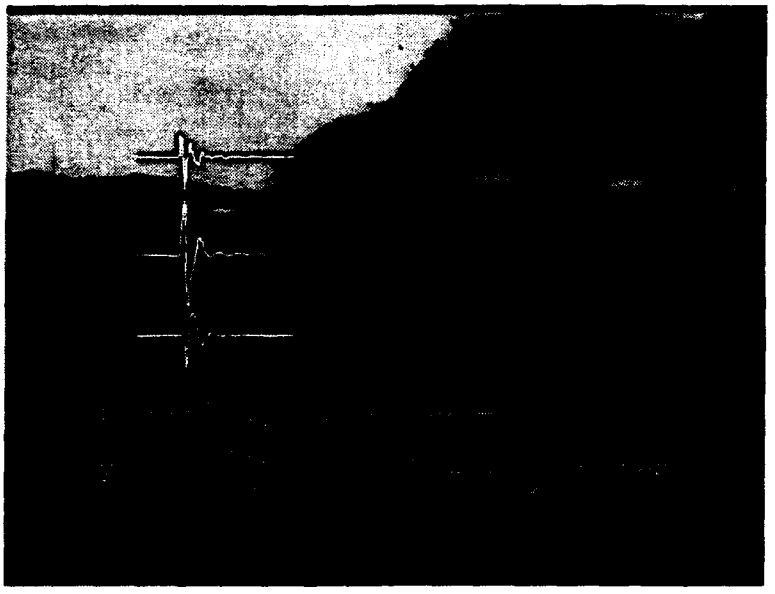


Figure 3: De-interlaced, de-jittered and composited field from the single, cylindrical explosion. The bottom two time series are the recovered camera displacements from the de-jittering process (x-tangential, y-vertical). The top three time series are ground velocities (vertical, top; radial, second; transverse, bottom) derived from a near-by accelerometer. Time denoted in the figure is elapsed time since the detonation of the surface delay.

The vertical bar in Figure 3 denotes the time in the waveforms that correlate with the video field from the explosion. Comparison of the ground motion record with the camera displacements illustrates the under damped pendulum response of the camera tri-pod. The near-source ground motions are completed many msec prior to this video image. The image also illustrates that there are still many dynamic processes taking place in the source region despite the lack of ground motion. Careful review of the animation reveals the importance of the initial shock from the explosive in generating the near-source ground motions. The P wave as it propagates from the initial shock to the camera can be seen as a reflectance change in the near-surface materials. These two observations indicate that for the recorded near-source ground motions that late time explosion phenomena including the material that is cast out into the pit do not contribute to these waveforms.

The same processing scheme was applied to the ripple-fired explosion. In this case, one can identify the non-electric detonating system as it operates, the detonation of the individual charges, the interaction of the motion between the individual charges and the spall of the material. The frame rate of the video is not fast enough to constrain the exact detonation time of all the surface delays. High speed film or video with frame rates as high as 500 frames/s are more appropriate for this task. Figure 4 illustrates one field from the ripple-fired explosion.

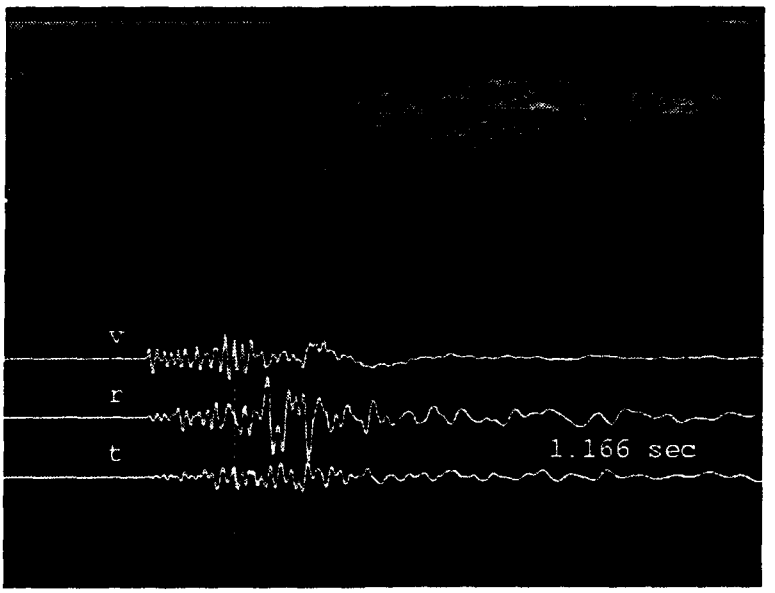


Figure 4: De-interlaced, de-jittered and composited filed from the ripple-fired explosion. The ground velocities and the camera are at a range of approximately 250 m from the explosion.

CONCLUSIONS AND RECOMMENDATIONS: The utility of combining video records and ground motion records from the near-source region of mining explosions has been demonstrated. This tool provides a unique opportunity for investigating the physical properties important in generating seismic waveforms. The simple examples presented in this paper argue that direct shock coupling of energy from the explosion is of primary importance in the generation of near-source waveforms and that the material cast by such explosions is of secondary importance. Analysis of the ripple-fired explosion documents the firing sequence and the cylindrical interaction of the individual charges in the source array. Spall processes quantified by the video occur at late time relative to the near-source motions.

Simple Hi-8 video with its improved resolution provides the starting point for this analysis procedure. The key to the work is the digitization of the video, the de-interlacing, the de-jittering and the animation with the recorded waveforms. A modest priced desk top computer such as a SGI Indigo-2 coupled with a video capture card provides the basis of the analysis system. A read/write laser disk system is needed as well for both the processing steps and the final assembly of the images.

This preliminary study has begun to explore the utilization of different types of data in the interpretation of the seismic source function. Additional work with multiple cameras intended to provide three-dimensional characterization of the source is planned. These images can be used to provide detailed temporal and spatial quantification of material motion in the source region. These same images in combination with sparsely sampled ground motion records can be used to provide some understanding of the two and three dimensional aspects of the seismic wavefield. We intend to explore the utilization of the video images as an interpolating tool between the point ground motion records.

An important key to these visualizations is the linking of temporal and spatial aspects of the problem in a logical way so that the scientists can interpret the important physical processes in the source. *Processed video records of the tests discussed in this paper will be displayed at the meeting for those interested in investigating the temporal and spatial relations in the video and ground motion data sets.*

REFERENCES:

Baumgardt, D. R. and K. A. Ziegler, Spectral evidence for source multiplicity in explosions: Application to regional discrimination of earthquakes and explosions, *Bull. Seismol. Soc. Am., 78,* 1773-1795, 1988.

Chapman, M. C., G. A. Bollinger and M. S. Sobel, Modeling delay-fired explosion spectra at regional distances, *Bull. Seismol. Soc. Am., 82,* 2430-2447, 1992.

Denny, M. D. and J. J. Zucca, Introduction: DOE Non-Proliferation Experiment, *Arms Control and Nonproliferation Technologies, First Quarter 1994,* 8-21.

Hedlin, M. A. H., J. A. Orcutt, J. B. Minster, and H. Gurrola, The time-frequency characteristics of quarry blasts and calibration explosions recorded in Kazakhstan, U.S.S.R., *Geophys. J., 99,* 109-121, 1989.

Hedlin, M. A. H., J. B. Minster and J. A. Orcutt, An automatic means to discriminate between earthquakes and quarry blasts, *Bull. Seismol. Soc. Am., 80,* 2143-2160, 1990.

Reamer, S. K., K.-G. Hinzen and B. W. Stump, Near-source characterization of the seismic wavefield radiated from quarry blasts, *Geophys. J. Int., 110,* 435-450, 1992.

Richards, P. G., D. A. Anderson and D. W. Simpson, A survey of blasting activities in the United States, *Bull. Seismol. Soc. Am., 82,* 1416, 1992.

Smith, A. T., High-frequency seismic observations and models of chemical explosions: Implications for the discrimination of ripple-fired mining blasts, *Bull. Seismol. Soc. Am., 79,* 1089-1110, 1989.

Stump, B. W., F. Rivière-Barbier, I. Chernoby and K. Koch, Monitoring a Test Ban Treaty Presents Scientific Challenges, *EOS, Trans. Am Geophys. U., 75,* 265-273, 1994.

ACKNOWLEDGMENTS: Some support for BWS was made possible by the Department of Energy and the Source Region Program at Los Alamos National Laboratory. John Smith, John Wiggins and R. Frank Chiappetta are thanked for their support in the field. D. Craig Pearson, Meredith Ness and Ben Smith were responsible for the data acquisition.

Effects on Pn, Pg, and Lg Amplitudes of Nuclear Explosion Waveforms Recorded in Southern California

G. Eli Baker[†], Vernon Cormier*, and J. Bernard Minster[†] [†](IGPP, UCSD), *(U Conn.)
AF Contract No. F49620-93-1-0508

Objectives:

The objective of our studies is to better understand what affects regional broadband waveforms. Isolated broadband seismic stations have been running for several years in large areas of the globe from which few seismic data had been available previously. Many of the data are collected for detection and discrimination of nuclear explosions, in which regional crustal phases play a major role. Such data have proved valuable for modeling of sources (e.g. Zhao and Helmberger, 1994), usually assuming one-dimensional structure and, because the data to synthetics misfits increase at higher frequency, using lowpass filtered data. Better understanding of the causes of variability in the waveforms at higher frequency will enhance the resolution and accuracy of results from source, structural, and discrimination studies. Our immediate focus is on understanding the effects of major topographic features on crustal phases.

Research Accomplished:

We have observed distinct and consistent differences between waveforms of Nevada Test Site (NTS) events recorded at 3 southern California broadband stations (figure 1). Differences in amplitude, frequency content, and character of secondary Pn arrivals at PAS vs. PFO suggest variations in upper mantle structure between the paths to the two approximately equidistant stations, and possible variations in near receiver scattering (figure 2). The PmP arrival is seen distinctly at PAS but is absent at LAC and PFO, suggesting variations in the crustal or Moho structure between the NTS-LAC-PFO path and the NTS-PAS path (Baker, et al, 1993). Increasing similarity of Pn waveforms with decreasing interevent spacing indicates a strong effect of near source scattering (figure 3a). Similarity of waveforms with comparable source magnitudes (which correlate very well with depth) indicates the importance of the source itself and of the surface reflection (figure 3b).

We focus on amplitude variations of Pn, Pg, and Lg caused by laterally heterogeneous structure. Lg propagation is of particular interest for its importance in discrimination and yield estimation . The relative amplitudes of Lg to Pg, at regional distances, form the basis for a useful discriminant between nuclear explosions and earthquakes (Taylor, et al, 1989). To help distinguish whether structure is affecting Pg or Lg, we compare both with Pn. For insight into the physics of propagation through laterally varying structures, both synthetic seismogram studies (Clouser, 1993) and direct observation of the effects on waveforms as they propagate through different structures (e.g. Bostock and Kennett, 1990) are useful. Synthetic seismogram studies are limited by the size and speed of computers, and by the approximations made in solving seismic wave propagation problems. Limits to the observational approach are largely due to imprecise knowledge of earth structure and insufficiently dense station spacing. To minimize these limitations, we use records of 10 NTS explosions recorded variously at 215 USGS/Caltech southern California network stations. The stations are more densely spaced than perhaps in any other network covering a comparable

area; they are 250-500 km distant from NTS; and they rest above what is likely the most comprehensively studied crust and upper mantle structure for a region of such extent.

We measured the rms amplitudes of Pn, Pg, and Lg. The largest subset of stations recording useful data for any one event was 114 for the Mb 4.3 explosion, *COSO*, on day 67, 1991. The Pn arrival times were handpicked, and the first 5 seconds of Pn were used. The first 10 seconds of Pg were used, starting with times calculated relative to Pn for a layer over a half space model (Helmberger and Engen, 1980). The Lg window was chosen to fall between group velocities of 2.8 and 3.6 km/sec. All three phases are prominent between 0.6 to 3 Hz, chosen to highlight Lg (Hansen, et al, 1990), and so were bandpass filtered within that range. The rms amplitude is defined as

$$A_{rms} = \sqrt{\frac{1}{M}\sum_{i=m_1}^{m_2} x_i^2 - \frac{1}{N}\sum_{j=n_1}^{n_2} x_j^2}$$

where x_i is the record of the phase of interest, m_1 and m_2 the denote the begin and end samples of the measurement window for the phase, and M is the number of points in that phase. N is the number of points in a pre-event noise window, with n_1 and n_2 denoting the begin and end samples of the noise window (after Zhang and Lay, 1994). The unknown site effect on amplification makes comparison of absolute amplitudes from station to station difficult, so we compare relative amplitudes. Figures 4, 5, and 6 show the geographical variations of Pn/Pg, Pn/Lg, and Pg/Lg amplitude ratios respectively. They are superimposed on a shaded relief image of topography, with the major southern California fault systems outlined. Figure 1 shows the same base map, with place names used in the discussion. The amplitude ratios shown are from the *COSO* explosion. The variations of amplitude ratios are very similar for all the events studied, although the absolute magnitudes of the amplitude ratios vary with the source. The actual values for this particular event vary, presumably coincidentally, from 0.06 to 2.6 for both Pn/Pg and Pn/Lg, and from 0.45 to 2.2 for Pg/Lg. The most obvious changes in amplitude ratios occur across a line delineated by the southern border of the Transverse Ranges and the eastern border of the Peninsular Ranges. The amplitude ratios of Pn/Pg and Pn/Lg increase with distance from NTS beyond this line. Amplitude ratios at stations in the Transverse Ranges and along the San Andreas fault remain relatively small. They continue to increase at sites in and beyond (i.e. away from NTS) the Peninsular Ranges. There is a sharp transition from the largest to much smaller amplitude ratios to the east of the Peninsular Ranges, where the mountains meet the Salton Trough. Pn and Pg recorded at stations from both sides of that boundary are shown in figure 7. The Pg/Lg amplitude ratios show no particular pattern, which may reflect the similar nature both phases, which consist of seismic waves reverberating in the crust.

It is not certain whether the pattern is due to Pg and Lg variations, or Pn variations, or both. Burdick et al (1991) hypothesized a steep gradient in the upper mantle beneath southern California based on the variation in Pn/Pg amplitude ratios observed for a suite of NTS events at 3 broadband stations, assuming this variation is due to a triplication. Conversely, that the pattern seems to vary with major crustal boundaries argues for a crustal cause and so for variation in Pg and Lg. We will accept the hypothesis for the moment that the variation is in the crustal phases, and ask what the cause might be. Scattering laterally or into the mantle from the root of the Transverse Ranges is an obvious hypothesis to consider. We note that no similar effect is seen along raypaths crossing the Sierra Nevada. This observation may bear on a current controversy regarding the existence of a root to the Sierra Nevada (eg. Jones, 1991; Sung and Jackson, 1992). The survival of crustal phases through the Salton Trough, followed by a sudden amplitude drop at stations just within the Pen-

insular Ranges, is suggestive of some effect of the basin-mountain boundary, perhaps of a large lateral velocity contrast. However, raypaths to stations at the southern base of the western Transverse Ranges, and to those across Banning Pass, do not cross any significant sedimentary basins but still have increased amplitude ratios. Further discussion of this in the context of preliminary 3-dimensional modeling with ray tracing is given by Vernon and Baker in this volume.

Conclusions and Recommendations:

The lack of coherent spatial variation of Pg/Lg amplitude ratios, and their somewhat smaller range of values and standard deviation, compared to Pn/Lg amplitude ratios, suggest that much of the path effects on Lg are mimicked by Pg. Thus Pn/Lg is more strongly affected by the path and Pg/Lg is more representative of the source. The latter should therefore be of greater utility for discrimination (eg. Taylor, 1989).

Intended future efforts include the collection of regional seismic data from events further away from but at a similar backazimuth to NTS, which should permit determination of whether the main source of amplitude variations is in Pn, Pg and Lg, or both. We also intend a systematic study of the correlation of amplitude variations with variations in topography and other widely available geophysical quantities (e.g. gravity).

Bibliography:

Baker, G.E., L.J. Burdick, and J.B. Minster, 1993, Regional broadband waveforms: individual station and three component array analysis of nuclear explosion sources crossing a southern California path, Proceedings 15th Annual Seismic Research Symposium, DARPA, PL-TR-93-2160 8-14 ADA271458

Bostock, M.G. and B.L.N. Kennett, 1991, The effect of 3-dimensional structure on Lg propagation patterns, *Geophys. J. Intl.*, **101**, 355-365

Burdick, L.J., C.K. Saikia, and N.F. Smith, 1991, *Explosion Source Phenomenology*, Geophys. Monog. **65**, Am. Geophys. Un., 197-209

Clouser, R.H., 1993, *Scattering of seismic waves by irregular surfaces*, Ph.D. Thesis, Penn. State Univ.

Hansen, R.A., F. Ringdal, and P.G. Richards, 1990, The stability of RMS Lg measurements and their potential for accurate estimation of the yields of Soviet underground nuclear explosions, *Bull. Seismol. Soc. Am.*, **80**, 2106-2126

Helmberger, D.V. and G.R. Engen, 1980, Modeling the long-period body waves from shallow earthquakes at regional ranges, *Bull. Seismol. Soc. Am.*, **70**, 1699-1714

Jones, C.H., 1991, Isostasy and the southern Sierra Nevada: seismic constraints, *Seismol. Res. Lett.*, **60**, 45

Sung, L., and D. Jackson, 1992, Crust and uppermost mantle structure under southern California, *Bull. Seismol. Soc. Am.*, **82**, 934-961

Taylor, S.R., M.D. Denny, E.S. Vergino, and R.E. Glaser, 1989, Regional discrimination between NTS explosions and western United States earthquakes, *Bull. Seismol. Soc. Am.*, **79**, 1142-1176

Zhang, T. and T. Lay, 1994, Analyses of short-period phase path effects associated with topography in Eurasia, Bull. Seismol. Soc. Am., **84**, 119-132

Zhao, L. and D.V. Helmberger, 1994, Source estimation from broadband regional seismograms, *Bull. Seismol. Soc. Am.*, **84**, 91-104

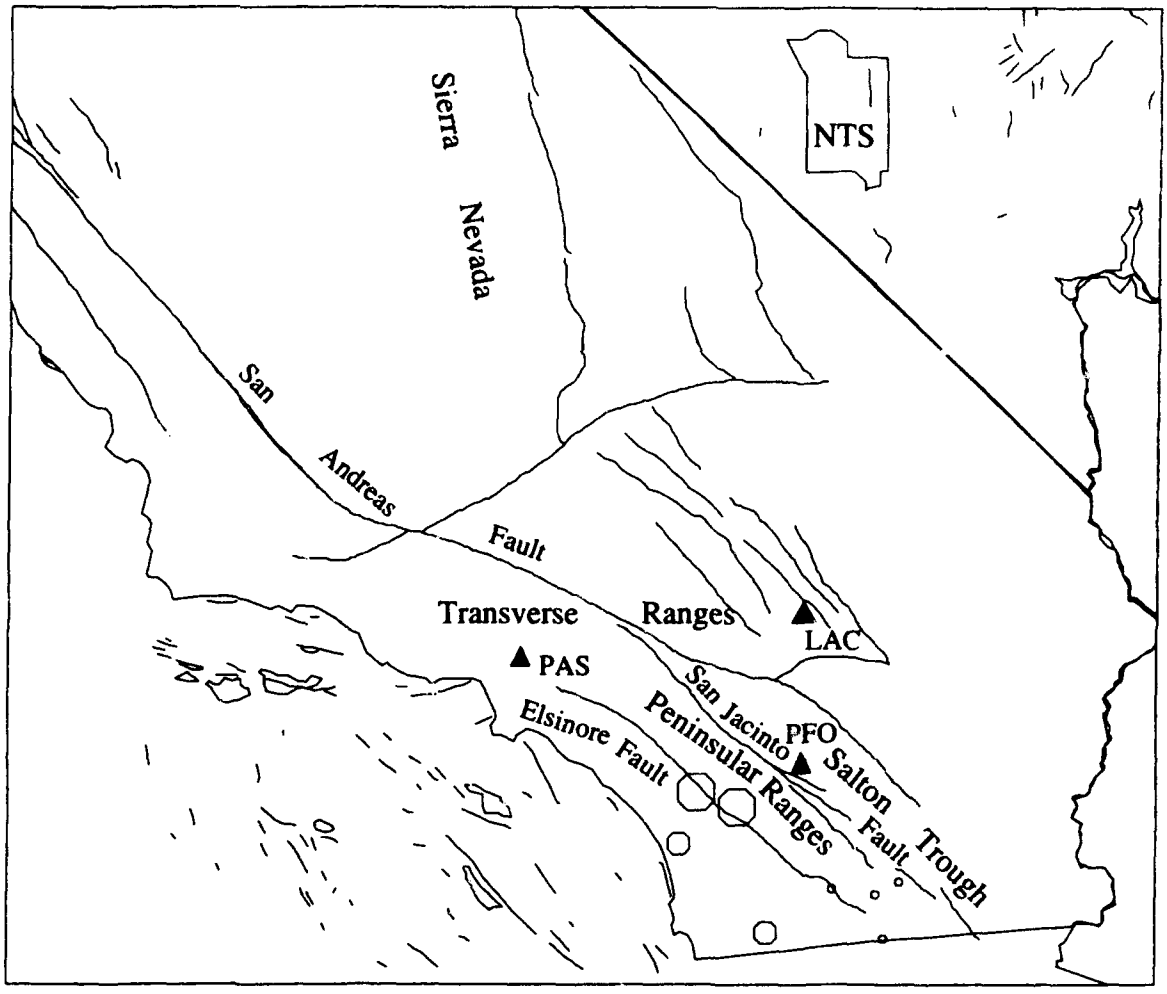


Figure 1: Southern California map, with place names discussed in text. Triangles indicate the 3 broadband stations. The 4 large and 4 small octagons indicate the station positions of the high and low Pn/Pg amplitude ratio records shown in figure 7.

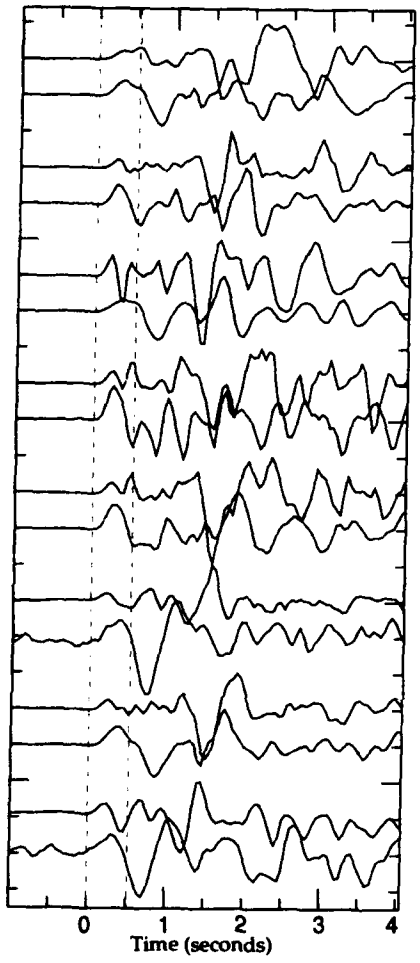


Figure 2: Pn of NTS events recorded at PFO (upper trace of each pair) and PAS (lowertrace of each pair). Dotted lines indicate firsthalf second, which is typically half a cycle at PAS, but approximately one and a half cycles at PFO.

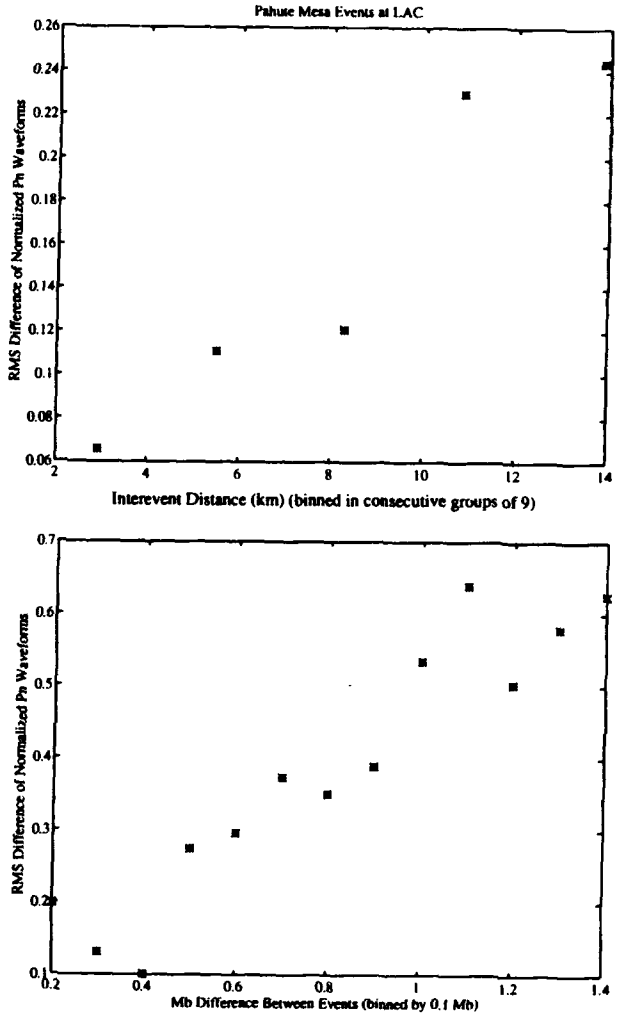


Figure 3: a) (top) RMS differences between normalized Pn waveforms of Pahute Mesa event pairs, recorded at LAC, binned in consecutive groups of nine event pairs, versus interevent distance. b) (bottom) RMS differences versus Mb with one event from Pahute Mesa and one from Yucca Flat.

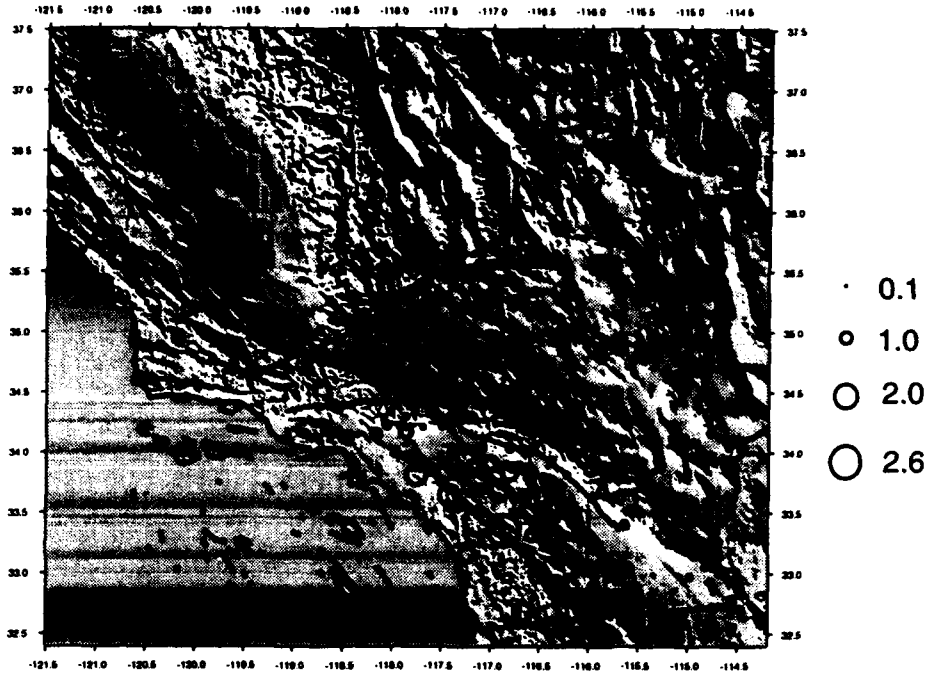


Figure 4: Pn to Pg amplitude ratios for the Nts event Coso, plotted over shaded relief image of southern California at the recording stations' positions. Circle sizes correspond to magnitude of the ratios.

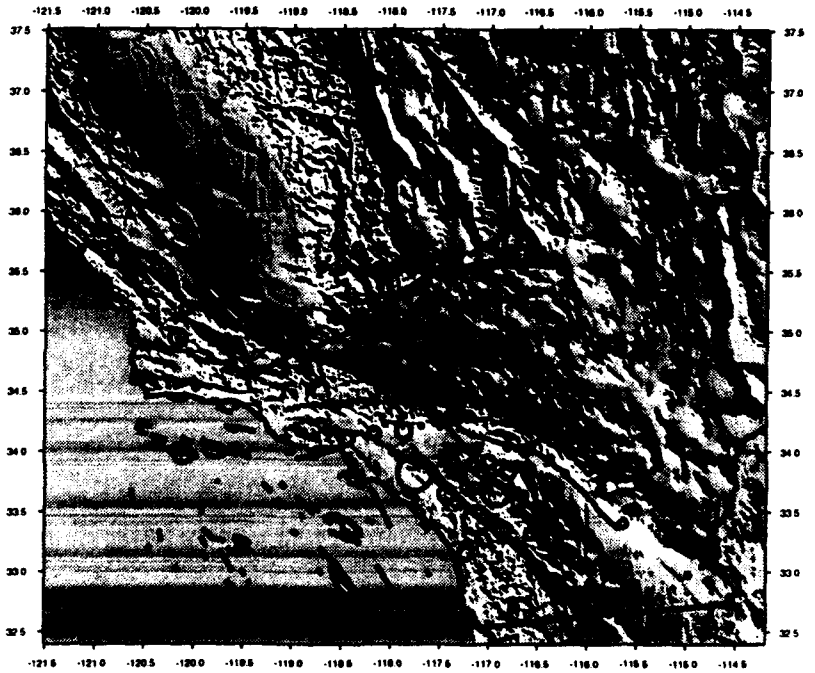


Figure 5: Same as above for Pn to Lg amplitude ratios.

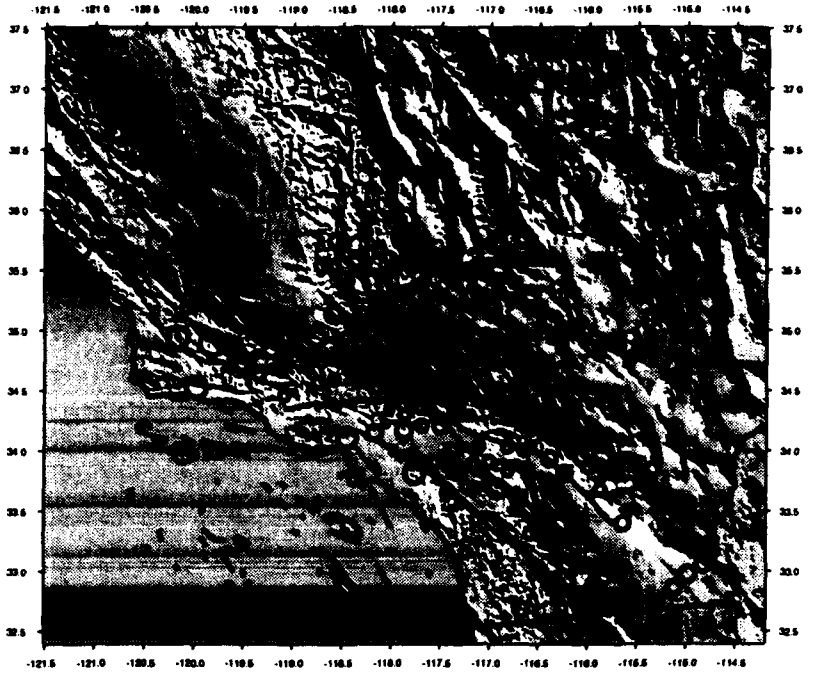


Figure 6: Same as figure 4, but for Pg-to-Lg amplitude ratios.

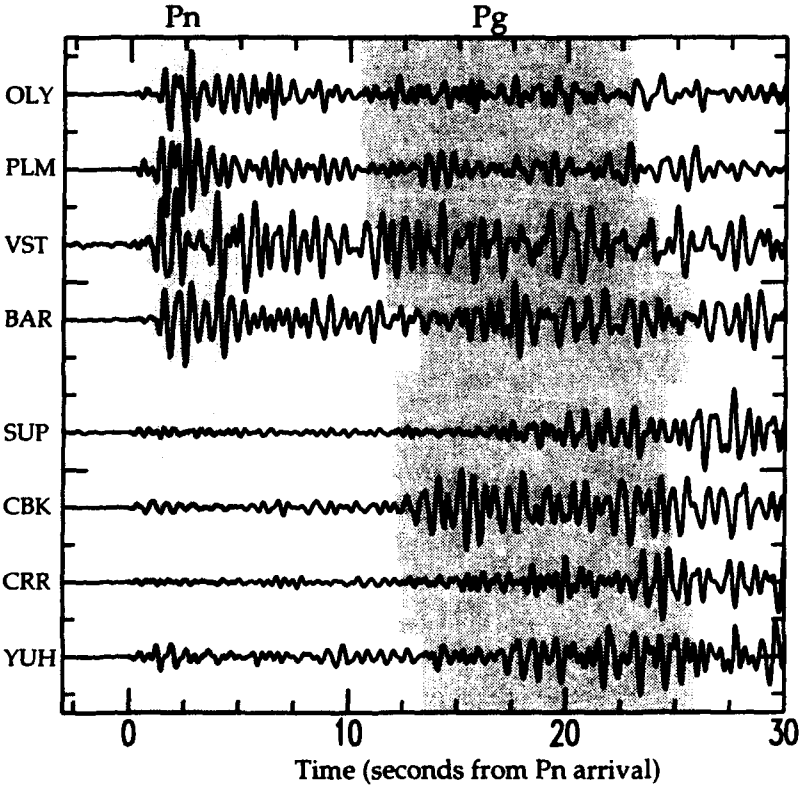


Figure 7: Pn (light gray) and Pg (darker gray) phases recorded at stations on either side of the Peninsular Ranges (top 4 traces)-Salton Trough (last 4 traces) boundary. Station locations indicated in figure 1.

Network Identification Capability Evaluation (NICE) of Regional Networks

T. G. Barker, K. L. McLaughlin and J. L. Stevens

Maxwell S-CUBED Division
P.O. Box 1620
La Jolla, CA 92038-1620

Contract No: F19628-93-C-0177

Objective

The objective of this program is to develop an interactive computer system capable of evaluating the factors affecting the identification performance of a network recording events at regional distances.

Research Accomplished

The computer program NICE, for Network Identification Capability Evaluation, was written to assess the ability of a seismic network to discriminate earthquakes from explosions. In this report on the progress during the first phase of a two-year project, we describe enhancements to the program which allow assessment of regional networks and discriminants in addition to the original capabilities to assess teleseismic networks. The enhanced program, called XNICE (with an X windows interface) simulates the detection, location and identification of a suite of events using a Monte Carlo approach. This approach allows one to isolate the effects of source type, propagation path, and choice of discriminants on the discrimination process. In addition, discriminant performance and network thresholds of detection, location and identification are assessed. XNICE generates the parameters of a sequence of events and computes the ground motions from the events at the stations of the network. The features of the ground motions used for discrimination are then measured, and discrimination scores are assigned to each event. From a suite of events, the performance of the network and the discriminants can be assessed. The program has the capability to compute signals from earthquakes, quarry blasts and both overburied and normally buried explosions.

The models of regional phases (*Pn, Pg, Lg, Sn* and *Rg*) include the effects of non-linear processes, in particular, spall. We use kinematic models of spall to incorporate the effects of mass movements associated with nuclear explosions and quarry blast charges. These spall movements change the source spectra, generally causing the measured slope above 1 Hz to increase. We use models of source spectra and the relative excitation of the sources to account for the differences in regional phase excitation for the various source types. We apply discriminants based on the spectral slopes from 1 Hz to 10 Hz of *Lg*, *Pg* and *Lg/Pg* to the events generated by XNICE. The models predict that spectral slopes for *Lg*, *Pg* and *Lg/Pg* are least for earthquakes, are greater for normally buried explosions and are greatest for quarry blasts. Spectral slopes of *Lg* are closer to earthquakes for overburied bombs, and can be indistinguishable at low magnitudes. Spectral slopes are higher for normally buried bombs than for earthquakes due to the slope of (1) the spall source spectrum and (2) of the excitation spectrum of shallow explosions relative to mid-crustal earthquakes. Quarry blast spectral slopes are largest due to the effects of spall and of extended source duration. These results are all consistent with numerous observations. Furthermore, we find that the population of spectral slopes of normally buried explosions separate from earthquakes more for an eastern U.S. earth structure than for a western structure. We also show that network detection levels strongly influence these results.

In addition, the X windows interface which has been installed is much easier to use than the question-and-answer format of the original program. In the following, we describe the architecture of the program, the means for doing regional analyses, and applications using an eastern U.S. earth structure.

XNICE

XNICE is comprised of four modules. The user communicates with the modules through the X interface, which also coordinates the modules. A flow chart of the system is shown in Figure 1. The modular design allows one to examine independently the effects of the seismic source, the wave propagation, the seismic network operation (location and detection) and discrimination rules on

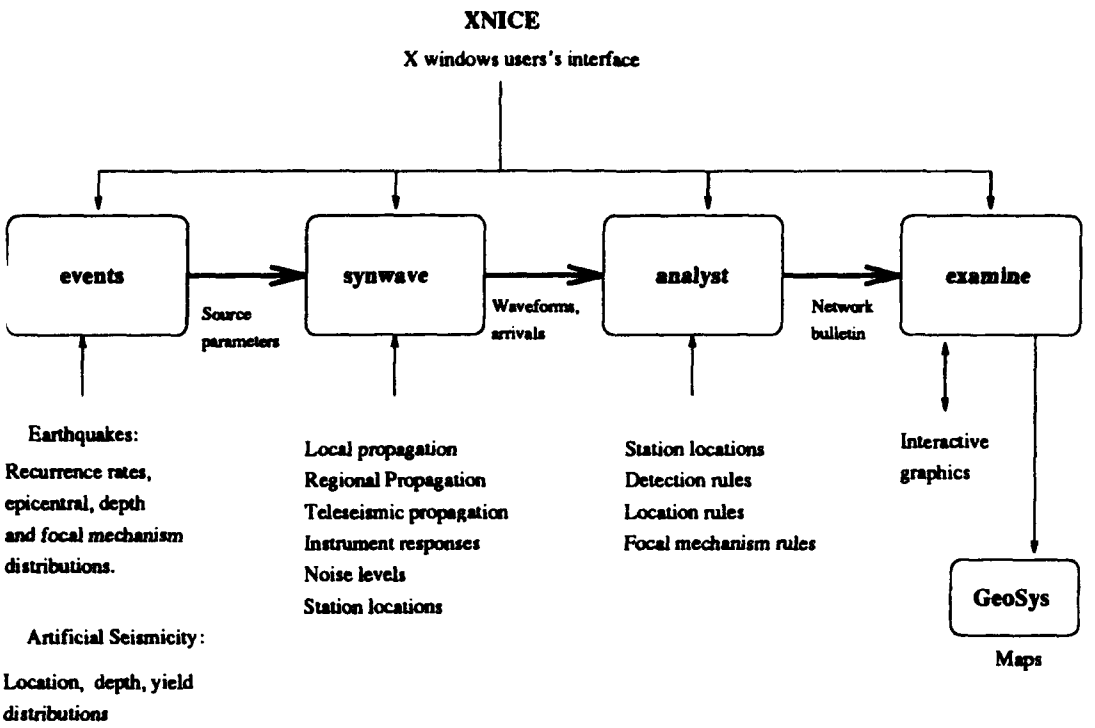


Figure 1. Flow chart of the XNICE system. The four major modules are controlled by the X windows interface. Graphic output can be supplied to GeoSys to make Graphics Information System (GIS) displays.

identification of events. The parameters of each module can be verified by direct comparison with observations. XNICE plots allow the user to examine a realization of the seismic events and details of the discrimination results. In addition, a link to the S-CUBED data visualization package GeoSys provides map drawings with contours and physical feature overlays.

Regional Propagation Modeling

A number of authors have derived empirical or heuristic expressions of regional phase propagation (see, for example, Goncz, *et. al.*, 1986 or Nuttli, 1975). We use a form, modified from Campillo, *et. al.* (1985), which includes the effects of propagation and source excitation explicitly. The observed signal amplitude (peak narrow-bandpass or spectrally averaged amplitude) at range Δ and frequency f has the form:

$$A(f,\Delta) = \Omega(f)\,\hat{G}(\Delta,f),\ \hat{G}(f,\Delta) = E(f)\,P(\Delta,f),$$

where $\Omega(f)$ is the source spectrum. The function $\hat{G}(f,\Delta)$ is an effective Green's function comprised of $E(f)$, the source excitation spectrum and a propagation term, specified by

$$log(P(\Delta,f)) = -n\,log(\Delta/\Delta_0) + log(e)\gamma(f)(\Delta - \Delta_0) + \varepsilon\ ,$$

where Δ_0 is a reference distance, $\gamma(f)$ is the anelastic attenuation parameter, n is a factor for geometric spreading (typically n = 5/6), and ε incorporates random effects of local station response and noise. The source excitation spectrum $E(f)$ depends on source type (earthquake, explosion, etc.) and source depth. The source excitation spectra are calibrated from calculations of synthetic seismograms or from observations of signals from different sources along common paths. The basic assumption underlying this approach in XNICE is that differences in spectral slopes for different types of sources and waves (Lg, Pg) are caused by differences in source $\Omega(f)$ and excitation $E(f)$.

Source Spectra

XNICE computes signals from four source types: earthquakes, quarry blasts, and both overburied and normally buried explosions. Earthquake source spectra are compuated using the formulation by Brune (1970). The equations given by Mueller and Murphy (1971) are used for nuclear explosion spectra. Like earthquakes, the spectra are flat at low frequencies and decrease as f^{-2} at high frequencies. We add to normally buried explosions a spall contribution which adds power near 1 Hz.

We model quarry blasts as the superposition of rows of charges fired in sequence, a well established paradigm. Following the modeling studies by Barker, *et. al.*, (1993), each charge consists of an explosion with an accompanying spall, which moves material from its original location. The source spectrum for each individual charge has an explosive part whose corner frequency is much higher than the frequencies of interest here, while the spall component peaks in the bandwidth of interest. The firing pattern spectrum F(ω) is flat at low frequencies and rolls off as f^{-1} above a corner frequency equal to the inverse of the total duration of the blast, which for larger blasts will be around 1 Hz or less. Barker, *et. al.* (1993) show that synthetic regional signals from the explosive and spall components are comparable.

Source Excitation Spectra

Ideally, one would find the source excitation spectra for each source type by recording signals from the different types along common propagation paths. This is possible in many areas for quarry blasts and earthquakes, although in many areas it is not. Of course, the number of nuclear test sites is small. When these recordings are available, $E(f)$, or $\Omega(f)E(f)$ can be inferred using analyses such as in Campillo (1985). Otherwise, we must rely on synthetic seismogram calculations.

We used synthetic seismograms to compute $E(f)$ for explosion, double-couple and point-force at the required depths. We recognize that the current technology for computing synthetic seismograms is limited to plane-layered models which do not completely represent the observed wavefields. We assume, however, that spectral differences in regional wavefields due to different sources can be predicted by the 1D synthetic calculations. The approach is to use relations derived from earthquake observations as a basis for calculating ground motions and rely on comparisons with synthetics to calculate motions from other sources with respect to earthquakes.Studies by Campillo, *et. al.* (1984) and by the authors of this report show that excitation of regional signals is nearly constant for sources within three depth regions: the very shallow crust, the mid-crust, and the lower crust. Most earthquakes have their hypocenters in the mid-crust while man-made sources will be in the upper crust. With this in mind, we write for the excitation functions for bombs and quarry blasts:

$$A_{src}(f,\Delta,z_{sc}) = \frac{E_{src}(f,z_{sc})}{E_{eqk}(f,z_{mc})} E_{eqk}(f_0)\Omega_{src}\, P_{obs}(\Delta,f) \ .$$

Where the subscripts *sc* and *mc* indicate that the source is in shallow crust and mid-crust, respectively. In practice, the spectral ratio is found from quotients of smoothed spectra computed by a wavenumber integration program.

Tests with an Eastern U.S. Structure

We have made initial tests of the XNICE regional capabilities using an eastern U.S. structure. In Figure 2, the normalized excitation functions are shown for this structure. We see that the *Lg* explosion and vertical force excitation decreases with frequency relative to the mid-crustal earthquake, with the vertical force having a steeper slope. For *Pg*, only the relative vertical force excitation decreases with frequency. We note that the *Lg* explosion and earthquake excitation functions differ by only 0.28 magnitude units at 1 Hz (for constant moment rate). Previous *Lg* excitation studies (Swanger, *et. al.*, 1982; Bennett, *et. al.*, 1987; McLaughlin, *et. al.*, 1988) have found that there is little difference in *Lg* peak excitation between shallow explosion and deeper earthquake excitation. Since the peak is near 1 Hz, the results in Figure 2 are not inconsistent with their findings.

Spectral slope discriminants have been tested in several areas using the slopes of *Lg* and *P* (*Pg* or *Pn*) spectra or equivalently the ratios of amplitudes at low frequencies to amplitudes at high frequencies. These studies all show that *Lg* and *Pg* spectra from earthquakes are richer in higher frequency energy than explosions. Quarry blasts also have been shown to have steeper spectral slopes than earthquakes (Bennett, *et. al.*, 1989).

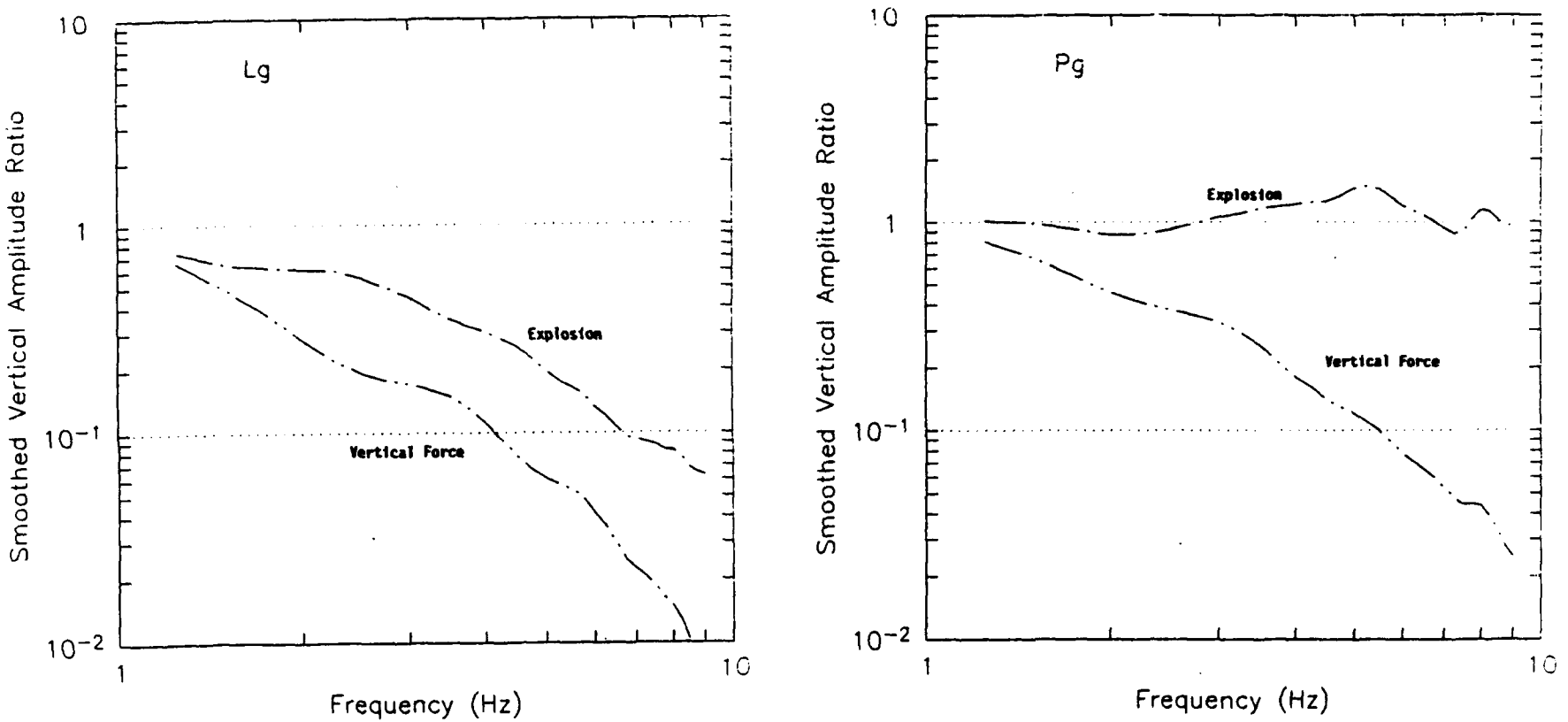


Figure 2. Normalized *Lg* and *Pg* excitation functions are shown for the eastern U.S. structure. Explosion and vertical force excitation are referenced to mid-crustal double-couple.

For an eastern U.S. structure, we show in Figure 3 a plot of the ratio of *Lg* spectral amplitude in the band from 1 to 2 Hz to the spectral amplitude in the 6 to 8 Hz band at stations on a uniform grid (this was done to isolate the effects of source and propagation from the effects of network geometry and location uncertainties). The events are located near the center of a square grid which is 5 degrees on a side. The ratios are plotted against $m_b(Lg)$. In this figure, the earthquake stress drop is held fixed at 100 bars to make the comparisons between source types more apparent. As can be seen in the figure (taken from the XNICE interface), the earthquakes have the lowest ratios (or the shallowest slopes). The quarry blasts have the highest *Lg* spectral ratios (steepest slopes). For lower magnitudes, the overburied bombs have ratios near those of earthquakes, but the ratios are larger for higher magnitudes. Normally buried bombs have higher ratios than earthquakes. The scatter in the normally buried bombs is due primarily to interference between the spall and explosive components at high frequencies, while the scatter in the quarry blasts is due to scalloping from the firing pattern and to low signal levels at high frequencies.

The causes of the different slopes can be seen in Figure 4, which shows spectra of the products of the *Lg* excitation and source functions $E(f)\Omega(f)$ for representative sources in the 1 to 10 Hz band. The spectra have been normalized to the values at 1 Hz. The earthquake spectra, for magnitude 2.5 and 3.5 events, show the effect of decreasing corner frequency with source size. The overburied bomb has a steeper slope primarily because the explosion excitation slope relative to the earthquakes is greater (Figure 2). The normally buried bomb source spectrum is peaked near 1 Hz due to the spall contribution, which causes the spectral ratio to be higher for the normally buried bomb than for the overburied bomb. The quarry blast spectrum is steepest due to both the source and excitation functions. Both the shallow crust excitation functions for the explosive and spall contributions to the quarry blast decay faster than the mid-crust earthquake. The finite duration of the quarry blast (in this case, 2.6 seconds) modulates the spectrum by a sinc function that decays as f^{-1} above about 0.4 Hz.

Figure 5 shows *Lg* spectral ratios for a larger set of events but recorded at a simulated network of 30 U.S. National Seismograph Network (USNSN) sites. The events are located near the center of the array at 37° N by 90° W (western Tennessee). At this time, we do not have noise data for many USNSN stations and no bulletins are yet available. Thus, we used a default value of 5 nm RMS ground noise at each site. The relative random variation from propagation is set at 0.2 magnitude units. We note that 295 out of the 440 events in the realization are plotted. The remainder were rejected primarily because the signal-to-noise levels in the high frequency measurement were less than 2, even though the signal levels at low frequencies were sufficient to make a magnitude measurement. Quarry blasts are not on the plot because the spectra fall off rapidly and the values at higher frequencies are below the specified signal-to-noise ratio of 2. Smaller overburied explosions do not appear on the plot because the higher frequency signals are in the noise, thus reducing the success rate of the discriminant. Referring to the spectral slope values on the figures, we see that the level for detecting and measuring earthquake spectral slopes is around 0.2 magnitude units more than the threshold for making a magnitude measurement. Since the spectral slope of the artificial sources is higher than for earthquakes, the threshold for measuring the spectral slope is even higher for these sources, about 1 magnitude unit.

Our results qualitatively support the use of *Lg* and *Lg/Pg* spectral ratios as a regional discriminant, but demonstrate the sensitivity of this discriminant to network detection thresholds.

Conclusions and Recommendations

This report describes the XNICE program, focusing on enhancements for regional discrimination of earthquakes from several artificial sources. We present a model for simulating the spectral slope discriminants, and test it using earth models for the eastern and western U.S. The model explicitly includes the effects of source spectrum and excitation on observed spectral amplitudes. For these tests, we calibrated the source excitation functions using spectral ratios of synthetic Green's functions. For populations of earthquakes, normally buried and overburied explosions and quarry blasts, we find that the relative values of spectral slopes (ratios of high to low frequency amplitudes) are consistent with observations of those source types at regional distances. We recognize that these results depend strongly on the relative slopes of the source spectra and excitation functions, which in turn depend on the earth structure. It is therefore important to test the model in different areas where there have been earth structure and discrimination studies, in particular, Europe. This will be a subject of research in the second year of this project.

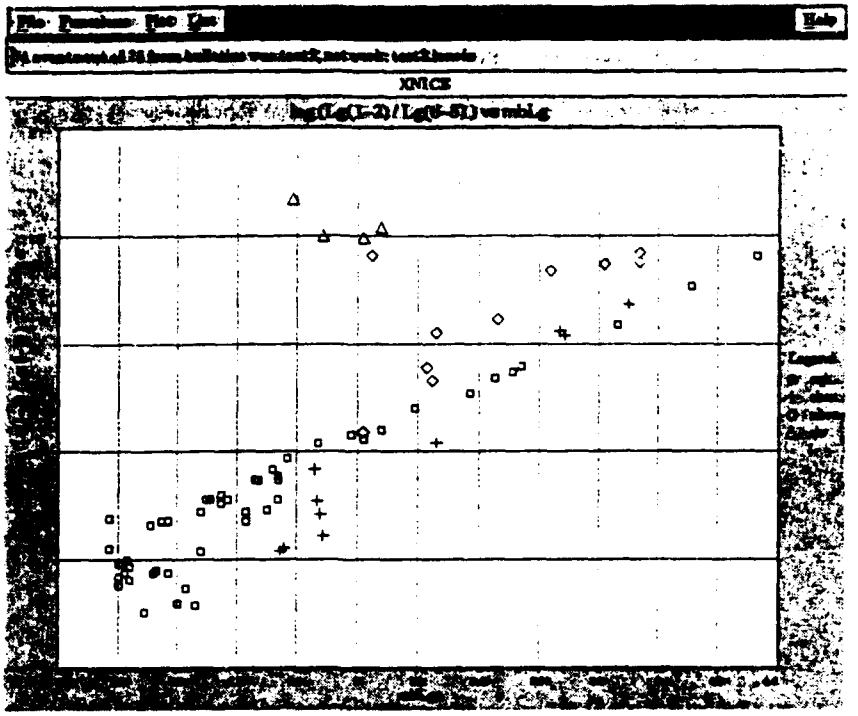


Figure 3. Plot of the ratio of *Lg* spectral amplitude in the band from 1 to 2 Hz to the spectral amplitude in the 6 to 8 Hz band averaged over stations on a uniform grid, for the eastern U.S. structure.

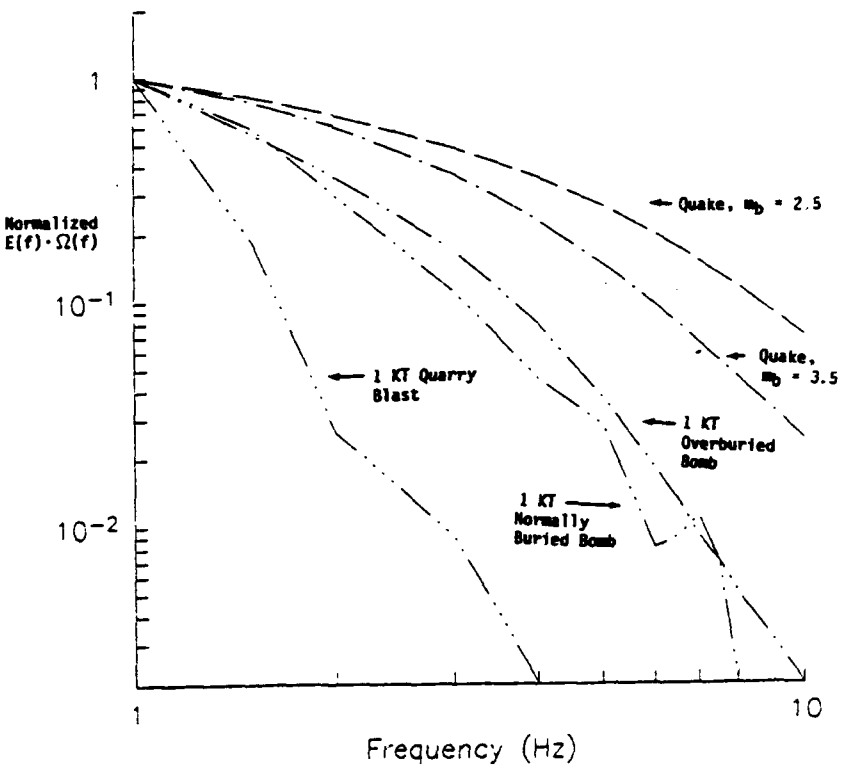


Figure 4. Spectra of the products of the *Lg* excitation and source functions $E(f)\ \Omega(f)$ for representative sources in the 1 to 10 Hz band. The spectra have been normalized to unity at 1 Hz. Note that the quarry blast spectrum has the steepest slopes and the earthquakes have the shallowest slopes.

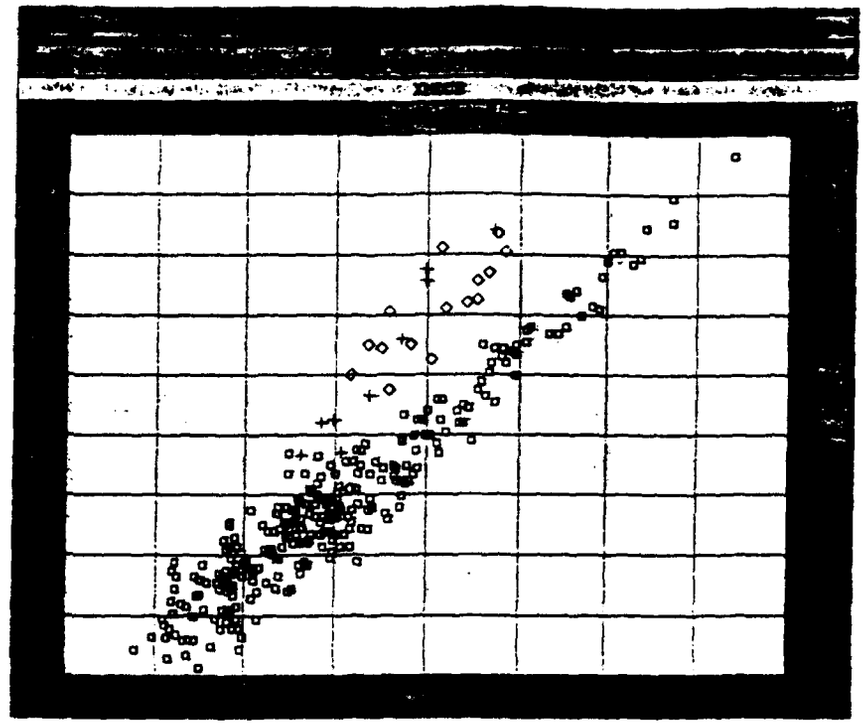


Figure 5. Plot of the ratio of *Lg* spectral amplitude in the band from 1 to 2 Hz to the spectral amplitude in the 6 to 8 Hz band averaged over stations in the USNSN with noise equal to 10 nm, for the eastern U.S. structure. The random propagation variation is 0.2 magnitude units.

We have completed most of the programming to test three other proposed regional discriminants : (1) *Rg* spectral slopes, (2) *Rg* to *Lg* ratios, and (3) M_0:m_b. These will be fully implemented in the first and second quarter of the second year.

Another enhancement which we will soon test is the effects of arrays on network performance. The focus will be on improvements in event location using azimuth and slowness information from array(s) and on the effects of improved detection levels due to the array(s). When these improvements have tested, we will apply the system to likely scenarios in the Middle East.

References

Barker, T.G., K.L. McLaughlin and J. L. Stevens (1993), "Numerical Simulation of Quarry Blast Sources," S-CUBED Technical Report to Air Force Geophysical Laboratory SSS-TR-93-13859.

Bennett, T. J., B. W. Barker and K.L. McLaughlin and J. R. Murphy (1989), S-CUBED Final Report to Air Force Geophysical Laboratory GL-TR-89-0114. ; ADA223148

Campillo, M., M. Bouchon and B. Massinon (1984), "Theoretical Study of the Excitation, Spectral Characteristics and Geometrical Attenuation of Regional Phases," *Bull. Seism. Soc. Am., 74(1)*, pp. 179-90.

McLaughlin, K. L., T. G. Barker, S. M. Day, B. Shkoller and J. L. Stevens (1988), "Effects of Depth of Burial and Tectonic Strain Release on Regional and Teleseismic Waveforms," S-CUBED Scientific Report to Air Force Geophysics Laboratory, SSS-R-88-9844. AFGL-TR-88-0314, ADA207541

Murphy, J. R. and T. J. Bennett (1982), "A Discrimination Analysis of Short-Period Regional Seismic Data Recorded at Tonto Forest Observatory," *Bull. Seism. Soc. Am., 72(4)*, pp. 1351-1366.

Patton, H. J. and S. R. Taylor (1993), "Analysis of *Lg* Spectral Ratios from NTS Explosions: Implications for the Source Mechanisms of Spall and the Generation of *Lg* Waves," submitted to *Bull. Seism. Soc. Am.*

Stump, B. W. and R. E. Reinke (1988), "Experimental Confirmation of Superposition from Small-Scale Explosions," *Bull. Seism. Soc. Am., 78*, pp. 1059-1073

Performance and Portability of Regional Seismic Waveform Discriminants in Different Tectonic Regions

Douglas R. Baumgardt
Zoltan Der

ENSCO, Inc., 5400 Port Royal Road
Springfield, Virginia 22151
Contract No. F19628-93-C-0103

OBJECTIVES

This paper reports on the progress of a project concerned with porting discriminants from known geographic regions, such as Scandinavia and the U.S., to other regions of the world, like the Middle East. A seismic discrimination research system, called the Intelligent Seismic Event Identification System or ISEIS, developed under an earlier project (Baumgardt et al, 1991) has been used to process events to extract discrimination waveform features and to view the processing results. Our goals are to examine the variabilities of performance of waveform discriminants for identifying nuclear explosions, chemical explosions, and earthquakes; to determine the possible causes of these variabilities; and to study effects of propagation path which will affect the porting of discriminants to other regions of the world.

RESEARCH ACCOMPLISHED

Many previous studies have demonstrated that the *Pn/Lg* amplitude ratio can be applied as a discriminant between mining explosion and earthquakes (Baumgardt and Young, 1990) and nuclear explosions and earthquakes (Bennett et al., 1989). However, Baumgardt (1990) showed the effects of propagation path blockage on observed *Lg* amplitudes recorded at large distances. Corrections need to be made for these effects when attempting to distinguish explosions and earthquakes which occur at different distances and different path geologies.

In our initial investigation, we have investigated the feasibility of porting the *Pn/Lg* discriminant determined in previous study (Baumgardt, 1993) for seismic arrays in Scandinavia to a new region, central Eurasia. We have reanalyzed some of the nuclear explosion and earthquake data, recorded at the CDSN station WMQ, originally studied by Bennett et al. (1989), along with some additional events, notably, the 1988 Lop Nor nuclear explosion in China. In our study, we have carefully analyzed all regional phase amplitude ratios and the variability of propagation paths from the regions to WMQ, shown on the shaded topographic map of the region on the right of Figure 1, and the possible effects of propagation path on the discriminant. Figure 1 left shows the locations of the earthquakes, plotted as square symbols, and the nuclear explosions, plotted as circle symbols. We have subdivided the study area into 7 regions, Mongolia, Lop Nor, Tien Shan (earthquakes near Lop Nor) , W Tien Shan, NE Tibet and NW Tibet.

For WMQ, *Pn/Lg* ratios measurements were made with the ISEIS system on both the midband (bz) and high frequency (sz) vertical-component channels, with sampling rates of 20 and 40 Hz, respectively. Figure 2 shows the discriminant in the 6-8 Hz band, measured on the bz channels, plotted versus the regions defined above. The CURRENT EVENT indicates the measurement for the September 29, 1988 Lop Nor explosion, whose events parameters are shown in the upper right of the diagram. The box at the bottom right of the figure shows the distances of the different regions from the Lop Nor region. The Lop Nor explosion and the Balapan explosions have about the same *Pn/Lg* but these two

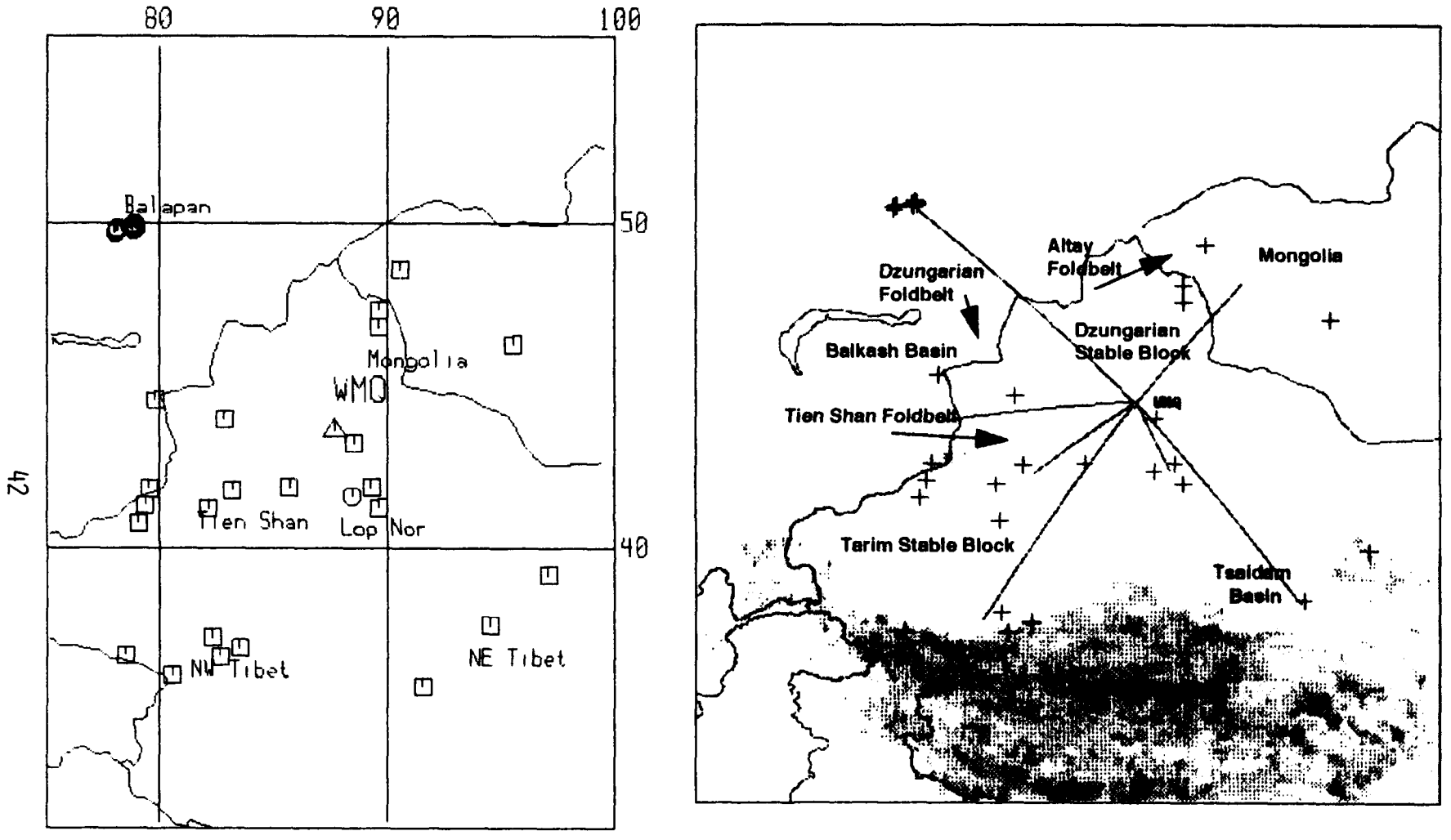


Figure 1: Maps showing locations of earthquakes and nuclear explosions recorded at the CDSN station, WMQ. Earthquakes are plotted on the left as squares and explosions as circles. Shaded topography and the source receiver paths as shown on the right. Tectonic features from Terman and Woo (1967).

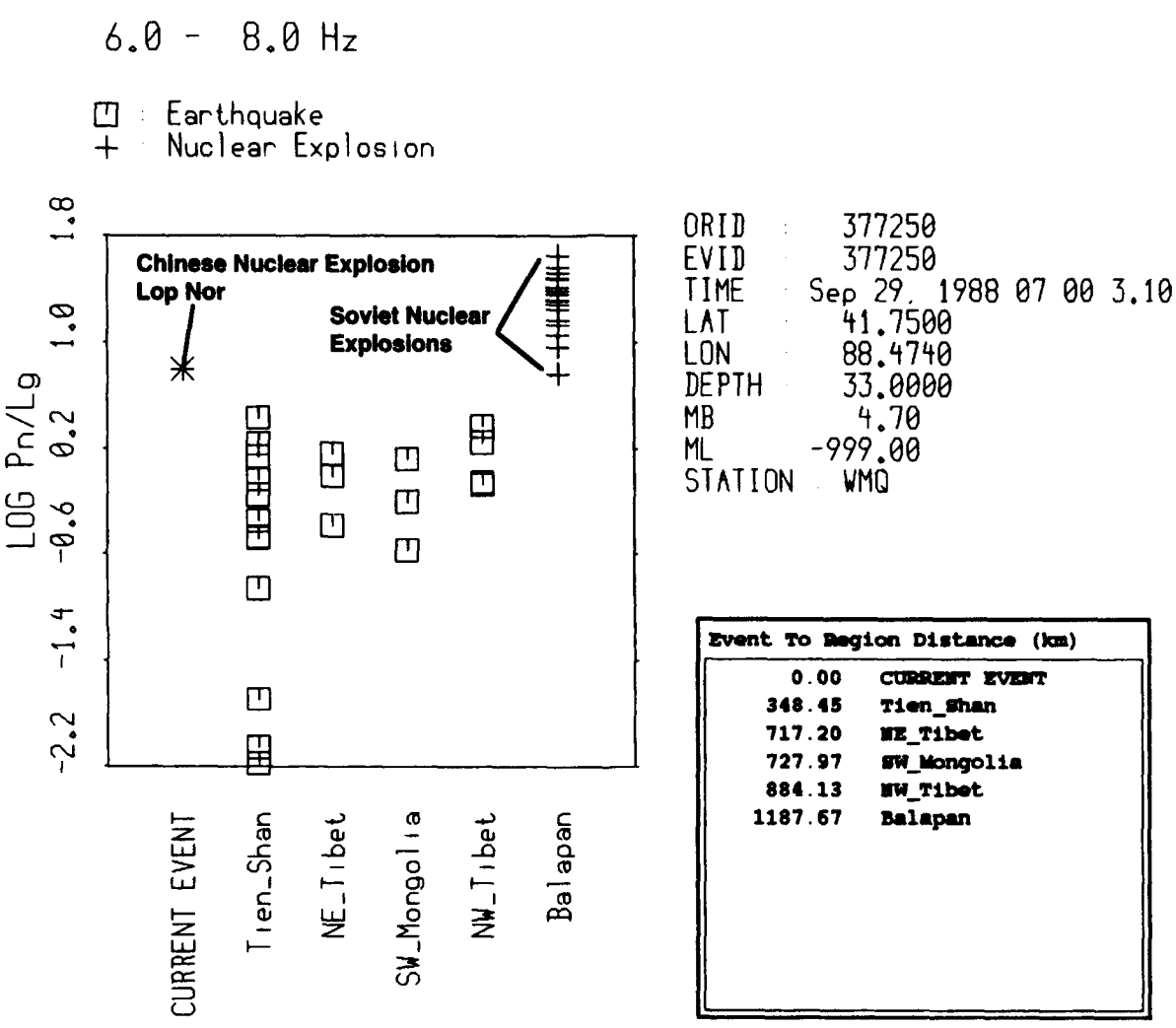


Figure 2: Scatter plot comparison of the Pn/Lg ratios in the 6-8 Hz band, recorded at WMQ, for the Lop Nor nuclear explosion compared with nearby earthquakes and Soviet nuclear explosions at the Balapan test site.

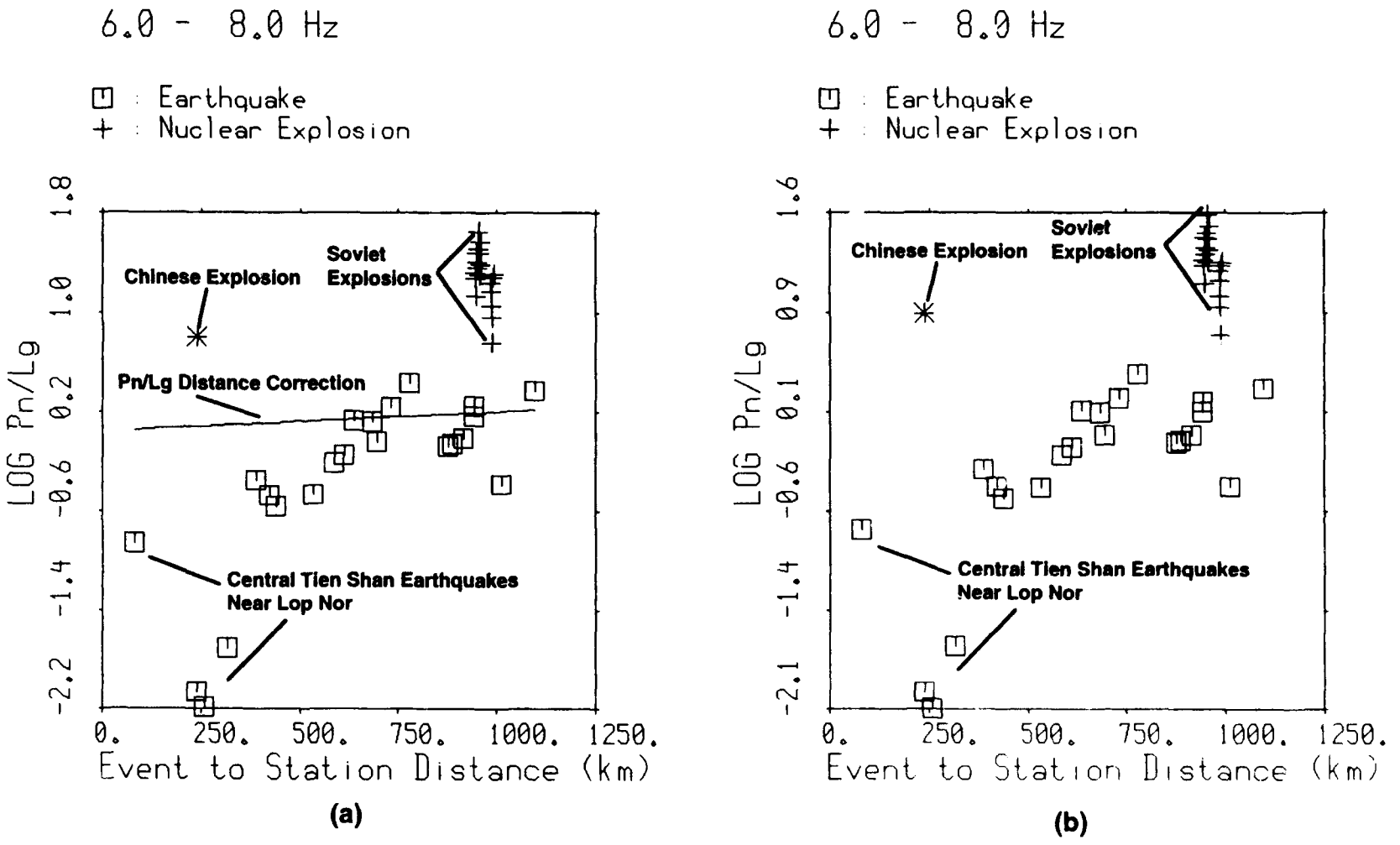


Figure 3: (a) Scatter plot of Pn/Lg ratios versus distance with distance correction curve shown. (b) Scatter plot corrected for distance.

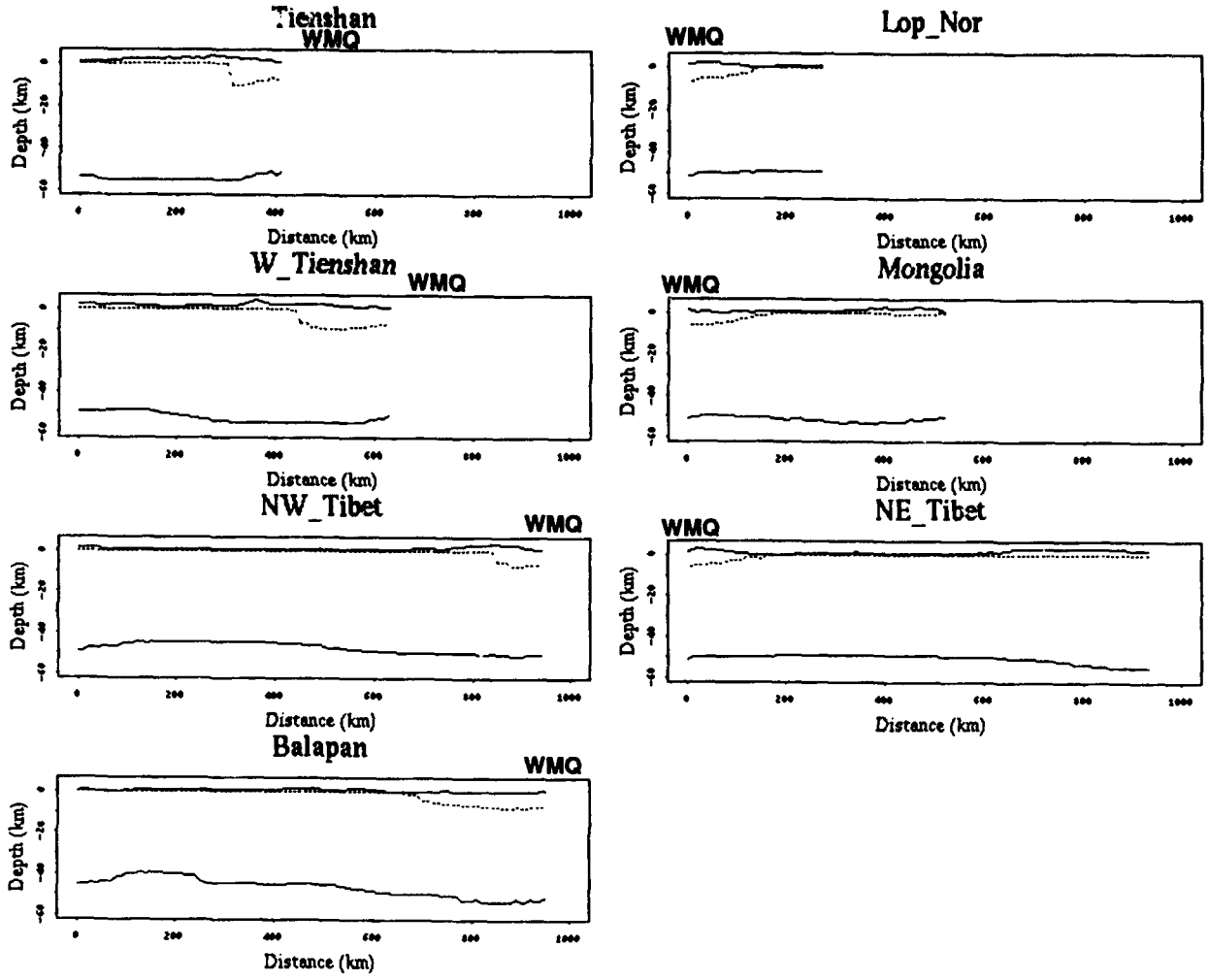


Figure 4: Crustal cross sections for the 7 regions to WMQ shown in Figure 1. Cross sections are plotted from west to east as left and right and the positions of WMQ are labelled.

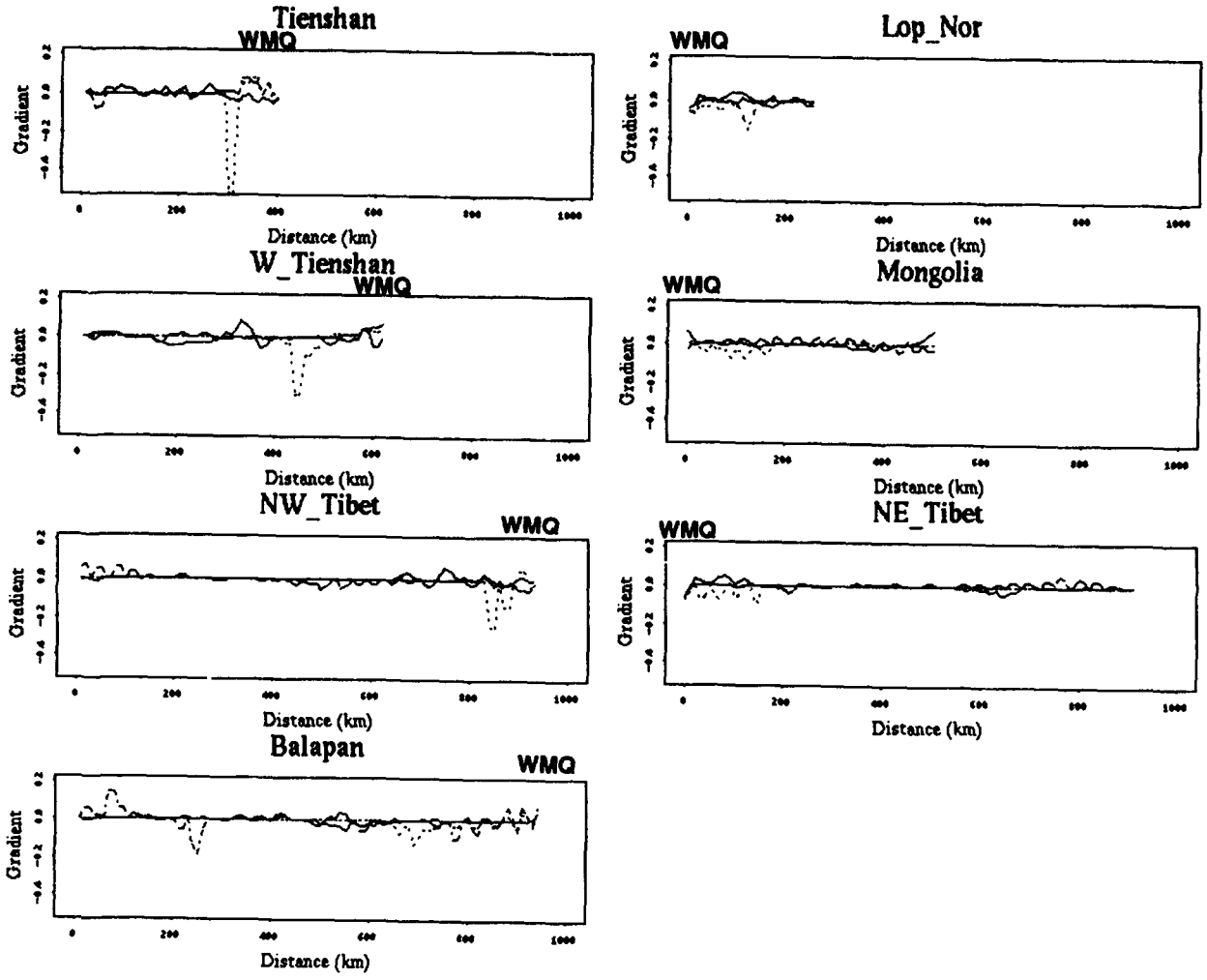


Figure 5: Gradients of the cross sections shown in Figure 4. Units of the gradients are elevation change (km) per distance change (km). As in Figure 4, west to east is left to right and positions of WMQ are labelled.

regions are 1188 km apart. The earthquakes show large variance in the log *Pn/Lg* ratios, whereas the nuclear explosion variance is much smaller.

Figure 3 shows the same points plotted as a function of distance. Clearly, the Lop Nor explosion is well separated from the nearby Tien Shan earthquakes. However, the Tien Shan earthquakes show a very strong increasing trend with distance. We have determined a distance correction for *Pn/Lg* ratios in Scandinavia, using data from the NORESS, ARCESS, and FINESA arrays. By fitting slopes to the amplitude ratios for station pairs covering several distance ranges, we build up a set of frequency dependent distance corrections. We regard these curves to be nominal for a shield type propagation path which may not be representative of central Eurasia. The one for 6 to 8 Hz is shown plotted as a curve in Figure 3(a). Using the slope of this curve, the *Pn/Lg* ratios have been corrected to a standard distance of 500 km and are shown in Figure 3 (b). This correction slightly shifts the Lop Nor point to a higher value that falls more in the Balapan group. Clearly, the shield correction is not adequate for the earthquake trend.

Figure 4 shows crustal cross sections for each of the paths in Figure 1 right. These plots shows cross sections of mean elevation, depth of sediments, and depth of the Moho. The data for these plots came from GIS server at Cornell University (Fielding, et al, 1992). Zhang, et al (1994) have suggested that variations in *Pn/Lg* ratio may be correlated to crustal parameters, such as average depth of the sediments. Baumgardt (1990) argued that a sharp change in the depth of sediments, relative to a change in distance, may disrupt the *Lg* waveguide and thus block *Lg*. To check this, we plot in Figure 5 the gradient of the crustal data shown in Figure 4.

This analysis shows that all the paths have significant variations in crustal parameters. Figure 3(a) shows that the best separation of the Lop Nor explosion and earthquakes occurs in central Tien Shan, which are the earthquakes near Lop Nor. Figures 4 and 5 show that WMQ is in a sedimentary basin. At about 300 km, the *Pn/Lg* ratios increase suddenly, perhaps caused by a local blockage. Beyond this distance, there appears to be a gradually increasing trend in the *Pn/Lg* ratios with distance with no apparent blockages, although that trend is much stronger than the Scandinavian trend. This may reflect partial blockages along all the paths, although differences in source mechanism and higher anelastic attenuation may also contribute to the variations in the *Pn/Lg* ratios for earthquakes.

CONCLUSIONS AND RECOMMENDATIONS

This study has shown that Scandinavian discriminants may not directly port to WMQ in China because of possible blockages of *Lg* beyond 300 km. The station WMQ is situated in the southern part of the fault-bounded Dzungarian Stable Block which contains up to 10 km of sediments (Terman and Woo, 1967), as shown in Figure 1 right. Earthquakes in or near Lop Nor occurred in the foldbelt between this basin and the Tarim Basin. This path seems to propagate *Lg* efficiently. All the other paths to WMQ pass through major fault bounded basins which may block the *Lg* arrivals. Tectonic features of this magnitude do not occur in Scandinavia, so that a more severe *Pn/Lg* correction will have to be inferred.

We conclude that crustal cross sections of the kind shown in Figures 4 and 5 can provide valuable information about possible blockages of *Lg* to determine of *Pn/Lg* discriminants can be directly to a new region. We plan to determine if quantitative measurements of path characteristics, such as those of Zhang, et al. (1994), correlate with *Pn/Lg* ratios measured at high frequencies and at regional distances which may be useful for correcting *Pn/Lg* discriminants for blockage effects on *Lg*.

REFERENCES

Baumgardt, D.R. (1990). Investigation of teleseismic *Lg* blockage and scattering using regional arrays, *Bull. Seism. Soc. Am.*, **80**, 2261-2281.

Baumgardt, D.R. (1993). Regional characteristics of mine blasts, earthquakes, mine tremors, and nuclear explosions using the Intelligent Seismic Event Identification System, Final Report, *SAS-TR-94-12*, ENSCO, Inc., Springfield, Va.

Baumgardt, D.R. and G.B. Young (1990). Regional seismic waveform discriminants and case-based event identification using regional arrays, *Bull. Seism. Soc. Am*, **80**, 1874-1892.

Baumgardt, D.R., S. Carter, M. Maxson, J. Carney, K. Ziegler, and N. Matson (1991). Design and development of the intelligent event identification system, *PL-TR-91-2298(I)*, Final Report, Volumes I,II, and III, ENSCO, Inc., Springfield, Va. Vol I: ADA248381

Bennett, T.J., B.W. Barker, K.L. McLaughlin, and J.R. Murphy (1989). Regional discrimination of quarry blasts, earthquakes, and underground nuclear explosions, Final Report, *GL-TR-89-0114*, S-Cubed, La Jolla, Ca. ADA223148

Fielding, E.J., B.L. Isacks, and M. Barazangi (1992). A geological and geophysical information system for Eurasia, *Technical Report No. 2*,. Cornell University, Ithaca, New York.

Terman, M.J. and C. C. Woo (1967). Atlas of Asia and Eastern Europe to support detection of underground nuclear testing, Vol. II, Tectonics, China and Mongolia, Prepared for ARPA by USGS.

Zhang, T. S.Y. Schwartz, and T. Lay (1994). Multivariate analysis of waveguide effects on short-period regional wave propagation in Eurasia and its application in seismic discrimination, Accepted for publication in *J. Geophys. Res.*

Identification of Rockbursts, Earthquakes, Chemical Blasts and Small Nuclear Explosions at Regional Distances

T. J. Bennett, B. W. Barker and J. R. Murphy
S-CUBED
11800 Sunrise Valley Dr., Suite 1212
Reston, Virginia 22091
Contract Nos. F 19628-91-C-0186 and F 19628-93-C-0093

Objective

Particularly important issues for Comprehensive Test Ban Treaty (CTBT) and non-proliferation monitoring are extending discrimination capabilities to lower magnitude levels and into new geographic regions. A consequence of this change in monitoring emphasis is that different types of seismic sources and nuclear testing scenarios begin to play a role in the discrimination problem. S-CUBED has been conducting research on regional seismic discrimination of several of these different source types. In particular, since the last review meeting, we have completed work on one contract aimed at assessing the nature of the seismic discrimination problem for rockbursts and related mining-induced events worldwide and at identifying some potential regional discrimination methods to distinguish them from other sources. Results from these studies indicate some promising differences in the relative excitation of regional phases and in their frequency content between rockbursts, earthquakes, and explosions. In addition, we are currently working on another project to investigate the identification problems associated with small or decoupled nuclear explosions near a low monitoring threshold (e.g. 1-kt decoupled, 2.5 m_b). Our initial efforts in this area have focused on using Mueller-Murphy source scaling to produce representative seismograms at regional array stations for these low-threshold nuclear explosions. These will then be used to test monitoring capability and discrimination techniques.

Research Accomplishments

With regard to rockbursts our observations were directed at data from two regions: Central Europe and South Africa. In both regions rockbursts have been frequent and occasionally large (with magnitudes sometimes exceeding 5 m_b). We analyzed digital waveform data from a variety of sources, including the ARPA regional arrays, SRO/ASRO, DWWSSN, Russian IRIS, and GSETT-2 stations, for rockbursts and contrasting source types with similar epicentral distances and propagation conditions. A variety of time-domain and spectral analyses were performed on the waveforms for selected events. For the far-regional and regional waveforms, we investigated the relative excitation of P, S, and L_g signals in both the time and spectral domains. For many larger events we compared complexity and spectra of the teleseismic P and M_S versus m_b between events.

Figure 1 shows the map of Central Europe with the location of several rockbursts, an earthquake, and a mineblast which were recorded by one or more of the far-regional stations shown. We performed band-pass filter analyses of the

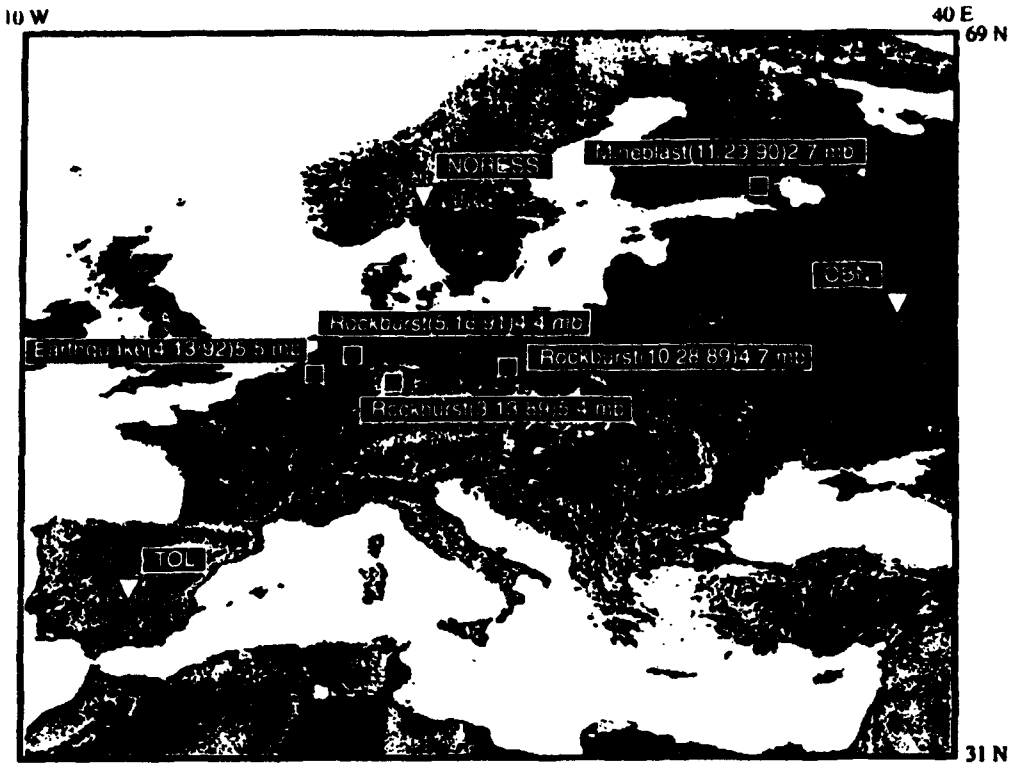


Figure 1. Locations of events and far-regional stations used in analyses.

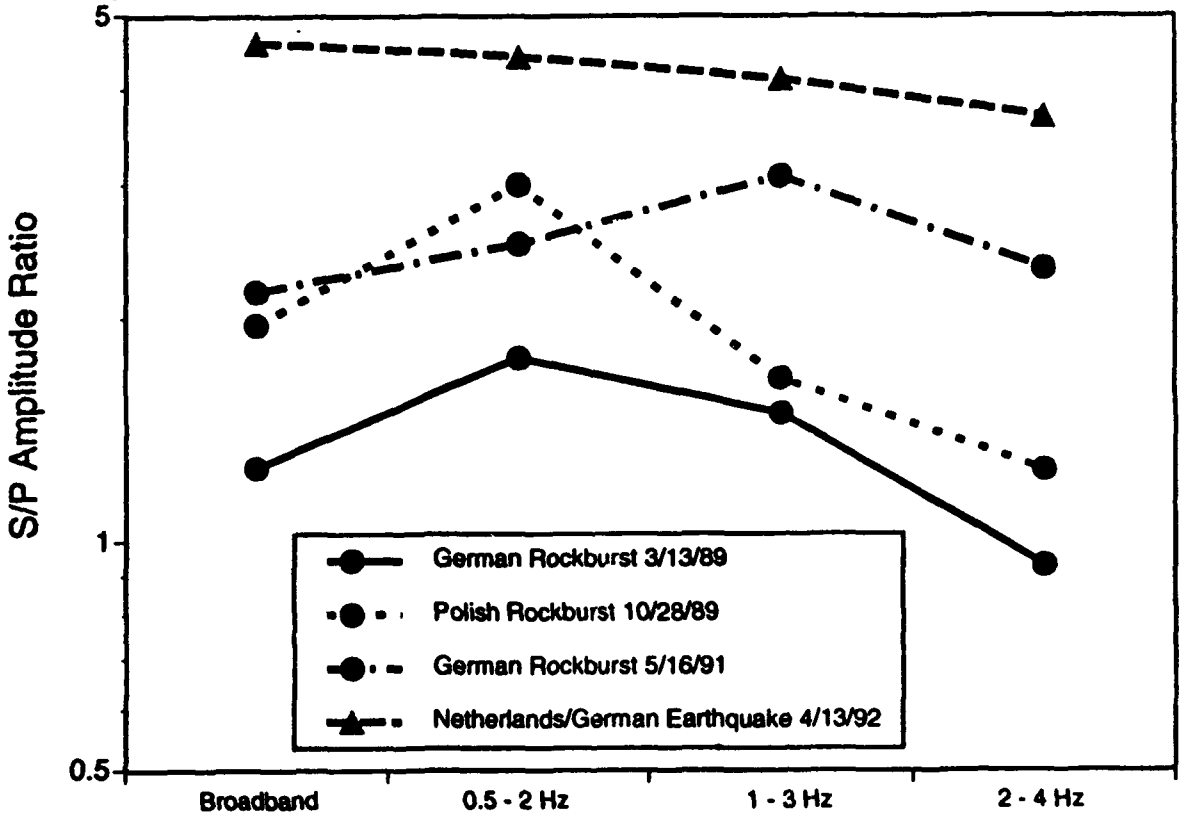


Figure 2. S/P ratios at NORESS for various filter passbands.

NORESS center-element, vertical-component records for the earthquake and the three rockbursts from Figure 1. The analyses revealed that S and S coda were the prominent secondary phase with little evidence of distinct L_g except at lower frequencies. S/P ratios were computed by dividing the maximum amplitudes in the respective phase windows for each frequency band. These S/P ratios are presented in Figure 2. The ratios are largest for the earthquake and less for the rockbursts at all frequencies. However, some rockbursts, like the 5/16/91 German event, tend to have S/P ratios closer to those of the earthquake at high frequencies. Referring back to Figure 1, it may be noteworthy in this regard that propagation paths would appear to be closest for the earthquake and the 5/16/91 rockburst which suggests that some of the greater differences in the high-frequency ratios between the earthquake and other rockbursts may be propagation related. The signal-to-noise ratio (S/N) was generally low for the small mineblast at this distance, particularly for high-frequency S, which prevented comparison of its S/P spectral ratio with other events. However, it should be noted that S/P ratios computed at far regional distances for nuclear explosions in other regions of Eurasia typically produce values well below one at frequencies above about 2 Hz (Bennett et al., 1992).

We also analyzed nearer regional observations for several Central European events with different source types. Figure 3 shows the locations of a Polish rockburst, a Netherlands earthquake, and a Swiss munitions blast, all having comparable magnitudes and recorded at GRFO. Figure 4 shows the vertical-component records for the three events. L_g phases produced the largest signals on the broad band recordings; while S phases, expected at the beginning or just prior to the L_g windows, are not separated or distinct on the records. The P_g phases are strongest for the Swiss munitions blast and Polish rockburst, and P_n is strongest for the rockburst. The maximum amplitude levels at GRFO were quite similar for all three events. Fourier spectral analyses of the P_n, P_g, and L_g signals showed S/N above one over a band from about 0.5 to 6 Hz. L_g/P_g spectral ratios over this band were somewhat oscillatory but tended to be highest (well above one) for the earthquake, least (well below one) for the explosion, and intermediate (above one) for the rockburst. This observation is in general agreement with results for South Africa where L_g/P spectral ratios were above one over a broad band for both rockbursts and earthquakes (Bennett et al., 1993).

Although teleseismic signals are not always apparent for rockbursts, we were able to compare teleseismic P spectra for some of the larger Central European events. We analyzed data from a common network of eight stations for the large German rockburst (4/13/89) and the Netherlands earthquake (4/13/92) shown in Figure 1 above and for a large Polish rockburst (6/29/89, 4.7 m_b). P/P spectral ratios, over the available frequency band from 0.5 to 4 Hz, revealed some differences between the events. The earthquake tended to be richer in high frequencies than the 4/13/89 German rockburst while the ratios for the 6/29/89 Polish rockburst and the earthquake tended to be flat with frequency. If these trends are related to source variations, they may indicate differences in mechanism between the German rockburst (thought to be more typical of a collapse event) and the Polish rockburst (probably more shear or earthquake-like).

Finally, M_S measurements are seldom reported for rockburst events; in most cases the events are too small to produce long-period surface waves at teleseismic station networks. For Central Europe and South Africa, we found a sample of nine rockbursts and three earthquakes with M_S measurements reported in the NEIC

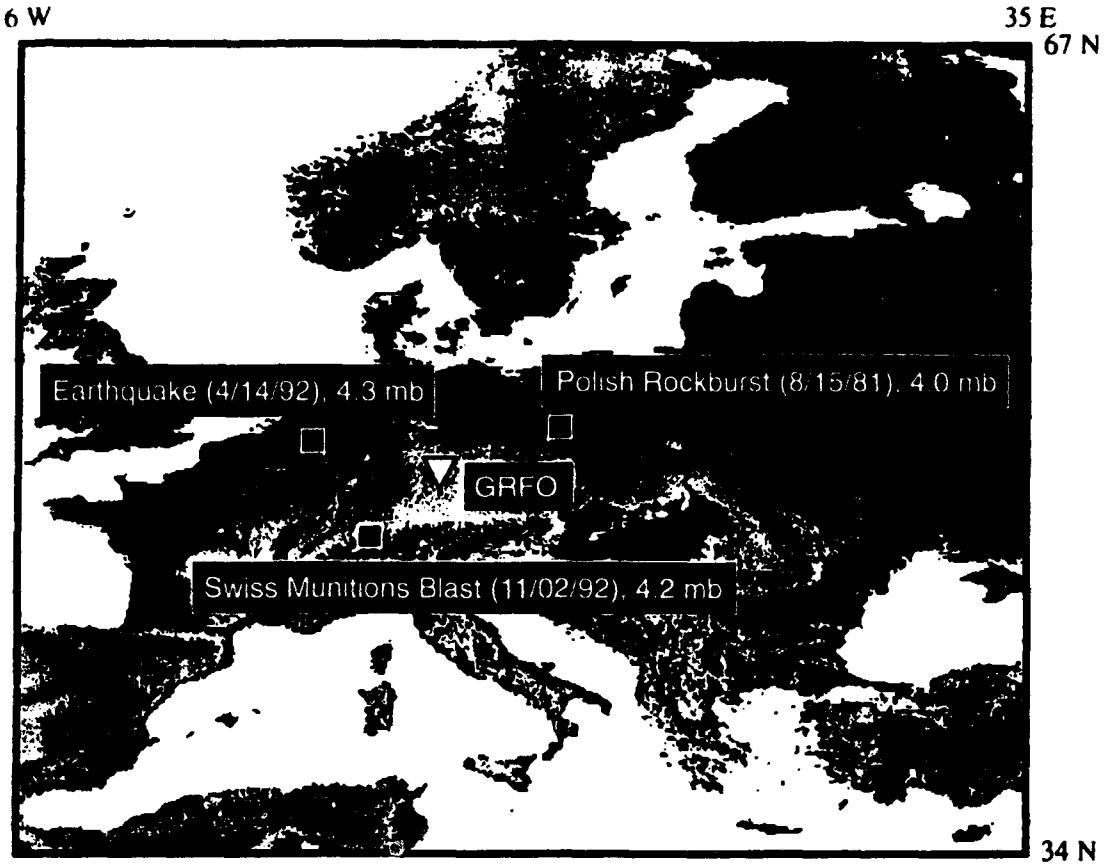


Figure 3. Locations of events used in discrimination analysis at GRFO.

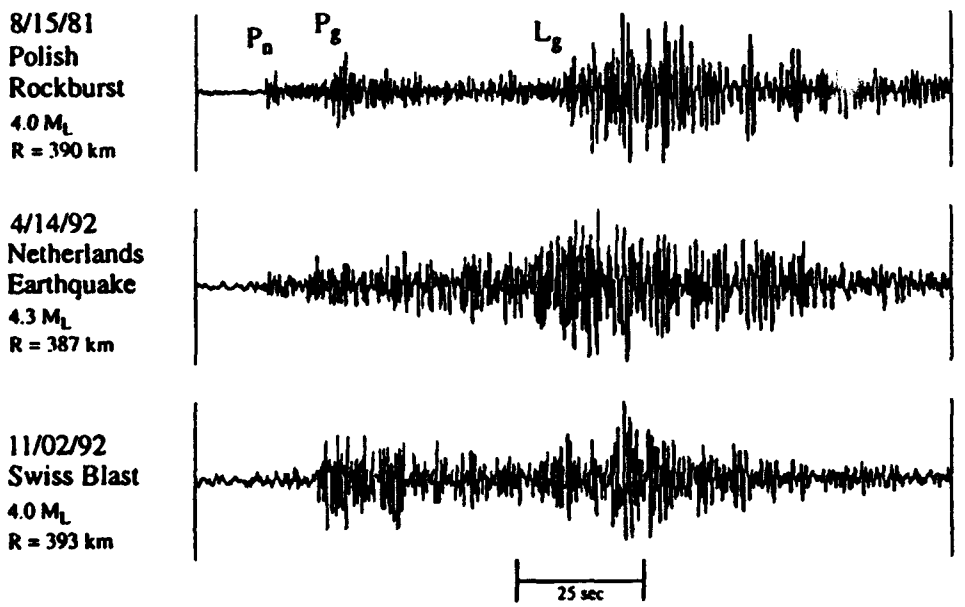


Figure 4. Vertical-component records at GRFO for three events from Figure 3.

catalogs. Four of the 12 events (including two of the earthquakes) had M_S values within 0.3 magnitude units of m_b, while four of the rockbursts had M_S values more than one magnitude unit lower than m_b. This tendency for rockburst M_S values to be low relative to m_b appears to be confirmed by other observations (Bennett et al., 1994) and suggests a potential problem for using the M_S/m_b discriminant to distinguish rockbursts from explosions.

With regard to our investigation of discrimination problems associated with small and decoupled nuclear tests, we have been attempting to simulate far-regional signals by applying source scaling theory to observed waveforms from larger events. Kvaerna (1991) used a simple frequency-independent magnitude scaling of NZ nuclear explosion signals to test detection threshold monitoring at the ARPA regional arrays. In our approach we have used the more elaborate Mueller-Murphy source scaling theory (Mueller and Murphy, 1971) which accounts for not only the reduction in amplitude but also the shift towards higher frequencies at lower yields. Furthermore, our ultimate interest goes beyond detection thresholds to investigation of the reliability of regional discrimination for low-yield and decoupled nuclear tests in the monitoring environment.

According to Mueller-Murphy source scaling theory, the source spectral ratio for a spherically-symmetric explosion model is given by

$$\frac{S_2(\omega)}{S_1(\omega)} = \frac{p_2(\omega)\, r_{el2}}{p_1(\omega)\, r_{el1}} \frac{\omega_{o1}^2 + i\,\omega_{o1}\,\omega - \beta\,\omega^2}{\omega_{o2}^2 + i\,\omega_{o2}\,\omega - \beta\,\omega^2}$$

where r_{el1} and r_{el2} are the elastic radii of the two sources at which the spherically symmetric pressures $p_1(\omega)$ and $p_2(\omega)$ act and

$$\omega_{oi} = \frac{\alpha}{r_{eli}} \quad \text{and} \quad \beta = \frac{\lambda + 2\,\mu}{4\,\mu}$$

with α the P-wave velocity and λ and μ the Lame constants characteristic of the source medium. At a common source depth in a fixed medium $p_2(\omega) = p_1(\omega)$, and the expression for the source spectral ratio is simplified. In the low-frequency limit the modulus of this source spectral ratio is equivalent to the cube of the ratio of the elastic radii, which just equals the ratio of the yields; and at the high-frequency limit it is equal to the ratio of the elastic radii, which just equals the cube-root of the yield ratio.

As an initial test of the methodology and to provide a relatively clean example, we have used this scaling theory to modify the available records at the ARPA regional arrays in Scandinavia (viz. NORESS, ARCESS and FINESA) from two NZ nuclear explosions (12/04/88, 5.7 m_b and 10/24/90, 5.7 m_b) and a Russian PNE (7/18/85, 5.0 m_b). Epicentral distances were between 1100 km and 2300 km. The signals were scaled down from their original yields (estimated from m_b) to fully-decoupled 1-kt and then added to available noise segments. The noise segments are about one hour in duration. The noise segments were arbitrarily selected and are thought to represent typical (not maximum or minimum) noise levels at each array.

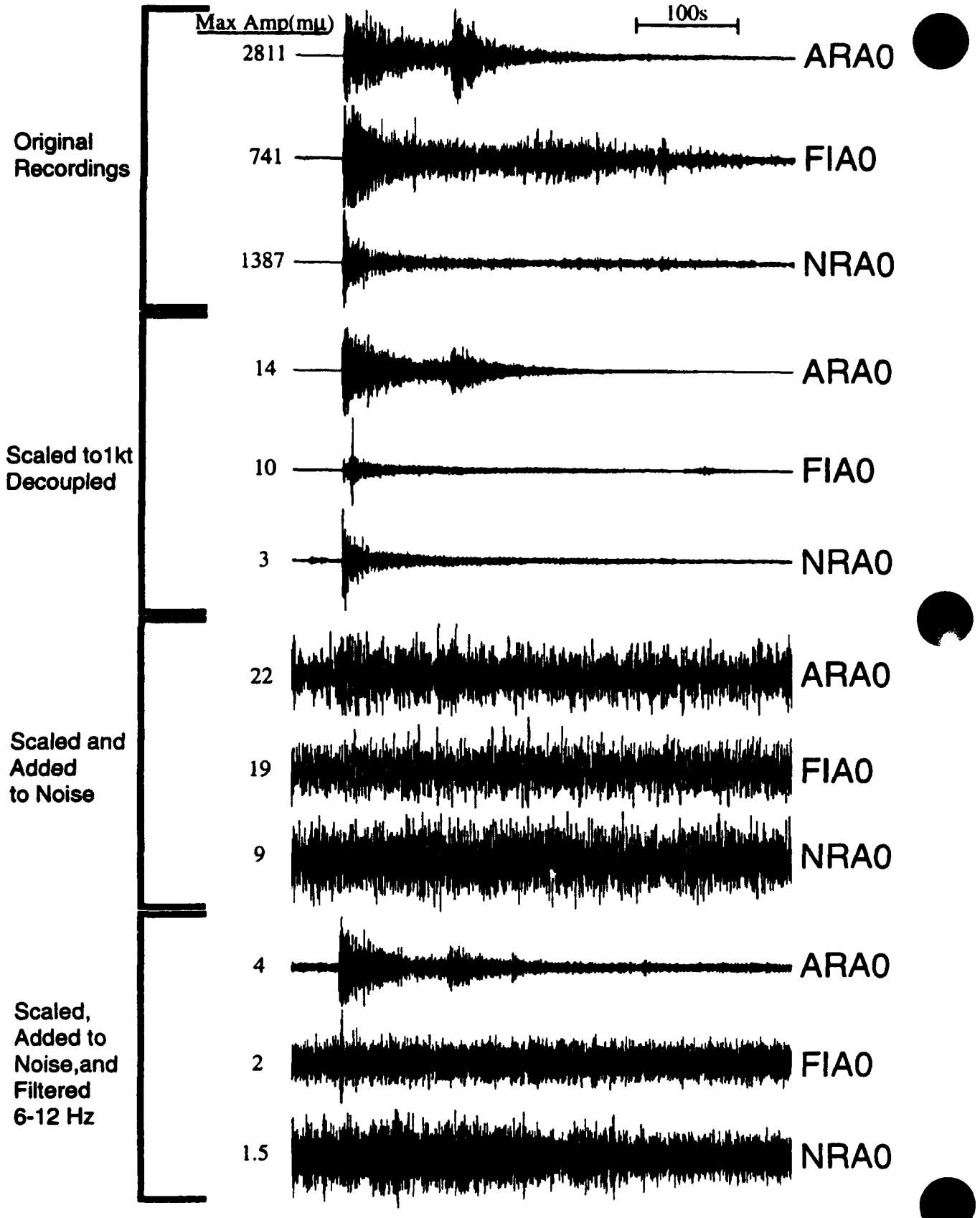


Figure 5. Examples of source-scaling process applied to NZ explosion at ARPA arrays.

Figure 5 illustrates the results of the scaling process for limited waveform segments which include the P through L_g windows for the center element at each array. The first group of three traces shows the original records for the 10/24/90 NZ explosion at each array. The next group shows the same signals scaled down to 1-kt decoupled using Mueller-Murphy theory. The reduction in amplitude is obvious while the frequency shift is more subtle. The third group of three traces shows the scaled traces added into the representative noise segments. The scaled signal amplitudes are at or below the broad-band noise levels and difficult to discern. The final group of traces shows band-pass filtered versions of the preceding group of traces for the passband 6-12 Hz; S/N was generally lower in other passbands. The 1-kt decoupled explosion signal is apparent only at ARCESS and barely rises above the background noise at FINESA. Such limitations on detectability and usable passband are expected to have important implications for discrimination monitoring at low thresholds.

Conclusions and Recommendations

For rockbursts our investigations suggest that there are differences in the relative amplitudes and frequency content of regional signals which may be useful in distinguishing between rockbursts, earthquakes, and explosions. However, other traditional discriminant measures (e.g. M_S versus m_b) may tend to provide false indication of rockburst events as explosions. Furthermore, anecdotal and other evidence indicates the possibility that at least some types of rockburst may be triggered deliberately, which suggests that the opportunity for clandestine testing of small nuclear weapons accompanying such events cannot be dismissed without additional investigation. For small or decoupled nuclear explosions approaching thresholds of interest, our preliminary results indicate that usable signals at regional to far-regional distances may be constrained to quite limited high-frequency bands. It seems critical that regional discrimination techniques be evaluated with consideration to the limitations on amplitude and frequency content of the signals expected from such small events.

References

Bennett, T. J., A. K. Campanella, J. F. Scheimer, and J. R. Murphy (1992). "Demonstration of Regional Discrimination of Eurasian Seismic Events Using Observations at Soviet IRIS and CDSN Stations," PL-TR-92-2090, ADA253275

Bennett, T. J., J. F. Scheimer, A. K. Campanella, and J. R. Murphy (1993). "Seismic Characteristics of Rockbursts for Use in Discrimination," PL-TR-93-2059, ADA266063

Bennett, T. J., M. E. Marshall, B. W. Barker, and J. R. Murphy (1994). "Characteristics of Rockbursts for Use in Seismic Discrimination," S-CUBED Report SSS-FR-93-14382.

Kvaerna, T. (1991). "Threshold Monitoring of Novaya Zemlya: A Scaling Experiment," NORSAR Semiannual Technical Summary, 1 Oct 1990 - 31 Mar 1991, NORSAR Sci. Rep. 2-90/91.

Mueller, R. A., and J. R. Murphy (1971). "Seismic Characteristics of Underground Nuclear Detonations. Part I. Seismic Spectrum Scaling," Bull. Seism. Soc. Am., 61, pp. 1675-1692.

Seismoacoustic Studies of the Norwegian Sea

Donna K. Blackman and John A. Orcutt
Institute of Geophysics and Planetary Physics
Scripps Institution of Oceanography, University of California San Diego

Contract No. F49620-94-1-0041

1. Objectives

The goal of the investigation in the Norwegian Sea is to assess the usefulness of SOSUS as a tool for seismology and to further our understanding of seismoacoustic wave propagation in ocean basins. Analysis of earthquake detection levels and our ability to characterize both natural and manmade seismic sources will determine how reliably the Navy hydrophone arrays can supplement, or even replace, seismometer arrays on land.

2. Setting and Approach for the Investigation

The Norwegian Sea offers a unique setting for assessing SOSUS use for seismology due to the existing combination of seismic activity, instrumentation and varied oceanographic conditions (Figure 1). The different seismic sources in the region provide a range of signal types and locations (e.g. Vogt, 1986): large oceanic earthquakes from transform faults along the plate boundary between Iceland and Svalbard; smaller oceanic earthquakes associated with volcanic eruptions along the rifting portion of the plate boundary; mining explosions on land; slope failure events on the continental shelf. Several types of recordings of Norwegian Sea seismic activity are available from instruments whose capabilities dovetail each other: the Global Seismic Network (GSN); the seismometer arrays in Norway and on Spitsbergen; and the SOSUS acoustic arrays. The geological and oceanographic character of the Norwegian basin differs from south to north and from east to west. The seafloor just north of Iceland is fairly shallow and smoothly varying; north of the Jan Mayen Fracture Zone, depths increase and the topography is generally rougher. The shape of the continental slope varies notably around the basin influencing the quality of coupling of acoustic to seismic energy at the sea/land interface. The southern part of the Nordic sea has a reasonably well developed sound (SOFAR) channel whereas to the north there is not a strong low velocity axis at the 1000m depth typical of the northern Atlantic. Winter ice cover significantly alters the sound profile of the ocean in the western Norwegian Sea (Hurdle, 1986).

The Norwegian Sea seismoacoustic investigation has three main phases: 1) acquisition and compilation of the different acoustic and seismic datasets; 2) characterization of the data and of the relationship between signal type and geophysical setting; 3) numerical simulation of the generation and propagation of acoustic energy (T-phases).

3. Initial Results From the First Phase

The first phase is currently underway with data from the Norwegian seismic arrays being transferred daily to Scripps Institution of Oceanography (SIO) for events detected by operators at the Center for Seismic Studies (CSS). The link to the SOSUS acquisition system is currently being installed at Keflavik by our colleague at the Naval Research Lab (NRL). These data will be archived at NRL and the location of acoustic events will be completed in the classified facility there. A more general synthesis of the historic patterns of seismicity in the Norwegian Sea is underway at SIO.

Preliminary analysis of 27 months of data from 1989 to 1992 suggests that several event locations determined by the Intelligent Monitoring System (IMS) at CSS may, in fact, reflect the location that the T-phase is converted at the slope (Figure 2). Out of 371 events listed by IMS for the period, 16% are located along the steep slope of the eastern Norwegian

Sea basin. Five of these slope events off Spitsbergen are co-detected by the GSN and are listed in the USGS Preliminary Determination of Epicenters (PDE) but with locations on the Knipovich spreading center. This suggests that acoustic energy from sources in the basin interior can propagate some distance in the ocean before coupling into seismic waves at the continental slope. Apparently the amplitude of these converted phases is large enough to influence the determination of epicenters by IMS. There are other interesting differences in the detection patterns indicated by the PDE vs IMS listings for the period: more PDE than IMS events occur on the Kolbeinsy ridge and the 4 out of 8 events that are listed by IMS are all located many km down-slope off the ridge axis; IMS detected 40% the number of events that the PDE listed for the Jan Mayen transform fault and one co-detected event was located by IMS down-slope from the PDE epicenter; more events were detected by IMS along the northeast Mohns ridge than are listed in the PDE and the converse is true for the southern Knipovich. We are reanalysing the arrivals for several of the co-detected events to assess the cause of the differences in IMS vs PDE source locations. Addition of the SOSUS data in the coming months will further allow us to investigate the nature of acoustic vs seismic propagation in the Nordic Seas.

As our acoustic and seismic database grows, our second-phase emphasis will be to catalogue events in terms of source magnitude, signal character on SOSUS vs at the land seismometers, source location (geographic and depth), and path of propagation in the basin. We can depend on standard techniques to obtain source parameters from the land array data. In contrast, acoustic T-phases are fairly complex with arrival energy often building over a period of many seconds to a maximum and then tailing off over as long as a few minutes. This complexity makes the task of using T-phases to determine source parameters rather difficult so we will initially use the land-derived parameters for co-detected events to develop an understanding of how T-phase character (onset time, frequency content, duration, amplitude) reflects source and propagation path parameters. For this observational phase of the project our goal is to determine how reliably we can locate and parameterize events that are too small to be detected by the land arrays but that are recorded by the hydrophone arrays.

The third phase will require computation of synthetic seismograms in complex media to understand the excitation and propagation physics of T-phases. Building on earlier simple models by Sereno and Orcutt (1985, 1986), the response of models of plane-layered structures with realistic water column structure will be computed. This wavenumber integration method will illustrate the character and composition of Pn, Sn and T arrivals as a function of structure, source mechanism and source depth. We will model the interaction of elastic and acoustic waves at a rough, sloping seafloor to understand the coupling of high phase velocity earthquake waves into lower phase velocity, acoustic waves using other advanced numerical approaches (Kirchoff-Helmholtz, Finite Difference (FD) and hybrid FD-Maslov methods).

4. References

Hurdle, B.G., The sound speed structure, in B.G. Hurdle (ed), *The Nordic Seas,* Springer-Verlag, New York, p155, 1986.

Sereno,T. and J. Orcutt, Synthesis of realistic oceanic Pn wave trains, J. Geophys. Res. 90, 12,755-12,776, 1985.

Sereno, T. and J. Orcutt, The propagation of Pn, in *Ocean Seismo-Acoustics,* T. Akal and J.M. Berkson, (eds), Plenum, 1986.

Vogt, P., Geophysical and geochemical signatures and plate tectonics, in B.G. Hurdle (ed), *The Nordic Seas,* Springer-Verlag, New York, p155, 1986.

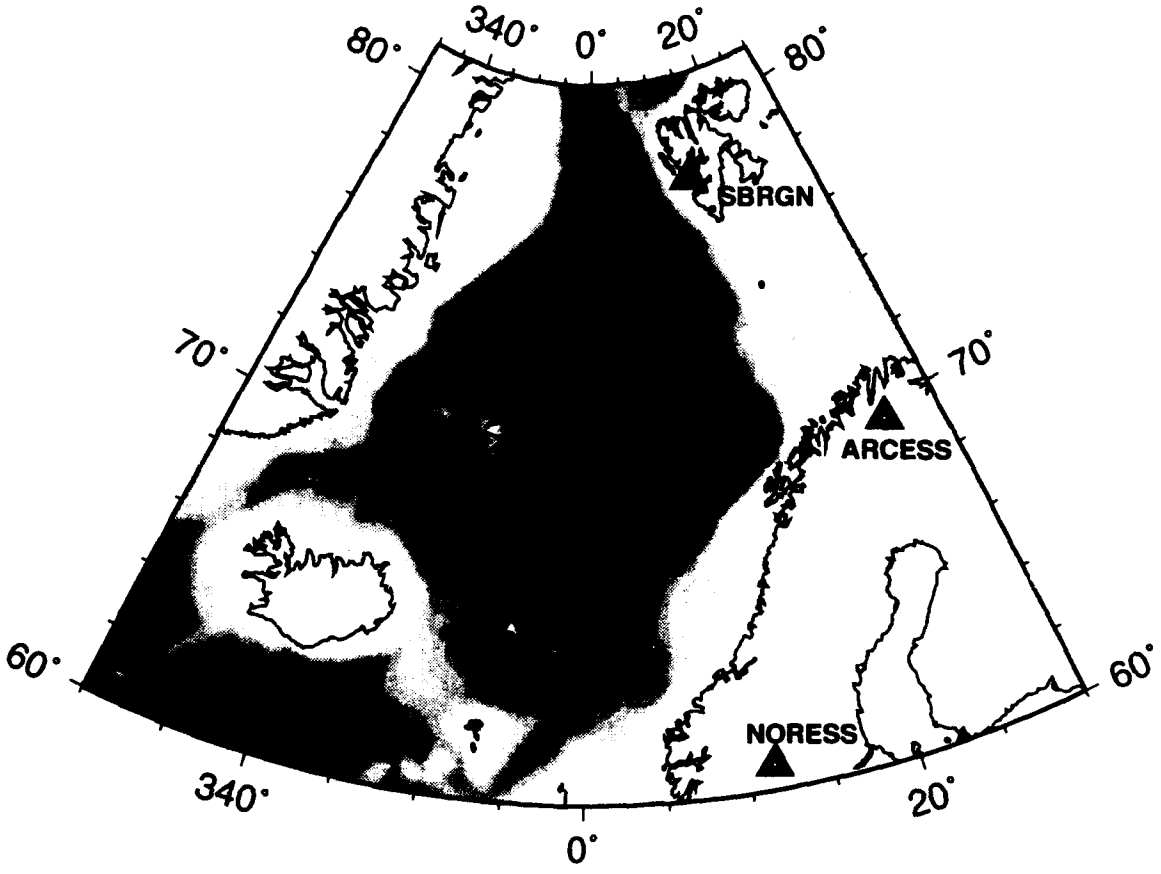


Figure 1. Map of the Norwegian Sea study area with Iceland to the south, Greenland to the west, Norway and Spits Bergen to the southeast and [illegible], respectively. Shading indicates seafloor depth with darkness increasing in steps of [illegible] from the 500m continental shelf edge to 4000m in the basin. The Jan Mayen Fractu[illegible] Zone (JMFZ) a source of large transform fault earthquakes is indicated. The spreading centers are shown by the shallow ridges: Kolbeinsy Ridge between Iceland and Jan Mayen; Mohns Ridge extending northeast from Jan Mayen; Knipovich Ridge striking north past Svalbard. The rift axes of the latter two ridges have deep valleys in contrast to the Kolbeinsy Ridge.

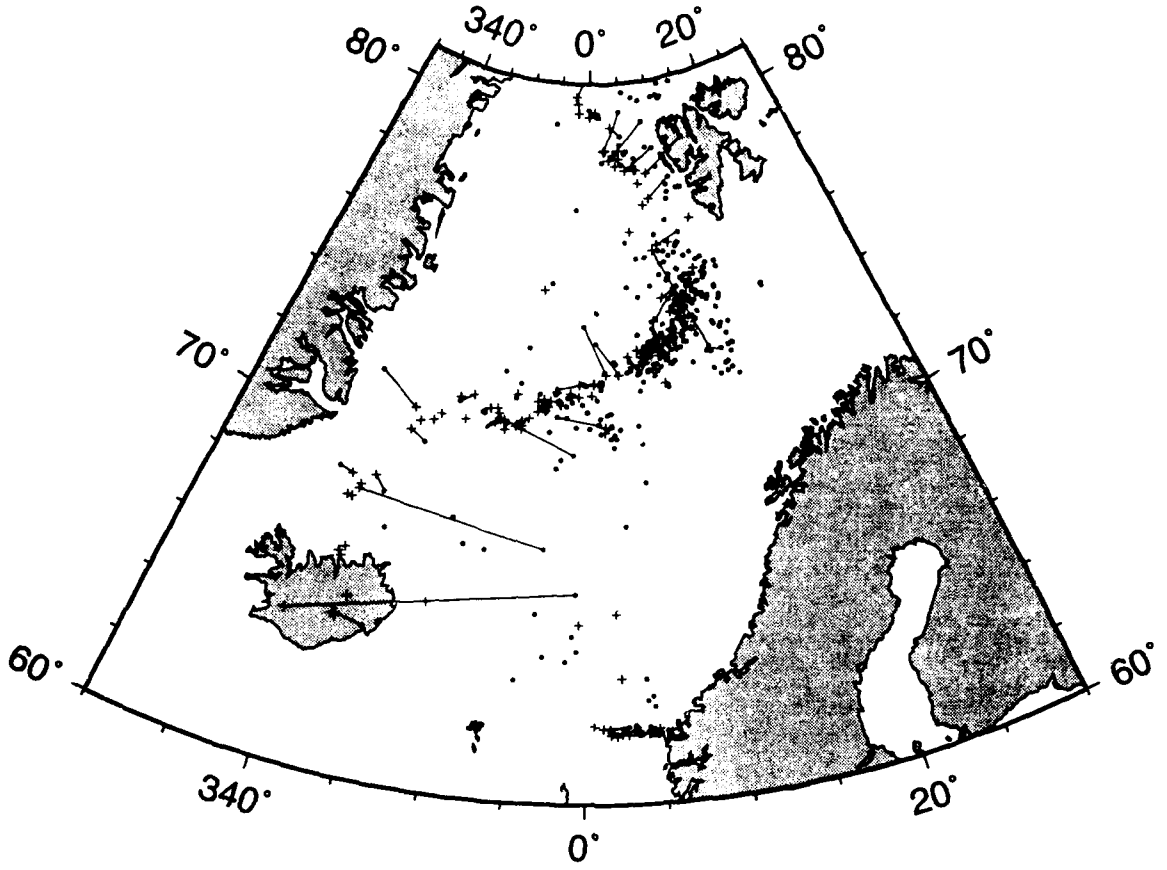


Figure 2. Earthquakes detected by the GSN (+) and by the land arrays (dots) from Oct 1989 to Dec 1992. This illustrates the number and distribution of events that we will observe during our study. 15% of the events were listed in both catalogues; the connecting lines show misfit between the PDE and the IMS locations- a problem we will address in our study. Smaller events will be detected by the SOSUS arrays alone and we will assess the accuracy with which we locate these sources.

RAY SYNTHESIS OF REGIONAL SEISMOGRAMS

Vernon F. Cormier[1], Tom Anderson[1], and G. Eli Baker[2]

[1]Department of Geology and Geophysics
University of Connecticut
Storrs, CT 06269-2045

[2]IGPP, Scripps Institution of Oceanography
University of California, San Diego
La Jolla, CA 92093-0225

CONTRACT NO: F49620-94-1-0059

OBJECTIVE

The crust and uppermost mantle are the most strongly laterally varying and heterogeneous regions of the Earth. The seismic phases Pn,Pg, Sn, Lg, and Rg, which are important to nuclear verification of small sources, are all strongly affected by this heterogeneity, complicating the transportability of methods to detect, discriminate and yield estimate in different regions. There is a need to predict the effects of heterogeneous crustal structure on regional phase propagation using geological and geophysical information for regions in which little or no seismic recording has occurred. The computational expense of a numerical solution of the wave equation in an arbitrarily heterogeneous model have thus far limited such predictions to primarily 2-D structure and low frequency bands. Ray based techniques of forward modeling, however, are sufficiently fast to allow practical predictions of efficiency of the propagation of regional phases in detailed 3-D structures. The effects of scattering by statistically distributed heterogeneity can also be incorporated in ray methods by single scattering theory. The objective of this project is to develop and apply the methods of dynamic ray tracing and superposition of Gaussian beams to forward model regional seismic phases in three-dimensionally varying models of the Earth's crust. Goals include (a) an understanding of what crustal structures are most important in determining the efficiency of regional phase propagation, (b) determining what type of non-seismic data (topography, surficially mapped geology, gravity, magnetics) are most useful in inferring 3-D crustal structure, and (c) testing the success of a fast ray-based modeling procedure in modeling detailed features of regional waveforms. Test regions of study are the region surrounding the Kyrgyz array in central Asia and the southern California regional array.

RESEARCH ACCOMPLISHED

Regional seismograms are synthesized by summing dynamically traced rays and/or superposing Gaussian beams (e.g., Cerveny, 1985) in models of the crust for southern California and the vicinity of the Kyrgyz array. Moho turning points of the rays comprising the Lg and Pg phase are projected in a map view to illustrate predicted efficiency of propagation. To simplify the description of rays and reduce model storage, the model parameters are assumed to be continuous functions of space. P and S velocity and density are parameterized by functions:

$$v(x,y,z) = a + b\tanh(z - h_1(x,y)/s_1) + c\tanh(z - h_2(x,y)/s_2)$$

where $h_1(x,y)$ and $h_2(x,y)$ specify the depth of the sedimentary basin/basement contact and depth of the Moho, respectively. The functions h_1 and h_2 are given as continuous

functions of horizontal coordinates by interpolating digitized surfaces by splines under tension. Additional tanh functions can be added, as needed, to model more interfaces. In southern California, h_1 and h_2 are inferred from surface topography and gravity data published in reviews of North American geology (;Pakiser and Mooney, 1989; Palmer and Bally, 1989). In the vicinity of the Kyrgyz array, h_1 and h_2 are taken from databases assembled by Fielding et al. (1993).

CONCLUSIONS AND RECOMMENDATIONS

Synthetics and ray diagrams predict strong regional variations in Pg and Lg efficiency in both Southern California and the Kyrgyz [illegible]es 1-2). A plot of SmS turning points (e.g., Bostock and Kennett , 1991) in Figure 2 strongly suggests that a strong transition observed in Pn/Lg amplitude ratios across the Salton Trough (Baker et al., 1994) is probably related to crustal thinning in this region. A common effect of crustal thickness variation is either compression or stretching of the Lg coda compared to that predicted in a crust of uniform thickness. It may be possible to incorporate this effect in the refinement of regional discriminants based on the Pn/Lg ratio.

With ray theory, it is simple to incorporate the effects of single scattering (e.g., Wu and Aki, 1982) by crustal and upper mantle heterogeneities in an ellipsoidal shaped volume enclosing the source and receiver. The first step in this procedure is to generate a catalogue of dynamic ray tracing results in volume elements of the model by shooting rays from source to receiver and from receiver to source. A small number of scatterers within the crust is sufficient to create Lg coda having realistic complexity. Intersections of focused rays shot from receiver to source and source to receiver can be used to infer locations of scatterers where scattering can be amplified.

REFERENCES

Baker, G.E., V.F. Cormier, and J.B. Minster, Effects on Pn, Pg, and Lg amplitudes of nuclear explosion waveforms recorded in southern California, *Proceedings 16th Annual Seismic Research Symposium* (this volume), AFOSR/DARPA, 1994, PL-TR-94-2217

Bostock, M.G., and B.L.N. Kennett, The effect of 3-dimensional structure on Lg propagation patterns, *Geophys. J. Int.*, 355-365, 1991.

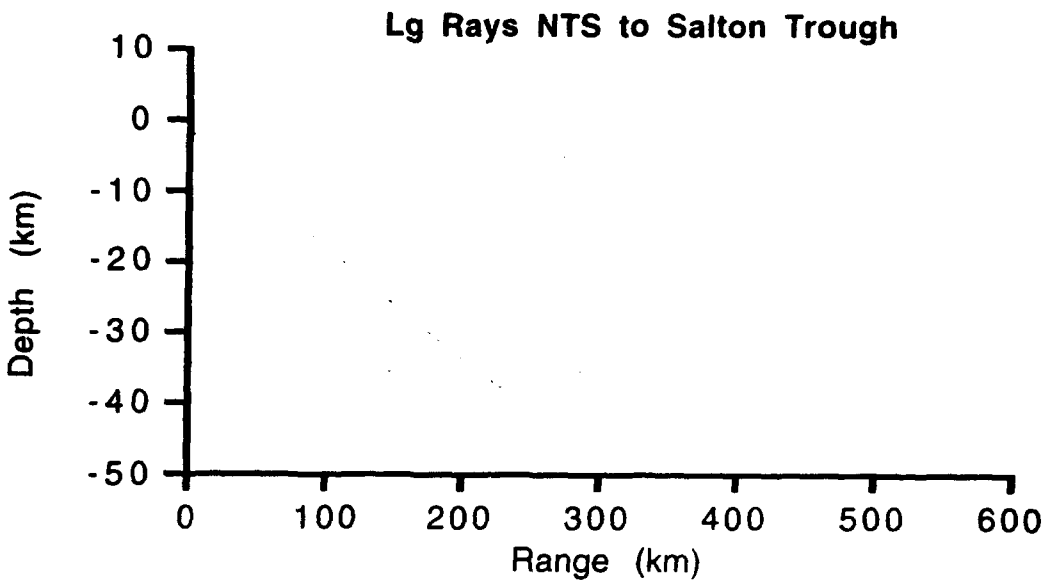
Cerveny, V., The application of ray tracing to the propagation of shear waves in complex media, in *Seismic Exploration* pp. 1-124, Treitel and Helbig, Vol. on Seismic Shear Waves, G. Dohr, ed., Geophysical Press, 1985.

Fielding, E., M. Barazangi, and B. Isacks, A network-accessible geological and geophysical database for Eurasia, North Africa, and the Middle East, *Proceedings 15th Annual Seismic Research Symposium*, AFOSR/DARPA, 1993, PL-TR-93-2160, ADA271458

Pakiser, L.C., and W.D. Mooney, eds., Geophysical framework of the continental United States, *U.S. Geological Survey, Memoir 172*, 1989.

Palmer, A.R., and A.W. Bally, eds., *The geology of North America, Volume A*, Geological Society of America, 1989.

Wu, R.S., and K. Aki, Scattering characteristics of elastic waves by an elastic heterogeneity, *Geophysics, 50*, 582-595, 1985.



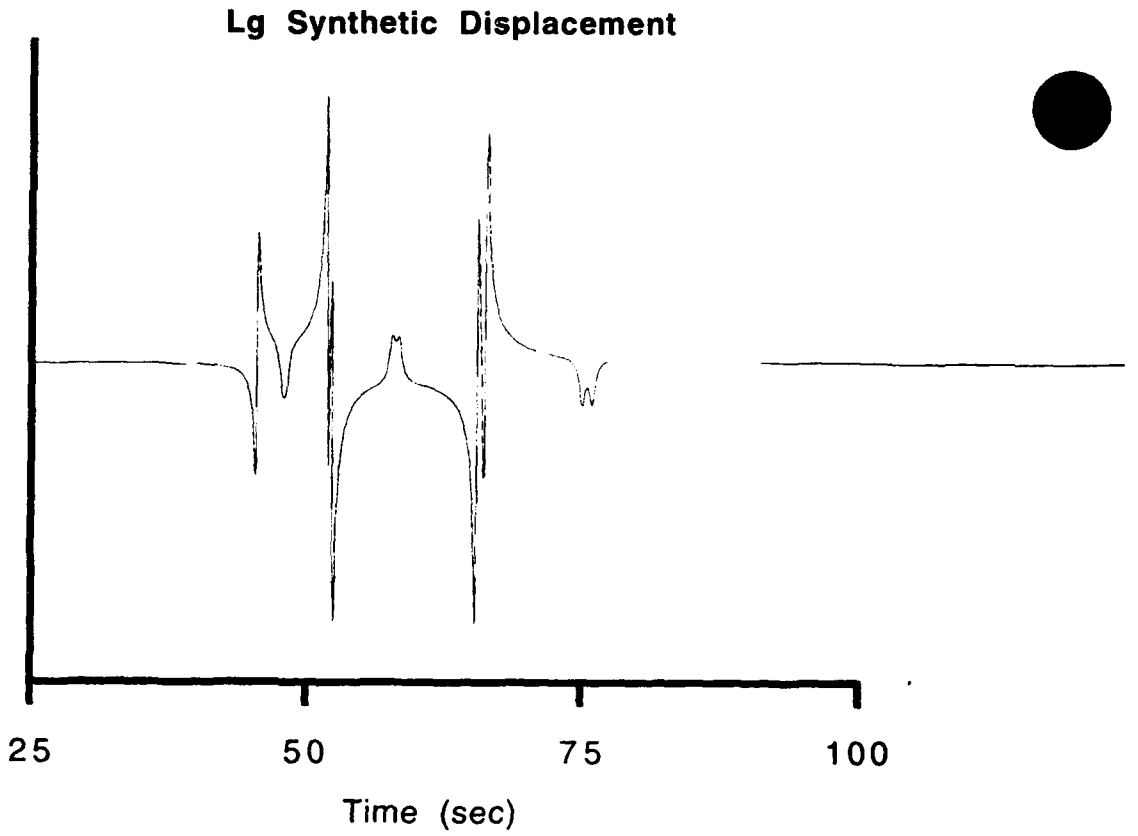


Figure 1. Top: SmS rays shot at a constant azimuth. Bottom: Synthetic Lg displacement calculated by summing dynamically traced shear waves in laterally homogeneous crust.

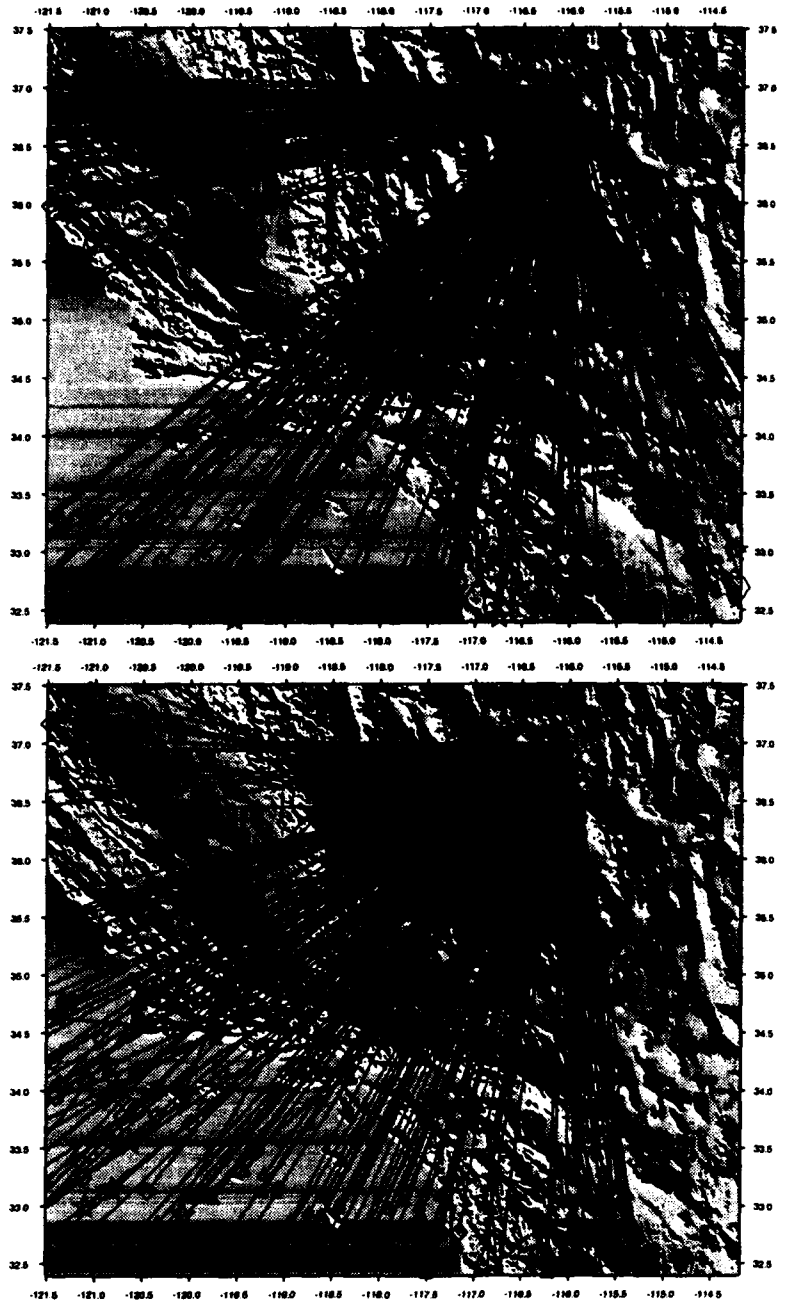


Figure 2. Lg ray trajectories constructed by connecting SmS turning points in a crustal model of southern California inferred from surface topography.

ENHANCING SURFACE WAVE SIGNALS USING THE UNDISTORTING GROUP FILTER

Anton M. Dainty
Phillips Lab/GPE
and
Alexander F. Kushnir
Moscow IRIS Data Center

Task #
76000908

OBJECTIVE

The objective of this research is to apply the undistorting group filter described in Kushnir et al. (1990) to the problem of extracting surface wave signals in the 5-30 sec period range from coherent noise using array recordings. The motivation for looking at these signals is they are used in the classic (and highly effective) mb-Ms teleseismic discriminant. However, there is difficulty in analyzing such signals for small events, even at regional distances, because of earth noise. While array analysis techniques have the potential to improve the signal to noise ratio, simple beamforming is most effective if the noise is not correlated between sensors; to achieve this, minimum element separations of 20 km or even greater may be needed, leading to very large array diameters for even a small number of sensors. It would be desirable to have processing methods that could exploit signals recorded at smaller arrays where noise is spatially coherent. Furthermore, it will be demonstrated by examples that better noise suppression may be achieved by appropriate analysis techniques than simple beamforming. Because the objective is to enhance signals for small events that may only be recorded at regional distances, far-regional as well near-teleseismic signals will be considered; preliminary studies indicate that long period measures such as seismic moment can be substituted for Ms at these ranges (e.g., Patton and Walter, 1993; Woods et al., 1993).

RESEARCH ACCOMPLISHED

As an initial test, presumed Soviet tests at the East Kazakh test site recorded at the NORSAR LP array (Figure 1) were examined. Vertical component (Rayleigh) surface wave recordings were used. At this near-teleseismic (38 deg) range, the surface wave train in the period range 10-30 sec is not strongly dispersed, and a velocity of 3.5 km/sec with an azimuth of 75 deg was found adequate for analysis purposes as representing the velocity and azimuth of the signal. Tests indicated that the method was not very sensitive to this parameter, variations of 0.5 km/sec or 10 deg of azimuth did not have a large effect.

The sampling rate of the data was one second. However, as part of the application of the undistorting group filter, an autoregressive model is fit to the inverse cospectral matrix of the traces. To obtain best results, the Nyquist frequency should not be much higher than the highest frequency in the data, otherwise a large section of spectrum between the Nyquist and the highest frequencies contains no information but is nonetheless being fit to the model. To limit the frequency content we low pass filtered the data to 0.1 Hz and decimated by a factor of two (Nyquist frequency = 0.25 Hz).

The filter transfer function is

$$K = H(f)G(f)/[g(f)H(f)G(f)],$$

where H(f) is the autoregressive estimate of the inverse cospectral matrix C(f), G(f) is the beamsteering vector, and g(f) is the complex conjugate of G(f). Capon (1970) gave this form with C(f) instead of H(f). To implement the filter, we chose a section of noise immediately before the event to estimate H(f). Then using this estimate, we apply the filter to the signal. There are two assumptions: (1) the noise does not change its statistical characteristics (stationarity) (2) the model is a good representation of these characteristics. A 14th order polynomial model was used in this study.

Figures 2, 3 and 4 show an example. The raw data traces are shown in Figure 2 with the 30 min data adaptation window (noise window) shown. Figure 3 shows a typical trace within the noise window filtered to 0.1 Hz LP, a simple beam at 3.5 km/sec, and the output of the undistorting group filter. The undistorting group filter suppresses the noise by about a factor of three relative to the simple beam. Figure 4 shows the application of the filter to the data; the three traces are as for Figure 3 but apply to the signal. The end of the noise adaptation window is shown on the Figure, the noise suppression for the undistorting group filter trace continues at a high level up to an hour afterward. The time signature of the surface waves is very similar on the beam and filter traces, indicating that the filter does not distort the signal. These results show that assumption (1) is met and the procedure may be used to enhance surface wave signals to a higher degree than simple beamforming.

Assumption (2) appeared to be most sensitive to the length of the data adaptation window. Figure 5 shows the same data as Figure 4, but only a 15 min adaptation window to the left of the mark is shown. We see that while the filter suppresses the noise well within the adaptation window, it immediately degenerates to a performance no better than the beam outside the adaptation window. This indicates the model is not a good representation of the noise.

An additional study was to test the filter performance for different noise conditions at NORSAR. In general, the higher the noise the better the performance relative to beamforming. This indicates that strong noise is more coherent than weak noise at NORSAR.

CONCLUSIONS AND RECOMMENDATIONS

The undistorting group filter can give superior enhancement of 10-30 sec surface wave signals at arrays if about 30 min of noise before the signal is available for noise adaptation. This is true even at NORSAR, where the noise is not very coherent because of the large sensor spacing. In future work we will look at arrays with closer spacing such as LASA, GRAFENBERG, PINYON FLAT and ALIBEK.

ACKNOWLEDGEMENTS

This preliminary study was carried out while the authors were visiting the NORSAR Data Processing Center, Kjeller, Norway; one of us (AFK) received financial support from NORSAR. The assistance of Drs. Frode Ringdal (Director), Svein Mykkeltveit, Jan Fyen and Tormod Kvaerna of NORSAR is gratefully acknowledged.

REFERENCES

Capon, J., Proc. IEEE v 58, p. 170, 1970.
Kushnir, A.F., V.M. Lapshin, V.I. Pinsky, and J. Fyen, Bull. Seis. Soc. Am., v. 80, p. 1934, 1990.
Patton, H.J., and W.R. Walter, Geophys. Res. Letts., v 20, p. 277, 1993
Woods, B.B., Kedar, S., and D.V. Helmberger, Bull. Seis. Soc. Am., v. 83, p. 1167, 1993.

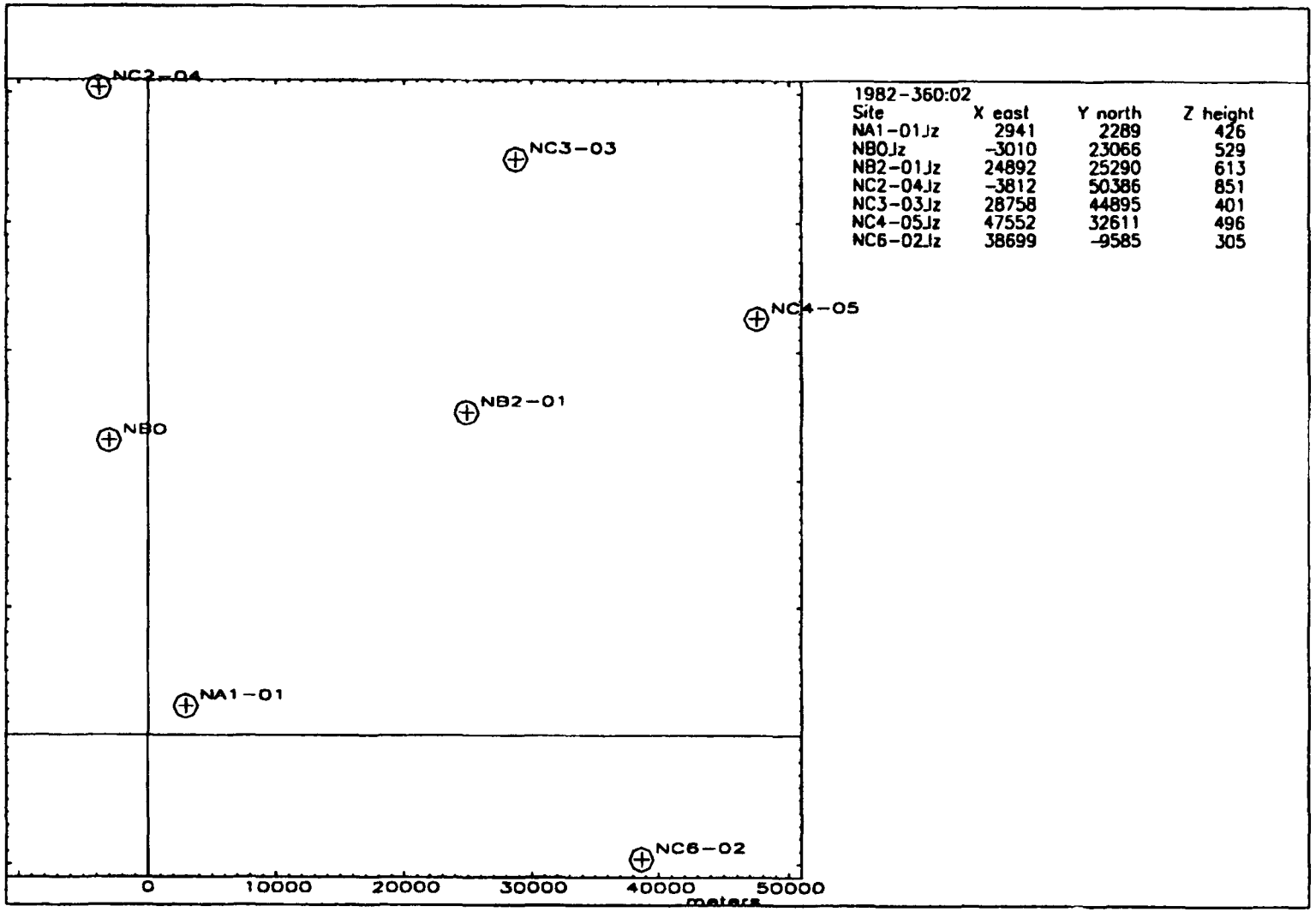


Fig. 1: NORSAR LP Array.

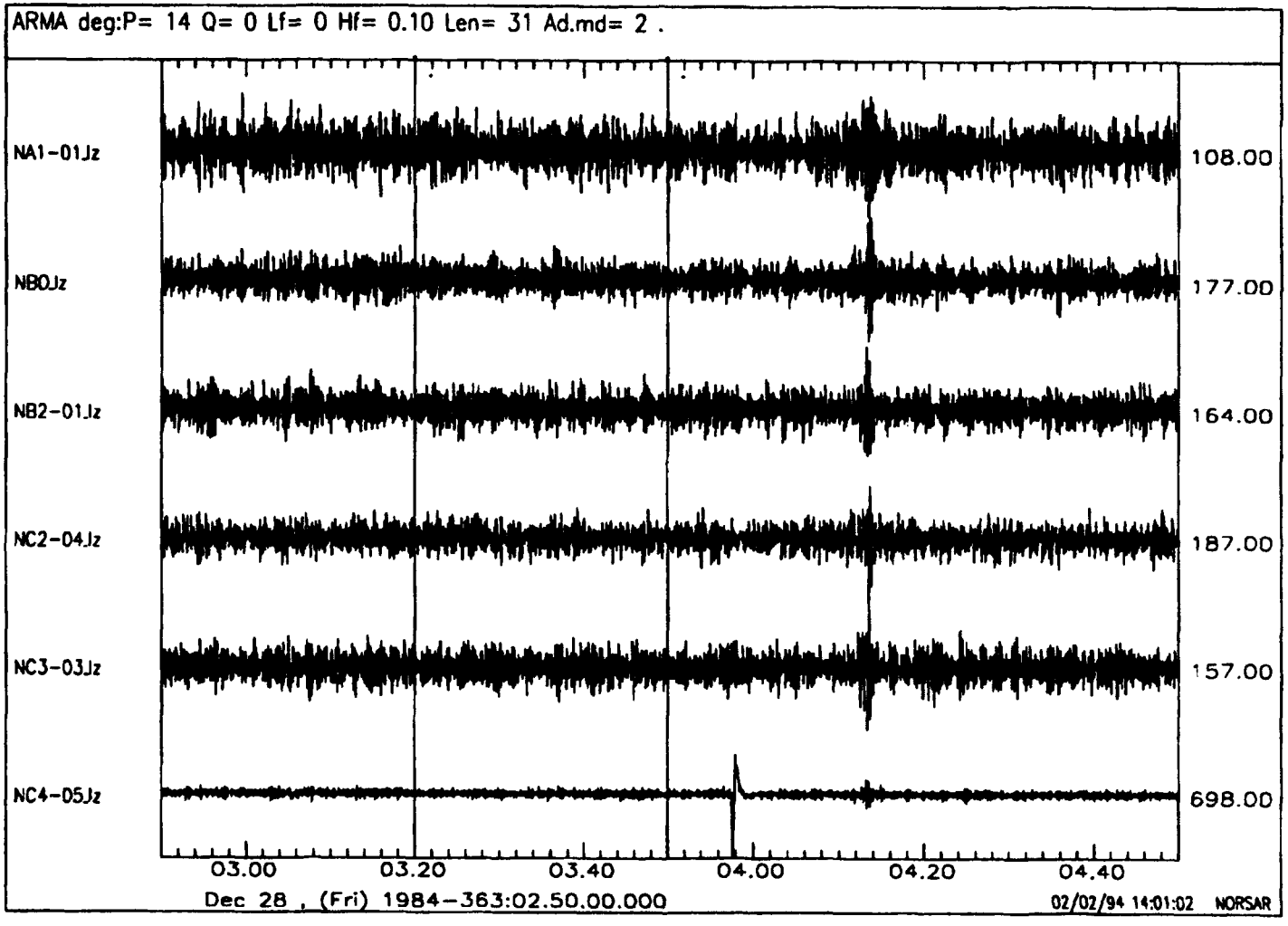


Fig. 2: Array seismograms from presumed East Kazakh test at NORSAR LP Array. Window is data adaptation window.

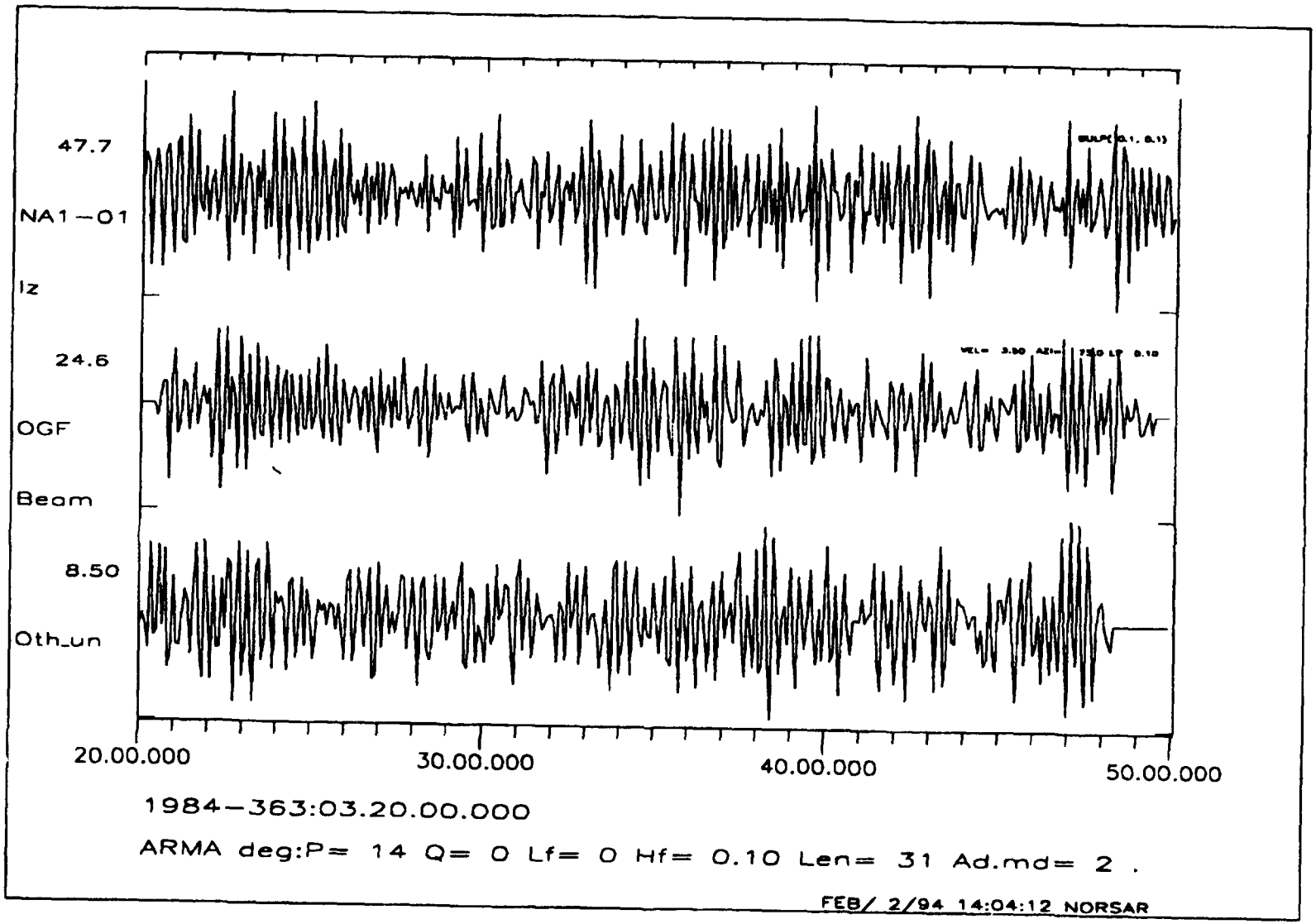


Fig. 3: Application of undistorting group filter to adaptation window in Fig. 2. Top trace, array seismogram for element NA1-01 filtered to 0.1 Hz LP; second trace, simple beam; third trace, filter output.

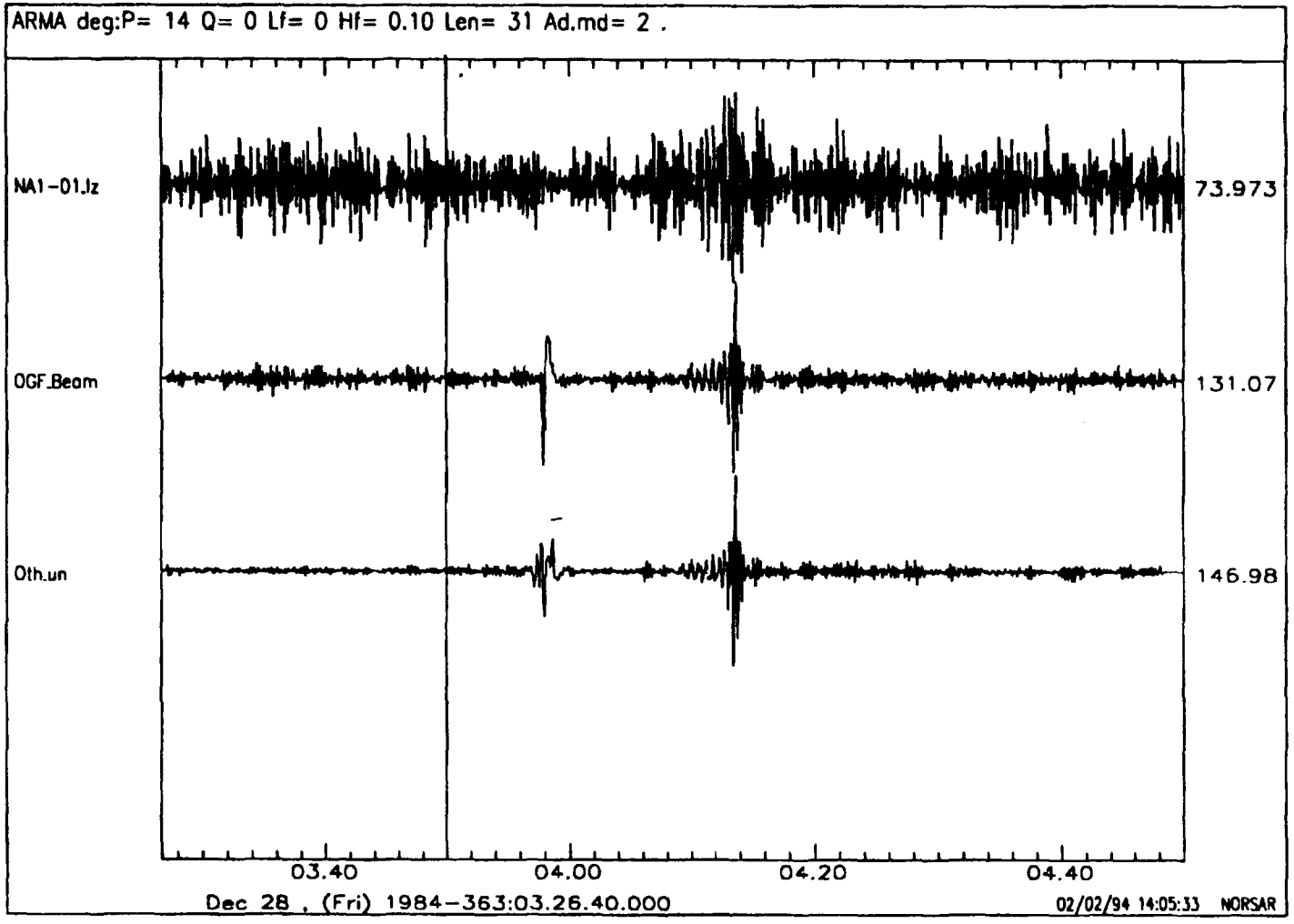


Fig. 4: Application of filter to data in Fig. 2 with data adaptation window in Fig 2. Traces as for Fig. 3.

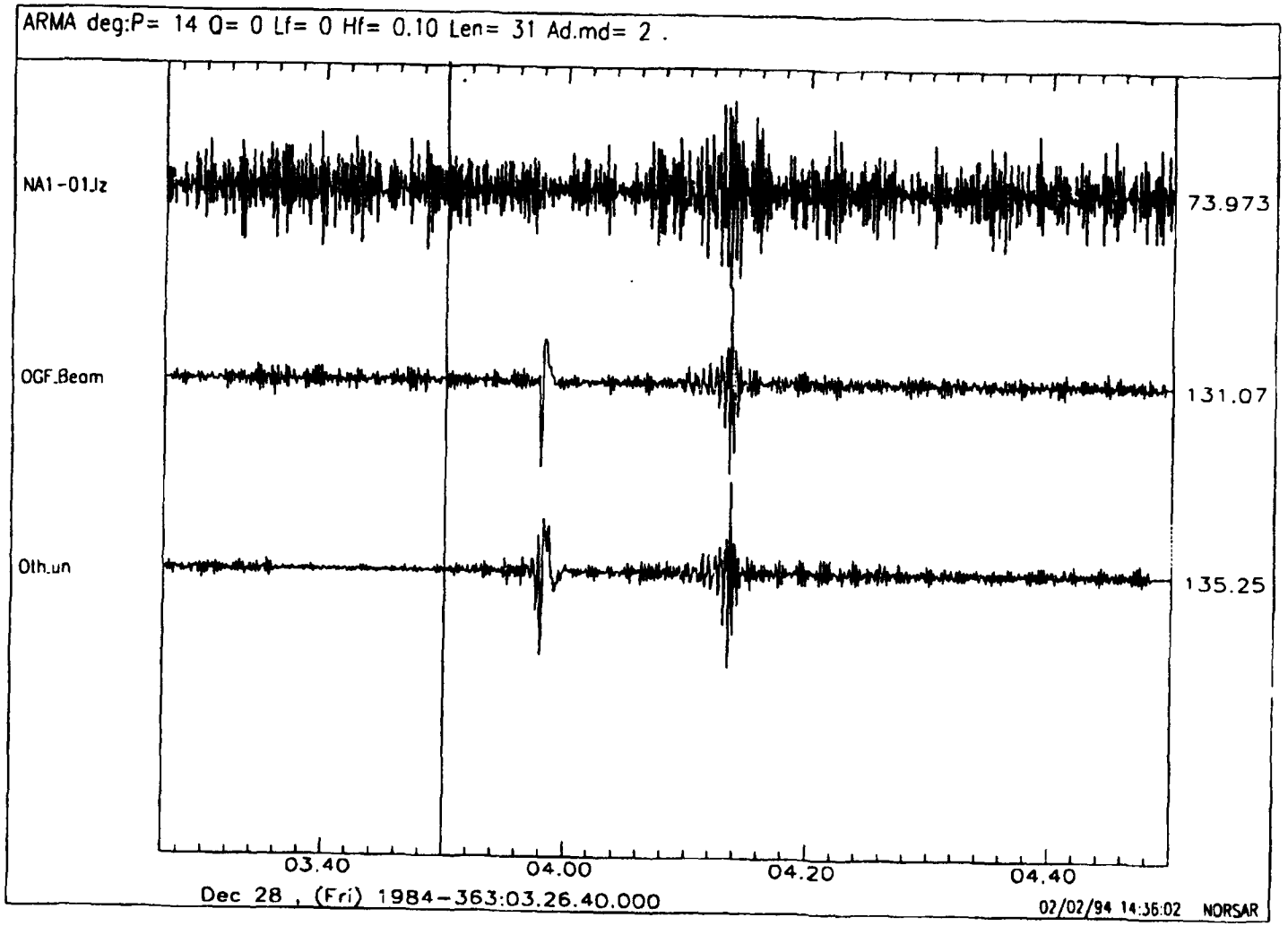


Fig. 5: Application of filter to data of Fig. 2, but with only 15 min data adaptation window. Vertical line is left edge of data adaptation window. Traces as for Figs. 3 and 4.

SEISMIC WAVE PROPAGATION IN SOUTH AMERICA

Lawrence A.Drake and Estela Minaya Ramos
Observatorio San Calixto
Casilla 12656
La Paz, BOLIVIA

Contract F49620-93-1-0433

Objective

Whitman and his coworkers (1992) have noted that for a portable seismic network deployed in Jujuy Province (24°S, 65°W), Argentina, P and S waves of short period propagate beneath the plateau much more efficiently from the north and northwest than from the west and south; likewise, Sn phases from regional crustal earthquakes in the Subandean foreland fold-thrust belt to the north propagate efficiently to the Jujuy network, while Sn is not observed from foreland earthquakes located at similar distances to the south of the network. Whitman and his coworkers suggest that, south of approximately 22°S, the upper mantle beneath the plateau and its adjacent foreland is more highly attenuating than the upper mantle further north. Similarly, Minaya and her coworkers (1989) and Ayala (1994) have observed that,at the World-Wide Standard Seismograph Network station at La Paz, Bolivia (LPB; 16°32'S, 68°06'W; 3292 m), there is much greater attenuation of Lg waves of periods of approximately 1.2 s from the Western Cordillera to the west of La Paz than from the Brazilian and Guyana Shields to the east; Ayala (1994) gives different formulas for Lg equivalent body wave magnitude and different exponential decays of the maximum amplitude of the Lg waves with distance (0.2/degree from the west, and 0.09/degree from the east). The Western Cordillera appears to be highly attenuating at these short periods. Isacks (1988), Ayala (1991) and Cahill and Isacks (1992) have mapped the warping of the Nazca plate under South America. It appears to be approximately flat from the Bucaramanga (07°08'N, 73°09'W) nest of earthquakes of intermediate depth in northern Columbia to 14°S in southern Peru. At 15°S there is a sharp flexure of the plate and its dip under Bolivia is approximately 30°. There is a gradual transition southward to nearly horizontal dip in the region from 28°S to 32°S beneath western Argentina. At 33°S there is another sharp flexure of the plate to a dip of approximately 30°. In addition, there is an 'elbow' in the Peru-Chile trench near Arica (18°29'S, 70°20'W) and this causes extreme complexity in the structure of the Eastern Cordillera and the Subandean Zone in central Bolivia (18°S, 66°W). Vega and Buforn (1991) have investigated the focal mechanisms of earthquakes in this region. As a result of the consequent 'elbow' in the Nazca plate, there are two main bands of associated deep earthquakes, one from 06°.5S, 71°.5W, to 11°.5S, 71°.0W, in western Brazil and southern Peru, and the other from 19°.0S, 63°.5W, to 28°.5S, 63°.0W, in southern Bolivia and northern Argentina (Okal et al., 1994). On 9 June

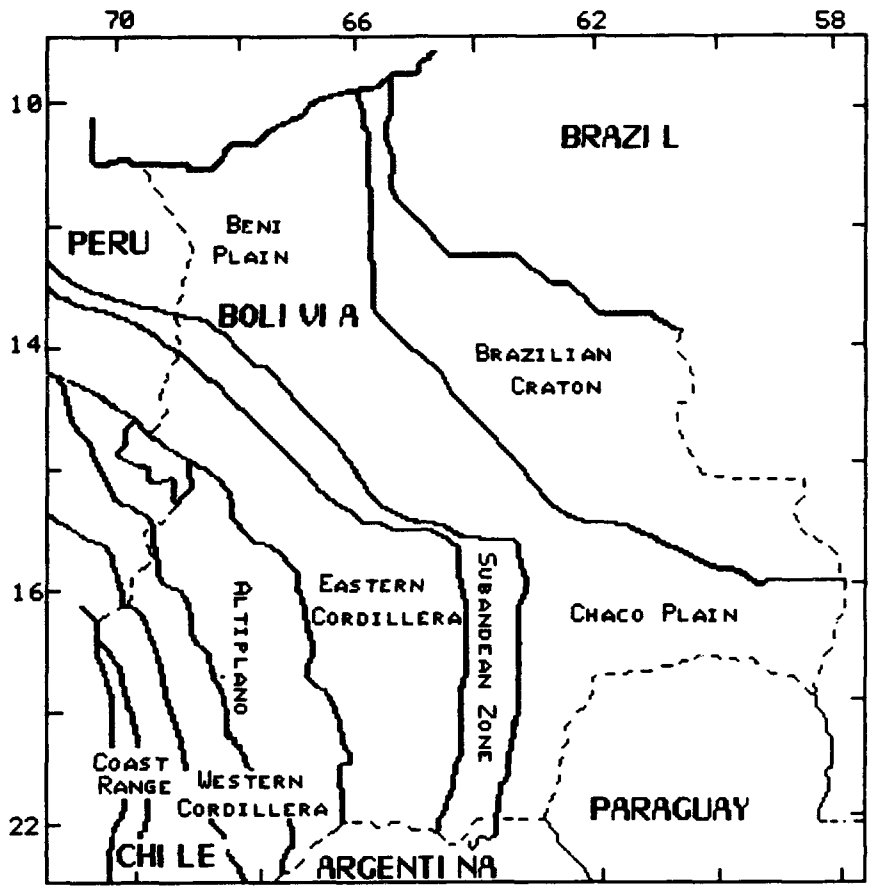


Figure 1. Morphological zoning of the Central Andes in the region of Bolivia.

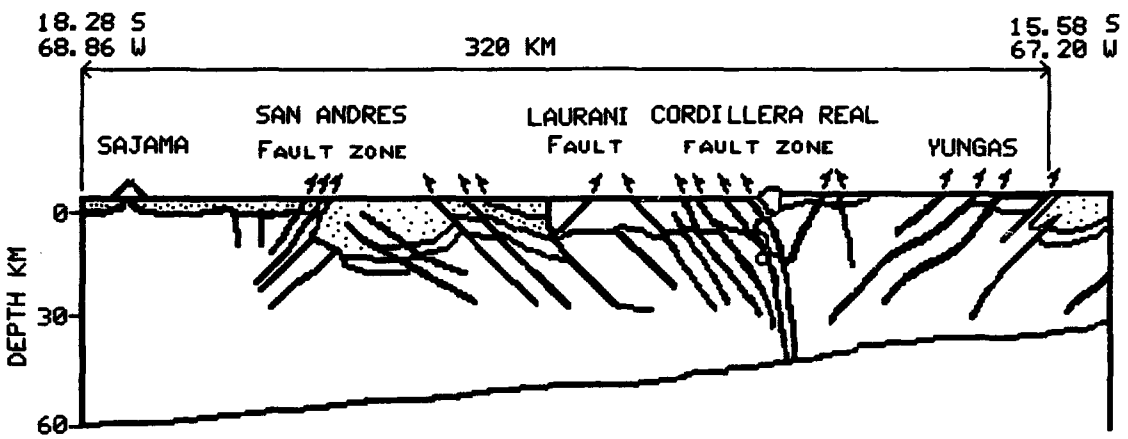


Figure 2. Geological and structural cross section northeast from Nevado Sajama.

1994, a deep event that was felt as far away as Toronto, in Canada, occurred between these zones (Harvard centroid time and location, 00:33:44.4, 13°.81S, 67°.20W, depth 657.4 km; Mw 8.3). The aim of this research is to study this extraordinary region in Bolivia and to its northwest and south, and model the propagation of Rayleigh and Love waves of long and short periods by the finite element method in the frequency domain.

TABLE 1

MODEL OF THE EASTERN CORDILLERA TO A DEPTH OF 920 KM

Layer thickness km	Compressional velocity km/s	Shear velocity km/s	Density g/cm³	Poisson's ratio	Quality factor Q
4.0	5.00	2.97	2.70	0.227	30
7.0	5.60	3.33	2.70	0.227	40
13.0	6.00	3.51	2.75	0.240	50
8.0	6.10	3.52	2.75	0.250	60
15.0	6.20	3.58	2.75	0.250	80
6.0	6.50	3.75	2.83	0.251	100
6.0	5.90	3.41	2.83	0.249	50
6.0	6.50	3.75	2.95	0.251	200
10.0	8.10	4.74	3.24	0.240	400
10.0	8.10	4.74	3.30	0.240	400
10.0	8.10	4.74	3.35	0.240	400
14.0	8.10	4.74	3.36	0.240	400
15.0	8.10	4.74	3.37	0.240	400
20.0	7.85	4.46	3.38	0.262	80
20.0	7.85	4.46	3.39	0.262	80
20.0	7.85	4.46	3.40	0.262	80
20.0	7.85	4.46	3.41	0.262	80
20.0	7.85	4.46	3.43	0.262	80
26.0	8.62	4.54	3.44	0.308	143
26.0	8.69	4.58	3.46	0.308	143
34.0	8.77	4.62	3.47	0.308	143
34.0	8.87	4.67	3.49	0.308	143
40.0	8.97	4.67	3.52	0.307	143
40.0	9.08	4.79	3.54	0.307	143
50.0	9.60	5.09	3.80	0.304	143
50.0	9.70	5.18	3.86	0.301	143
50.0	9.80	5.26	3.92	0.298	143
50.0	9.89	5.35	3.98	0.293	143
50.0	9.99	5.43	4.05	0.290	143
50.0	10.97	6.13	4.39	0.273	312
50.0	11.05	6.17	4.42	0.273	312
50.0	11.14	6.21	4.45	0.275	312
50.0	11.22	6.25	4.48	0.275	312
50.0	11.30	6.28	4.51	0.277	312

Research Accomplished

The Bolivian Andean Cordillera forms part of the Andean chain, which originated in two major orogenic cycles of the Phanerozoic, the Late Precambrian-Paleozoic Preandean Cycle and the Mesozoic-Cenozoic Andean Cycle (Omarini et al., 1991). During the Preandean Cycle, huge depocenters developed successively further westward, from the Subandean Ranges in Bolivia and northern Argentina to the Longitudinal Valley and Coastal Cordillera in Chile (Figure 1; Castaños and Rodrigo, 1978, p. 41; Instituto Geográfico Militar, 1985, p. 166; Ahlfeld, 1972, p. 40). During the Andean Cycle, four magmatic

TABLE 2

TOP 20 M OF MODEL OF THE ALTIPLANO REGION

Layer thickness km	Compressional velocity km/s	Shear velocity km/s	Density g/cm³	Poisson's ratio	Quality factor Q
7.0	4.50	2.70	2.50	0.219	20
7.0	5.00	2.97	2.70	0.227	30
6.0	5.40	3.21	2.70	0.227	40

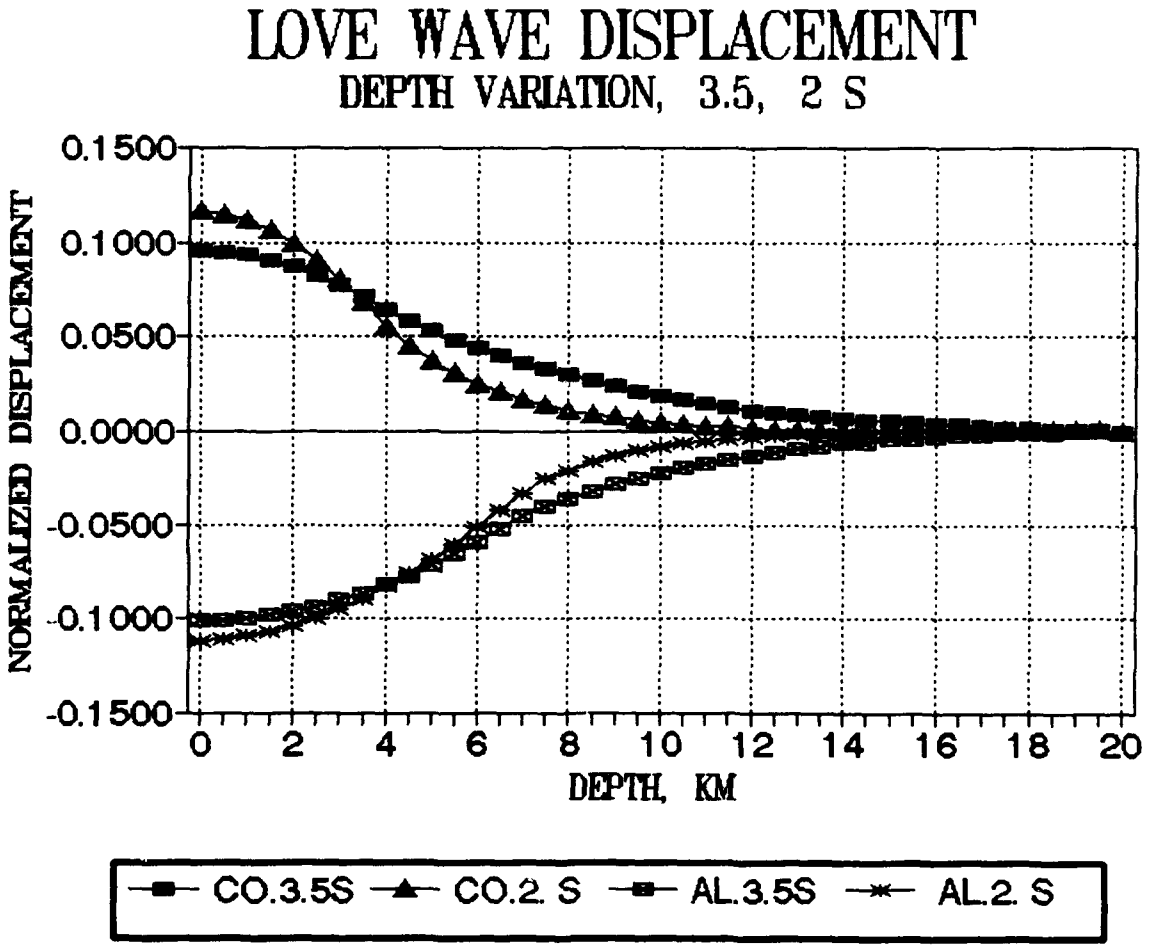


Figure 3. Normalized variation of fundamental Love mode displacement with depth at periods of 3.5 s and 2.0 s for the regions of the Eastern Cordillera and the Altiplano.

arc systems developed successively eastward: a Jurassic-Early Cretaceous arc in the Coastal Cordillera, a Mid-Cretaceous arc in the Longitudinal Valley, a Late Cretaceous-Paleogene arc in the Chilean Precordillera and the Miocene-Holocene arc in the Western Cordillera (Dorbath et al. 1993). In the region of Main Andean Thrust, between the Eastern Cordillera and the Subandean Ranges in northern Bolivia, there is overlap of approximately 230 km of Neogene age (Roeder, 1988; cf. Allmendinger et al., 1990). This is what keeps the marine

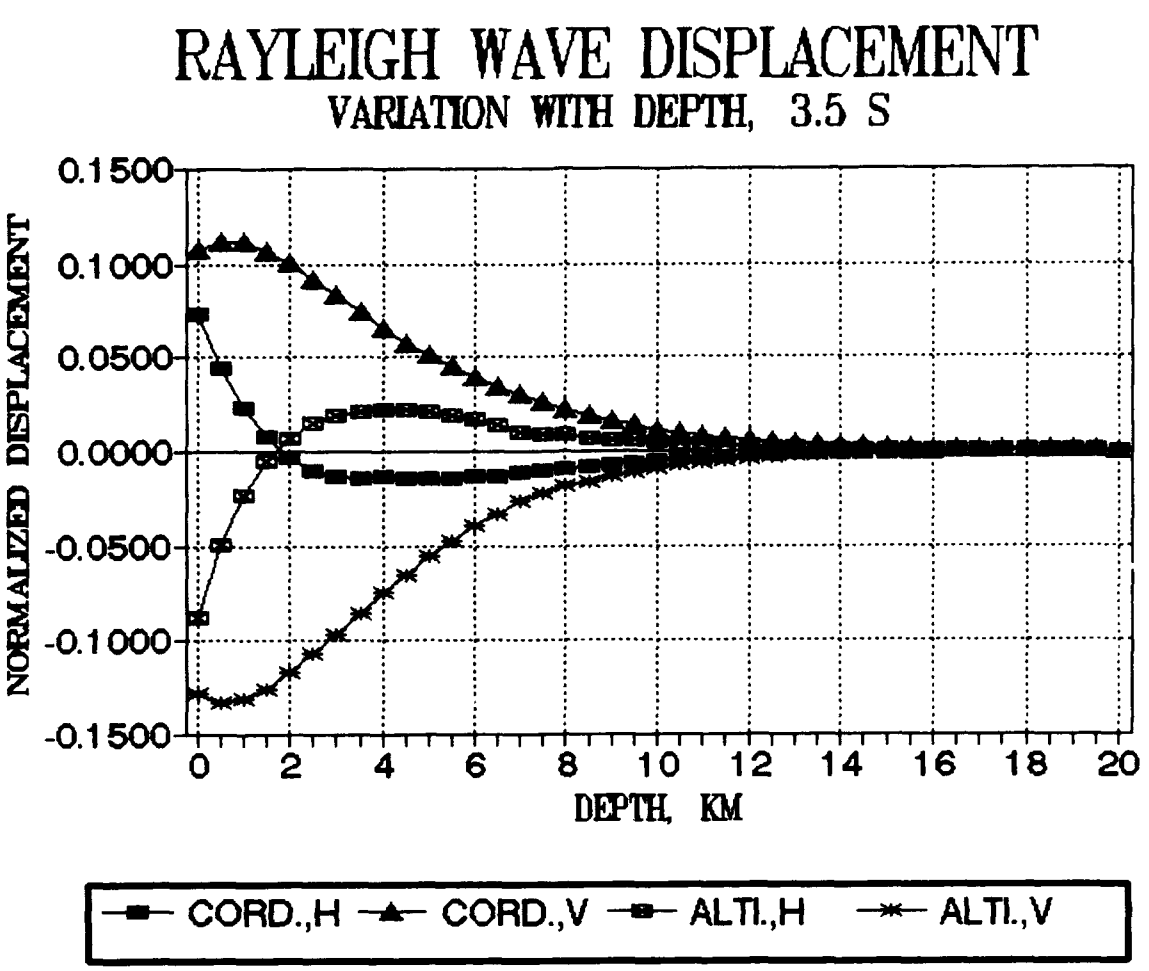


Figure 4. Normalized variation of horizontal and vertical fundamental Rayleigh mode displacement with depth at a period of 3.5 s for the regions of the Eastern Cordillera and the Altiplano.

limestones near Copacabana on Lake Titicaca and the tightly folded Silurian diamictites, arenites, quartzites and lutites, exposed abundantly in road cuts between Cochabamba and Caracollo, at an elevation of approximately 3800 m above sea level. The Main Andean Thrust appears to be steeply dipping and the Cordillera Real fault system, at the southwestern border of the Cordillera Real, marks a subvertical boundary, dipping slightly to the southwest, which, from the surface down to a depth of 140 km, separates two strongly contrasting velocity units. The depth to the Moho below the Altiplano is approximately 60 km and, below the Eastern Cordillera, is approximately 50 km. The propagation of Love and Rayleigh waves, including Lg and Rg waves, along the profile of Figure 2 has been modelled by the finite element method (Lysmer and Drake, 1972; Drake and Bolt, 1989). The horizontally layered structures representing the regions of the Eastern Cordillera and the Altiplano are shown in Tables 1 and 2 (Ocola et al., 1971; James, 1971; Wigger et al., 1991; Dziewonski and Anderson, 1981; Dziewonski et al., 1975; Morelli and

Dziewonski, 1993). The normalized variation of Love wave displacement with depth (Lysmer and Drake, 1972) at periods of 3.5 s and 2.0 s for the regions of the Eastern Cordillera and the Altiplano is shown in Figure 3. The normalized variation of Rayleigh wave horizontal and vertical displacement with depth (Lysmer and Drake, 1972) at a period of 3.5 s for the regions of the Eastern Cordillera and the Altiplano is shown in Figure 4.

Conclusions and Recommendations

It can be seen from the shapes of the fundamental Love modes in Figure 3 and from the shapes of the fundamental Rayleigh modes in Figure 4 that the models of the regions of the Eastern Cordillera and the Altiplano in Bolivia so far published do not account for much change in these waves when they cross these regions. Absorption of Lg in the Western Cordillera is probably connected with heat and the volcanism there since the beginning of the Neogene (Omarini et al., 1991). At present, an enormous amount of seismic investigation is taking place into the irregular earth structure in the region of Bolivia (Beck et al., 1994; Soler, personal communication; Okal et al., 1994). The results of this investigation will need to be incorporated into finite element and other models in order to understand better the propagation of seismic waves in the region of Bolivia.

References

Ahlfeld, F.E. (1972). Geología de Bolivia, Amigos del Libro, Cochabamba.

Allmendinger, R.W., Figueroa, D., Snyder, D., Beer, J., Mpodozis, C. and Isacks, B.L. (1990). Foreland shortening and crustal balancing in the Andes at 30°S latitude, Tectonics 9, 789-809.

Ayala, R.R. (1991). Deriva continental y tectónica de placas con relación a la evolución de la placa de Nazca y los Andes Centrales, Revista: Academia Nacional de Ciencias 6, 98-118 (Bolivia).

Ayala, R.R. (1994). Magnitud m_{bLg} para sismos sudamericanos, Revista Geofísica, Instituto Panamericano de Geografía e Historia (in press).

Beck, S., Wallace, T., Myers, S., Swenson, J., Tinker, M., Brazier, R., Silver, P., Kuehnel, R., Drake, L.A., Minaya, E., Alcala, R., Soler, P., Baby, P., Guillier, B., Zandt, G., Rock, D., Ruppert, S., Tellería, J. and Barrientos, S. (1994). A passive broadband seismic experiment in the Central Andean Cordillera: the BANJO and SEDA experiments, Asamblea Regional de Sismología en América del Sur, Brasilia, Brasil (Abstract).

Cahill, T. and Isacks, B. (1992). Seismicity and shape of the subducted Nazca plate, J. Geophys. Res. 97, 17,503-17,529.

Castaños, A. and Rodrigo, L.A. (1978). Sinopsis Estratigráfica de Bolivia: Parte de Paleozoico, Academia Nacional de Ciencias de Bolivia, La Paz.

Dorbath, C., Granet, M., Poupinet, G. and Martinez, C. (1993). A teleseismic study of the Altiplano and the Eastern

Cordillera in northern Bolivia: new constraints on a lithospheric model, J. Geophys. Res. 98, 9825-9844.
Drake, L.A. and Bolt, B.A. (1989). Finite element modelling of surface wave tranmission across regions of subduction, Geophys. J. Int. 98, 271-279.
Dziewonski, A.M. and Anderson, D.L. (1981). Preliminary Earth reference model, Phys. Earth planet. Interiors 25, 297-356.
Dziewonski, A.M., Hales, A.L. and Lapwood, E.R. (1975). Parametrically simple Earth models consistent with geophysical data, Phys. Earth planet. Interiors 10, 12-48.
Instituto Geográfico Militar (1985). Atlas de Bolivia, Geomundo, Barcelona.
Isacks, B.L. (1988). Uplift of the Central Andean Plateau and bending of the Bolivian Orocline, J. Geophys. Res. 93, 3211-3231.
James, D.E. (1971). Andean crustal and upper mantle structure, J. Geophys. Res. 76, 3246-3271.
Lysmer, J. and Drake, L.A. (1972). A finite element method for seismology, in Methods in Computational Physics (B.A. Bolt, ed.), Academic Press, New York, 181-216.
Minaya, E., Ayala, R.R., Alcócer, I. and Cabré, R. (1989). Ondas Lg de sismos sudamericanos, Revista Geofísica, Instituto Panamericano de Geografía e Historia 31, 115-146.
Morelli, A. and Dziewonski, A.M. (1993). Body wave traveltimes and a spherically symmetric P- and S-wave velocity model, Geophys. J. Int. 112, 178-194.
Okal, E., Kirby, S., Engdahl, E.R. and Huang W.-C. (1994). Deep earthquakes beneath South America and their physical significance, Asamblea Regional de Sismología en América del Sur, Brasilia, Brasil (Abstract).
Ocola, L.C., Meyer, R.P. and Aldrich, L.T. (1971). Gross crustal structure under Peru-Bolivia Altiplano, Earthquake Notes 42 (3-4), 33-48.
Omarini, R., Reutter, K. and Bogdanic, T. (1991). Geological development and structures,in Central Andean Transect, Nazca Plate to Chaco Plains: Southeastern Pacific Ocean, Northern Chile and Northern Argentina, Global Geosience Transect 6 (R. Omarini and H.-J. Götze, eds.), American Geophysical Union, Washington, 5-12.
Roeder, D. (1988). Andean-age structure of Eastern Cordillera (Province of La Paz, Bolivia), Tectonics 7, 23-39.
Vega, A.J. and Buforn, E. (1991). Focal mechanism of intraplate earthquakes in Bolivia, South America, Pure and Applied Geophysics (PAGEOPH) 136, 449-458.
Whitman, D., Isacks, B.L., Chatelain, J.-L., Chiu, J.-M. and Perez, A. (1992). Attenuation of high-frequency seismic waves beneath the Central Andean Plateau, J. Geophys. Res. 97,19,929-19,947.
Wigger, P.J., Araneda, M, Giese, P., Heinsohn, W.-D., Röwer, P., Schmitz, M. and Viramonte, J. (1991). The crustal structure along the central Andean transect derived from seismic refraction investigations, in Central Andean Transect, Nazca Plate to Chaco Plains: Southeastern Pacific Ocean, Northern Chile and Northern Argentina, Global Geosience Transect 6 (R. Omarini and H.-J. Götze, eds.), American Geophysical Union, Washington, 13-19.

Elastic and Anelastic Structure Beneath Eurasia

Göran Ekström, Adam M. Dziewonski, Wei-jia Su and Gideon P. Smith

Department of Earth and Planetary Sciences
Harvard University
Cambridge, MA 02138

Contract No. F49620-92-J-0392

Objective

We are adapting the seismic tomographic techniques developed in global scale studies to the regional scale problem of mapping the elastic and anelastic material properties beneath Eurasia. The first objective of this research is to obtain a tomographic seismic velocity model for the structure beneath Eurasia with a horizontal resolution corresponding to at least $l = 20$, consistent with the widest possible range of seismological observations. A second objective is to evaluate the utility of such three-dimensional models in event location algorithms.

Research Accomplished

In order to achieve reliable higher resolution models, our approach is to develop new datasets and to gradually modify the model parameterizations so as to resolve increasingly more detailed structures. We validate the models by performing predictive calculations of independent observations, such as absolute event locations and other seismological datasets.

Over the past year, we have made progress in four main areas:

(1) We have obtained a spherical harmonic degree 12 global mantle model of P and S wave velocities based on waveform data, ISC travel times, and new waveform measurements of absolute and differential travel times.

(2) By relocation of a set of large explosions with known hypocentral coordinates, we have verified that the new 3-dimensional model significantly improves teleseismic locations with respect to those obtained from the standard travel time tables IASP91, JB, and PREM.

(3) With the purpose of better constraining the velocities in the top 200 km of the upper mantle, we have collected a very large dataset of Love and Rayleigh dispersion measurements in the period range 35–140 seconds.

(4) The new dispersion observations have been used together with previous datasets in a three-dimensional, $l \leq 20$ inversion for S-wave velocities in the upper mantle.

Degree 12 P and S model - A joint dataset of ISC and digital data were used to simultaneously invert for P and S models of the Earth. This type of joint inversion may provide answers to the question of the nature of elastic heterogeneity in the Earth's mantle. The deviation of the ratio $\gamma(r) = (d \ln v_S)/(d \ln v_P)$ from a proportionality constant varying only as a function of r would indicate a chemical rather than thermal cause of heterogeneity. It has been known for some time that the P and S velocity anomalies are correlated. In a joint

inversion which uses this as an a priori weak assumption, it possible to obtain realistic and practically useful models of P wave heterogeneity even in areas where P wave coverage is scarce.

The data used in the joint inversion include: (1) direct P and PKP arrivals reported in the ISC Bulletins for years 1964 to 1990; (2) body wave and mantle wave waveforms; (3) travel-times of S and SS phases measured from long-period seismograms and (4) the differential travel-times of $SS - S$ and $ScS - S$. For the starting model we assumed that the ratio $d\ln v_S/d\ln v_P$ is constant; a proportionality of 1.85 seems to be consistent with most of the data. Figure 1 shows a cross section through the Earth and the variations in P and S velocity mapped in the model PS12WM13. There is a fairly good overall correlation between the P and S velocity perturbations, but the proportionality coefficient is greater than the starting value in the upper mantle as well as in the lowermost mantle.

The effect of 3-dimensional Earth structure on event locations - Teleseismic and regional travel times are affected by elastic heterogeneity on many length scales. It will continue to be difficult to deterministically account for the smaller scale structures in travel time calculations, but an important question remains whether larger scale structure, which can be mapped by the methods described here, contribute significantly to the travel time residual patterns. A second question is whether any systematic location biases exist which can be removed by properly accounting for large scale heterogeneity in the location algorithm. Figure 2 shows that the effect of three-dimensional variations in P wave velocities, as described by the model PS12WM13, is significant at teleseismic distances, and that P residuals can range up to ± 2 seconds in the teleseismic distance range.

In order to investigate whether we can improve event locations using PS12WM13, we extracted ISC travel times for 26 explosions with known locations and origin times and relocated these in four different Earth models: JB, PREM, IASP91, and the three-dimensional model PS12WM13. The r.m.s. difference between the known origin time and location and those predicted by individual models is shown in the Table below. Both the best origin times and the best locations are found using the PS12WM13 model.

Model	*rms misfit to known origin time (s)*	*rms misfit to known location (degrees)*
JB	2.3	0.098
PS12WM13	0.7	0.076
PREM	1.0	0.106
IASP91	0.9	0.098

Table 1. Root mean square difference between known hypocentral parameters and those found by inverting traveltimes using a particular velocity model.

The improvement in location is also demonstrated in Figure 3, which shows the mislocation due to the PS12WM13 model versus that due to the PREM model for each of the explosion events. The location errors are systematically lower using the PS12WM13 model. The IASP91 tables, which were specifically produced to update the JB tables, give locations no closer than those found by the JB tables.

New dispersion measurements and a degree 20 model of the upper mantle - We have developed an new automated matched filter technique for measuring the amplitude and phase of fundamental mode surface waves. Using CMT solutions for 4 years and data from

the digital stations around the world (GSN, GEOSCOPE, CDSN, etc.) we have collected more than 10,000 good quality $R1$ and $G1$ dispersion and amplitude measurements. We have inverted these data for high resolution phase velocity maps up to spherical harmonic degree 36. We have also derived a new S wave velocity model, S20U7L5, for the Earth's upper mantle parameterized in terms of spherical harmonics up to degree 20 and radially by Chebyshev polynomials up to degree 7. In addition to the surface wave data, we have also included other S wave sensitive data such as waveforms and traveltimes. The degree 20 model shows many of the features seen in previous tomographic images, but with sharper horizontal definition. The deep expression of continental shields is the most prominent anomaly in the top of the mantle, but the new model also confirms the expression of mid-oceanic ridges as slow anomalies through the top 200 km of the mantle. Figure 4 shows the S wave velocity perturbation with respect to the global average beneath Eurasia at a depth of 75 km. A 10% variation in S velocities is seen between the stable shields and tectonically active areas. The new model shows greater velocity variations in the uppermost mantle than our previous models, and provides a good fit to the surface wave dispersion data, which are highly sensitive to heterogeneity at these depths. Figure 5 shows a comparison between observed and predicted phase anomalies for Love waves at 45 seconds period.

Conclusions and Recommendations

By combining a large number of diverse seismological observations, we have made progress towards obtaining higher resolution tomographic images of the regional scale elastic structure beneath Eurasia. Large and regional scale heterogeneity in the mantle is shown to bias seismically derived event locations, and significant improvements in locations can be achieved by correcting for known elastic heterogeneity in the Earth's mantle.

References

Dziewonski, A. M., B. H. Hager and R. J. O'Connell, Large scale heterogeneity in the lower mantle, *J. Geophys. Res.*, **82**, 239-255, 1977.

Dziewonski, A. M., Mapping the lower mantle: Determination of lateral heterogeneity in P velocity up to degree and order 6, *J. Geophys. Res.*, **89**, 5929-5952, 1984.

Ekström, G., J. Tromp, and E. W. Larson, Measurements and models of global surface wave propagation (abstract), *EOS, Trans. Am. Geophys. Un.*, **74**, 438, 1993.

Su, W.-J. and A. M. Dziewonski, Predominance of long-wavelength heterogeneity in the mantle, *Nature*, **352**, 121-126, 1991.

Su, W.-J., R. L. Woodward and A. M. Dziewonski, Deep origin of mid-oceanic ridge velocity anomalies, *Nature*, **360**, 149-152, 1992.

Su, W.-J. and A. M. Dziewonski, Joint 3-D inversion for P- and S-velocity in the mantle (abstract), *EOS, Trans. Am. Geophys. Un.*, **74**, 556, 1993.

Su, W.-J., L. Woodward and A. M. Dziewonski, Degree-12 Model of Shear Velocity Heterogeneity in the Mantle, *J. Geophys. Res.*, **99**, 6945–6980, 1993.

Woodhouse, J. H., and A. M. Dziewonski, Mapping the upper mantle: three-dimensional modeling of Earth structure by inversion of seismic waveforms, *J. Geophys. Res.*, **89**, 5953-5986, 1984.

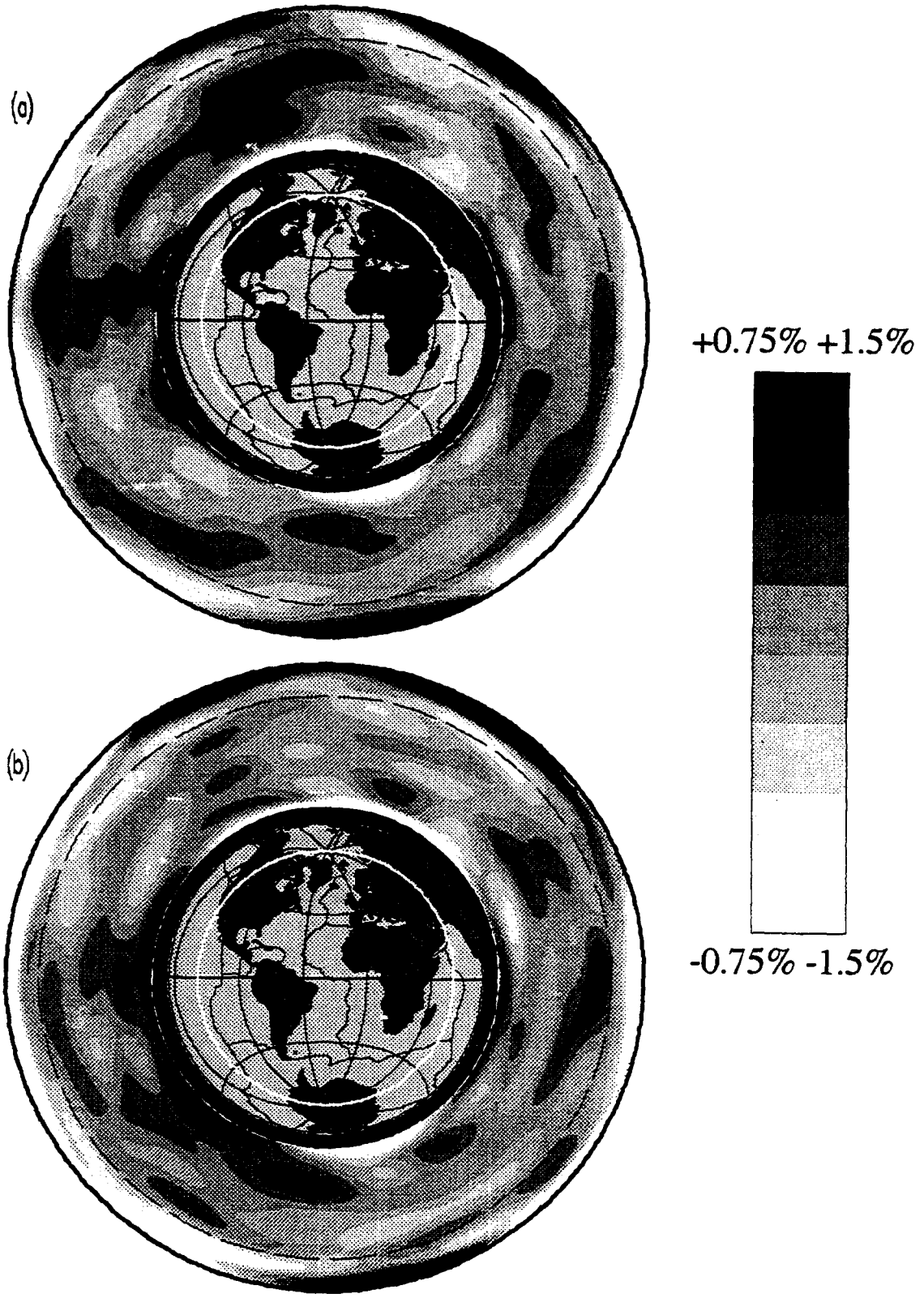


Figure 1. Cross sections through the model PS12WM13 showing the P (top) and S (bottom) wave velocity variations. The left scale ($\pm 0.75\%$) refers to P wave velocities.

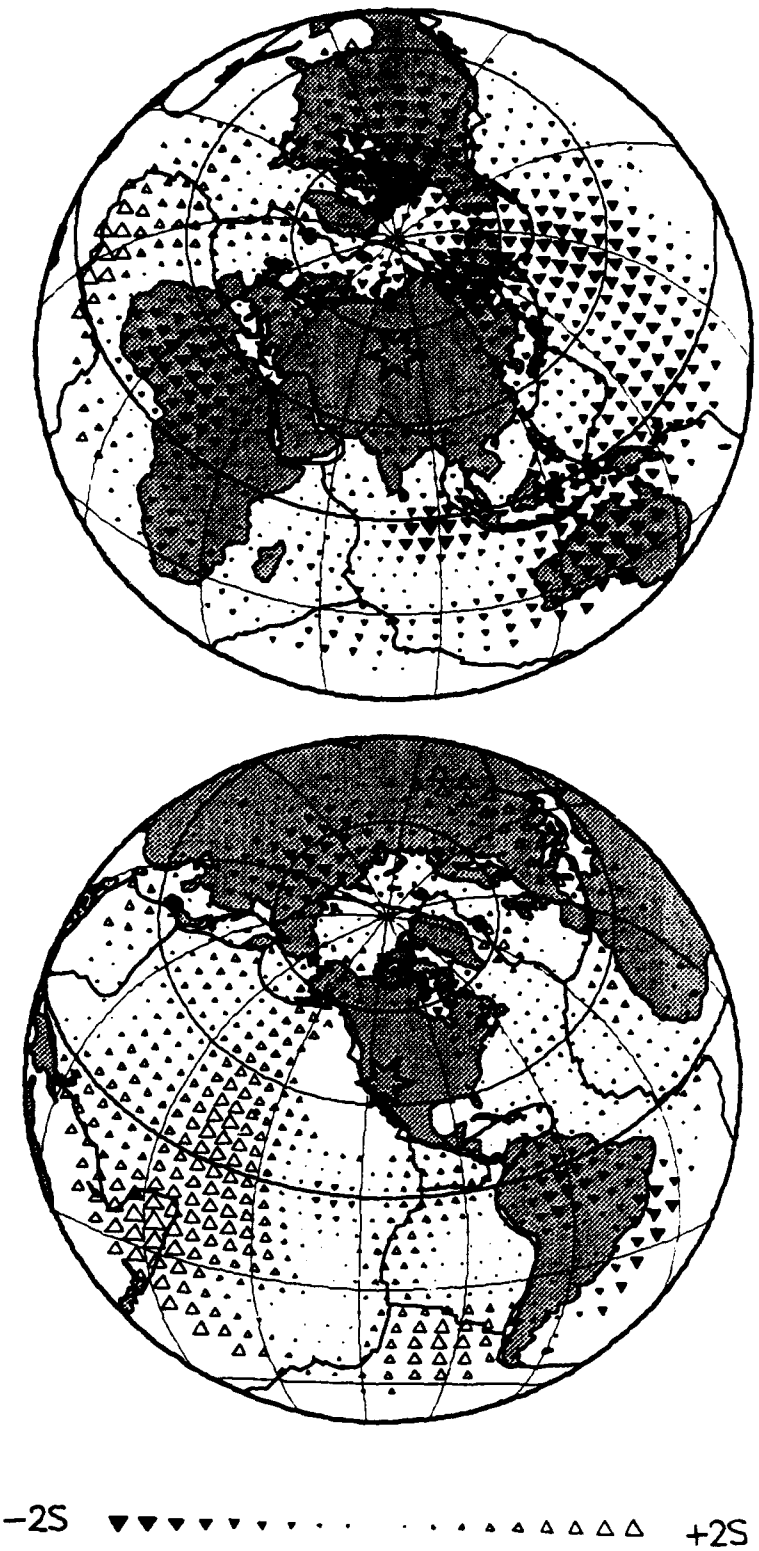


Figure 2. Azimuthal maps centered on the Kazakhstan (top) and Nevada (bottom) nuclear test sites. Triangles show the P travel time anomalies predicted by the model PS12WM13 to hypothetical stations located in the distance range 20° to 100°.

Year	*Month*	*Day*	*Time*	*Latitude*	*Longitude*	*Depth*	m_b
1977	8	10	22 00 00.10	50.956	110.983	0.0	5.0
1983	7	10	3 59 59.99	51.362	53.306	0.0	5.3
1983	7	10	4 04 59.94	51.367	53.327	0.0	5.3
1983	7	10	4 09 59.85	51.380	53.340	0.0	5.3
1983	9	24	5 00 00.03	46.783	48.315	0.0	5.2
1983	9	24	5 05 00.03	46.788	48.297	0.0	5.1
1983	9	24	5 10 00.08	46.767	48.311	0.0	5.0
1983	9	24	5 15 00.14	46.749	48.303	0.0	5.2
1983	9	24	5 19 59.93	46.754	48.289	0.0	5.4
1983	9	24	5 25 00.00	46.766	48.274	0.0	5.3
1984	7	21	2 59 59.81	51.358	53.319	0.0	5.4
1984	7	21	3 04 59.71	51.390	53.351	0.0	5.3
1984	7	21	3 09 59.84	51.371	53.337	0.0	5.4
1971	11	6	22 00 00.06	51.472	179.107	0.0	0.0
1968	1	19	18 15 00.10	38.634	-116.215	0.0	0.0
1968	4	26	15 00 00.10	37.295	-116.456	0.0	0.0
1988	7	7	15 05 30.07	37.252	-116.377	0.0	5.6
1967	5	20	15 00 00.20	37.130	-116.064	0.0	0.0
1969	9	10	21 00 00.10	39.406	-107.948	0.0	0.0
1973	5	17	16 00 00.00	39.793	-108.366	0.0	0.0
1967	12	10	19 30 00.10	36.678	-107.208	0.0	0.0
1965	7	15	14 16 08.10	37.197	-74.352	0.0	5.0
1969	11	30	3 32 59.70	49.924	78.956	0.0	6.0
1971	4	25	3 32 59.90	49.769	78.034	0.0	5.9
1972	8	16	3 16 59.80	49.765	78.059	0.0	5.0
1972	11	2	1 27 00.20	49.927	78.758	0.0	6.1

Hypocentral parameters of 26 explosions used in the relocation experiment.

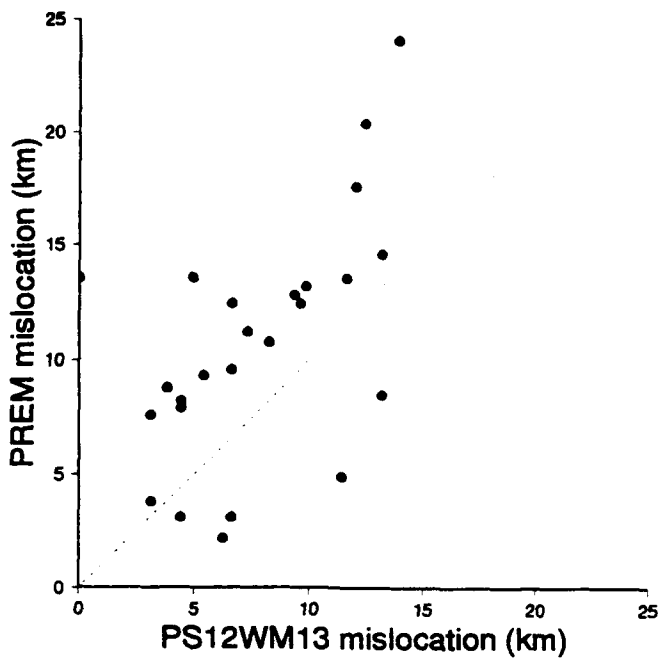


Figure 3. Mislocations from known epicenters using model PS12WM13 versus PREM.

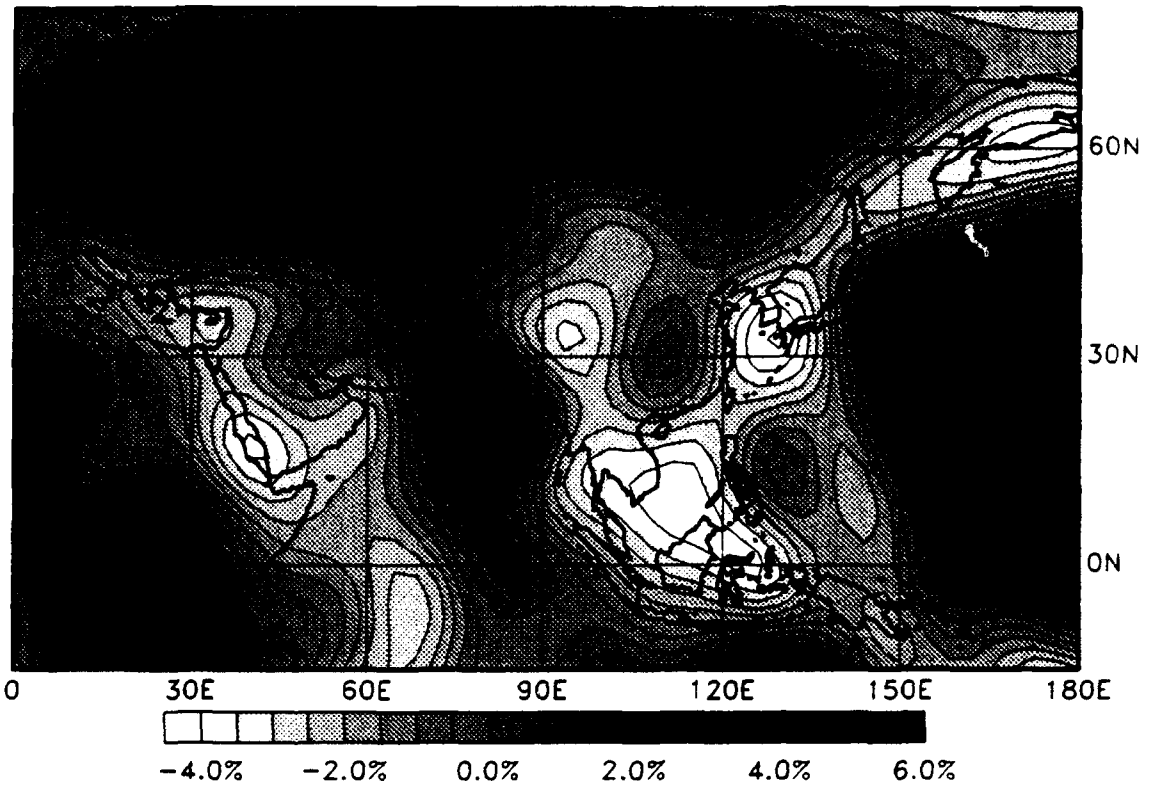


Figure 4. Shear wave velocity perturbations at 75 km depth beneath Eurasia as imaged in the new degree 20 model S20U7L5.

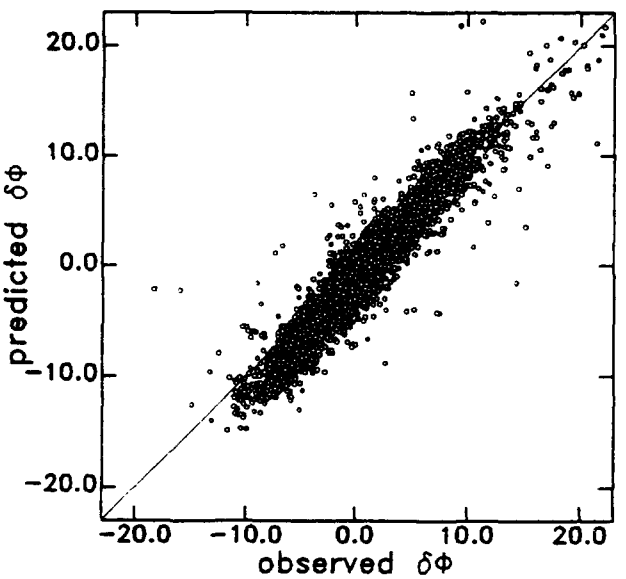


Figure 5. Observed and predicted phase anomalies for Love waves at 45 sec period. The observations are derived from 4311 globally distributed measurements of Love wave dispersion. The predictions are made from the model S20U7L5 and a global model of crustal thickness.

A Network-Accessible Geological and Geophysical Database for Eurasia, North Africa, and the Middle East: Digital Database Development for the Middle East and North Africa

Eric Fielding, Muawia Barazangi, Bryan Isacks, and Dogan Seber

Institute for the Study of the Continents (INSTOC)
Cornell University, Ithaca, NY 14853
e-mail: "eric@geology.cornell.edu" -or- "seber@geology.cornell.edu"

Contract #F19628-93-K-0030

OBJECTIVE

With the anticipated completion of multilateral comprehensive nuclear test ban and nonproliferation treaties in the near future, it is essential for the monitoring efforts that multidisciplinary information on any given region is readily available and accessible in a digital, on-line format via electronic networks for use by concerned researchers and decision makers. Our objective is to collect and organize all available seismological, geophysical, topographical, and geological datasets for the Middle East and North Africa into a digital information system that is accessible via the Internet from Cornell and can be utilized by display programs running at the International Data Center (IDC) and by other ARPA/AFOSR/DOE/AFTAC researchers. We are concentrating the area of data acquisition on the Middle East and North Africa to complement our previous work in Europe and Central Asia. We store the data in an information system (GIS). The information system is organized to extract and usefully display the information most relevant to verification and detection, and data products are released via the Internet. The work includes assembly and digitization of available datasets such as crustal reflection and refraction profiles, gravity and magnetic maps, and other geological and geophysical map information on sedimentary basins and crustal thicknesses and details of crustal structure. Digital waveforms will also be made available in the future for selected areas, including both earthquakes and chemical explosions.

RESEARCH ACCOMPLISHED

We have begun a comprehensive effort to compile and digitize information on the crustal structure of the Middle East and North Africa to expand our existing database for Eurasia developed under previous contracts. Our first work has been in the Middle East where we are locating and digitizing published data on the depth of the Moho and basement and crustal velocity and density structures, primarily as interpreted from seismic refraction, gravity, and drill hole datasets. We are also maintaining a comprehensive bibliography of all the relevant references in a computer database. All data are being stored in our Arc/Info Geographic Information System (GIS), the most widely used full-featured GIS. The format of the files being released is detailed in our recent report (Fielding and others, 1994).

We are releasing preliminary versions of our datasets as they are completed via the Internet. We continue to add more information to our database and plan to issue further interim releases as we progress toward our goal of a complete crustal structure database as well as other types of geophysical and geological databases for the Middle East and North Africa. We hope that these interim releases will be useful to and used by other ARPA/AFOSR/DOE/AFTAC researchers studying the propagation of seismic phases in the Middle East and North Africa. In the first data release, described in our Scientific Report #1 (Fielding and others, 1994), we present some of the data interpretations country by country, including Egypt, Iran, Israel, Jordan, and Saudi Arabia. In the future, we will be integrating these individual observations and our own analyses into a regional gridded database of the best available information on crustal structure and velocities. This database can then be used to derive crustal structure profiles along any path through the region to compare with observations or simulate the propagation of regional seismic phases as described in the final report of our previous contract (Fielding and others, 1993).

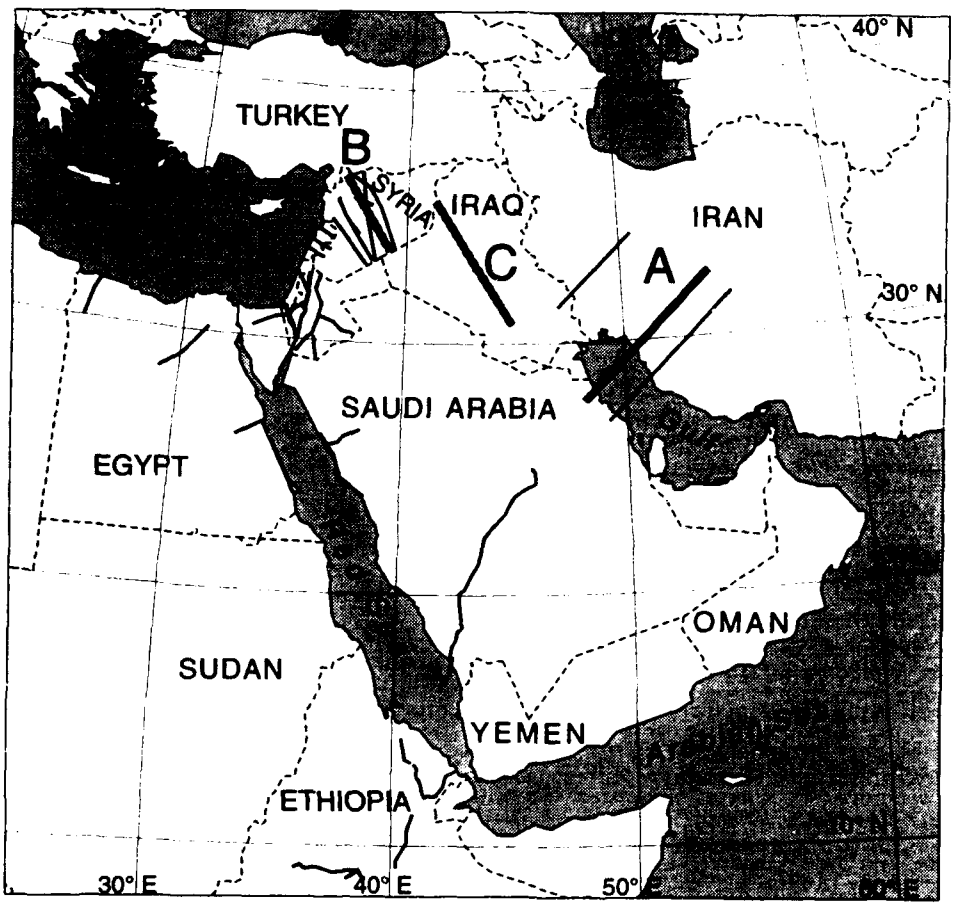


Figure 1: Map of the Middle East, showing locations of crustal profiles. Both refraction and gravity profiles are shown as *medium black lines*. *Thick gray lines* and *letters* mark locations of profiles shown in Figure 2. Coastlines are *thin solid lines*, and international borders are *dashed lines*. A ten-degree latitude-longitude grid is overlain as *very thin solid lines*. Map is in a transverse Mercator projection centered at 42°E longitude.

Figure 1 shows a number of seismic refraction lines and gravity profiles of various types that have been collected and interpreted in many of the countries of the region. We are digitizing the locations of the lines, the interpreted sections, and the velocity-depth profiles from published papers. We also digitize the interpreted contours of the depth of Moho or other crustal boundaries where they are included in the published works. Several

Gravity Profiles

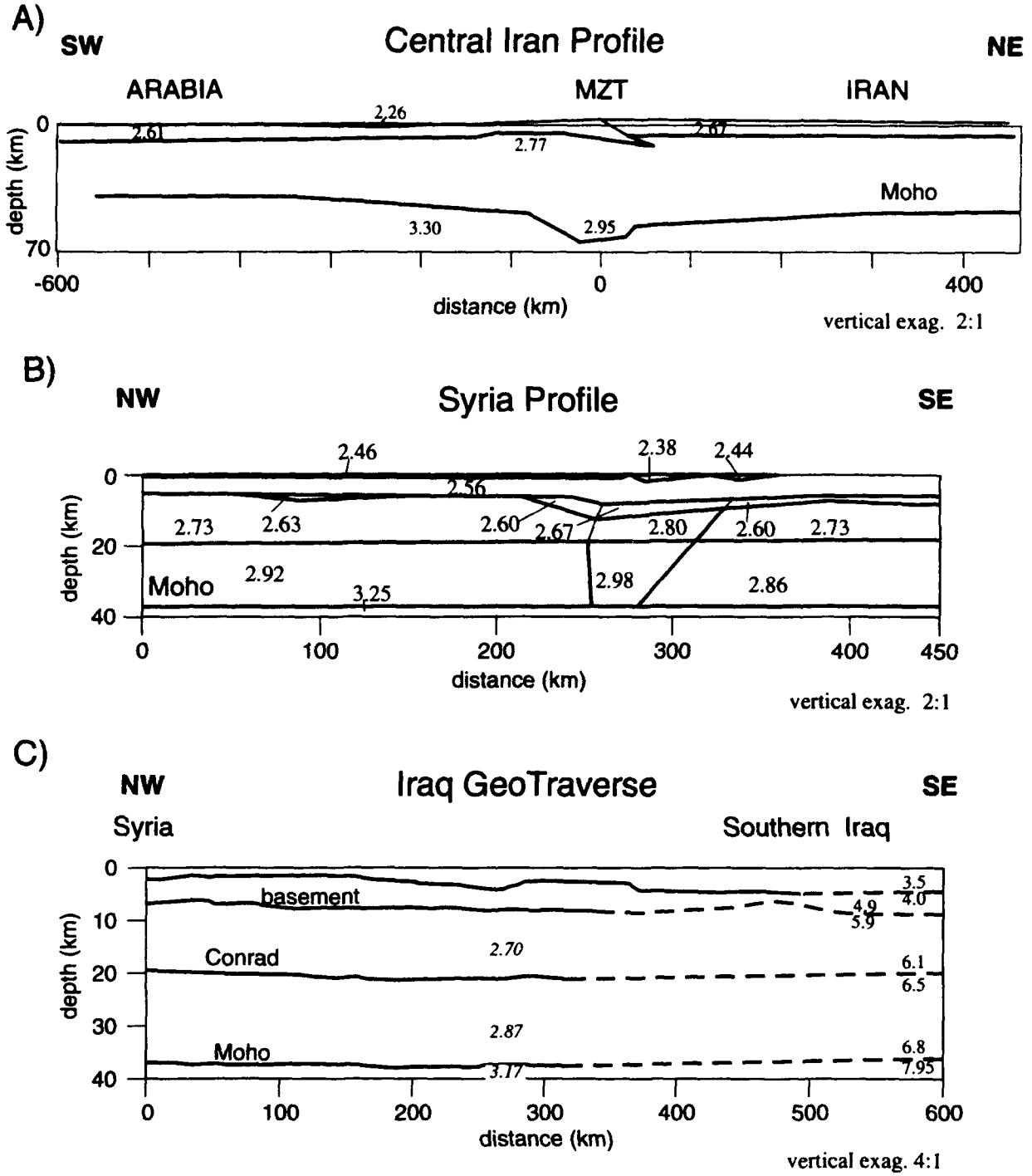


Figure 2: Three crustal density profiles interpreted from gravity data in Iran, Iraq, and Syria. The Iran profile *(a)* was digitized from Snyder and Barazangi (1986). One of the profiles interpreted at Cornell from Syria *(b)* is from Best and others (1990), and the profile through Iraq *(c)* is from the unpubliished Hussein Al-Rahim (1993). Locations are marked on Figure 1. Densities are shown in g-cm^{-3} with the crustal interfaces *(thick solid lines)*. The profiles have been vertically exaggerated for better readability.

Much data on the depth of sedimentary basins comes from the extensive petroleum exploration in the Middle East and North Africa, and we have started to digitize and incorporate some of this voluminous data into our databases. Some of this valuable data is only available at Cornell. We have digitized a preliminary map of the thickness of sedimentary cover for most of the Middle East (Figure 3), prepared by Beydoun (1989) primarily from well and reflection profile data. It shows the major variations in sedimentary thickness for the area. The western part of the Arabian plate, the Arabian shield, has Precambrian basement exposed at the surface, and the basement slopes eastward under sediments up to 14 km

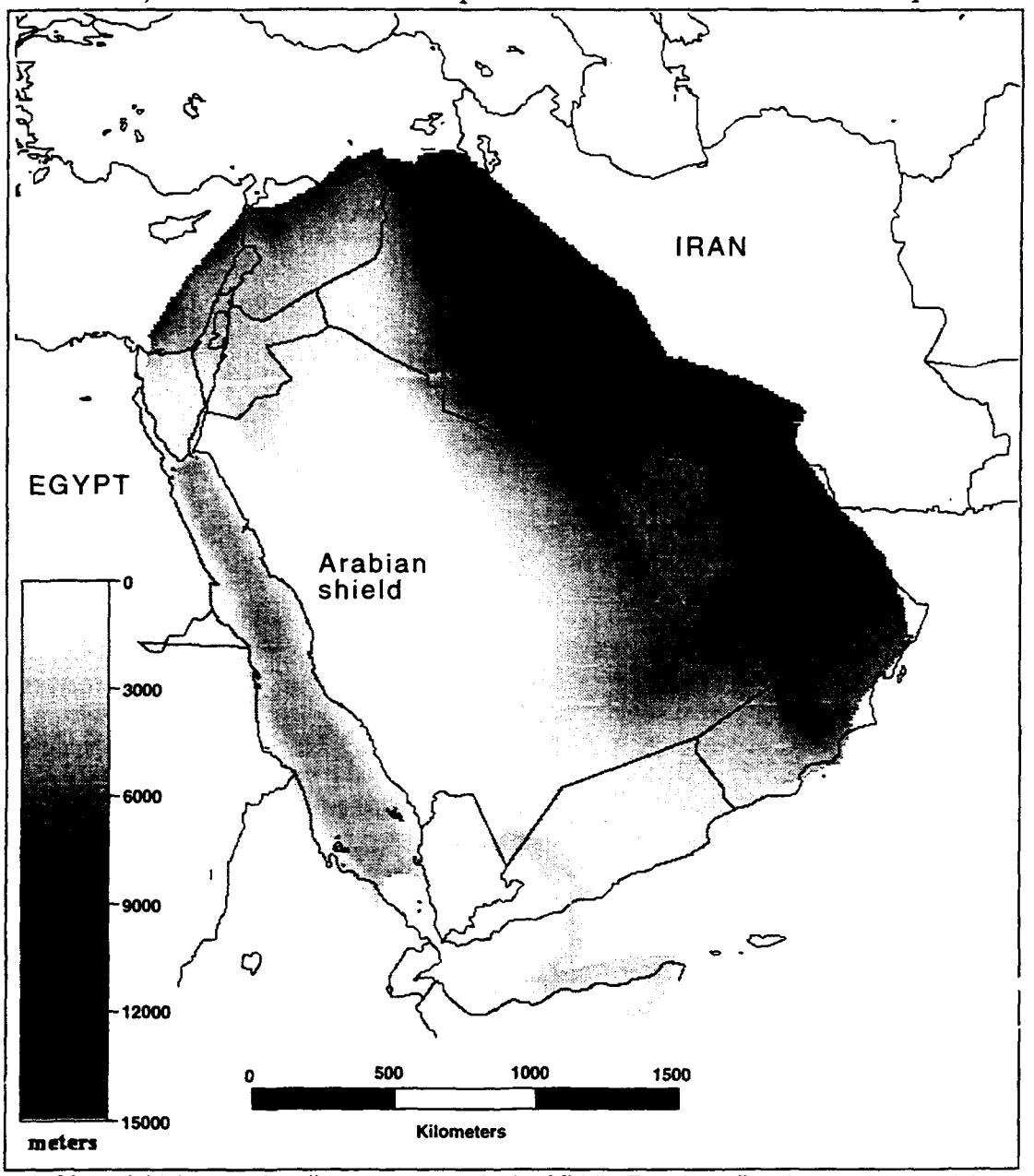


Figure 3: Map of thickness of sedimentary cover in the Middle East from Beydoun (1989). Thicknesses from gridded dataset are shown in gray shades according to key *(left)*. Values range from zero sediment thickness where Precambrian basement is exposed on Arabian shield to ~15 km in western Iran. Other geographic overlays, scale, and map projection are similar to Figure 1.

thick in the Zagros. To the west of the Arabian shield, a steep scarp forms the edge of the Red Sea rift zone with up to 4.5 km of sediments.

We are building our bibliographic database in the Macintosh program called HyperCard (which comes bundled with every Macintosh). References to books, journal articles, reports and other published literature are stored with the usual information on title, date, authors, journal, page numbers, etc. and with searchable keywords on the content. Automatically (by keyword search) or manually selected subsets of the HyperCard dataset can be extracted and formatted in a variety of formats. This is becoming a comprehensive database of crustal structure, geology, and geophysics literature for the Middle East and North Africa, and we have copies of nearly all the references, including many hard-to-find reports, in our files. We continue to add to this bibliographic database, but we released a preliminary version to aid other researchers (Fielding and others, 1994).

We are utilizing the rapidly accelerating Internet network to share datasets with ARPA/AFOSR/DOE/AFTAC and other interested researchers. We are releasing these databases in several different forms. We continue using the well-established "anonymous FTP" protocol as a basic interface to the data. The FTP server on "hugo.geo.cornell.edu" in directory "pub/arpa" has both our new releases under our present contract and our earlier databases from previous contracts. We continue to have many ARPA and Air Force researchers contact us about our Eurasia crustal structure databases. Some researchers have been interested in access via the time-honored method of "anonymous ftp", and others via our network data server. An operational version of a network "raster server" program that allows "client" programs to access our crustal structure datasets over the Internet has been running continuously since August 1992.

We are also installing a World-Wide Web (WWW) protocol server at Cornell to provide a more sophisticated hypertext and graphics interface to our datasets and associated descriptions. The WWW protocol is rapidly increasing in popularity on the Internet due to the excellent Mosaic client program available from the National Center for Supercomputing Applications (NCSA). In particular, the Mosaic client and Gopher or WWW servers can be used to create custom figures on a remote system that can be viewed on a local workstation. Versions of NCSA Mosaic now run on most X workstations, Macintoshes and PC-compatibles under Windows. Our WWW server is accessible from Mosaic via the URL (Uniform Resource Locator) "http://www.geo.cornell.edu". We will expand on the information available in this server, and explore the possibilities for making custom figures generated from our databases. Eventually, all of our unrestricted Middle East and North Africa databases can be incorporated into our WWW server. We encourage researchers to contact us about gaining access to our databases at the computer mail addresses listed on the first page of this paper.

CONCLUSIONS AND RECOMMENDATIONS

To monitor the anticipated multilateral comprehensive nuclear test ban and nonproliferation treaties, we recommend that multidisciplinary information on any given region be readily available and accessible in digital form via the Internet for use by concerned researchers and decision makers. New data, both seismological/geophysical and geological, are required to constrain advanced theoretical and modeling efforts in order to better understand seismic waves produced by very low magnitude events at regional distances. For these monitoring efforts to be successful, researchers must be able to detect, characterize, calibrate, discriminate, and verify any suspect event for most regions on earth. As important to the success of any monitoring strategy, such data must be swiftly accessible to researchers via networks in order to integrate with real-time recorded events to provide ground-truth for fast verification purposes.

Our ongoing efforts are of direct relevance to the ongoing IDC at CSS and the planned test of the experimental international monitoring system, the GSETT-3 (Group of Scientific Experts Technical Test 3) established by the Conference on Disarmament, as well as the planned National Data Center. Our digital seismic and non-seismic databases and results can profitably be used by this system for calibration and verification purposes.

REFERENCES

Best, J.A., M. Barazangi, D. Al-Saad, T. Sawaf, and A. Gebran, Bouguer gravity trends and crustal structure of the Palmyride Mountain belt and surrounding northern Arabian platform in Syria, *Geology, 18,* 1235-1239, 1990.

Beydoun, Z.R., Hydrocarbon potential of the deep (pre-Mesozoic) formations in the Middle East Arab countries, in *Technical Papers Presented at the Seminar on Deep Formations in the Arab Countries: Hydrocarbon Potential and Exploration Techniques*, Abu Dhabi National Oil Company, Abu Dhabi, UAE, 1989.

Fielding, E.J., Barazangi, M., and Isacks, B.L., A geological and geophysical database for Eurasia, *ARPA Final Technical Report, Cornell University, Ithaca, NY,* 38 p., 1993.

Fielding, E.J., Barazangi, M., and Isacks, B.L., A geological and geophysical information system for Eurasia, the Middle East, and North Africa: digital database development for the Middle East and North Africa, *Scientific Report #1, Phillips Laboratory,* 73 p., 1994.

Hussein Al-Rahim, A.M., Geophysical Transect Project Northwest–Southeast Iraq, *M.S. Thesis, University of Baghdad* (in Arabic), 1993.

Seber, D., M. Barazangi, T. Chaimov, D. Al_saad, T. Sawaf and M. Khaddour, Upper crustal velocity structure and basement morphology beneath intracontinental Palmyride fold-thrust belt and north Arabian platform in Syria, *Geophys. J. Int., 113,* 752-766, 1993.

Snyder, D. B., and M. Barazangi, Deep crustal structure and flexure of the Arabian Plate beneath the Zagros collisional mountain belt as inferred from gravity observations, *Tectonics, 5 (3),* 361-373, 1986.

Preliminary Assessment of Seismic CTBT/NPT Monitoring Capability

Mark D. Fisk
Mission Research Corporation

and

Henry L. Gray and Gary D. McCartor
Southern Methodist University

Contract No. F19628-C-93-0117

OBJECTIVE

Our recent work has focussed on assessing regional event identification capabilities using a method we developed for outlier detection. This is motivated by the fact that historical underground nuclear tests have been performed in only a few regions. Thus, in most regions, seismic monitoring of a Comprehensive Test Ban Treaty (CTBT) or a Non-Proliferation Treaty (NPT) is a problem of identifying unusual events, i.e., outliers. Our procedure may be fully automated to flag events warranting special attention and to test all appropriate assumptions to ensure validity of the results. In addition, the method allows straightforward control of false alarm rates and a natural way to rank events. We have applied this approach to seismic events in very diverse geological regions, recorded by the ARCESS and GERESS arrays, CDSN station WMQ, and LLNL stations KNB and MNV.

We also examined effects of contaminated training data by intentionally including quarry blasts or rock bursts in earthquake training sets to determine if the outlier test can detect them and to assess potential impacts on monitoring performance. We also examined Pn/Lg transportability before and after applying distance corrections to assess (1) regional attenuation effects on transportability and (2) how precisely a discrimination threshold must be transported in order to be effective. Last, we repeated our identification analysis of the 31 December 1992 Novaya Zemlya event, after first applying distance corrections.

RESEARCH ACCOMPLISHED

Data Sets. We primarily used ISEIS feature data provided by Baumgardt (1993a) for seismic events recorded by the ARCESS and GERESS arrays and CDSN station WMQ. ARCESS events include earthquakes near Steigen, Norway, and near Spitsbergen, quarry blasts on the Kola Peninsula and in the Kiruna region of Sweden, and 3 underground nuclear explosions on Novaya Zemlya. GERESS events include 10 earthquakes and 13 quarry blasts in the Vogtland region of Germany and 30 rock bursts in the Lubin region of Poland. WMQ events include 23 earthquakes in China and nearby countries, 16 nuclear explosions in Kazakhstan, and 1 nuclear explosion at Lop Nor. In addition, we used feature data provided by Patton and Walter (1994) for 59 earthquakes and 89 nuclear explosions at NTS, recorded by KNB and MNV. Locations of the seismic stations, arrays and most events are depicted in Figure 1. The events are summarized in Table 1. Discriminants used here include Pn/Lg and Pn/Sn in 3-5, 4-6, 5-7, 6-8 Hz bands, and an Lg spectral ratio. Of these, only Pn/Lg in the 6-8 Hz band and Lg spectral ratio measurements were available for KNB and MNV. Also, Sn was measured for only 2 of 17 explosions at WMQ.

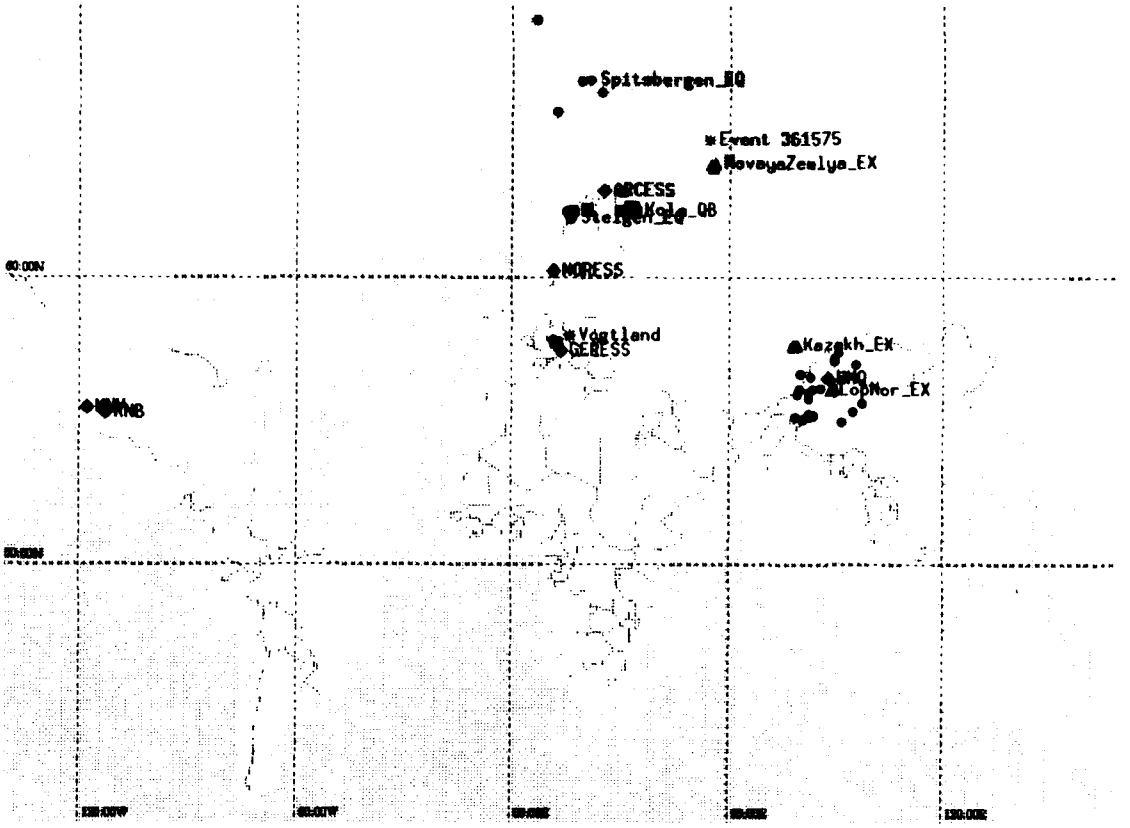


Figure 1. Locations of ARCESS, GERESS, CDSN station WMQ, LLNL stations KNB and MNV, and most of the seismic events used in our event identification study.

Outlier Detection Approach. If a station exists or has been installed recently, the first step is to collect a set of events as soon as the station starts recording. A fundamental assumption is made that the number of nuclear tests in a new region will be relatively small compared to the number of earthquakes, chemical mining blasts or rock bursts. If this assumption fails, i.e., if a region is aseismic and with no mining activity, then any new event would be suspicious, warranting further investigation. Since there are only a small number of mining blasts that occur annually above magnitude 3.0, our primary concern for monitoring above this threshold is to be able to distinguish explosions from earthquakes. (Monitoring down to magnitude 2.5 poses greater difficulty.) A standard set of discriminants is used, unless we have information about particular ones that work best for a given region. Here we used the discriminants listed above, provided they were available. In general, the outlier test can rigorously include any discrete or continuous discriminant. Distance corrections are applied if information is available. Each event is then tested as an outlier of the remaining data set using a hypothesis test based on the generalized likelihood ratio. (Details of the outlier test and previous applications are provided by Baek et al., 1992; Fisk et al., 1993; Fisk and Gray, 1993; Fisk, 1993.) Events flagged as outliers can be investigated further using, possibly, non-seismic means. The significance level of the test is an input parameter which controls the false alarm rate, i.e., the percentage of earthquakes flagged as outliers.

For situations in which more training information is available, we developed a classification test, based also on the likelihood ratio methodology (e.g., Baek et al., 1993; Fisk et al., 1993), which provides improved identification accuracy. In this case, training data for all available classes are used and the event in question is allocated into one of two or more classes. Here we concentrated on monitoring results obtained using the outlier test.

Table 1: Data sets used in our study.

Array/Station	Events	Distance (km)	Magnitude
ARCESS	24 Steigen EQs	385-480	1.0-3.2
	5 Spitsbergen EQs	795-1320	1.5-2.9
	53 Kola QBs	300-430	2.0-3.2
	39 Kiruna QBs	250-295	1.6-2.0
	3 NZ EXs	1100	>3.9
GERESS	10 Vogtland EQs	140-260	1.4-3.2
	13 Vogtland QBs	165-210	2.0-2.6
	30 Lubin RBs	340-350	1.8-3.3
WMQ	23 EQs	100-1100	4.2-5.9
	16 Kazakh EXs	950	4.8-6.1
	1 Lop Nor EX	240	4.7
KNB	59 NTS EQs	295-310	2.1-5.9
	89 NTS EXs	280-315	2.4-5.5
MNV	37 NTS EQs	250-260	2.2-5.9
	78 NTS EXs	190-245	2.6-5.5

Monitoring applications. Sequentially using each of the nuclear explosions and quarry blasts in each region as a new explosion, each event was tested against the earthquakes to determine the percentage that are detected as outliers. Each earthquake was also tested using the leave-one-out procedure to estimate the false alarm rate. We set the significance level at 0.01. For ARCESS, using the Steigen and Spitsbergen earthquakes to train the outlier test, 3 of 3 Novaya Zemlya nuclear explosions, 50 of 51 (98%) Kola quarry blasts, and 36 of 39 (92%) Kiruna quarry blasts were flagged as outliers once distance corrections were applied to the discriminants, and there were no false alarms. For GERESS, using the Vogtland earthquakes to train the outlier test, 13 of 13 Vogtland quarry blasts were detected as outliers and there were no false alarms. For WMQ, 17 of 17 Kazakh and Lop Nor nuclear explosions were flagged as outliers with 1 false alarm out of 23 earthquakes. For the LLNL stations, 74 of 78 (95%) and 71 of 89 (80%) NTS nuclear explosions were detected as outliers at MNV and KNB, respectively, with one false alarm at each station.

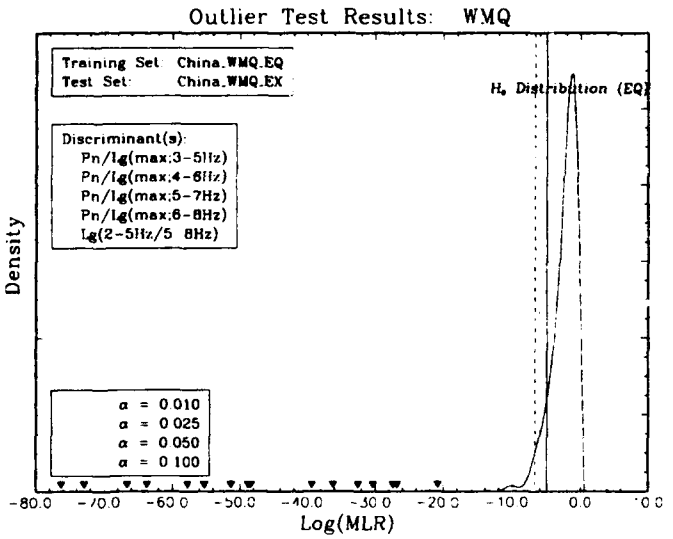


Figure 2. Example of outlier test results for events at WMQ.

Figure 2 shows outlier test results for the 17 explosions observed at WMQ. The distribution shown is of the likelihood ratio when the

event being tested is from the same group as the earthquake training set. The vertical lines represent critical values of the test for various significant levels. Events whose likelihood ratio fall to the left of the critical value are identified as outliers at a given significance level. The triangles depict values of the likelihood ratio for the explosions being tested. This plot shows that all 17 explosions are flagged as outliers of the earthquake group at 0.01 significance level. It also illustrates how the outlier test combines multivariate data into a single variable which can be ranked in a straightforward and statistically consistent manner.

Contaminated training set study. We have assumed to this point that the data sets in each region consist of earthquakes and at most one explosion. In practice, we should also be concerned with the situation in which quarry blasts and rock bursts may contaminate earthquake training sets when trying to detect a nuclear explosion. Although there are likely to be only a small number of quarry blasts above magnitude 3, it is possible that a couple of large quarry blasts might contaminate the earthquake training set. Large rock bursts could also be present. The purpose of this study was to determine how a lack of ground-truth affects our ability to monitor using the outlier test.

To address this problem, we first selected 2 Vogtland quarry blasts and inserted them in the Vogtland earthquake set. To make the problem interesting, we chose the 2 that are most like the earthquakes. We then ran the outlier test on each event in the training set using the leave-one-out procedure and the same discriminants as above. Note that even if one quarry blast is left out of the training set to be tested, one contaminating event still remains. If an outlier is detected, it is removed from the set and the remainder are tested again. In this case, both quarry blasts were flagged on the first pass. If the 2 quarry blasts are not removed from the earthquake training set, 2 of the remaining 11 Vogtland quarry blasts are undetected when tested. This analysis was repeated by randomly selecting 2 Kola quarry blasts and inserting them in the Steigen earthquake set. Only one blast was detected on the first pass, but once removed, the other was also detected. If the 2 Kola quarry blasts are not removed from the Steigen earthquake training set, 7 of the remaining 51 quarry blasts are undetected when tested. However, even if both Kola quarry blasts were not detected, the outlier test was still able to detect all 3 Novaya Zemlya nuclear explosions. (ARCESS was the only array for which we have data of these three types.) As a related study, we contaminated the Vogtland earthquake set with 30 Lubin rock bursts and then tested the Vogtland quarry blasts. All 13 Vogtland quarry blasts were still flagged as outliers.

These results show that the outlier test can be used to detect contaminating events in data sets which lack ground-truth. If they are not detected, the probability of detecting an explosion may be affected significantly, e.g., by 10-20%, although it did not affect the ability to identify the Novaya Zemlya explosions as outliers. Contamination by rock bursts did not reduce the capability to detect mining explosions in the case examined.

Transportability of Pn/Lg. Figure 3 shows plots of uncorrected and distance-corrected Pn/Lg in the 6-8 Hz band for events observed at ARCESS, GERESS, WMQ, MNV, and KNB. The discrimination threshold for uncorrected Pn/Lg at WMQ is roughly an order of magnitude greater than those at the other stations. The distance-corrected thresholds are all fairly similar except for the threshold at ARCESS, which differs by almost an order of magnitude. (Distance corrections for ARCESS events were obtained from Sereno, 1990, and may be invalid for frequencies above 5 Hz. At present, however, these are the best corrections available.) Note that even for the distance-corrected case, a threshold obtained for KNB would lead to several missed nuclear explosions at WMQ. Similarly, the threshold for WMQ would lead to roughly a 30% false alarm rate at KNB. Since there is virtually no separation between the earthquake and explosion groups, the threshold must be set very precisely in order to have high detection and low false alarm rates. Station and specific path corrections might improve Pn/Lg transportability, but it may be unlikely that a set of

events, needed to derive station corrections, are recorded at two or more common stations. Also, explosion and earthquake data will likely be too sparse to obtain specific path corrections and theoretical modeling will have to be very precise to succeed.

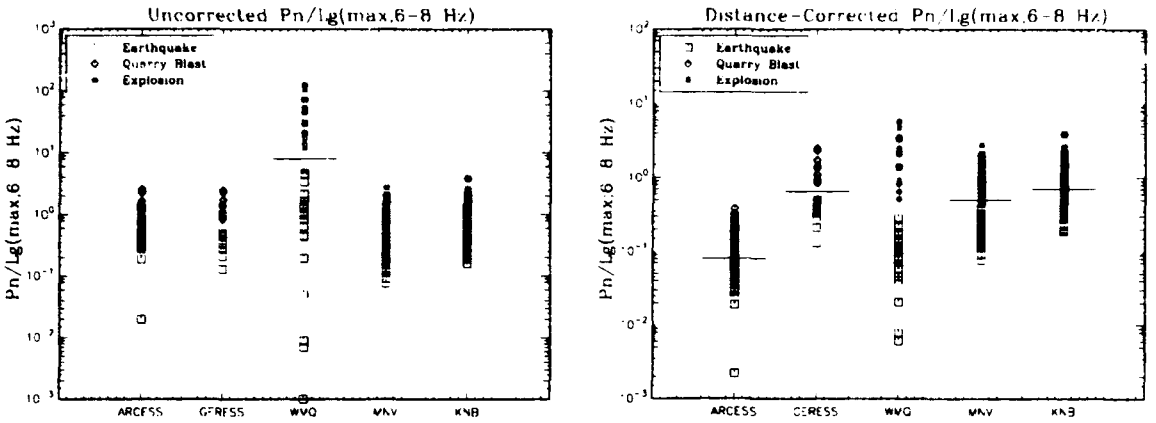


Figure 3. Scatter plots of uncorrected (left) and distance-corrected (right) Pn/Lg in the 6-8 Hz band for events observed at ARCESS, GERESS, WMQ, MNV, and KNB. The horizontal lines depict discrimination thresholds for each station.

Identification Results for the 921231 Novaya Zemlya Event with Attenuation Corrections. Several ARPA contractors previously analyzed the identification of a 31 December 1992 event on Novaya Zemlya. They generally agreed that this event was not a nuclear detonation. Results obtained by Baumgardt (1993b), Fisk and Gray (1993), and Pulli and Dysart (1993) suggest that this event was much more like Kola Peninsula mining blasts than earthquakes in Scandinavia and near Spitsbergen, in apparent contradiction to a statement by the Seismological Service of the Ministry of Defense, Russian Federation, that no blasting had occurred on the Novaya Zemlya test range on the day in question (Ryall, 1993).

The discriminants used to obtain these results were based on Pn and Sn measurements of ARCESS recordings. No corrections were made for attenuation, although all authors recognized their importance on the outcome of identification tests since the epicentral distances of the 921231 event and reference events ranged from 300 to 1300 km and it is well known Pn/Sn is affected by distance. More rapid attenuation of Sn with distance relative to Pn would cause the 921231 event to have higher Pn/Sn ratios than a similar event occurring in the Steigen or Kola Peninsula regions due to the longer path from Novaya Zemlya. It was speculated that applying distance corrections may lead to Pn/Sn ratios that are more consistent with earthquakes than with quarry blasts.

Using distance corrections reported by Sereno (1990), we reanalyzed the identification of the 921231 event. We applied outlier and classification tests using Pn/Sn(max) in 4-6, 5-7, 6-8, 8-10, and 8-16 Hz bands for waveforms recorded by ARA0. For comparison, we again used 3 nuclear explosions at NZ, the Kola and Steigen data sets, and 5 earthquakes near Spitsbergen. Figure 4 shows scatter plots of the amplitude ratios before and after applying distance corrections. The objectives of this study were to resolve the apparent discrepancy and to assess the impact of attenuation on regional event identification. The following results and observations were obtained. (Further details are provided by Fisk, 1993.)

First, there is sufficient evidence to reject the 921231 event as a member of the Novaya Zemlya nuclear explosion group at 0.01 significance level, using either the outlier or

classification tests. This is consistent with the results of Fisk and Gray (1993) as expected since the epicentral distances for the Novaya Zemlya events are all very similar; thus, attenuation corrections should have little effect on the identification relative to this group.

Second, there was insufficient evidence, based on outlier tests, to reject the 921231 event as a member of either the quarry blast or earthquake groups, at 0.05 significance or lower. Classification between the earthquake and quarry blast alternatives led to rejection of this event as a member of the Kola quarry blast group at 0.05 significance level, although it was also rejected as a member of the earthquake group using Pn/Sn in the five frequency bands. Omitting the 6-8 Hz band, the 921231 event was accepted as an earthquake at 0.05 significance. These results are quite different than those of Fisk and Gray (1993), Baumgardt (1993) and Pulli and Dysart (1993), who found that the 921231 event was much more consistent with identification as a mining blast than as an earthquake. Although identification of this event is still inconclusive, it is no longer inconsistent with the statement by the Seismological Service of the Ministry of Defense, Russian Federation. This study also demonstrates that distance corrections can have a significant impact on event identification and should be applied routinely.

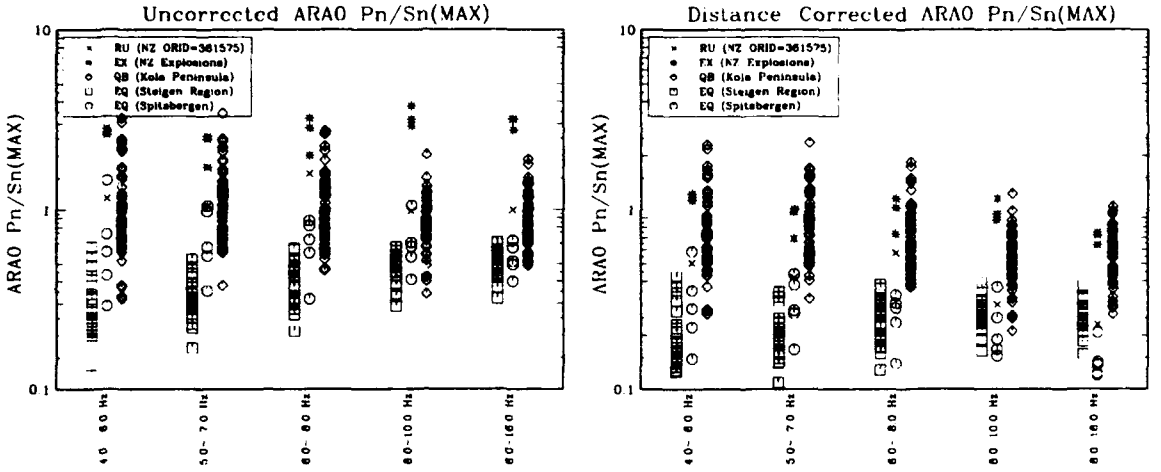


Figure 4. Pn/Sn amplitude ratios in five frequency bands before (left) and after (right) applying distance corrections.

Among other important monitoring issues, we found that distance-corrected Pn/Sn values for the 3 Novaya Zemlya nuclear tests fall within the values for the Kola quarry blast group (Figure 4). This implies that a more effective discriminator between nuclear explosions and mining blasts is needed. Spectral and cepstral variances, presence of cepstral peaks, and presence of Rg have been considered to identify mining blasts, but adequate utility of any is yet to be demonstrated.

CONCLUSIONS AND RECOMMENDATIONS

Our results show that useful monitoring can be performed currently at magnitude 3 and above using the outlier detection approach. Between 92–100% of the explosions and quarry blasts were detected as outliers of the earthquake groups in the various regions, except at KNB where the detection rate was 80%, and there was one false alarm at KNB, MNV and WMQ. Overall, 264 of 290 (91%) explosions were detected and there were only 3 false alarms out of 158 earthquakes (1.9%), slightly higher than the target rate of 1%. These results were obtained for very diverse regions and for a wide range of epicentral distances and magnitudes. One or more additional discriminants that work about as well as Pn/Sn and

Pn/Lg, but that are relatively uncorrelated, or information which allows us to choose the best discriminants in a given region, should improve the monitoring capability further.

Contaminated training data did not reduce the monitoring capability for the cases studied but remains a cause for concern, especially at a low magnitude threshold. We also found that it is very important to distance-correct discriminants in order to obtain accurate identification results. Transporting discriminants looks very difficult and must be done very precisely in order to have a reasonable probability of detecting an explosion without having an unmanageable number of false alarms world wide. A key benefit of the outlier approach is that it does not require transporting discrimination thresholds, while providing high detection probabilities and low false alarm rates in regions studied thus far.

Future research should focus on investigating ways to select the best regional discriminants in the absence of nuclear explosion training data and on investigating other discriminants such as a regional M_S-m_b, autoregression analysis of Lg, waveform complexity, etc. In addition, reliable methods are needed to distinguish nuclear explosions from chemical mining blasts. Last, a distance-correction data base should be established.

REFERENCES

Baek, J., H.L. Gray, and W.A. Woodward (1992). A Generalized Likelihood Ratio Test in Outlier Detection or Script Matching, Technical Report, Department of Statistical Science, Southern Methodist University, Dallas, TX.

Baek, J., H.L. Gray, W.A. Woodward and M.D. Fisk (1993). A Bootstrap Generalized Likelihood Ratio Test in Discriminant Analysis, submitted to *Comp. Stat. and Data Anal.*, Southern Methodist University, Dallas, TX.

Baumgardt, D.R. (1993a). Private Communication.

Baumgardt, D.R. (1993b). Seismic waveform feature analysis and discrimination of the December 31, 1992 Novaya Zemlya event, Paper in volume compiled by Ryall (1993).

Fisk, M.D. (1993). Event Identification Analysis of the 31 December 1992 Novaya Zemlya Event with Attenuation Corrections, MRC-R-1459, Mission Research Corp., Santa Barbara, CA.

Fisk, M.D. and H.L. Gray (1993). Event Identification Analysis of the Novaya Zemlya Event on 31 December 1992 using Outlier and Classification Likelihood Ratio Tests, Paper in volume compiled by Ryall (1993), MRC-R-1449, Mission Research Corp., Santa Barbara, CA.

Fisk, M.D., H.L. Gray and G.D. McCartor (1993). Applications of Generalized Likelihood Ratio Tests to Seismic Event Identification, PL-TR-93-2221, Phillips Laboratory, Hanscom AFB, MA, ADA279479.

Patton, H. and W. Walter (1994). Private Communication.

Pulli, J.J. and P.S. Dysart (1993). Identification analysis of the Dec. 31, 1992 Novaya Zemlya event, Paper in volume compiled by Ryall (1993).

Ryall, A. (1993). The Novaya Zemlya Event of 31 December 1992 and Seismic Identification Issues, Supplemental volume of papers to Proceedings of the 15th Annual Seismic Research Symposium, 8-10 September 1993, Vail, CO, PL-TR-93-2160, ADA271458.

Sereno, T.J. (1990). Attenuation of Regional Phases in Fennoscandia and Estimates of Arrival Time and Azimuth Uncertainty using Data Recorded by Regional Arrays, SAIC-90/1472, Science Applications International Corp., San Diego, CA.

Location of Regional Seismic Events Using Single-Station Broadband Data

Cliff Frohlich and Lian-She Zhao
Institute for Geophysics
University of Texas at Austin
Austin, TX 78759-8397

Contract No. F49620-94-1-0287

OBJECTIVES

In this study we evaluate methods that utilize both traveltime and waveform data to obtain accurate locations for relatively small seismic events. Our ultimate objective is to develop the capacity to locate events which have available only one or a few regionally recorded broadband waveforms, often contaminated by high levels of background noise. For single-station data our approach is to obtain the back azimuth by analyzing radial and tangential seismogram components, and to find distance and focal depth by comparison of observed and synthetic waveforms. If two or more stations are available, we augment this by using a grid-search technique to find the optimum location.

RESEARCH ACCOMPLISHED

Determination of Station Back Azimuth

We determine the station-event back azimuth by rotating the seismogram to find the direction which minimizes the tangential-component energy in the P_{nl} time window. For example, consider the P waveforms recorded at station BKS (Berkeley, CA) for an earthquake occurring 26 April 1992 (Figure 1a). For an azimuth of 317°, the earliest arriving signal (P_{nl}) is quite strong on the radial component but invisible on the tangential component, however, it is clearly visible on both components for an azimuth of 329° based on the location given by UC Berkeley. The minimum-energy direction is 317° regardless of whether the time window chosen for analysis has a length of 35, 40, or 45 sec (Figure 1b).

For laterally homogeneous media the tangential-component energy should be exactly zero for the P_{nl} phase at regional distances. Thus, as long as the velocity structure is one-dimensional the back azimuth determined in this way does not depend on the details of the layered velocity structure or the nature of the earthquake source. However, the event-station back azimuth so determined may be in error if there is significant lateral variation in the velocity structure along the event-station path, due to dipping layers or other geological structures which "bend" the P_{nl} rays.

Determination of Distance and Depth

If we possess a reasonable model for regional velocity structure, we compare observed broadband waveforms with synthetics calculated for a range of possible event-station distances and focal depths. We assume a trapezoidal source-time function and use routine methods described by Zhao and Helmberger (1994a) to calculate body and surface-wave synthetics and to perform a grid search over a range of distances, depths, and focal mechanisms. If our regional velocity model is reasonable and if the signal/noise ratio is

adequate these methods applied to data from a single station will generally provide well-constrained distance and depth information, even when the focal mechanism is poorly constrained.

To make this method practical we have put some effort into streamlining the grid search scheme. For example, we utilize a cross-correlation method for comparison of observation and synthetics which automatically determines the time shift which corresponds to an optimum fit. Such efficiencies make it possible to search a larger range of model parameters. Nevertheless, unlike the determination of back azimuth, in the determination of distance and focal depth a considerable amount of subjective judgment is sometimes necessary, especially in cases where the velocity structure is poorly known or where there may be complexity in the source-time function. Our continuing research focuses on ways to reduce this subjectivity, and methods to improve location determination for smaller events.

As an example, we apply these methods to waveforms recorded at PAS (Pasadena, CA) for the 15 September 1992 earthquake in southern California, using velocity model SC of Dreger and Helmberger (1991) to calculate synthetics. The minimum misfit occurs for an event-station distance of 210 km and depth of 8 km (Figure 2a). Changes in distance of 10 km and changes in depth of only 3 km produce misfits that are 5-10% higher than the optimum value. Inspection of the waveforms show the source of these misfit increases (Figure 2b): changing the focal depth changes the separation between the two pulses making up the P_{nl} waveform; changing the distance changes the separation between the P_{nl} and surface wave arrivals.

More Stations

If we have data for an event from more than one station, we apply the above methods for each station to determine the apparent back azimuth $\Theta_{j\text{obs}}$, distance $\Delta_{i\text{obs}}$, and focal depth. Then, if we have n well-determined distances, and m well-determined back azimuths, we apply a grid search over trial locations to minimize errors of any given form, say, the L_2 norm:

$$e_2 = \frac{1}{n+m}\left(\sum_{i=1}^{n}(\Delta_{i\text{obs}} - \Delta_{i\text{cal}})^2 + \omega^2 \sum_{j=1}^{m}(\Theta_{j\text{obs}} - \Theta_{j\text{cal}})^2\right)$$

where $\Theta_{j\text{cal}}$ and $\Delta_{i\text{cal}}$ are the back azimuth and distance for the trial locations, and ω is a weight factor. We normally use $\omega = 1$, which means that 5 km of distance and 5 degrees of back azimuth have the same importance. For focal depth we use a simple average of all the well-determined values.

Further Examples

To illustrate the procedure described above we have investigated locations for six earthquakes (Table 1). These include events in the Hindu Kush and in California with magnitudes between 3.6 and 6.5.

Two Hindu Kush earthquakes: For these events we used a single station, GAR (Garm). For the 5 March 1990 event the event-station distance is 320 km with uncertainty of 5 km or less, compared to 336 km and 315 km for the locations reported by PDE and ISC. The back azimuth from waveform data is roughly the same as that of PDE, 134° For the 26 May 1989 earthquake, the event-station distance is 445 km, compared to 439 km and 434 km for PDE

and ISC. The back azimuth is 77° from broadband velocity data, since the signal to noise ratio of the east-west component of the displacement is low, 5° smaller than that of PDE.

Two northern California earthquakes: For these events we determined the locations in Table 1 using two stations, BKS and STAN (Stanford, CA). The model used is from Dreger (personal communication, 1993). For the 8 March 1992 earthquake, the back azimuths was 316° as determined from waveforms for both stations; the event-station distance was 325 km for BKS and 390 km for STAN. The two single-station locations were separated by about 20 km, and thus best joint location lay in the middle, about 10 km from the single-station hypocenters.

For the 26 April 1992 earthquake, the back azimuths determined from waveform data were again the same, being 317° for both BKS and STAN (Figure 1). From Berkeley location, the back azimuth for BKS is 325°, for STAN 329°.

15 September 1992 southern California earthquake: For this event we determined a location using 3 stations (Table 2), PAS (Pasadena, CA), GSC (Goldstone, CA), and ISA (Isabella, CA). The model used to study these two southern California earthquakes is the SC model derived by Dreger and Helmberger (1991). As discussed previously, from waveforms at PAS we obtained a source depth of 8 km. Table 2 gives comparison of locations by different agencies.

4 January 1993 Southern California Earthquake: This earthquake is small (M_L=3.6). At station GSC the broadband and filtered waveforms (Figure 3a) are noisy, with some apparent long-period contamination. This long-period signal remains even after it is filtered to resemble a Wood-Anderson long-period (walp) instrument. We can remove this long-period signal by filtering to resemble a short-period WWSSN response (Figure 3a).

By minimizing the energy of the first 18 seconds of the tangential component short-period WWSSN waveform, we obtain a back azimuth of 127°, and waveform matching gives an event-station distance of 130 km. For the reported PDE location, the back azimuth at GSC is significantly different, 178°, and the event-station distance is 112 km. The fits of the synthetics to the filtered data are good (Figure 3b), thus we believe that the single-station distance is reasonable. However, the new location is 106 km away from PDE location. Presumably the gross discrepancy in back azimuth determination occurs because of lateral variation in structure between the epicenter and GSC. If we possessed more detailed information about the velocity structure variations along the path it would be possible to model the Pnl energy on the tangential component and get better estimation of back azimuth.

CONCLUSIONS AND RECOMMENDATIONS

When a reasonable along-path velocity structure and relatively noise-free broadband data are available, the single-station methods described here provide quite accurate locations. For example, for southern California, the model SC (Dreger and Helmberger, 1991) is good enough to locate nearly all earthquakes with magnitude of 4.5 and larger.

However, our preliminary results suggest that the principal difficulty with smaller events is signal-noise ratio at periods of 10 sec. This contaminates both the Pnl and surface wave phases, complicating our attempts to find well-constrained fits to the observations. Nevertheless, it may be possible to make robust fits for events with magnitude 3.5 and

smaller in regions where a reliable, detailed regional velocity structure allows us to model short-period seismic records. Thus, our future research will focus on developing a library of stations for which we can obtain well-determined near-station structural information, and on relocating small regional events near these stations.

References

Dreger, D. S. and D. V. Helmberger (1991). Source parameters of the Sierra Madre earthquake from regional and local body waves, *Geophys. Res. Lett.*, **18**, 2015-2018.

Zhao, L.-S., and D. V. Helmberger, Source retrieval from broadband regional seismograms; Hindu Kush region, *Phys. Earth Planet. Inter* , **78**, 69-95, 1993.

Zhao, L.-S., and D. V. Helmberger, Source estimation from broadband regional seismograms, *Bull. Seism. Soc. Am.*, **84**, 91-104, 1994a.

Zhao, L.-S., and D. V. Helmberger, Regional moments, energy levels, and a new discriminante, Submitted to *Bull. Seism. Soc. Am.*, 1994b.

Table 1. New earthquake relocations determined using methods described in this study, and locations reported by PDE and by Harvard.

Ev	Date	Time	Mag	Location (New)			Location (PDE)			Location (CMT)		
HK	900305	20:47	6.0	36.97°	72.90°	10	36.85°	73.01°	33	37.04°	72.85°	18
HK	890526	01:08	4.6	39.64°	75.41°	35	39.44°	75.38°	26			
NC	920308	03:43	5.5	40.00°	-125.01°	17	40.23°	-124.29°	13	40.25°	-124.10°	15
NC	920426	07:41	6.5	40.14°	-125.11°	20	40.42°	-124.60°	20	40.25°	-124.61°	15
SC	920915	08:47	5.2	34.16°	-115.93°	8	34.06°	-116.36°	9	34.49°	-116.67°	15
SC	930104	00:32	3.6	34.59°	-115.67°	11	34.29°	-116.77°	6			

The date information is year-month-day, origin time is hours and minutes. The location is latitude, longitude, and depth in km. SC - Southern California earthquake; NC - northern California; HK - Hindu Kush.

Table 2. Event-station distances (first number) and back azimuths (second number) for the earthquake of 15 September 1992.

Station	Single-station Relocation		3-Station Relocation		PDE		CMT	
PAS	210	98°	206	90°	167	93°	143	74°
GSC	155	-	152	148°	143	163°	90	172°
ISA	280	141°	287	125°	262	132°	208	128°

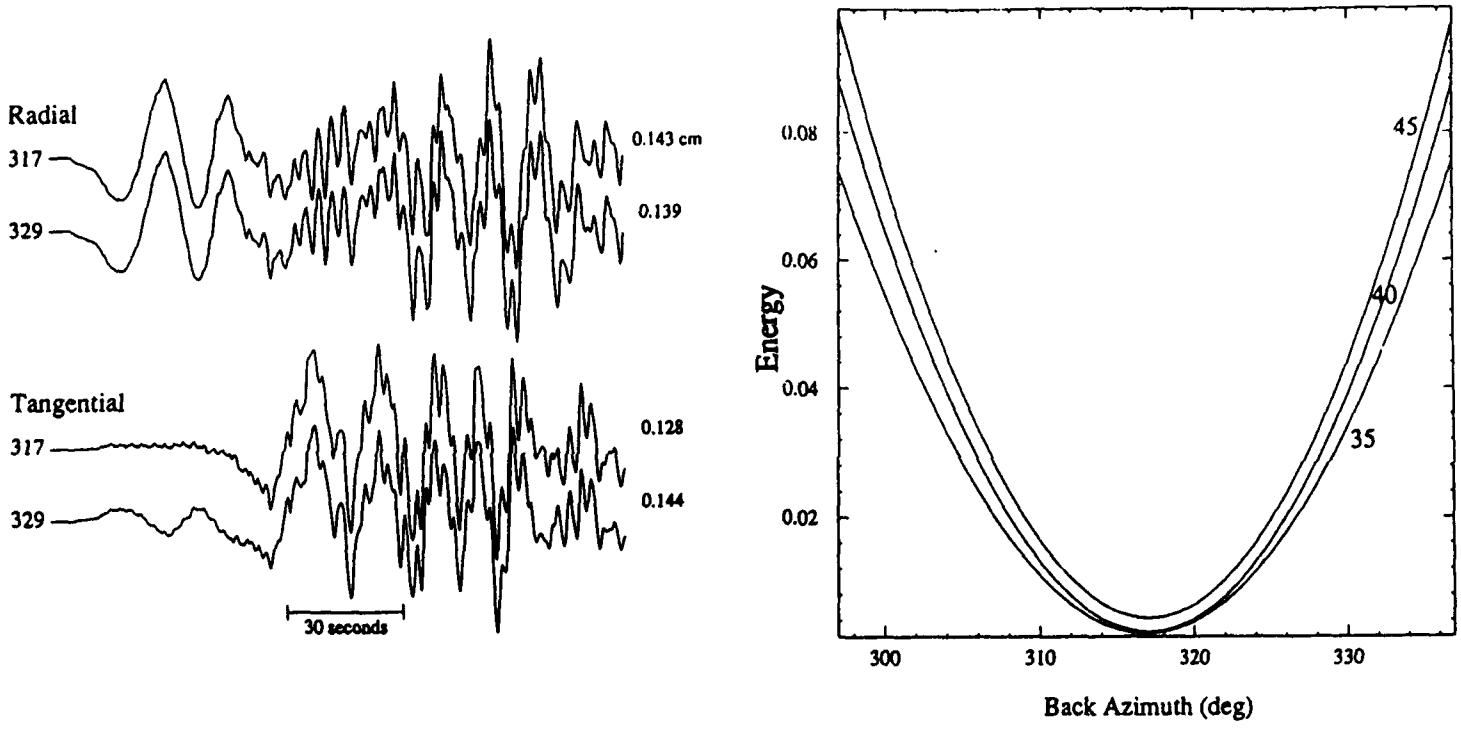


Figure 1. Example demonstrating how single-station data constrain event-station azimuth. For the northern California earthquake of 26 April 1992, Figure 1a displays radial and tangential seismograms recorded at station BKS (Berkeley, CA) corresponding to station-event back azimuths of 317° and 329°. Traces are normalized to maximum amplitude, designated by numbers to the right of each trace. Note that there is little or no arriving energy for the tangential-component P_{nl} phase (approximately the earlier 45 seconds of the waveform) for a back azimuth of 317°. Figure 1b plots the sum of displacement squared (proportional to arriving energy) and demonstrates that the back azimuth with the minimum energy tangential component is the same regardless of whether time windows of 35, 40, or 45 sec are chosen.

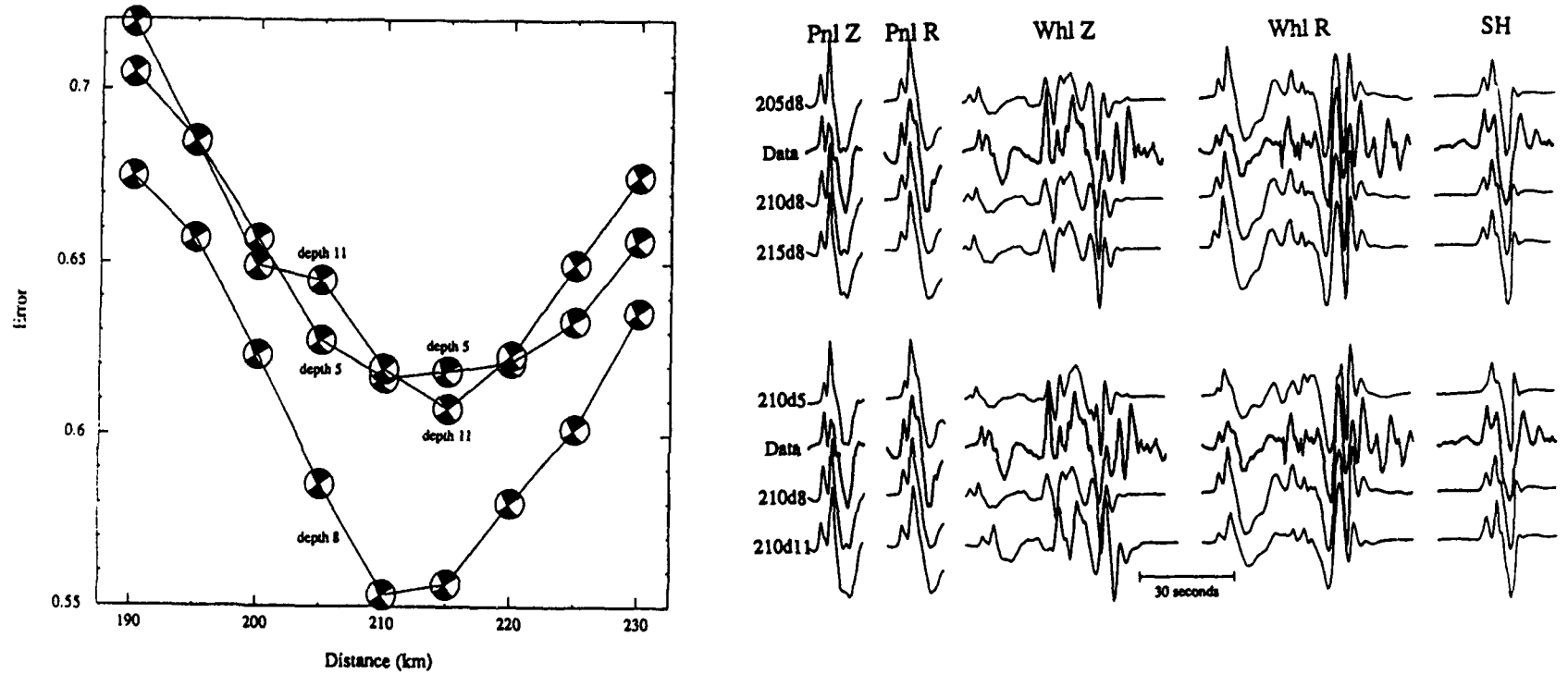


Figure 2. Example demonstrating how single-station data can constrain event-station distance and source depth. Figure 2a demonstrates how the misfit between synthetic and observed waveforms depends on distance, depth, and mechanism for waveforms recorded at station PAS (Pasadena, CA) for the 15 September 15 1992 southern California earthquake. Figure 2b compares the observed waveform to synthetics calculated for several distances and depths surrounding the optimum values of 210 km and 8 km.

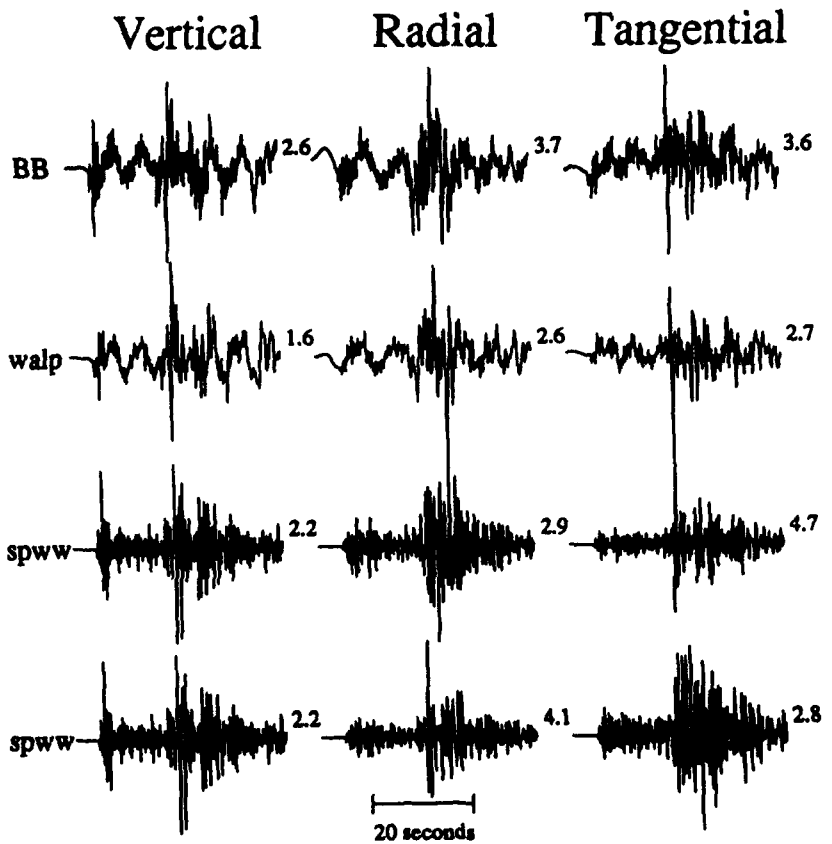


Figure 3a. For the earthquake of 4 January 1993, broadband (BB) records at station GSC for a small earthquake in southern California filtered to resemble Wood-Anderson long-period (walp) and short-period WWSSN (spww) band passed waveforms. The bottom radial trace is plotted assuming the back azimuth is 178° as determined from the PDE location, all other traces assume the back azimuth is 127° as determined from minimizing tangential component energy. Numbers to the right of each trace are maximum amplitudes in unit of 10^{-4} cm.

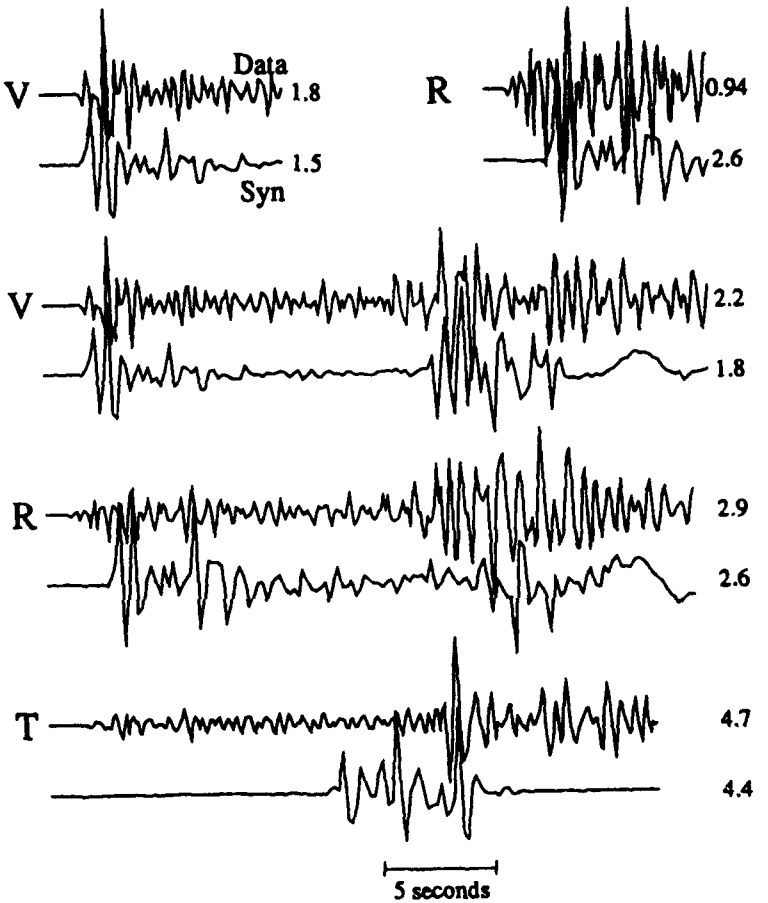


Figure 3b. For the earthquake of 4 January 1993, comparison of observations (top trace) and synthetic data (bottom trace) filtered to resemble a short-period WWSSN instrument. The synthetics are for the best-fitting distance (130 km) and depth (11 km). Traces are: top trace, vertical and radial components of Pnl phase; second and third traces; whole seismogram for vertical and radial components; bottom trace, whole seismogram for tangential component. Numbers to the right of each trace are maximum amplitudes in unit of 10^{-4} cm.

STUDIES OF EARTHQUAKES ON AND NEAR THE LOP NOR, CHINA, NUCLEAR TEST SITE

Liping Gao and Paul G. Richards*
Lamont-Doherty Earth Observatory, Palisades, NY 10964
(* also, Dept. of Geological Sciences, Columbia University)
F49620-94-1-0057

OBJECTIVE

The estimation of focal mechanisms and moment tensors of the earthquakes in the vicinity of a nuclear test site is crucial in understanding the tectonic release associated with explosions at the site. With a record of 100 seismic events a year around the Lop Nor test site (within 500 km), focal mechanisms or moment tensor results have been available for only a few events, and these are at $m_b > 5$. Most of the events in the area are smaller, and are not recorded teleseismically. Only in recent years, have digital records become available. They have provided an opportunity to understand the seismicity and earthquake characteristics in the Lop Nor area, and will be the basis for discrimination studies.

RESEARCH ACCOMPLISHED

We obtained the locations and magnitudes of a large set of seismic events, occurring in the years 1970 and 1972-1989, within 4° lat/long of the Lop Nor test site (Figure 1). The numbers of events above magnitudes 2, 3, 4, 5, 6 are respectively 2757, 884, 164, 31 and 4. Though much of this seismicity is diffuse, most of the activity is concentrated in the Tian Shan area. Two sub-parallel lineaments can be identified (Figure 1). One of them is presumably associated with the main Tian Shan fault system and another, about 150 km to the south, appears to terminate in the vicinity of the test site (Figure 1). Near the test site, around 2° in lat/long, the USGS/PDE has reported a total of 65 events (including 16 explosions) during 1953-1991 (some explosions are listed as earthquakes); but there are 972 seismic events in the Chinese catalog from 1972-1989, indicating that in fact this region has quite high seismicity.

Since most of the events in the area are small ($m_b < 5$) they can be well-recorded only at regional distances, and we needed to adopt a method that is able to retrieve the focal mechanisms by using few stations. The only nearby digital station is in Urumqi (WMQ), about 240 km northwest from the test site. Fan and Wallace (1991) and Gao and Wallace(1993) used the first tens of seconds of the seismic records to study the focal mechanism. Zhao and Helmberger (1993) have used the whole waveform at regional distances to search for fault plane solutions. In this study, we apply an inversion scheme that uses both body and surface waveforms to retrieve the focal mechanisms. The procedure is similar to that of Fan and Wallace (1991). The Green's functions of the fundamental faults SS, DS, and 45DS are calculated by reflectivity. Then these Green's functions are converted to the types associated with moment tensor elements. Thus we build up the linear relationship $\mathbf{Gm} = \mathbf{D}$, where $\mathbf{G}$ consists of Green's functions associated with the moment tensor elements, $\mathbf{m}$ is the model parameter to be inverted (the moment tensor

elements), and **D** is the observed waveform data. The moment tensor **m** is estimated by single value decomposition. In the inversion, the waveform is divided into body wave segments and surface wave segments, and a time shift is allowed between the segments. Thus the errors in the inversion caused by possible mislocations of events can be avoided.

The structure along the wave propagation path is very important in the focal mechanism inversions. The Lop Nor test site is in an intermontane basin and surrounding hills (Matzko, 1992, 1994). Along the path from Lop Nor to station WMQ are parts of the edge of the Tarim basin and Tian Shan (Figure 1). The crustal structure along the path is no doubt very complex. There are efforts to study the structures around the Tian Shan area (e.g. Mangino and Ebel,1992; Roecker, et al., 1993), but the detailed structures of the eastern part of Tian Shan and the northeast Tarim basin are not very clear. Here, we have attempted to obtain a simple approximate crustal structure for the path to WMQ by using an explosion on 9/29/1988, with $m_b = 4.26$ (Douglas et al. 1993), recorded at station WMQ. This appears to be the only digital data available from a Chinese station at a regional distance for a Chinese nuclear explosion. This event is relocated by Douglas et al. (1993) at 41.759°N, 88.400°E. We take the model from Mangino and Ebel (1992) as a starting point and reduce it to a simple 3-layer crustal model. We then modify the parameters (α, β and thickness) by trial and error to fit synthetics to the observations. The synthetics for this event are calculated for a simple isotropic source. The final model and the comparison of the waveforms are shown in Table 1 and Figure 2. After the simple crustal model is obtained, the Green's functions are calculated for each earthquake in our data set. In this study, we have collected waveforms from IRIS for WMQ of events indicated in the Chinese catalog. The time window for the catalog is from 1972-1989, and year 1970, but the digital data from WMQ are available only for 1988-1989, i.e. only for two years. Within the data collected, only the events within 2° of Lop Nor and with high signal-to-noise ratio (usually $m_b \geq 3.0$), are studied. In this way, we have obtained regional data for a total of 15 events with location known and close to Lop Nor.

Figure 3 shows two examples of the results with whole waveforms. One of the events occurred on 3/4/1988, with $m_b = 4.0$ (distance to WMQ 170 km) and the other on 5/25/1989 with $m_b = 3.9$ (distance to WMQ 223 km). Both events show reverse faulting. The locations of these events are shown in Figure 4. Figure 4 also shows the results of 13 other events we inverted in this study plus some results from Gao and Wallace (1994) and one event on 10/2/1993 with a CMT result. The focal mechanisms of the earthquakes in Figure 4 show a domination of reverse faulting in the area. At the test site and nearby, some of the events show a left-lateral strike-slip faulting pattern. The P axis from the focal mechanisms trend in N-S, NE-SW, and NW-SE directions.

SUMMARY AND RECOMMENDATIONS

Although the USGS/PDE and ISC catalogs indicate little seismic activity in the vicinity of the Lop Nor test site, the Chinese catalog used in our study shows that in fact this region has quite high seismicity. In this report, we have studied 15 earthquakes in the vicinity of Lop Nor, digitally recorded by the nearby CDSN station WMQ. The process of collecting other data, such as digital recordings from Borovoye, Kazakhstan, and analog data from Chinese stations (one of them is WMQ) is well underway. The ability to invert for focal mechanisms using few regional stations (the extreme is single station inversion) provides an opportunity to investigate the small to intermediate earthquakes in the Lop Nor area. And the vast data base of these events will also make the region of the Chinese test site an excellent source of data for discrimination research.

REFERENCES

Douglas, A., P.D. Marshall, and K.H. Jones, Body-Wave Magnitudes and Locations of Explosions at the Chinese Test Site, 1967-1989, Atomic Weapons Establishment report No. O 12/93, 1993.

Fan and Wallace, The determination of source parameters for small earthquakes from a single, very broadband seismic station, *Geophys.Res.Lett.*, **18**, 1385-1388, (1991.

Gao and Wallace, Seismotectonics of the Lop Nor region, Northwest China (in preparation), 1994.

Gao and Wallace, Aftershocks of the June 1990 Rudbar-Tarom earthquake: evidence for slip partitioning, submitted to JGR, 1994.

Mangino S. and J. Ebel, The receiver structure beneath the Chinese Digital Seismography Network (CDSN) stations: preliminary results, Phillips Laboratory, PL-TR-92-2149, 1992.

Matzko, R., Geology of the Chinese Nuclear Test Site Near Lop Nor, Xinjiang Province, China. 14th DARPA/AF Symposium, 1992, Tucson, AZ., 297-303, 1992.

Matzko, J.R., Geology of the Chinese nuclear test sties near Lop Nor, Xinjian Uygur Autonomous Region, China, *Engineering Geology*, **36**, 173-181, 1994.

Richards, P.G., W.-Y. Kim and G. Ekström, Initial Visit to the Borovoye Geophysical Observatory, North Kazakhstan, 14th DARPA/AF Symposium, 1992, Tucson, AZ.,344-350, 1992.

Roecker, S.W., T.M. Sabitova, L.P. Vinnik, Y.A. Burmakov, M.I. Golvanov, R. Mamatkanova, and L. Munirova, Three-Dimensional Elastic Wave Velocity Structure of the Western and Central Tien Shan, *Jour. Geophy. Res.*, **98**, 15779-15796, 1993.

Zhao and Helmberger, Source Estimation from Broadband Regional Seismograms, *Bull. Seis. Soc. Am.*, **84**, 91-104, 1993.

Table 1. Crustal structure model

depth (km)	α (km/s)	β (km/s)	ρ (Mg/m^3)
0 to 7	5.00	2.68	2.00
7 to 38	6.80	3.58	2.60
38 to 46	7.50	4.20	2.63
below 46	8.00	4.50	3.40

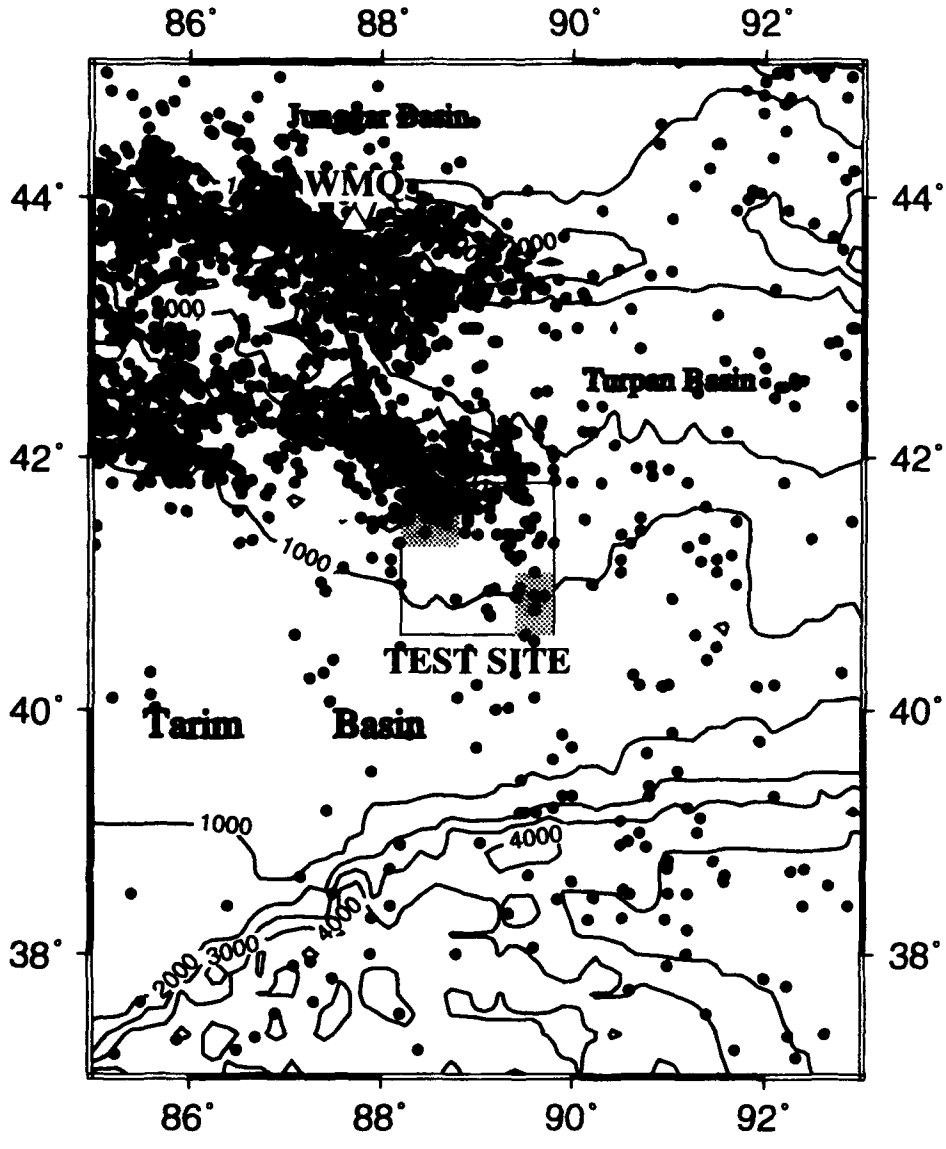


Figure 1. Seismicity near Lop Nor (Catalog from the State Seismological Bureau of China, 1970-1989). Seismic activity is concentrated in the Tian Shan area. The shaded area at the lower right corner of the test site is the site for atmospheric tests, and the shaded area at the upper left is the underground explosion site. Contour lines show elevation with 1000 m increments.

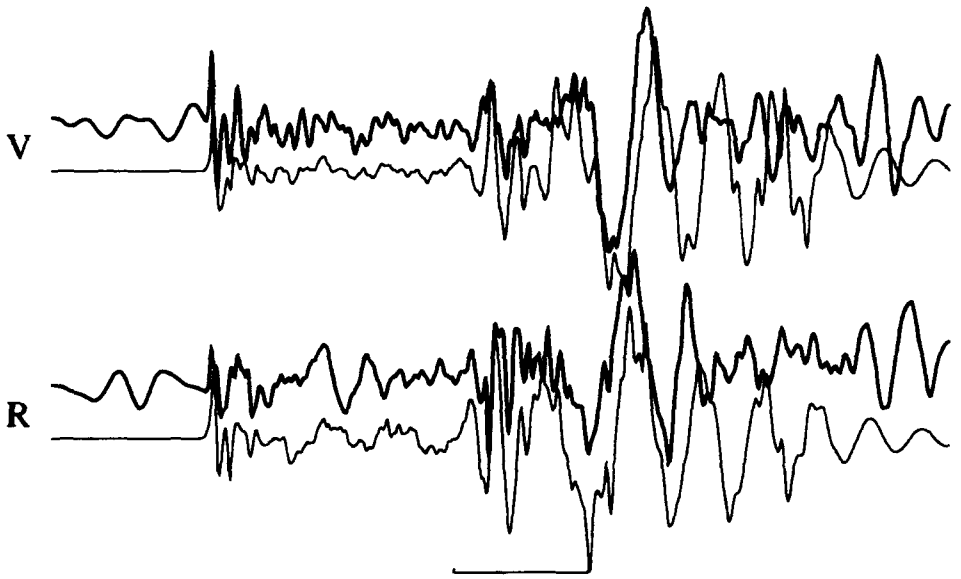


Figure 2. Waveform comparisons of an isotropic source within the crustal model of Table 1, and the explosion observations at WMQ (1988/9/29). The thick upper traces are observations and the lower thinner traces are synthetics. Both are filtered with a low pass filter having a corner frequency of 0.25 Hz.

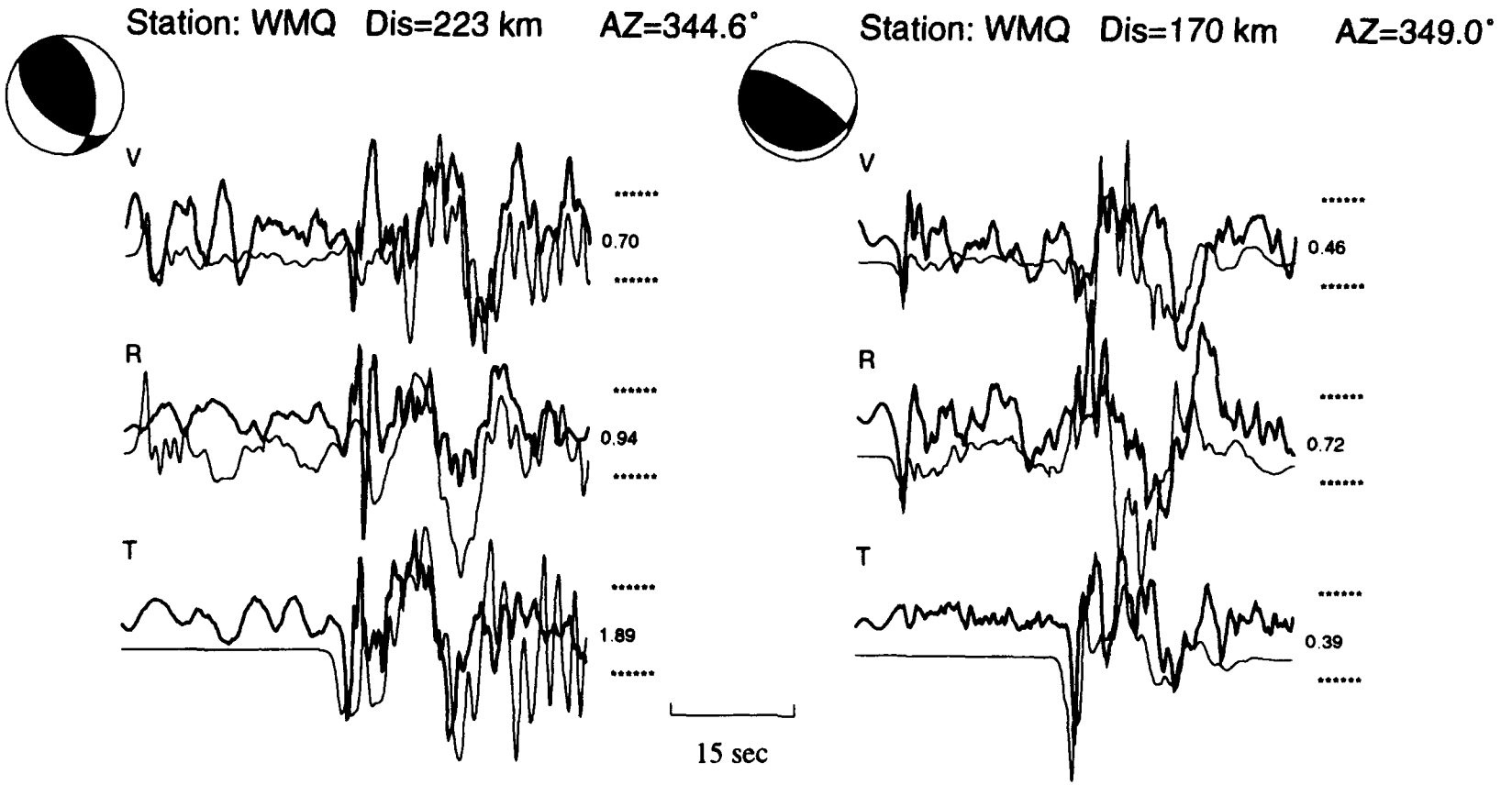


Figure 3. Two examples of the waveform fits for the inversion. Left panel: event on 1988/03/04, mb = 4.0; right panel: event on 1989/05/25, mb = 3.9. The respective focal mechanisms are shown at the upper left corners. Both events show reverse faulting mechanisms. Low pass filter at corner frequency 0.25 Hz applied.

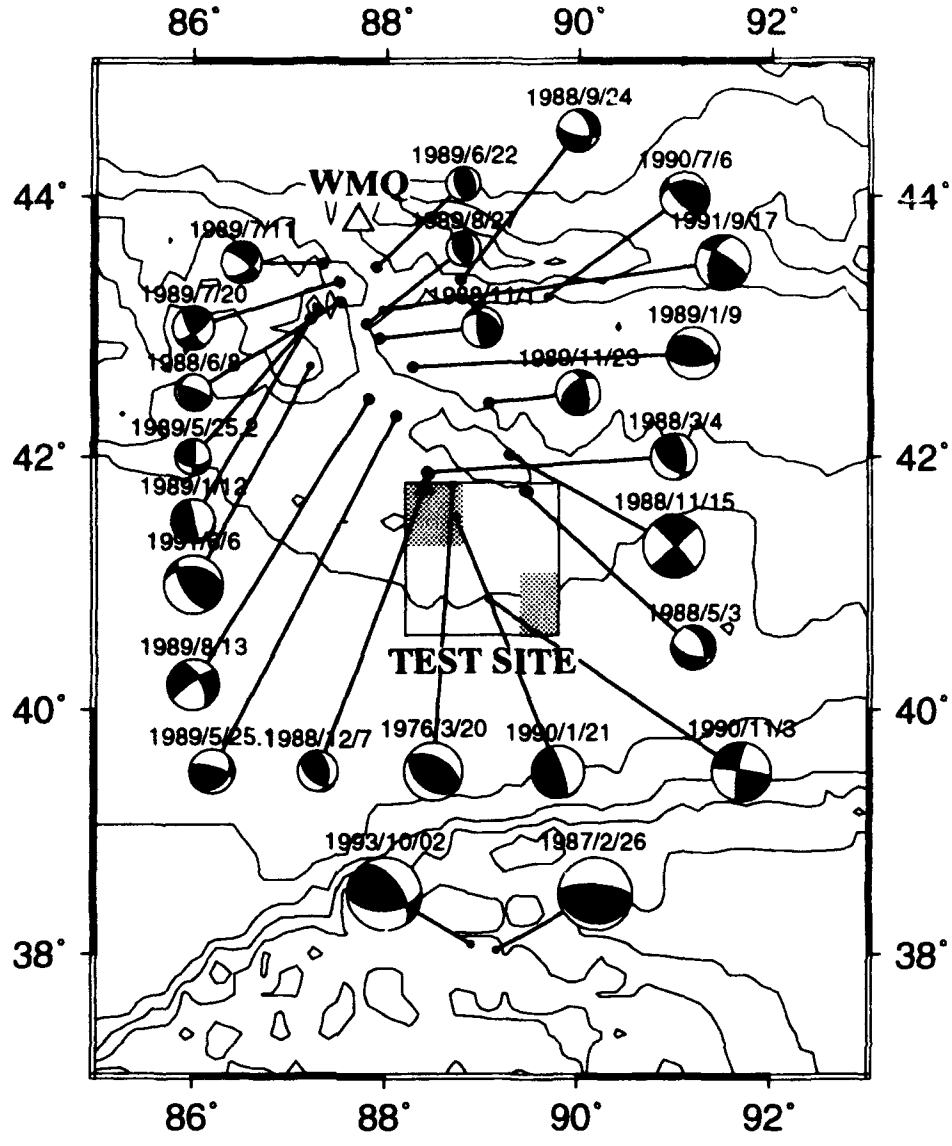


Figure 4. Inversion results for the earthquakes from 1988-1993, including results from Gao and Wallace (1994), and a CMT solution for the 1993/10/02 event. The focal mechanisms show that reverse faulting dominates in the Tian Shan-Lop Nor area. At the test site and nearby, events with left lateral strike-slip mechanisms are also present, indicating tectonic complexities in the area. The black triangle in the test site is the location of the explosion on 1988/9/29.

RADIATION FROM SEISMIC SOURCES IN CYLINDRICAL CAVITIES

R. L. Gibson, Jr., M. N. Toksöz, and W. Dong

Earth Resources Laboratory
Department of Earth, Atmospheric, and Planetary Sciences
Massachusetts Institute of Technology, Cambridge, MA 02139

Contract No. F49620-92-J-0413

OBJECTIVE

Our goal is to understand the effects of the geometry of the explosion source cavity on seismic wavefields for the purposes of developing potential nuclear discrimination methods. We address this goal by performing numerical simulations of the radiation of elastic waves by explosion sources located in cylindrical cavities of finite length. We utilize the indirect boundary element method to compute the seismic displacement fields in a homogeneous, isotropic formation surrounding the cavity, which provides a simple model of a tunnel in which an explosion source might be located. A comparison of the P and S-wave radiation patterns for cavities of different aspect ratios shows that as the aspect ratio decreases (i.e., the cavity changes from very slender to a more equidimensional shape), the amplitude of the S-wave relative to the P-wave decreases substantially. Moving the source from the exact center of the cavity towards one end of the tunnel causes the radiation pattern to approach that of a single point force because the near end of the cavity has a more significant effect than the more distant end.

RESEARCH ACCOMPLISHED

Introduction

Observations of seismic waves generated by nuclear explosions show that the idealized model of an explosion in an isotropic medium with its uniform P-wave radiation pattern is not adequate to describe the behavior of true nuclear sources (e.g., Wallace et al., 1983, 1985; Priestley et al., 1990). While several aspects of the explosion process such as spall or tectonic release contribute to source complexity, deviations from the simple model of a spherical source cavity in an isotropic elastic medium will also have a major impact on source radiation. Zhao and Harkrider (1992) developed analytic expressions for the radiation from an explosion source located off-center in a solid sphere embedded in an infinite isotropic medium. They showed that in this case the source also generates strong S-waves in the far-field and that the effects of this off-center source are strongest at high frequencies. In contrast, Glenn et al. (1985), Glenn et al. (1986), and Rial and Moran (1986) considered the effect of changing the cavity shape from spherical to ellipsoidal and estimated several properties of the radiated seismic waves using a variety of numerical and approximate analytical methods. Like the off-center source in the spherical cavity, a strong S-wave can be radiated by a source located in the center of an ellipsoidal cavity, especially as the cavity becomes more and more needle-like.

In this work, we have considered the radiation of elastic waves by an explosion source located in a cylindrical cavity rather than the spherical or ellipsoidal geometries. The displacement fields

generated by an explosion source in such a cavity, which serves as a model of a tunnel drilled into the surrounding medium, are modeled with an indirect boundary element method. Although our implementation requires that the source must be on the axis of the cavity, it may be located anywhere along the axis relative to the ends of the cavity. We have computed displacement fields and the associated P and S-wave radiation patterns for several configurations of tunnel and source. Our results show that the radiation patterns change significantly as the source is moved from the center of the cavity towards the end, that the relative amplitudes of P and S-waves are sensitive to the aspect ratio of the cavity, and that the patterns are somewhat sensitive to frequency.

Method

The indirect boundary element method (BEM) has recently been applied to the calculation of acoustic and elastic wavefields in and around infinite boreholes in both homogeneous and plane layered media (Bouchon, 1993; Dong, 1993). In addition, the method has been extended to apply to semi-infinite cavities in order to model the radiation from seismic sources on or near the bottom end of a borehole (Dong, 1993). The basic idea of this approach is that the effects of the diffracting boundary on the displacement fields in the elastic medium can be represented by a set of fictitious sources located on the boundary, the cavity wall. Once these fictitious sources and the Green's functions for the elastic medium are known, the wavefield generated by the source inside the cavity can be calculated for a point outside the cavity. Our work extends these earlier results to include the second end of the cylindrical cavity to model the displacement fields generated by an explosion source located inside a tunnel.

The algorithm begins by discretizing the wall of the cylindrical cavity into rings on the cylinder and circular annuli on the top and bottom capping surfaces. Axial symmetry is assumed, so that the source must be located on the tunnel axis. In general, there must be at least 3 elements within the smallest wavelength involved in the calculation. After the discretization, the magnitudes of fictitious volume injection sources for the fluid inside the borehole and vertical and radial force sources for the elastic medium must be determined on each element. This is accomplished by enforcing the appropriate boundary conditions for continuity of stress and displacement. Hence, the stress and displacement generated by each fictitious source must be determined, which is accomplished using the discrete wavenumber approach to evaluate integrals over horizontal wavenumber (Dong, 1993). Then, once the initial displacement field created by the primary explosion source in the fluid is computed, the matrix of boundary condition equations can be solved for the magnitude of each of the individual sources on the boundary elements.

Although the method is relatively straightforward to implement once appropriate expressions for each of the Green's functions are determined, there are some practical difficulties. In particular, the integrals for the displacement and stresses generated by the elements on the ends of the cavity converge very poorly, making accurate numerical solution difficult. Previous implementations of this method applied a premature truncation of the integrals, resulting in serious errors in the computed wavefields (Mandal et al., 1993). We have performed some comparisons of our BEM solutions with finite difference results, with good results in most cases. In general, the two methods give very similar results for P-wave radiation patterns, but the finite difference code tends to yield slightly larger shear wave amplitudes.

Results

We applied the indirect BEM to a cavity 80 m long inside a medium with P-wave velocity 4000 m/s, S-wave velocity 2200 m/s and density 2.2 g/cm^3. The acoustic velocity of the cavity filling material was set to 10000 m/s to simulate the shock wave created by a nuclear explosion. Displacement fields were computed for receivers at a distance of 10000 m from the source to obtain the far-field radiation pattern, and time domain synthetic seismograms were generated by convolving the frequency domain response with a Ricker wavelet. Radiation patterns were then estimated by rotating the seismograms into spherical coordinates to isolate the P and S-waves on the radial and tangential components and picking the maximum amplitude of the envelope of the different traces. Figure 1 shows the radiation patterns for several aspect ratios of the cavity, where we define the aspect ratio as the ratio of the length of the cavity to its diameter. These patterns were computed for a 1 Hz source wavelet. The pattern for the aspect ratio of 10 is very similar to that estimated by Rial and Moran (1986), though our S-wave is larger relative to the P-wave. As the cavity becomes more equidimensional, the relative amplitude of the S-wave is predicted to decrease, and the P-wave radiation pattern becomes more spherical.

The proximity of the cavity end is also very important in controlling the far field radiation pattern (Figure 2). As the source is moved closer to the end of the cavity, the reradiation of energy by the near end begins to dominate the signals seen in the far-field. In Figure 2, the source is moved from the center of the cavity towards the lower end of the vertical cavity. The resulting patterns are essentially equivalent to the radiation pattern of an idealized vertical point force, reproducing the shapes of such patterns, relative amplitudes of P and S-waves, and the polarity changes of the waves with direction (Aki and Richards, 1980). When the source is moved half way from the cavity center to the end of the tunnel (20 m), the S-wave signal is already significantly larger than the P-wave.

The radiation patterns obtained when the acoustic velocity is set to 330 m/s (to model a conventional explosion in an air-filled cavity) are very similar to those in Figure 2, except that the P-wave signals are slightly larger in the downwards direction and the S-wave signals are slightly larger in the upwards direction. Apparently, for this very slow acoustic wave velocity, the wavelength is close enough to the size of the cavity that the asymmetry of the source/cavity arrangement has a stronger effect on the far-field signals than for the nuclear model.

We have also repeated the calculations for the model of the nuclear explosion using a wavelet of 5 Hz (Figure 3). In this case, the patterns are distorted so that the idealized point force radiation pattern is not obtained for the source 1 m from the end of the cavity. Instead, there is still a significant P-wave signal traveling horizontally from the source tunnel. This case is very interesting, since the seismograms in the two vertical directions have opposite polarizations as if they were generated only by the vertical point force. However, since there is no nodal direction, the phase changes gradually near the horizontal direction, yielding unusual phase shifts as a function of propagation direction.

CONCLUSIONS AND RECOMMENDATIONS

The BEM is a useful approach for simulating the far-field response of explosion sources located along the axis of finite length cylindrical cavities. Computational results show that the radiation patterns are sensitive to both the cavity aspect ratio and the location of the source along the

axis. As the cavity becomes more equidimensional and the aspect ratio decreases, the amplitude of the shear wave generated by the explosion decreases until the radiation pattern becomes similar to that of an ideal explosion. However, for a high aspect ratio cavity, moving the source towards the end of the tunnel yields a radiation pattern like that of a vertical point force at lower frequencies (e.g., 1 Hz). As frequency increases, the pattern is somewhat distorted.

While these results provide some useful guidelines in understanding the behavior of explosions located in tunnels, future research is needed to perform more complete and realistic simulations. In particular, the BEM algorithm can be extended to apply to irregular cavity profiles. This has already been done for application to full waveform acoustic log synthesis (Bouchon and Schmitt, 1989). In addition, we would recommend further work on calibrating the method with accurate finite difference codes to simulate the far-field radiation of wavefields by off-axis sources. This latter problem can not be solved with the BEM.

REFERENCES

Aki, K., and Richards, P.G., 1980. *Quantitative Seismology*, vol. 1, Freeman and Company, San Francisco.

Bouchon, M., 1993. A numerical simulation of the acoustic and elastic wavefields radiated by a source in a fluid-filled borehole embedded in a layered medium, *Geophysics*, *58*, 475–481.

Bouchon, M. and D. P. Schmitt, 1989. Full-wave acoustic logging in an irregular borehole, *Geophysics*, *54*, 758–765.

Dong, W., 1993. Elastic wave radiation from borehole seismic sources in anisotropic media, Ph.D. thesis, Massachusetts Institute of Technology.

Glenn, L. A., A. J. C. Ladd, B. Moran and K. A. Wilson, 1985. Elastic radiation from explosively-loaded ellipsoidal cavities in an unbounded medium, *Geophys. J. R. astr. Soc.*, *81*, 231-241.

Glenn, L.A., B. Moran, A.J.C. Ladd, K. Wilson, J.A. Rial, 1986. Elastic radiation from explosively-loaded axisymmetric cavities, *Geophys. J. R. astr. Soc.*,, *86*, 119–136.

B. Mandal, C.A. Schultz, W. Dong, M. Nafi Toksöz and W. Rodi, 1994. Research in nuclear test monitoring: explosions in non-spherical cavities; investigation of enhanced backscattering, *Annual Technical Report*, Air Force Office of Scientific Research, Contract F49620-92-J-0413, M.I.T.

Priestley, K. F., W. R. Walter, V. Martynov and M. V. Rozhkov, 1990. Regional seismic recordings of the Soviet nuclear explosion of the joint verification experiment, *Geophys. Res. Lett.*, *17*, 179-182.

Rial, J. A. and B. Moran, 1986. Radiation patterns for explosively-loaded axisymmetric cavities in an elastic medium: analytic approximations and numerical results, *Geophys. J. R. astr. Soc.*, *86*, 855-862.

Wallace, T.C., D.V. Helmberger, and G.R. Engen, 1983. Evidence of tectonic release from underground nuclear explosions in long-period P waves, *Bull. Seism. Soc. Am.*, *73*, 593–613.

Wallace, T.C., D.V. Helmberger, and G.R. Engen, 1985. Evidence of tectonic release from underground nuclear explosions in long-period S waves, *Bull. Seism. Soc. Am.*, *75*, 157–174.

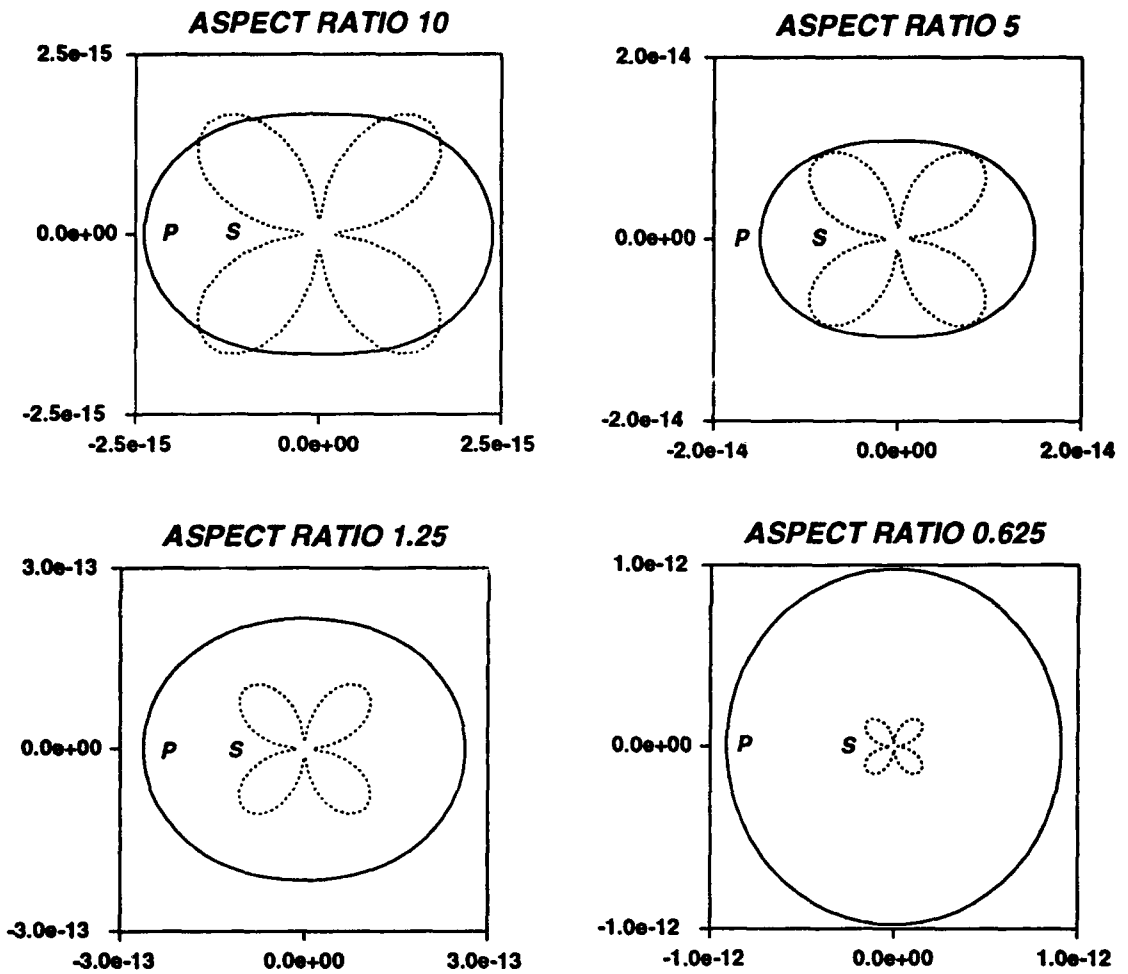


Figure 1: Radiation patterns for tunnels 80 m long with several aspect ratios, obtained from synthetic seismograms with a central frequency of 1 Hz. The velocities of the surrounding medium are given in the text. Note that the cavity is oriented vertically with respect to these patterns, and that the P-wave radiation is largest in the direction perpendicular to the cavity for large aspect ratio.

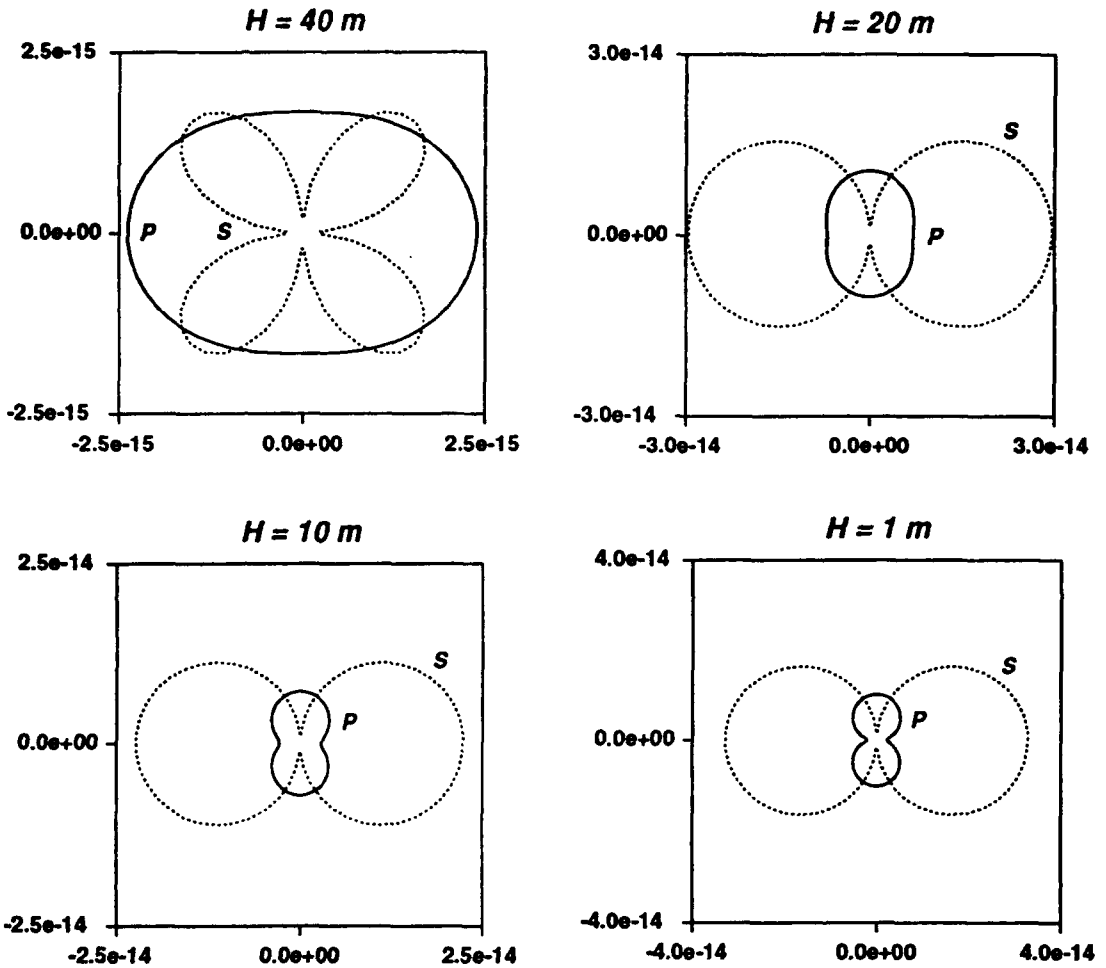


Figure 2: Radiation patterns for several source locations in the 80 m long cavity with an aspect ratio of 10 and a source center frequency of 1 Hz. The distance from the end of the cavity is given by H so that the figure in the upper left (H =40 m) shows the radiation patterns for a source located in the center of the cavity. When the source is off-center, it is located towards the lower end of the cavity.

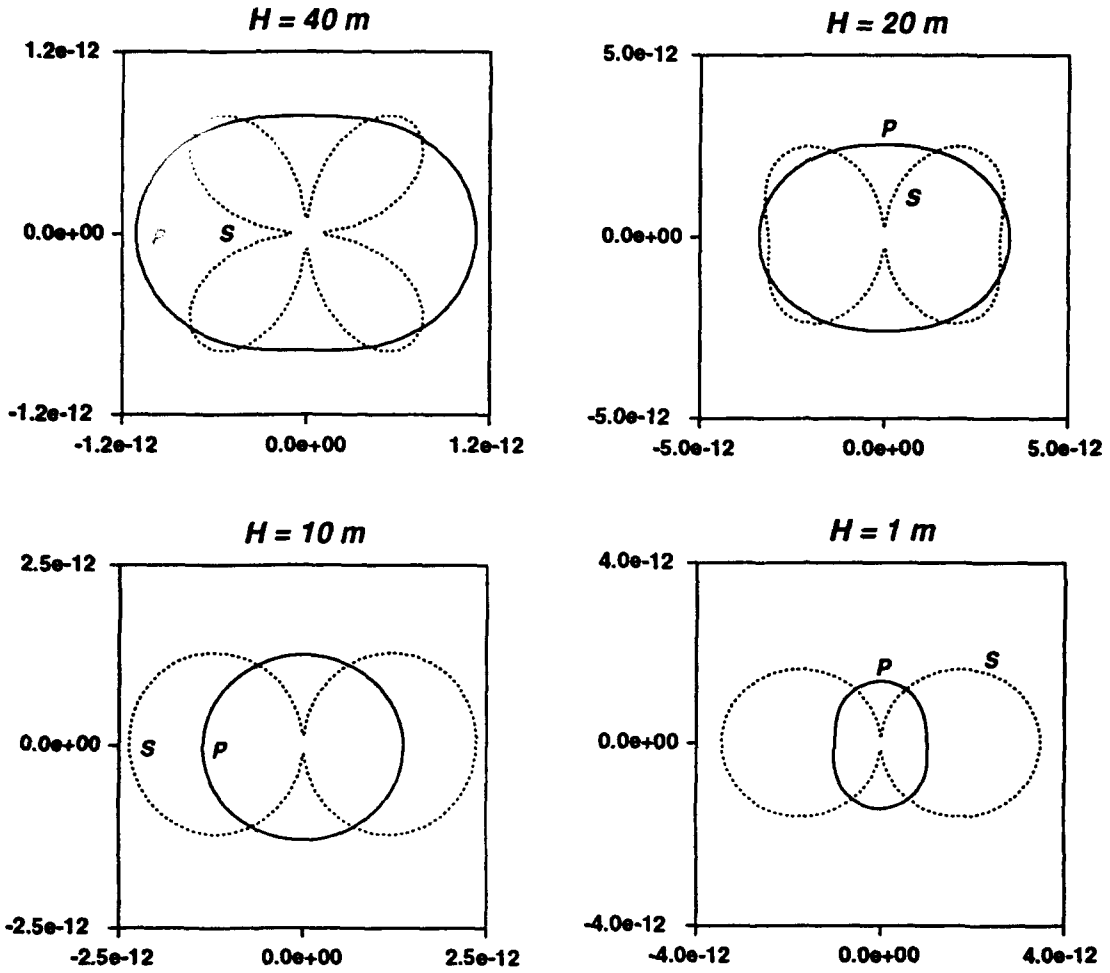


Figure 3: Radiation patterns for several source locations in the 80 m long cavity with an aspect ratio of 10 and a source center frequency of 5 Hz. The format of the figure is the same as Figure 2. Comparison to Figure 2 shows that increasing source frequency has a significant effect on these far-field radiation patterns.

GEOPHYSICAL RESEARCH LETTERS, VOL. 21, NO. 6, PAGES 493-496, MARCH 15, 1994

The U.S. Government is authorized to reproduce and sell this report.
Permission for further reproduction by others must be obtained from
the copyright owner.

Modal fields: A new method for characterization of random seismic velocity heterogeneity

John A. Goff
University of Texas Institute for Geophysics, Austin

Klaus Holliger and Alan Levander
Rice University, Houston, Texas

Abstract. Geologically and petrophysically constrained synthetic random velocity fields are important tools for exploring (through the application of numerical codes) the seismic response of small-scale lithospheric heterogeneities. Statistical and geophysical analysis of mid- and lower-crustal exposures has demonstrated that the probability density function for some seismic velocity fields is likely to be discrete rather than continuous. We apply the term "modal" fields to describe fields of this sort. This letter details a methodology for generating synthetic modal fields which satisfy the von Kármán covariance function. In addition, we explore some of the mathematics of "modality", and define a modality parameter which quantifies the variation between end members binary and continuous fields.

Introduction

The von Kármán covariance is gaining increased recognition as a useful tool for stochastic modeling of a wide range of random geophysical fields. This parameterized model provides quantitative estimation of basic physical characteristics, including rms variation, characteristic or outer scale, Hausdorff (or fractal) dimension, and, in two- or three-dimensional form, structural anisotropy. *Von Kármán* [1949] initially used it to characterize random fluctuations in the velocity field of a turbulent medium. More recently, it has been used to model seafloor morphology [e.g., *Goff and Jordan*, 1988] and seismic velocity perturbations [e.g., *Wu and Aki*, 1985; *Frankel and Clayton*, 1986; *Gee and Jordan*, 1988; *Holliger et al.*, 1993, 1994; *Levander et al.*, 1994].

Like any second-order statistic (i.e., power spectrum, variogram), the von Kármán covariance is a limited description of a random field. It contains no information on the phase distribution or, equivalently, on the functional form of the probability density function. With only a covariance description it is impossible, for example, to distinguish a continuous Gaussian-distributed field from a discrete binary field. The importance of this limitation was recently recognized in published work by *Holliger et al.* [1993] on characterization of lower crustal seismic velocity variations. In that work and subsequent work on Archean upper and middle crustal rocks by *Levander et al.* [1994], petrophysical properties of various crustal exposures were used to generate realistic models of in-situ seismic velocity fields. Both studies found that the von Kármán covariance function was an excellent representation of the second-order statistics of seismic velocity fields. However, they also recognized that the velocity field of some parts of the crystalline crust can be discrete (Figure 1); i.e., that the crustal exposures consist of a small number of compositionally distinct lithologies, each having a different velocity. This observation contrasts with the more generally assumed continuous Gaussian distribution for random velocities [e.g., *Wu and Aki*, 1985, *Frankel and Clayton*, 1986. We use the term "modal" to designate fields with discrete probability densities.

If we consider two random velocity fields, each with identical covariance (including rms variation), but one binary and the other Gaussian distributed, the respective seismic responses can differ significantly. For example, a binary field may generate 2-3 times the backscattered energy as a Gaussian-distributed field with the same covariance [*Holliger et al.*, 1994]. Larger impedance contrasts associated with modal fields also imply increased P to S conversions compared to Gaussian-distributed fields.

There are two principal goals for this letter, one purely practical and the other more philosophical. The first is to detail a methodology for generating synthetic random fields with specific discrete distributions and known von Kármán covariance statistics. Synthetic fields are realistic representations of random velocity heterogeneities which can be used to simulate the seismic response to such fields [e.g., *Frankel and Clayton*, 1986] For example, *Holliger et al.*, [1993] and *Levander et al.* [1994] have demonstrated qualitatively that finite difference simulations on modal fields with von Kármán covariance statistics successfully reproduce the character of some crustal seismic data. The methodology for creating synthetic modal fields involves (1) generating a Gaussian-distributed synthetic via a Fourier method, and (2) mapping the probability space from Gaussian to discrete distributions. Considerable effort is devoted to mapping the relationship between the covariance function of the starting Gaussian-distributed field and that of the resulting modal field.

The second goal is to explore some of the mathematics of "modality". We find that the mapping between Gaussian and modal fields with von Kármán covariance provides a rigorous definition of a modality parameter which varies continuously between 2 (binary distribution) and ∞ (Gaussian-continuous distribution). This parameter quantifies the "discreteness" in a probability distribution. We believe that, along with properties associated with covariance (i.e., rms fluctuation, characteristic scales, fractal dimension), modality is an essential property of a random velocity field to characterize before wavefield propagation through that field can be predicted or understood.

Copyright 1994 by the American Geophysical Union.

Paper number 94GL00311
0094-8534/94/94GL-00311$03.00

The von Kármán Covariance Model

We consider a spatially homogeneous, zero-mean random field $h(\mathbf{x}_1)$, a function of vector position $\mathbf{x}_1$. With regard to seis-

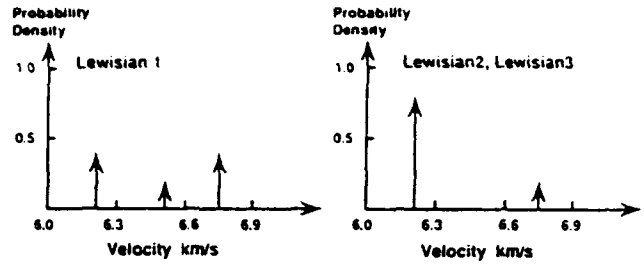


Figure 1. Velocity populations from crystalline rock estimated from geologic maps and petrophysical data from the Lewisian gneiss complex (Archean upper, middle, and lower crust) [*Levander et al.*, 1994]. These examples display a variety of modal probability density functions, reflecting the occurrence of two or three compositionally distinct lithologies.

mic velocity variations, $h(\mathbf{x}_1)$ can be considered as a small-scale random velocity field superimposed on a deterministic, smoothly varying large-scale velocity field [e.g., *Holliger et al.* , 1993]. The covariance can be defined in terms of the 2-point expectation

$$C_{hh}(\mathbf{x}) = E[h(\mathbf{x}_1)h(\mathbf{x}_1 + \mathbf{x})] , \qquad (1)$$

where $\mathbf{x}$ represents a lag vector and E the expectation operator.

The following presentation of the von Kármán covariance model closely follows that of *Goff and Jordan* [1988], which contains an exhaustive reference list on this subject. We represent the von Kármán covariance model by

$$C_{hh}(\mathbf{x}) = H^2 G_\nu(r(\mathbf{x})) / G_\nu(0) , \qquad (2)$$

where H is the rms velocity variation and G_ν is defined by

$$G_\nu(r) = r^\nu K_\nu(r), \quad 0 \le r < \infty, \quad \nu \in [0,1] . \qquad (3)$$

K_ν is the modified Bessel function of the second kind and order ν. G_ν is plotted by *Goff and Jordan* [1988] at several values of ν. $G_\nu(r)$ are a class of monotonically decaying covariance functions. Fields corresponding to this covariance representation are aperiodic. The order parameter ν controls the behavior of $G_\nu(r)$ at the origin; its slope at $r = 0$ is zero for $\nu = 1$ and infinite for $\nu = 0$. $G_{1/2}(r)$ is simply an exponential function.

The function $r(\mathbf{x})$ can be used to express structural anisotropy, typically an elliptic function which modifies the lag scale along specified eigenvectors [*Goff and Jordan*, 1988]. The form of $r(\mathbf{x})$ has no bearing on the formulation presented here. For simplicity we will limit consideration to the isotropic case $r(\mathbf{x}) = k_0|\mathbf{x}| \equiv k_0 x$. Generalization to elliptic anisotropic functions is trivial. The covariance model considered here is specified by three parameters H, k_0, and ν. The Hausdorff (or fractal) dimension D associated with (2) is $D = N + 1 - \nu$, where N is the Euclidean dimension of the coordinate vector $\mathbf{x}$ [e.g., *Goff and Jordan*, 1988]. The parameter ν is identical to the Hurst number [e.g., *Feder*, 1988]. The power spectrum is calculated by Fourier transform of the covariance (see *Goff and Jordan* [1988] for functional form). The isotropic von Kármán power spectrum contains a corner wavenumber at k_0. At higher wavenumbers there is a power-law (fractal) behavior, the exponent of which is controlled by ν, while at lower wavenumbers the spectrum is flat.

Synthetic Modal Fields

To generate a Gaussian-distributed random field in one, two, or three dimensions with known second order statistics is straightforward. We compute a Fourier spectrum on a regularly spaced wavenumber grid by multiplying the square-root of the power spectrum model by a phase factor $\exp(i\phi)$, where ϕ is a random number uniformly distributed on the interval $[0,2\pi)$. Hermetian symmetry is enforced, and the space-domain image is then obtained by inverse Fourier transform. The uniformly distributed phase ensures a Gaussian probability distribution.

Non-Gaussian fields can be derived from Gaussian fields through a mapping of probability distribution space [e.g., *Christakos*, 1992]. We consider the special case of a "modal" field $h(\mathbf{x}_1)$ which can take on discrete values $H_1 < H_2 < \ldots < H_n$ with respective probabilities ρ_i ($\rho_1 + \rho_2 + \ldots + \rho_n = 1$). Fields can be rescaled and mean shifted following transformation. For simplicity assume that $h(\mathbf{x}_1)$ has zero mean and unit variance. Beginning with a zero mean, unit-variance Gaussian-distributed field $g(\mathbf{x}_1)$ with covariance represented by the notation $C_{gg}(\mathbf{x})$, a modal field may be generated through the following equations

$$h(\mathbf{x}_1) \equiv \begin{cases} H_n, & g_{n-1} < g(\mathbf{x}_1) < g_n = +\infty \\ \vdots & \\ H_i, & g_{i-1} < g(\mathbf{x}_1) < g_i \\ \vdots & \\ H_1, & g_0 = -\infty < g(\mathbf{x}_1) < g_1 \end{cases} , \qquad (4)$$

$$\rho_i = \int_{g_{i-1}}^{g_i} p(g(\mathbf{x}_1))\, dg(\mathbf{x}_1) . \qquad (5)$$

The density function $p(g(\mathbf{x}_1))$ is simply a Gaussian function with zero mean and unit variance. Equations (4) and (5) are a generalized form of non-conditional indicator simulation [e.g., *Journel and Isaaks*, 1984]. Figure 2 shows an example of a mapping from a Gaussian-distributed field to a binary field.

An alternative method for generating modal fields with arbitrary discrete values is the generalized telegraph signal (e.g., *Banik et al.* [1985], and references therein). This methodology, based on Markov autoregressive time series modeling, is severely limited; the Hurst number is always 0.5, and simulations can be generated only in 1 dimension.

Probability distribution mappings such as (4) and (5) will alter the form of the covariance. Where both Gaussian mapped fields have zero mean and unit variance, the relationship between the covariance of the mapped field $C_{hh}(\mathbf{x})$ and the covariance of the Gaussian field $C_{gg}(\mathbf{x})$ is given by [*Christakos*, 1992]

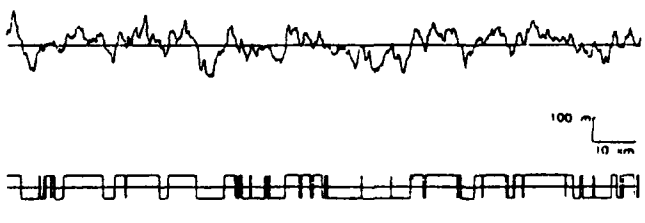


Figure 2. Demonstration of the mapping algorithm (4) for a simple binary case. Top profile is Gaussian-distributed with von Kármán covariance parameters (equation (2)) H = 50 m, $k_{0,c}$ = 0.70 km^{-1}, and ν_c = 0.80. The bottom binary profile has been mapped from the Gaussian-distributed profile using $\rho_1 = \rho_2 = 0.5$ and $H_1 = -H_2 = 50$ m. The resulting von Kármán covariance parameters for the binary field, which can be determined from Table 1, are H = 50 m, k_0 = 0.57 km^{-1}, and ν = 0.37.

$$C_{hh}(\mathbf{x}) = \frac{1}{2\pi\sqrt{1-C_{gg}^2(\mathbf{x})}} \int_{-\infty}^{+\infty}\int_{-\infty}^{+\infty} h(\mathbf{x}_1)h(\mathbf{x}_1+x) \times \exp\left[-\frac{g^2(\mathbf{x}_1)-2C_{gg}(\mathbf{x})g(\mathbf{x}_1)g(\mathbf{x}_1+\mathbf{x})+g^2(\mathbf{x}_1+\mathbf{x})}{2(1-C_{gg}^2(\mathbf{x}))}\right] \times dg(\mathbf{x}_1)dg(\mathbf{x}_1+\mathbf{x}), \quad (6)$$

where h is specified by the mapping equation (4). Hence, to generate a modal field which satisfies the probability distribution mapping in (4) and a particular covariance model $C_{hh}(\mathbf{x})$, one must first ascertain $C_{gg}(\mathbf{x})$ such that equation (6) is satisfied.

von Kármán Modal Fields

Unfortunately, determination of an analytic relationship between $C_{gg}(\mathbf{x})$ and $C_{hh}(\mathbf{x})$ using equation (6) appears to be an intractable problem. However, extensive trial-and-error solutions have lead us to conclude empirically that modal fields mapped from Gaussian fields with von Kármán covariance also have von Kármán covariance. This section presents some results of a systematic exploration of the relationship between covariance parameters of starting Gaussian fields and those of mapped modal fields. The latter are determined by fitting a von Kármán model to a numerical integration of equation (6).

In the following tabulations, the rms parameter H is not considered because it is irrelevant. Tabulated values of H_1, H_2,..., H_n are chosen for intuitive clarity; i.e., the mean and variance of the resulting modal function $h(\mathbf{x}_1)$ are not necessarily 0 and 1 respectively. The mean is subtracted and variance rescaled to unity prior to application of equations (4) and (6). For clarity, we append the subscript c (for "continuous") to denote the covariance parameters used to generate the starting Gaussian-distributed field (i.e., $k_{0,c}$ and ν_c). The parameter r_k is the ratio between k_0 (corner wavenumber, or lag scaling parameter) for the mapped modal field and $k_{0,c}$ for the starting Gaussian-distributed field. This value is general for all $k_{0,c}$.

Binary Fields

Binary fields are the simplest of modal fields. The binary field covariance parameters k_0 and ν depend only on the three parameters $k_{0,c}$, ν_c, and ρ_1 ($\rho_2 = 1 - \rho_1$). Because the binary field is set to zero mean and unit variance, the parameters H_1 and H_2 are determined by ρ_1 (see Table 1). There are two important results evident in Table 1. First, binary field values of the Hurst number ν are roughly 1/2 the corresponding value of ν_c, and in all cases less than 0.5. This is consistent with heuristic arguments that slopes are always negatively correlated for binary fields [*Holliger et al.*, 1993]. Second, ν is not dependent on the proportion of the binary field designated to H_1 versus the proportion designated to H_2 (specified respectively by ρ_1 and $\rho_2 = 1 - \rho_1$). This implies a fundamental one-to-one relationship between the fractal dimension of a binary field and the fractal dimension of the corresponding Gaussian-distributed field defined by the mapping equation (4). We designate this relationship functionally as $\nu_2(\nu_c)$. The following empirical equation approximates this relationship:

$$\nu_2(\nu_c) \equiv \begin{cases} \nu_c/2 - 0.12(\nu_c - 0.5), & \nu_c \geq 0.5 \\ \nu_c/2 - 0.05(\nu_c - 0.5), & \nu_c \leq 0.5 \end{cases}. \quad (7)$$

Table 1. Von Kármán covariance parameters determined for binary fields mapped from Gaussian-distributed field

	$\rho_1 = 0.5$		$\rho_1 = 0.59$		$\rho_1 = 0.70$		$\rho_1 = 0.85$	
ν_c	r_k	ν	r_k	ν	r_k	ν	r_k	ν
0.99	0.78	0.43						
0.90	0.80	0.40	0.81	0.40	0.84	0.40	0.95	0.40
0.80	0.82	0.37						
0.70	0.83	0.33	0.84	0.33	0.86	0.33	0.99	0.33
0.60	0.84	0.29						
0.50	0.85	0.25	0.87	0.25	0.90	0.25	1.05	0.25
0.40	0.86	0.20						
0.30	0.87	0.16	0.90	0.16	0.93	0.16	1.12	0.16
0.20	0.88	0.11						

The parametric form for the von Kármán covariance function is given in equation (2). Binary fields are generated by the mapping equation (4) with $n = 2$, $H_1 = -1$, $H_2 = +1$ (prior to removing mean and rescaling to unit variance), ρ_1 as shown in table, and $\rho_2 = 1 - \rho_1$. Binary field covariance parameters are determined by fitting equation (2) to a numerical integration of equation (6). The starting Gaussian field is generated with $\nu = \nu_c$ as shown in table. The parameter r_k represents the ratio between the value of k_0 for the binary field and $k_{0,c}$ for the starting Gaussian-distributed field. This value is general for all starting and mapped values of k_0.

Ternary Fields and Fractional Modality

Ternary fields are substantially more in complex than binary fields; k_0 and ν are dependent on the relative values of H_1, H_2, and H_3, the respective probabilities ρ_1, ρ_2, and ρ_3, as well as the starting parameters $k_{0,c}$ and ν_c. It is impractical to present the entire phase space in tabulated form. Table 2 displays some representative examples which enable an intuitive understanding of the relationships among these parameters. Two principal conclusions are drawn from Table 2. First, when H_1, H_2, and H_3 are evenly separated and have roughly similar probabilities, a maximum value of ν is obtained which is approximately equal to $2\nu_c/3$ (exact for $\nu_c = 0.5$). Similar investigation of higher mode fields confirms an approximate $\nu_c(n\text{-}1)/n$ progression for the maximum possible value of ν for a given modal value n (exact for $\nu_c = 0.5$). We designate these values as $\nu_n(\nu_c)$. The following empirical equation provides a good representation

$$\nu_n(\nu_c) \equiv \nu_2(\nu_c) + (\nu_c - \nu_2(\nu_c))(n-2)/n, \quad (8)$$

where $\nu_2(\nu_c)$ is given by equation (7).

The second conclusion derived from Table 2 is the following: the closer the ternary field comes to being a binary field, either by bringing one of the H_i values closer to another or by decreasing one of the probabilities ρ_i, the closer ν gets to ν_2. This is a fundamentally intuitive result, and implies that morphological "modality", including non-integer or fractional modality, can be quantified by the relationship between ν and ν_c. For example, if we estimate ν in the range $\nu_2 < \nu < \nu_3$, its modality should have a value between 2 and 3. Replacing n in equation (8) with the designated modality parameter M, the following can be derived

$$M(\nu_c, \nu) \equiv 2(\nu_c - \nu_2(\nu_c))/(\nu_c - \nu). \quad (9)$$

M can vary from a 2 (binary field) to ∞ (continuous field).

Table 2. Von Kármán covariance parameters determined for ternary fields mapped from Gaussian-distributed fields.

ν_c	H_1	H_2	H_3	ρ_1	ρ_2	ρ_3	k_0	ν
0.5	-1.0	0.0	1.0	0.39	0.24	0.37	0.90	0.33
"	-1.0	0.25	1.0	"	"	"	0.89	0.32
"	-1.0	0.50	1.0	"	"	"	0.89	0.30
"	-1.0	0.75	1.0	"	"	"	0.89	0.28
"	-1.0	1.0	1.0	"	"	"	0.87	0.25
0.9	-1.0	0.0	1.0	0.39	0.24	0.37	0.87	0.55
"	-1.0	0.25	1.0	"	"	"	0.86	0.53
"	-1.0	0.50	1.0	"	"	"	0.85	0.50
"	-1.0	0.75	1.0	"	"	"	0.83	0.45
"	-1.0	1.0	1.0	"	"	"	0.80	0.40
0.5	-1.0	0.0	1.0	0.51	0.22	0.27	0.92	0.33
"	"	"	"	0.62	0.20	0.18	0.93	0.32
"	"	"	"	0.73	0.09	0.18	0.98	0.30
"	"	"	"	0.79	0.03	0.18	0.97	0.26
"	"	"	"	0.81	0.01	0.18	0.96	0.25
0.9	-1.0	0.0	1.0	0.51	0.22	0.27	0.88	0.55
"	"	"	"	0.62	0.20	0.18	0.89	0.53
"	"	"	"	0.73	0.09	0.18	0.92	0.49
"	"	"	"	0.79	0.03	0.18	0.91	0.43
"	"	"	"	0.81	0.01	0.18	0.89	0.40

The parametric form for the von Kármán covariance function is given in equation (2). Ternary fields are generated by the mapping equation (4) with $n = 3$ and H_i (prior to removing mean and rescaling to unit variance) and ρ_i ($i = 1, 2, 3$) as shown in table. See Table 1 for further details.

We believe that morphological modality, as defined in equation (9), is a very useful concept for quantifying an important aspect of the "non-Gaussian" nature of seismic velocity fields found in the crust, and discrete random fields in general. Modality need not be confined to purely modal fields. If we are interested in quantifying the morphological modality of any field $h(\mathbf{x}_1)$ that has von Kármán-type covariance statistics, the following general steps are required: (1) estimate the covariance parameters k_0 and ν for $h(\mathbf{x}_1)$, (2) estimate the probability density function $p(h)$ for $h(\mathbf{x}_1)$ (for modal fields this requires estimating the total number of modes n, the value of each mode H_i, and their respective probabilities ρ_i ($i = 1,...,n$)), (3) define the probability mapping between $p(h)$ and the Gaussian probability density with zero mean and unit variance (i.e., equation (4) for modal fields), (4) through trial-and-error application of equation (6), determine covariance values $k_{0,c}$ and ν_c of a Gaussian-distributed field $g(\mathbf{x}_1)$ which, given the probability mapping between $g(\mathbf{x}_1)$ and $h(\mathbf{x}_1)$, will produce a field with identical covariance statistics to $h(\mathbf{x}_1)$, and finally (5) determine modality M using equation (9).

Conclusions

Recent work suggests that the degree of "discreteness" or "modality" in velocity heterogeneity can be important. This letter provides two valuable tools for investigating the seismic response to random modal fields: (1) a detailed method for generating synthetic modal fields which conform to von Kármán covariance statistics and (2) a definition for a modality parameter.

Synthetic fields are necessary for finite difference simulations, frequently the only means available to investigate wave propagation in highly heterogeneous media. Generating modal synthetic fields involves the following steps: (1) for given mode n, values $h(\mathbf{x}_1) = H_i$ ($i = 1,...,n$), corresponding probability density function ρ_i and von Kármán covariance parameters k_0 and ν, determine corresponding parameters $k_{0,c}$ and ν_c for starting Gaussian-distributed field $g(\mathbf{x}_1)$ through trial-and-error application of equation (6), (2) generate a realization $g(\mathbf{x}_1)$ using a Fourier method, (3) map $g(\mathbf{x}_1)$ via equations (4) and (5) to generate a zero mean, unit-variance modal field $h(\mathbf{x}_1)$, and (4) rescale $h(\mathbf{x}_1)$ to desired rms H and add a desired mean value

The relationship between ν_c and ν found through a systematic exploration of mappings between Gaussian and modal fields (Tables 1 and 2) led us to an empirical definition (equations (8) and (9)) of morphological "modality" M. This parameter quantifies "discreteness" in the velocity distribution. We believe that, along with properties associated with covariance, modality is a critical component to predicting the seismic response to random velocities within the Earth, particularly the crust.

Acknowledgments. We thank two anonymous reviewers for comments. This work was supported by AFOSR grant F49620-94-1-0100. UTIG contribution #1044. Crustal Heterogeneity Initiative (CHI) cont. #9.

References

Banik, N.C., I. Lerche, J.R. Resnick, and R.T. Shuey, Stratigraphic filtering, Part II: Model spectra, Geophysics, 50, 2775-2783, 1985.

Christakos, G., *Random field models in Earth sciences*, 474 pp., Academic Press, San Diego, 1992.

Feder, J., *Fractals*, 183 pp., Plenum Press, New York, 1988.

Frankel, A., and R.W. Clayton, Finite difference simulations of seismic scattering: Implications for the propagation of short-period seismic waves in the crust and models of crustal heterogeneity, *J. Geophys. Res.*, *91*, 6465-6489, 1986.

Gee, L.S., and T.H. Jordan, Polarization anisotropy and fine-scale structure of the Eurasian upper mantle, *Geophys. Res. Lett.*, *15*, 824-827, 1988.

Goff, J. A., and T.H. Jordan, Stochastic modeling of seafloor morphology: Inversion of Sea Beam data for second-order statistics, *J. Geophys. Res.*, *93*, 13,589-13,608, 1988.

Holliger, K., A. Levander, and J. A. Goff, Stochastic modeling of the reflective lower crust: petrophysical and geological evidence from the Ivrea Zone (Northern Italy), *J. Geophys. Res.*, *98*, 11,967-11,980, 1993.

Holliger, K., A. Levander, R. Carbonell, and R. Hobbs, Some attributes of wavefields scattered from Ivrea-type lower crust, *Tectonophysics*, in press, 1994.

Journel, A. G., and E. H. Isaaks, Conditional indicator simulation: Application to a Saskatchewan uranium deposit, *Math. Geology*, *16*, 685-718, 1984.

Levander, A., R.W. England, S.K. Smith, R.W. Hobbs, J.A. Goff, and K. Holliger, Stochastic characterization and seismic response of upper and middle crustal rocks based on the Lewisian gneiss complex, Scotland, *Geophys. J. Int.*, in press, 1994.

von Kármán, T., Progress in the statistical theory of turbulence, *J. Mar. Res.*, *7*, 252–264, 1948.

Wu, R.-S., and K. Aki, The fractal nature of the inhomogeneities in the lithosphere evidenced from seismic wave scattering, *Pure Appl. Geophys.*, *123*, 805-818, 1985.

J. A. Goff, University of Texas Institute for Geophysics, 8701 N. MoPac Expy, Austin, TX 78759. (e-mail: goff@utig.ig.utexas.edu)

K. Holliger and A. Levander, Department of Geophysics, Rice University, PO Box 1892, Houston, TX 77001.

(Received October 21, 1993; revised January 13, 1994; accepted January 21, 1994)

A HYPOTHESIS-TESTING APPROACH TO DISCRIMINANT ANALYSIS WITH MIXED CATEGORICAL AND CONTINUOUS VARIABLES WHEN DATA ARE MISSING

H.L. Gray, W.A. Woodward, and G.D. McCartor
Southern Methodist University
Department of Statistical Science
Dallas, TX 75275

and

M.D. Fisk
Mission Research Corporation
Santa Barbara, California

CONTRACT NO. F19628-93-C-0199

OBJECTIVE

In several recent papers, Gray, et al. have developed methodology based on the maximum likelihood estimator for detecting outliers. These results have been applied very successfully by Mark Fisk at Mission Research Corporation. One problem, however, arises that can effect the success of the method -- missing data. That is, in many cases, various features may be missing in a number of the events. When this is the case the likelihood function cannot be calculated and the algorithm "crashes." The purpose of this research is to adjust the methodology in a statistically sound manner in order to allow for missing data.

RESEARCH ACCOMPLISHED

In Baek, Gray, Woodward, Miller, and Fisk (1994) (subsequently abbreviated BGWMF) techniques are given for a hypothesis-testing approach to discriminant analysis. In Miller, Gray, and Woodward (MGW) (1993) a similar hypothesis-testing approach is used for discriminant analysis and outlier detection when some of the data are missing. That paper, however, only considers the case in which all variables are continuous and, in fact, normally distributed.

In this paper we remove those restrictions and extend the methodology to mixtures of continuous and categorical data when both training sets (continuous and discrete) may have missing data. We study three algorithms for accomplishing this.

(1) The INDICATOR algorithm - This algorithm begins by converting each categorical variable with j categories into j - 1 indicator variables. This results in a larger number of variables (unless all categorical variables are already binary, in which case the data set is unchanged). These indicator variables can be analyzed using techniques for quantitative data. In this algorithm we make the (obviously incorrect) assumption that all variates are continuous and, in fact, normally distributed. We then perform discriminant analysis using the transformed data and the techniques of MGW.

(2) The FULL algorithm - Next, we model the joint distribution of each observation in the following manner: Suppose each observation consists of p categorical variables and q continuous variables. The categorical variables define r cells of a contingency table in which the observation could fall, where r is the product of the number of categories possible within each categorical variable. We assume that the observation will fall into cell i (i = 1, ..., r) with probability p_i, and that the conditional distribution of the continuous part given that the discrete part places the observation into cell i is multivariate normal with mean μ_i and Σ_i. We then employ the EM algorithm to obtain maximum likelihood estimates of parameters in this model and compute maximized likelihoods of the available data, and bootstrap the ratio of maximized likelihoods, as was done in BGWM.

(3) The COMMON algorithm - This algorithm is essentially the same as the FULL algorithm, except that we assume a common covariance matrix across all multinomial cells. That is, the conditional distribution of the continuous part given that the discrete part places the observation into cell i is assumed multivariate normal with mean μ_i and Σ, with Σ no longer depending on i. This reduces considerably the number of parameters that need to be estimated and makes possible calculation of the likelihood ratio statistic when some cells may be sparsely represented, or not represented at all.

Simulation studies are conducted to compare and contrast the performance of each of these procedures with regard to their ability to accurately control the Type I error rate, and with regard to their power.

Suppose we wish to classify a (p+q)-dimensional random vector **V** into one of two populations π_1 or π_2. Suppose further that **V** can be partitioned as **V** = (**X**, **Y**), where **X** = $(X_1, X_2, ..., X_p)$ is a p-dimensional vector of categorical variables and **Y** = $(Y_1, Y_2, ..., Y_q)$ is a q-dimensional vector of continuous variables. Suppose that for i = 1, ..., p, the variable X_i takes on one of the r_i possible values 1, 2, ..., r_i. Then the vector **X** takes on one of $r = \prod_{i=1}^{p} r_i$ possible values. We let Ψ denote the set of all possible values of the vector **X**. Finally, suppose that training samples $\{\mathbf{V}_i^{(1)}\}$, i = 1, ..., N_1 from π_1 and $\{\mathbf{V}_i^{(2)}\}$, i = 1, ..., N_2 from π_2, each having the same structure as **V**, are available, and that data may be missing at random from any part of **V** or from the training samples.

The generalized likelihood ratio test (GLRT) procedure for classifying V into π_1 or π_2 is based on a hypothesis testing approach. That is, the classification of V is done by testing

$$
\begin{aligned}
&H_0: \ V, V_1^{(1)}, V_2^{(1)}, \ldots, V_{N_1}^{(1)} \in \pi_1; V_1^{(2)}, V_2^{(2)}, \ldots, V_{N_2}^{(2)} \in \pi_2 \\
&\qquad\qquad \text{versus} \\
&H_1: \ V_1^{(1)}, V_2^{(1)}, \ldots, V_{N_1}^{(1)} \in \pi_1; V, V_1^{(2)}, V_2^{(2)}, \ldots, V_{N_2}^{(2)} \in \pi_2.
\end{aligned} \tag{1}
$$

The two misclassification probabilities that we will be interested in are P(2|1) and P(1|2), where P(i|j) denotes the probability of classifying V into π_i when in fact $V \in \pi_j$. We will refer to $\alpha = P(2|1)$ as the significance level for the test and P(2|2) as the power.

Let m denote the number of elements in V that are missing and let $V_{(2)} = (X_{(2)}, Y_{(2)})$denote the (p - m)-variate vector of available data in V. Similarly, let $m_i^{(j)}$ denote the number of elements missing from $V_i^{(j)}$ and let $V_{i(2)}^{(j)}$ denote the $(p - m_i^{(j)})$-variate vector of available data in $V_i^{(j)}$ (j = 1, 2; i = 1, 2, ..., N_j). We assume that π_1 has joint density function $f(V|\theta^{(1)})$ and that π_2 has joint density function $f(V|\theta^{(2)})$, where f is some parametric density function with parameters $\theta^{(1)}$ and $\theta^{(2)}$ for populations π_1 and π_2, respectively. Then, under H_0, the likelihood of V and the training samples is given by

$$
L_{01}(\theta^{(1)}| V, V_1^{(1)}, V_2^{(1)}, \ldots, V_{N_1}^{(1)}) L_{02}(\theta^{(2)}| V_1^{(2)}, V_2^{(2)}, \ldots, V_{N_2}^{(2)}),
$$

where

$$
L_{01}(\theta^{(1)}| V, V_1^{(1)}, V_2^{(1)}, \ldots, V_{N_1}^{(1)}) = f_2(V|\theta^{(1)}) \prod_{i=1}^{N_1} f_{1i}(V_i^{(1)}|\theta^{(1)}),
$$

$$
L_{02}(\theta^{(2)}| V_1^{(2)}, V_2^{(2)}, \ldots, V_{N_2}^{(2)}) = \prod_{i=1}^{N_2} f_{2i}(V_i^{(2)}|\theta^{(2)}),
$$

$f_2(V|\theta^{(1)})$ is the marginal density function for $V_{(2)}$ evaluated at $V_{(2)}$ with parameters $\theta^{(1)}$, and $f_{ji}(V_i^{(j)}|\theta^{(j)})$ is the marginal density function for $V_{i(2)}^{(j)}$ evaluated at $V_{i(2)}^{(j)}$ with parameters $\theta^{(j)}$. Under H_1, the likelihood of V and the training samples is given by

$$
L_{11}(\theta^{(1)}| V_1^{(1)}, V_2^{(1)}, \ldots, V_{N_1}^{(1)}) L_{12}(\theta^{(2)}| V, V_1^{(2)}, V_2^{(2)}, \ldots, V_{N_2}^{(2)}),
$$

where

$$
L_{11}(\theta^{(1)}| V_1^{(1)}, V_2^{(1)}, \ldots, V_{N_1}^{(1)}) = \prod_{i=1}^{N_1} f_{1i}(V_i^{(1)}|\theta^{(1)}),
$$

$$L_{02}(\theta^{(2)}|\, V, V_1^{(2)}, V_2^{(2)}, \ldots, V_{N_2}^{(2)}) = f_2(V|\theta^{(2)}) \prod_{i=1}^{N_2} f_{2i}(V_i^{(2)}|\theta^{(2)}),$$

and $f_2(V|\theta^{(2)})$ is the marginal density function for $V_{(2)}$ evaluated at $V_{(2)}$ with parameters $\theta^{(2)}$. We emphasize that these are the likelihood functions for the available data rather than the likelihood functions for the complete data since f_2 and f_{ji} (j = 1, 2; i = 1, 2, ..., N_j) are marginal densities for the available part of each observation, rather than the likelihood functions for the complete data.

The GLRT procedure is based on the ratio

$$(2) \qquad LR = \frac{\sup_{(\theta^{(1)}, \theta^{(2)})} L_{01}(\theta^{(1)}|\, V, V_1^{(1)}, V_2^{(1)}, \ldots, V_{N_1}^{(1)}) L_{02}(\theta^{(2)}|\, V_1^{(2)}, V_2^{(2)}, \ldots, V_{N_2}^{(2)})}{\sup_{(\theta^{(1)}, \theta^{(2)})} L_{11}(\theta^{(1)}|\, V_1^{(1)}, V_2^{(1)}, \ldots, V_{N_1}^{(1)}) L_{12}(\theta^{(2)}|\, V, V_1^{(2)}, V_2^{(2)}, \ldots, V_{N_2}^{(2)})}$$

$$= \frac{L_{01}(\hat{\theta}_0^{(1)}|\, V, V_1^{(1)}, V_2^{(1)}, \ldots, V_{N_1}^{(1)}) L_{02}(\hat{\theta}_0^{(2)}|\, V_1^{(2)}, V_2^{(2)}, \ldots, V_{N_2}^{(2)})}{L_{11}(\hat{\theta}_1^{(1)}|\, V_1^{(1)}, V_2^{(1)}, \ldots, V_{N_1}^{(1)}) L_{12}(\hat{\theta}_1^{(2)}|\, V, V_1^{(2)}, V_2^{(2)}, \ldots, V_{N_2}^{(2)})},$$

where $\hat{\theta}_0^{(j)}$ and $\hat{\theta}_1^{(j)}$ are maximum likelihood estimates of $\theta^{(j)}$ (j = 1, 2) under the null and alternative hypotheses, respectively. That is, $\hat{\theta}_0^{(1)}$ is the MLE of $\theta^{(1)}$ based on the sample $\{V, V_1^{(1)}, V_2^{(1)}, \ldots, V_{N_1}^{(1)}\}$, $\hat{\theta}_0^{(2)}$ is the MLE of $\theta^{(2)}$ based on the sample $\{V_1^{(2)}, V_2^{(2)}, \ldots, V_{N_2}^{(2)}\}$, and $\hat{\theta}_1^{(1)}$ is the MLE of $\theta^{(1)}$ based on the sample $\{V_1^{(1)}, V_2^{(1)}, \ldots, V_{N_1}^{(1)}\}$, and $\hat{\theta}_1^{(2)}$ is the MLE of $\theta^{(2)}$ based on the sample $\{V, V_1^{(2)}, V_2^{(2)}, \ldots, V_{N_2}^{(2)}\}$.

Equivalently, the test procedure may be based on the statistic

$$(3) \qquad \lambda = \log(LR) = \lambda_{01} + \lambda_{02} - \lambda_{11} - \lambda_{12},$$

where

$$(4) \qquad \lambda_{01} = \log f_2(V|\hat{\theta}_0^{(1)}) + \sum_{i=1}^{N_1} \log f_{1i}(V_i^{(1)}|\hat{\theta}_0^{(1)}),$$

$$\lambda_{02} = \sum_{i=1}^{N_2} \log f_{2i}(V_i^{(2)}|\hat{\theta}_0^{(2)}),$$

$$\lambda_{11} = \sum_{i=1}^{N_1} \log f_{1i}(V_i^{(1)}|\hat{\theta}_1^{(1)}), \text{ and}$$

$$\lambda_{12} = \log f_2(V|\hat{\theta}_1^{(2)}) + \sum_{i=1}^{N_1} \log f_{2i}(V_i^{(2)}|\hat{\theta}_1^{(2)}).$$

A key step in evaluating λ for a given sample is the computation of the maximum likelihood estimates and the corresponding maximized log-likelihood functions λ_{01}, λ_{02}, λ_{11}, and λ_{12} in equation (4). This is no trouble when the data are complete, as illustrated by (BGWM). However, in the presence of missing data, the usual expressions for maximum likelihood estimates are no longer valid. In this case, maximum likelihood estimates are obtained via the EM algorithm (Dempster, Laird, and Rubin (1977)). The EM algorithm is an iterative procedure for obtaining parameter estimates which maximize the likelihood function of the available data. It involves two key steps:

(E -step) - Using current estimates $\hat{\theta}^{(k)}$ (where k now denotes the current iteration step, rather than designating π_1 or π_2), estimate the values of the complete data sufficient statistics by computing their expectations given the available data.

(M-step) - Determine the values of the parameters which maximize the likelihood for the complete data based on the current estimates of the complete data sufficient statistics, thus yielding $\hat{\theta}^{(k+1)}$.

The EM algorithm iteratively performs E- and M-steps until the sequence $\{\hat{\theta}^{(k)}\}$converges to an adequate approximation to the MLE. To evaluate the test statistic λ of equation (3), we must implement the EM algorithm four times. That is, $\hat{\theta}_0^{(1)}$ and λ_{01} are based on the sample $\{V, V_1^{(1)}, V_2^{(1)}, \ldots, V_{N_1}^{(1)}\}$, $\hat{\theta}_0^{(2)}$ and λ_{02} are based on the sample $\{V_1^{(2)}, V_2^{(2)}, \ldots, V_{N_2}^{(2)}\}$, $\hat{\theta}_1^{(1)}$ and λ_{11} are based on the sample $\{V_1^{(1)}, V_2^{(1)}, \ldots, V_{N_1}^{(1)}\}$, and $\hat{\theta}_1^{(2)}$ and λ_{12} are based on the sample $\{V, V_1^{(2)}, V_2^{(2)}, \ldots, V_{N_2}^{(2)}\}$.

The decision rule is described as follows: small values of λ provide evidence in favor of H_1, hence, V is classified into π_2 if $\lambda \le \lambda_\alpha$, otherwise v is classified into π_1. The cut-off value λ_α is chosen so that $P(2|1) = \alpha$, the desired significance level for the test. Since the null distribution of λ is not known, the critical value is approximated by the parametric bootstrap (Efron 1979). For some large integer B, B bootstrap samples $\{V^*, V_1^{*(1)}, V_2^{*(1)}, \ldots, V_{N_1}^{*(1)}\}$ are simulated from a distribution with density $f(V|\hat{\theta}^{(1)})$ and B bootstrap samples $\{V_1^{*(2)}, V_2^{*(2)}, \ldots, V_{N_2}^{*(2)}\}$ are simulated from a distribution with density $f(V|\hat{\theta}^{(2)})$, where $\hat{\theta}^{(1)}$ and $\hat{\theta}^{(2)}$ are MLEs obtained from the samples $\{V_1^{(1)}, V_2^{(1)}, \ldots, V_{N_1}^{(1)}\}$, and $\{V_1^{(2)}, V_2^{(2)}, \ldots, V_{N_2}^{(2)}\}$, respectively. (Notice that in this case, $\hat{\theta}^{(1)} = \hat{\theta}_1^{(1)}$ and $\hat{\theta}^{(2)} = \hat{\theta}_0^{(2)}$.) When there are missing values, the simulated bootstrap samples should also have missing values in a configuration similar to that in the actual data. For each bootstrap sample, the test statistic λ is computed, thus generating a random sample $\{\lambda_1^*, \lambda_2^*, \ldots, \lambda_B^*\}$ of variates that have approximately the same distribution as λ under H_0. For an α-level

test, the cut-off value λ^*_α is chosen as the α-th empirical quantile of $\{\lambda^*_1, \lambda^*_2, \ldots, \lambda^*_B\}$. Finally, V is classified into π_1 if $\lambda > \lambda^*_\alpha$; V is classified into π_2 if $\lambda \leq \lambda^*_\alpha$.

As was pointed out in (MGW), this test procedure is only an approximation to the true GLRT procedure since the critical value is obtained via bootstrapping and we may further relax our approximation to the true GLRT procedure by relaxing the number of iterations performed by the EM algorithm. That is, we may choose a stopping criterion for the EM algorithm that does not continue iteration until convergence has been obtained to a high degree of accuracy. Whatever the stopping criterion, bootstrapping the test statistic insures an approximate α-level test. As in (MGW), it would appear that very little power is lost by only performing a very few iterations of the EM algorithm, as opposed to carrying out iterations until MLEs are obtained with a high degree of accuracy.

We have performed simulations of each of the three algorithms (INDICATOR, FULL, and COMMON) based on several different parameter configurations in order to determine how well the algorithm controls the Type I misclassification probability as desired, and to assess the power P(2|2) of each algorithm. We also keep track of how many times the algorithm fails to classify the observation at all. These failures occur when for some reason the simulated data fails to yield full-rank estimates of all required covariance matrix parameters. This results in an undefined test statistic λ. This happens most frequently in the FULL algorithm, and is caused by a very few number of observations falling into one or more of the multinomial cells. It happens occasionally in the INDICATOR algorithm when at least one possible value of a categorical variable is not represented. Failures may occur when the test statistic is undefined for the sample which we are trying to classify, and also when the statistic is undefined for attempted bootstrap samples. We see in our simulations that the COMMON algorithm is least susceptible to these types of failures. Full details of the results of these simulations along with a careful documentation of each algorithm employed will be available in a more detailed paper to be distributed at the poster session. Code for performing outlier detection in the presence of missing data is available through Mission Research Corporation.

CONCLUSIONS AND RECOMMENDATIONS

In this paper, we have extended the results of BGWMF and MGW to perform discriminant analysis with categorical and continuous variables when data are missing. We presented three algorithms for doing so. In simulation studies, we have observed that the INDICATOR algorithm has a tendency to yield a higher Type I error rate than desired. The FULL algorithm often fails due to singular parameter estimates when some value of the discrete part is sparsely represented. The COMMON algorithm seems to avoid these problems, and is therefore the preferred algorithm, especially when samples are small and the assumption of a common covariance matrix across all multinomial cells is reasonable.

REFERENCES

Baek, J., Gray, H. L., Woodward, W. A., and Miller. J. W. (1993), "A Bootstrap Generalized Likelihood Ratio Test in Discriminant Analysis."

Dempster, A. P., Laird, N. M., and Rubin, D. B. (1977), "Maximum Likelihood Estimation from Incomplete Data via the *EM* Algorithm" with discussion, *J. Royal Stat. Soc.*, ,1-38.

Efron, B., (1979), "Bootstrap Methods: Another Look at the Jackknife," *Annals of Statistics*, 7, 1-26.

Little, R. J. A. & Rubin, D. B. (1987) *Statistical Analysis with Missing Data*. New York: Wiley.

Little, R. J. A. & Schluchter, M. D. (1985) Maximum likelihood estimation for mixed continuous and categorical data with missing values. *Biometrika* 72, 497-512.

Krzanowski, W. J. (1980) Mixtures of continuous and categorical variables in discriminant analysis. *Biometrics* 36, 493-499.

Krzanowski, W. J. (1982) Mixtures of continuous and categorical variables in discriminant analysis: a hypothesis-testing approach. *Biometrics* 38, 991-1002.

Miller, J. W., Gray, H. L., and Woodward, W. A. (1993), "A Bootstrap Generalized Likelihood Ratio Test in Discriminant Analysis."

Olkin, I., & Tate, R. F. (1961) Multivariate correlation models with mixed discrete and continuous variables. *Ann. Math. Statist.* 32, 448-65

High Frequency 3-Component Waveform Inversion for Source and Structural Parameters

by
Roger A. Hansen and Danny J. Harvey
Department of Physics
University of Colorado
Campus Box 583
Boulder, CO 80309-0583

Contract No: F49620-94-1-0109

Objective:

We are continuing a study aimed at obtaining fundamental understanding of regional wave propagation by attempting to match synthetic seismograms with real data. In the process we have learned much about the behavior of P, S, Lg and Rg and how they relate to earth structure, source characteristics and source-receiver geometry. Previously, we reported on a two phase study in which we identified and analyzed a set of local and regional seismic events recorded near the former Soviet test site at Semipalatinsk. We then applied full waveform inversion to selected events to extract source and structure parameters. We found that for certain source-receiver paths we could do a very good job of matching complete seismograms on radial and vertical components up to a frequency of one Hertz including P, S and Rg phases using shallow explosion sources. For other source-receiver paths the fits were not so good using shallow explosion sources, however we obtained good fits on all three components by assuming a 5 km deep earthquake source. These results indicate that waveform inversion can be used to discriminate small shallow explosions from small relatively shallow earthquakes. The current objectives are to utilize the structural parameters obtained earlier in a moment tensor inversion process to more fully characterize the source processes. Single station inversions for station KKL (of the NRDC network in operation during 1987-1988), are used to estimate the ability of single station 3-component waveforms to discriminate explosion sources.

Research Accomplished

We used seismic data recorded as part of the NRDC program conducted during 1987. The NRDC network was operated by the University of California, San Diego and consisted of three stations that surrounded the Shagan River and Degelen Mountain areas of the Eastern Kazakhstan Soviet test site. Although there were three stations in the NRDC network, throughout most of the year only one or two stations were operational and the most consistent station was KKL (Karkaralinsk). All of the results in this study are based upon data collected at KKL. We used as our data source the NRDC Information Product which was compiled by IRIS' Joint Seismic Program Center and distributed through the IRIS Data Management Center.

The instrumentation at KKL consisted of surface 1 Hz 3-component seismometers and a borehole 0.2 Hz 3-component seismometer all recording at two different gain levels (on 16-bit digitizers) and at 250 sps. The site was on granitic bedrock and generally exhibited low noise characteristics. All of the results presented in this study are based upon the borehole instruments that were at a depth of 100 m.

The region around KKL is an active mining area with many shallow explosions and generally exhibits low natural seismicity. Most seismicity in the area is of the "in-
d type and is associated with the large nuclear explosions at the former Soviet test
s

A total of 69 events were used in this study. These events were determined by scanning through one year's worth of data recorded at KKL looking for any events that had clearly identifiable P and S arrivals and whose S-P times were consistent with distances of less than 500 km. Event epicenters were determined by using the S-P distances along with back azimuth estimates that were obtained from polarization analysis. All events were assumed, initially, to be shallow mining blasts. A map of the 69 events used in this study is shown in figure 1.

Although the epicenters determined from a single station location are subject to some scepticism, we think that they are fairly good as indicated by the clustering that would be characteristic of mining operations especially to the west, south and southwest. These directions also correspond to the source-receiver paths for which we can best fit the data. The locations to the north however are not particularly clustered, even though we know that this is an active mining region. This direction also represents source-receiver paths for which we have difficulty fitting synthetic seismograms to the data.

Figure 2 shows the unfiltered KKL vertical components for all events sorted by azimuth and distance. All of the times are relative to the first P arrival time. The labels on the left of each trace give the distance and back azimuth in degrees to each event which can be used to identify the events in figure 1. Probably the most interesting characteristic of the data that can be seen from this figure is the great variability in the excitation of Rg. If one looks carefully at the data it appears that events to the south and west systematically show larger Rg amplitudes than events to the north or east (with the exception of the very local events). The data shown here represent a rich source of information that provide us with the means for learning about local and regional wave propagation. Further description of this data and the structural inversions can be found in Harvey (1993).

We conducted a two phase study in which we characterized a number of small events in Eastern Kazakhstan in the distance range of 10 to 320 km and we inverted full waveform data for structural and source parameters. We found that there was a strong variability in Rg propagation characteristics as a function of azimuth for the single station we used in this study. We quantified this variability in terms of Rg dispersion function and amplitude characteristics as a function of azimuth. We inverted for near surface structural parameters using observed Rg dispersion and found reasonable azimuthal variations.

We used full waveform inversion to determine structural and source parameters for events to the south of KKL. Although we only performed the structural inversion

for one event, we found that the inverted structural model worked well for predicting wave propagation effects for other events in the near vicinity of the event used in the inversion. Waveform inversion was used to refine single station relative locations of presumed mining explosions resulting in a reduction of event clustering from several tens of km to several km.

The inverted structural model was used for computing theoretical seismograms for a number of events that were not in the vicinity of the original event cluster used in the inversion. A sudden change in the observed waveforms was successfully modeled by changing the source from a shallow explosion to a 5 km deep double couple. No other changes in the structural parameters were required in order to accomplish this fit.

We have demonstrated the ability to invert full waveform data up to a frequency of 1 Hertz for both structural and source parameters and to produce excellent matches between observed and theoretical seismograms. We have shown that waveform matching can be used to discriminate between small shallow explosions and small relatively shallow earthquakes. Both the Rg and S phases play an important role in this waveform based discrimination. All of these results were obtained using a reasonable and fairly simple structural model with no lateral scattering.

Although we have experienced remarkable success with this particular study, there are many questions that remain unanswered and much more work to be done. In the obvious next step we applied an approach of source inversion that utilizes a moment tensor formulation to the data at station KKL. This allows for the evaluation of the capability of a single seismic station to determine an explosive source with a data set of mining explosions. Furthermore, in this report we have concentrated on trying to evaluate to what frequency we can match waveforms for the close-in data in the top few traces of Figure 2.

As an example, we present the analysis of the 3-component KKL recording for the event on May 23, 1987 at a distance of 21 kilometers from KKL (figure 3). The method of moment tensor inversion is that of Hansen (1989) as applied to seismic events in Norway by Hansen et. al. (1989) and Bungum et. al. (1990). This procedure consists of filtering the data to the band of interest and then matching the waveforms to synthetic seismograms in both a forward and an inverse sense. Green's functions are calculated using the Locked Mode Approximation method of Harvey (1981) in order to model both body and surface waves simultaneously. In our case here, we are able to model the high frequency surface waves, or Rg waves, from these close-in events, obtaining zeroth order moment tensors. The moment tensor representation is then decomposed into standard equivalent sources of explosion, double couple, and compensated linear vector dipole. The results of the fit to the May 23 event are given in figure 4. Here we see the fit of the 3-component data with the synthetic seismogram plotted below each data trace up to a frequency of 4 hertz. Note that the transverse component is quite small relative to the vertical and radial components. To the right of Figure 4 is the P-wave focal sphere calculated from the moment tensor solution. The best double couple (which only consist of 4.5% of the solution) is shown as the fault planes, while the nearly 30% explosion and 66% CLVD are expressed as a contour plot of amplitude on the focal sphere. (Similar results are obtained for more limited frequency ranges for this and other events within this data set). Experience with

earthquake solutions within Norway indicate that this is obviously the solution of an explosive source that has some spatial and temporal extent folding into the CLVD part of the zeroth order moment tensor. Such a source may well be a ripple fired mining blast. A sonogram of the P-wave train for this event is shown in Figure 5, illustrating a scalloping effect as a function of frequency indicative of a ripple fired blast. The fact that the CLVD component appears to have a horizontal rather than vertical extent may well be due to the extended explosive source.

Conclusions and Recommendations

Preliminary results demonstrate the ability to invert full waveform data up to a frequency of 4 hertz for close in data obtaining non-double couple moment tensor solutions for obvious mining blasts with excellent matches between observed and theoretical seismograms. Such waveform matching can be used to discriminate between shallow explosions and small relatively shallow earthquakes through an interpretation of equivalent force representations of the moment tensor solution.

We recommend a continuation of such waveform matching to much larger distances and in other regions of interest to determine and quantify the repeatability of these results as compared to known events including the three large NRDC chemical explosions and the Soviet JVE nuclear explosion. In subsequent studies the existing 1-D waveform inversion method will be further developed and applied to a large amount of data in the distance range of 10 to 3000 km, and from a variety of geologic and seismic settings. The first step in this process is to define the frequencies, distances, and geologic regions for which lateral scattering plays a secondary role and which can be represented well with 1-D structure. The major thrust of this study will be to verify the utility of waveform inversion for the purpose of seismic discrimination, to invert for crustal and upper mantle structure in Eurasia, to define the operating bounds of existing 1-D inversion methods in terms of geology, distance and frequency, and to identify, develop, and evaluate several tractable theoretical approximations for handling lateral scattering in an effective manner.

References

Bungum, H., Alsaker,A., Kvamme,L., & Hansen,R., 1991. Seismicity and seismotectonics of Norway and nearby continental shelf areas, *J.Geophys. Res.*, **96**,2249-2265.

Hansen,R. 1989. Surface wave modelling and source parameter inversions of Norwegian earthquakes recorded at local and regional distances, EOS Trans, AGU.

Hansen,R., Bungum,H., and Alsaker,A. 1989. Three recent larger earthquakes offshore Norway, *Terra Nova*, **1**, 284-295.

Harvey,D. 1981. Seismogram synthesis using normal mode superposistion: the locked mode approximation, *Geophys. J. R. astr. Soc.*, **66**,37-61.

Harvey,D. 1993. Full Waveform Inversion of Structure and Source Parameters using regional data recorded in eastern kazakhstan. PL-TR-93-2078, ADA266405.

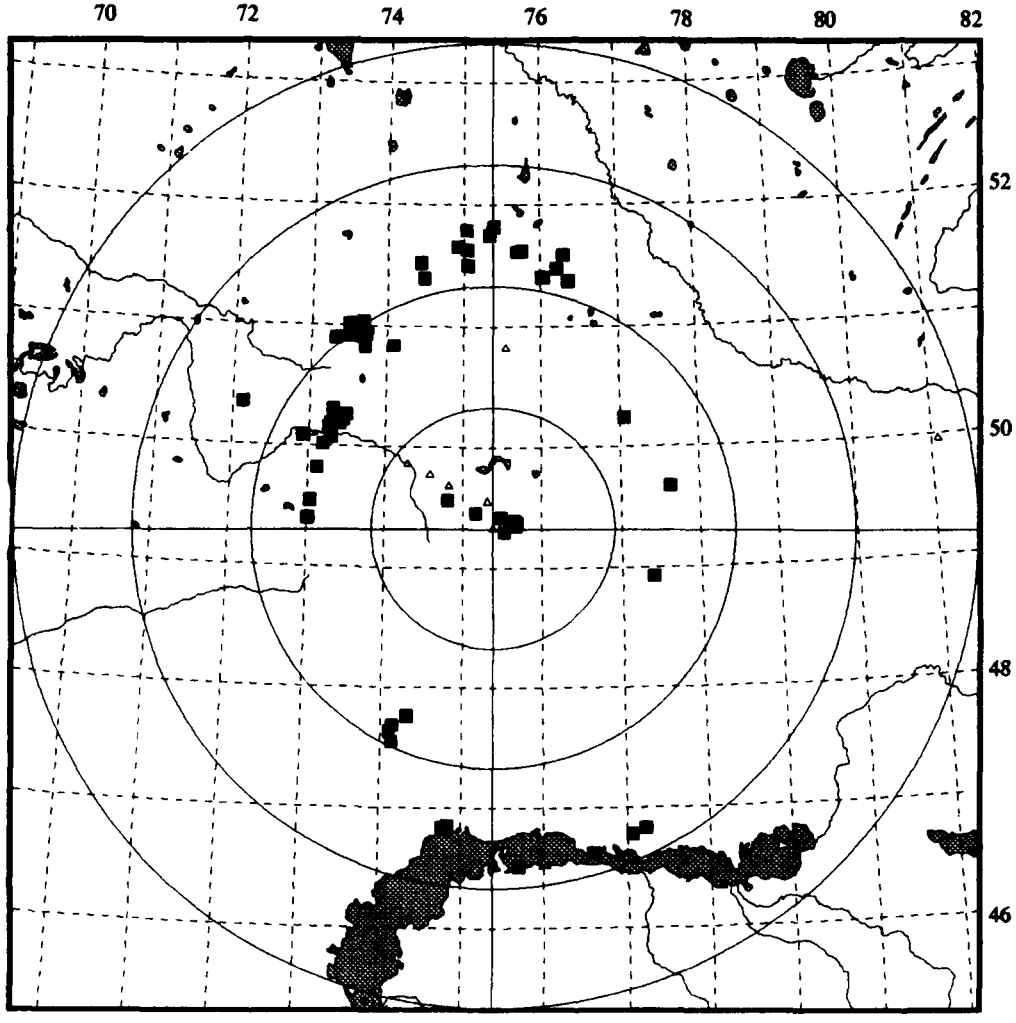


Figure 1. Event map centered at station KKL. Squares are events and triangles are stations. Circles are at one degrees distances from KKL.

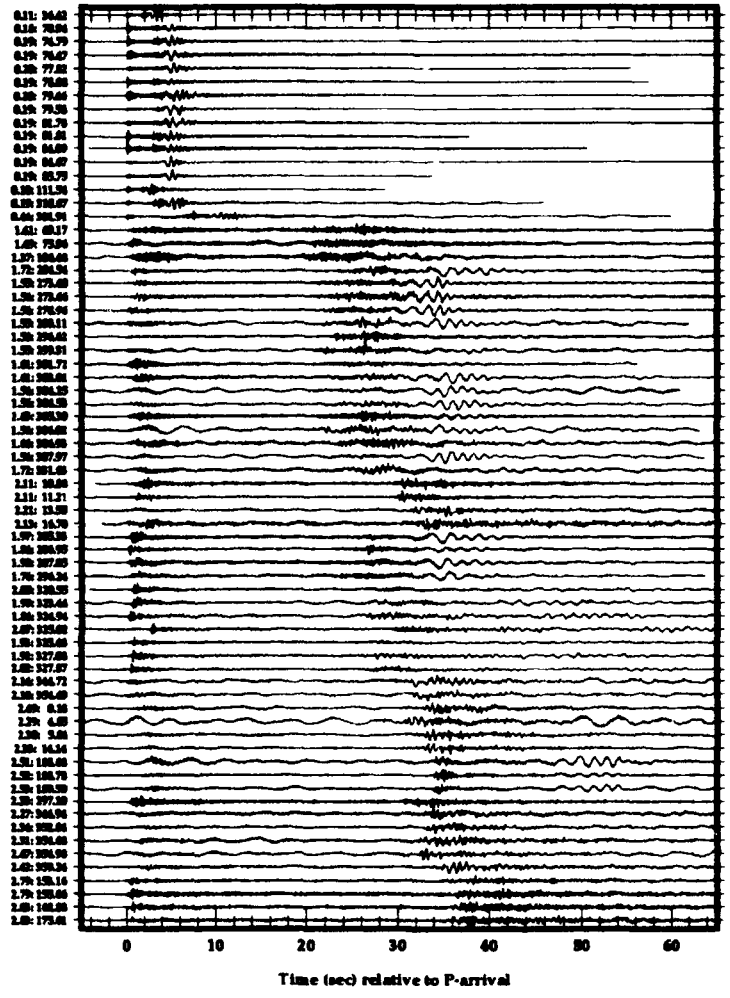


Figure 2. Unfiltered vertical component seismograms recorded by the borehole instrument at station KKL for the 69 events used in this study. Distance and back azimuth in degrees are given for each trace.

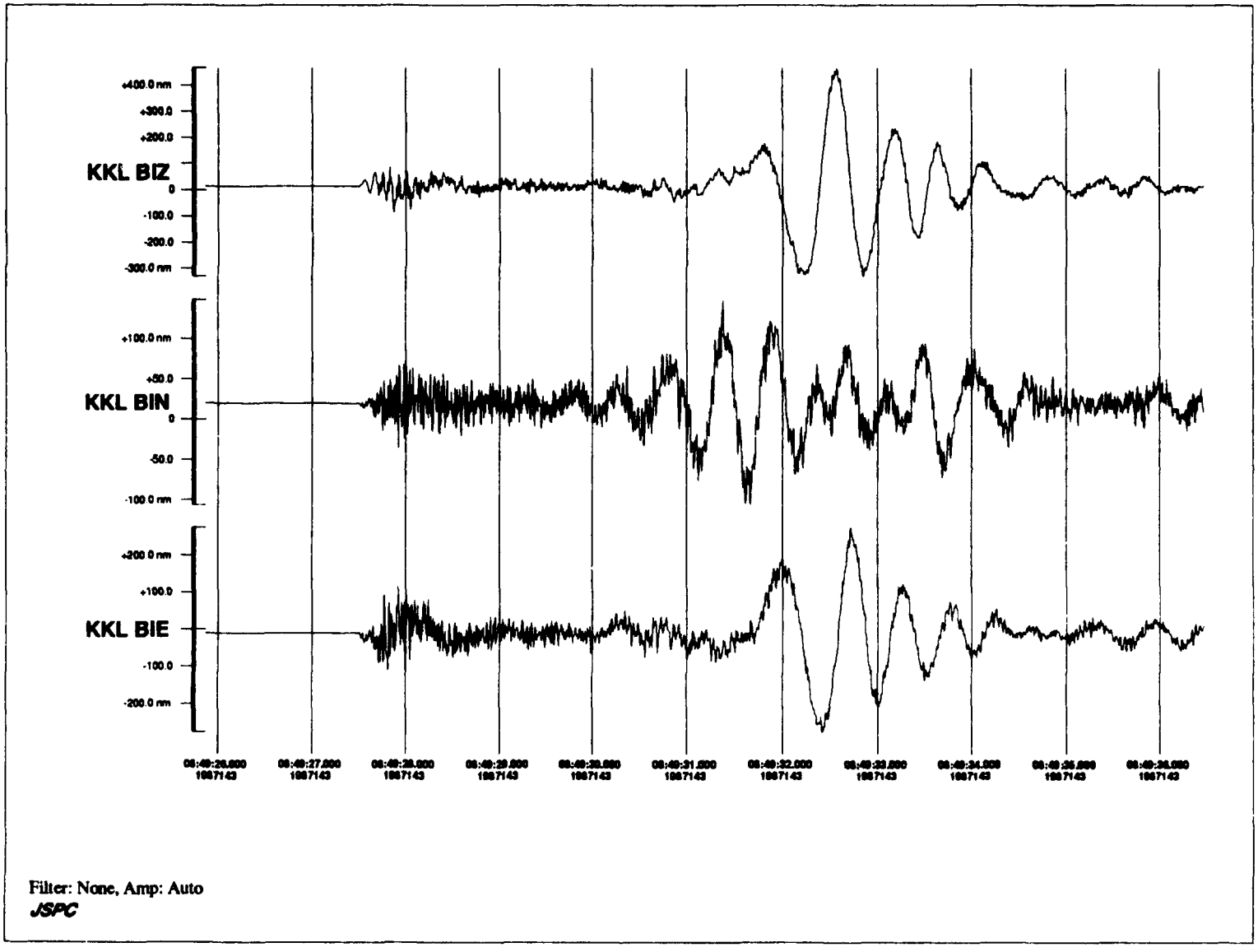


Figure 3. Three Component seismogram from a mining blast a distance of 21 kilometers.

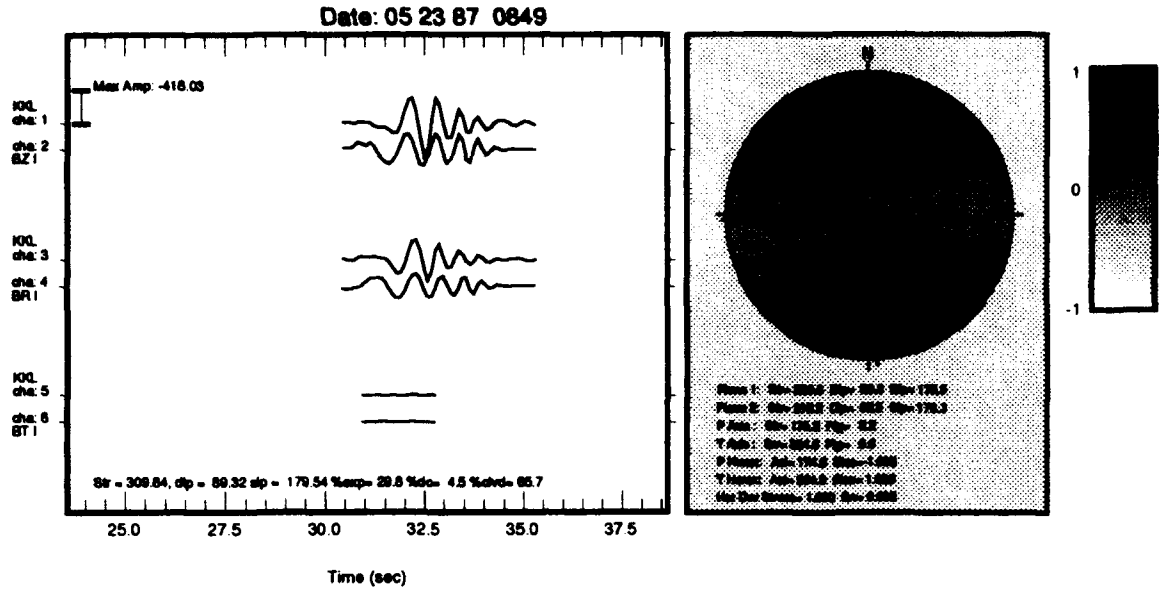


Figure 4. Results of moment tensor inversion for a mining explosion near station KKL. The figure show fits of the 3component data (top traces) the synthetic data (lower traces) in a least squares sense. To the right is the P-wave focal sphere calculated from the moment tensor where the amplitude is contour plotted, and the 4.5% best fit double couple is illustrated by the solid lines.

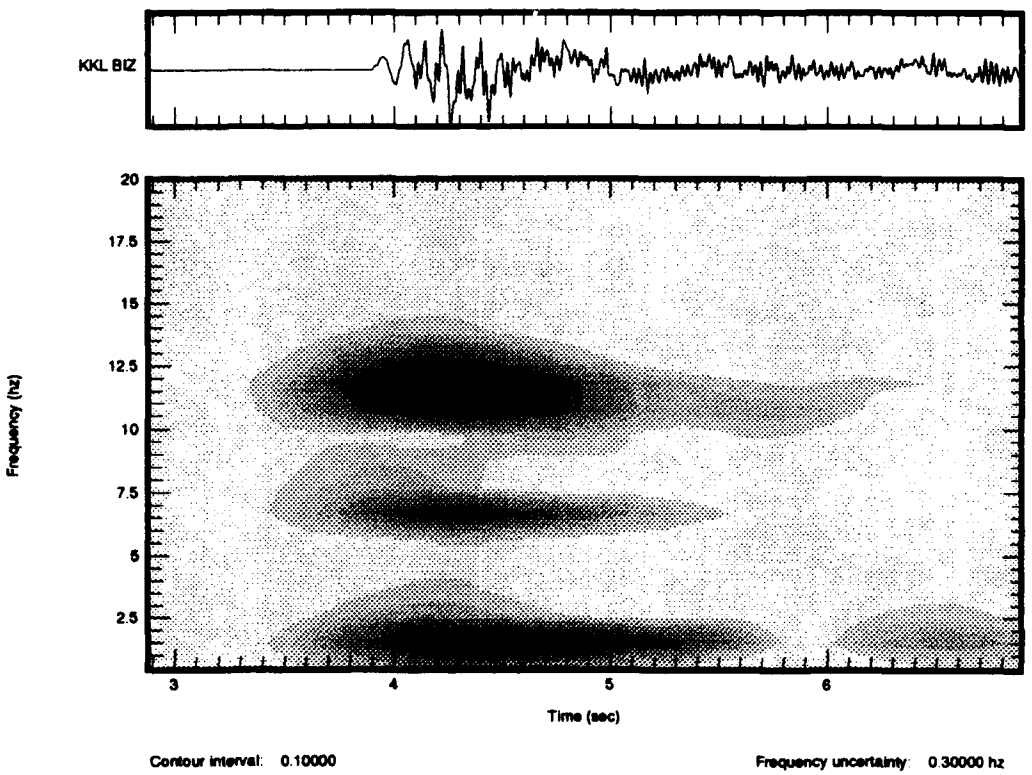


Figure 5. Sonogram of the P-wave train for the event illustrated in Figure 4. Note the scalloping effect as a function of frequency.

THEORETICAL RAYLEIGH AND LOVE WAVES FROM EXPLOSIONS IN NON-SPHERICAL CAVITIES AND FROM TECTONIC RELEASE IN COMPRESSIVE STRESS FIELDS

D. G. HARKRIDER
Seismological Laboratory, California Institute of Technology,
Pasadena, CA 91125
F49620-93-1-0221

A. BEN-MENAHEM
Earth Resources Laboratory, Massachusetts Institute of Technology,
Cambridge, MA 02142
F49620-93-1-0424

OBJECTIVE

To determine if the earthquake like surface wave radiation almost always accompaning underground explosions and usually explained by tectonic stress release might in some instances be due to an explosion in a horizontal tunnel.

RESEARCH ACCOMPLISHMENTS

In order to simulate the tunnel environment and to obtain simple analytic albeit approximate and quick results without the need for the time expensive, totally numerical results of a finite difference calculation, Ben-Menahem and Mikhailov (1994) developed a spherical mapping approximation for the evaluation of displacement fields from explosions in non-spherical cavities embedded in an elastic medium. In their approximation the explosion generated stress distribution is mapped onto the surface of an equivalent virtual spherical cavity completely surrounding the true cavity. The analytical results express the displacement field in terms of a multipole expansion of spherical eigenvectors. For our tunnel simulatuion, we use their results for a right circular cylindrical cavity.

Terminating their expanion at order two, they showed that the symmetric cavities are equivalent to a second order seismic moment tensor solution where the diagonal elements are directed along the principal cavity-axes. If we terminate the expansion at this order, the time functions for each moment tensor component depend on whether they are associated with P or S waves. This is typical of all finite sources which can be modeled by a point source moment tensor because of symmetry. At very long periods, this radiation field is the same as that due to the rapid formation of a spherical cavity in the presence of tensile stress and differs only by sign if the initial stress is compression. The two sources differ at shorter periods only by their respective moment tensor time functions. Because of this, the algebra needed in determining their surface wave excitation is essentially the same. The tectonic release of the closely related cavity in a compressive stress field is interesting in that its isotropic part is the negative of an associated explosion and would tend to mask the actual size of the explosion. For periods of 20, 10, and 1 seconds in the chosen source medium, it was found that the time finctions were essentially step functions in moment for cavity radii much less than one kilometer and even at a radius of 1 km., only the 1 second radiation showed a significant difference in P and S moments.

We show 20-sec Rayleigh and Love wave radiation patterns for the horizontal right cylinder with diameter to length ratios ranging from a finite length line source (zero diameter) to a disk (zero length). The diameter to length ratio is parameterized by the angle θ_0 shown in Figure 1. The radiation patterns

shown are for θ_0=0 (finite line), 22.5, 45, 50.3, 67.5, and 90 (disk) degrees. As pointed out by Ben-Menahem and Mikhalov (1994), for θ_0 = 50.3 degrees, the cylinder at long periods has the same radiation pattern as a spherical cavity , ie. no azimuthal dependence for Rayleigh waves and no Love waves. The source depth is 0. 6 km in an elastic propagation model of the Western US (Wang and Herrmann, 1989). In the Figures, the symmetry axis of the cylinder is in the x direction or zero azimuth (up on the figure). The equivalent tectonic release model shown is that created by the rapid formation of a spherical cavity in a plane tensile stress field in the horizontal direction, τ_{xx}

The Rayleigh wave radiation patterns (solid line) agree with the Rayleigh wave pattern for a homogeneous half space shown in Ben-Menahem and Mikhailov (1994). The Love wave radiation pattern for all the sources is identical to a vertical strike-slip fault with a strike 45 degrees from the axis of symmetry. The tectonic release model used in this paper was chosen because, other than the strengths of its moments, its analytic expression was identical to the horizontal right cylinder. Also, it has been suggested that a more realistic model of the tectonic regeme associated with underground explosions in some regions might be plane compression or tension rather than the pure shear assumed for NTS. For pure shear field, τ_{xy}, the Love wave radiation pattern is again identical to vertical strike-slip fault but with the strike shifted 45 degrees from that shown here.

Since at a period of 20 seconds all that differs between the various source models are the moment tensor comnponets M_{11}, M_{22} and M_{33}, we show their values at the top of each radiation pattern. Also because of this, it should be noted that the radiation patterns and the relative excitation between Rayleigh and Love waves are a function of the relative weights of the 3 moment tensor components and not their absolute values. Their absolute values are determnined by the explosion pressure or initial stress for the tectonic source and their respective cavity dimensions.

The Rayleigh and Love radiation patterns are almost identical for the tectonic release and the flat disk sources. They are shown in Figure 2 and labeled "SPHERE" and "THETA=90" respectively. In Figure 3, we show the patterns for a thin rod source and our next step in diameter to length ratio, θ_0 = 22.5 degrees. Theu are labeled "THETA=0." and "THETA=22.5" respectively. For the zero diameter source, the radiation pattern for Rayleigh waves has been rotated from the flat disk pattern by 90 degrees with the maximum lobes at right angles to the cylinder axis. There is also a small lobe along the axis. The presence of this small lobe is very dependent on the Rayleigh depth eigenfunctions and is not visible in the 10 second pattern. For the wider cylinder "THETA=22.5", it is not visible. We note also that as the cylinder gets wider, the lobes on the Rayleigh wave pattern get larger relative to Love waves. In fact in Figure 4, we see that by the time θ_0 = 45 degrees the Rayleigh wave pattern is an oval with very small Love waves which have disapeared by θ_0 = 50.3 and the Rayleigh wave pattern is a circle. In Figure 5, we show the pattern for the remaining cylinder shape, θ_0 = 67.5. Here the pattern is again larger in the x direction or the axis of the cyinder. This peanut shape is interesting in that this pattern is what we would expect if we included the explosion with its associated tectonic release pattern of Figure 2. Of course the shape would depend on the "F" factor, ie. ratio of tectonic relese moment to explosion moment.

CONCLUSIONS AND RECOMMENDATIONS

If this approximation is valid, we have shown that tunnel explosions can generate significant Love waves almost eaual in size to the explosion generated Rayleigh waves. Also for certain geometries, these explosions can mimic the oval or peanut shapes sometimes associated with explosions plus tectonic release. We recommend that this simple but elegant solution be verified with existing finite-difference calculations.

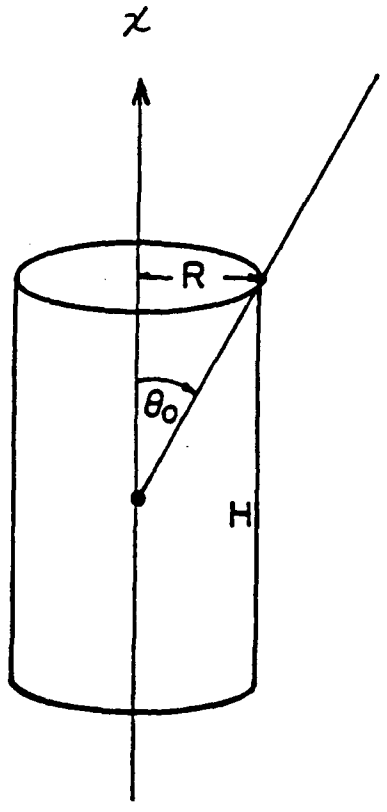
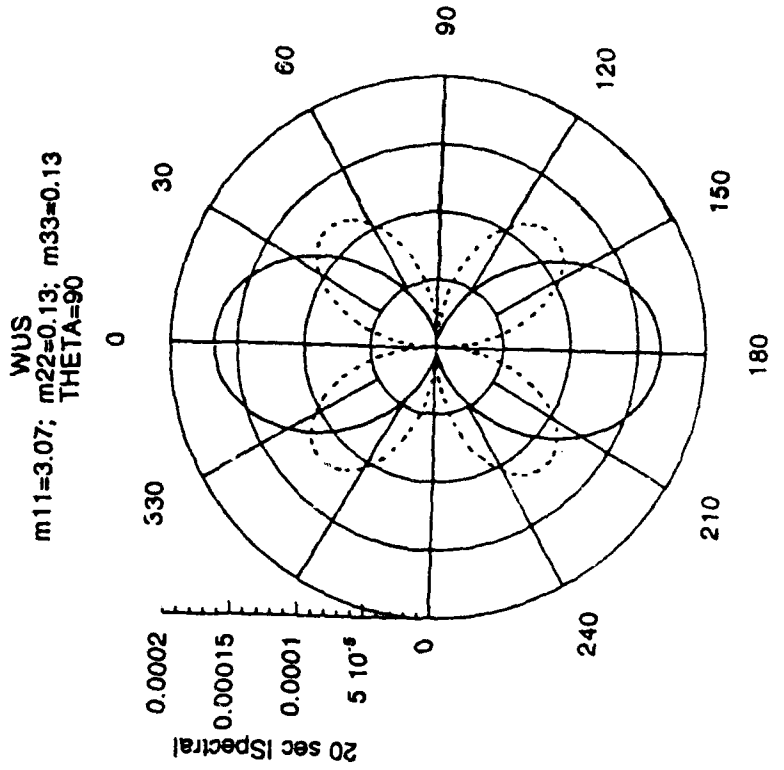


Figure 1


WUS
m11=3.07; m22=0.13; m33=0.13
THETA=90
20 sec ISpectral
0.0002
0.00015
0.0001
5 10⁻⁵
0
30
60
90
120
150
180
210
240
270
300
330

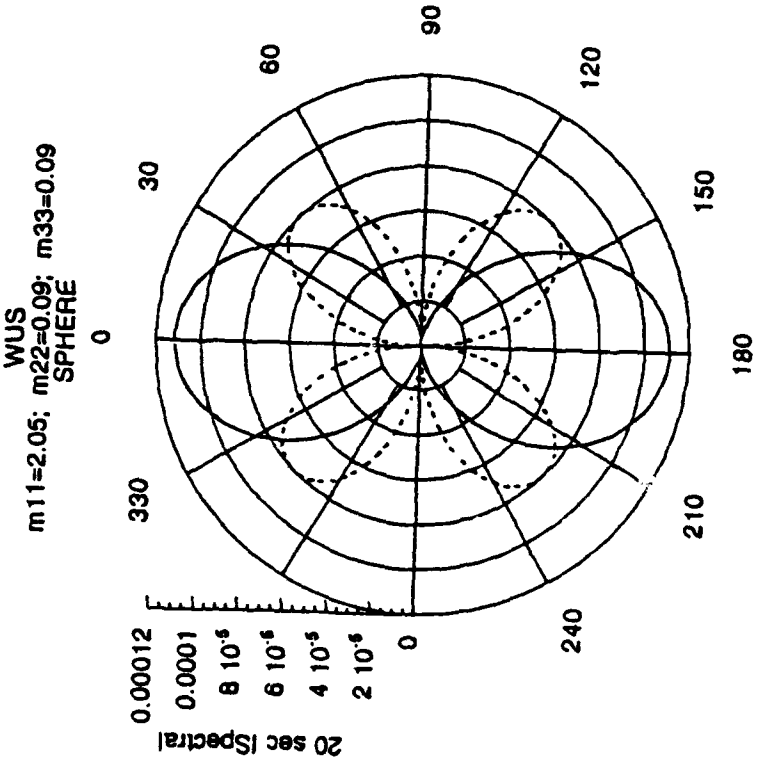
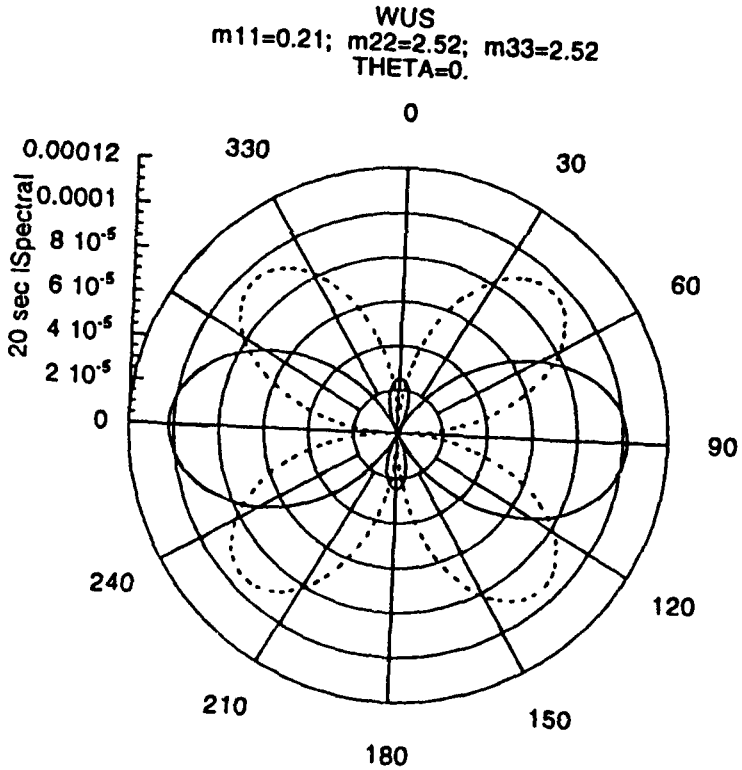

WUS
m11=2.05; m22=0.09; m33=0.09
SPHERE
20 sec ISpectral
0.00012
0.0001
8 10⁻⁵
6 10⁻⁵
4 10⁻⁵
2 10⁻⁵
0
30
60
90
120
150
180
210
240
270
300
330

Figure 2


WUS
m11=0.21; m22=2.52; m33=2.52
THETA=0.
20 sec lSpectral
0.00012
0.0001
8 10-5
6 10-5
4 10-5
2 10-5
0
0
30
60
90
120
150
180
210
240
330

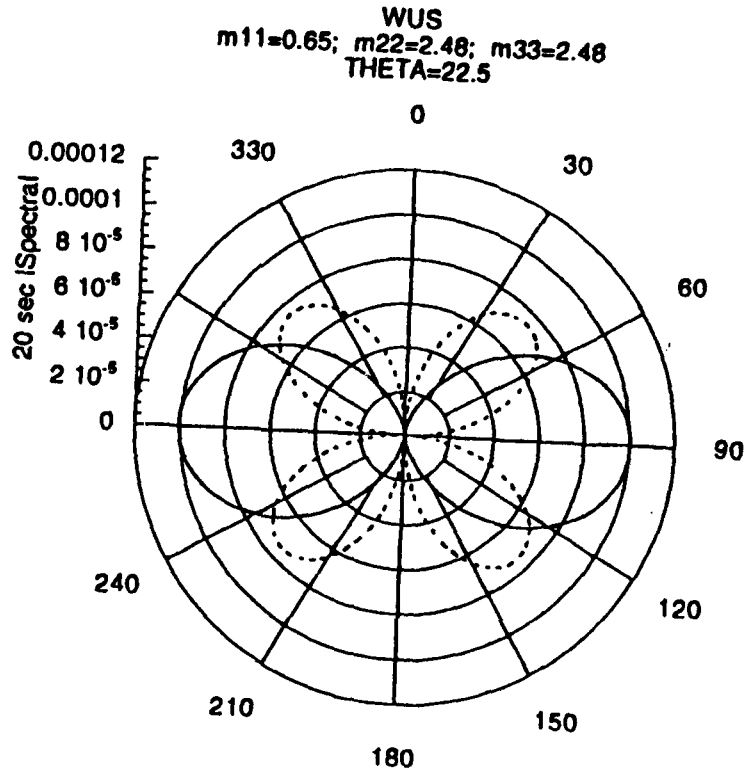
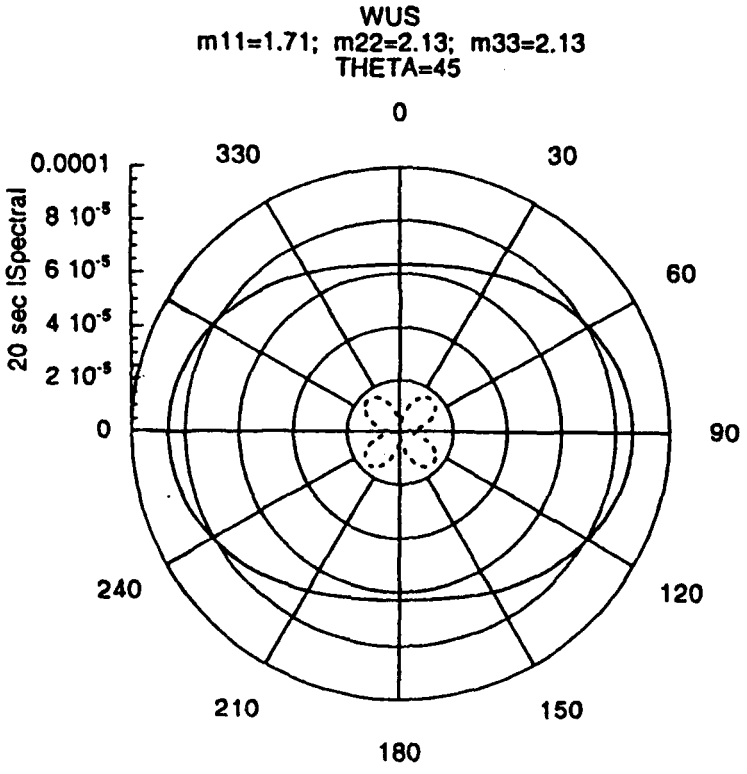

WUS
m11=0.65; m22=2.48; m33=2.48
THETA=22.5
20 sec lSpectral
0.00012
0.0001
8 10-5
6 10-5
4 10-5
2 10-5
0
0
30
60
90
120
150
180
210
240
330

Figure 3


WUS
m11=1.71; m22=2.13; m33=2.13
THETA=45
0
30
60
90
120
150
180
210
240
270
300
330
0.0001
8 10-5
6 10-5
4 10-5
2 10-5
0
20 sec lSpectral

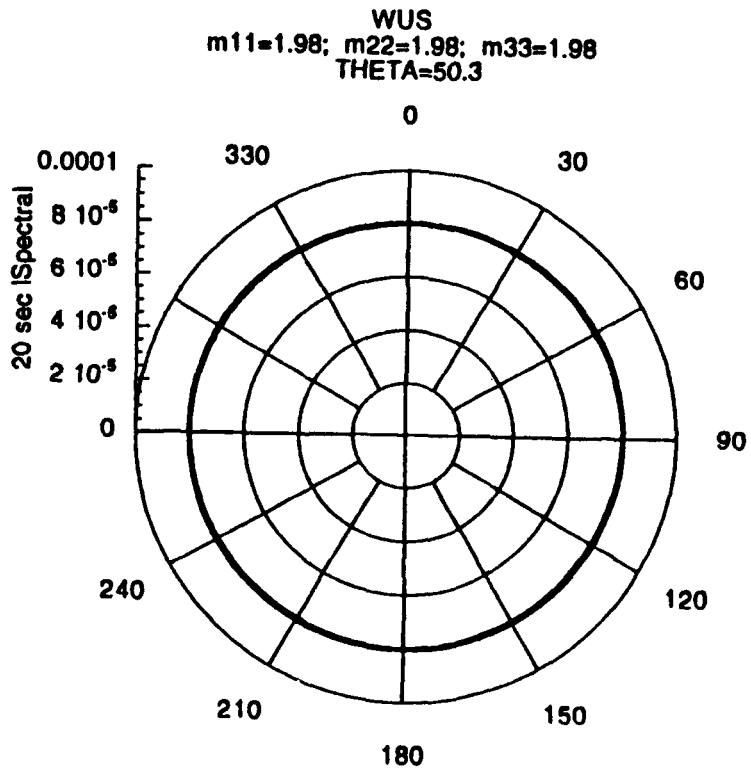

WUS
m11=1.98; m22=1.98; m33=1.98
THETA=50.3
0
30
60
90
120
150
180
210
240
270
300
330
0.0001
8 10-5
6 10-5
4 10-5
2 10-5
0
20 sec lSpectral

Figure 4

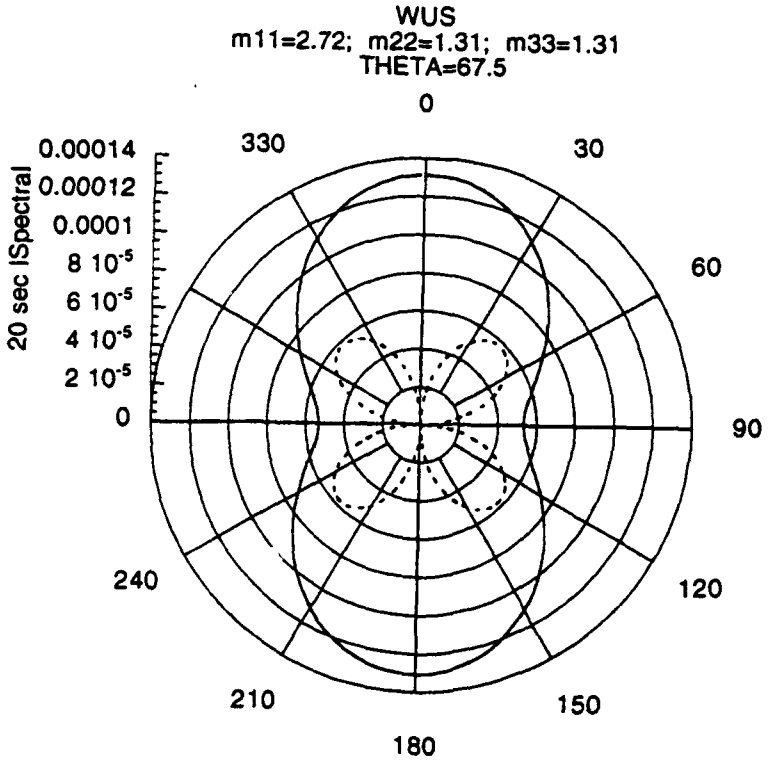

WUS
m11=2.72; m22=1.31; m33=1.31
THETA=67.5
0
30
60
90
120
150
180
210
240
270
300
330
0.00014
0.00012
0.0001
8 10-5
6 10-5
4 10-5
2 10-5
0
20 sec lSpectral

Figure 5

Imaging Prominent Crustal Scatterers and Constraining Source Depth Using the Piñon Flat Broad-band 3-Component Array

Michael A. H. Hedlin, J. Bernard Minster, Frank L. Vernon and John A. Orcutt
Institute of Geophysics and Planetary Physics
Scripps Institution of Oceanography, University of California at San Diego

Contract No. F19628-93-K-0021

1. Objectives

We analyze the P coda recorded by seismic arrays to investigate the origin of high amplitude apparent secondary arrivals. Broad-band 3-Component (3-C) array data collected in 1991 at the Piñon Fat Observatory (PFO) in southern California yield compelling evidence that some of these arrivals are due to strong crustal scatterers associated with both topographic and buried heterogeneities located near this array. We find such scattered phases in the P-coda of both local and teleseismic seismograms. In some instances, these secondary arrivals may be incorrectly interpreted as direct arrivals, including so-called "depth phases", particularly when they are detected by single stations. We show that by imaging the apparent source of these arrivals using array data it is possible to remove this ambiguity if an unambiguous scatterer is identified. Conversely, by treating the location of the free-surface reflection as an apparent near-source scatterer we can also use the imaging technique to help constrain the source depth.

2. Research Accomplished

In this paper we extend earlier analyses of prominent near-receiver crustal scatterers (ex. Hedlin, 1991; Hedlin *et al.* 1991, 1994) in several ways. Instead of restricting our analysis to surface scatterers excited by teleseismic wavetrains we have adapted the technique to accommodate scatterers located anywhere in a layered Earth excited by regional events. We have introduced a polarization analysis into the technique that allows the analysis of 3-C array data.

We have applied the enhanced technique to broad-band small-aperture array data collected at the Piñon Flat Observatory (PFO) in 1991 with the intent of scanning the local crustal volume for prominent scatterers. We have found that strong evidence linking prominent buried scatterers with local tectonic features and surface scatterers with local topography.

2.a Brief review of the imaging technique

The technique has been summarized in a number of other papers (ex. Hedlin, 1991; Hedlin *et al.* 1991, 1994) and so only a brief review will be given here. In essence, the technique is adapted from diffraction summation migration (Hedlin *et al.*, 1991). We consider each scatterer as a secondary source which is excited by incident regional or teleseismic wavetrains with a delay estimated from elementary ray theory. Given an array recording of the scattered waves, enough information exists to locate and image the secondary source using a modified beamforming technique. The algorithm combines raytracing, polarization analysis and beamforming to produce 3-dimensional images of local scatterers after suppressing the direct waves from the primary source and back-projecting the residual wavefield, through a one-dimensional crust, to the secondary point(s) of origin. The polarization analysis is applied to each station separately prior to the beamforming.

2.b Spatial resolution

A parameter central to the understanding of spatial resolution is the time delay that exists between arrivals of the incident (parent) and the secondary (scattered) phases at the array. To illustrate this point we consider an array and a single scatterer both located at the surface of a homogeneous Earth receiving waves from a teleseism located directly beneath. It is easy to see that a circle passing through the scatterer, centered at the array, describes all possible surface locations which have the same time delay as the scatterer. It can be shown that, in general, locations which have a common delay time τ lie on a surface described by:

$$|R_{as}| = \tau / [|\mathbf{p_s}| - |\mathbf{p_i}| \cos(\theta)]$$

where θ is the angle between the vectors pointing from the array to the primary source and to the scatterer. When the scattered slowness, $\mathbf{p_s}$, is greater than the incident slowness, $\mathbf{p_i}$, (e.g. P to R_g or P to S scattering) this describes an ellipsoid of revolution with one focus at the center of the array, major axis pointing to the primary source and eccentricity equal to $|\mathbf{p_i}| / |\mathbf{p_s}|$. The circle described above is simply the trace of a vertically oriented ellipsoid on the horizontal plane. When the primary source is not directly beneath, the ellipsoid tilts from the vertical and the time-delay curve on the free-surface becomes elliptical. When the incident and scattered wave velocities are equal (e.g. P to P scattering) the eccentricity equals 1 and the surface is a paraboloid of revolution.

This observation is important because the manner in which time delay surface appears in the plane, or volume, being imaged determines the resolution of point scatterers and allows us to predict how scatterers that might be symmetrical might become distorted in the image. If two scatterers lie on the same time-delay surface it will be relatively difficult to resolve them since, by definition of the curve, their seismic offspring will arrive at the array at the same time. Resolution along constant time-delay surfaces will be relatively poor and will be determined by the rate at which the slowness of scattered waves changes along the constant time-delay curves. If the slowness of scattered waves recorded at the array happens to be invariant for all scatterers on the same time delay surface, we would have no ability to resolve any of the individual scatterers. If, as is often the case, the slowness is slowly varying along a time-delay curve the resolution will likely be poor, and directly proportional to the aperture of the array. Resolution along paths orthogonal to the time-delay surfaces is determined by the temporal resolution of the scattered wave sources. As we (Hedlin, Minster & Orcutt, 1994) found in our analysis of teleseismic signals because of the protracted nature of the incident wavetrains it was necessary to perform deconvolution of the seismic recordings prior to imaging to compact the signal in time and obtain acceptable time-resolution. As we will see, in our analysis of small, local and regional events, the short source times involved make this additional processing unnecessary.

To test the resolution of scatterers in a layered Earth we have calculated and analyzed Wavenumber Integration synthetics. In the simulation shown in Figure 1 a synthetic source (an omnidirectional, impulsive explosion identified by a star) excites scattering at the layer interfaces (horizontal lines). Since the combined primary and scattered energy is recorded by a small-aperture array (located at the free-surface) the recorded layer conversions occur within small areas (identified by the triangles). As a result, this simulation allows us to gauge resolution of *point* scatterers located in a layered crust and excited by a regional event. We can also use the technique to compare 3-C with single (vertical) component arrays and compare different 3-C array geometries. In the top half of Figure 1 we display the time delay we expect should exist between the direct P energy and P-SV scattered arrivals. The conversions occur where the time delay curves become tangent to the interfaces - this equals the point at which the time delay is a minimum (i.e. Fermat's principle is obeyed). As discussed above, in a homogenous model, the constant time-delay surfaces for P-SV scattering are ellipsoids of revolution which have one focus at the center of the array. In this example, abrupt discontinuities in the time delay-surfaces occur at impedance contrasts. The time-delay surface in a low velocity layer connects to another surface of lower eccentricity in a neighboring high-velocity layer.

The lower half of Figure 1 contains the image calculated from this simulation. The unsuppressed direct energy is located at the array and clearly is insignificant relative to the P-SV conversions. Both are imaged with high time-resolution but rather limited slowness-resolution. The energy that appears in the figure between the ellipses associated with the P-SV conversions arrives roughly 5 s after the direct energy and is due to the P-P bounce at the lower interface.

These images were calculated by taking advantage of the full SAA2 array. To demonstrate the resolution possible with a single 3-C station we have included Figure 2 (top). Steering the station for vertically polarized energy we see that the time-resolution is unchanged however the slowness-resolution is poor (since with a single station all we have to constrain the direction of propagation is polarization analysis). Surprisingly, a single 3-C station still outperforms a full single component (vertical) array. In Figure 2 (bottom) we display the SV image calculated by recording the synthetics with a virtual NORESS array. The P-SV conversions have little influence on the vertical components (the particle motion is largely

horizontal) and are barely resolved. This image contains uncorrected direct energy (at the origin) and energy due to the P-P bounce at the lower interface (appearing at 30 km).

2.c Analysis of small-aperture data recorded in southern California

We have applied our imaging technique to regional and teleseismic events recorded by the 28 station broad-band (.0083 to 40 Hz) 3-C small-aperture SAA2 array deployed at the Piñon Flat Observatory (PFO). During the winter months of 1991 the array collected triggered (100 sa/s) recordings of 130 local and 140 regional and teleseismic events as well as continuous (20 sa/s) recordings of these, and other smaller, events.

One event (which occurred on day 057) occurred 85 km from the array at a back-azimuth of 35°. The coda contains a significant phase delayed 2.25 s after the P wave onset (Figure 3). A *f*-**k** analysis indicates that the onset phase arrives from the azimuth of the event, at a phase velocity of 6.2 km/s while the later phase arrives from a back azimuth of 14° at 12 km/s. In Figure 4 we consider a profile through the crust and upper mantle that passes through the array and bears 14°. In the upper figure we display the time delays we predict should exist between the arrivals of the energy directly from the event and via single P-P scattering interactions that occur in this vertical plane. Given that our assumptions (regarding the velocity model and the scattering) are reasonable the source of the late energy should lie somewhere on the 2.25 s curve (not shown). The lower half of Figure 4 contains an image calculated from this event using the 19 available 3-C stations. The energy adheres to the 2.25 s curve and despite the imperfect slowness-resolution it is clear that an isolated source exists at roughly 30 km depth and roughly 20 km to the NNE of the array. The proximity of this location to the San Andreas fault is intriguing. The depth is puzzling, however, since at 30 km it is well below the seismogenic zone. We are not yet close to understanding what this scatterer might be due to and what, if any, relationship it bears to the San Andreas fault.

2.d Depth determination

One reason that we have adapted the beam-stack imaging technique to accommodate regional events and layered Earth models is that it seems well suited to the problem of depth determination of regional events. By forcing the algorithm to consider ray paths from the primary event that bounce off the free surface we can iteratively solve for the source depth by selecting the source depth that places the free-surface bounce at the free surface. We have just recently considered this modification and will discuss preliminary results.

3. Conclusions and Recommendations

An analysis of synthetics has shown that 3-C arrays provide much higher resolution of buried scatterers than a single component array or a single 3-C station.

Some events recorded in southern California by a broad-band array appear to have excited deeply buried scatterers. The event discussed in this paper is one of a cluster that were recorded by the SAA2 array. The other events in the cluster recorded in the triggered mode also, not surprisingly, contained the same phase in the coda. Other large events in the vicinity appear to have not excited a scatterer at this location indicating that if a scatterer is located here it is highly directional. We will be using the continuous data, which provides tighter spatial coverage, to test the existence of this scatterer and explore, more fully, its directionality.

4. References

Hedlin, M.A.H., Analysis of seismic coda to identify regional sources and image strong crustal scatterers, PhD thesis - University of California at San Diego, 1991.

Hedlin, M.A.H., Minster, J.B. and Orcutt, Beam-stack imaging using a small aperture array, *Geophysical Research Letters*, **18**, 1771-1774, 1991.

Hedlin, M.A.H., Minster, J.B. and Orcutt, Resolution of prominent crustal scatterers near the NORESS small-aperture array, *Geophysical Journal International*, in press, 1994.

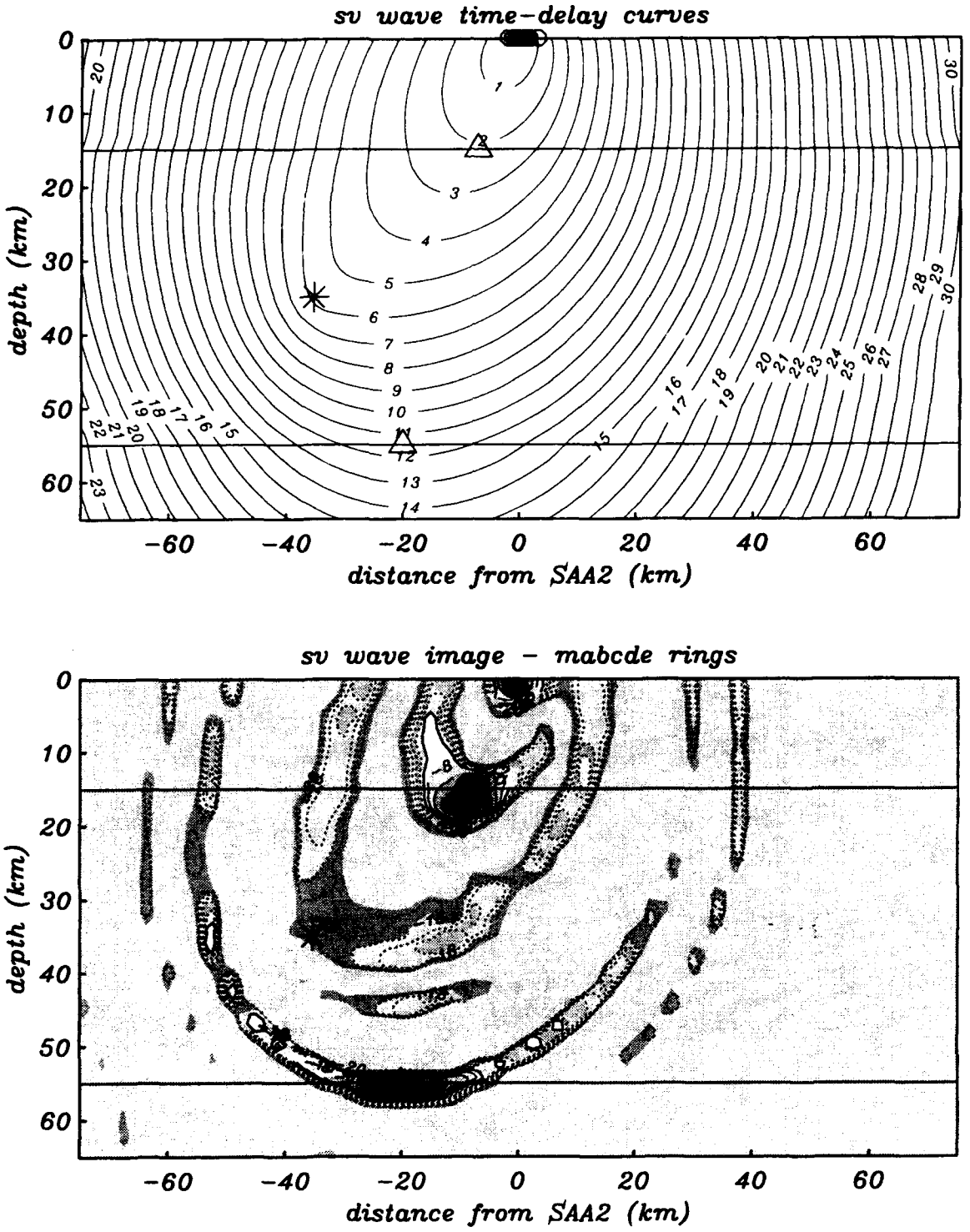


Figure 1 In this figure we consider synthetics calculated in a 2 layer crust overlying a high velocity half-space. In this simulation an explosion (star) and P-SV conversions at the interfaces (triangles on the horizontal lines) are recorded by a 3-C array at the free-surface. The top figure shows the time delays we expect SV energy, due to single scattering interactions, should have relative to the direct P energy. The lower figure shows the image calculated when steering the array for scattered SV energy. In this, and all subsequent images, contour values indicate amplitudes in dB relative to the largest value in the image.

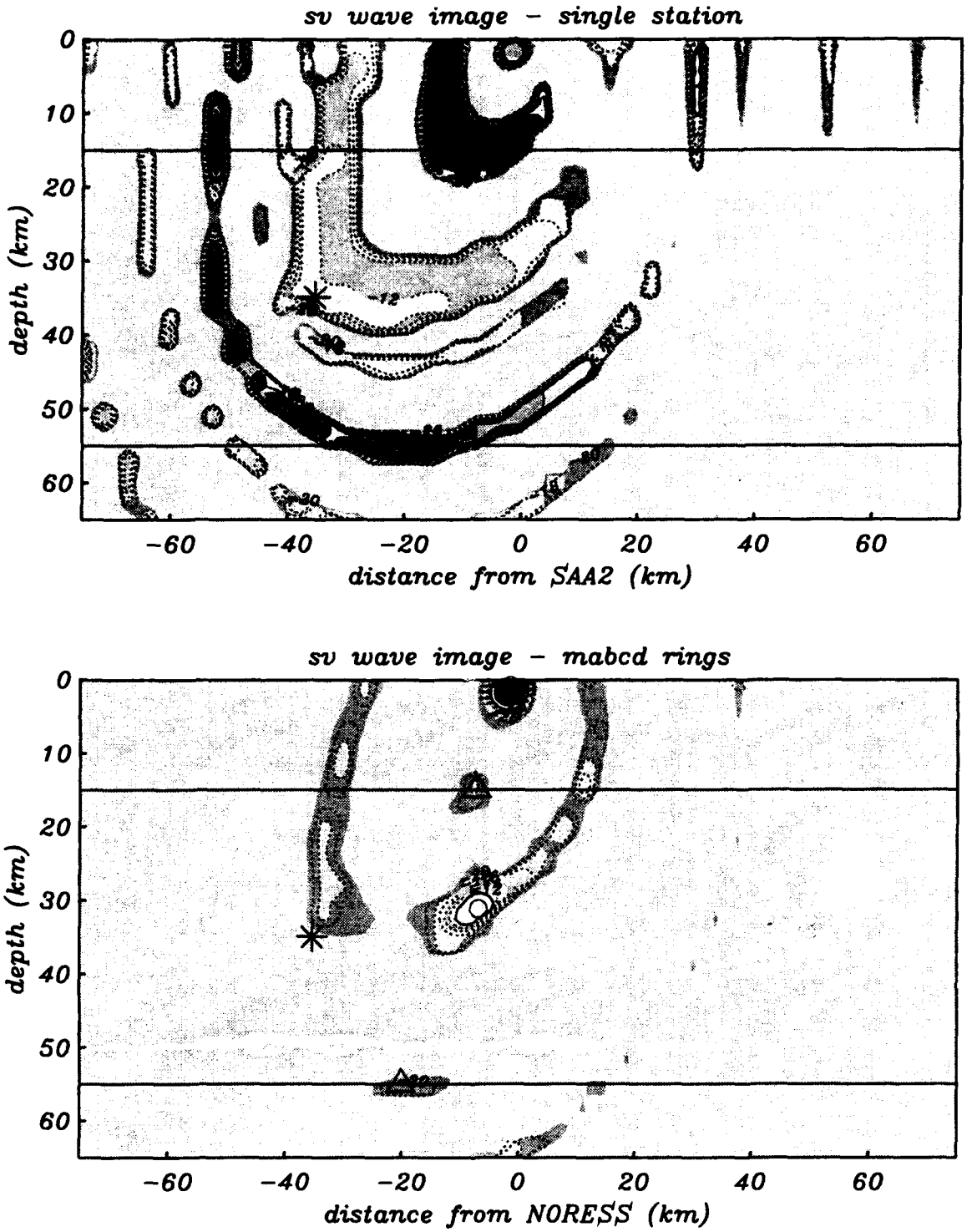


Figure 2 The top figure shows the image obtained from a single 3-C station. The lower figure shows the image calculated by deploying the single component NORESS array at the free-surface rather than a 3-C array.

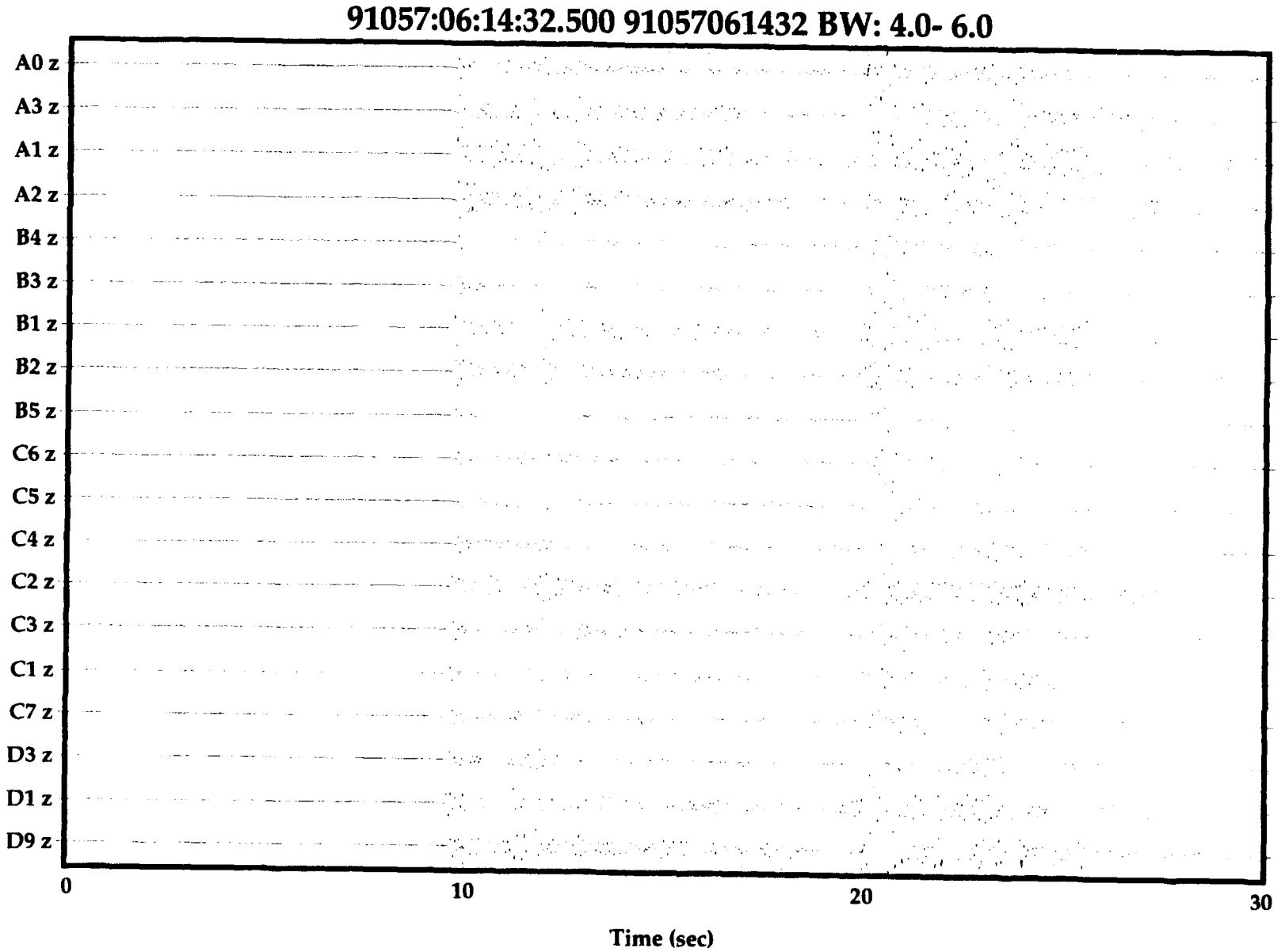
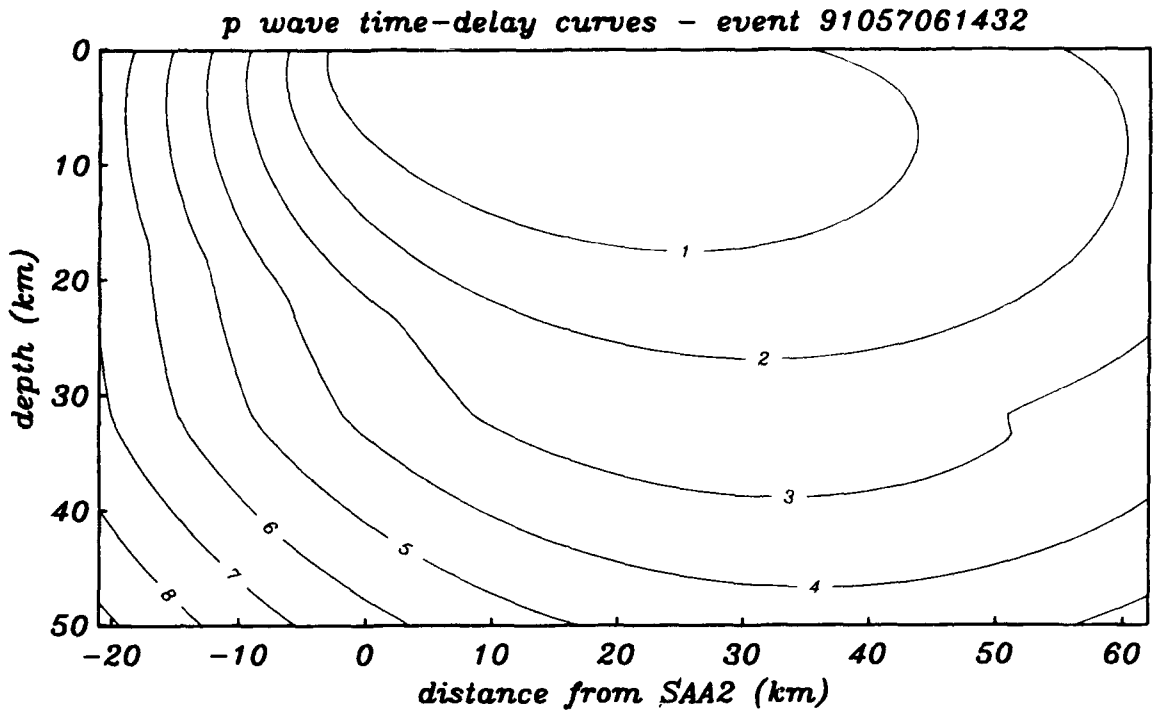


Figure 3 Vertical component recordings of a local earthquake. The P onset at 0.75 s is followed 2.25 s by a high velocity phase that arrives from 35° the azimuth to the event.



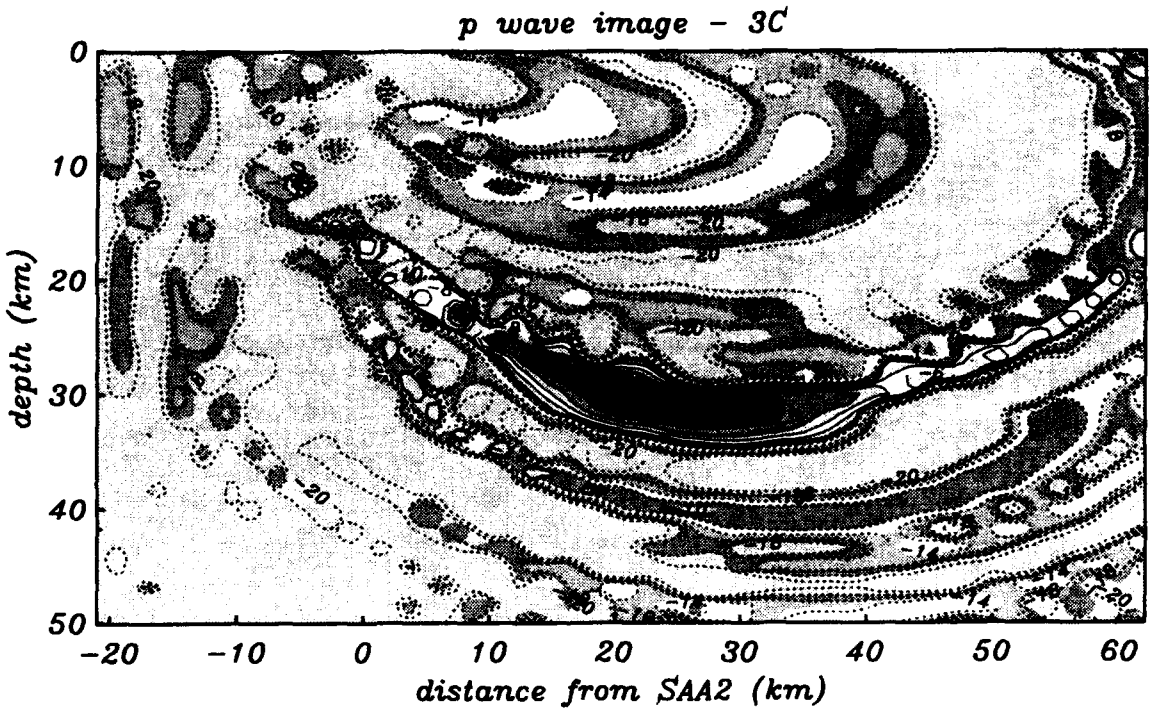


Figure 4 An image calculated using the data introduced in Figure 3. The top figure shows the time delay we expect should exist between direct P energy from the earthquake and single P-P scattered energy. In the image displayed in the lower figure energy is concentrated at a location roughly 30 km deep and 20 km north of the array.

RESEARCH IN REGIONAL EVENT DISCRIMINATION USING Ms:m_b AND AUTOREGRESSIVE MODELING OF LG WAVES

Eugene Herrin, Valeriu Burlacu, Henry L. Gray, Jack Swanson,
Paul Golden and Billie Myers
Southern Methodist University
Contract No.: F19628-93-C-0057

Part 1 Regional Ms:m_b

In this project we investigated the capability of the GSE Alpha array at Lajitas (TEXESS) to measure Ms (20 sec) for regional events. We used the prototype posthole KS 36000 broadband sensor and the straight sum of the nine vertical GS-13 elements of the array to measure spectral amplitude of the Rayleigh waves at a period of 20 sec. Magnitudes calculated from the two data sets were nearly identical. A suite of 25 aftershocks from the Northridge, CA earthquake of 17 January 1994, with an epicentral distance of approximately 1500 km from Lajitas, were chosen as a data set for the initial investigation. A m_b 5.0 aftershock on 19 January 1994 was chosen as a reference event. The data from both the broadband sensor and the summed array were low-pass filtered using a 6 pole, zero phase Butterworth filter with a corner at 10 seconds, removing the very energetic regional phases. A multiple filter analysis (MFA) was then performed on the filtered data. A multiple filter plot and the initial fundamental mode Rayleigh dispersion curve resulting from this analysis are shown in Figure 1. Figure 2 shows the application of a carefully determined filter that is phase-matched to the reference event. This master phase-matched filter was then adjusted for small differences in epicentral distances and applied to 24 Northridge aftershocks The events were selected based on local magnitudes that ranged from ML 3.0 to 5.0. Spectral Ms for each event was measured at a period of 20 sec. The results are tabulated in Table 1, with the following conclusions:

1.) sp array and bb surface wave magnitudes are essentially the same
2.) USGS m_b is on the average about 0.3 units less than ML.
3.) Ms could be reliably determined for events with m_b about 3.5 and greater.
4.) Lajitas m_b was determined using an array beam with an azimuth of 272° and a horizontal phase velocity of 8.4 km/s.
5.) Pn arrivals for Lajitas with m_b less than about 3.3 were heavily contaminated by background noise.

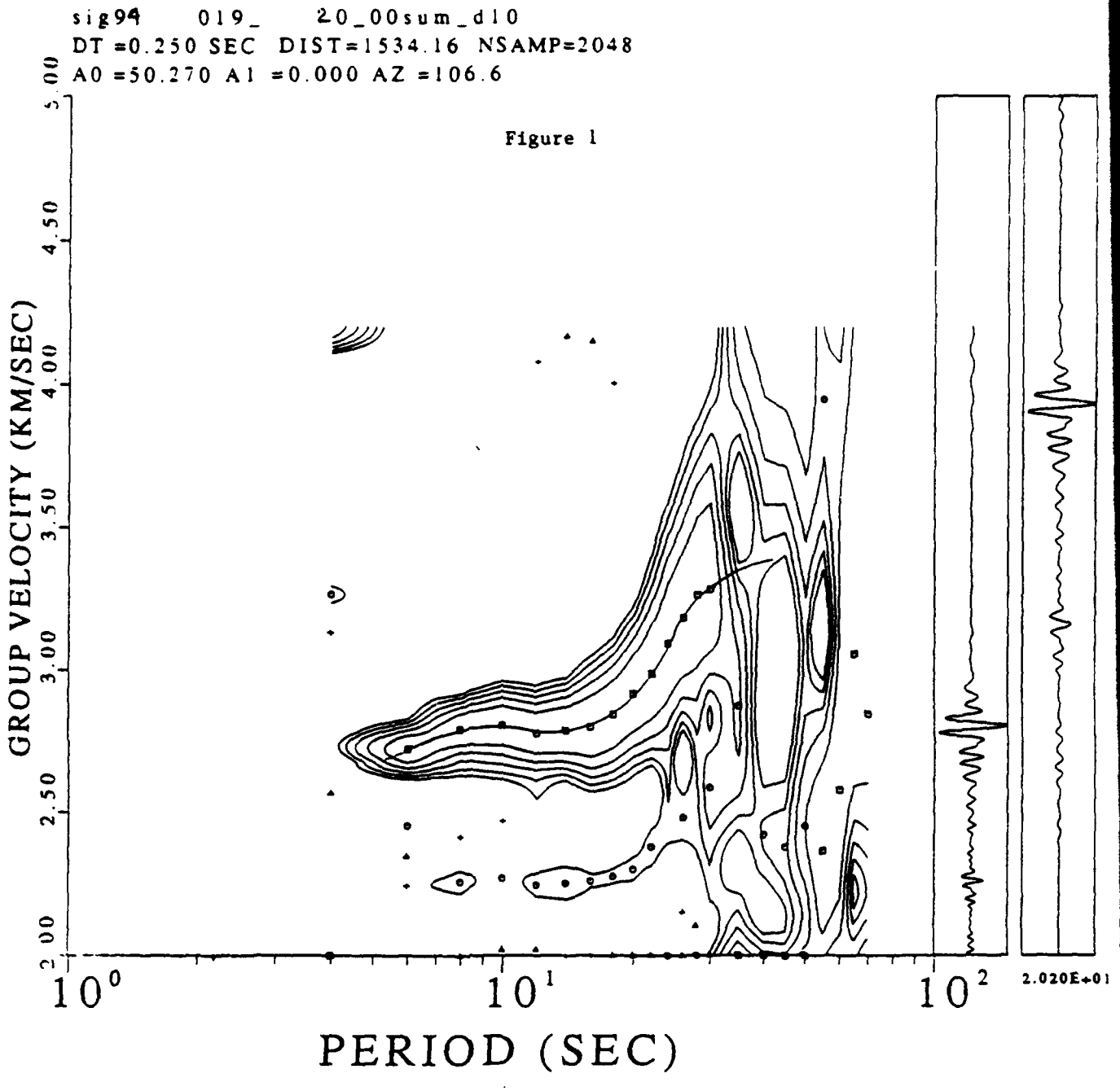
Part 2 Autoregressive Modeling of Lg

The autoregressive spectral model is

$$x(n) = -\sum_{k=1}^{p} a(k)x(n-k) + u(n)$$

where p is the order of the process, a(k) are the coefficients and u(n) is the white noise driving process.

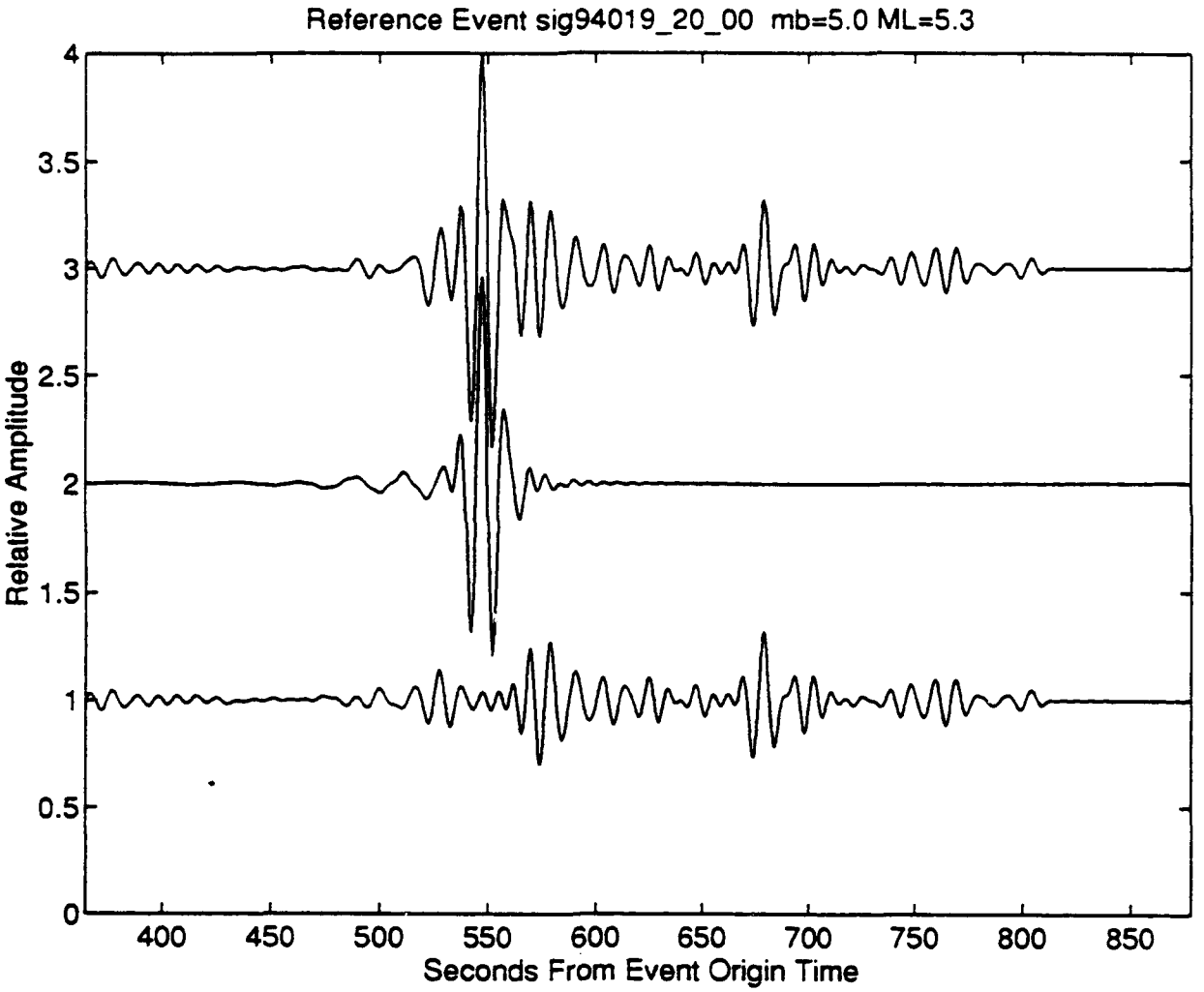
In this study an order 3 was used. This model consists of one complex pole and one real pole, the latter being located at zero frequency for the events studied here. The initial data is from the CSS Ground Truth Data Base recorded at GERESS. The data consisted of explosions and earthquakes in the Vogtland area that are tabulated in Table 2. Figure 3 illustrates the third order autoregressive spectrum (AR(3)) for a quarry blast. The frequency and reciprocal pole position of the complex pole in AR (3) models were calculated for the Lg arrival for all events. A value of 1.0 indicates that the reciprocal pole is on the unit circle, 0.0 indicated a position at the origin. Neither a value of 0.0 or 1.0 can occur in practice.



Multiple-filter plot of the reference event sig94019_20_00, mb=5.0 ML=5.3, showing the fundamental Rayleigh-wave group velocity dispersion curve. This event was used to develop the phase-matched filter for the Northridge, California to Lajitas, Texas travel path.

Wave-form to the far right is the input waveform plotted on a linear time scale. The inside waveform is the input signal plotted on a non-linear time scale corresponding to group velocity arrival on the multiple-filter plot.

Figure 2



Results of phase-matched filtering of the reference event:

Top trace is the input waveform of reference event sig94019_20_00.

The middle trace shows the estimated fundamental Rayleigh-wave component of the complex input signal.

The bottom trace is a plot of the residual after the estimated fundamental Rayleigh (middle trace) is removed from the input signal.

Table 1

Selected Aftershocks of the Northridge (Los Angeles, California) Earthquake 17 January, 1994

Event Identification	dy/mo/yr	Time (GMT)	Reported mb	Reported ML	Dist (km)	Azimuth (degrees)	P-wave (pn) magnitude (mb)	Surface-wave (sp) magnitude (LR)	Surface-wave (bb) magnitude (LR)
Reference Event-									
sig94019_20_00	19Jan94	21:09:26.4	5.0	5.3	1534.2	106.6	5.23	5.31	5.34
sig94029_08_00	29Jan94	11:20:35.9	4.5	5.0	1513.4	107.3	4.59	5.39	
sig94019_20_01	19Jan94	21:11:43.1	4.6	4.8	1521.7	106.9	4.43	4.90	4.85
sig94024_04_00	24Jan94	04:15:18.8	4.4	4.7	1512.4	107.5	4.33	3.76	
sig94019_12_00	19Jan94	14:09:11.9	4.3	4.5	1512.4	106.3	4.24	4.07	4.07
sig94019_04_00	19Jan94	04:40:46.1	4.1	4.5	1518.0	106.8	4.07	3.89	
sig94024_04_02	24Jan94	05:54:21.0	4.1	4.4	1519.6	107.4	4.14	3.66	
sig94024_04_01	24Jan94	05:50:24.3	4.2	4.3	1519.6	107.4	4.23	3.81	
sig94019_08_01	19Jan94	09:13:08.6		4.2	1531.8	106.5	4.18	3.16	3.23
sig94019_04_01	19Jan94	04:43:12.4		4.1	1531.3	106.7	4.24	3.61	3.62
sig94019_12_01	19Jan94	9:13.0		4.1	1505.5	106.9	4.04	3.51	3.47
sig94019_04_04	19Jan94	4:04.0		3.9	1507.6	106.8	4.02	3.27	
sig94032_04_01	1Feb94	07:40:19.1		3.8	1521.6	106.8	3.60	3.00	
sig94019_12_02	19Jan94	15:03:46.6		3.7	1502.1	107.2	3.60		
sig94019_16_02	19Jan94	19:50:07.8	3.3	3.7	1503.8	107.1	3.37		
sig94019_04_02	19Jan94	05:14:57.3		3.6	1502.7	107.0	3.39		
sig94019_20_02	19Jan94	21:27:50.2		3.5	1528.0	107.1	3.71		
sig94019_04_03	19Jan94	06:23:41.1		3.5	1501.1	107.3	3.16		
sig94032_08_00	1Feb94	09:59:10.1		3.4	1524.1	107.1	3.16		
sig94031_04_00	31Jan94	04:55:50.2		3.4	1516.9	107.2	3.14		
sig94019_16_01	19Jan94	17:46:51.8		3.3	1503.6	107.4	3.18		
sig94019_08_02	19Jan94	11:06:03.0		3.2	1501.5	107.2	2.84		
sig94019_08_00	19Jan94	07:58:32.9		3.1	1508.3	106.9	3.23		
sig94019_16_00	19Jan94	17:02:11.0		3.1	1513.1	106.7	2.45		
sig94032_16_01	1Feb94	18:23:34.9		3.0	1517.2	107.2	2.52		

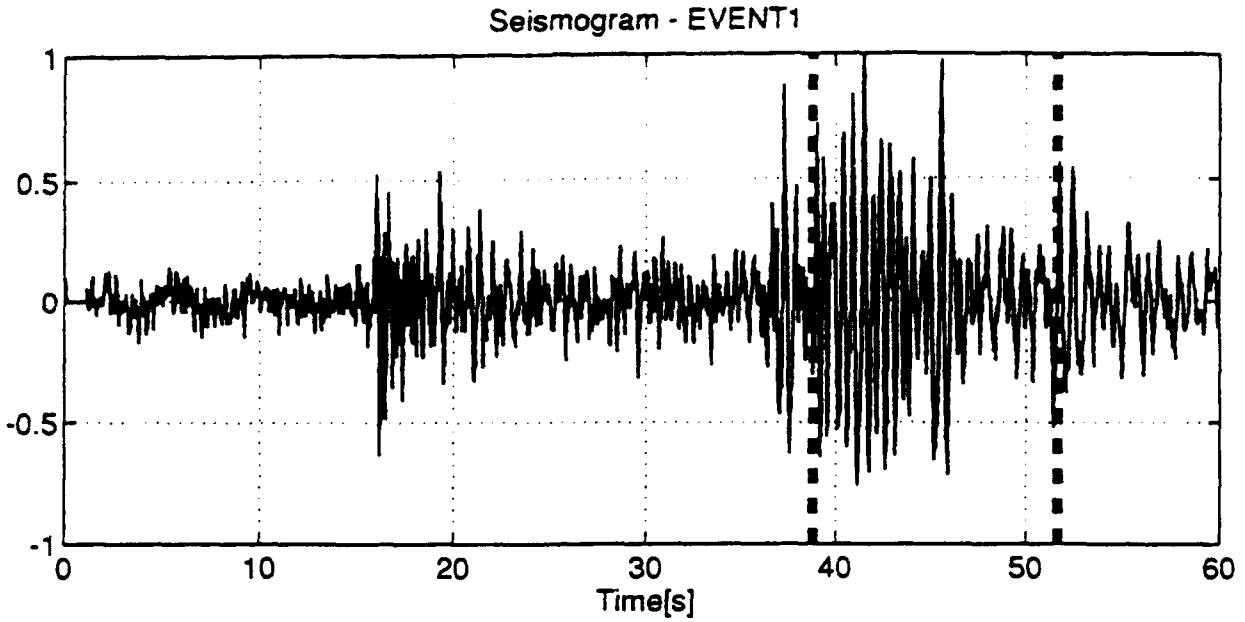
Earthquakes and explosions from Vogtland area used in this study

Table 2

Even] #	Date	Lat(N)	Long(E)	Depth	M	Yield(kg)	Origin time	Eq/Qb
1	3/11/91	50.207	12.685	0	1.98	3,265	12:03:23.986	qb/V
2	3/21/91	50.207	12.685	0	2.05	3,982	12:04:14.701	qb/V
3	3/22/91	50.207	12.685	0	2.03	2,835	12:33:25.332	qb/V
4	3/23/91	50.207	12.685	0	1.99	2,025	12:00:55.800	qb/V
5	3/24/91	50.296	12.225	12.9	2.18		05:05:04.447	eq
6	3/24/91	50.279	12.228	12.9	1.5		05:35:21.047	eq
7	3/24/91	50.277	12.24	13.9	1.4		06:57:59.309	eq
8	3/24/91	50.278	12.22	12.4	1.65		09:38:33.436	eq
9	3/24/91	50.294	12.223	12.7	2.07		14:33:27.988	eq
10	3/24/91	50.293	12.224	12.5	1.8		15:00:44.532	eq
11	3/24/91	50.293	12.224	9	1.73		15:41:03.515	eq
12	3/25/91	50.298	12.222	12.9	2.37		14:54:13.507	eq
13	3/25/91	50.292	12.213	12.4	1.54		22:31:45.761	eq
15	5/2/91	50.207	12.713	0	1.93	3,575	11:06:10.221	qb/NS
16	5/2/91	50.184	12.186	0	2.03		12:47:33.067	qb/nk
18	5/10/91	50.79	12.07	-999	1.43		20:02:51.112	eq
19	5/19/91	50.36	12.371	0	2.06		03:22:10.0	eq
20	5/23/91	50.207	12.713	0	2.12	3,135	11:01:05.259	qb/NS
21	5/25/91	50.207	12.713	0	2.13	3,135	11:01:28.688	qb/NS
22	5/26/91	50.207	12.713	0	2.14	2,907	11:00:32.367	qb/NS
23	5/28/91	50.207	12.685	0	2.01	3,575	11:03:51.425	qb/V
24	6/20/91	50.207	12.685	0	1.98	1,998	11:01:16.808	qb/V
25	6/20/91	50.293	12.803	0	1.8		11:45;35.486	qb/D
26	6/22/91	50.207	12.685	0	2.15	2,886	10:58:34.818	qb/V
27	6/27/91	50.207	12.685	0	1.93	3,515	11:04:39.629	qb/V

V - Vintirov; NS - Nove Sedlo; nk - not known; D - Depoltivice

Figure 3


Seismogram - EVENT1
1
0.5
0
-0.5
-1
0
10
20
30
40
50
60
Time[s]

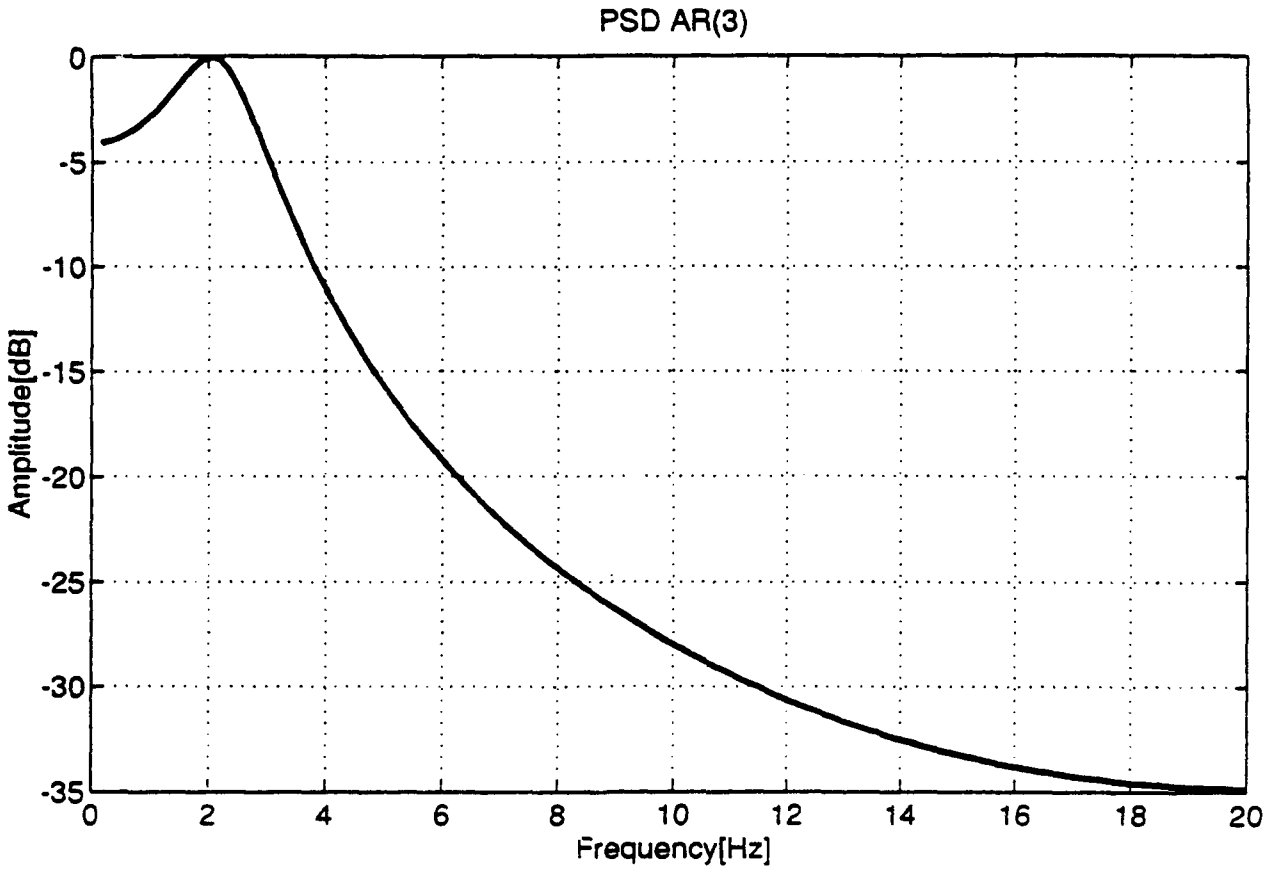

PSD AR(3)
0
-5
-10
-15
-20
-25
-30
-35
Amplitude[dB]
0
2
4
6
8
10
12
14
16
18
20
Frequency[Hz]

Figure 4
Absolute pole position as function of frequency

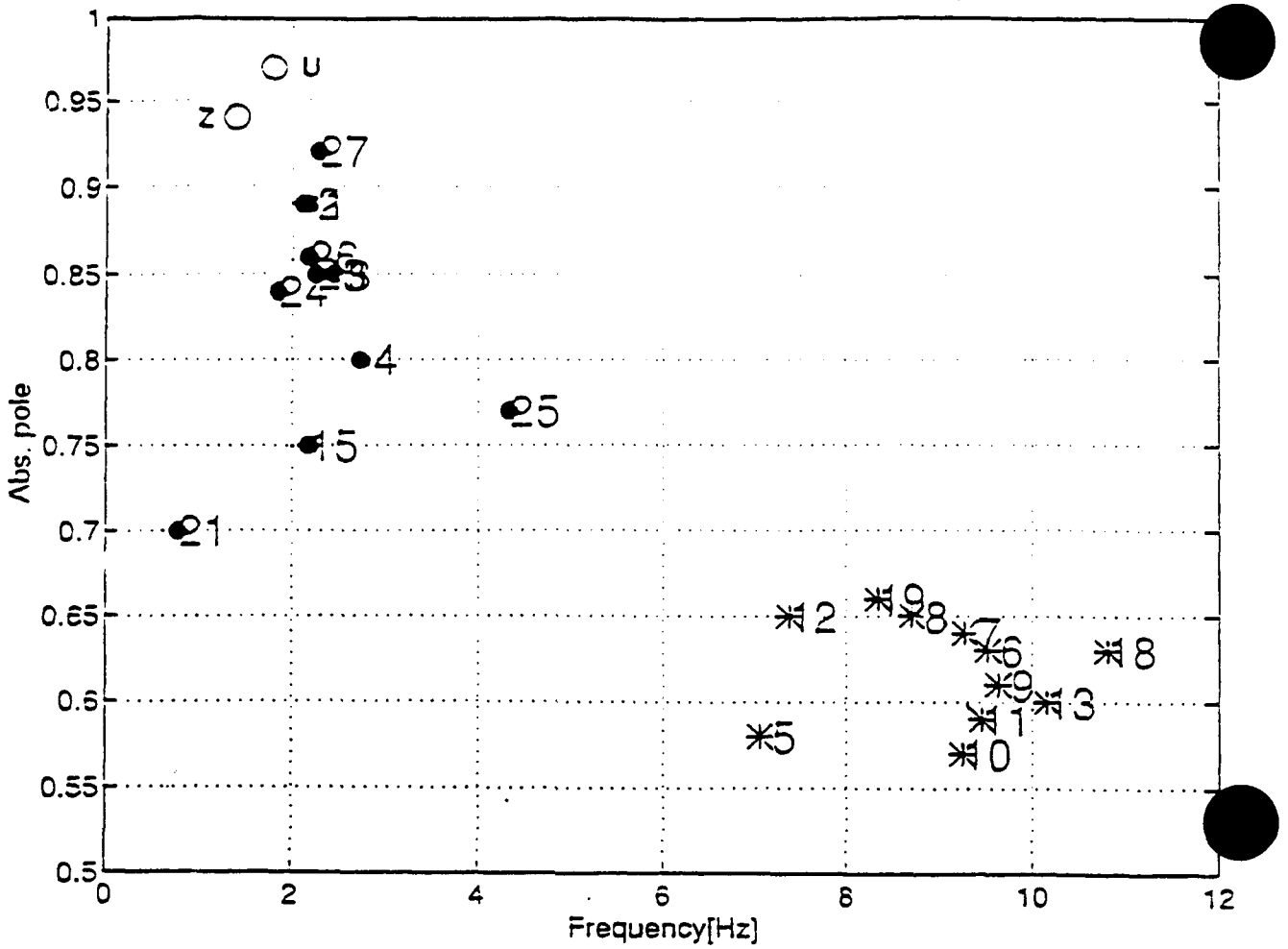


Figure 4 shows the reciprocal pole position versus frequency for the analysed events. Solid circles are explosions and stars are earthquakes. The two open circles represent surface and buried explosions in southern Russia, recorded at Garm. Figure 4 shows a clear separation of explosions and earthquakes with the latter having broad AR (3) spectra with weak poles above 6 Hz while the explosions all show a much stronger pole at frequencies less than 5 Hz.

Further studies will concentrate on (1) lowering the practical threshold for determining Ms of regional events and (2) determining the transportability of the AR (3) - Lg method to other areas.

QUANTIFICATION OF SMALL SOURCES

R. B. Herrmann† and K. D. Hutchenson
Department of Earth and Atmospheric Sciences
Saint Louis University
†rbh@slustl.slu.edu
TEL: 314/658-3131, FAX: 314/658-3117

AFOSR Contract No. F49620-93-1-0276

OBJECTIVE

This paper addresses the problem of source estimation using regional seismic network data by focusing on modeling Rg waveform data from local mining blasts. In the context of a CTBT such a study may be viewed negatively because of restrictions on the use of the Rg wave, e.g., one must have observations at relatively short distances, typically less than 300 km. A counter argument is that there may be cases in which both Rg is observed and it is necessary to classify an event, and hence all information must be used and understood. This may occur when a seismic monitoring system is physically close to the a region under study.

Another reason for having such a capability is that the Rg wave provides redundant information about the source that can be used together with regional/teleseismic P and regional Lg to test the validity of the local magnitude scale by providing an independent seismic moment estimate and perhaps to the extrapolation of the successful teleseismic $M_S - m_b$ discriminant to regional distances.

RESEARCH ACCOMPLISHED

We have completed several studies on the moment-yield relation for chemical explosions (Al-Eqabi, 1994; Hutchenson, 1994). Al-Eqabi (1994) examined USGS refraction data for shots in the metamorphic Paleozoic rocks in Maine. The shots were 1 ton in size and were single explosions. Averaging 10 shots, the mean seismic moment is 3×10^{18} dyne-cm for 1T.

Hutchenson (1994) used both regional seismic network data from the Central Mississippi Valley Seismic Network operated by Saint Louis University and also from temporary deployments of DR-2000 recorders for several chemical explosions at strip mines (November, 1991 and August, 1992) and at a USGS refraction profile shot point (October, 1991).

The Rg data were processed using tools from Computer Programs in Seismology to determine group velocities, to use match filters to isolate modes, to perform cross-correlation analysis to estimate phase velocities, and to invert the dispersion curves for a shallow velocity model. Although the shear-wave velocity model was determined using existing programs, the determination of the Q_β structure had to be done by trial and error pending the development of a robust waveform inverter under this contract. The Q_β structure was estimated using a combination of forward synthetics, spectral ratios, and the dispersion inversion program. The only test of the consistency of the Q_β structure is similarity of seismic moment estimates from

the different vertical component trace observations.

As an example, we discuss the strip mine explosions at the Delta Mine near Marion, Illinois in November, 1991. Two events, having yields of 50 and 64 tone were monitored. Figures 1 and 2 show the locations of the stations used in the analysis.

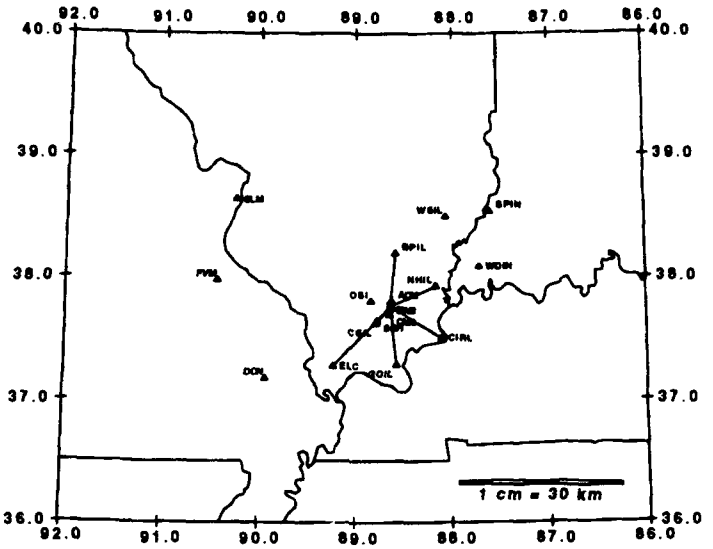


Fig. 1. Central Mississippi Valley Seismic Network Stations used to study the Delta Mine source near Marion, Illinois.

Figures 3 and 4 show the observed data and the synthetic seismogram fits for the two sets of instruments. Each synthetic is generated using a velocity - Q model inferred for that station. There was significant variability in the individual seismic moment estimates, roughly a factor of 40 from the lowest to the highest. The estimates from the regional seismic network were typically higher than those from the near-in digital instruments. Such variation may be due to source radiation patterns, incorrect path velocity - Q models, absolute instrument calibration and perhaps unresolved very shallow structure beneath the more distance stations.

Figure 5 presents the moment - yield results from Hutchenson (1994). A clear separation is seen between the regional CMVSN values and the near-in DR2000 estimates. For reference the linear moment- log yield relation proposed by Denny and Johnson (1991) is show with 1T ~ $1.0 x 10^{18}$ dyne-cm. In addition the same trend shifted vertically upward to fit the mean of the Al-Eqabi (1991) observations is also shown.

CONCLUSIONS AND RECOMMENDATIONS

- These seismic-moment estimates for commercial strip mining (delayed shot) surface explosions are systematically higher than Denny and Johnson (1991) estimates for tamped, buried explosions. This may be due to the complex seismic wavefield associated with surface movement of rock.

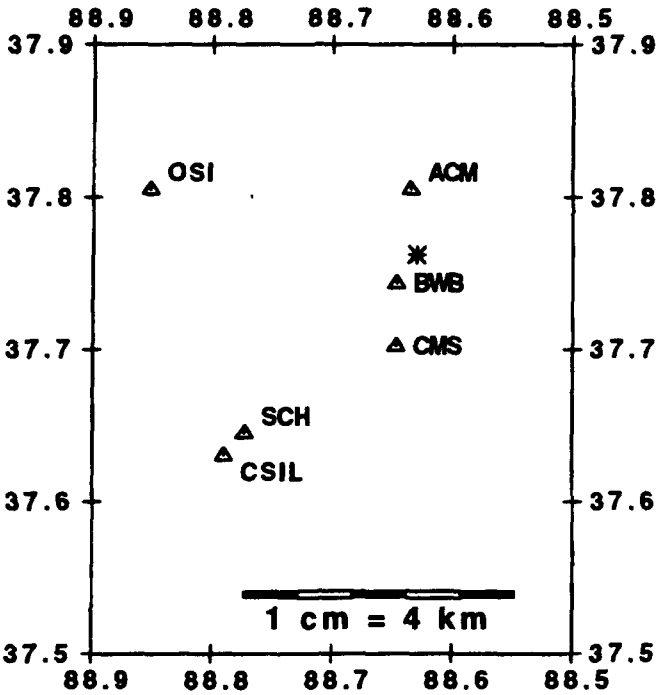


Fig. 2. Portable digital stations used to study the Delta Mine source near Marion, Illinois.

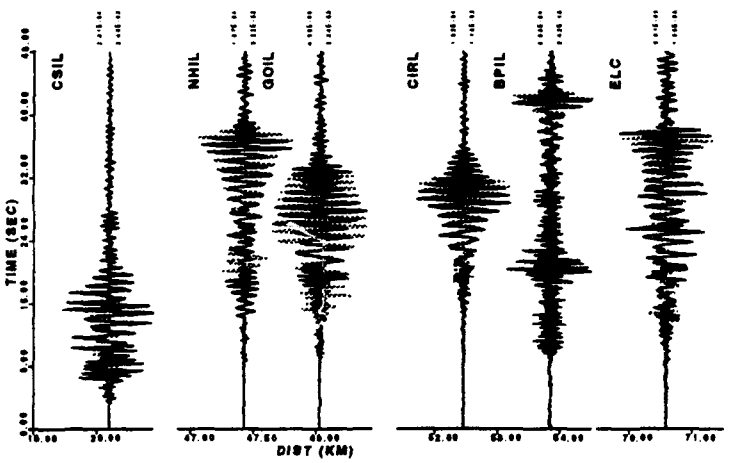


Fig. 3. Waveform overlay showing the match between the recorded waveform (bold) and the calculated synthetic (shaded) in the 0.5 to 5.0 Hz bandwidth for each of the paths from Marion, IL, for the 08 September 1992 strip-mine blast.

- Single station techniques can be used to estimate seismic-moments and also infer yields. Until a proper waveform inversion procedure is developed, which would permit a sensitivity analysis of model and source parameters, the scatter observed is greater than desired in a CTBT environment, but probably on the same order of improper regional magnitude scales for P or Lg.

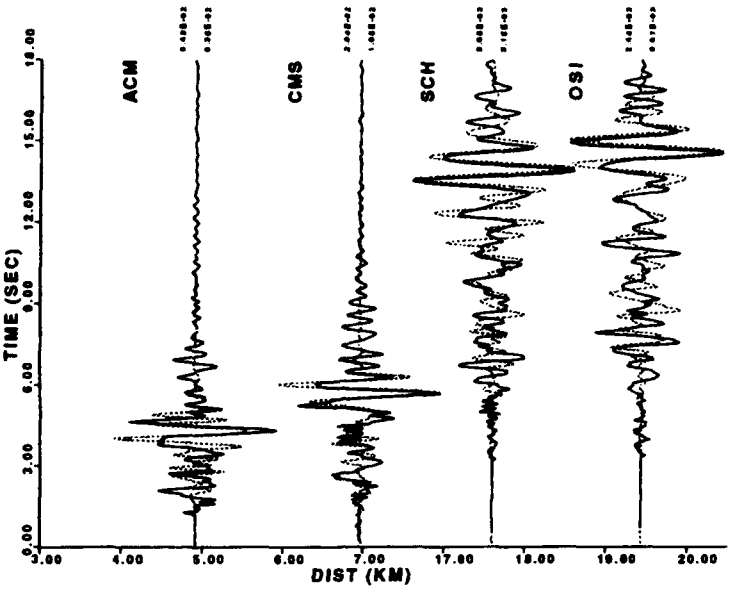


Fig. 4. Waveform overlay showing the match between the recorded waveform (bold) and the calculated synthetic (shaded) in the 0.5 to 5.0 Hz bandwidth for each of the paths from Marion, IL, for the 8 September 1992 strip-mine blast. The fit for the fundamental mode Rg is good, with the majority of the higher modes matching reasonable well.

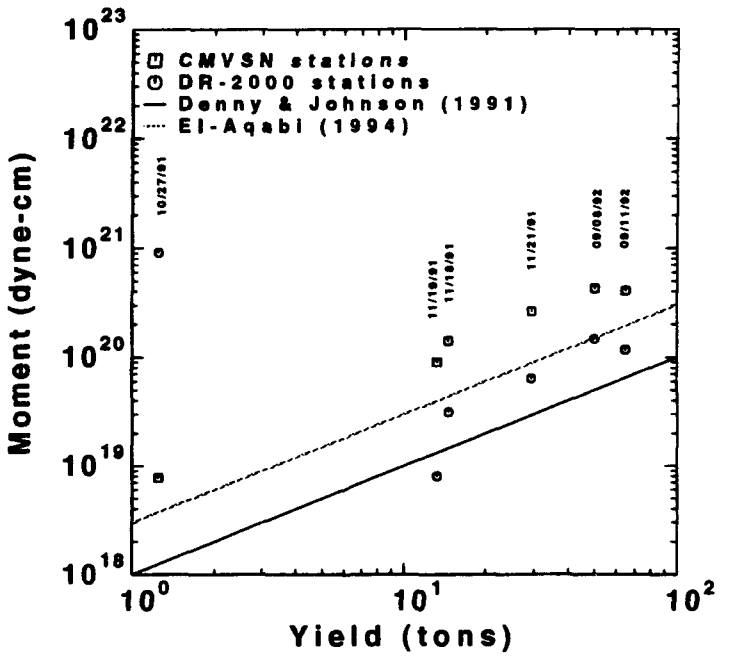


Fig. 5. M_L vs yield for events used in this study, shown recorded as averages for each of the two networks. The solid line is the relationship determined by Denny and Johnson (1991), the dashed line that determined by El-Aqabi (1994).

- To the extent that an $M_S - m_b$ discriminant may work for small events, it is necessary that controlled field experiments be performed at regional distances to understand seismic-moment yield relations and the value of longer period discriminants. Specifically deployment of broadband sensors along different profiles and in tight arrays to improve low frequency S/N is required.

REFERENCES

Al-Eqabi, G. I. (1994). Analysis and inversion of the dispersion and waveforms of short period Rayleigh waves (Rg) in Maine, *Ph. D. Dissertation,* Saint Louis University.

Denny, M. D., and L. R. Johnson (1991). The explosion seismic source function: models and scaling laws reviewed, in *Explosion Source Phenomenology,* S. R. Taylor, H. J. Patton and P. G. Richards, eds., American Geophysical Union, 268pp.

Hutchenson, K. D. (1994). shallow structure of the Illinois Basin from fundamental and higher-mode regional surface wave dispersion, *Ph. D. Dissertation,* Saint Louis University.

Hutchenson, K. D., and R. B. Herrmann (1994). Determination of shallow surface shear-wave velocity and Q_β from near-regional monitoring of strip-mine blasts, *Bull. Seism. Soc. Am.* (under revision).

Near Real Time Seismic Magnitude and Moment Measurements

Eystein S. Husebye , C. Deniz Mendi, and Bent O. Ruud
Institute of Solid Earth Physics, University of Bergen,
Allégaten 41, N-5007 Bergen, Norway
AFOSR Grant F49620-94-1-0278

Objective

Understanding seismic wave propagation in the heterogeneous lithosphere in the context of nuclear test ban monitoring.

Research accomplished

We demonstrate event magnitude can be reliably estimated in near real time conditioned on the design of the signal detector being of STA/LTA type where STA is a short term signal power or *rms* estimate. Using real data we demonstrate the Random Vibration Theory relation that $A_{max} \sim (2 \ln N)^{1/2} A_{rms}$ is valid for non-stationary seismic signals. Using Rayleigh's theorem we also established a relation between A_{rms} and the flat portion of the source spectra. These A_{max} and A_{rms} estimation procedures were used for determining conventional magnitudes and moment magnitudes for 29 events recorded locally by the Norwegian Seismograph Network (NSN). The procedure outlined by Sereno *et al.* (1988) was used and also their geometrical spreading and attenuation parameters derived from analysis of NORSAR recordings. Our magnitude and moment magnitude estimates for 5 different frequency bands are in good agreement with the NORSAR M_L estimates derived from the conventional magnitude formulas in combination with empirical correction tables. We also constructed conventional magnitude correction tables from the Sereno *et al.*'s spreading and attenuation parameters for a variety of signal frequency bands. Near real time A_{max} and/or A_{rms} or correspondingly event magnitudes would be of significance in automatic phase association analysis, bulletin production for local and regional seismic networks and the earthquakes monitoring performances of such networks.

Introduction

The concept of earthquake magnitude was firstly introduced by C.F. Richter in 1935. He proposed a logarithmic amplitude scale tied to the first arriving P wave as a measure for the relative size of local southern California earthquakes. Despite the diversity of record measurements, tied to the maximum amplitudes of P, S and surface waves, all

magnitude scales are of similar forms;

$$M = \log\left(\frac{A}{T}\right) + q(r,f) + c \tag{1}$$

where M is the magnitude, A the maximum phase amplitude, T is the period (sec), q accounts for geometrical spreading and attenuation as a function of distance r (km) and signal frequency (f) while c is a station correction term. The problem considered is that of automating event magnitude and moment estimation.

On line A/T estimation

Obviously for near real time magnitude/moment estimation, the A/T term must be an integral part of the signal detector design. The most popular ones in use are the so-called sliding window STA/LTA type which is a comparison of short and long term trace amplitude (a_i) averages (e.g., Ruud and Husebye, 1992). Common STA definitions are of the forms;

$$STA(abs) = \frac{1}{n}\sum_{i=1}^{n}|a_i| \tag{2}$$

$$STA(rms) = \left[\frac{1}{n}\sum_{i=1}^{n}a_i^2\right]^{\frac{1}{2}} \tag{3}$$

Our preference is for the *rms* related STA-LTA definitions also because signal *rms* is related to the signal power spectrum via the Parseval's theorem.

The task is to estimate peak time domain amplitudes for the first arrival of P-waves or the dominant L_g-phase in case of local events that is the A/T-term in eq(1). From the Random Vibration Theory (RVT) results of Cartwright and Longuet-Higgins (1956) we have the relation;

$$E(A_{max}) = A_{rms}f(N) \tag{4}$$

where E is expectation, N is the number of extremes (peaks and troughs) and A_{rms} is the *rms* value of the signal. In the case of STA trace window, $A_{rms} = STA(rms)$. We have for $f(N)$,

$$f(N) = (2\ln N)^{\frac{1}{2}} \tag{5}$$

The validity of the simple linear relationship in eq(5) was confirmed by extensive analysis of real data; an example is given in Fig. 1. Whether we prefer to measure magnitude (M_L) or moment (M_0), the A_{max} term is estimated from bandpass filtered traces, and thus must be corrected for the instrument response.

Magnitude and moment measurements

The A/T-term derived via the signal detector parameter $STA(rms)$ sufficies for event magnitude estimation given that a tabulation of the distance dependent q-term in eq(1) are available. If this is not the case, we may introduce specific estimates of the geometrical spreading and attenuation (Q) effects. Following Sereno *et al.* (1988), we write for the amplitude spectrum of displacement at epicenter distance r;

$$|A(f,r)| = S(f)G(r,r_0)\exp\left[\frac{-\pi ft}{Q(f)}\right] \tag{6}$$

where f is frequency, $S(f)$ source spectra, $G(r,r_0)$ geometrical spreading function with a reference distance (r_0), and $Q(f)$ the attenuation function.

At local distances the dominant signal in the records is the L_g-phase whose source spectrum in case of an earthquake is expressed as (Sereno *et al.*, 1989);

$$S(f) = S_0 H(f,f_c) \tag{7}$$

$$H(f,f_c) = \left(1+(1-2B)\left(\frac{f}{f_c}\right)^2 + B^2\left(\frac{f}{f_c}\right)^4\right)^{-1/2} \tag{8}$$

where S_0 is the low frequency spectral source level, f_c is the corner frequency of the source spectrum, B is the amount of overshoot (Xie, 1993). We have the following relations for f_c and S_0 regarding M_0;

$$f_c = cS_0^{-1/3}; \qquad S_0 = \frac{M_0}{4\pi\rho\beta^3} \tag{9}$$

where β is the crustal shear wave velocity, ρ the crustal density and c a scaling constant. For moment/magnitude estimation, we must establish a relationship between the amplitude spectrum of the displacement ($|A(f,r)|$) and the near 'real-time' record parameters, A_{rms} or A_{max}, namely;

$$|A(f_{0i},r)| = \sqrt{\frac{\Delta T}{2\Delta f_i}}\,A_{rms}; \qquad i=1,\ldots,5 \tag{10}$$

$$|A(f_{0i},r)| \cong \frac{1}{2\Delta f_i}\,A_{max} \quad ; \qquad i=1,\ldots,5 \tag{11}$$

where f_{0i} represents the center frequencies of the 5 bandpass filters used in data analysis, $|A(f_{0i},r)|$ is the amplitude spectrum at frequency f_{0i} and distance r, ΔT is the window length in *sec* and Δf_i is the bandwidth of the i^{th} filter.

Under certain assumption, the $H(f,f_c)$ is negligible and combining eq(7,9-11) gives;

$$\log M_{0(max)} \cong \log A_{max} - \log 2\Delta f_i + \log 4\pi\rho\beta^3 - \log G(r,r_0) + \frac{\pi ft}{Q(f)}\log e \tag{12}$$

$$\log M_{0(rms)} = \log A_{rms} + \frac{1}{2}\log\frac{\Delta T}{2\Delta f_i} + \log 4\pi\rho\beta^3 - \log G(r,r_0) + \frac{\pi ft}{Q(f)}\log e \tag{13}$$

Note that P, S and L_g-phases from explosions and earthquakes have different source representations. Further methodological details in Mendi and Husebye (1994).

Data analysis and results

In this section we demonstrate that the approach detailed in the previous section appears to be valid for calculating magnitudes and moments for the 29 local earthquakes and explosions listed in Table 1 and recorded by stations in the Norwegian Seismograph Network (NSN). Firstly, the event moments were estimated and then converted to event magnitudes (Table 2) using the formulas and the parameter values given in Table 3. These moment magnitudes are denoted $ML(Ser)_{max}$ and $ML(Ser)_{rms}$. We computed $ML(Ser)$ for 5 frequency bands as indicated in Table 2 and also conventional event magnitudes using various types of correction curves taken from NORSAR, Alsaker *et al.* (1991), and the Helsinki Observatory (Table 3). The obtained averaged event magnitudes are similar at the lower frequencies, irrespective of epicenter distance except the ML_H which are consistently high by ca. 0.6 magnitude units. Frequency dependence of the magnitude estimates is obvious from the Table 2 results, but there is hardly any difference between the $ML(Ser)_{rms}$ and $ML(Ser)_{max}$ estimates. The attenuation parameter may be important in this respect so we recalculated the $ML(Ser)$ magnitudes for $\gamma = 0.20$ and $\gamma = 0.14$ equivalent to increased signal attenuation. Its effect is to increase the *f4* and *f5* magnitudes by only 0.1 magnitude and thus negligible at distances less than say 300 km.

Discussion

In this study, we have explored the possibility of estimating event magnitude in near real time. At this stage of development we have concentrated on demonstrating that A_{max} and/or A_{rms} and hence event magnitudes and moments can be obtained from signal detector outputs of the STA/LTA types.

Our preference is for the moment magnitude estimation approach simply because of its anchoring on physical source representation and well established wave propagation parameters. The relative consistency of $ML(Ser)$ magnitudes (Table 2) implies that it should be possible to construct correction tables, the $q(r, f)$-term in eq(1), from the spreading and attenuation parameters in eq(13). Such correction curves are shown in Fig. 2 for the center frequencies and bandwidths of the bandpass filters used and the Alsaker *et al.* (1991) and NORSAR correction curves are included for comparison. In Table 2 the ML_A magnitudes are very similar to the $ML(Ser)$ ones as expected from Fig. 2 since the epicenter distances seldom exceed 250 km. Likewise, the NORSAR reported M_L magnitudes are in average 0.3 units below the $ML(Ser)$ ones. This is also easily explained from Fig. 2 since the NORSAR epicenter distances are mostly in the 300 -600 km range where the associated correction curve is lower by ca. 0.3 units.

Conclusions and recommendations

Near real time event magnitude estimates are feasible and would be invaluable for estimating network monitoring capabilities also in near real time. Such estimates are tied to noise level estimates from the individual network stations in combination with a grid search procedure (e.g. Sereno *et al.*, 1989; Ringdal and Kværna, 1992). Another application now under consideration is to use near real time magnitude estimates as a part of automated epicenter location schemes (Ruud *et al.*, 1993).

References

Alsaker, A., L. B. Kvamme, R. A. Hansen, A. Dahle and H. Bungum (1991). The M_L scale in Norway, *Bull. Seism. Soc. Am.* **81**, 379-398.

Cartwright, D. E. and M. S. Longuet-Higgins (1956). The statistical distribution of the maxima of a random function, *Proc. Roy. Soc. London, Ser. A237*, 212-223.

Mendi, C. D. and E. S. Husebye (1994). Near real time seismic magnitude and moment measurements, *Annali di Geofisica*, in press.

Richter, C. F. (1935). An instrumental earthquake magnitude scale, *Bull. Seism. Soc. Am.* **25**, 1-32.

Ringdal, F. and T. Kværna (1992). Continuous seismic threshold monitoring, *Geophys. J. Int.* **111**, 505-514.

Ruud, B. O. and E. S. Husebye (1992). A new three-component detector and automatic single station bulletin production, *Bull. Seism. Soc. Am.* **82**, 221-237.

Ruud, B. O., C. D. Lindholm and E. S. Husebye (1993). An exercise in automating seismic record analysis and network bulletin production, *Bull. Seism. Soc. Am.* **83**, 660-679.

Sereno, T. J., S. R. Bratt and T. C. Bache, (1988). Simultaneous inversion of regional wave spectra for attenuation and seismic moment in Scandinavia, *J. Geophys. Res.* **93**, 2019-2035.

Sereno, T. J. and S. R. Bratt (1989). Seismic detection capability at NORESS and implications for the detection threshold of a hypothetical network in the Soviet Union, *J. Geophys. Res.* **94**, 10,397-10,414.

Xie, J. (1993). Simultaneous inversion for source spectrum and path Q using L_g with application to three semipalatinsk explosions, *Bull. Seism. Soc. Am.* **83**, 1547-1562.

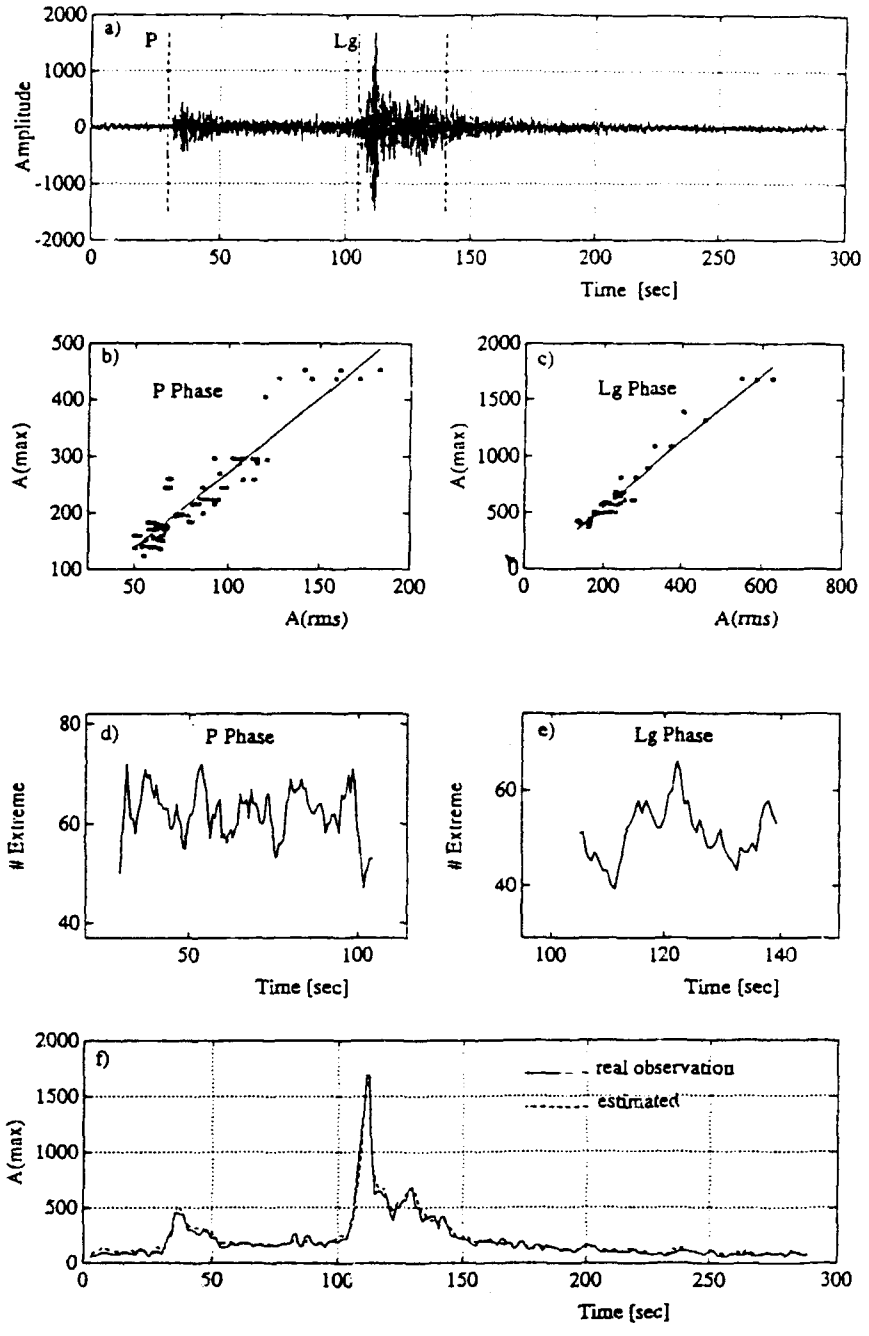


Fig. 1. $A_{max} - A_{rms}$ analysis for station KMY unfiltered recordings of Event 4 in Table 2 at an epicentral distance of 795 km. **a)** original vertical trace record. **b)** and **c)** A_{max} versus A_{rms} for P- and L_g-phases respectively. The window length used in the evaluation of A_{rms} is 2.5 sec. **d)** and **e)** number of extremes N for P- and L_g-phases. **f)** Observed and estimated A_{max} using eq(5). The two curves match each other almost perfectly.

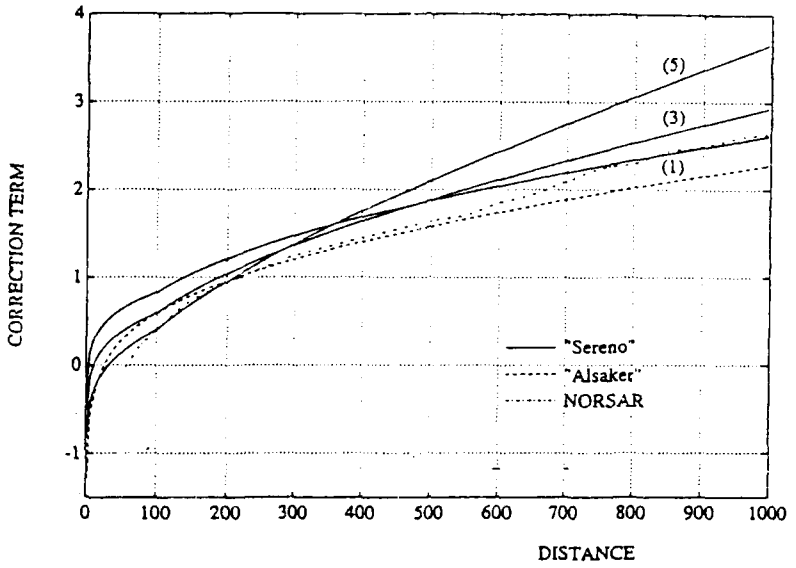


Fig. 2. Generating distance - correction curves from the Sereno *et al.*, 1988 spreading and attenuation parameters as listed in Table 3. For comparison the corresponding Alsaker *et al.*, 1991 and NORSAR (T = 0.45 sec) curve are shown. The correction curves derived from Sereno *et al.*, 1988 are plotted for the filters *f1*, *f3* and *f5*. In Table 2 the $ML(Ser)$ and ML_A magnitude estimates are very similar which is also expected from Fig. 2 since epicenter distances generally are less than 250 km. The NORSAR reported magnitudes (M_L column in Table 2) are in average 0.3 units lower as expected since the corresponding epicenter distances are in the 300 - 600 km range. Note that the different correction curves are similar out to ca. 350 km that is the distance range where the majority of local events are recorded.

Magnitude Formulations	*Reference*
$\log M_0 = 1.03\,ML(Ser) - 17.1$ (EQ) $\log M_0 = 1.04\,ML(Ser) - 17.7$ (EXP) $Q_0 = 560;\ \gamma = 0.26$ $r_0 = 100\,km;\ \mu = 1;\ \nu = 1/2$ $\rho = 2.7\,gr/cm^3;\ \beta = 3.5\,km/s$	Sereno et. al. (1989)
$ML_N = \log(100\,A) + F(\Delta, T)$	NORSAR
$ML_A = \log A + 0.91 \log \Delta + 0.00087\,\Delta - 1.31$	Alsaker et. al. (1991)
$ML_H = \log A + 1.27 \log \Delta - 1.44$	Helsinki Seismological Observatory

Table 3. Listing of correction formulas as used for the estimated magnitudes tabulated in Table 2. M_0 = moment, A = peak amplitude in nm and Δ = epicentral distance in km. $F(\Delta, T)$ correction function is shown in Fig. 2 for T = 0.45 sec.

No	Date	Time	Location		M_c	M_L	H	#	Source
	(d/m/y)	(h.min:sec)	(LatN)	(LonE)			(km)	Stat.	Type
1	26/08/93	10.34:32.0	59.05	5.77	2.6	2.2	0	8	EXP
2	26/08/93	19.22:04.9	61.11	4.07	2.8	2.5	18	8	EQ
3	10/09/93	13.11:23.8	58.34	6.36	2.7	2.0	0	5	EXP
4	13/09/93	05.25:14.4	66.34	5.67	3.9	3.2	11	10	EQ
5	15/09/93	09.58:38.1	60.60	4.79	2.1	1.6	0	7	EXP
6	15/09/93	15.31:29.7	67.11	20.84	3.2	1.8	0	4	EXP
7	21/09/93	13.15:21.1	58.33	6.31	3.0	2.5	0	7	EXP
8	28/09/93	16.44:53.9	58.49	10.62	2.9	2.3	15	5	EQ
9	28/09/93	16.57:42.1	60.46	5.15	1.6	1.4	0	6	EXP
10	29/09/93	14.12:21.5	58.15	6.31	2.8	2.2	0	6	EXP
11	02/10/93	08.30:55.3	60.39	5.02	1.8	1.5	0	6	EXP
12	03/10/93	23.48:35.5	60.06	7.29	2.5	1.8	15	7	EQ
13	04/10/93	20.21:48.3	61.94	1.44	2.3	1.0	11	5	EQ
14	07/11/93	23.40:44.0	67.84	20.08	2.5	1.7	15	4	EQ
15	07/11/93	23.43:17.2	66.28	7.02	3.1	2.5	25	4	EQ
16	08/11/93	14.28:17.3	59.91	2.72	2.4	1.5	15	7	EQ
17	12/11/93	19.54:36.0	59.69	12.86	3.4	2.9	16	6	EQ
18	15/11/93	15.04:25.6	62.17	3.27	2.7	1.9	15	5	EQ
19	21/11/93	01.53:56.3	60.18	4.96	2.6	2.1	12	6	EQ
20	27/11/93	18.57:52.7	60.47	11.66	3.1	2.2	0	5	EXP
21	13/12/93	09.00:09.5	56.75	2.74	3.1	2.6	12	6	EQ
22	27/12/93	05.20:46.3	61.29	2.79	3.3	3.6	14	8	EQ
23	03/01/94	22.12:59.8	61.76	4.19	2.6	2.4	17	7	EQ
24	07/01/94	09.06:22.6	60.60	2.43	2.3	1.8	23	5	EQ
25	15/01/94	00.00:26.2	65.23	7.58	2.8	1.6	2	3	EQ
26	19/01/94	09.16:54.8	66.36	14.60	2.4	1.4	0	3	EXP
27	21/01/94	01.26:14.1	65.98	11.89	3.1	2.1	19	2	EQ
28	25/01/94	03.07:58.3	62.46	5.07	2.6	1.9	20	5	EQ
29	26/01/94	17.27:47.1	66.84	13.58	3.0	2.3	0	5	EXP

Table 1. Listing of all the events used in analysis. The focal parameters are taken from the monthly bulletins for the Norwegian Seismic Network (NSN) as published by the University of Bergen. The M_c and M_L notations reflect NSN coda wave magnitude and NORSAR reported M_L (L_g-waves) magnitude, respectively. We have introduced a few modifications in parameter listing; all presumed explosions (EXP) are given zero focal depth. The separation of events into EXP and EQ (earthquake) populations are not based on specific classification criteria. Potential errors here would not significantly change our analysis results.

No	M_L	M_c	$ML(Ser)_{max}$					$ML(Ser)_{rms}$					ML_N	ML_A	ML_H
			f1	*f2*	*f3*	*f4*	*f5*	*f1*	*f2*	*f3*	*f4*	*f5*	*f2*	*f2*	*f2*
1	2.2	2.6	2.5	2.3	2.2	2.0	2.0	2.6	2.4	2.3	2.1	2.1	2.3	2.3	2.9
2	2.5	2.8	2.9	2.8	2.7	2.6	2.5	3.0	2.9	2.8	2.6	2.5	2.8	2.7	3.3
3	2.0	2.7	2.5	2.3	2.2	2.1	2.0	2.6	2.5	2.4	2.2	2.1	2.3	2.3	2.9
4	3.2	3.9	3.7	3.7	3.6	3.5	3.5	3.7	3.6	3.5	3.2	2.9	3.8	3.6	4.1
5	1.6	2.1	2.1	1.9	1.8	1.6	1.5	2.2	2.0	1.9	1.7	1.6	1.8	1.8	2.4
6	1.8	3.2	2.0	1.8	1.9	2.3	2.3	2.1	1.9	2.0	2.3	2.3	1.9	1.9	2.4
7	2.5	3.0	2.7	2.6	2.5	2.5	2.4	2.8	2.7	2.6	2.5	2.4	2.6	2.5	3.1
8	2.3	2.9	2.3	2.2	2.3	2.3	2.1	2.4	2.3	2.3	2.2	1.8	2.2	2.2	2.8
9	1.4	1.6	1.6	1.4	1.3	1.1	0.9	1.8	1.5	1.4	1.2	1.1	1.3	1.3	1.8
10	2.2	2.8	2.5	2.4	2.3	2.1	2.0	2.7	2.5	2.4	2.2	2.0	2.4	2.4	3.0
11	1.5	1.8	1.8	1.5	1.3	1.2	1.1	1.9	1.7	1.5	1.4	1.2	1.3	1.4	2.0
12	1.8	2.5	2.1	2.0	1.9	1.8	1.7	2.2	2.1	2.0	1.9	1.7	1.8	1.9	2.5
13	1.0	2.3	1.8	1.5	1.5	1.4	1.3	1.9	1.6	1.5	1.3	1.2	1.5	1.5	2.0
14	1.7	2.5	2.3	2.2	2.1	1.8	1.6	2.4	2.3	2.1	1.8	1.5	2.1	2.1	2.7
15	2.5	3.1	2.9	2.9	2.8	2.5	2.5	3.0	2.9	2.7	2.4	2.2	2.9	2.8	3.5
16	1.5	2.4	2.1	1.8	1.7	1.6	1.5	2.1	1.8	1.7	1.6	1.5	1.7	1.7	2.3
17	2.9	3.4	3.1	2.9	2.9	2.8	2.7	3.2	3.0	2.8	2.6	2.3	3.0	2.9	3.5
18	1.9	2.7	2.4	2.3	2.2	2.1	2.0	2.5	2.3	2.3	2.1	1.9	2.2	2.2	2.8
19	2.1	2.6	2.4	2.3	2.2	1.9	1.8	2.4	2.3	2.3	2.1	1.9	2.1	2.1	2.7
20	2.2	3.1	2.6	2.5	2.3	2.2	2.1	2.7	2.6	2.4	2.1	1.9	2.5	2.5	3.1
21	2.6	3.1	2.4	2.3	2.3	2.4	2.4	2.5	2.3	2.3	2.2	2.0	2.3	2.3	2.9
22	3.6	3.3	3.6	3.4	3.2	3.0	2.9	3.7	3.4	3.2	2.9	2.7	3.4	3.3	3.9
23	2.4	2.6	2.9	2.7	2.7	2.5	2.4	2.9	2.8	2.7	2.5	2.4	2.6	2.6	3.3
24	1.8	2.3	2.2	2.1	2.0	1.8	1.7	2.3	2.1	2.0	1.8	1.7	2.0	2.0	2.6
25	1.6	2.8	2.0	1.8	1.8	1.9	1.9	2.1	1.9	1.9	1.8	1.7	1.8	1.8	2.4
26	1.4	2.4	2.0	1.7	1.5	1.3	1.3	2.1	1.8	1.5	1.4	1.4	1.7	1.7	2.2
27	2.1	3.1	2.4	2.3	2.2	2.1	2.0	2.5	2.4	2.3	2.2	2.1	2.2	2.2	2.9
28	1.9	2.6	2.3	2.0	1.9	1.7	1.6	2.3	2.1	1.9	1.7	1.5	1.9	1.9	2.5
29	2.3	3.0	2.4	2.3	2.2	2.1	1.9	2.5	2.4	2.3	2.1	1.9	2.2	2.2	2.8

Table 2. Magnitude estimates for the events listed in Table 2. *f1*, *f2*, *f3*, *f4* and *f5* represent different frequency bands which are 1-2 Hz, 1.5-3 Hz, 2-4 Hz, 3-6 Hz and 4-8 Hz, respectively. Column M_L is L_g event magnitudes as reported by NORSAR using NORESS recordings while M_c is coda magnitude based NSN recordings as reported in the bulletin. $ML(Ser)_{max}$ is magnitude estimates tied to maximum amplitude observations (eq(12)) while $ML(Ser)_{rms}$ are corresponding moment magnitude estimates tied to the *rms* values (eq(11)). ML_N, ML_A and ML_H are magnitude estimates similar to $ML(Ser)_{max}$ except that the distance correction terms used are those of NORSAR, Alsaker *et al.*, 1991 and Helsinki (Table 3). Since these are frequency independent only magnitude in the *f2* band are listed.

Numerical Modeling of Crustal Phase Propagation in Irregular Waveguides

R.-S. Jih
Analytical Systems Engineering Corporation

Contract Number: F19628-93-D-0004, Task 3 (11 April 1994 --)

Project Objective

The long-term objective of this project is to improve the fundamental understanding of seismic wave excitation and propagation by exploiting the full potential of linear finite-difference method in modeling various seismological problems directly related to the treaty monitoring issues. Current emphasis is placed on improving the capability of modeling P_n , P_g , S_n , L_g , and R_g in complex geological / geophysical environments.

Research Accomplished

1. Quantitative assessment of R_g apparent attenuation due to rough topography

Two-dimensional linear elastic (P–SV) finite-difference [LFD] experiments illustrate that reflection of R_g due to rough topography is an efficient process, and that the bulk of the energy which is not transmitted across the topography is either converted to body waves or reflected back (Figure 1). The scattered P and S waves are radiated as coda to teleseismic distances, and some P–SV energy is trapped in the crustal waveguide as P_g , S_g , and L_g (Figures 2 and 3). The body waves appear to radiate from the changes in slope and to first order can be visualized as being from point diffractors along the rugged free-surface (Figure 1; see also McLaughlin and Jih, 1986). For most models tested, the R_g -to-S conversion is more efficient than that of R_g -to-P. The spatial Q values associated with rough topographic profiles, inferred from the logarithm of the transmitted power spectrum, range from 15 to 80, which are consistent with the Q_β of the uppermost crust in many places of the world (Jih, 1993c). Seven candidate roughness statistics have been tested with twenty seven random topographic profiles. The goal of this exercise was to determine which of these parameters can best characterize the roughness, and when a seismic phase is considered, which roughness statistics can best quantify the propagation efficiency. Despite differences in the definitions, some of these parameters share certain functional relationships or even correlate linearly (Jih, 1993c). Regressing the R_g propagation efficiency and scattering loss on these roughness parameters indicates that, with the exception of the Durbin-Watson statistics (also called the von Neumann ratio), most naturally defined roughness measures could be useful in predicting R_g propagation characteristics of uncalibrated paths (Figure 4). Similar statistical analysis is being conducted with the L_g phase.

2. Visualization of SV L_g propagation in irregular waveguides

LFD method is also utilized to model the propagation and scattering of L_g waves in a suite of crustal models. Each canonical model contains a laterally heterogeneous crust superimposed on the homogeneous mantle. The heterogeneities examined include rough interfaces, rugged free-surface topography, as well as embedded thick sedimentary layers. The pure L_g wave packet is injected into a stratified portion of the grid as the reference initial condition to trigger all LFD calculations (*e.g.*, Figures 5 and 6). An obvious advantage of this approach is that the effect due to different types of heterogeneity on L_g phase can be isolated and evaluated easily. Both abrupt changes in the Moho topography and a thick contained sedimentary layer can cause strong L_g -to-S_n conversions (Figure 7). The physical mechanisms underlying the conversion are different for these two structures, however. The early L_g

observed for paths from Novaya Zemlya island to Scandinavia, as reported by Baumgardt (1991), can be illustrated with LFD calculations (*e.g.*, Figure 6). Alluvial basin structures cause strong reverberations as well as very strong L_g -to-R_g conversions. If the principle of seismic reciprocity is invoked, R_g -to-L_g conversion could be an important mechanism of L_g excitation for certain structures, as Patton and Taylor (1994) recently observed with Yucca Flat explosions. Unlike the case for R_g, free-surface topography alone does not affect the L_g propagation as much as do other types of heterogeneity (Figure 5).

Conclusions and Recommendations

This paper studies the scattering of R_g and L_g into body waves by topographic irregularities and other heterogeneities along the propagation paths using 2-D finite-difference simulations. For the R_g waves, rough topography is the most important means of scattering (Jih, 1993abc). The velocity heterogeneity in the near-surface structure would be another, which was addressed in our earlier study (*cf.* McLaughlin and Jih, 1987, and Jih, 1993b). The present study expands the scope of that of McLaughlin and Jih (1986) in that statistical descriptors of the surface roughness are explored, and the relationships to apparent attenuation effects on R_g phase are examined in a quantitative manner. Numerical modeling demonstrates that R_g scattering can be an important contributor to the formation of coda waves, in support of the observational studies by Greenfield (1971), Gupta and Wagner (1992), and many others. An accurate prediction of the regional phases in areas of high proliferation concern requires a decent understanding of the attenuation / scattering mechanisms along the propagation paths. Synthetic seismograms are particularly useful for regions where earthquake or explosion data are not available.

References

Baumgardt, D. R. (1991). High frequency array studies of long range L_g propagation and the causes of L_g blockage and attenuation in the Eurasian continental craton, *Report PL-TR-91-2059(I)*, Phillips Laboratory, Hanscom Air Force base, MA., ADA236984.

Greenfield, R. J. (1971). Short-period P-wave generation by Rayleigh-wave scattering at Novaya Zemlya, *J. Geophys. Res.*, **76**, 7988-8002.

Gupta, I. N. and R. A. Wagner (1992). Evidence of R_g -to-P scattering in teleseismic P coda of East Kazakh explosions, *Bill. Seism. Soc. Am.*, **82**, 2139-2152

Jih, R.-S. (1993a). Directional excitation of R_g due to ripple-fired explosions: a 2-dimensional finite-difference calculation, in *Proceedings of Numerical Modeling for Underground Nuclear Test Monitoring Symposium*, S. R. Taylor and J. R. Kamm, eds., *Los Alsmos National Laboratory Report No. LAUR-93-3839.*

Jih, R.-S. (1993b). User's manual of FD2: a software package for modeling seismological problems with 2-dimensional linear finite-difference method, *Report TGAL-93-06*, Teledyne Geotech, Alexandria, VA.

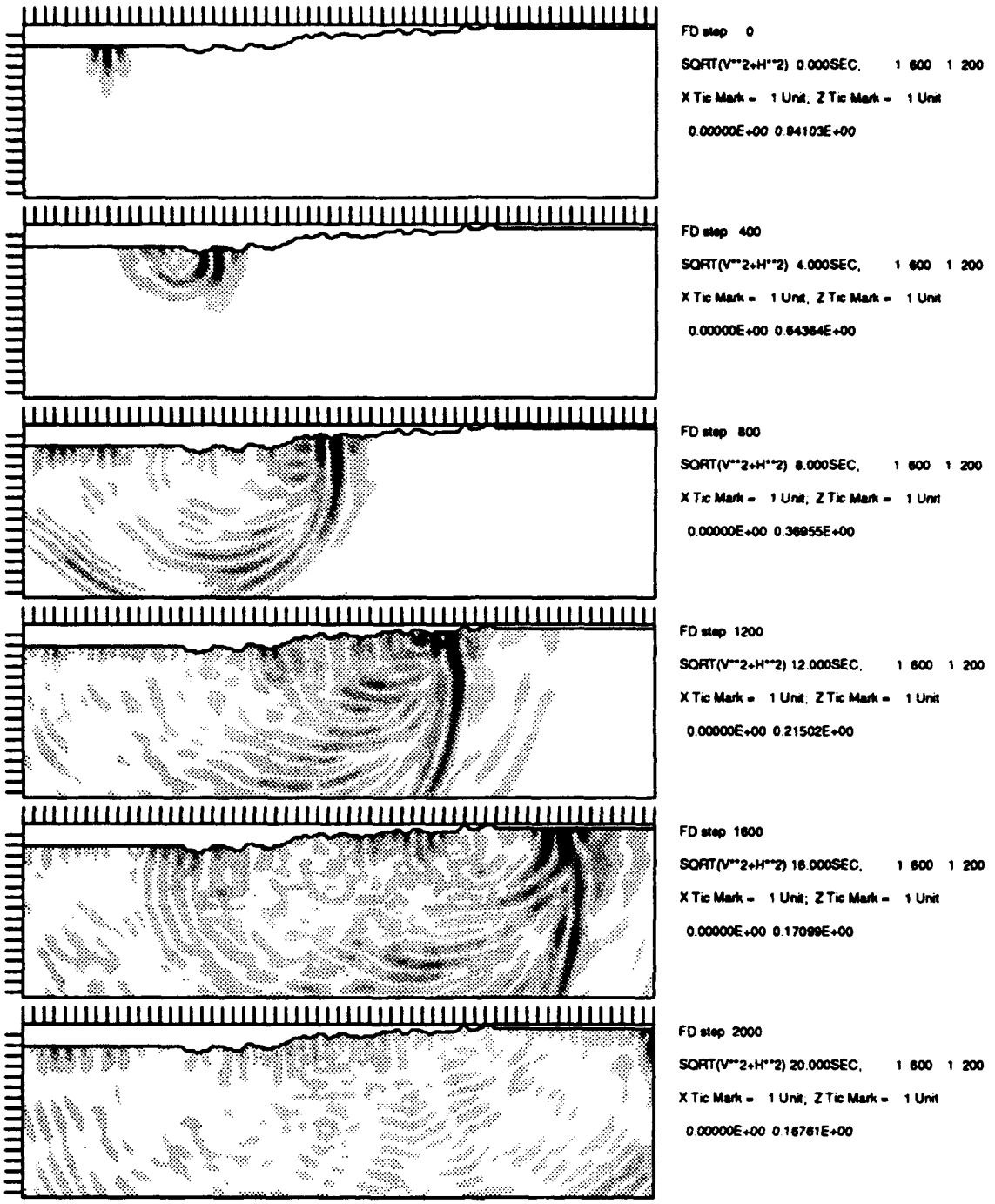
Jih, R.-S. (1993c). Statistical characterization of rugged propagation paths with application to R_g scattering study, *Report TGAL-93-07*, Teledyne Geotech, Alexandria, VA.

Jih, R.-S., K. L. McLaughlin and Z. A. Der (1988). Free boundary conditions of arbitrary polygonal topography in a 2-D explicit elastic finite difference scheme, *Geophysics*, **53**, 1045-1055.

McLaughlin, K. L. and R.-S. Jih (1986). Finite-difference simulations of Rayleigh wave scattering by 2-D rough topography, *Report AFGL-TR-86-0269*, Air Force Geophysics Laboratory, Hanscom AFB, MA, ADA179190.

McLaughlin, K. L. and R.-S. Jih (1987). Finite-difference simulations of Rayleigh wave scattering by shallow heterogeneity. *Report AFGL-TR-87-0322*, Air Force Geophysics Laboratory, Hanscom AFB, MA, ADA194961.

Patton, H. J. and S. R. Taylor (1994). Analysis of L_g spectral ratios from NTS explosions: implications for the source mechanisms of spall and the generation of L_g waves (*Bull. Seism. Soc. Am.*, in press)



Rg, Profile 43 (Seed 12345, Pr(1)=0.20), Grid 600*500, dX=dZ=100m

Figure 1: Snapshots of the displacement field due to a Rayleigh wave incident upon topographic profile No.43, shown at every 4 seconds. Shading in each snapshot is proportional to $\sqrt{U^2 + W^2}$ where U and W are the displacement along the X and Z directions, respectively, of the grid. The darkness of the plot is normalized to the maximum in each frame. The corners act as point sources radiating converted body waves (mainly *S* wave), as previously reported by McLaughlin and Jih (1986) and Jih *et al.* (1988).

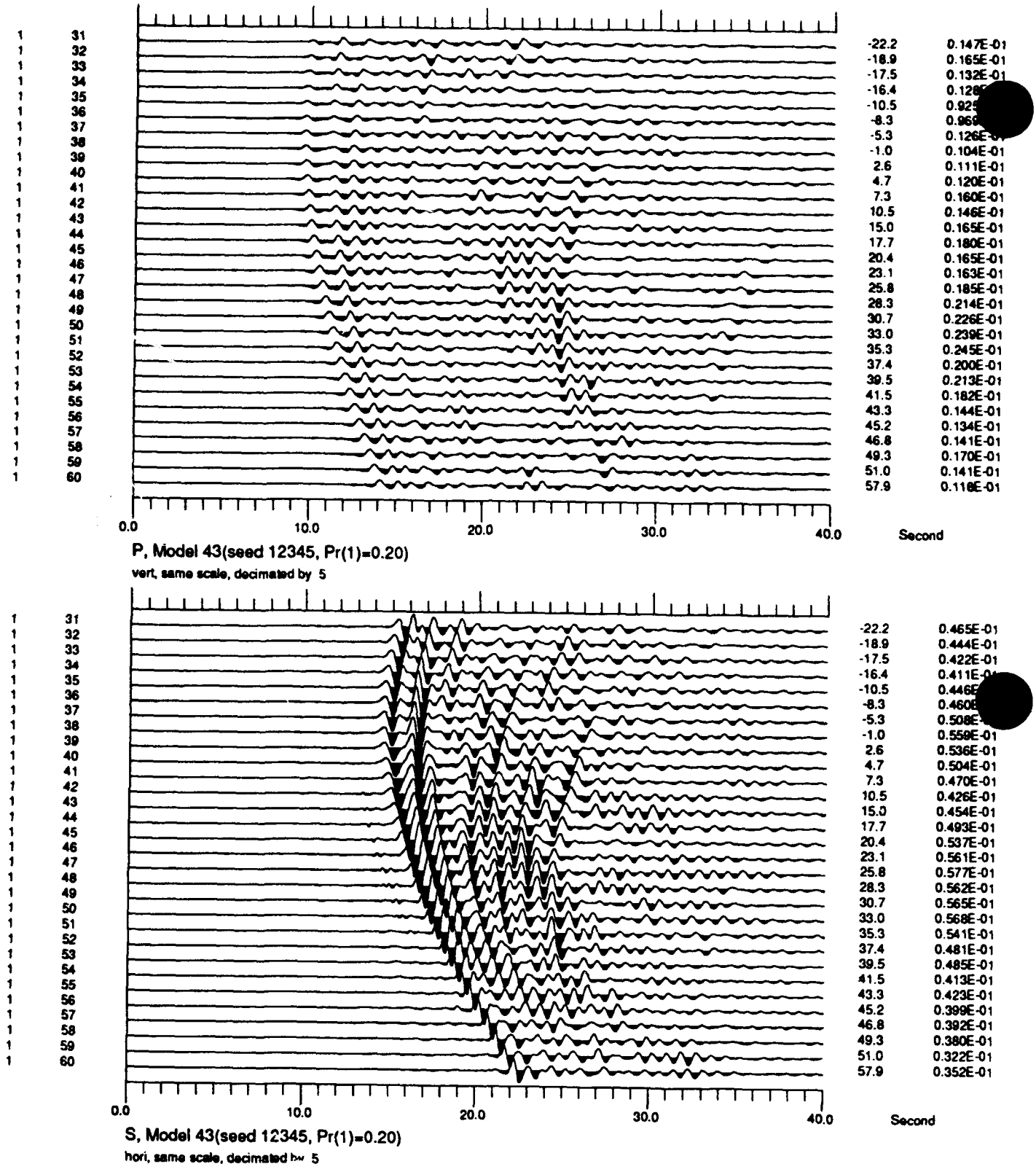


Figure 2. Seismic sections of the converted *P* wave (top) and *S* wave (bottom) displacements of model No.43. The take-off angle and the maximal zero-to-peak amplitude of each synthetic are shown on the right. Note that the converted *SV* waves typically have a peak amplitude two to three times larger than that of the the converted *P* waves. Scattered *S* waves with slownesses appropriate for trapping in the crust will generate L_g waves observed at regional distances. In this example, about one third to half of these synthetics would contribute primarily to L_g energy.

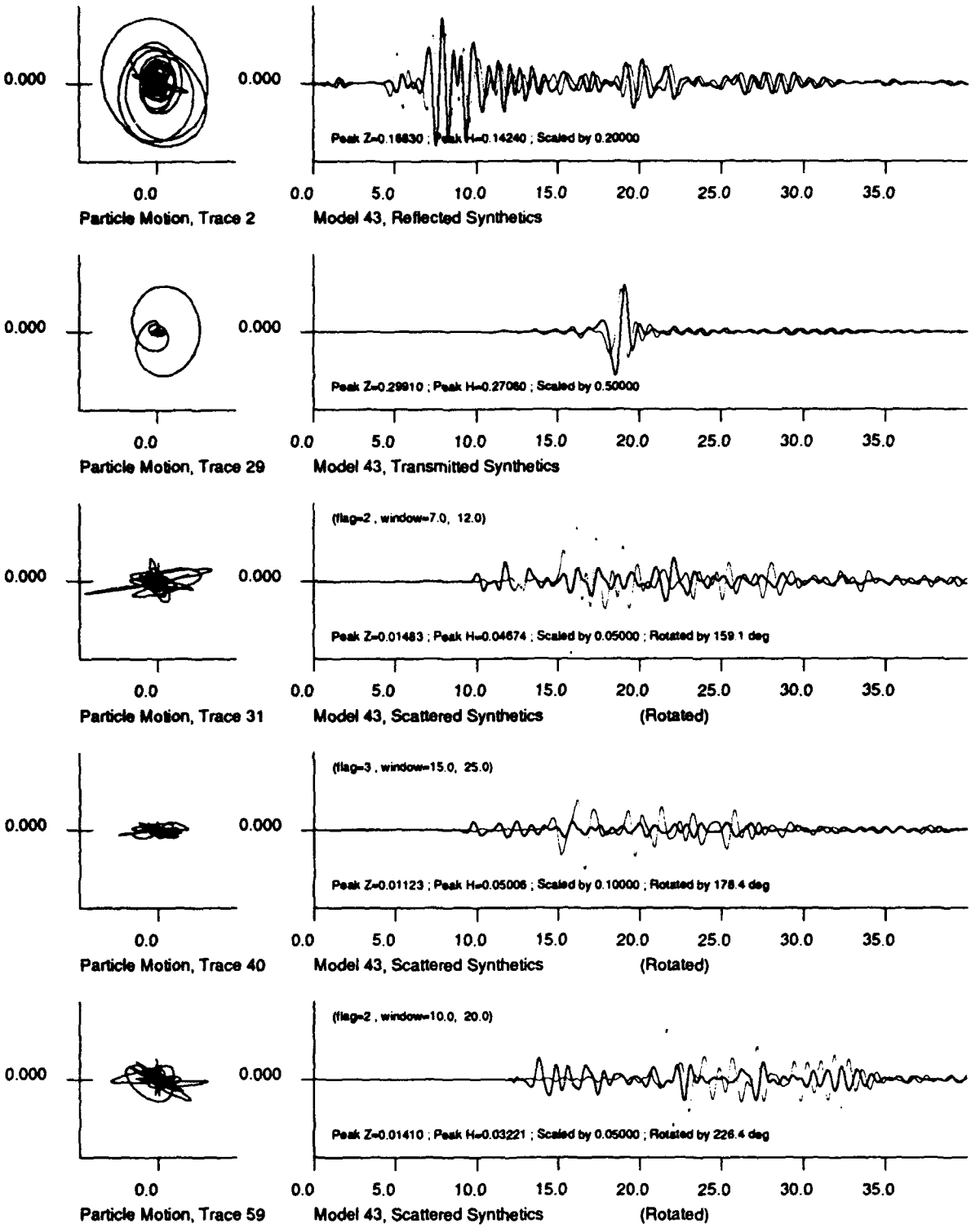


Figure 3. Five synthetics corresponding to the reflected R_g waves (No.2, top), the transmitted R_g waves (No.29), and scattered body waves (No.31, No.40, and No.59), respectively, for the topographic profile No.43. For scattered energy, the *P* and *S* waves are shown in solid and dashed curves, respectively. Scattered *S* waves appear to contain more energy than do the *P* waves (see also the particle motions on the left). In realistic gelogic structures, a significant fraction of the scattered *S* wave energy would be trapped in the crust and observed as L_g or coda waves, due to their obligue take-off angles.

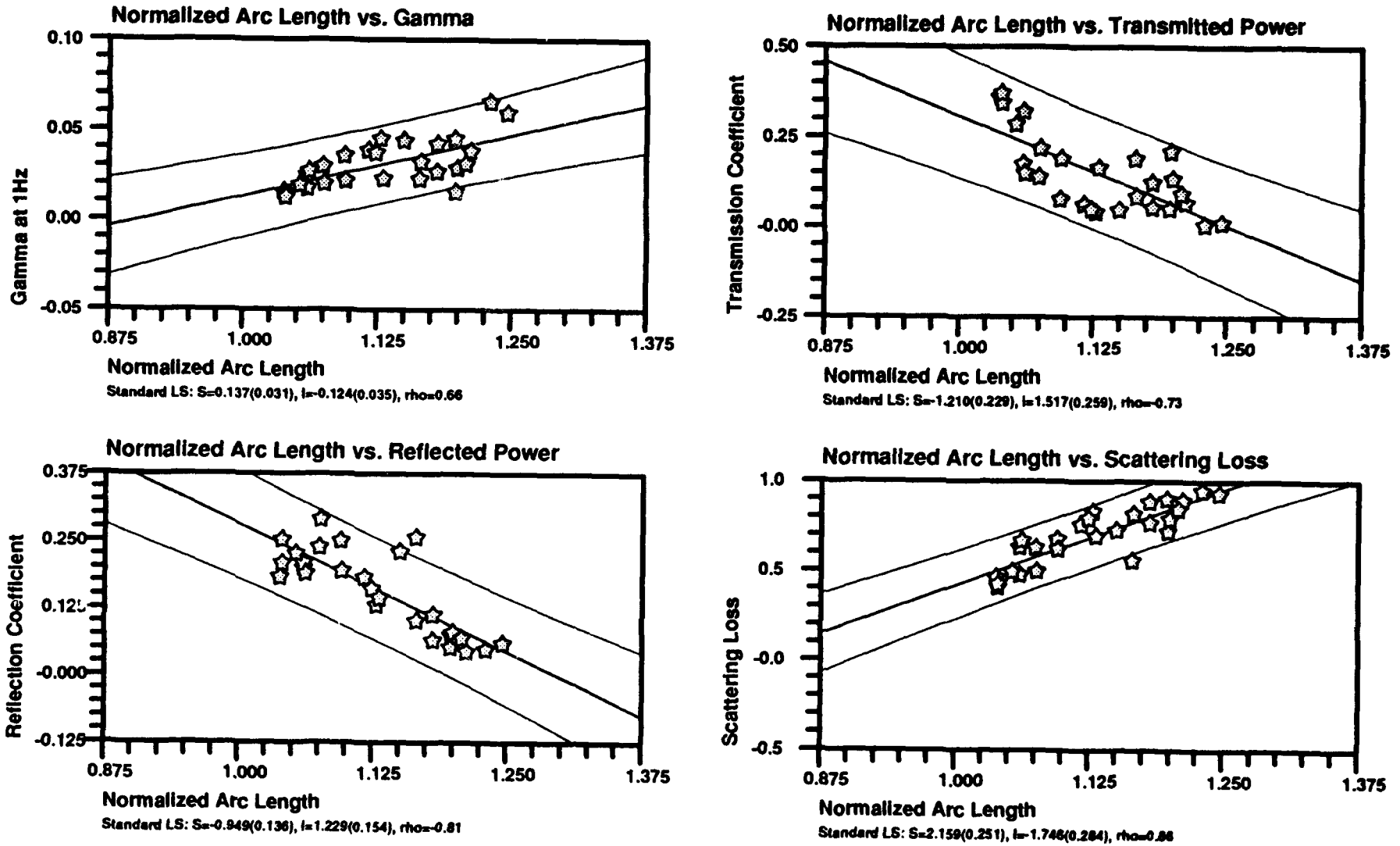
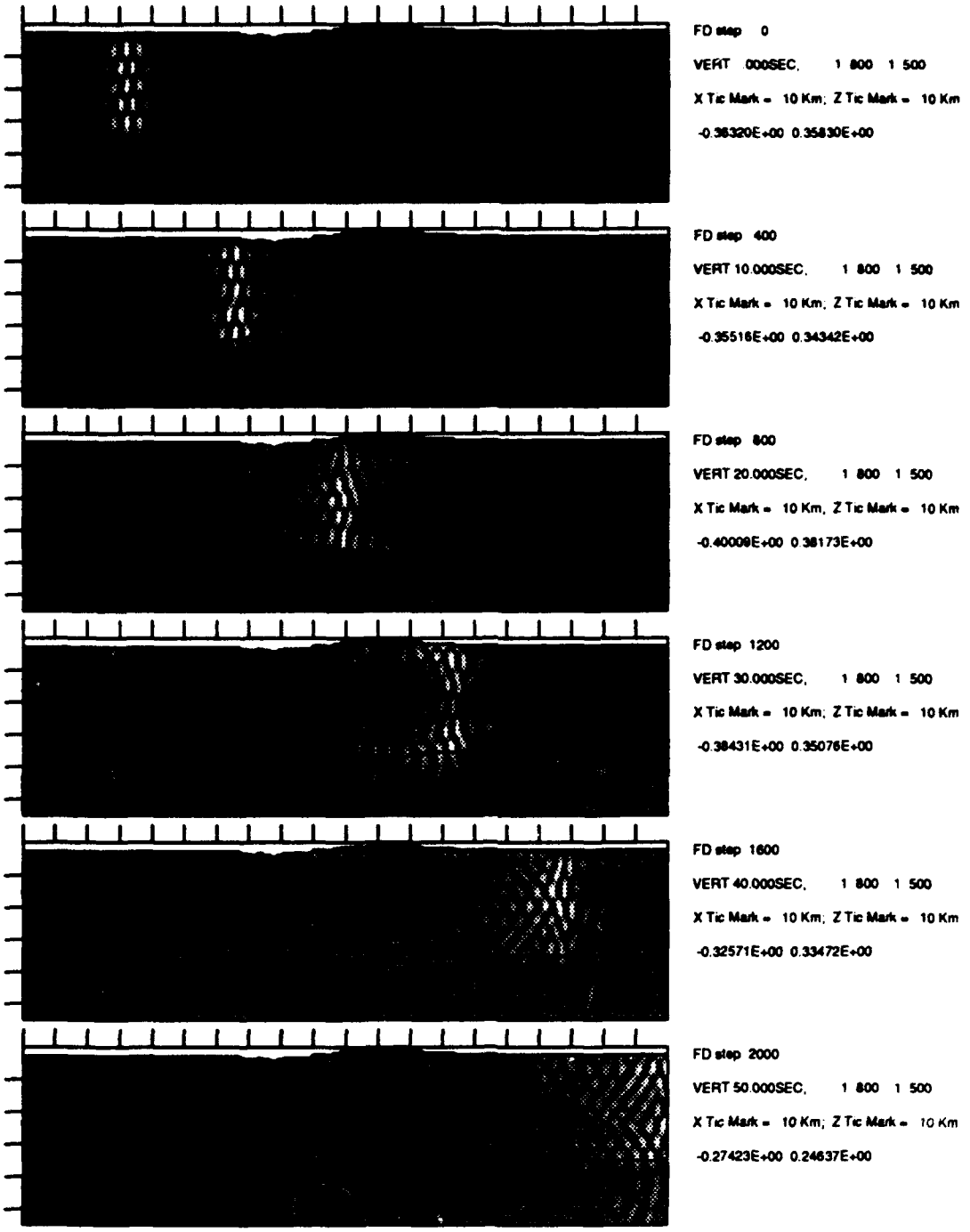
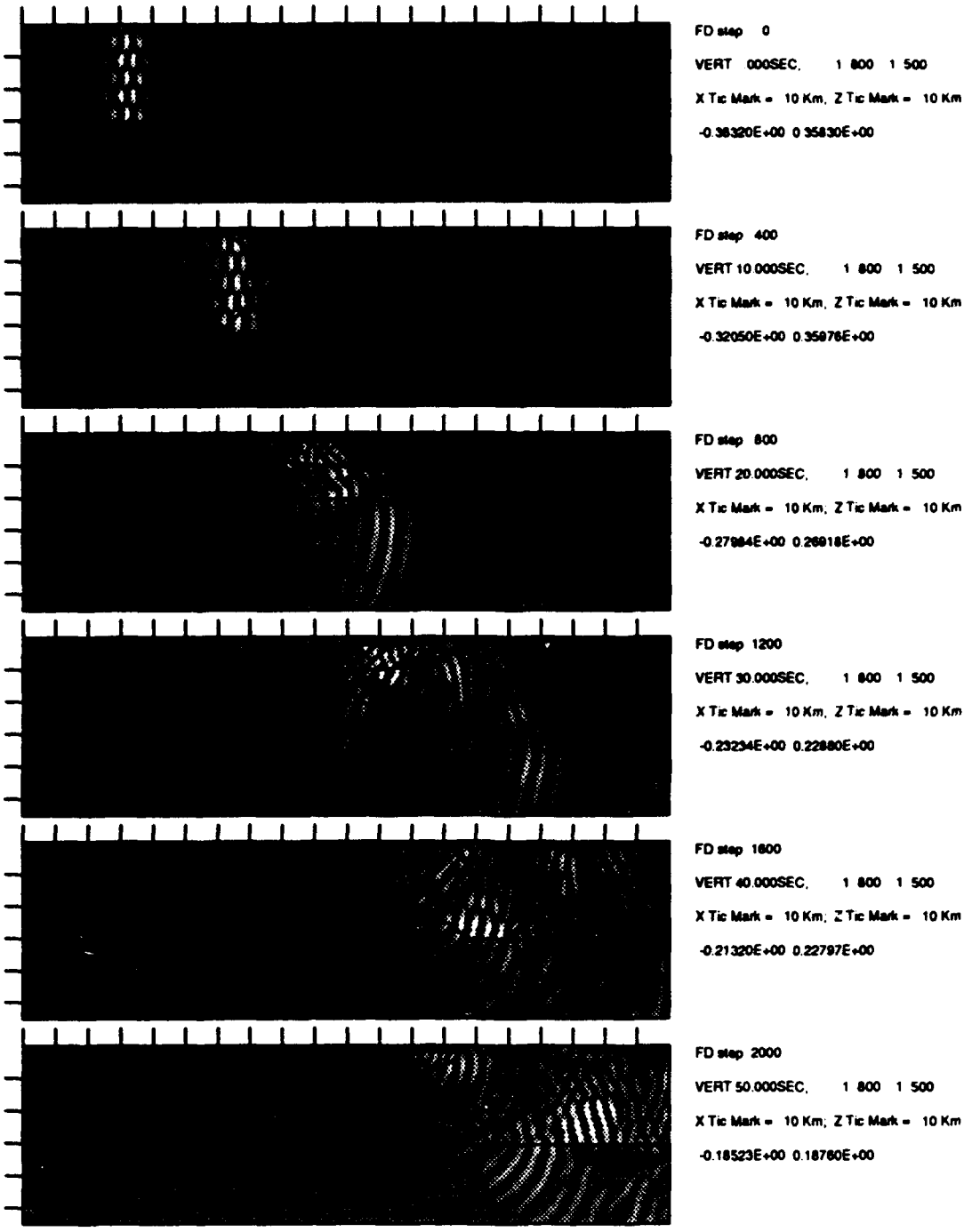


Figure 4. Regressing the attenuation coefficients [γ] (top left), transmitted power [T] (top right), reflected power [R] (bottom left), and scattering loss [1-T-R] (bottom right), respectively, on the normalized arc length, Ω_7, which is one of the seven roughness measures analyzed. A flat free surface would correspond to an Ω_7 of 1. Rougher topographic profiles have larger γ's and smaller T's, as expected. In the roughness range of interest, however, rougher profiles also tend to have weaker reflection, due to the stronger scattering. As a result, the total scattering loss, defined as 1-T-R, correlates with Ω_7 fairly well (ρ = 0.86).



LFD Simulation of Lg Propagation/scattering, Model 2a, Grid 800*500, dX=dZ=250m

Figure 5. The vertical-component snapshots of L_g wave propagation of Model 2a in which the Moho is fully compensated. The elevation change of this topographic profile is relatively small as compared to the thickness of the homogeneous crust, and hence the transmission of L_g is fairly efficient. This is very different from the case of R_g where scattering by rough topography would cause very strong apparent attenuation, as illustrated in Figure 1.



LFD Simulation of Lg Propagation/scattering, Model 0Fc, Grid 800*500, dX=dZ=250m

Figure 6. The vertical-component snapshots of L_g wave propagation in the basin model 0Fc. The Moho uplift causes strong S_n conversion (*cf.*, at 20 second). A weaker S_n conversion also occurs at the pinched end of the basin where part of the energy trapped in the basin starts to leaks out of the basin.

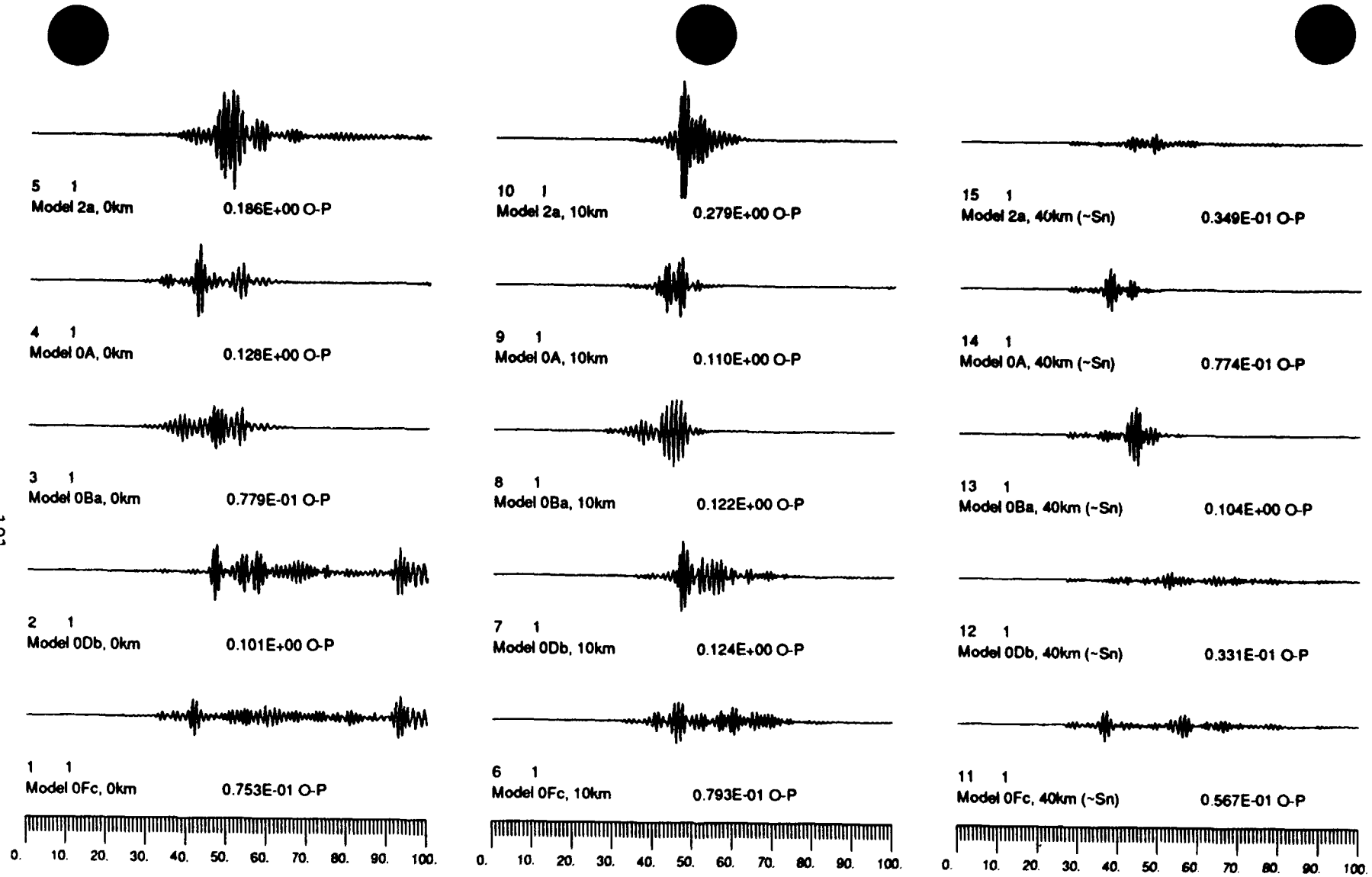


Figure 7. L_g synthetics recorded at 3 depths (0km, 10km, and 40km) after crossing a heterogeneous zone of 155.5 km wide for models 2a (a fully compensated topographic model), 0A (a model with Moho uplift), 0Ba (a model with gradual continent-to-oceanic transition), 0Db (a model with thick contained basin), and 0Fc (a model with both contained basin and Moho uplift), respectively. Both Moho uplift and the thick contained sediment could cause L_g-to-S_n conversion (*e.g.*, models 0A, 0Ba, and 0Fc). The contained sedimentary basins in models 0Db and 0Fc also generate L_g-to-R_g conversion with peak amplitudes of converted R_g waves comparable to those of the transmitted L_g waves. By seismic reciprocity, R_g-to-L_g could be strong in certain structures.

NEAR-SOURCE OBSERVATIONS OF THE NPE

Lane R. Johnson and T. V. McEvilly

Center for Computational Seismology, Lawrence Berkeley Laboratory,
and Seismographic Station, University of California,
Berkeley, California 94720

Contract No. F49620-94-1-0197

OBJECTIVE

The general objective of this research effort is the detection and discrimination of underground explosions through the study of radiated seismic waves. Particular emphasis is on the study of physical processes in the source region through the development of improved models for the generation and propagation of elastic waves. Such models are tested by the collection and analysis of broad-band seismic data at near and regional distances. The most recent phase of the research has included the analysis of near-source seismic data from the Non Proliferation Experiment (NPE) for the purposes of checking seismic scaling relationships and exploring possible differences between nuclear and chemical explosions.

RESEARCH ACCOMPLISHED

The NPE was conducted by the Department of Energy at the Nevada Test Site in September 1993 and provided a unique opportunity to test may of the critical issues related to seismic verification research. The NPE was a chemical explosion with a yield of about 1.1 kilotons which was detonated at a depth of 389 meters in Rainier Mesa. Included in the experiment was the deployment of a large number of seismic recording stations both within Rainier Mesa and on the surface above the explosion, yielding a very complete set of three-component broad-band seismic waveform data in the near-source distance range. The waveform data recorded by three of the participating groups, Southern Methodist University, Los Alamos National Laboratory, and UC Berkeley, have been jointly analyzed to obtain estimates of the explosion parameters and the uncertainties in these estimates.

Prior to the NPE a surface reflection profile was obtained along a north-south line on the surface of Rainier Mesa about 600 meters to the west of the explosion epicenter (Majer et al, 1994). The data from this profile were processed using conventional seismic reflection techniques, including common-depth-point stacking, velocity semblance, and migration. The results were interpreted with the aid of the geological information obtained from drill holes (Baldwin et al., 1994) to yield a one-dimensional model of the P velocity for Rainier Mesa in the vicinity of the NPE. This model was also constrained to agree with the travel times of the direct P wave observed from the NPE. The S velocity and density were derived from the P velocity using ratios consistent with measurements of velocity and density obtained from the drill holes. The net result is the model shown in Figure 1.

The general features of the velocity model include rather low velocities in the weathered layer at the surface, but these increase rapidly in the cap rock of the mesa, the Rainier Mesa Tuff. There is a decrease in velocity part way through this unit (depth of 80 meters) and a further decrease at its bottom. The underlying unit, the Paintbrush Tuff, has very low velocities, but the velocities increase before reaching the depth of the NPE (389 meters) in the Tunnel Beds Unit. Below the explosion depth there is a further increase in the velocity and then the Paleozoic basement is encountered at a depth of about 775 meters.

two inversions show good agreement in their general features. This agreement can be quantified by comparing the parametric models which were fit to the spectral moduli and are shown as dotted lines in the figures. This parametric model had the form

$$|M(f)|^2 = \frac{P_1^2}{1 + 2(2P_4^2 - 1)(f/P_2)^{P_3} + (f/P_2)^{2P_3}} + P_5$$

where

P_1 is the low frequency level, or scalar moment
P_2 is the corner frequency
P_3 is the high frequency decay rate
P_4 is the damping parameter (1 for critical damping)
P_5 is the variance of the signal independent white noise

This model was fit to the estimated spectral moduli of the NPE by a maximum likelihood procedure with the damping constrained to be critical ($P_4 = 1.0$), with the following results:

	SMU	LANL
scalar moment	25.6 10^{13} *Nm*	25.3 10^{13} *Nm*
corner frequency	2.6 *Hz*	2.6 *Hz*
high-frequency decay	2.5	2.7

Based on the analysis of this study, these properties of the NPE source appear to have been estimated with an uncertainty of approximately 5%.

The spectral parameters estimated for the isotropic moment tensor of the NPE were converted to source properties using the scaling relationships of Denny and Johnson (1991). The working point properties which were used in these calculations were as follows:

P velocity	$\alpha = 2.6$ *km/sec*
S velocity	$\beta = 1.2$ *km/sec*
density	$\rho = 1.9$ *gm/cc*
pressure	$P_o = 7.2$ *MPa*
gas porosity	$GP = 1\%$

The calculations yielded the following estimated source properties for the NPE:

scalar moment	$M_o = 25\ 10^{13}$ *Nm*
static RDP	$\Psi_\infty = 1600\ m^3$
yield	$W = 1.7$ *kt*
cavity radius	$R_c = 20$ *m*
elastic radius	$R_s = 150$ *m*

These estimates appear to be reasonable, although the yield of 1.7 kt is significantly greater than the announced yield of 1.1 kt.

CONCLUSIONS AND RECOMMENDATIONS

The NPE was a valuable exercise because it was specifically designed to gather data which could be used to study verification issues. In the case of the present study, this meant that sufficient high-quality waveform data were available to compare independent moment tensor inversions and thus obtain an estimate of the uncertainty in the results. Further comparisons of this type are possible and should be performed, such as the comparison with free-field data and inversions obtained from regional data.

The present study allowed a consideration of one source of uncertainty in the moment tensor inversion method, the effect of incomplete sampling of the data space. However, another aspect

The data used in this study were all obtained with similar instrumentation. The seismometers were accelerometers with nominal natural frequencies of 100 Hz. Each station had three components. The data were digitally recorded at a sampling interval of 0.004 sec. Much of the data recorded within 600 meters of the explosion epicenter showed accelerations greater than 1 g and contained evidence of spall, and such data were not included in the analysis. The data included in the analysis was all recorded at ranges between 600 and 2200 meters, with a fairly complete distribution of azimuths. The number of recording stations available was 14, or 42 seismograms.

The wave-form data were subjected to the standard moment tensor inversion method (Stump and Johnson, 1977). Past experience with this method has indicated that reliable results can be obtained when the inversion is performed with at least 15 seismograms representing a sufficient range in azimuth and distance. The amount of data available in the present study was considerably more than this and provided an opportunity to perform a check on the consistency of the moment tensor estimates. Thus the data were divided into two independent sets, with each set having 7 stations (21 seismograms) and similar distributions in range and azimuth. One of the data sets was recorded by Southern Methodist University (SMU) and the other by Los Alamos National Laboratory (LANL), and these institution names will be used to designate the two data sets.

The moment tensor inversions were performed with complete seismograms consisting of 8.1 sec of data, although most of the large amplitude phases arrive in the first 4 sec. Green functions for the inversion were calculated using the one-dimensional model shown in Figure 1. The basic results of the inversions are shown in Figures 2 and 3. In both cases the moment tensor is dominated by its diagonal elements, as one would expect for a simple explosion. Thus a good approximation to the explosive part of the source is provided by the isotropic moment tensor (average of the three diagonal elements), and the spectrum of this function is shown in the lower panel of the figures.

The availability of two estimates for the moment tensor of the NPE, obtained with independent data sets, provides a partial check on one of the difficulties present in most methods of estimating seismic source parameters, the uncertainty introduced by the incomplete sampling of data space. Such an uncertainty is always present in an inverse problem such as this when the number of recording stations is finite. The simple hypothesis followed in interpreting the results of this study is that those features of the moment tensor which are common to the two inversions are most likely to be reliable features of the actual source, while those features which are different provide a measure of the uncertainty of the moment tensor which can be attributed to the incomplete sampling of data space.

A comparison of the time domain estimates of the moment tensor in Figures 2 and 3 shows good agreement with regard to the basic feature, a simple step function with a finite rise time on the diagonal elements. There is also approximate agreement concerning the small oscillations on the flat part of the step function. However, the amplitudes of the step functions show a variability between components which has a different pattern in the two inversions, suggesting that this feature of the results is not well determined. This is not surprising in view of the fact that three integrations with respect to time have to be performed in going from the observational data to the moment tensor estimates, and low-frequency instability is characteristic of such integrations. With respect to the much smaller off-diagonal elements of the moment tensor, there is some agreement between the two inversions with respect to sign but some disagreement with respect to the shape. This leads to the general assessment that a small signal is present in these off-diagonal elements, but the uncertainty is comparable to the amplitude of the signal.

The comparison of the time domain estimates suggests that the best determined feature of the moment tensor is the isotropic part, and this conclusion is reinforced by the comparison of the spectra shown in Figures 2 and 3. The spectra of the isotropic part of the moment tensors for the

which requires a similar investigation is the effect of the velocity model used in the inversion. A single velocity model, thought to be reasonably accurate because it was based upon reflection data and information from drill holes, was used in both of the inversions, so it is possible that systematic errors in this model could affect the estimates of the moment tensor and in turn bias the estimates of source properties. For instance, inaccurate values for the velocity and density at either the source or receiver location can directly influence the estimate of yield. In addition, the scaling relationships depend upon the working point properties and so any inaccuracies here are translated directly into the estimates of source properties. The NPE appears to be good opportunity to explore matters such as these, as the available information on material properties is much better than in most cases, and it should be possible to place realistic bounds upon the uncertainty that they introduce into the final results.

The moment tensor inversion results of this study coupled with the scaling relationships of Denny and Johnson (1991) result in an estimate of the NPE yield which is significantly greater than the announced yield. It is important to understand the reason for this difference. The scaling relationships are primarily empirical and, although both nuclear and chemical data were used in their construction, there were few data on moment versus yield in the range around 1 kt. The question of interest here is whether separate scaling relationships are required for nuclear and chemical explosions.

References

Baldwin, M. J., R. P. Bradford, S. P. Hopkins, D. R. Townsend, and B. L. Harris-West, Geologic characteristics of the NPE site in the U12n.25 drift of N-tunnel, Nevada Test Site, in Proceedings of the Symposium on the Non-Proliferation Experiment Results and Implications, M. D. Denny et al. (eds), Lawrence Livermore National Laboratory, Livermore, CA, CONF-9404100, 1994.

Denny, M. D., and L. R. Johnson, The explosion seismic source function: models and scaling laws reviewed, in Explosion Source Phenomenology, Geophys. Monograph 65, American Geophysical Union, Washington, D.C., 1991.

Majer, E. L., L. R. Johnson, E. K. Karageorgi, and J. E. Peterson, High-resolution seismic imaging of Rainier Mesa using surface reflection and surface-to-tunnel tomography, in Proceedings of the Symposium on the Non-Proliferation Experiment Results and Implications, M. D. Denny et al. (eds), Lawrence Livermore National Laboratory, Livermore, CA, Conference 9404100, 1994.

Stump, B. W., and L. R. Johnson, The determination of source properties by the linear inversion of seismograms, Bull. Seismol. Soc. Am., 67, 1489-1502, 1977.

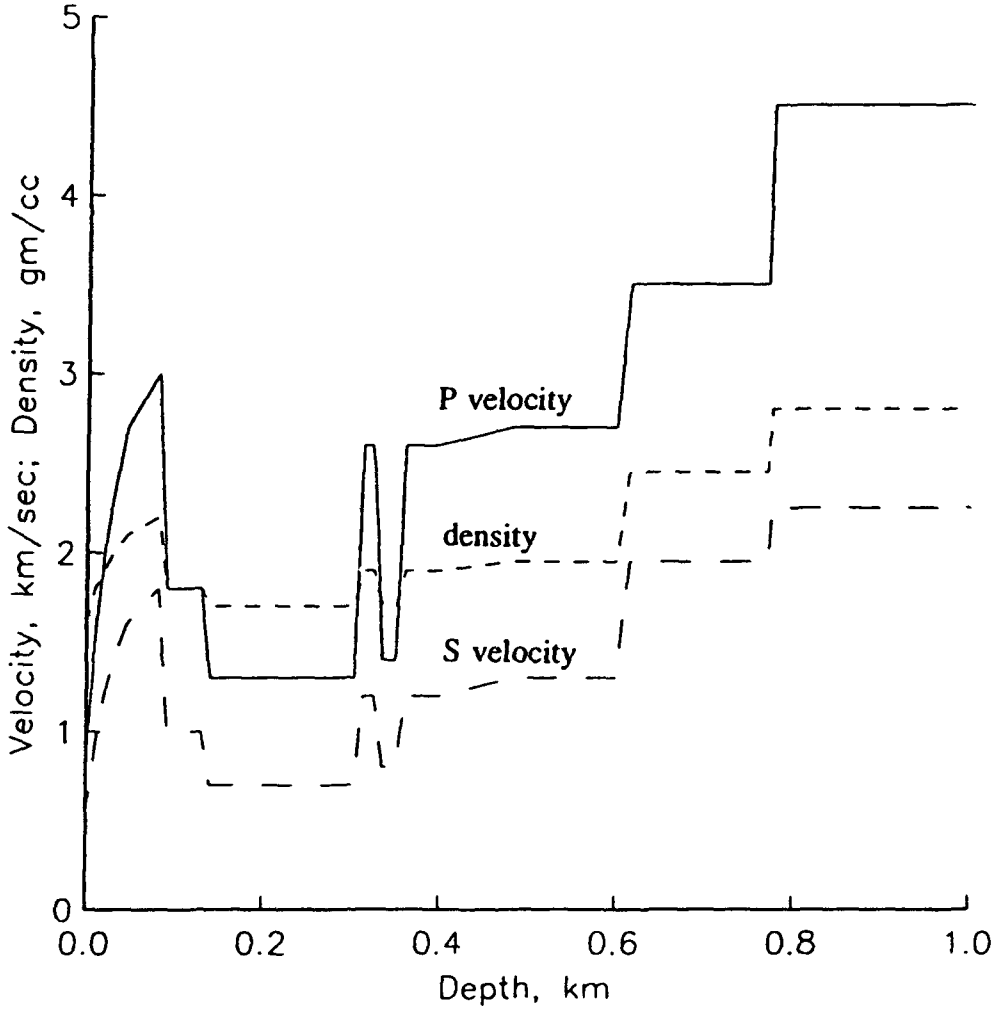


Figure 1. Velocity and density model for the upper part of Rainier Mesa in the vicinity of the NPE.

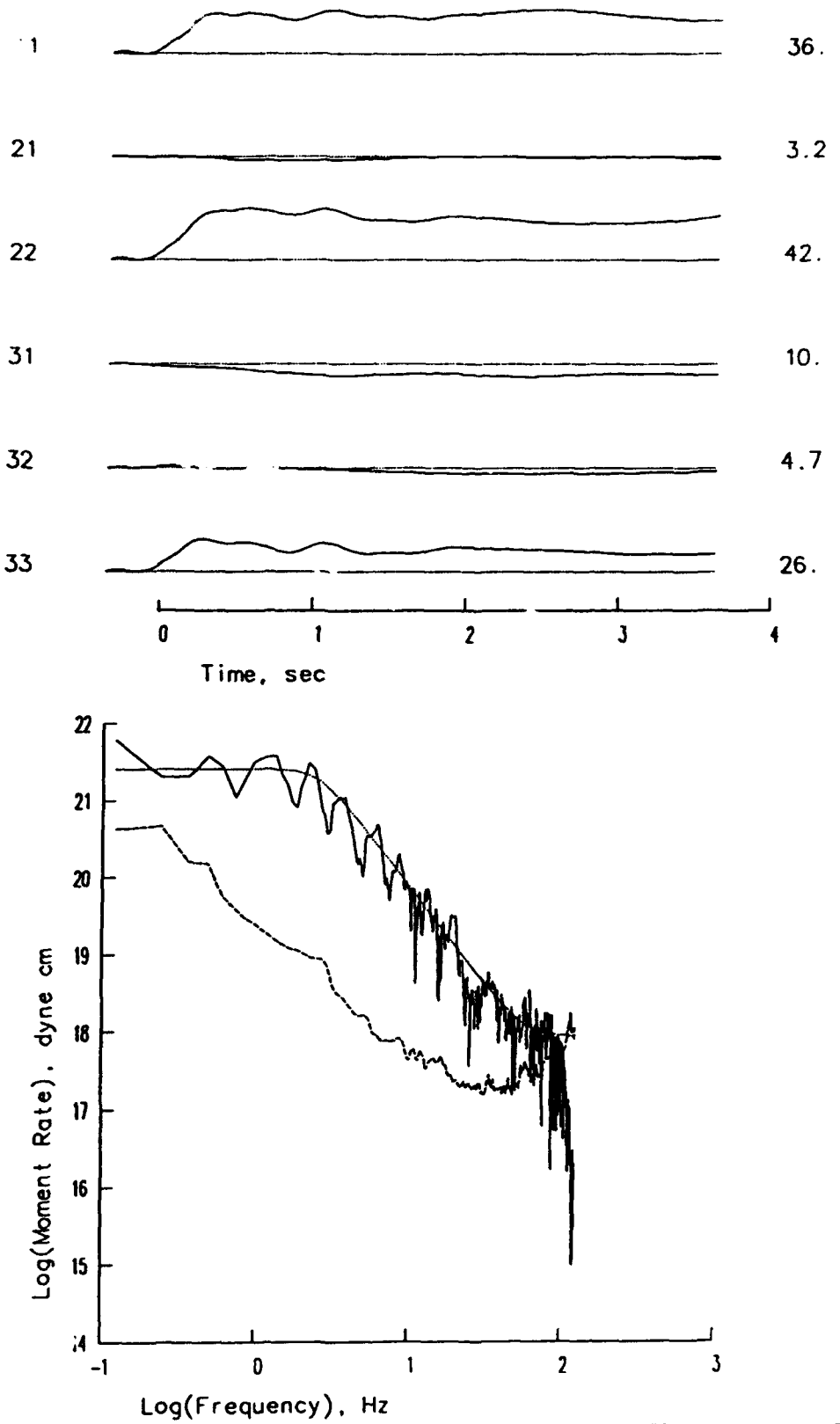
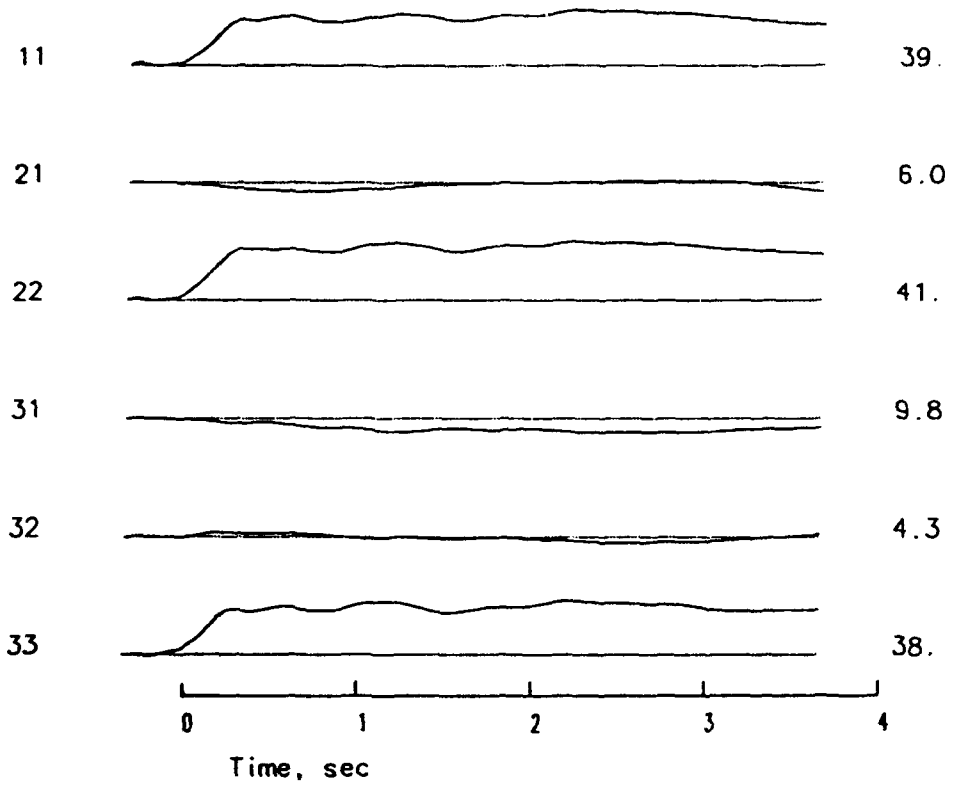


Figure 2. Moment tensor estimates obtained from the inversion of the SMU waveform data. The top panel shows estimates for the six elements of the force moment tensor. The directions are chosen so that 1 is north, 2 is east, and 3 is down. The numbers on the right are maximum values in units of 10^{13} *Nm*. The bottom panel shows the modulus of the Fourier transform of the isotropic moment rate tensor. The dashed line is an estimate of the uncertainty in the estimate and the dotted line is a parametric model which was fit to the modulus.



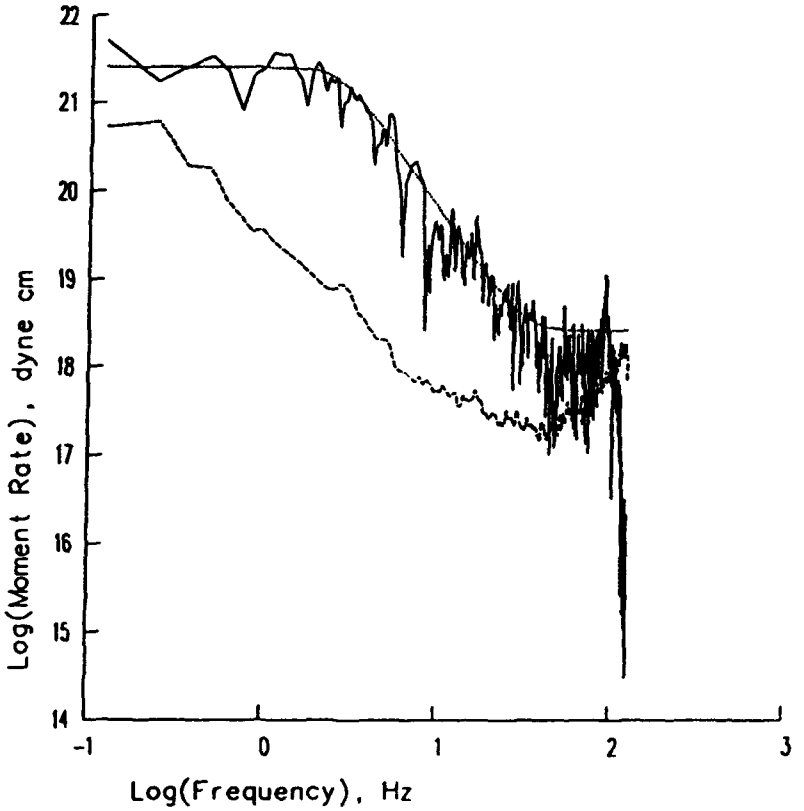


Figure 3. Similar to Figure 2, except that the moment tensor estimates were obtained from the inversion of the LANL waveform data.

Polarization Anisotropy and Small-Scale Structure of the Continental Upper Mantle

THOMAS H. JORDAN AND JAMES B. GAHERTY

Department of Earth, Atmospheric and Planetary Sciences
Massachusetts Institute of Technology, Cambridge, MA 02139

AFOSR Grant F49620-92-J0404

Objectives and Approach

The technologies of nuclear-monitoring seismology are built, in part, on studies of wave propagation at regional distances (< 2000 km). One poorly understood aspect of regional propagation is the forward scattering of high-frequency signals by small inhomogeneities. The objective of our research is to erect quantitative, stochastic models of small-scale heterogeneity that are suitable for assessing scattering effects at regional distances.

Although crustal and upper-mantle heterogeneities are thought to be responsible for the strong multiple scattering recorded on essentially all high-frequency seismograms at regional distances, there have been few attempts to quantitatively decribe the small-scale heterogeneity. The task is especially challenging for the mantle because there is no feasible way to image small-scale structures at these great depths (discounting the rather meager returns from reflection profiling). The geological study of upper-mantle outcrops and xenoliths gives some guidance regarding the range of plausible rock types and the fabrics of rock formations [Nicolas and Christensen, 1987; Kern, 1993], but their dimensions are too limited to extract the parameters needed to describe regional wave propagation, even in the special tectonic regions where they are found.

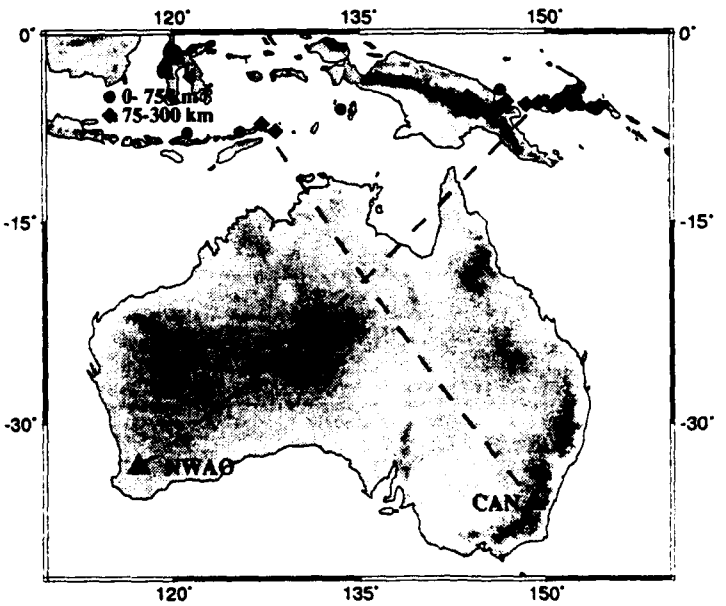


FIGURE 1. Two Australian corridors analyzed in this study. Model AU3 was derived from three-component seismograms recorded at NWAO from 20 shallow and intermediate-depth earthquakes in the New Britain region. Data were were also obtained from the Banda Sea-CAN corridor to test for azimuthal anisotropy, which was not observed (Fig. 2a).

Our approach is to model small-scale heterogeneity by a bootstrap from low to high frequencies. We first use low-frequency (< .05 Hz), phase-coherent waves to derive anisotropic, path-

averaged models of crustal and upper-mantle structure. We have developed methods for extracting phase delays and amplitudes from three-component seismograms that have delivered new information about impedance discontinuities and velocity gradients in the upper mantle; the analysis of an Australian-crossing corridor is presented below. The second step is to interpret the polarization anisotropy in terms of heterogeneity at subwavelength scales. We have formulated stochastic models that specify the small-scale heterogeneity of the continental upper mantle as samples of Gaussian random fields with self-affine (fractal) scaling at high wavenumbers. The models include fields where the local properties are hexagonally anisotropic with a nearly horizontal, but randomly oriented, axis of symmetry. The low-frequency inversions yield good values for the magnitude and depth extent of the heterogeneity, although they place only crude bounds on its characteristic (outer) scale lengths and no constraints whatsoever on its high-wavenumber behavior. The third step, and a major focus of our current theoretical efforts, is to design experiments to estimate the outer scales and fractal dimensions from high-frequency, phase-incoherent data.

Research Accomplishments

Observational Studies. To get better vertical resolution of anisotropic structure, we have developed new observational techniques to extract large, rich data sets in a self-consistent way from three-component seismograms. We have applied these methodologies to several corridors, including one in the western Pacific (Tonga-Kermadec to Oahu), presented by Gaherty, Jordan, and Gee [1994], and two crossing the Australian continent, discussed in this report. Most of the Australian data were collected along paths from earthquakes in New Britain to the station NWAO, although we also analyzed some nearly orthogonal paths from the Banda Sea to CAN (Fig. 1). The path lengths ranged from 35° to 43°.

We employed *ScS* reverberations to identify, locate and measure the impedance contrasts of upper-mantle discontinuities. Revenaugh and Jordan [1991] summarize the technique and describe the results of stacking reverberations for 18 paths, including a reflectivity profile for New Britain-NWAO corridor (their Fig. A12). This profile shows well-developed Hales (H) and Lehmann (L) discontinuities with positive impedance contrasts of 4.9% and 2.1%, respectively, located at average apparent depths (based on PREM) of 56 km and 249 km. The latter appears to deepen towards the center of the Australian craton. No discontinuity with a negative *SV* impedance contrast (i.e., G discontinuity = lid-LVZ boundary) is observed. The New Britain-NWAO stack also identifies transition-zone discontinuities at PREM apparent depths of 411 km (+4.4%), 499 km (+.8%), and 662 km (+4.1%).

We measured over 800 frequency-dependent travel times from *S* and *SS* body waves and *R* and *G* surface waves using the isolation-filter techniques of Gee and Jordan [1992]. The isolation filters were synthesized by phase- and group-velocity windowing during mode summation, and the travel times were represented as phase-delays referenced to a starting model. The phase-delay observations, which spanned the 10-45 mHz band, were interpreted using the Gee and Jordan's theory of generalized seismological data functionals (GSDFs); the Fréchet kernels accounted for all diffraction and (one-dimensional) mode-coupling effects, as well as the effects of interference remaining after the isolation filtering.

The data invariably show appreciable polarization anisotropy; e.g., splitting of *SV*- and *SH*-polarized shear waves by up to 10 s and *R* and *G* surface waves by up to 20 s (Fig. 2). We did

not observe any significant azimuthal anisotropy, however. While the two orthogonal paths in Fig. 1 have slightly different dispersion curves, they display essentially the same splitting (Fig. 2a). We infer that waves propagating over distances of 40° or so average out azimuthal anisotropy, at least in Australia.

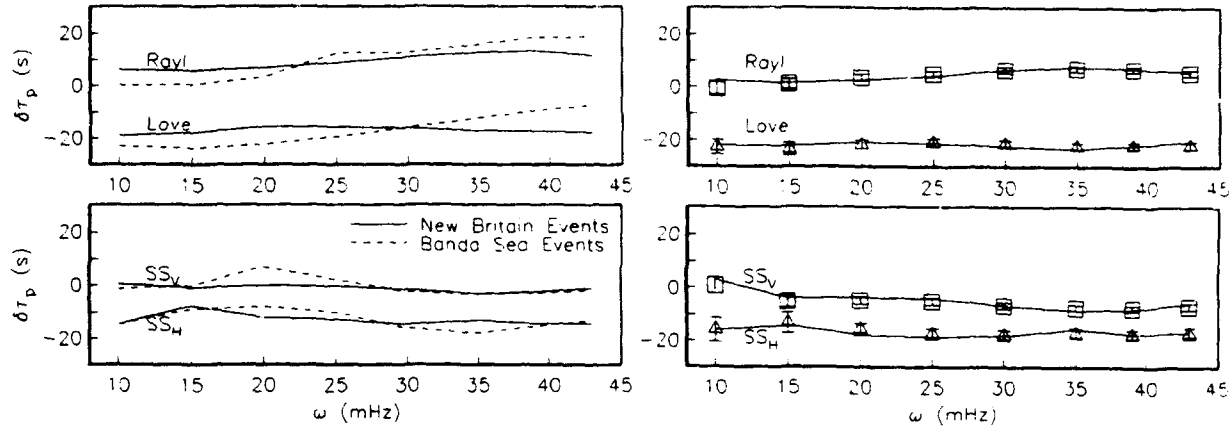


FIGURE 2. Phase delays of surface waves (*top*) and *SS* waves (*bottom*), expressed as residuals in seconds with respect to the isotropic starting model, AU1. *Left panel* shows the comparison between average measured residuals for the two crossing, approximately orthogonal corridors in Fig. 1. Data for the New Britain-NWAO corridor are shown as solid lines; data for the Banda Sea-CAN corridor as dashed lines. Although there are small differences in the dispersion, the amount of shear-wave splitting is essentially identical, indicating that the azimuthal components of anisotropy are small at these epicentral distances. *Right panel* is a comparison of the average data for the New Britain-NWAO corridor (points with 1-σ error bars) with AU3 (solid lines).

The impedance contrasts and the vertical travel times from the *ScS* reverberations were combined with the frequency-dependent phase delays derived from the GSDF method, and the resulting data set was inverted for a radially anisotropic (transversely isotropic), path-averaged structure. Down to the base of the transition zone, we allowed the density ρ and two to five elastic parameters (v_{PV}, v_{PH}, v_{SV}, v_{SH}, and η) to vary linearly in layers separated by discontinuities, whose depths were also allowed to vary. In the lower mantle, the model was fixed to the isotropic structure of PREM [Dziewonski and Anderson, 1981]. An isotropic starting model with this parameterization, AU1, was constructed to fit approximately the *ScS* reverberations and *PSV* phase delays. Two iterations of the linearized inversion were performed; in each, radial anisotropy was allowed to develop in the two mantle layers below the M and above the L discontinuities. The resulting model, AU3, is presented in Fig. 3, and its fit to the average *SS* and surface-wave phase-delays is illustrated in Fig. 2b. Its match to the *ScS* reverberation data is similarly good.

AU3 has an *S*-wave anisotropy ratio, $(v_{SH} - v_{SV}) / v_{SH}$, of about 3% in the layer between the H and L discontinuities, and no anisotropy below this depth. Inversion experiments allowing deeper anisotropy yielded models with small anisotropy below L, usually with a negative *SH/SV* ratio, and no better fits to the data. These results are thus consistent with the hypothesis of Revenaugh and Jordan [1991] that the L discontinuity is the boundary separating an anisotropic mechanical boundary layer (lithosphere) from the nearly isotropic sublithospheric mantle. AU3 has a positive *SV* impedance contrast at the L discontinuity, as required by the *ScS* reverberation data, but a negative *SH* contrast, in general agreement with *SH* models like SNA of Grand and

Helmberger [1984], which show an *SH* low-velocity zone (LVZ) in this part of the upper mantle. The Voigt-Reuss-Hill isotropic average of AU3 does not vary significantly across the L discontinuity, so that there is no need to invoke incipient melting as a mechanism for generating this LVZ. AU3 has higher velocities than the Pacific model of Gaherty et al. [1994] down to 400 km, indicative of a continental tectosphere that extends below the L discontinuity [cf. Lerner-Lam and Jordan, 1987].

We note that Bowman and Kennett's [1993] SOZ model, derived from high-frequency S_n travel times measured at regional distances across central and western Australia, also has an LVZ (though it is about 40 km shallower). This supports Gee and Jordan's [1988] explanation for what they called the "S_n discrepancy": that the first-arriving, high-frequency S_n waves, regardless of their polarization, propagate with average speeds at or above the low-frequency *SH* velocity. This behavior may be indicative of strong scattering of S_n waves in a laminated, anisotropic lithosphere of the sort discussed below.

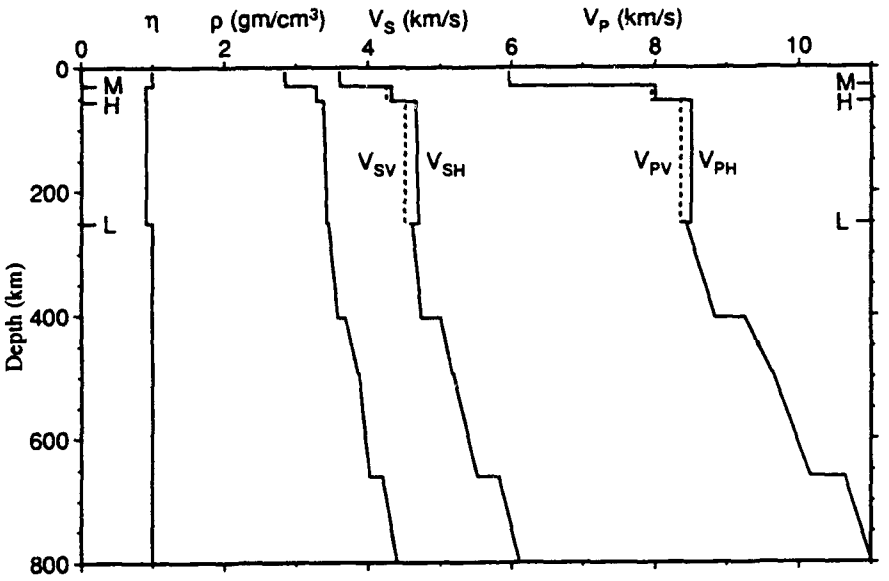


FIGURE 3. Model AU3, representing path-averaged structure of the upper mantle along the New Britain-NWAO corridor. The model is radially anisotropic between the M and L discontinuities and isotropic elsewhere. Where they differ, horizontally and vertically polarized velocities are shown by solid and dashed lines, respectively. AU3 is consistent with Revenaugh and Jordan's [1991] hypothesis that L represents the transition from an anisotropic lithosphere to a more isotropic sublithosphere. Note that L is an impedance increase for *SV* waves, as required by the *ScS* reverberation data, but an impedance decrease for *SH* waves.

Theoretical Studies. Although polarization anisotropy is ubiquitously observed for waves that propagate through the Earth's upper mantle [Anderson and Dziewonski, 1982], surprisingly little work has been done to understand how this phenomenon is related to the local properties of mantle rocks. It is known that olivine and pyroxene—both highly anisotropic minerals—dominate upper-mantle mineralogies, and that these minerals can be aligned by the flow fields of plate tectonics [Estey and Douglas, 1986; Nicolas and Christensen, 1987; Kern, 1993]. But not much can be said about the vertical and horizontal scale lengths over which this alignment is coherent. The deficiency is particularly acute in the continents, which are associated with a

thick, chemically heterogeneous tectosphere [Jordan, 1988] having a complex (and largely unknown) metamorphic history.

We have formulated stochastic models that specify the small-scale heterogeneity of the continental upper mantle as samples of Gaussian random fields with self-affine (fractal) scaling at high wavenumbers. The parameters of two-point correlation functions for these fields include k_z and k_h, the characteristic (outer-scale) wavenumbers in the vertical and horizontal directions, respectively, and a fractal dimension D. The models include rough, isotropic (RI) fields, where the elastic properties are locally isotropic, and rough, anisotropic (RA) fields, where the local properties are hexagonally anisotropic with an axis of symmetry $\hat{\mathbf{n}}(\mathbf{x})$ that is nearly horizontal, but randomly oriented. We distinguish two cases: *equidimensional stochastic heterogeneity*, which has an aspect ratio near unity ($a \equiv k_z / k_h \sim 1$), and a *stochastic laminate*, which has a large aspect ratio ($a >> 1$).

For stochastic laminates, we have derived effective-media representations valid in the limit $\omega / \bar{c} << k_z$ by the averaging procedure of Backus [1962]. This approximation does not require any ordering between the wavenumber of the seismic data functional, $\omega / \bar{c}$, and the characteristic horizontal wavenumber of the heterogeneity, k_h. For equidimensional heterogeneity, we have obtained effective-media representations valid for $k_h \sim k_z << \omega / \bar{c}$ by slowness averaging.

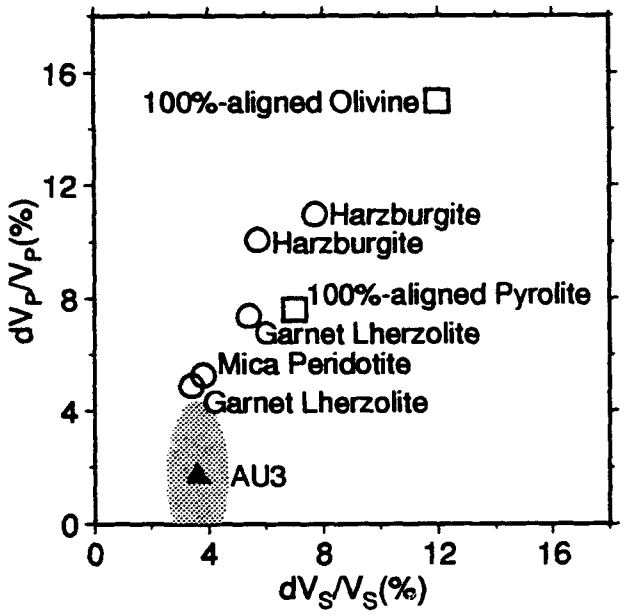


FIGURE 4. Plot of the *P* anisotropy ratio against the *S* anisotropy ratio, comparing AU3 (triangle) and its 50% confidence ellipse (shaded region) against theoretical values for anisotropic stochastic laminates with various assumptions of local anisotropy. The models include both the predictions for ideally aligned, hypothetical compositions (squares) and local anisotropies measured by Christensen [1994] in a suite of peridotitic xenoliths (circles). The magnitude of the shear-wave anisotropy observed in Australia falls at the lower end of the range predicted by the stochastic models, while the compressional-wave anisotropy is significantly smaller. The comparison can be improved by modifying the laminate models to have fast axes dispersed out of the horizontal plane.

The upper-mantle anisotropy observed for trans-Australian paths can be explained by both RI and RA models, but the former requires a laminated structure in order to yield an effective medium that is radially anisotropic. The laminated RI model is unsatisfactory, however, because it implies an RMS variation in the local isotropic properties on the order of 10%, much larger than the 3% or less predicted by realistic mantle petrologies [Gee and Jordan, 1988]. Acceptable transversely isotropic averages can be obtained from RA models with plausible local anisotropy in both the equidimensional and laminate approximations, however. Fig. 4 compares the

anisotropy ratios for AU3 against a series of models for stochastic laminates with different local anisotropies. The models include both theoretical compositions (pure olivine and pyrolite with ideal alignment; data summarized by Estey and Douglas [1986]) and local anisotropies from a suite of peridotitic xenoliths measured by Christensen [1994]. The AU3 shear-wave anisotropy lies at the lower end of the range predicted by these particular stochastic laminates, while the compressional-wave anisotropy is significantly smaller. Similar results are obtained for equidimensional stochastic models.

The *P*-wave anisotropy is not well constrained by the observations, however, and it may be underestimated in AU3. Moreover, the models were constructed assuming the fast axis is locally horizontal everywhere, thus maximizing the predicted anisotropy. By allowing for stochastic variations in the dip of this axis, we can decrease the amount of low-frequency anisotropy by an arbitrary factor, thus reducing the amount of anisotropy predicted by the laminate models in Fig. 4. Therefore, the anisotropy in AU3 can be plausibly explained by simple RA models. Such models do not require that the horizontal correlation length k_h^{-1} be large and are thus consistent with anisotropy resulting from structures frozen in during ancient episodes of tectonic deformation [Silver and Chan, 1991; Helffrich et al., 1994].

Conclusions and Recommendations

We conclude that the L discontinuity is an expression of the rapid extinction of lithospheric anisotropy with depth. This feature, which is constrained by the reverberation data to have a thickness less than about 30 km, is presumably controlled by thermally activated processes, one possibility being the transition from dislocation creep to diffusion creep conjectured by Karato [1992]. Our model explains why a low-velocity zone is observed in stable continents at depths of 200-250 km for *SH* waves, but not for *SV* waves [Revenaugh and Jordan, 1991]. The description of the region above the L discontinuity as an anisotropic, heterogeneous mechanical boundary layer is consistent with the petrology of kimberlite xenoliths. In particular, the L discontinuity appears to mark the maximum depth from which kimberlite magmas can propagate upwards via magma-fracture [Spence and Turcotte, 1990], and it thus sets the maximum equilibration depth observed in the kimberlite nodules [Boyd and Gurney, 1986].

High priority should be given to testing the models described here against additional data sets in order to place tighter bounds on the stochastic parameters. At this stage, it is particularly important to resolve the ambiguity in the aspect ratio $a = k_z / k_h$, which is a critical parameter in the description of high-frequency scattering at regional distances. The concept of an anisotropic stochastic laminate ($a >> 1$) has several attractive features; e.g., the forward multiple scattering of high-frequency waves by such structures can potentially explain the S_n discrepancy [Gee and Jordan, 1988] and the *P*-wave "shingling" commonly observed on long-range refraction profiles [Fuchs and Shulz, 1976; Cipar et al., 1993]. But models with high aspect ratios cannot easily satisfy the large splitting observed for vertically propagating *SKS* waves [Silver and Chan, 1991; Helffrich et al., 1994]. It may be that a varies strongly both laterally and vertically in the subcontinental mantle.

Additional theoretical efforts are needed to design methods to estimate the outer scales and fractal dimensions from broadband recordings of seismic signals at regional distances. We are exploring the use of frequency-dependent signal (first-motion) velocities for this purpose. If

successful, we will incorporate the high-frequency constraints into models derived from the low-frequency analysis.

Acknowledgements

We thank Nick Christensen for the use of his unpublished nodule data, and Lind Gee for her help in developing the data-processing and inversion codes.

References

Anderson, D. L., and A. M. Dziewonski, Upper mantle anisotropy: evidence from free oscillations, Geophys. J. R. Astr. Soc., 69, 383-404, 1982.

Backus, G. E., Long-wave elastic anisotropy produced by horizontal layering, *J. Geophys. Res.*, *67*, 4427-4440, 1962.

Bowman, J.R. and B.L.N. Kennett, The velocity structure of the Australian shield from seismic travel times, *Bull. Seism. Soc. Am.*, *83*, 25-37, 1993.

Boyd, F. R., and J. J. Gurney, Diamonds and the South African lithosphere, *Science*, *232*, 472-477, 1986.

Cipar, J , K. Priestley, A. V. Egorkin, and N. I. Pavlenkova, The Yamal Peninsula-Lake Baikal deep seismic sounding profile, *Geophys. Res. Lett.*, *20*, 1631-1634, 1993.

Christensen, N. I., Seismic properties of mantle xenoliths: clues to the interpretation of deep seismic observations beneath the kimberlite province of Yakutsia, preprint, January, 1994.

Dziewonski, A. M., and D. L. Anderson, Preliminary reference earth model (PREM), *Phys. Earth Planet. Inter.*, *25*, 297-356, 1981.

Estey, L. H., and B. J. Douglas, Upper-mantle anisotropy: a preliminary model, *J. Geophys. Res.*, *91*, 11393-11406, 1986.

Fuchs, K., and K. Schulz, Tunneling of low-frequency waves through the subcrustal lithosphere, *J. Geophys.*, *42*, 175-190, 1976.

Gaherty, J. B., T. H. Jordan, and L. S. Gee, Depth extent of polarization anisotropy in the western Pacific upper mantle, *J. Geophys. Res.*, to be submitted, August, 1994.

Gee, L. S., and T. H. Jordan, Polarization anisotropy and fine-scale structure of the Eurasian upper mantle, *Geophys. Res. Lett.*, *15*, 824-827, 1988.

Gee, L. S., and T. H. Jordan, Generalized seismological data functionals, *Geophys. J. Int.*, *111*, 363-390, 1992.

Grand, S. P., and D. V. Helmberger, Upper mantle shear structure of North America, *Geophys. J. R. Astr. Soc.*, *76*, 399-438, 1984.

Helffrich, G., P. Silver, and H. Given, Rapid shear wave splitting variation in continental compressional tectonic regions, *Geophys. J. Int.*, in press, 1994.

Karato, S., On the Lehmann discontinuity, *Geophys. Res. Lett.*, *19*, 2255-2258, 1992.

Jordan, T. H., Structure and formation of the continental tectosphere, *J. Petrology Special Lithosphere Issue* , 11-37, 1988.

Kern, H., P- and S-wave anisotropy and shear-wave splitting at pressure and temperature in possible mantle rocks and their relationship to the rock fabric, *Phys. Earth Planet. Inter.*, *87*, 245-256, 1993.

Lerner-Lam, A. L., and T. H. Jordan, How thick are the continents?, *J. Geophys. Res.*, *92*, 14007-14026, 1987.

Nicolas, A., and N. I. Christensen, Formation of anisotropy in upper mantle peridoütes–a review, in *Composition, Structure and Dynamics of the Lithosphere-Asthenosphere Boundary*, K. Fuchs and C. Froidevaux (eds.), A.G.U. Geodyn. Ser. 16, A.G.U., Washington, D.C., pp. 111-123.

Revenaugh, J.R. and T.H. Jordan, Mantle layering from *ScS* reverberations, 3, The upper mantle, *J. Geophys. Res.*, *96*, 19,781-19,810, 1991.

Silver, P.G. and W.W. Chan, Shear-wave splitting and subcontinental mantle deformation, *J. Geophys. Res.*, *96*, 16,429-16,454, 1991.

Spence, D. A., and D. L. Turcotte, Buoyancy-driven magma fracture: a mechanism for ascent through the lithosphere and the emplacement of diamonds, *J. Geophys. Res.*, *95*, 5133-5139, 1990.

The Character of Lg-Waves from a Mode and Ray Point of View

H. Keers, K. Vogfjörd, G. Nolet, R. Phinney

Department of Geological and Geophysical Sciences
Princeton University
Princeton, NJ 08544

Contract number: F49620-94-1-0077

OBJECTIVE

The objective of our research is to find ways to compute synthetics of Lg-waves in complicated heterogeneous media. Lg-waves are the most prominent phases on regional seismograms. As such they are important in studying seismic sources and the structure of the crust and upper mantle.

In our study we look at Lg-waves from both a mode and a ray point of view (Kennett, 1986). The validation of the ray methods, by comparing them to the mode sum is the primary reason for this study. Both methods have been among the most successful in computing synthetics in heterogeneous media. However the ray method tends to be less difficult from a computational point of view.

To gain physical understanding we start by considering the propagation of Lg-waves in a simple layer over a halfspace. A comparison of the seismograms, computed using the two different methods is presented and an interpretation of the Lg-waves in terms of modes and rays is given. Subsequently we discuss the effects of an undulating Moho on the wave propagation; in doing so we emphasize ray theory, because of its computational advantages over mode theory. First we discuss one-point ray tracing and point out the limitations of two-point ray tracing. Because of the limitations of classical ray theory we also study the application of graph theory to this kind of models.

RESEARCH ACCOMPLISHED

Lg-waves in simple layered media

In order to understand the ray-mode duality of Lg-waves in layered media we take a simple layer over a halfspace model, see table 1. The source that we use is a strike-slip point source, at 8 km depth. All seismograms are calculated for points on a line through the source, perpendicular to the strike direction. For this preliminary investigation we only study SH waves. The calculated synthetics are all convolved with the WWSSN short period instrument response, which acts as a passband with corner frequencies of 1Hz and 3Hz.

Modes - Using the locked mode approximation of normal mode theory, synthetics have been calculated. The epicentral distance was 500 km. Figure 1 shows seismograms in which the first ten, twenty, forty and hundred modes are used. After comparing the seismograms we

conclude that ten modes are clearly not enough to model the whole Lg wavetrain. If twenty modes are used then the first half of the seismogram is reasonably well modelled, when compared with the seismogram in which hundred modes have been used. If forty modes are used then the result is quite satisfactory; except for the fact that the last part of the seismogram is not well modelled. It appears that we need around sixty additional modes in order to get one more arrival.

The latest arriving energy of each mode corresponds with the Airy phase. Even though the Airy phases are associated with a concentration of energy, they are not visible on the seismograms as separate arrivals, as suggested for example by Kovach and Anderson (1964). Rather, the formation of the different multiples is a consequence of a more complex superposition of the various modes.

Rays - In a simple layer over halfspace model it is easy to calculate all the ray paths from the source to the receiver, as well as the traveltimes and amplitudes of each ray. The amplitudes depend on the radiation pattern of the source, the pathlength of the ray and the reflection coefficient of the Moho. Using these quantities ray synthetics can readily be computed. An example of such synthetics are shown in figures 2 and 3. The only rays that contribute significantly to the seismogram are the super-critically reflected rays. In this case (epicentral distance of 500 km) there are twenty-one super-critical reflected rays. The twenty-second multiple has an amplitude that is a factor of 0.7×10^{-4} smaller than the twenty-first multiple, due to leakage of energy into the mantle. All super-critical reflected rays are clearly visible as separate arrivals, providing a simple interpretation of the seismogram in terms of rays. Because the reflection coefficient is complex the multiples have different phases. It should be noted that head-wave energy is not modelled with this method.

Mode-Ray duality - In figure 2 the mode and ray seismograms for different epicentral distances are presented. The overall agreement between the two methods is very good. In figure 3 blow-ups of the seismograms for an epicentral distance of five hundred kilometers are given. It appears that there are two major differences: the first difference is the presence of energy in the mode synthetic between the multiples. This is for instance visible in figure 3c, between 166s and 168s, and between 169s and 171s. This energy is not present in the ray synthetics. The second difference is the last multiple. This multiple is not present in the mode summation. Currently we believe that the energy in between the multiples is associated with (multiple) head-waves. Head-wave and multiple head-wave arrivals are not accounted for. The second discrepancy can be explained either by the incompleteness of the mode sum, such that more than 100 modes need to be taken into account, or by the failure of ray theory for rays reflected near critical angles.

It should be noted that in more complicated layered media not all ray arrivals are visible as separate arrivals, thus making the interpretation of the seismogram in terms of rays more complicated.

Lg-waves in simple heterogeneous media

As a next step we study the behavior of Lg-waves in a layer over a halfspace model with

an undulating Moho. From a modal point of view, in the high frequency approximation the waveforms should be identical to the model with a flat Moho and a crustal thickness equal to the average crustal thickness between source and receiver. If the high frequency approximation is not made, then the modes couple and the computation of synthetics becomes more difficult (Maupin, 1990).

Rays - From a ray point of view the first thing to do is one-point ray tracing. The situation is sketched in figure 4. The Moho is described by a given function f. The thickness of the crust at the horizontal coordinate x is given by $h + f(x)$. If, after n reflections the horizontal coordinate of the ray is x_n then after $n+1$ reflections the horizontal coordinate of the ray is given by

$$x_{n+1} = \psi_n + [h + f(\psi_n)] / \tan \theta_{n+1} \tag{1}$$

where ψ_{n+1} and θ_{n+1} are given by

$$\psi_n = x_n + [h + f(\psi_n)] / \tan \theta_n \tag{2}$$

and

$$\theta_{n+1} = \theta_n - 2 \arctan f'(\psi_n). \tag{3}$$

Note that these formulas hold if $x_n < \psi_n < x_{n+1}$. Similar formulas can be derived if x_n, ψ_n and x_{n+1} are permuted. It can be shown that $(x_n, \cos \theta_n)$ are canonically conjugate coordinates, i.e. the one-point ray tracing system can be written in terms of a Hamiltonian system.

For simplicity we took a simple sinusoid for f, with a wavelength of 100 km and an amplitude of 0.1 km. The average thickness is 20 km, the same as used in the layer over halfspace model. Figure 5 shows the results of the one-point ray tracing for *SmS* through 7×*SmS*. For *SmS* the first multipathing occurs for epicentral distances of 400 km.

For epicentral distances of 800 km and larger it becomes hard to do two-point ray tracing for *SmS*. If the undulation of the Moho becomes larger, then it turns out that it is hard to do any two-point ray tracing, and in fact the ray behavior is chaotic.

Graph-theoretical Rays - Because of these difficulties with two-point ray tracing in media with curved interfaces, it is worthwhile to investigate the possibility to use other methods, such as graph theory. Graph theory enables fast calculation of raypaths and travel times in complicated media, avoiding the problems mentioned above, and makes first order scattering computation possible. The method entails approximating ray paths with shortest-time paths between nodes in a grid and using Dijkstra's algorithm (Dijkstra, 1959) to search over all permissible raypaths between a source and a receiver. The search is made more efficient, by applying a sorting algorithm (Moser, 1991), making computation-time proportional to $n \log n$, where n is the number of nodes in the model.

The method finds only the shortest-time path; ray paths representing later arrivals can however be found by formulating them as constrained shortest paths. Scattered ray-paths

can be found by requiring the rays to visit a set of nodes. Moho reflections can also be obtained by stacking duplicates of the crust, the number of duplicates depending on the number of Moho reflections desired. For example, to obtain ray paths and travel times for *SmS* one duplicate of the crust is required, whereas for *2×SmS* a quadruplicated stack is needed. For one reflection the model consists of three interfaces: surface, Moho and surface. The source is located at a node on the surface, on one side of the model and the shortest-time ray paths are found to the nodes on the other surface, requiring the paths to go through the nodes on the intermediate interface, representing the Moho. We have made such an adaptation of the method, to obtain first arrivals for multiple Moho reflections of SH waves. Our initial model is the same as before. The nodes are 1 km apart on each copy of the Earth's surface and the Moho. To limit the ray paths to Moho reflections, nodes on one interface are only connected to nodes on the next one.

Ray paths of *SmS* first-arrivals in this model are shown in Figure 6. As distance increases beyond 140 km, the bounce-points of the first-arriving rays center around the peaks on the Moho, with fewer and fewer rays leaving the source ending up as first arrivals. Thus only a fraction of the energy leaving the source is present in these first arrivals. As the number of Moho multiples increases, even less of the source's energy is present in the first arrivals. Except for the reflection from each Moho peak, the first arrivals in this model are not geometric rays, as the reflection angles from the Moho deviate up to 0.07 deg from Snell's law, but rather represent diffracted waves from the peaks on the undulating Moho. Travel-time deviations from those of a flat Moho, are extremely small, due to the small amplitude of the Moho perturbation. Therefore, although the triplications produced by the sinusoidal Moho are not obtained with this method, the travel-time curve is nearly identical to the one obtained with the normal ray tracing method.

CONCLUSIONS AND RECOMMENDATIONS

We have come to a good understanding of Lg-waves from both a mode and a ray point of view in a simple layer over halfspace model, with a flat discontinuity. From a mode point of view the seismogram consists of the superposition of all modes. An interpretation in terms of Airy phases does not appear to be useful. From a ray point of view the seismogram consists of all crustal multiples that are critically reflected. The agreement between the seismograms obtained using these two methods is striking. The main difference is that head-waves are not modelled by the ray method in plane layered media.

If the Moho is undulating then the two-point ray tracing becomes much more complicated. It is nevertheless possible to do two-point ray tracing as long as neither the amplitude of the undulation nor the epicentral distance are too large. The graph theoretical traveltime results are nearly identical to those obtained with normal ray theory, thus providing a promising application of graph theory.

Further research should focus on the calculation of seismograms in media with one or possibly more curved interfaces. The possibilities and limitations of classical ray theory should be investigated, as well as the supplementary role that graph theory can play. It is also

necessary to compute seismograms in more complicated layered media, using both methods. As a next step P-SV waves need to be considered.

REFERENCES

Dijkstra, E. W., 1959. A note on two problems in connection with graphs. *Numer. Math.*, **1**, 269-271.

Kennett, B. L. N., 1986. Lg waves and structural boundaries. *Bull. seism. Soc. Am.*, **76**, 1133-1141

Kovach, R. L. and Anderson, D. L., 1964. Higher mode surface waves and their bearing on the structure of the Earth's mantle, *Bull. seism. Soc. Am.*, **54**, 161-182.

Maupin, V., 1992. Modelling of laterally trapped surface waves with application to Rayleigh waves in the Hawaiian swell, *Geoph. J. Int.*, **110**, 553-570.

Moser, T. J., 1991. Shortest path calculation of seismic rays, *Geophysics*, **56**, 59-67.

Table 1	layer #	thickness (km)	S-velocity (km/s)	density (g/cm3)
	1	20	3.5	2.7
	2	2000	4.6	3.3
	3	inf	1000	1000

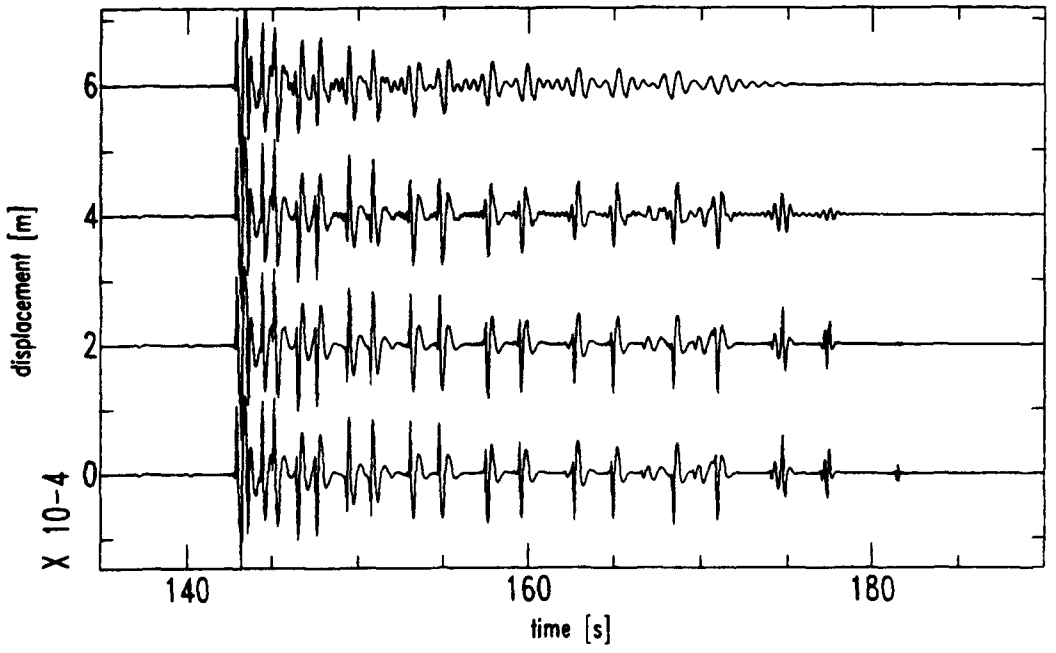


Figure 1. Mode-seismograms using (from top to bottom) 10, 20, 40 and 100 modes. The epicentral distance is 500 km.

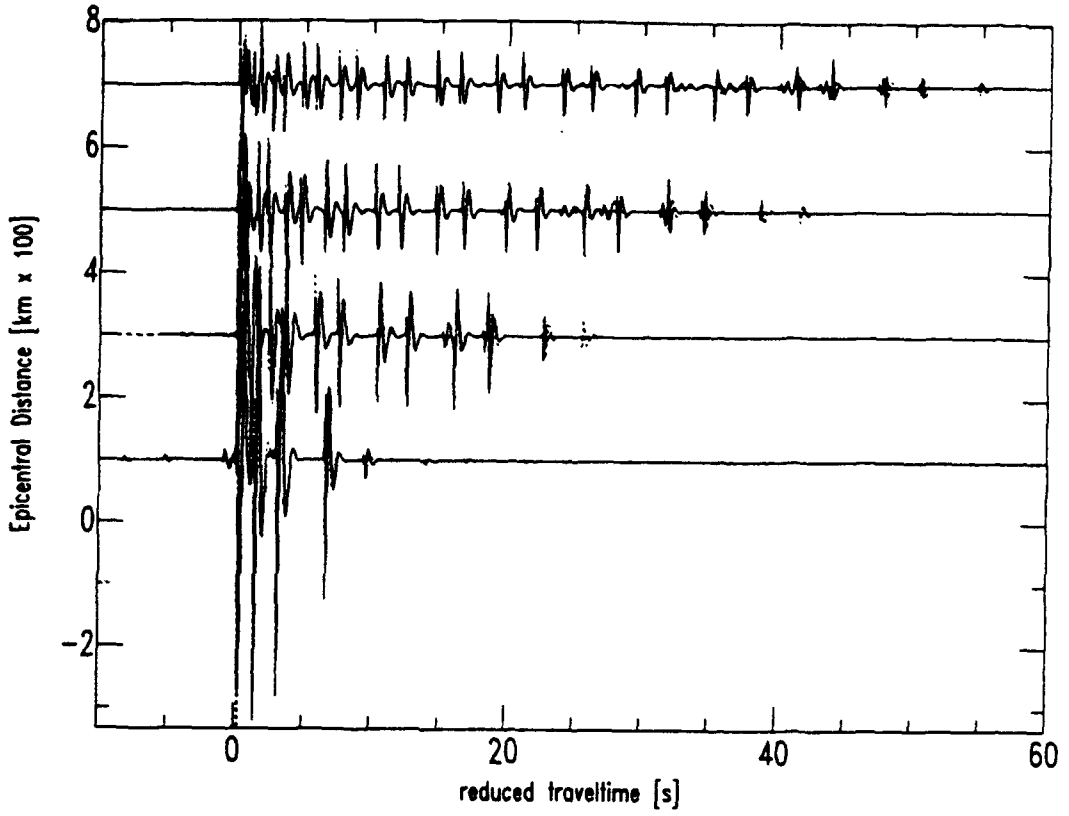


Figure 2. Comparison between seismograms computed using mode theory (solid) and ray theory (dashed). Epicentral distances are 100 km (bottom), 300 km, 500 km and 700 km (top). The reduced velocity is the S-wave velocity of the crust (3.5 km/s).

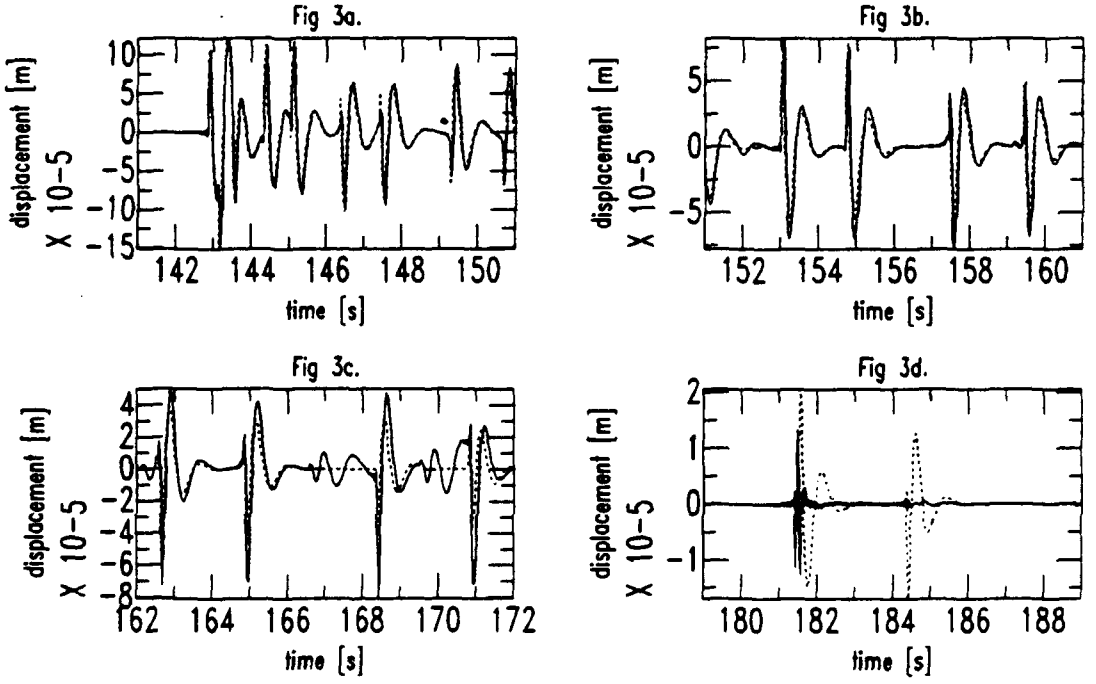


Figure 3. Comparison between seismograms computed using mode theory (solid lines) and ray theory (dashed lines). The epicentral distance is 500 km.

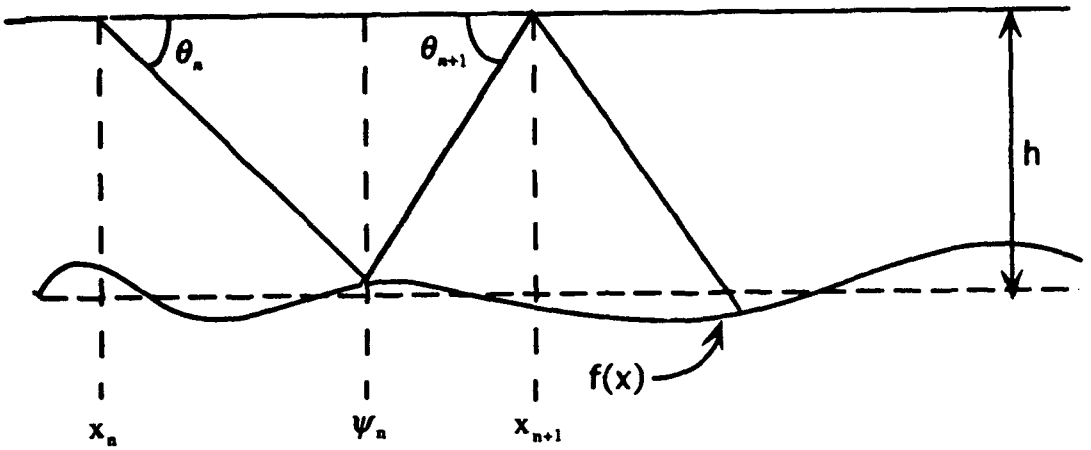


Figure 4. Geometry of layer over halfspace model with undulating discontinuity.

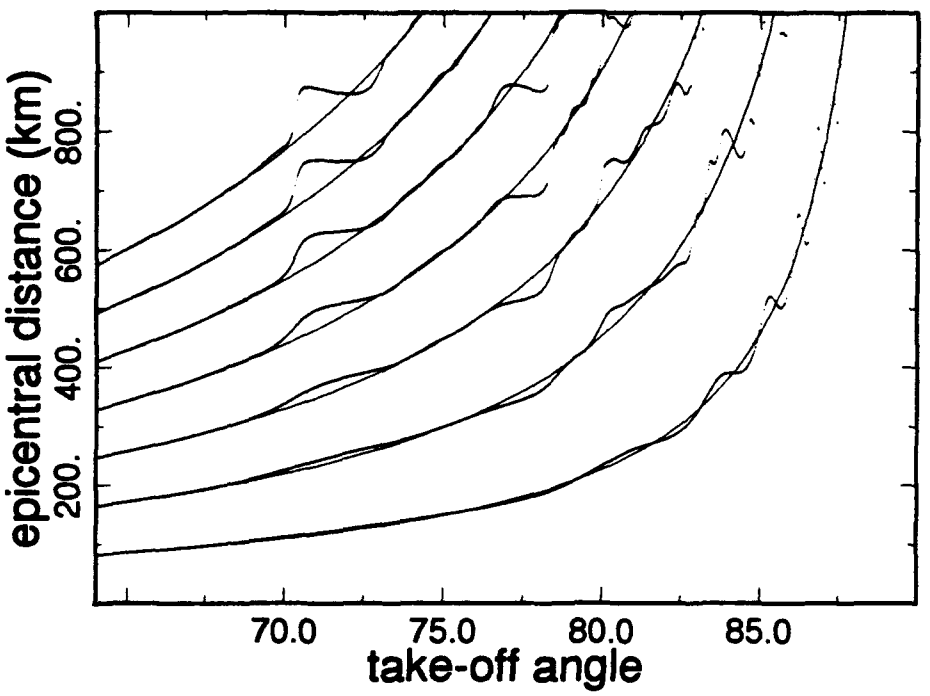


Figure 5. Epicentral distance as a function of take-off angle for *SmS* (bottom curve) through 7×*SmS* (top curve). Also plotted are the background values for a crust with a thickness of 20 km.

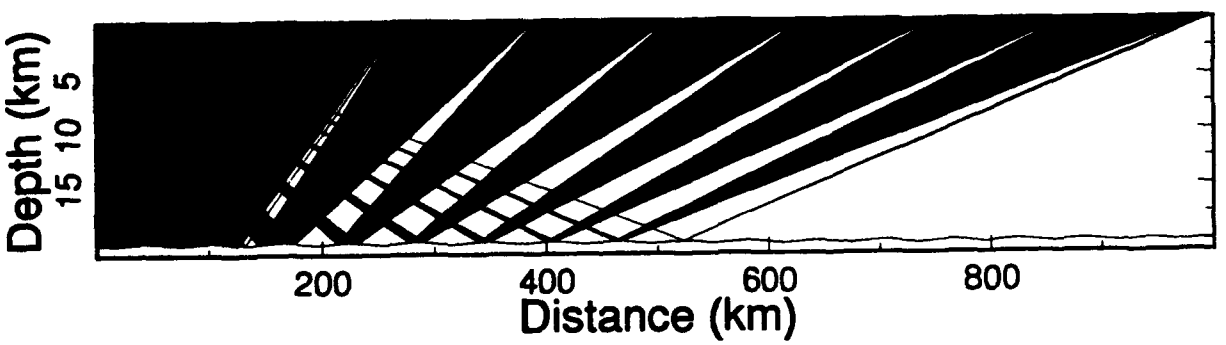


Figure 6. Ray paths for *SmS* from a surface source in a 20-km-thick crust, with sinusoidally undulating Moho of amplitude 0.1 km and period 60 km. Vertical exaggeration ×10.

The Exploitation of Regional and Teleseismic Waveforms

B.L.N. Kennett
Research School of Earth Sciences, Australian National University,
Canberra ACT 0200, *Australia*

Grants: F49620-94-1-0110, F49620-94-1-0022

OBJECTIVES

The principal objectives of the many strands of research which have been carried out under these grants are the exploitation of the information content of seismograms at regional and teleseismic distances in order to improve both the characterisation of events and also information about seismic structure on regional scales.

The aim of the work on seismic structure in three dimensions is to exploit the waveforms of surface waves which are frequently the largest features in the seismogram to delineate the main characteristics of shear wave structure in the lithosphere. The analysis is carried out using relatively low frequency waves but the available resolution is generally limited by station distribution. Such structural information should be valuable for predicting the characteristics of wave propagation at regional to far-regional distances. The major area of study is the Asian continent using GSN, GEOSCOPE, CDSN and other broad-band stations. Theoretical studies are being undertaken to try to extend the approach to higher frequencies where more complex wave propagation features have to be included, and are complemented by field studies in Australia using a regularly spaced network of portable broad-band instruments. Such field studies are also useful in establishing how it would be possible to undertake structural studies for regions where lithospheric structure is unknown.

The major aim of our work with teleseismic events is to improve the characterisation of seismic sources by attempting a unified determination of source mechanism and location. If the location of an event is well known, the estimation of the components of the seismic moment tensor can be readily accomplished. However, if the location is poor, the correlation of phases may lead to misidentification of later arrivals with a consequent error in the source mechanism. S wave information can be exploited using broad-band records but the optimum procedures for comparison of observed and theoretical seismograms are not clear when the data has a wide range of frequencies.

The presence of three dimensional heterogeneity within the Earth on a wide range of scales has been demonstrated in many studies, yet nearly all location procedures on a global scale use one-dimensional models. In the context of nuclear monitoring it is very important to be able to make an effective combination of information at local and regional distances with teleseismic results. The same approach is also necessary for constructing synthetic seismograms for realistic 3-D Earth models. It is possible to exploit techniques from computational geometry to provide a representation of Earth structure which can include detail where needed but also use a sparse parametrisation where velocities are slowly changing.

A further objective has been to characterise the influence of small scale heterogeneity within the Earth on the nature of arrivals at different frequencies. Later phases on a seismogram are normally lower frequency and are picked against the background of

other phases. These influences need to be taken into account in designing improved location algorithms.

RESEARCH ACCOMPLISHED

The following sections summarise the different aspects of the research undertaken and represents contributions from a number of members of the Seismology group, in particular, Alet Zielhuis, Oli Gudmundsson, Malcolm Sambridge and Cheng Tong.

Structural Studies

The major emphasis in the work on regional seismic structure has been on the refinement of a 3-D shear wave velocity model for the upper mantle below Central and East Asia by assembling and processing more data. The number of propagation paths crossing the region has now been almost doubled since last year to a total of 210 seismograms recorded at the regional GSN, GEOSCOPE, and CDSN stations.

The waveforms of Rayleigh waves and S multiples on vertical component seismograms have been analysed using the technique of partitioned waveform inversion developed by Nolet (1990), using synthetic seismograms calculated by modal summation. Nonlinear optimisation techniques are used to find the 1-D dimensional velocity structure which provides the best fit to an individual seismogram. Such a 1-D structure should represent the integral of the shear velocity along the propagation path. After assessing the errors in the path integrals for a particular wavepath, a set of uncorrelated linear constraints on the velocity-depth profile of the wave path can be constructed. The final 3-D model for shear velocity is obtained from the inversion of the linear constraints provided by all the wave paths, with a low weight given to any ignoring constraints with large errors.

For the inversion of waveforms from each seismogram we use a starting model with crustal thickness close to the average crustal thickness along the propagation path. If appropriate, models with a different crustal thickness for source and receiver location are used to calculate the excitation of the modes. The average crustal thickness, and thickness at source and receiver location, are calculated on the basis of the digital map of crustal thickness by Fielding et al. (1993). From a set of starting models with crustal thickness ranging from 25 to 70 km, increasing in steps of 2.5 km, models that best approximate the crustal thickness for source, path, and receiver structure are chosen. The large variations in crustal thickness in Central Asia limit the frequency range over which the assumptions built into the partitioned waveform inversion are valid. So that, depending on the variations along the path, the portion of the seismogram including the fundamental mode is low-passed filtered with an upper limit of 15-20 mHz and the S body wave portion is low-pass filtered with a 35-50 mHz uuper limit.

Figure 1 shows a section through the 3-D shear wave model at 140 km depth. The Indian craton is characterized by high velocities which extend below the southern part of the Tibetan Plateau. High velocities are also present below the Tarim basin. The apparent northeast trending boundary of this anomaly is not resolved. The northern part of the Tibetan Plateau has lower velocities at this depth.

The partitioned waveform inversion procedure has so far been used for Rayleigh waves on the vertical component; work is underway on assessing the application of this procedure to horizontal component information (both Love and Rayleigh waves). The primary

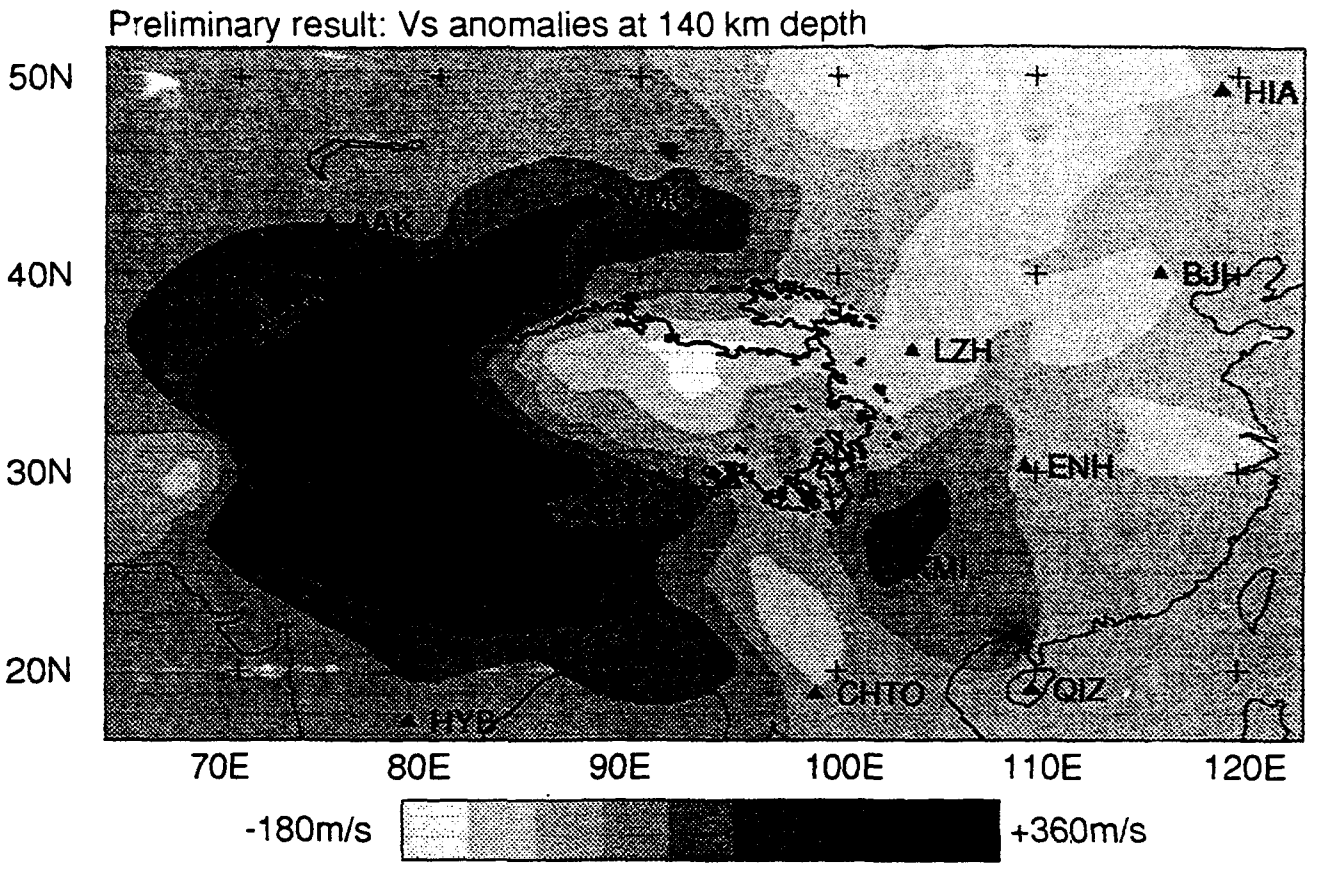


Figure 1. Horizontal section through Asian 3-D shear wave model at 140 km depth, with a reference velocity of 4.5 km/s. The location of stations are indicated by triangles. The coastline and the 4000m topography of the Tibetan Plateau are outlined in black

assumption in the method is that the propagation occurs along a great circle path but in the presence of complex structure polarisation anomalies can be significant particularly at high frequency and it remains to be seen whether such effects cause major problems. The influence of structural changes is being investigated by using ray tracing for surface waves through models derived from *a priori* information.

Research is also being conducted into the representation of the seismic wavefield in three-dimensional structures and a new algorithm has been devised to represent the propagation of guided wavetrains which includes inter-mode coupling as well as transfer between different plane wave components.

Source Inversion

The extraction of the characteristics of a seismic source from a limited set of seismograms requires the exploitation of as much of the information on each seismogram as possible. In particular when the sampling of the focal sphere by P waves is sparse it is important to use as much S wave information as possible (including P to S conversions) to improve the definition of the resulting source mechanism.

Experimental tests with a small array of portable broadband seismographs near Can-

berra (in a tectonic setting similar to the eastern US) have shown that we can pick up S waves above the microseismic peak for distances out to 90°. The typical frequency is 0.3-0.4 Hz so that the accuracy of onset picking is not large. However the detection of S waves for a distant event of itself provides a primary discriminant in favour of an earthquake source.

For larger events we can separate the determination of earthquake location from source mechanism, and proceed by making a nonlinear inversion for the source location and then a linear inversion for the components of the moment tensor description of the source. The linear inversion depends on the comparison of observed and theoretical seismograms for portions of the seismogram. Such an approach relies on the alignment of the observed and theoretical traces so that the identification of later phases is correct.

For smaller events the quality of location estimates is not as good and so there needs to be a close integration of the location and source estimation procedures. Most well established source mechanism estimation schemes work with low-pass filtered data, in order to achieve stability in the source estimate. Also the use of low-passed data avoids problems in the comparison of seismograms. When higher frequency data is used it is possible to get an erroneous measure of the level of match between two records when there is a time shift of a full cycle in a waveform. In order to assess suitable methods of comparing seismograms we have used recordings of the same event at broadband stations 150-300 km apart to examine the influence of near receiver conditions on the caharcter of the recorded seismograms. The best results for the estimation of time shifts between the two records have been achieved by using Lp norm comparators with p around 1.5.

Comparison of observed and synthetic seismograms will give satisfactory results if the same parts of the seismogram are being compared. However, if the location estimate is poor, the identification of later seismic phases may be in error. If these misidentified phases are used in an inversion scheme there will be a consequent error in the source mechanism. Since the timing of later phases can also be of advantage in improving locations, there will need to be a recursive process in which the location is first determined using the largest phases which are then used in a preliminary source determination. The theoretical seismograms for this presumed mechanism can then be used to associate other later phases which can be used in a revised location procedure, followed by a further source estimation step.

Location Studies

For accurate event detection, phase identification and location, all available information about local and regional scale earth structure should be taken into account. This presents the problem of building composite two and three dimensional earth models from different local and regional seismic models. For example a local 3-D model may be appropriate within the source region and a continental or oceanic path at regional scales.

A major difficulty exists in combining models (or travel time tables) which have very different length scales and character. A local source region model will have wavespeed variations over very short length scales compared to regional models. In addition the path between source and receiver may be affected by large scale features, e.g. major tectonic boundaries, or subduction zones. At present the only completely flexible way

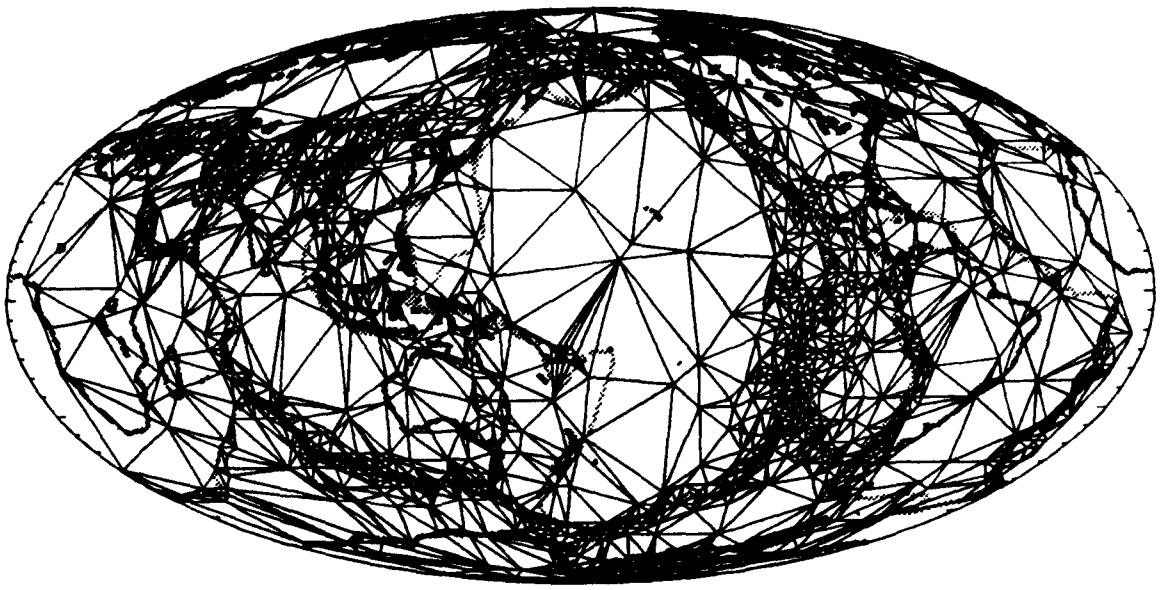


Figure 2. Tessellation of an a priori model of global seismic velocities

to handle large variations in scale length is to parameterize the entire regional, or global, model on a regular grid at the length scale of smallest feature. This involves an extremely large regular 3-D mesh of seismic wavespeeds (or travel time table) which is impractical over regional scale source/receiver separations, even with modern super-computers.

A powerful and flexible mechanism has been developed for solving this problem, which takes advantage of techniques from the field of computational geometry. The new approach allows one to build arbitrarily complex seismic structures from an irregular distribution of velocity mesh points. The complete freedom allowed in choosing the position of mesh points means that large 3-D seismic models can be built from smaller composite models by concentrating mesh points in the places where they are needed, i.e. to represent short scale features. The irregular distribution of mesh points are connected using a unique tessellation method known as 'Delaunay triangulation' which produces a set of triangles in 2-D, or tetrahedra in 3-D. The tessellation produced in this way provides an excellent basis for interpolation when combined with a new procedure known as 'natural neighbour interpolation'. The result is an approach which provides smooth, accurate and efficient interpolation of wavespeeds (or travel times) anywhere in the model.

The flexibility of the method is demonstrated in figure 2. An irregular set of grid points has been chosen over the surface of the earth, concentrated in regions which are expected to have slower than average seismic velocities between depths of 0-100 km. The tessellation produced by the new procedure is shown (centered on the Pacific) and connects each grid point to its set of nearest neighbours on the sphere. The large range in density of grid points results in a set of triangles whose size varies considerably across the surface (The average length of a triangle edge varies by two orders of magnitude in this case). The important feature of the tessellation is that the triangles are as least 'long

and thin' as possible which is the best shape for accurate interpolation of the seismic wavespeeds specified at the vertices. The efficiency of the method means that fully 3-D models can be easily handled as well as much greater range of length scales than shown here. For example one could just as easily incorporate a small (20 km spacing) detailed model within the global mesh to represent source or receiver structure without changing the long scale features in the model.

The new approach represents an extremely versatile and efficient means of parameterizing and interpolating 3-D models from irregularly distributed mesh points. In addition to building seismic models for event location it seems likely that it would have also applications in other areas where complex two and three dimensional geophysical models are used, e.g. numerical modelling of tectonic processes using finite element methods, and Seismic Tomography for large scale earth structure.

Influence of Heterogeneity

When a wavefront passes through heterogeneous structure it acquires significant complexity. In particular, perturbations in phase which record the local variations in wave speed are introduced. Thus the wavefront registers information about heterogeneous structure which may be remotely recorded and subsequently inverted for a heterogeneous model. However, as the perturbed wavefront advances to a remote recorder its complexity evolves. Advanced portions of the wavefront expand in space and mask to some degree the delayed portions by a process often referred to as wavefront healing. Inherent in this process is a loss of phase information which is frequency dependent. Wavefront healing is essentially a geometrical diffraction effect and simple geometrical arguments or mathematical analysis lead one to estimate its importance by the first Fresnel zone of constructive interference. That involves, however, an essentially qualitative or order-of-magnitude argument.

In an attempt to quantify the effect of wavefront healing on the measurement of traveltime we have performed a sequence of synthetic experiments. We start with a simple plane wave. Complexity is introduced to the plane wave by the thin-lens approximation as it passes through an imaginary lens of heterogeneity. We then follow the evolution of the introduced complexity as the perturbed wavefield advances through a homogeneous medium using frequency-wavenumber migration. Having propagated the wavefield a given distance we measure the traveltime from densely spaced seismograms is subjected to filtering and compare the detailed spatial variation of traveltime to the initial phase perturbations. Of course, if we measured the full wavefield we could in theory migrate it back to the initial condition and thus recover all of its detail. Instead, in earthquake seismology we generally have sparse recordings of the wavefield and extract only a very simple measure from the seismogram, namely traveltime. And this simple measure does not allow us to recover all the detail of the initial condition.

Wavefront healing imposes a low-pass spatial filter on the resolution power of traveltime measurements. The shape of this filter is roughly described by a second order Butterworth function and therefore has a sharp cutoff in wavenumber or scale. The variation of the width of the spatial filter with propagation distance and frequency is described by the Fresnel zone. This holds for measurements of traveltime by a picking procedure or by correlation.

CONCLUSIONS AND RECOMMENDATIONS

Seismograms contain a rich amount of information about the nature of the seismic source and the propagation path between source and receiver. However, being able to exploit this information to best advantage still presents a variety of problems.

The characteristics of wave propagation can be simplified by working at relatively low frequencies but at the expense of potential resolution in the nature of structure. The use of low passed seismograms can stabilise the estimates of source mechanisms for events but also increases the level of interference between the main arrivals and any depth phases. The most promising approach is to try to combine procedures based on the phase information of high frequency records with the waveform analysis suitable for lower frequencies. This can be achieved by suitable use of broad-band data systems with adequate high-frequency response e.g. Guralp CMG3, Streckeisen STS-2.

The extension of source inversion procedures to smaller events requires the adaptation of current approaches to higher frequency and noisier data. For such data it is important to combine the processes of location and source mechanism determination so that errors in location do not result in mis-identification of later phases with the introduction of error in the source estimates.

For improved event location using a limited set of global stations it is desirable to have as effective a 1D dimensional model as possible for the construction of initial locations. A update of the iasp91 model is currently being tested which provides improved fits to the times of core phases, which are particularly important for coverage of some oceanic areas. For suspect events, the final location should then be determined using a 3-D model and the tools which we are developing for building variable resolution with a flexible parametrisation should enable the use of nonlinear location procedures for realistic 3-D models.

Current methods for extracting medium scale variations in seismic structure across a region based on the analysis of seismic surface waves work very well for lower frequency waves. In association with a carefully designed configuration of portable instruments it is possible to get the major features of the structure of a region of 1000x1000 km with about a year of recording and a similar time period for analysis. A prerequisite for improvements in such classes of analysis techniques for seismograms is improved modelling of the interactions of seismic waves with three-dimensional structures. Progress has been made with the representation of the surface wavetrain but a full solution will be computationally intensive.

References

Fielding, E., Barazangi, M. & Isacks B.L., 1993. A geological and geophysical information system for Eurasia. *Semiannual Technical Report 3*, Phillips Laboratory, Hanscom AFB, MA

Nolet, G., 1984. Partitioned waveform inversion and two-dimensional structure under the Network of Autonomously Recording Seismographs, *J. Geophys. Res.*,95. 8499-8512.

BOROVOYE, KAZAKHSTAN, (BRVK) SEISMIC DATA ANALYSIS

Won-Young Kim, Paul G. Richards[1], Vitaly I. Khalturin[2], and Tatyana G. Rautian[2]
Lamont-Doherty Earth Observatory, Palisades, NY 10964
([1] also, Dept. of Geological Sciences, Columbia University;
[2] also, Institute of Physics of the Earth, Russian Academy of Sciences, Moscow)

F49620-92-J-0497

OBJECTIVES

The seismographic station Borovoye (BRVK) in Kazakhstan provides high-quality digital data due to its low noise environment. In light of the availability of this unique data, our objective has been to determine accurately the instrument responses and to analyze regional as well as teleseismic waveform data recorded at BRVK for determining geophysical properties in the crust and upper mantle under Central Asia.

We have also used BRVK data, plus analog data from many other seismic stations in Central Asia, to improve the documentation of nuclear and chemical explosions at the Semipalatinsk, Kazakhstan test site.

RESEARCH ACCOMPLISHED

We have carried out three projects:

- a method is developed to determine the response of digital seismographs from their transient calibration pulses when there is no recourse to direct measurements;
- an application of the method, for accurate determination of instrument responses for BRVK STsR-TSG seismographs by inversion of the transient calibration pulse and available frequency-amplitude response information;
- a major survey of regional seismic data for explosions at the Semipalatinsk test site, that has documented the occurrence of eighteen small nuclear explosions (since confirmed), not previously described in the open literature.

Determination of the Response of Digital Seismographs at Borovoye, Kazakhstan by Inversion of Transient Calibration Pulse Shapes

A method is developed to determine the response of digital seismographs from their transient calibration pulses when there is no recourse to direct measurements. Based on linear system theory for small input signal, the digital seismograph is represented by a set of first- and higher-order linear filters characterized by their cutoff frequency and damping constant. The transient calibration pulse is parameterized by a set of instrument constants, and the problem is linearized for small perturbation with respect to their nominal values. The calibration pulse shape is iteratively inverted in the time domain using a linearized, generalized inverse technique.

The method is used to determine instrument responses of the digital seismographs at Borovoye (BRVK) in Kazakhstan as well as a digital seismograph at Kislovodsk (KIV) in Northern Caucasus, Russia. The results of the calibration pulse shape inversion for these seismographs indicates that the method is efficient and the results are reliable even when microseismic noise is present in the recorded transient calibration pulse. Because the calibration

pulse generated by the input step acceleration signal emphasizes the lower frequencies due to $(i\omega)^{-3}$ scaling of the impulse response, the reliability of the solution at high frequencies is limited at the frequency where the spectral amplitude drops to approximately one part in one thousand from its peak value. The iterative inversion proceeds as: 1) recorded and synthetic calibration pulses are aligned in time and baseline adjusted; 2) kernels for the inversion is formed; 3) parameter correction is found from inversion; 4) parameter is updated and the iteration continues until it converges.

Application of the Method, for Accurate Determination of Instrument Responses

Calibration Pulse Shape Inversion for STsR-TSG system: We analyze the responses of the various seismographs of STsR-TSG system (also called TSG). The TSG system is one of the better system operated at BRVK and it has been in operation since Feb. 1973 (see Table 1; and Richards et al., 1992). Nominal instrument constants of these seismographs were obtained from:
1) seismometer free period, damping and digital sensitivity (in count/μ) given in Adushkin & An (1990);
2) frequency-amplitude calibration tables of the TSG system available at the Borovoye Observatory.

Although it was reported that the TSG system is carefully calibrated every year, only information on the amplitude responses and overall gains and no phase information were available to us. On a more routine basis, transient calibration pulses are generated and recorded to check the overall digital sensitivity of the system. We obtained digital recordings of such calibration pulses from all seismometers of the TSG system. The calibration pulses were recorded on Feb. 8, 1988 (15:00). These calibration pulses are generated by feeding a boxcar calibrating signal with duration of 8 msec (two Heaviside steps) into the seismometer damping coils. The recorded calibration pulse corresponds to the seismograph response to an *impulse* in ground acceleration. The recorded calibration pulse is equivalent to the multiplication of the system transfer function for ground displacement by $(i\omega)^{-2}$ (see e.g., Herrmann, 1977).

Table 1. Characteristics of the STsR-TSG Seismic System at Borovoye Station.

Seismometer	Data channel	T_s[(a)] (s)	ξ_s[(b)]	Gain (count/μ)	f_n[(c)] (Hz)	dt[(d)] (msec)	Channel number
KS		1.5	0.7	4500	1.5	26	7, 8, 9
DS		20.0	0.5	50	0.1	312	19, 20, 21
KSM	High-gain	1.5	0.35	100000	1.0	26	10, 11, 12
	Low-gain			1000		26	3, 4, 5
DSM	High-gain	28.0	0.5	1000	0.07	312	22, 23, 24
	Low-gain			10		312	15, 16, 17
KSVM	High-gain (Z)	1.5	0.35	4600	1.0	26	2
	Low-gain (Z)			50		26	1

(a) T_s = Seismometer natural period,
(b) ξ_s = Seismometer damping constant,
(c) f_n = normalization frequency where the nominal gain is measured,
(d) dt = Sampling interval.

We parameterized the responses of all seismometers (channels) of the TSG system in terms of cutoff frequencies and damping constants of a set of linear first- and second-order filters. The transfer functions of each seismograph obtained from the inversion are represented by complex poles and zeros in the complex *s*-plane.

TSG-KSM Seismograph: For example, the short-period KSM seismograph consists of:
1) seismometer with natural period, $T_s = 1.5$ s and damping $\xi_s = 0.35$ (Adushkin & An, 1990);
2) second-order high-pass filter with cutoff frequency, $f_{H2} \approx 0.65$ Hz and damping, $\xi_{H2} \approx 0.71$;
3) third-order Butterworth low-pass filter with cutoff frequency, $f_{L3} \approx 8$ Hz.

Calibration pulses recorded on the 3-component, short-period KSM seismograph are plotted in Figure 1. The calibration pulses of both horizontal components are similar to each other, but the vertical-component pulse is slightly different. The recorded calibration pulse is inverted for the six instrument constants: T_s, ξ_s, f_{H2}, ξ_{H2}, f_{L2}, K. A stable solution is obtained after three iterations. In each iteration, we perturbed the initial values by about 5 %. The instrument constants obtained from the best fit waveform inversion are given in Table 2 and comparisons between the vertical-component, recorded and synthetic calibration pulses are shown in Figure 1. The final solution shows that instrument constants of all three components have similar values with relatively small deviations from the nominal values.

The spectral amplitude responses of all vertical-component channels of the TSG system at BRVK determined in this study are plotted in Figure 2. The amplitude responses obtained from the calibration pulses are compared with the frequency-amplitude responses given in response table which were determined independently at BRVK. Overall good agreements between the two independent measurements over a wide frequency band indicate that the instrument calibration of various seismographs at BRVK station appear to be stable.

However, the instrument responses of some 3-component channels suggest significant departures of seismometer constants from their nominal values. Among the five seismographs of the TSG system, the basic 3-component, short-period KS and long-period DS seismographs show significant differences among their three components. The vertical components differ from the two horizontal components, more than between the two horizontals. The recorded calibration pulses of the short-period KSM and corresponding long-period DSM seismographs are best resolved for their instrument constants.

Table 2. TSG-KSM 3-component instrument constants from inversion

	Seismometer		High pass		Low pass	rms fit
	T_s (sec)	ξ_s	f_{H2} (Hz)	ξ_{H2}	f_{L2} (Hz)	
Nominal	1.500	0.350	0.650	0.707	8.00	34.521
Z	1.481 (-1.4%)	0.332 (-5.4%)	0.630	1.042	8.13	1.249
NS	1.515 (+1.0%)	0.345 (-1.4%)	0.636	1.049	8.47	1.781
EW	1.520 (+1.3%)	0.349 (-0.3%)	0.644	1.034	8.77	2.365

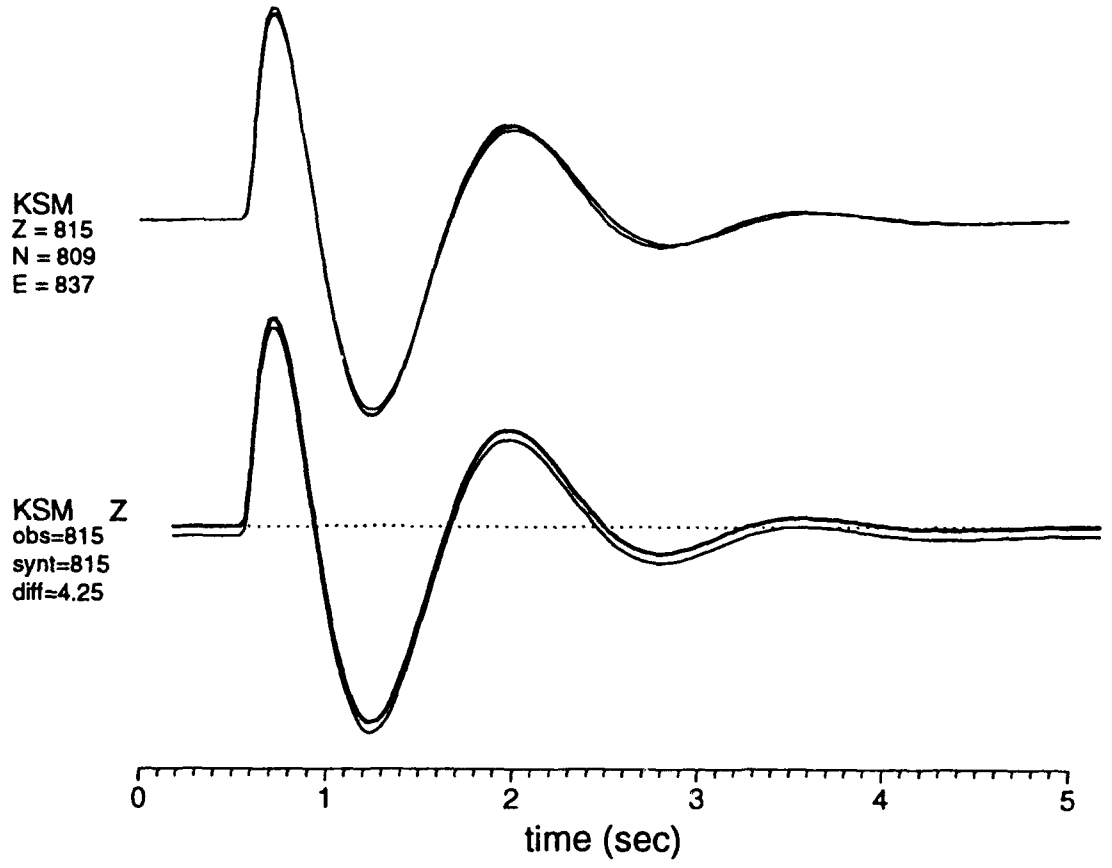


Fig. 1. (*upper traces*) A comparison among the calibration pulses recorded by the 3-component, short-period KSM seismograph. There are slight differences in the three traces indicating deviations of instrument constants among the three components. (*lower traces*) A comparison between the vertical-component, recorded (*thick trace*) and synthetic calibration pulses after the waveform inversion (*thin trace*). Synthetic pulse calculated with the final instrument constants is plotted with small vertical offset to show the overall fit. Recorded-synthetic trace is plotted (*dotted trace*).

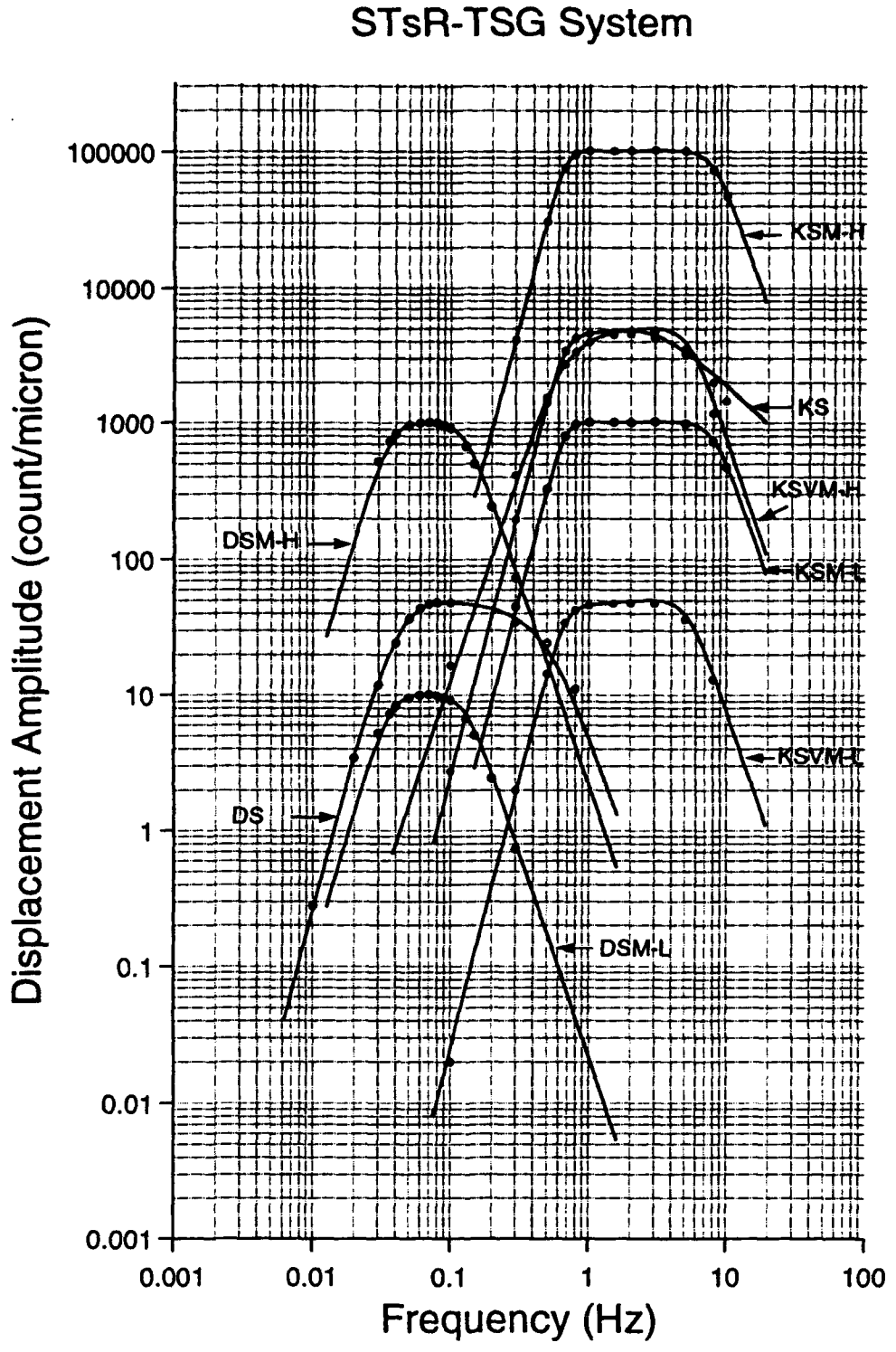


Fig. 2. A summary figure showing spectral amplitude responses of the all vertical-component seismographs of the TSG system. In each seismograph, frequency-amplitude responses given in the log book at BRVK (*circles*) and the amplitude responses obtained after the calibration pulse shape inversion (*solid lines*) are plotted together for comparison.

A Study of Small Explosions and Earthquakes during 1961 - 89 near the Semipalatinsk test site, Kazakhstan

A lengthy technical report (Khalturin, Rautian, and Richards; 1994) was completed in Spring 1994 and is available from the authors. It reviewed the then available open literature on locations, origin times and magnitudes for Semipalatinsk explosions. It documented the occurrence of a number of additional small nuclear explosions, and chemical explosions and one earthquake, not previous known from open publications on this test site.

In June 1994, a Russian paper (Gorin et al, 1993) became available in the west, giving an apparently complete chronology of 348 underground nuclear explosions (UNEs) at Semipalatinsk. This paper confirmed 18 of the small nuclear explosions we had documented in early 1994, and permits an evaluation as follows:

Openly known prior to 1994	Degelen	158
	Balapan	100
	Murzhik	23
Additional from our 1994 report		18
		299

Therefore the number of "new" events from the 348 UNEs listed by Gorin et al (1993) is

$$348 - 299 = 49 \text{ events.}$$

Of these 49 we have since learned of (teleseismic) detections (NORSAR or Hagfors) for 3 events; and 19 events were included in multiple shots where the other shot is known. There remain 27 events that (as of July 21) are unexplained in our project.

CONCLUSIONS AND RECOMMENDATIONS

The calibration pulse shape inversion method is efficient in determining instrument constants even when there is substantial microseismic noise present in the calibration pulse. The reliability of the solution at high frequencies appears to be limited up to the frequency where the spectral amplitude drops to a factor of one thousand smaller than the peak amplitude. The calibration pulse generated by the input step acceleration signal emphasizes the low frequency content due to $(i\omega)^{-3}$ scaling to the transfer function.

In this study, a lack of detailed knowledge on the input calibrating signal prevents determination of the absolute instrument sensitivity. The transient calibration technique which can provide accurate starting time and amplitude of the input calibrating signal would be very useful for determining the overall sensitivity and phase response.

The broadband nature of BRVK digital records provides an opportunity to examine seismic velocities and discontinuities in the upper mantle beneath Central Asia.

The new information on Semipalatinsk events can be used for special studies of multiple events, and for discrimination research.

References

Adushkin, V. V. and V. A. An (1990). Seismic observations and monitoring of underground nuclear explosions at Borovoye Geophysical Observatory, *Izv. Acad. Sci. USSR, Phys. Solid Earth*, 1023-1031, no. **12**.

Gorin, V.V., G.A. Krasilov, A.I. Kurkin, A.L. Maltsev, A.M. Matushchenko, S.L. Orlov, A.V. Pichugin, S.G.Smagulov, V.G. Strukov, V.I. Filippovskiy, K.V. Kharitono, A.K. Chernyshev, and M.V. Shumayev, Semipalatinsk: Chronology of Underground Nuclear Explosions, and their Primary Radiation Effects (1961 - 1989), in Russian from *Byulletin Tsentra Obschestvennoy Informatsii Po Atomnoy Energii*, **9**, 21-32, 1993; in English from JPRS-UST-94-004-L, 23 March 1994.

Herrmann, R. B. (1977). On the determination of the impulse response of seismograph systems with emphasis on the SRO system, *Earthquake Notes*, **48**, No. 1-2, 3-23.

Khalturin, V.I., T.G. Rautian, and P.G. Richards, A Study of Small Explosions and Earthquakes during 1961 - 89 near the Semipalatinsk test site, Kazakhstan, Technical Report to LLNL and AFOSR, 25 pages plus 12 Tables and 13 Figures, 1994.

Richards, P. G., W. Y. Kim and G. Ekström (1992). The Borovoye Geophysical Observatory, Kazakhstan, *EOS*, **73**, 201-206.

Anatomy of Regional Phases and Source Characterization of the Soviet Joint Verification Experiment, Underground Nuclear Explosion

Charles A. Langston
Department of Geosciences
440 Deike Building
Pennsylvania State University
University Park, PA 16802
(814) 865-0083
cal@geosc.psu.edu

Contract #F49620-93-1-0207

Objective

Regional broadband data from the 1988 Soviet JVE explosion show dramatic excitation of high frequency SH waves. Generally ascribed to "tectonic release", the source of high frequency shear waves from underground nuclear explosions remains an enigma since cavity relaxation models generally have relatively little shear wave excitation at high frequency. The primary objective of this research is to determine sources of shear wave radiation operating in the explosion and to evaluate how such sources of high frequency shear waves impact event discrimination. Secondary objectives include understanding the nature of crustal wave propagation in Kazakhstan, particularly understanding the excitation and waveshape of Pn, Pg, Sn,, Sg, Rayleigh and Love waves and the influence of the explosion and tectonic release source functions on these phases.

Research Accomplished

Introduction

Extensive synthetic seismogram computations and data analyses were performed to understand, in a complete sense, the nature of regional waveforms recorded by the NRDC instrument deployment for the 1988 Soviet JVE underground nuclear test. The approach used in this research was simple and, perhaps, naive. Regional phases are studied empirically by many seismologists but understanding of their exact path and interaction with crustal structure is usually vague. I have assumed that the various phases and waves seen in the data can be understood and modeled in terms of reasonably simple plane-layered earth structure models in conjunction with kinematic point source models. Such a direct approach can be very naive in relying implicitely on such simple 1D structure, particularly when lateral heterogeneity and wave scattering effects can be seen in the data in some frequency bands. However, a complete understanding of the excitation and propagation of regional phases is required to understand empirical source discrimination techniques or to develop new discrimination techniques.

NRDC Broadband Data

The NRDC deployment of seismic stations in Kazakhstan in 1988 to record the Soviet JVE explosion collected a unique set of seismic signatures written by an underground nuclear test (Priestley et al 1990). Stations Karkaralinsk (KKL) and Bayanual (BAY) were both situated at 255 km from the shot point and recorded spectacular near-regional waveforms. As Figure 1 shows, the displacement data appear to be relatively simple showing very simple regional P and S phases and a well-dispersed Rayleigh wave. Tangential motions are particularly interesting showing a high-amplitude SH pulse, particularly at BAY. The Soviet JVE explosion is not considered to have a significantly large tectonic release component at long periods (Sykes and Ekstrom, 1989) yet these short-period regional data show that SH waves were excited quite efficiently from the source. Walter and Patton (1990) attempted to use these shear waves to estimate the orientation of tectonic release from the explosion using general observed amplitudes and wavenumber synthetic seismograms but found the result to be non-unique. In this study, I use details of the data along with the known behavior of wave propagation in plane layered media to constrain source models. The data were corrected for instrument response and absolute time was calibrated using satellite clock times recorded by the University of Wisconsin at both sites.

A close look at the body wave phases (Figure 2) shows that the P waveforms are simple and consistent between stations. The mantle head wave (or turning wave) Pn has separated from the Moho reflection, PmP by about 1 to 2 seconds. Because absolute time is available, it is clear that velocity structure to BAY is just slightly faster than that along the KKL path. Pn has moved out about a half second more at BAY compared to KKL but PmP at BAY is just a small fraction of second earlier than PmP at KKL. The shear waves are interesting and show clear source radiation pattern effects. Based on the close similarity of P phases between the stations, we can expect the S wave phases to arrive a nearly the same times also, with BAY arrivals coming in slightly earlier. However, vertical S and tangential S at BAY is much larger later in the waveform compared to KKL S waves. A long-period bandpass filtered record clearly shows Sn and SmS phases occur at about the same time at both stations (Figure 3). Yet the large amplitude S phase (denoted as SmS') occurs 1 to 2 seconds <u>after</u> expected SmS. Moreover, the long-period bandpass shows that BAY tangential S is actually smaller than that at KKL, just the opposite as seen at higher frequency. Progressively higher frequency bandpass filters show that this secondary SH phase becomes quite distinct at both stations. Although first arriving SmS at BAY is slightly advanced because of faster crustal velocity, the large secondary phase arrives simultaneously at both stations. Furthermore, there is a clear polarity change between BAY and KKL for this phase even at 4Hz! The polarity change and change in relative amplitudes between stations strongly suggests a fault model. The reduction in amplitude of this phase at long-period further suggests that the net moment on the fault must be small and that dislocation movement was highly oscillatory.

These straightforward observations strongly suggest that there are two source of shear wave radiation from the JVE source. The first source is one directly related to processes going on at the shot point. Sn and Sg at long-period come in as expected with

slight time shifts between stations due to differing velocity structures. These S waves are inferred to be excited by stress relaxation around the explosion cavity. The later arriving high-frequency SmS' phase, on the other hand, must be excited by a source 1 to a few km south of the JVE source because of near-simultaneous arrival times at both stations. Since the path to BAY is slightly faster, the high-frequency S wave source must be slightly farther from BAY compared to KKL. Assuming that initial SmS comes from the explosion, bounds can placed on location of the secondary source and these are shown in Figure 4. Figure 4 was constructed assuming that the high frequency S phase is SmS and that it has a relative time delay at BAY of 0.35 sec which is enough to counter the 0.35 sec time advance of SmS travel time due to velocity structure. Circles on Figure 4 denote the distance from the JVE that P waves and Rayleigh waves from the explosion can travel in one second, the approximate relative time shift from first SmS and SmS'. It is interesting to note that the inferred secondary source falls near where the expected Rayleigh wavefront would be about 1 second after the initial explosion. I propose that the strong-motion Rayleigh wave induced oscillatory motion on a fault in this location.

Synthetic Seismograms

The data directly speak to the nature of the JVE source(s), but can the waveforms be fit by this kind of source model? The key to understanding the S waveforms lies in the simplicity of the P waveforms. Figure 5 shows two synthetic seismogram calculations for P and SH waves. These models are taken from a suite of trial-and-error model calculations in an attempt to model the high frequency S wave arrival as purely being due to crustal structure. The principal observation made in these computations was that any reasonable structure (a structure with reasonable Poisson ratios) that stretched out the duration of the SH wave also stretched out the duration of the P waveform. Separate crustal phases from the Moho and lower crust seen in the SH waveform also were produced in the P waveform. Clearly, the P waveform data at both stations show very compact PmP and lower crust P arrivals (Figure 2). This, in conjunction with the observed high-frequency SH polarity change, frequency dependence, and timing, strongly suggests that crustal structure effects are not the source of the secondary SH waves.

Figure 6 shows a fault model which can explain the observed SH waveforms. The vertical strike-slip Green's function representing the stress relaxation part of the JVE source is summed with an oscillating vertical strike-slip source with a polarity change. Clearly, with only two stations, determining the orientation of the relaxation part of the tectonic release and the explosion-driven fault motions of the secondary source is a non-unique problem. However, the synthetics show that is quite straightforward to match the main features of the SH waveforms with this kind of model.

Knowledge of the crustal structure effect allows a detailed look at the explosion source itself through simple observation and modeling of the P waveforms. The filtered P waveform data are remarkably simple in character (Figure 1). Indeed, this simplicity is extremely useful in observing the RDP of the explosion source. At this range, Pn has only separated 1 to 1.5 seconds from PmP. Synthetic seismogram calculations (Figure 5) and well-known theoretical considerations of the characteristics of headwaves show

that Pn behaves like the integral of the far-field source function, or has the shape of the RDP itself. If Pn is an actual turning wave in the mantle due to a positive upper mantle velocity gradient, then it should behave more like the time derivative of the RDP. The data for Pn, as well as PmP, show that the JVE explosion RDP must have significant overshoot.

Previous Soviet Deep Seismic Sounding studies in the region (Leith, 1988) found high Pn velocity. This is reflected in the crustal model of Figure 7. The amplitude ratio of Pn to PmP in the BAY data suggest that Pn may actually be a turning wave in a positive upper mantle velocity gradient. If this assumed, then the Pn waveform itself is an image of the time derivative of the source RDP. Figure 2 shows that there must be a large amount of overshoot to the RDP. This problem does not go away if Pn is assumed to be a pure head wave. Indeed, it becomes much more difficult to explain the observed negative swings in the data since the RDP itself must have a negative swing. The source models of von Seggern and Blandford (1972) and Haskell (1967) were investigated but it was found that these models were incapable of producing of producing the observed overshoot in Pn or PmP. The Mueller and Murphy (1971) source model, however, is more oscillatory and produces larger overshoots comparable to the data.

Conclusions and Recommendations

"Tectonic release" in the 1988 Soviet JVE explosion is seen to be composed of two parts. The first in time and space is that due to cavity relaxation and dominates at longer periods. The second is inferred to be caused by explosion-driven block motions located 1 to several kilometers south of the shotpoint. This induced faulting must incorporate oscillatory dislocation with little net moment. It is speculated that strong-motion explosion Rayleigh waves drive this block motion. This observation implies that high frequency S waves seen in explosion seismograms are caused by a random excitation process at high frequencies and is controlled by the fracture heterogeneity of the near-source medium.

The explosion RDP is seen to have significant overshoot. The Mueller-Murphy source model is more effective in modeling this overshoot than are models by von Seggern and Blandford or Haskell.

References

Haskell, N.A. (1967). Analytic approximation for the elastic radiation from a contained underground explosion, *J. Geophys. Res.*, *72*, 2583-2587.

Mueller, R.A., and J.R. Murphy (1971). Seismic characteristics of underground nuclear detonations: Part I, seismic scaling law of underground detonations, Bull. Seism. Soc. Am., 61, 1675-1692.

Priestley, K., W. Walter, V. Martynov, and M. Rozhkov (1990). Regional seismic recordings of the Soviet nuclear explosion of the joint verification experiment, *Geophys. Res. Lett.*, *17*, 179-182.

Sykes, L.R., and G. Ekstrom (1989). Comparison of seismic and hydrodynamic yield determinations for the Soviet joint verification experiment of 1988, *Proc. Natl. Acad. Sci.*, *86*, 3456-3460.

von Seggern, D., and R. Blandford (1972). Source time functions and spectra for underground nuclear explosions, *Geophys, J. R. astr. Soc.*, *31*, 83-97.

Walter, W.R., and H.J. Patton (1991). Tectonic release from the Soviet joint verification experiment, *Geophys. Res. Lett.*, *17*, 1517-1520.

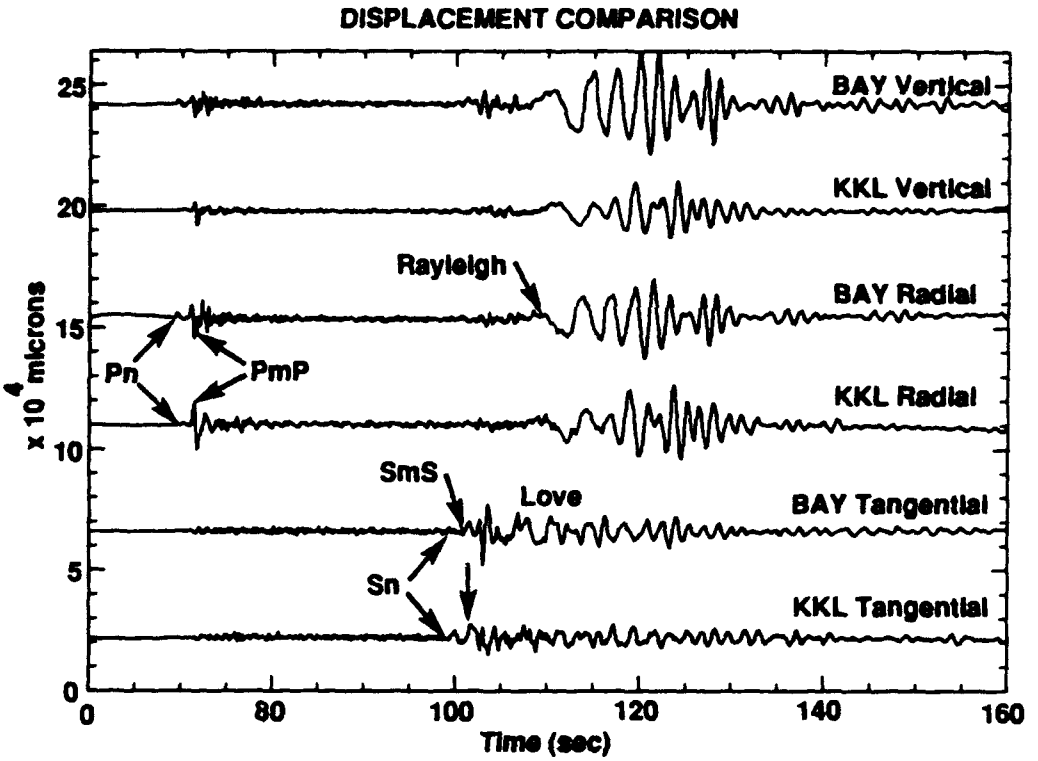


Figure 1: Corrected displacement data recorded at BAY and KKL. Phases are annotated.

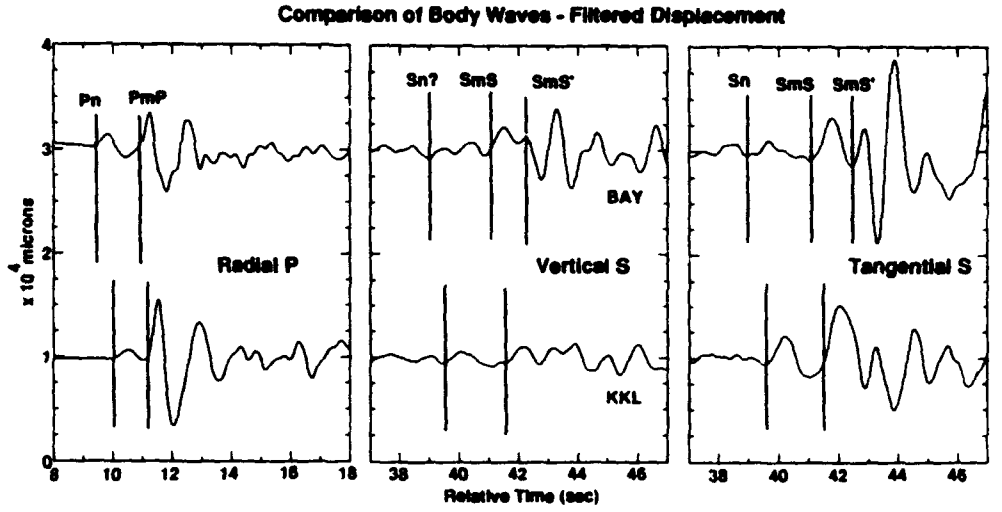


Figure 2: Comparison of observed body waves in time and amplitude. The data have been lightly low-passed filtered with a 2 pole, causal Butterworth filter with a corner frequency of 1 Hz. Phases are annotated. Note the small time advances of Pn and PmP at BAY compared to KKL. Also note that SmS' is significantly delayed compared to the SmS at BAY.

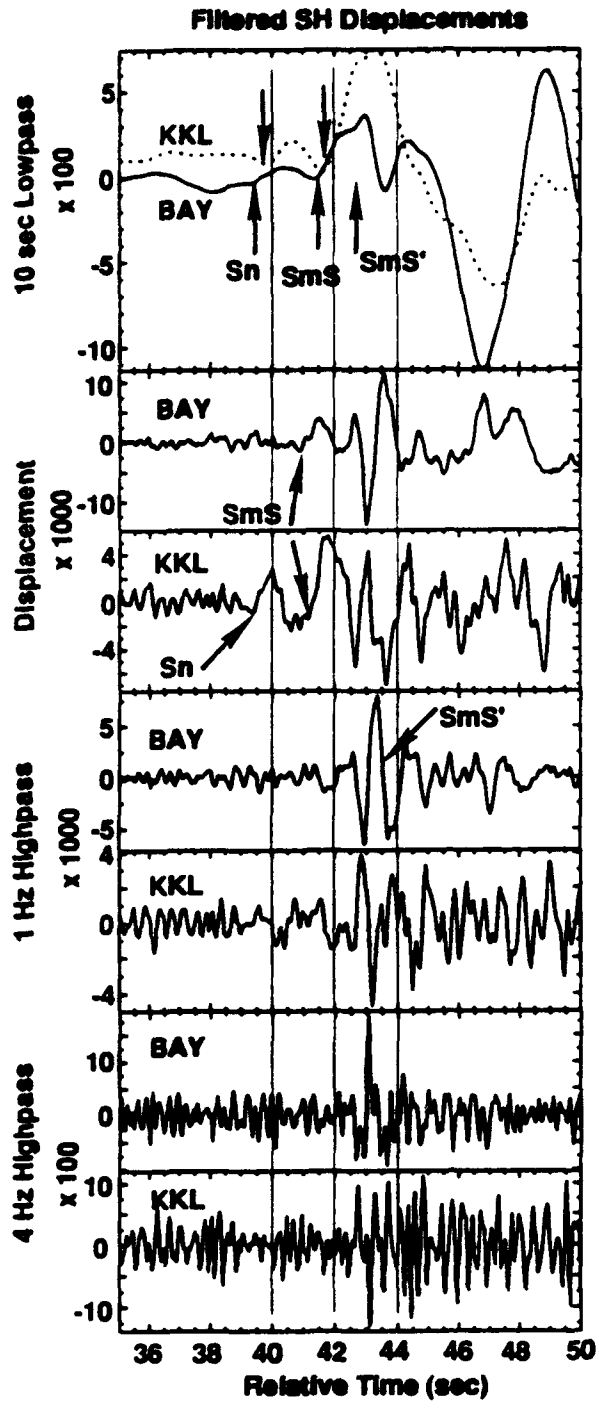


Figure 3: Comparison of the displacement data at BAY and KKL using lowpass and highpass 2-pole, causal Butterworth filters. Vertical lines are for time reference. Phases are annotated. Identification of Sn and SmS is possible at both stations for the lowpassed data and is consistent with the relative time shifts seen in the P wave data. The path to BAY is slightly faster. However, SmS' becomes dominant at higher frequecies and shows a clear polarity change between stations. SmS' also arrives at nearly the same time at both stations unlike Sn or SmS, implying a different source location.

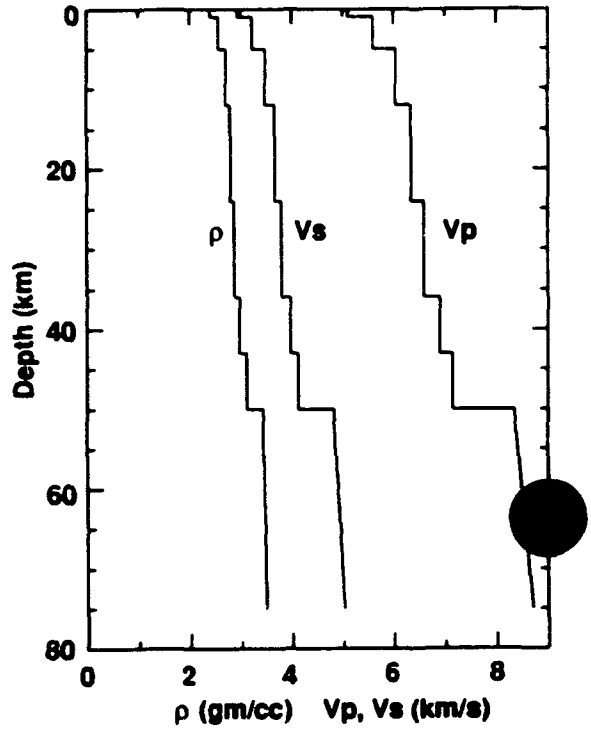


Figure 7: Crust and upper mantle assumed in the synthetic seismogram calculations. Based on Soviet DSS results for the area (Leith, personal communication).

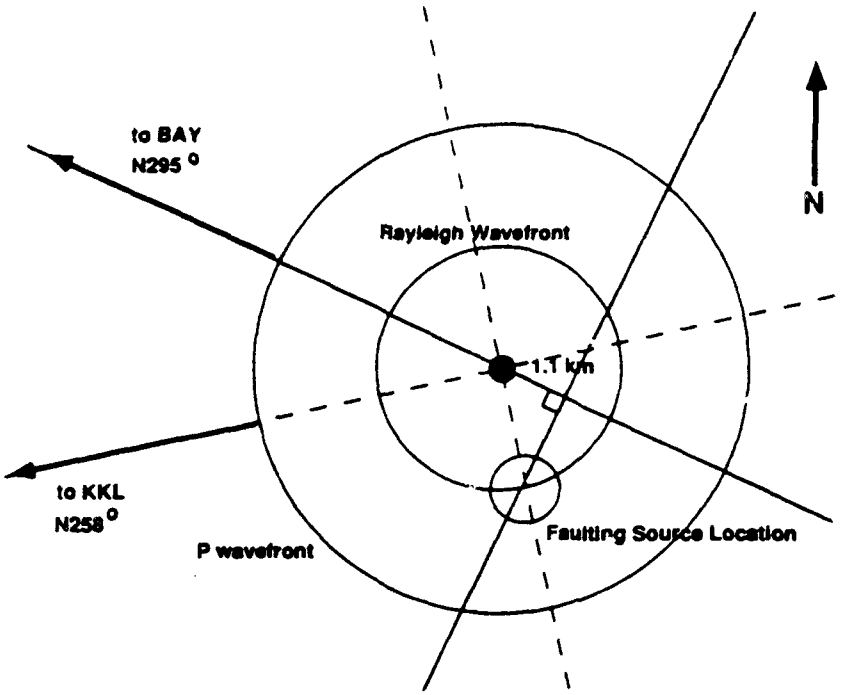


Figure 4: Sketch of the relative location of the SmS' source relative to the JVE shotpoint. SmS' must be delayed by the same amount as the time advance due to velocity structure to BAY relative to KKL (0.35 sec). Therefore, the SmS' source must be farther from BAY than KKL. The diagram shows the graphical solution. Also shown are the expected P and Rayleigh wavefront locations at 1 sec after detonation of the explosion. One second is the approximate relative time of SmS' to SmS at both stations.

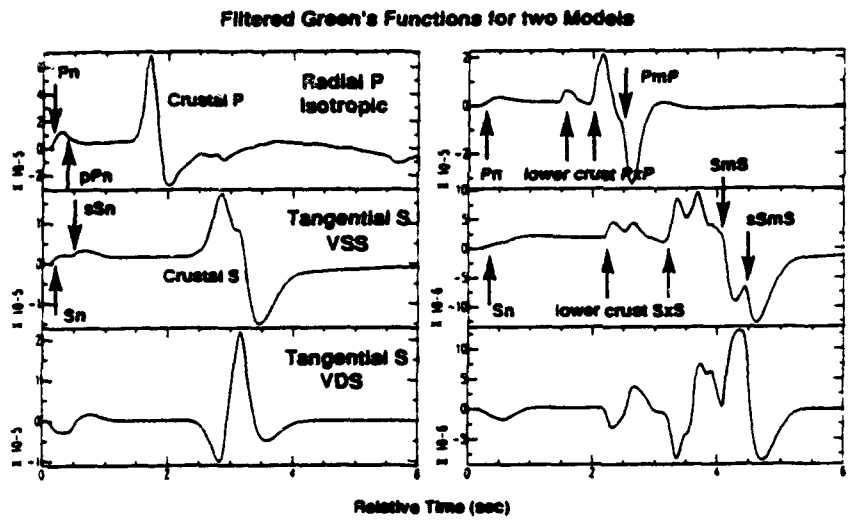


Figure 5: Comparison of two synthetic seismogram computations for P and SH waveforms. The left panel shows synthetics for a model based on DSS results for the area (Figure 7). Crustal P and S phases are composed of reflections from lower crustal interfaces. Small modification of this model spreads on relative arrival times as shown in the right panel. Seismograms become complex and do not match the character of the data in Figure 2. PxP and SxS are reflections from lower crustal interfaces. Thus, SmS must be a simple, compact phase similar to the that seen for PmP in the data.

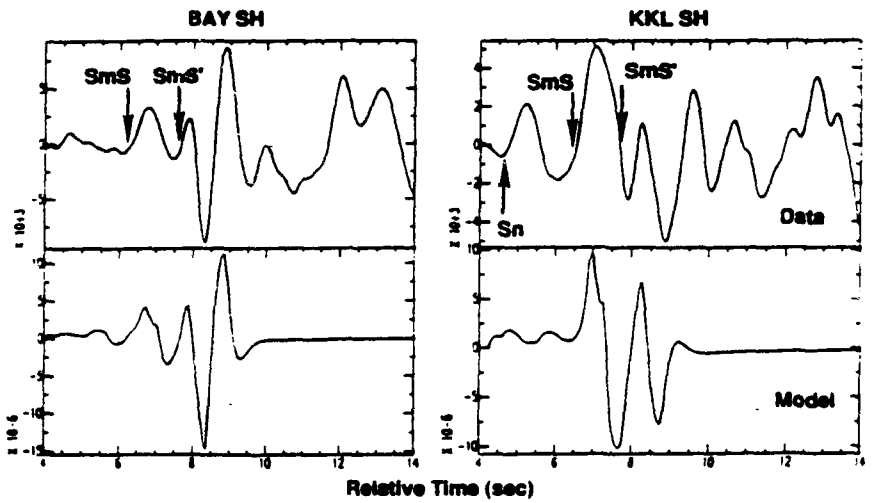


Figure 6: Comparison of data and synthetic for the two-source model of tectonic release. The SmS' source consists of a strike-slip fault with relative dislocation of 0.5, -1.0 and 0.5 separated at 0.5 second intervals. Amplitudes are arbitrary in this plot.

CALIBRATION OF REGIONAL WAVE DISCRIMINANTS IN DIVERSE GEOLOGICAL ENVIRONMENTS: TOPOGRAPHIC CORRELATIONS

Thorne Lay and Tianrun Zhang
University of California, Santa Cruz

Contract #F49620-94-1-0247

Objective: This research is directed at improving the performance of regional wave discriminants by developing empirical and, potentially, theoretical wave propagation corrections for Pn/Lg and Sn/Lg ratios, as well as for Lg amplitudes. It will hopefully provide fundamental advances in our understanding of the regional wavefield. The basic idea is that by establishing the influence of large-scale crustal waveguide structure on the amplitude ratios of regional phases, the scatter in those ratios can be reduced, thereby enhancing the discriminant performance. We are exploring surrogates for waveguide structure such as surface topography and bathymetry characteristics, along with independently constrained parameters such as crustal thickness, sedimentary basin thickness, and crustal attenuation. A combined empirical and modeling approach is being undertaken to systematically explore the influences of large-scale irregularities in the crustal waveguide, as a preliminary step toward a predictive capability of reliable a priori path calibration for regions for which we may have no prior wave propagation experience.

Research Accomplished: The current research effort commenced on May 1, 1994, so only a few months work has been completed at this time. However, the research effort builds directly upon work initiated under prior grants from ARPA and AFOSR. Our earlier work has established that there are strong correlations between regional phase amplitude ratios and gross characteristics of the crustal path from the source to the receiver for explosions and earthquakes in Eurasia. Strong correlations have been found between surface topographic characteristics, including mean elevation and *rms* roughness of the surface, and the regional phase amplitude ratio Sn/Lg for explosions at the Semipalatinsk test site (Figure 1; Zhang and Lay, 1994a). This suggests a strong partitioning of high frequency wavefield energy between crustal and upper mantle lid phases, controlled by irregularity of the waveguide. Surface scattering probably plays a direct role, especially in the generation of the Lg and Sn energy by Rg scattering near the source, but the trends in Figure 1 indicate that overall waveguide characteristics that are manifested in surface

topography and its roughness (via isostatic compensation) are important and quantifiable. Less significant correlations have been found for upper mantle distance P/Lg behavior and surface topography for Semipalatinsk explosions (Zhang and Lay, 1994a), but we are just beginning to analyze a data set of Pn observations for NTS explosions to explore the behavior of waves that do not dive into the mantle.

Zhang and Lay (1994b) have also found correlations with bathymetric characteristics of the underwater segment for Lg phases from Novaya Zemlya explosions (Figure 2). The extent of necking of the waveguide along the continental shelf, which is coupled to bathymetric and sedimentary basin variations, appears to have a strong influence on relative amplitude of Lg phases. In our most recent work, conducted under the current contract, we (Zhang, Schwartz and Lay, 1994) have analyzed a large data set of Eurasian nuclear tests and small earthquakes, finding that the thickness of sedimentary basins traversed on the regional path, along with attenuation effects predicted by an Lg coda Q model (Pan et al., 1992), influence Pn/Lg ratios at regional to upper mantle triplication distances. We have explored the relative importance of crustal thickness, surface roughness, sediment thickness, and attenuation structure of the crust using a multivariate analysis (Figure 3, 4). The waveguide properties considered tend to be highly correlated with each other, thus it is as of yet difficult to isolate specific characteristics that control the regional phase energy partitioning. A two parameter model, involving the path attenuation term, $\gamma\Delta$, and maximum sediment thickness on each path, reduces the variances for separate earthquake and explosion data sets by 40% and 27%, respectively. However, nearly equal performance is given by models combining path attenuation and surface topography measures, thus it is likely that several factors are important. It is encouraging that regional Lg coda Q models appear to have the potential to reduce scatter in Lg phase amplitudes, but we have found significant correlations with Sn amplitude variations and P coda amplitude variations as well, suggesting that these models are not purely crustal measures. Based on these exploratory efforts, it appears possible to use independent constraints on crustal properties to develop corrections that significantly reduce the scatter in regional phase discriminants. This could have tremendous significance for our ability to transport discriminants to regions sampling significantly different paths than the well-studied ones associated with old test sites.

Under this research effort, we are also conducting finite difference and normal mode synthesis of regional phases to explore the physics underlying the empirical trends that have been found. This extends, and complements, our earlier work on Lg excitation (Xie and Lay, 1994a) and propagation effects on Lg scaling (Xie and Lay, 1994b). Initial work with a finite difference method also indicates a greater role for crustal

thickness in the generation of Lg than has been previously recognized, in that crustal thicknesses of less than 6 km cannot support large numbers of Rayleigh wave overtone modes in the appropriate frequency band for typical continental Lg signals. Thus, blockage of Lg transport across ocean-continental boundaries is strongly influenced by overall change in crustal thickness rather than by details of the transitional structure (Zhang and Lay, 1994c). This is distinctive from the behavior of fundamental mode energy.

Conclusions and Recommendations: At this time it is too early to confidently state whether or not propagation corrections based on independently obtained measures of the crustal structure on a given path will in fact reduce the scatter in regional discriminants effectively. Our initial work has been in a relatively low frequency (0.2-3 Hz) passband, where we find that there is in fact significant variance reduction in the P/Lg or Sn/Lg amplitude ratios using path corrections. Whether this will hold for the higher frequency band (2-8 Hz) where Pn/Lg appears to have discrimination potential is uncertain. We recommend that available broadband observations of quarry blasts, earthquakes, and nuclear tests be explored using multivariate analysis to establish empirical relations to waveguide characteristics wherever possible. This should be accompanied by development of realistic three-dimensional waveguide modeling capabilties, including short-wavelength inhomogeneities and surface and internal boundary topography, to quantify the existing correlations. Systematic relationships between attenuation properties and waveguide structure also should be explored.

References:

Pan, Y., B. J. Mitchell, J. Xie and J. Ni (1992). Lg coda Q across northern Eurasia, in Proceedings of the 14th Annual PL/Darpa Seismic Research Symposium, 311-317, PL-TR-92-2210, ADA256711.

Xie, X.-B., and T. Lay (1994a). The excitation of explosion Lg: a finite-difference investigation, *Bull. Seism. Soc. Am.*, **84**, 324-342.

Xie, X.-B., and T. Lay (1994b). The scaling law slope of the Lg phase, *Bull. Seism. Soc. Am.*, submitted.

Zhang, T., and T. Lay (1994a). Analysis of short-period regional phase path effects associated with topography in Eurasia, *Bull. Seism. Soc. Am.*, **84**, 119-132.

Zhang, T., and T. Lay (1994b). Effects of crustal structure under the Barents and Kara Seas on short-period regional wave propagation for Novaya Zemlya explosions: Empirical relations, *Bull. Seism. Soc. Am.*, in press.

Zhang, T., and T. Lay (1994c). Why the Lg phase does not travel across oceanic paths, *Bull. Seism. Soc. Am.*, in preparation.

Zhang, T., S. Y. Schwartz, and T. Lay (1994). Multivariate analysis of waveguide effects on short-period regional wave propagation in Eurasia and its application in seismic discrimination, *J. Geophys. Res.*, in press.

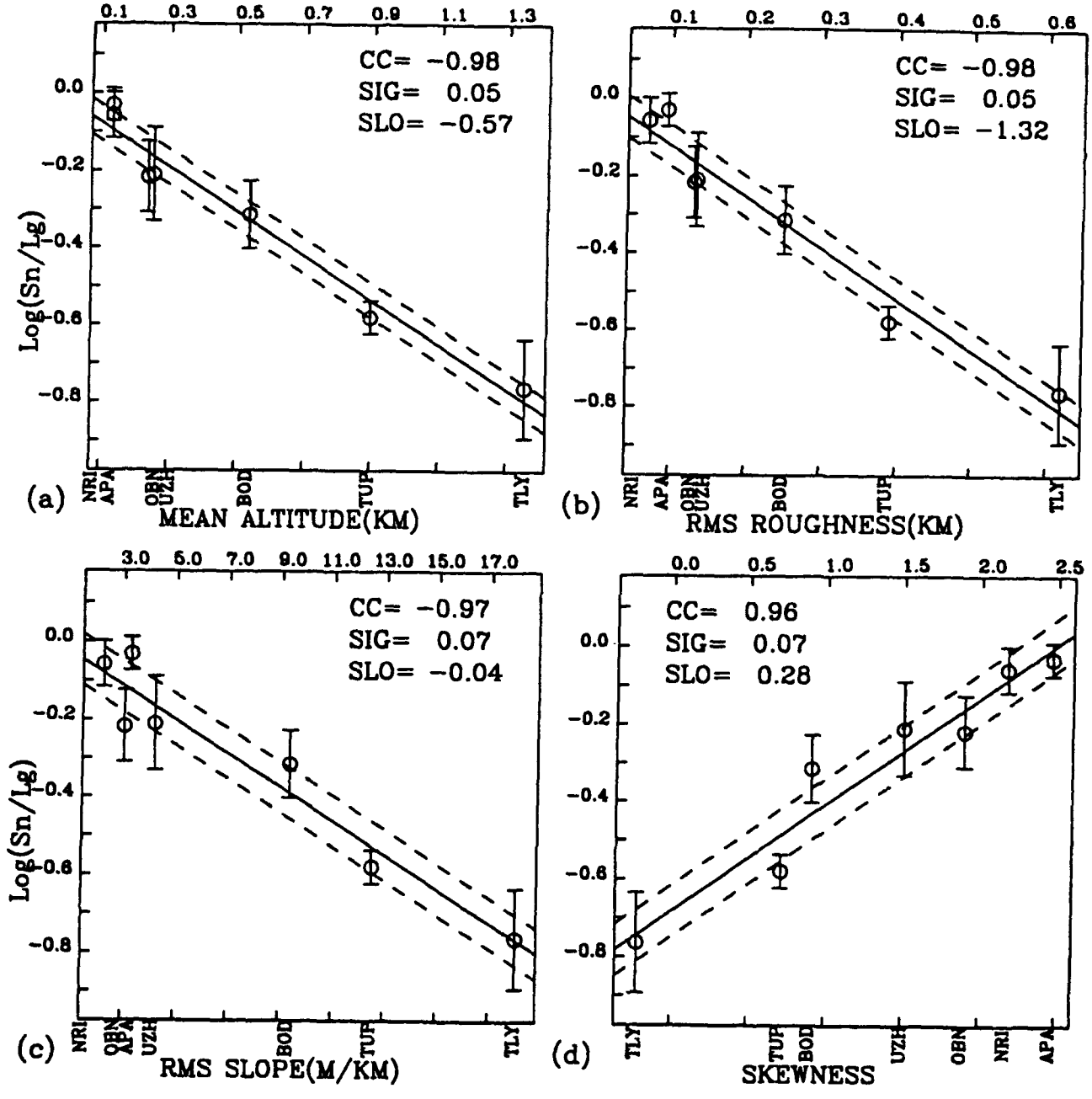


Figure 1. The relationship of Sn/Lg with path topographic character, similar to Figure 3. Note the strong correlations. From Zhang and Lay (199).

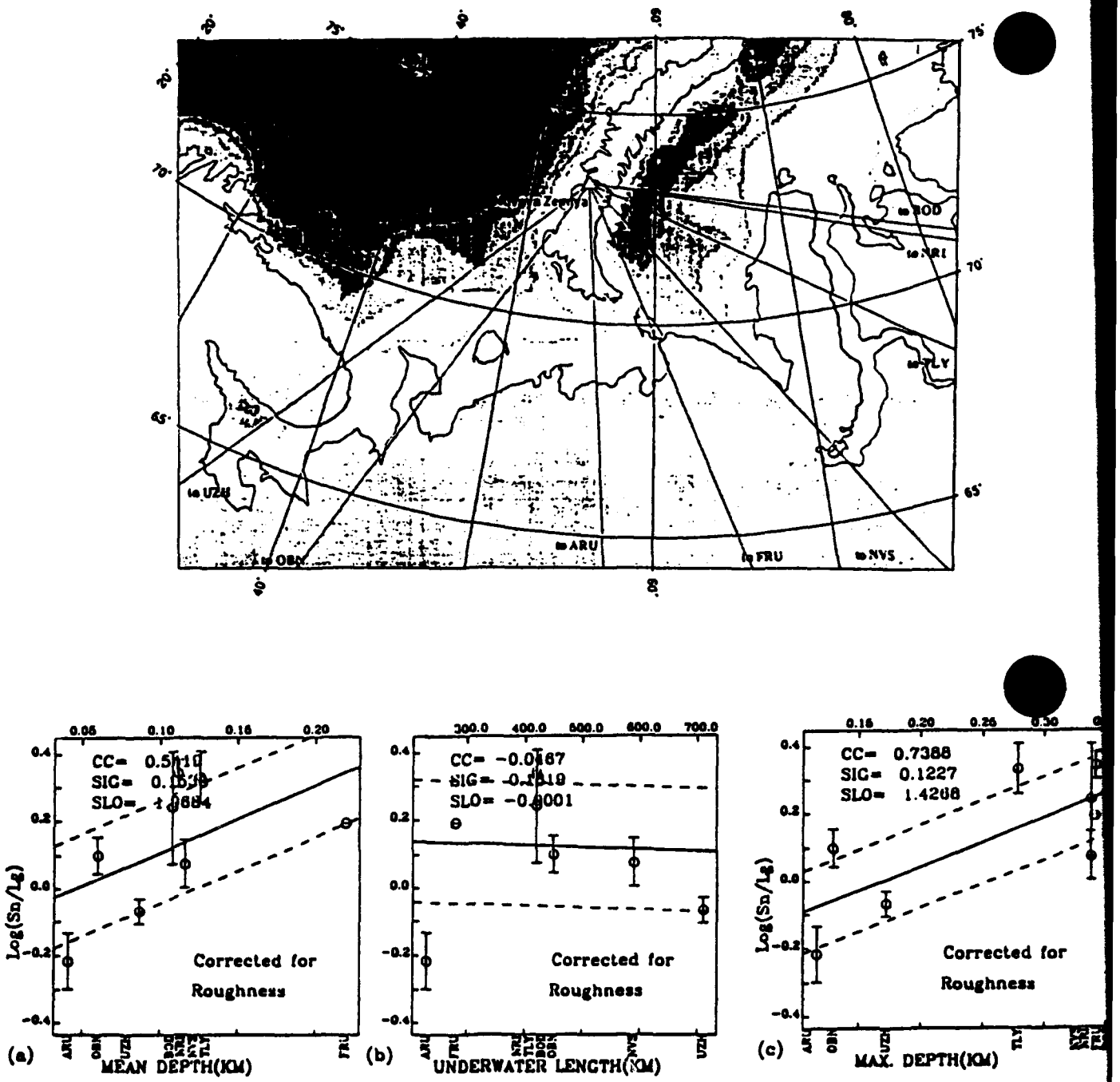


Figure 2. Top: Bathymetric map around the Novaya Zemlya test site, showing great-circle paths to Eurasian stations for which energy partitioning is compared to path properties. Bottom: Plots of Sn/Lg RMS values, corrected for topographic roughness trends using the Eurasian correlations shown in Figure 4, versus (a) mean depth on the underwater leg, (b) length of the underwater leg, and (c) maximum depth of the underwater leg on the path to each station. From Zhang and Lay, 1994b).

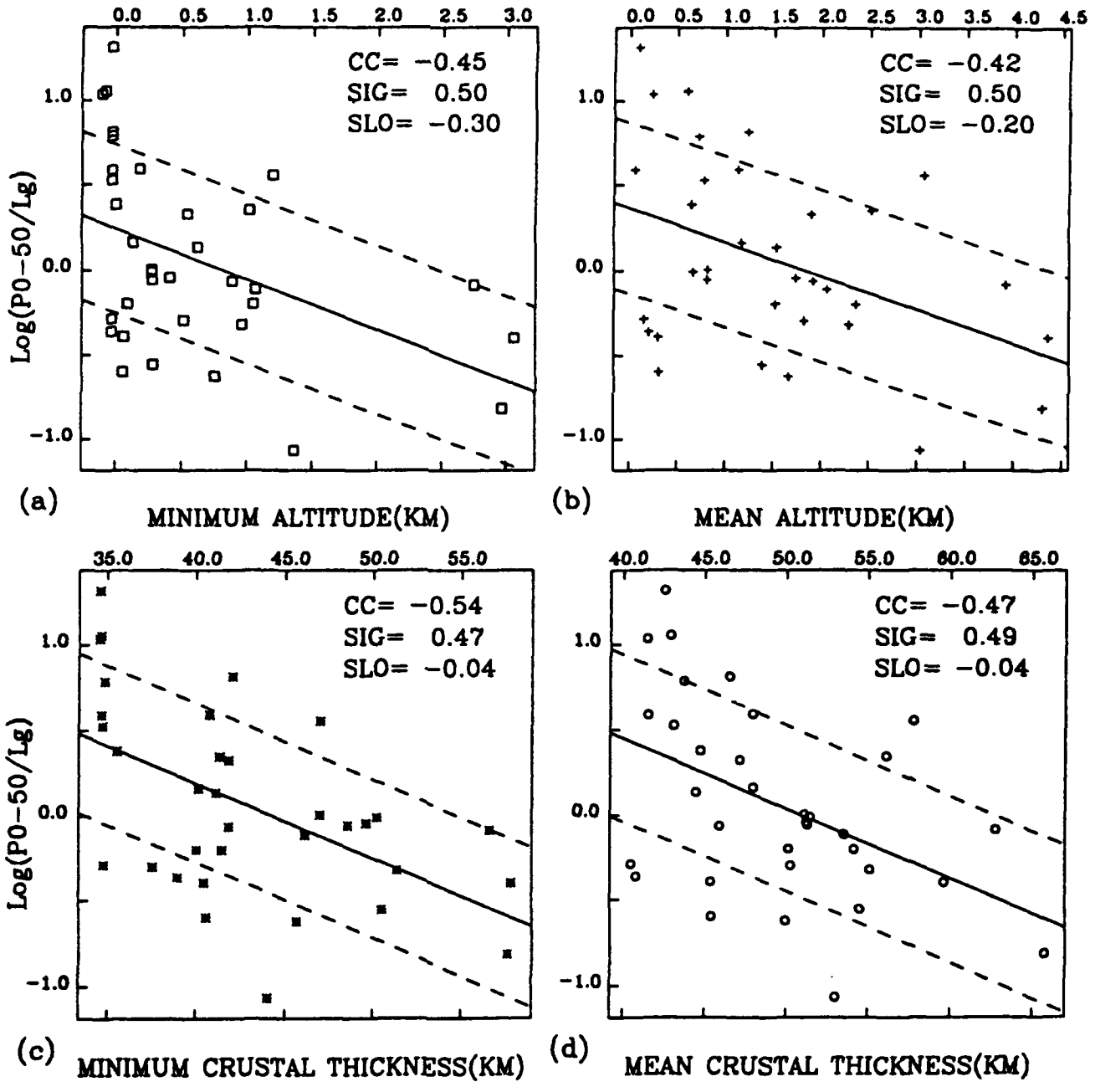


Fig. 3. *Log P/L$_g$* ratio variations with a) minimum and b) mean altitude, c) minimum and d) mean crustal thickness for earthquake data. CC stands for correlation coefficient, SIG is standard deviation of linear correlation, SLO is the slope of the linear regression.

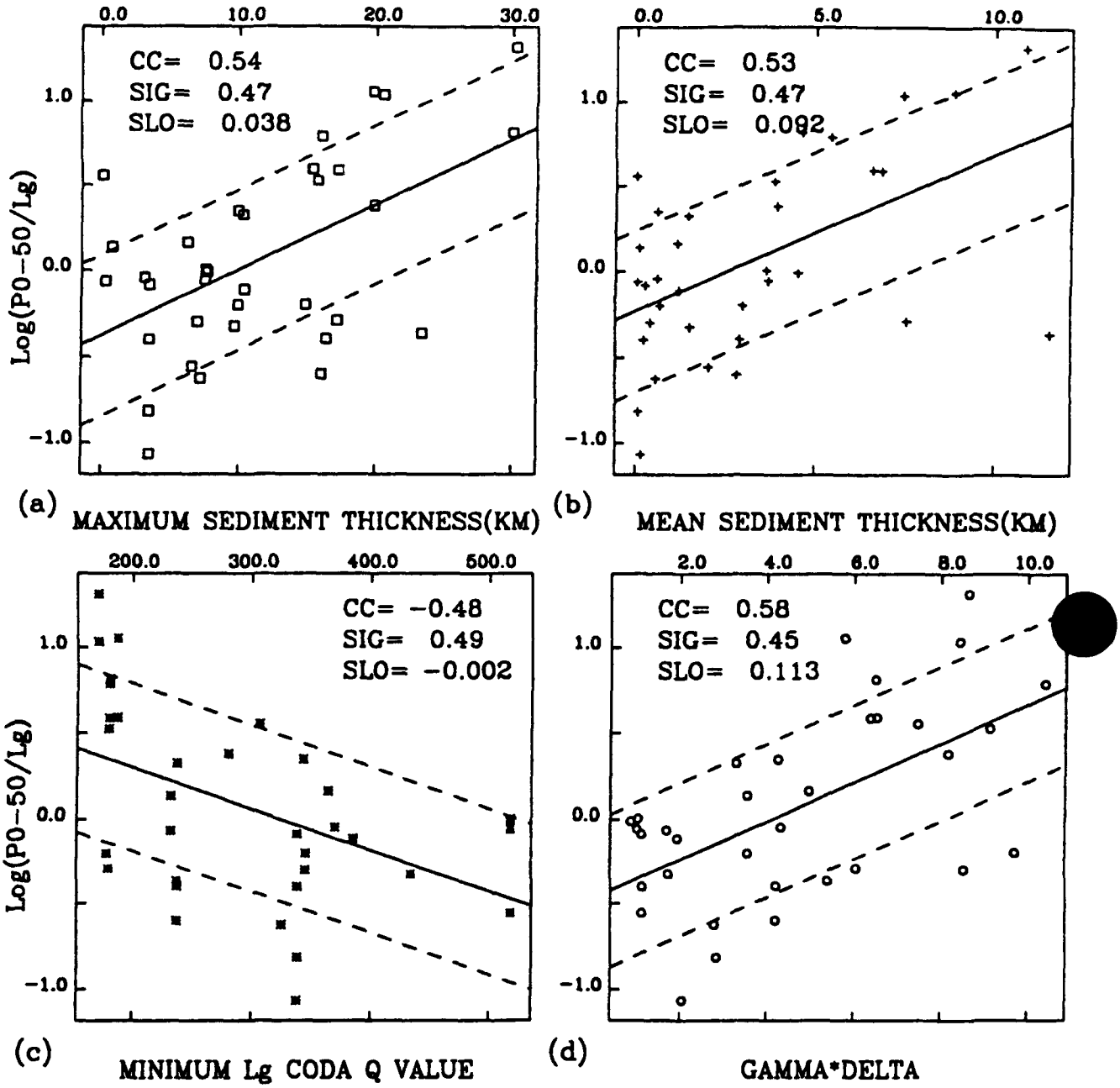


Fig. 4. *Log P/L_g* ratio variations with a) maximum and b) mean sediment thickness, c) minimum Q value and d) the attenuation term $\gamma\Delta$ for earthquake data.

SEISMIC SOURCE CHARACTERIZATION WITH EMPIRICAL GREEN'S FUNCTION AND RELATIVE LOCATION TECHNIQUES

Y. Li, W. Rodi and M. N. Toksöz

Earth Resources Laboratory
Department of Earth, Atmospheric, and Planetary Sciences
Massachusetts Institute of Technology, Cambridge, MA 02139

Contract Nos. F49620-93-1-0424, F49620-94-1-0282

OBJECTIVE

The objective of this project is to assess the usefulness of the empirical Green's function method (e.g. Hartzell, 1978; Mueller, 1985) and relative event location techniques (e.g. Jordan and Sverdrup, 1981) in characterizing and discriminating seismic sources for nuclear monitoring. The principle underlying these methods is that relative properties between events can be extracted from regional and teleseismic data more reliably than the absolute properties of the events when path propagation effects are not accurately known. We seek to determine the practical requirements for this principle to hold, and to develop relative source parameter estimation techniques that are useful for seismic event discrimination.

RESEARCH ACCOMPLISHED

The work reported here is a continuation of earlier research reported by Toksöz *et al.* (1993). In this paper we apply the empirical Green's function (EGF) method in two ways. First, we use it in the conventional way to estimate the source time functions of several events in central Asia, including both nuclear explosions and earthquakes. Second, we apply the EGF method to directly compare earthquakes and explosions. The results of doing the latter does not strictly isolate relative source parameters from earth structure effects but may still lead to a basis for event discrimination. The last section of the paper tests the hypothesis that a relative event location approach exploiting waveform information can achieve good teleseismic location accuracy with only a small number of stations.

Nuclear Explosions and Earthquakes in Central Asia

Relative source time functions (RSTF) have been estimated for five underground nuclear explosions and nine earthquakes in central Asia by using regional and teleseismic P waveforms of nearby smaller events as empirical Green's functions. Two of the explosions are at the Kazakhstan test site (KTS) and the other three are at the Xinjiang test site (XTS). RSTFs of the five explosions (m_b=5.3 to 6.5) are each dominated by a simple pulse with a source duration of 0.4 to 0.8 s (Figure 1a), reflecting the rapid energy release over a small volume. We estimated the RSTF of one of the explosions (920521, m_b=6.5) with three different EGF events to test consistency (Figure 1a). Two explosions have a significant secondary pulse with a pulse width similar to that of the first pulse. The secondary phases are associated with the spall slapdown phenomenon. The total source durations of the five explosions range from 0.4 to 1.6 s.

In contrast, RSTFs of earthquakes (m_b=5.5 to 6.6) in the vicinity of these test sites typically comprise multiple source pulses with a total source duration from a few to several tens of

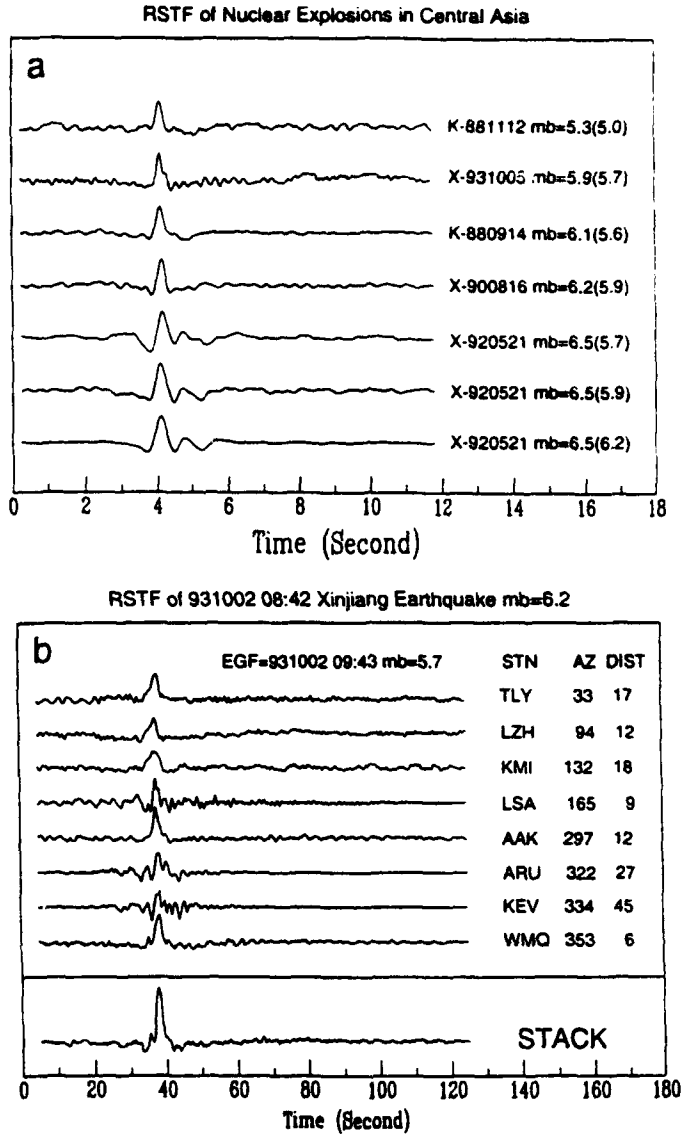


Figure 1: (a) Estimated RSTFs of two explosions at KTS and three explosions at XTS. The source durations for the five explosions range from 0.4 to 1.6 s. The numbers in brackets are m_b magnitude for the EGF events. The three bottom traces are RSTFs of the 920521 explosion estimated with three different EGF events. (b) Eight single station estimates of RSTF for Xinjiang earthquake (931002, m_b = 6.2) and the stacked RSTF trace. The total source duration of the event is about 9 s. Note that the time scales in frames (a) and (b) differ by a factor of 10.

seconds, indicating the complex source process involves a fault dimension of several tens of kilometers. The RSTF of the 931002 earthquake (m_b=6.2) in southern Xinjiang was estimated using the regional and teleseismic broadband P waveforms at eight stations from a nearby aftershock (m_b=5.7) as the EGFs. These single-station estimates were stacked to obtain an averaged RSTF (Figure 1b). The mainshock consists of two subevents: a smaller precursor followed by a larger one 2 s later. The total relative source duration of the mainshock is about 9 s. The location of the earthquake pair is about 300 km south of XTS. This result and other events we analyzed show that the time duration and structure of RSTFs estimated with the EGF method easily discriminate large explosions from moderate earthquakes (m_b > 5.5) in

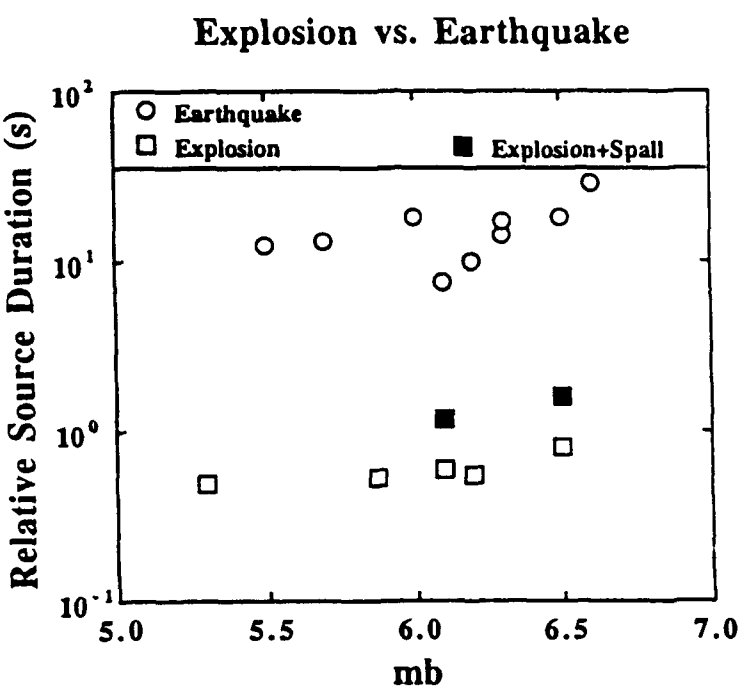


Figure 2: Comparison of relative source durations for earthquakes and explosions in central Asia. Note that the source durations for explosions are typically less than those of earthquakes with the same magnitudes by a factor of about 10.

central Asia (Figure 2).

Nuclear Explosions as EGF Events

To further investigate the potential use of the EGF method in nuclear monitoring and discrimination, we used the seismograms of small explosions as EGFs and deconvolved them from the seismograms of earthquakes. The results of this deconvolution are strictly not a relative source time function but can be considered an "apparent source time function" (ASTF). Our hope is that the difference between such ASTFs and the RSTFs of explosions can be the basis for event discrimination. Figure 3a shows broadband, vertical-component seismograms for four XTS explosions (920521, 900816, 931005, and 940610, m_b = 5.7 to 6.5) and two Xinjiang earthquakes (931002-0842 and 931002-0943, m_b = 6.2 and 5.7) recorded at station COL, which is about 60 degrees from XTS. The locations of the two earthquakes are about 300 km south of the XTS. We used the smallest explosion (940610, m_b = 5.7) as the EGF event and deconvolved its seismogram from those of the three larger explosions and the two earthquakes. Figure 3b shows the deconvolution results. For explosions, the RSTF of the each event consists of a simple pulse with duration of 0.45 to 1.6 s. For the 931002-0943 earthquake (m_b = 5.7), the ASTF trace shows two secondary pulses with different polarities following the first pulse. The secondary pulses are associated with the depth phases (pP and sP). The deconvolution trace of the 931002-0842 earthquake (m_b = 6.2) shows an even more complex structure and longer duration. We interpret that the complex structure is caused by the combined effects of the depth phases and a complex source time function of the earthquake (Figure 1b).

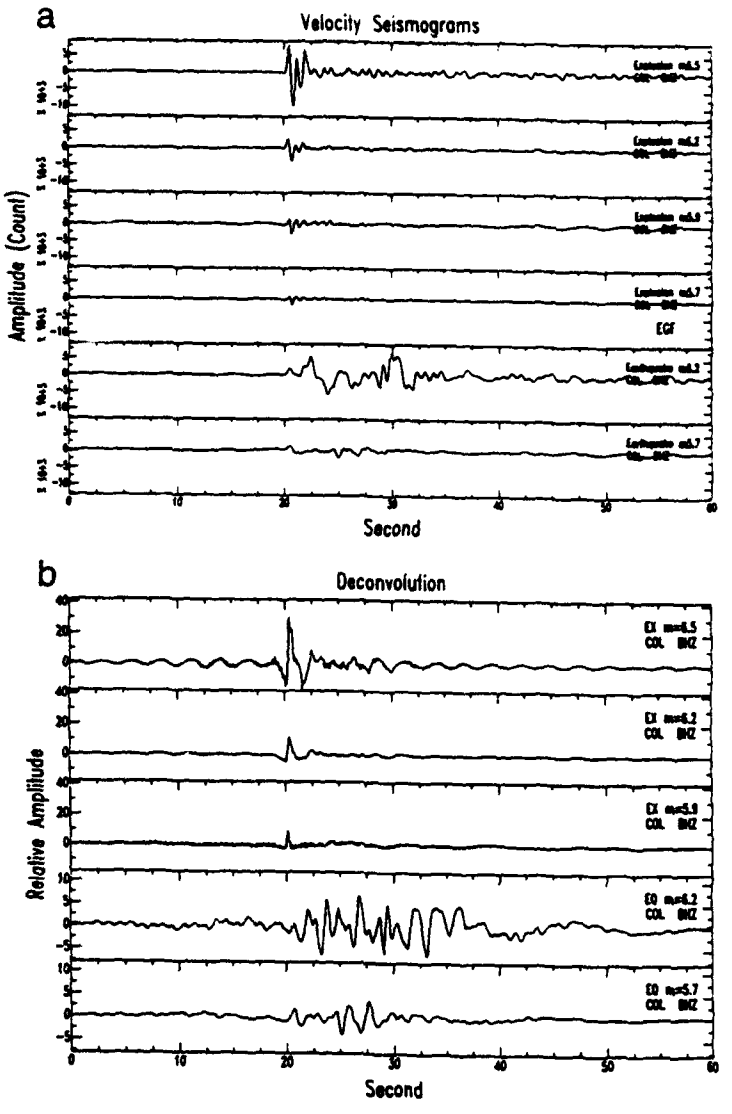


Figure 3: (a) Broadband, vertical component seismograms recorded at station COL for four nuclear explosions at XTS and two earthquakes in southern Xinjiang. The waveforms of the smallest explosion $m_b = 5.7$ was used as the EGF. (b) Apparent STFs for the explosions and earthquakes. Note the complex structure and longer duration of the deconvolution results for the earthquakes.

Comparison of Local Earthquakes and Quarry Blasts

The goal of monitoring the CTBT is to detect, locate, and identify explosions, blasts, and earthquakes as small as $m_b = 2.5$. We explore the possibility of using the EGF method to distinguish quarry blasts and earthquakes at local distance. Figure 4a shows the locations of two earthquakes ($m_c = 3.1$ and 2.8) and seven quarry blasts ($m_c = 1.4$ to 2.0) at Littleton, Massachusetts, as well as the location of a short-period station (DNH) of the MIT seismic network. The epicentral separations among the events are about 5 km and the depths of the earthquakes are estimated to be a few to ten kilometers. The epicentral distance to station DNH is about 70 km. Short-period, vertical component seismograms of the two earthquakes and three larger blasts ($m_c = 1.9$ and 2.0) are shown in Figure 4b. We stack the seismograms of

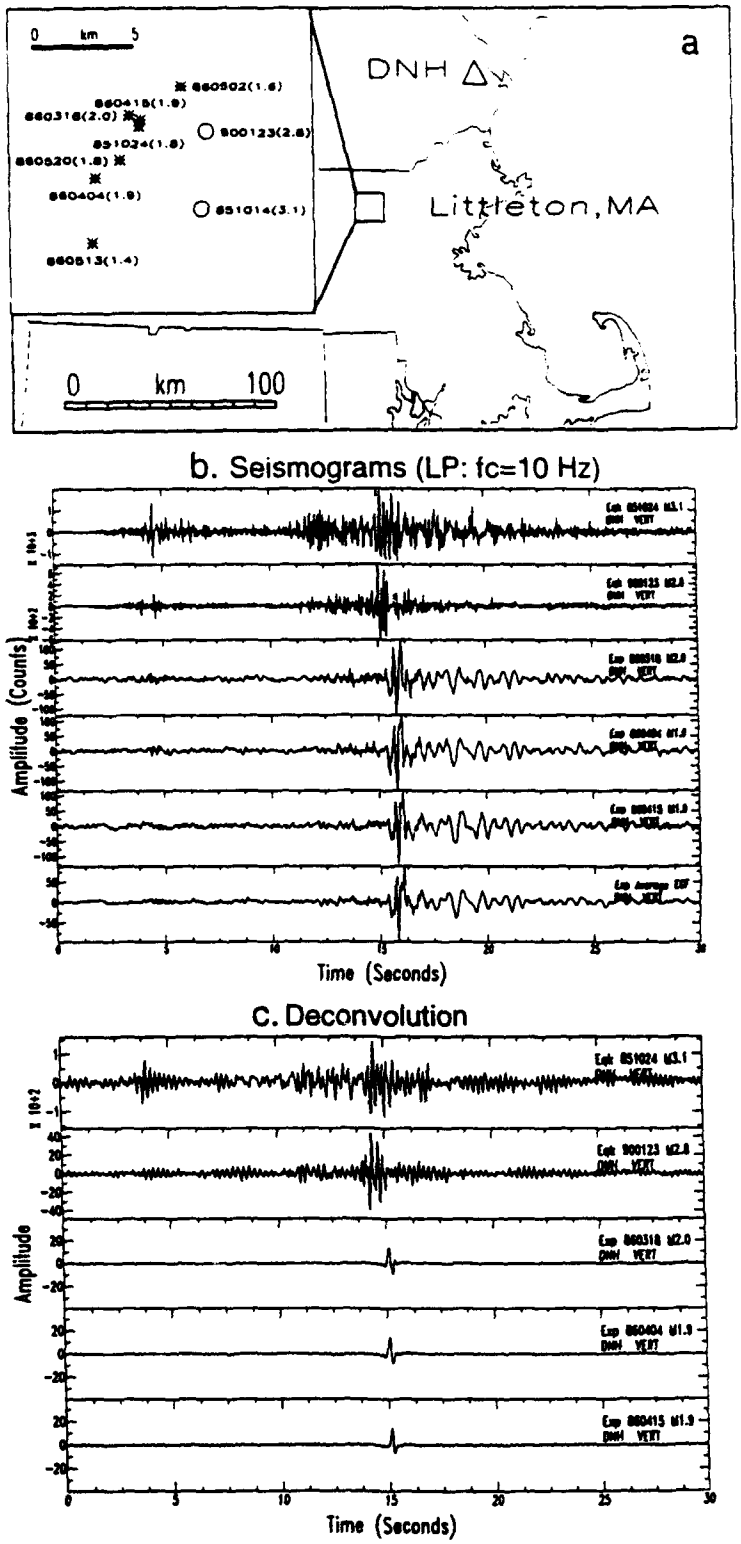


Figure 4: (a) Locations of quarry blasts (stars) and earthquakes (circles) at Littleton, MA and seismic station DNH. The numbers are events' ID and duration magnitudes. (b) Short-period, vertical component seismograms of two earthquakes and four blasts at Littleton, MA, recorded at station DNH. The bottom trace is used as the EGF. (c) Deconvolution results. Note the difference between the earthquakes and quarry blasts.

the seven blasts to obtain an average seismogram for the quarry blasts, plotted at the bottom of Figure 4b. The stacked seismogram was used as the EGF and deconvolved from seismograms of the larger blasts and earthquakes to obtain ASTFs for the events (Figure 4b). The RSTFs of the blasts are simple pulses while the ASTFs of the earthquakes show a complex structure. The secondary phases are probably related to depth phases, complex structure near the source and complexity of the source itself. This example suggests that the EGF method may be a useful tool for discriminating small earthquakes from quarry blasts.

Relative Locations of Balapan Explosions

Our relative location approach uses cross correlation of waveforms to determine accurate differential arrival times between pairs of events in a cluster. Differential times from multiple stations and phases are inverted to determine the event location pattern within the cluster. We have applied this method to teleseismic data from explosions occurring from 1987 to 1988 at the Balapan test site in Kazakhstan. Thurber *et al.* (1993) located these explosions with high accuracy (100 m) using satellite images. We determined differential arrival times for P and, in some cases, PcP phases for ten teleseismic stations and five of the well-located explosion (see Figure 5a). The event pair used for each differential time comprised a common reference event (event 94) and one the remaining four events. The data set totaled 47 differential arrival times.

Figure 5b compares our locations based on differential arrival times to the locations determined by Thurber *et al.* (1993), which we consider to be the true locations of the explosions. For comparison, we have shifted our location pattern so that the reference event (94) resides at its true location. We see that the locations of the remaining four events differ from their true locations by 2–3 km. The location pattern is basically correct and differs primarily in size rather than relative positioning of events. The larger size of our cluster may be due to the use of global traveltime tables in the inversion, which do not reflect the correct local velocity structure for the Balapan site.

This result shows that relative event location based on waveform correlation can achieve, with a small number of data, relative location accuracies which are comparable, or better, than those resulting from much larger data sets of absolute arrival time picks.

CONCLUSIONS AND RECOMMENDATIONS

Our results to date show that relative location and EGF methods are of potential value for nuclear monitoring. By using waveform information, our location method achieves good location accuracy with sparse data, compared to conventional location methods. Further, we have shown that source duration, as estimated by the EGF method, effectively discriminates large explosions and earthquakes. We have also shown that the EGF method can be adapted to directly compare earthquake and explosion seismograms, thus expanding the potential applicability of the method for discrimination. We recommend that these methods of relative source parameter estimation be tested further with an eye towards their use in discrimination of small events from regional data.

REFERENCES

Hartzell, S., 1978. Earthquake aftershocks as Green's functions, *Geophys. Res. Lett.*, *5*, 1–4.

Jordan, T.H. and Sverdrup, K.A., 1981. Teleseismic location techniques and their application to earthquake clusters in the south-central Pacific, *Bull. Seism. Soc. Am.*, *71*, 1105–1130.

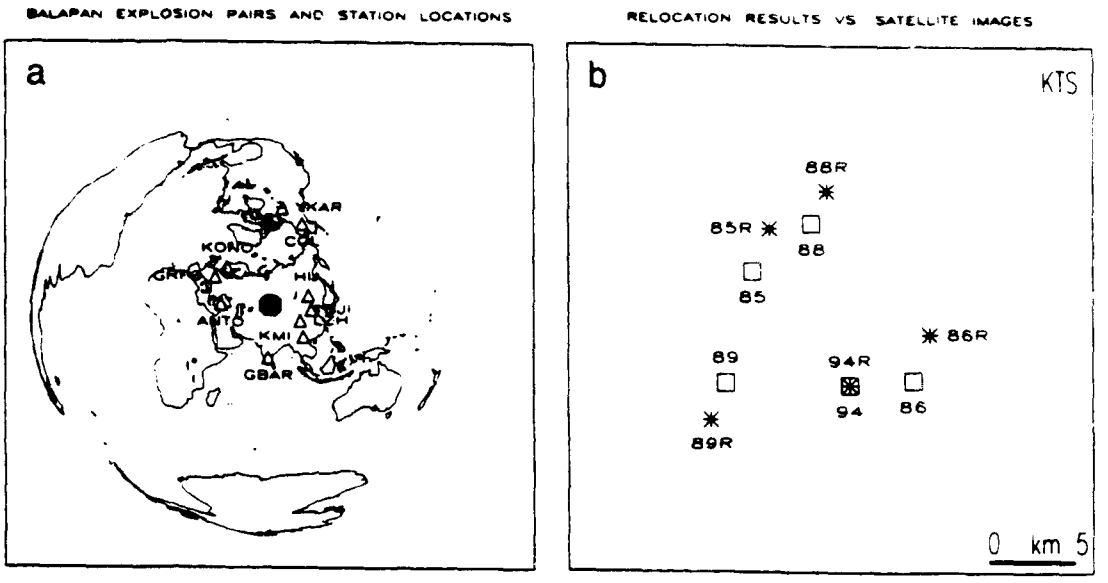


Figure 5: (a) Map of the world showing locations of the five Balapan nuclear explosions (circles) at KTS and locations of the seismic stations (triangles) used in this study. (b) Comparison of our relocation results (stars) with the locations determined with the satellite image analysis by Thurber *et al.* [1993].

Mueller, C., 1985. Source pulse enhancement by deconvolution of an empirical Green's function, *Geophys. Res. Lett., 12,* 33–36.

Thurber, C.H., Quin, H.R., and Richards, P.G., 1993. Accurate locations of explosions in Balapan, Kazakhstan, 1987 to 1989, *Geophys. Res. Lett., 20,* 399–402.

Toksöz, M.N., Li, Y., and Rodi, W., 1993. Seismic source characterization with empirical green's function and relative location techniques, *Papers Presented at the 15th Annual PL/ARPA Seismic Research Symposium*, Vail, Colorado, PL-TR-93-2160, ADA271458.

Seismic Studies of the Caspian Basin and Surrounding Regions

Stephen Mangino and Keith Priestley

Department of Earth Sciences
Bullard Laboratories
University of Cambridge
Cambridge CB3 0EZ, England

Contract No. F49620-92-J-0475

Objective

Our objective is to characterize the crust and upper mantle velocity structure of the south Caspian Basin using both body-wave receiver function and surface wave dispersion techniques. To accomplish this we installed a network of 6 digital three component seismic stations in the former Soviet republics of Turkmenistan and Azerbaijan. This extended abstract describes the Caspian Seismograph Network (CSN) and discusses some observations and preliminary results.

Research Accomplished

During May, June, and December 1993 we installed a network of 6 three-component seismograph stations in the former Soviet republics of Turkmenistan and Azerbaijan. The Turkmenian stations are located near Krasnovosdk (KRV), Nebit Dag (NBD), Dana Tag (DTA) and Kizyl Atrek (KAT) (Figure 1). In Azerbaijan the stations are located near Lenkoran (LNK) and Baku (BAK) (Figure 1). In June 1994 we relocated the BAK station 100 km west to Shemaha (SHE). The Turkmenian stations are operated in cooperation with Dr. B. Karryev from the Institute of Seismology of Turkmenistan, and the Azerbaijan stations are operated in cooperation with Dr. S. Agamirzoev from the Geophysical Expedition of Azerbaijan. In addition to CSN data our research incorporates data from the IRIS seismograph station near Ashkabat, Turkmenistan (ABKT) (Figure 1).

Data at each CSN station is recorded on a Refraction Technology 72a-02 data logger that is equipped with either Omega or GPS timing and an external hard disk. Four stations (KRV, DTA, KAT and LNK) record ground motion using a Guralp CMG-3T triaxial broadband (BB) feedback seismometer. Stations NBD, BAK and SHE have three component Teledyne SL-210/220 long period (15 second free period) (LP) pendulum seismometers. All stations record data continuously. To determine the instrument transfer function each station is calibrated with a simple step function, a cosine function, and a pseudo-random binary input. The pseudo-random binary input (RB) (Berger et al., 1979) consists of a series of fixed amplitude step functions which vary randomly in duration. These calibrations were done in order to determine the instrument response to an accuracy of 1 percent in amplitude and 1° in phase.

The task of data processing and archival can be summarized into three steps. First, all CSN raw data files are permanently archived to tape. The amount of raw data, depending on station 'uptime' can exceed 2 Giga bytes for every two months of network operation. Second, individual events are identified with respect to the Preliminary Determination of Epicenter (PDE) and Quick Epicentral Determination (QED) Bulletins. Third, the data is converted into SAC format and all file headers are updated with the appropriate source and station information. A number of local and regional events have also been recorded that are not identified in either the PDE or QED. To date we have recorded a sufficient amount of data for a detailed receiver function analysis beneath most stations, and anticipate by the

conclusion of the experiment enough common great-circle path surface wave data for a detailed surface wave analysis of the region between each station.

Previous Work

The south Caspian Basin is an anomalous aseismic depression that is surrounded by active fold and thrust belts that are part of the east-west trending Alpine-Himalayan Belt. The Basin is bounded to the north by a narrow seismogenic zone extending from the Caucasus Mountains in Azerbaijan, through the Apsheron-Balkhan Sill, to the Kopet Dag Mountains of Turkmenistan. To the west in Azerbaijan and to the south along the Iranian border the Basin is bounded by the active fold and thrust belts of the Talesh and Alborz Mountains, respectively. Located to the east of the Caspian Sea are the Turkmenian Lowlands which are structurally a part of the south Caspian Basin.

Deep seismic sounding data collected in the early 1960's suggests that the crust of the south Caspian Basin and west Turkmenian Lowlands consists of 2 layers; a thick sedimentary layer (15-20 km) with a P-wave velocity of 3.5-4.0 km/s which overlies a 12-18 km thick 'basaltic' layer with a P-wave velocity of 6.6-7.0 km/s (Neprochnov 1968; Rezanov and Chamo, 1969). It has been suggested that the south Caspian Basin represents a section of 'ocean-like crust' that may be either a relic of an older Paleozoic-Triassic ocean, or alternatively a marginal sea which developed behind a Mesozoic-Paleogene ocean (Berberian and King 1981; Berberian 1983). The 'ocean like' crust hypothesis is supported by the observation of L_g blockage and efficient S_n propagation for the paths that cross the south Caspian Basin (Kadinsky-Cade et al., 1981). The northward movement of the Iranian plate with respect to the Eurasian plate is causing compressional deformation throughout this region (Jackson and McKenzie 1984). A focal mechanism analysis of earthquakes that occurred within the seismic belts bordering the Basin suggest that the crustal shortening between Iran and Eurasia is being accommodated primarily along thrust and strike-slip faults in the Alborz and Talesh Mountains, and to a lesser extent, by northern Caspian continental crust thrust over the south Caspian Basin 'ocean-like' crust (Priestley et al., 1994).

Receiver Function Analysis: CSN Station NBD

The source equalization method of (Langston 1979; Ammon 1991) is used to isolate the converted shear phases which are primarily recorded on the horizontal components of ground motion. Individual or stacked radial component receiver functions are then used to estimate the receiver structure with models composed of either vertically heterogeneous and laterally homogeneous horizontal layers, or two-dimensional models composed of planer dipping layers. Key indicators of planer dipping structure beneath a recording station are: (1) a systematic polarity variation of scattered energy on the tangential response as a function of azimuth; and (2), a moveout with respect to the direct P-wave, of multiply reflected and converted phases as a function of the incident P-wave azimuth to the dipping layer (Langston 1977). A primary concern is the contamination of the radial receiver function with scattered energy which can be estimated by analysis of the tangential receiver function. By varying the width of the Gaussian filter in the source equalization procedure, all, or part of the bandwidth available can be examined. In some cases, lower frequency receiver functions are simpler than their higher frequency counterparts (Mangino et al., 1993) and are potentially less-biased by small scale (relative to wavelength) lateral heterogeneity.

To model the crust and upper mantle structure beneath station NBD the time domain inversion procedure of Ammon et al. (1990) is employed. The data is linearized in a Taylor series about the starting model, obtained from forward modelling. Each model layer is perturbed and a waveform derivative is determined for each perturbation. The L_2 norm between the model synthetic receiver function and the observed data, with a side constraint of model smoothness, is then minimized. A Poisson's ratio of 0.25 is used to relate P- to S-wave velocity. The resulting solution model synthetics that do not fit the most coherent

phases in the data are discarded, and the remaining solution models represent the crustal structure beneath the station. It is important to recognize a limitation of this technique's inability to constrain absolute depth-to-interface velocity. Herein lies the importance of apriori information which can be used to select a model or 'family' of models if a range solution models exist.

Figure 2 shows the NBD radial and tangential (0.01-0.5 Hz) receiver functions. Large amplitude arrivals present on the NBD radial response indicate the receiver structure beneath NBD contains prominent velocity contrasts. In comparison with the radial, motion on the tangential is low for the north-easterly backazimuths. This is consistent with, but not necessarily limited to, the response of one-dimensional model. The difference between the radial and tangential response as a function of azimuth suggests some lateral heterogeneity. As backazimuth increases to more easterly approaches, motion on the tangential between 12-14 seconds increases and eventually exceeds the motion on the radial receiver function. For the present analysis, the 41° backazimuth two event stack is modelled in detail below.

Figure 3 shows the inversion results for the NBD 2 event stack. The most important model features are a strong positive gradient from the surface to 4 km depth, a 3-4 km thick high velocity layer, and a strong decrease in velocity between 8-9 km depth. Between 10 to 20 km depth, the 'mid-crust' average velocity is between 5.8-6.2 km/s. At a depth of 20-24 km, velocity increases to 6.8-7.2 km/s, and has a positive gradient through the 'lower crust' to a depth of 34 km, where velocity jumps by 0.5 km/s to 8.0-8.2 km/s. The most prominent and suspect model feature is the 4 km thick high velocity layer in the upper crust. This 'layer' is the most significant contributor to the large amplitude arrivals in the first 10 seconds of data. The broad direct arrival is matched with Ps conversions from the top of the positive gradient in layers 1-4. The large negative motion between 2-3 seconds are fit with reverse polarity Ps conversions from the base of the shallow high velocity layer. First order multiples from the top and bottom of this 'layer' also contribute to the response. Direct comparison of the radial and tangential response (Figure 2) indicate the shear wave energy is predominately confined within the vertical plane. Therefore, it is difficult to attribute this model feature to an artifact of scattering. Speculation on the significance of this 'layer' within a relatively simple crustal structure is premature until the adjacent stations are modelled in detail.

Surface Wave Observations

Shown in Figure 4 are vertical component seismograms from a mid-Atlantic ridge earthquake that were recorded at stations LNK and KRV. These stations lie on almost the same great circle path from the epicenter and both stations have identical instrumentation. Previous analysis of short-period seismograms has shown that the higher frequency (0.5-2.0 Hz) crustal phase L_g is not observed for paths that cross the south Caspian Basin (Kadinsky-Cade et al., 1981). Figure 4 shows that both the shorter period and longer period surface wave train is strongly attenuated or scattered across the south Caspian Basin.

Conclusions and Recommendations

A receiver function and surface wave analysis of CSN and ABKT data is currently in progress. The main advantage of modelling the lithosphere using these techniques lies in the relatively low cost and logistical simplicity compared with active source seismic reflection and refraction surveys. Upon completion of this research, in light of what we have learned from the body and surface wave analysis, the next logical step is to examine regional phase propagation across the study area. To date we have recorded over 110 local and regional events. Shown in Figure 5 are the local and regional raypaths for the first 9 months of network operation. Analysis of this unique data set, as well as using data from nearby stations should enable us to characterize and develop un-biased discriminats based on regional phases that do not include the effects of averaging over large distances.

Reference

Ammon, C. J., The isolation of receiver effects from teleseismic P waveforms, *Bull. Seism. Soc. Am.*, **81**, 2504-2510, 1991.

Ammon, C. J., G. E. Randall and G. Zandt, On the resolution and non-uniqueness of receiver function inversions, *J. Geophys. Res.*, **95**, 15303-15318, 1990.

Berberian, M., The southern Caspian: A compressional depression floored by trapped, modified oceanic crust, *Can. J. Earth Sci.*, **20**, 163-183, 1983.

Berberian, M. and G. C. P. King, Towards a paleogeography and tectonic evolution of Iran, *Can. J. Earth Sci.*, **18**, 210-265, 1981.

Berger, J., D. C. Agnew, R. L. Parker and W. E. Farrell, Seismic system calibration: 2. Cross-spectral calibration using random binary signals, *Bull. Seism. Soc. Am.*, **69**, 271-288, 1979.

Jackson, J. A., and D. McKenzie, Active tectonics of the Alpine-Himalayan Belt between western Turkey and Pakistan, *Geophys. J. R. Astr. Soc.*, **77**, 185-264, 1984.

Kadinsky-Cade, K., M. Barazangi, J. Oliver, and B. Isacks, Lateral variations of high-frequency seismic wave propagation at regional distances across the Turkish and Iranian Plateau's, *J. Geophys. Res.*, **86**, 9377-9369, 1981.

Langston, C. A., The effect of planer dipping structure on source and receiver responses for constant ray parameter, *Bull. Seism. Soc. Am.*, **67**, 713-724, 1977.

Langston, C. A., Structure under Mount Rainier, Washington inferred from teleseismic body waves, *J. Geophys. Res.*, **84**, 4749-4762, 1979.

Mangino, S. G., G. Zandt and C. J. Ammon, The receiver structure beneath Mina, Nevada, *Bull. Seism.. Soc. Am.*, **83**, 542-560, 1993.

Neprochnov, Y. P., Structure of the earth's crust of epi-continental seas: Caspian, Black, and Mediterranean, *Can. J. Earth Sci.*, **5**, 1037-1043, 1968.

Owens, T. J., and R. S. Crosson, Shallow Structure effects on Broadband Teleseismic P Waveforms, *Bull. Seism.. Soc. Am.*, **78**, 96-108, 1988.

Priestley, K., C. Baker and J. Jackson, Implications of earthquake focal mechanism data for the active tectonics of the south Caspian Basin and surrounding regions, *Geophys. J. Int., (in press)*, 1994.

Rezanov, I. A. and S. S. Chamo, Reasons for absence of a 'granitic' layer in basins of the South Caspian and Black Sea type, *Can. J. Earth Sci.*, **6**, 671-678, 1969.

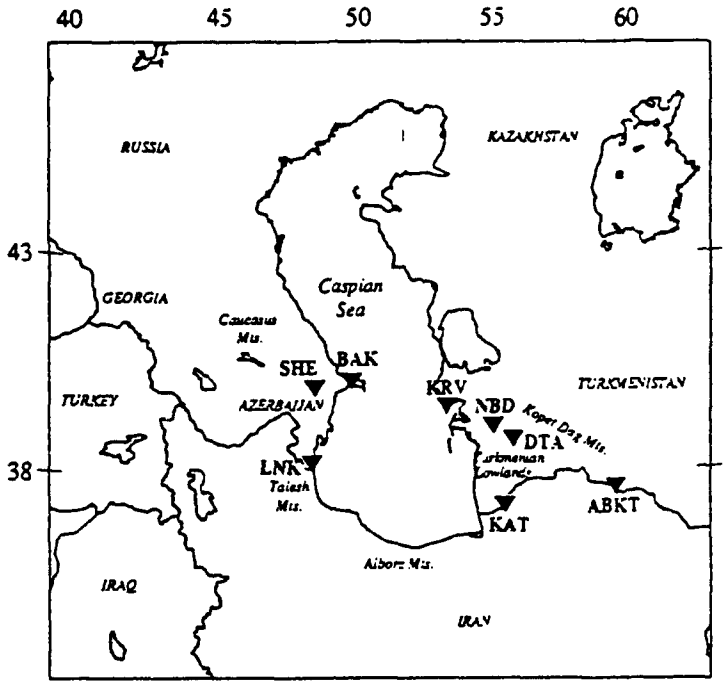


Figure 1. Map of the Caspian Sea and surrounding regions

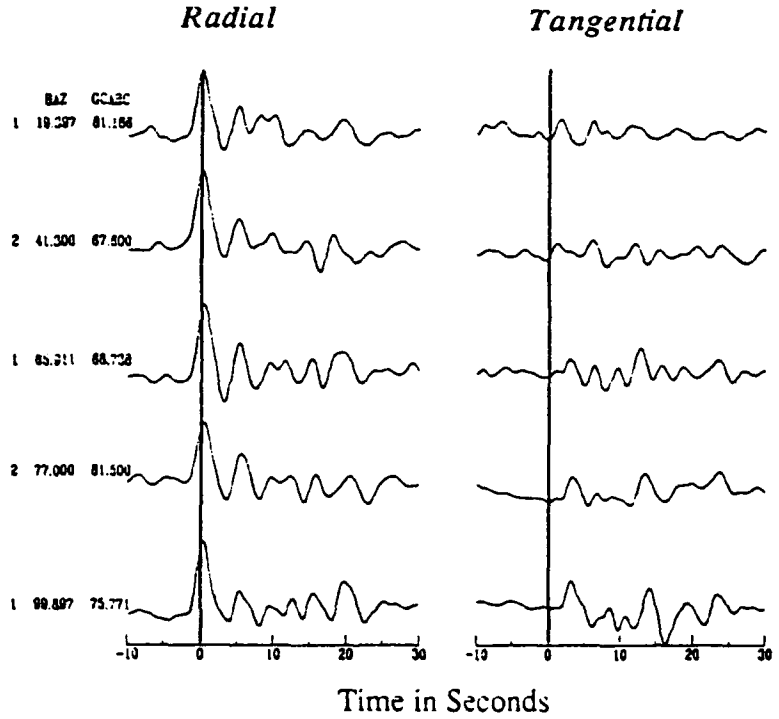


Figure 2. NBD receiver functions clockwise from north about the station, relative amplitudes are preserved. The number of events stacked, epicentral distance and backazimuth is shown at left of each trace pair.

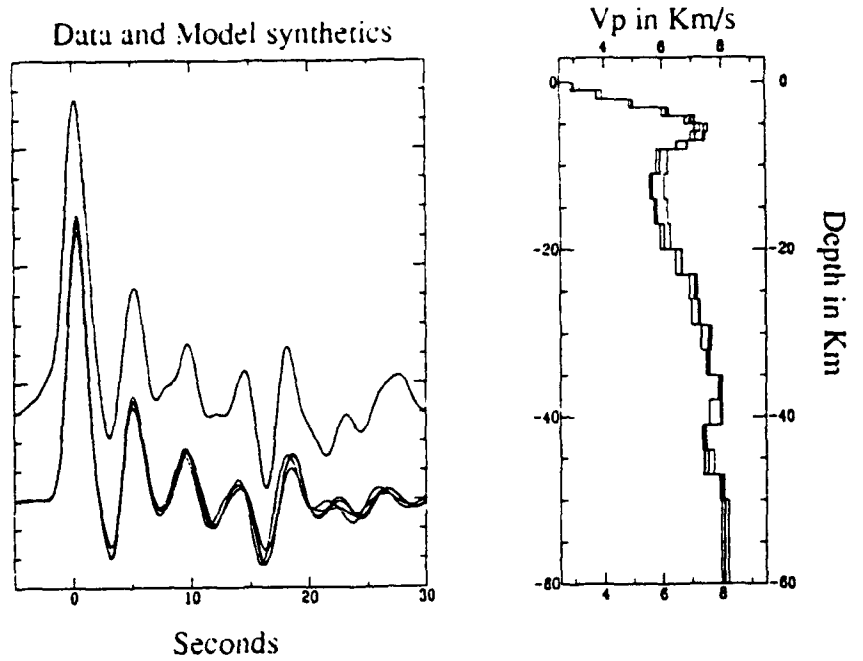
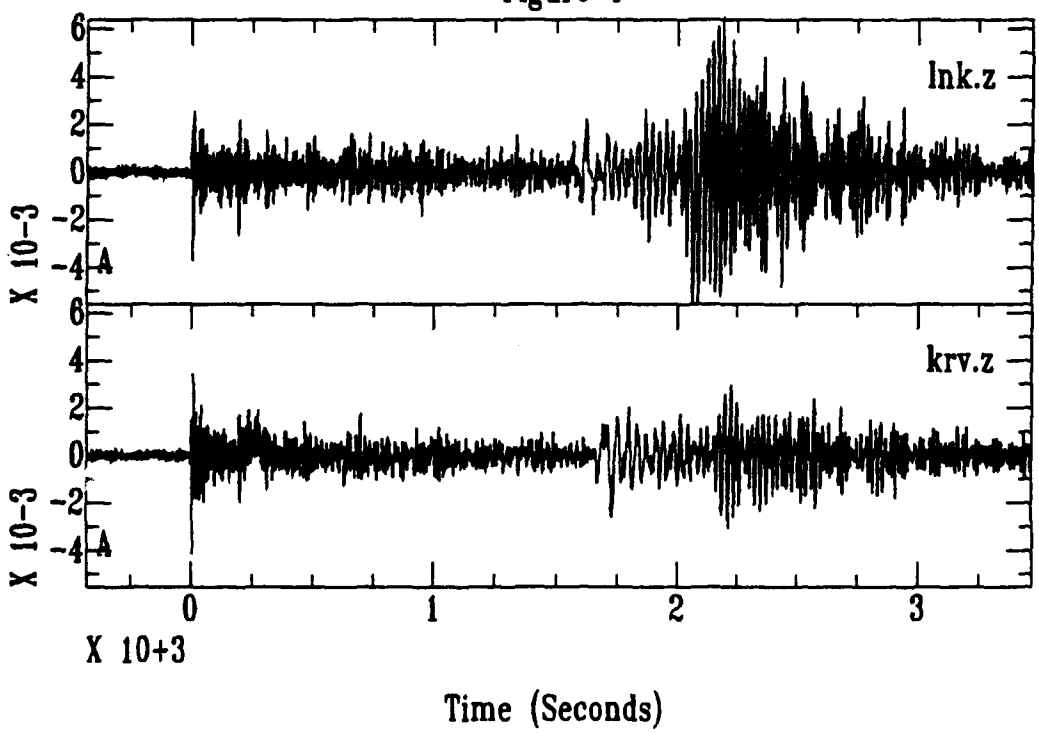
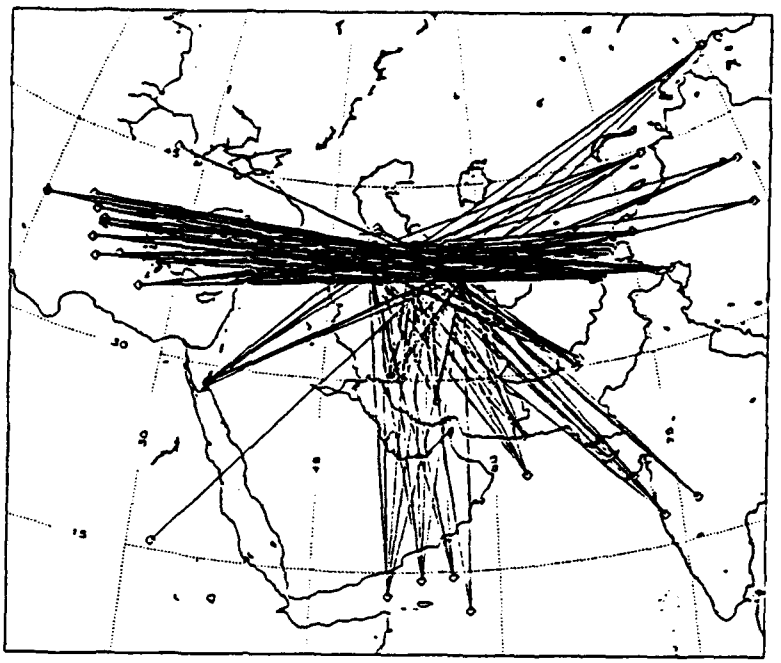


Figure 3. Inversion results for station NBD (right), and the model synthetic receiver functions (lower left) compared to the stacked data (upper left).

Figure 4





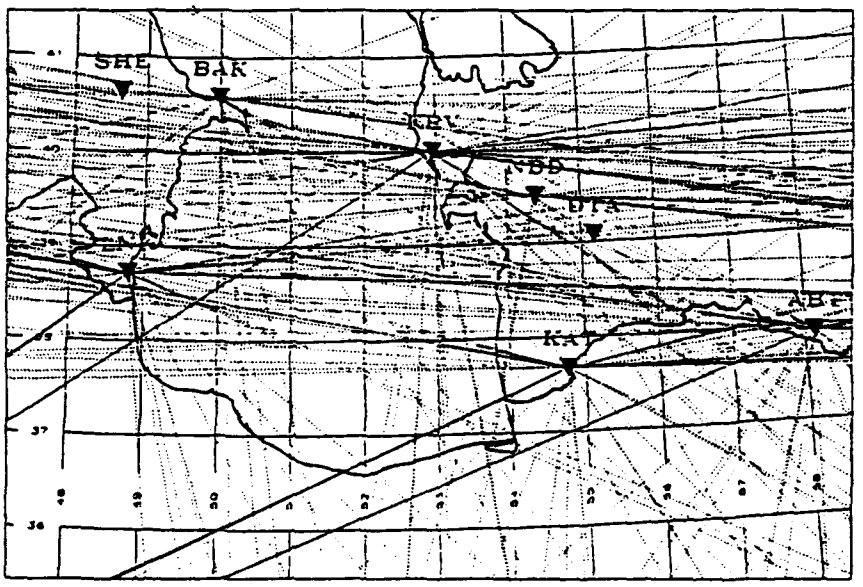


Figure 5. The first nine months of regional data with their corresponding raypaths to each CSN station and station ABKT (top). Shown below is a 1x1 degree grid expansion of the South Caspian Basin and surrounding regions.

Studies of Lithospheric Structure in Southwestern North America Part II: Lithospheric Structure of the Sierra Nevada: 1993 Field Observations of the NPE and the Southern Sierra Nevada Continental Dynamics Project

Kate C. Miller and G. Randy Keller
Department of Geological Sciences
The University of Texas at El Paso
El Paso, Texas 79968
Contract No: F49620-92-J-0438

Objective

As part of the University of Texas at El Paso's ongoing effort to record regional seismic refraction data using sources at the Nevada Test Site (NTS), our group has collaborated with members of the Southern Sierra Nevada Continental Dynamics Project (SSCD), a consortium of research universities funded by a number of government agencies to spearhead a coordinated program of seismic and electrical studies of the Death Valley, southern Sierra Nevada, and San Joaquin Valley regions of California. The aim of this project is to establish the nature of the crust and upper mantle of these regions, for a variety of basic scientific and practical purposes. During the 1993 field work, a special effort was made to record the Non-Proliferation Experiment (NPE) at the Nevada Test site in addition to collecting two other seismic refraction/wide-angle reflection profiles. These data are allowing us to develop refined models of the crustal and upper mantle structure of the southern Sierra Nevada and to evaluate alternative hypotheses for its uplift and for Basin and Range extension. They also provide important insights into the propagation of regional phases across complex geologic structure.

Research Accomplished

Background

The Southern Sierra Nevada Continental Dynamics (SSCD)* Project is a multidisciplinary, multi-institutional investigation of the cause of the uplift of the Sierra Nevada and its relationship to extension in the adjacent Basin and Range province. A broad range of geologic and geophysical data are being collected as part of this project. To investigate the lithospheric structure of this area and the propagation of regional seismic phases through it, two seismic experiments were designed: (1) a major, crustal and

*The SSCD Working Group includes representatives from Duke Univ., Caltech, Univ. of Colorado, Princeton Univ., U.C. Riverside, Univ. of Texas at El Paso, San Diego State Univ., Stanford Univ., China Lake Naval Weapons Center, and the U.S. Geological Survey.

upper-mantle scale, refraction survey using shots in drill holes and the NPE as sources, recorded by IRIS-PASSCAL, U.S. Geological Survey, and Geological Survey of Canada seismograph systems, and deployed along N-S and E-W and (2) a teleseismic converted wave survey using IRIS-PASSCAL, and French supplied seismographs. The government agencies funding the SSCD project are the National Science Foundation, United States Geological Survey, the Air Force Office of Scientific Research, the Department of Energy, the Naval Air Weapons Station China Lake, and the Lawrence Livermore National Laboratory.

Geophysical Background

Seismic observations of the lithospheric structure of the Sierra Nevada have produced conflicting interpretation (See Jones et al., 1994 and Savage et al., 1994 for recent summaries). Refraction profiles along the axis of the range have been interpreted to show a crust more than 50 km thick (Eaton, 1966; Pakiser and Brune, 1980). Disagreements over the identifications of phases and their interpretation has led to an alterative interpretation of a crust only about 40 km thick (Prodehl, 1979). Seismic profiles transverse to the range were initially interpreted to require a thin (30 km thick) crust with very low mantle velocities (7.65 to 7.88 km/s) beneath the range (Carder et al., 1970; Carder, 1973). Again, alternative interpretations suggest that a thick crust might also be consistent with the observations (Pakiser and Brune, 1980). Ray-tracing models through both structures appear to indicate that the thinner crust better fits the observations (Bolt and Gutdeutsch, 1982). Abnormally low heat flow is consistent with the presence of a thick root (Roy et al., 1972). However, Crough and Thompson (1977) argue that the surface heat flow reflects the heat flux into the crust over 10 m.y. ago and does not reflect the modern tectonic configuration. Accordingly, the asthenosphere could have risen to near the base of the crust within the last 10 m.y. or so, presumably at the time extension began in Death Valley. Consistent with this idea, Mooney and Weaver (1989) show that the maximum depth of regionally recorded seismicity decreases from over 25 km beneath the San Joaquin Valley to about 15 km beneath the Sierra Nevada. This latter depth is comparable to the depth of seismicity beneath the Basin and Range to the east. This decrease could be due to elevation of the brittle-ductile transition as a result of asthenospheric heating from below.

Several seismic reflection and refraction profiles have been shot in the San Joaquin Valley area by the U.S. Geological Survey (e. g. Holbrook and Mooney, 1987; Colburn and Mooney, 1986; Wentworth et al., 1987) These data give both velocity and structural information north and south of our seismic profile, but give little information on the crustal transition from the San Joaquin Valley to the Sierra Nevada. In the western part of the valley the crust is approximately 26-28 km thick with velocities approaching 7.2 km/s in the lower crust (Holbrook and Mooney, 1987). Recent analysis of microearthquake data in the eastern part of the San Joaquin Valley by Miller and Mooney (1994) (sponsored in part by this contract), suggest that crustal thickness may approach 38 km in this region with lower crustal velocities of 6.7 km/s. Seismic reflection data in this region display prominent, but still enigmatic west-dipping reflections in the middle to lower crust. One goal of the 1993 refraction work is to better understand the implications of these reflections for the tectonic evolution of the Sierra Nevada.

Somewhat surprisingly, relatively little geophysical research has been done in the Death Valley area. The only seismic refraction line indicates a roughly 30 km thick crust to

the east of Death Valley with a mean crustal P-wave velocity of about 6.1 km/s (Prodehl, 1979). The eastern end of the COCORP line across the Mojave Desert crosses the southern part of Death Valley, where a zone of reflections considered to represent Moho are about 30 km deep (Serpa et al., 1988). A large gravity high and topographic low that trends along the valley have been attributed to either outcrops of dense metamorphic rocks at the valley margins or thinner crust under Death Valley than under regions to the east and west. To our knowledge, no real quantitative attempt has been made to separate crustal thinning from lateral density contrast as the cause of these features. In May of 1994, the University of Texas at El Paso (UTEP) group reshot the easternmost of the SSCD shotpoints along with three other shots to the southeast. The result is a series of interlocking profiles which will greatly enhance our knowledge of structure and wave propagation in the southern Basin and Range.

Equipment, Logistics, and Cooperation.

The bulk of the seismic recording equipment for the SSCD refraction and teleseismic surveys was provided by the national IRIS-PASSCAL instrument center at Stanford University, the U.S. Geological Survey in collaboration with UTEP, and the Geological Survey of Canada. The total number of recorders deployed numbered between 600 to 700 instruments.

In September 1993, three seismic refraction/wide-angle reflection profiles were recorded: (1) a 325-km-long, north-south profile extending from just east of Mono Lake south across the Garlock fault, (2) a 400-km-long, east-west profile extending from Death Valley west across the Sierra Nevada to near the San Andreas fault, and (3) a 480-km-long, east-west profile deployed for the NPE. This profile extended from Beatty, Nevada, west across the Sierra Nevada along the previously recorded east-west profile and continued nearly to the Pacific Ocean. A total of 24 explosions including the NPE were recorded in in-line and fan geometries.

Over 50 individuals from more than a dozen institutions cooperated in the SSCD experiment. The bulk of leg work for permitting of shot points, roadways, trails, and ways-to-go along the teleseismic and refraction surveys was done by the university participants working with a Post Doctoral Research Fellow from Lawrence Livermore National Laboratories. The permits for the shot points and refraction survey points were signed by the U.S. Geological Survey. Some amount of helicopter reconnaissance was needed for both the permitting and survey of the refraction lines in the Sierra Nevada and Death Valley areas. It was necessary that all groups worked closely together to successfully deploy the large number of instruments along the seismic profiles.

For the NPE explosion at the Nevada Test Site, the SSCD project fielded some 350 portable seismic recorders. Stations were equipped with a mixture of 3-component and vertical geophones, with both short period and broad-band responses. The various sensors were interleaved to give: (a) a 450 km profile across the Sierra Nevada at 2 km station spacings and (b) local arrays placed both in a circle around Owens Lake and in 3 smaller apertures, at Darwin Plateau, Horse Shoe Meadow, and Mineral King (Figure 1). The arrays and 25 of the profile stations were also used to record earthquakes for several weeks. These events include a magnitude 3+ Death Valley event and the 5+ event in Oregon.

Discussion

The data were distributed to the SSCD members in March, 1994 and await complete interpretation of the crustal structure information. This is a complex process which includes forward and inverse modeling of travel times for the various seismic phases observed in the data as well as amplitude modeling.

A record section for the profile NPE (Figure 2) presents an outstanding picture of the Pn phase as it propagates across the Sierra Nevada, San Joaquin Valley, and San Andreas fault regions. This phase is clear all across the record section to the westernmost stations which were deployed just east of Carmel, California. Large variations in the amplitude relations between Pn and later arriving phases such as PmP, suggest significant complexities in upper mantle structures. An understanding of such variations is important to treaty verification efforts. The broad band recording do show that longer period Lg type waves are clearly affected by the Sierra Nevada. We are combining these observations into model of seismic wave propagation across the region for both scientific and nuclear discrimination purposes.

Preliminary results from analysis of the refraction data and teleseismic converted waves by SSCD members indicate that the crust of the southern Sierra Nevada is relatively thin, in the range of 35 km or less. Further analysis of the NPE record will help answer questions about the nature of the upper mantle in the southern Sierra Nevada.

Conclusions and Recommendations

The NPE effort has provided an unique opportunity to record detailed data on upper mantle structure across California in order to answer major crustal and nuclear monitoring questions. Since the Pn phase plays a major role in Comprehensive Test Ban Treaty verification efforts, long range recordings of this phase are very important in order to provide data on waveform variations as it propagates through complex structures. This project is an excellent example of the kind of significant results that can be obtained when universities and government agencies cooperate and pool resources.

References

Bolt, B.A., and R. Gutdeutsch, 1982. Reinterpretation by ray tracing of the transverse refraction seismic profile through the California Sierra Nevada, Part 1, Bull. Seis. Soc. Am. 72:889-900.

Colburn, R. H., and W. D. Mooney, 1986, Two-dimensional velocity structure along the synclinal axis of the Great Valley, California, Bull. Seismol. Soc. Am., v. 76, pp. 1305-1322.

Carder, D.S., 1973. Trans-California seismic profile, Death Valley to Monterey Bay, Bull. Seis. Soc. Am., v. 63, pp. 571-586.

Carder, D.S., A. Qamar, and T.V. McEvilly, 1970. Trans-California seismic profile, Pahute Mesa to San Francisco Bay, Bull. Seis. Soc. Am., v. 60, pp. 1829-1846.

Crough, S.T., and G.A. Thompson, 1977. Upper mantle origin of the Sierra Nevada uplift, Geology, v. 5, pp. 396-399.

Eaton, J.P., 1966. Crustal structure in northern and central California from seismic evidence, in Bailey, E.H., ed., Geology of Northern California, Calif. Div. Mines Geol. Bull., v. 190, pp. 419-426.

Holbrook, W. S., and W. D. Mooney. 1987. The crustal structure of the axis of the Great Valley, California, from seismic refraction measurements, Tectonophysics, v. 140, pp. 49-63.

Jones, C.H., H. Kanamori, and S.W. Roecker, 1994. Missing roots and mantle drips: Regional Pn and teleseismic arrival times in the Southern Sierra Nevada and Vicinity, California, J. Geophys. Res., v. 99, pp. 4567-4601.

Miller, K.C. and W.D. Mooney, 1994. Crustal structure and compositoin of the southern Foothills Metamorphic Belt, Sierra Nevada, California, from seismic data, J. Geophys. Res., v. 99, p. 6865-6880.

Mooney, W.D., and C.S. Weaver, 1989. Regional crustal structure and tectonics of the Pacific coastal states: California, Oregon, and Washington: in Pakiser, L.C., and W.D. Mooney (eds.), The Geophysical Framework of the United States, Geol. Soc. Am. Monograph 172.

Pakiser, L.C., and J.N. Brune, 1980. Seismic models of the root of the Sierra Nevada, Science, v. 210, pp. 1088-1094.

Prodehl, C., 1979. Crustal strucutre of the western United States, USGS Prof. Paper, 1034, 74 pp.

Savage, M.K., Lili, J. P. Eaton, C. H. Jones, and J. N. Brune, 1994. Earthquake refraction profiles of the root of the Sierra Nevada, Tectonics, in press.

Serpa, L., B. deVoogd, L. Wright, J. Willemin, J. Oliver, E. Hauser, and B. Troxel, 1988. Structure of the central Death Valley pull-apart basin and vicinity from COCORP profiles in the southern Great Basin, Geol. Soc. Am. Bull., v. 100, pp. 1437-1450.

Wentworth, C.M., M.D. Zoback, A. Griscom, R.C. Jachens, and W.D. Mooney, 1987. A transect across the Mesozoic accretionary margin of central California. Geophys. J.R. Astr. Soc., v. 89, pp.105-110.

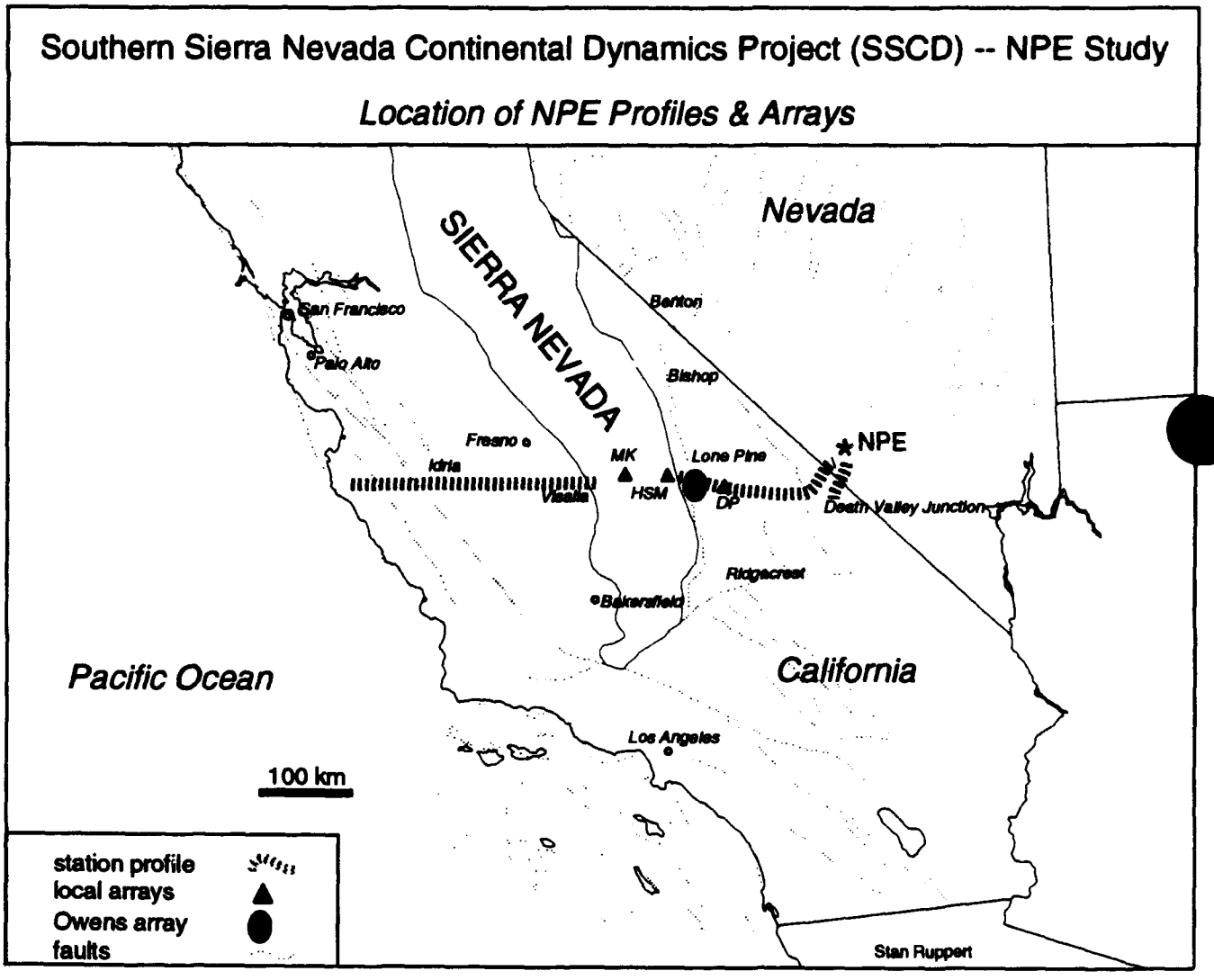


Figure 1. Index map showing the profile of seismic recordings obtained for the NPE.

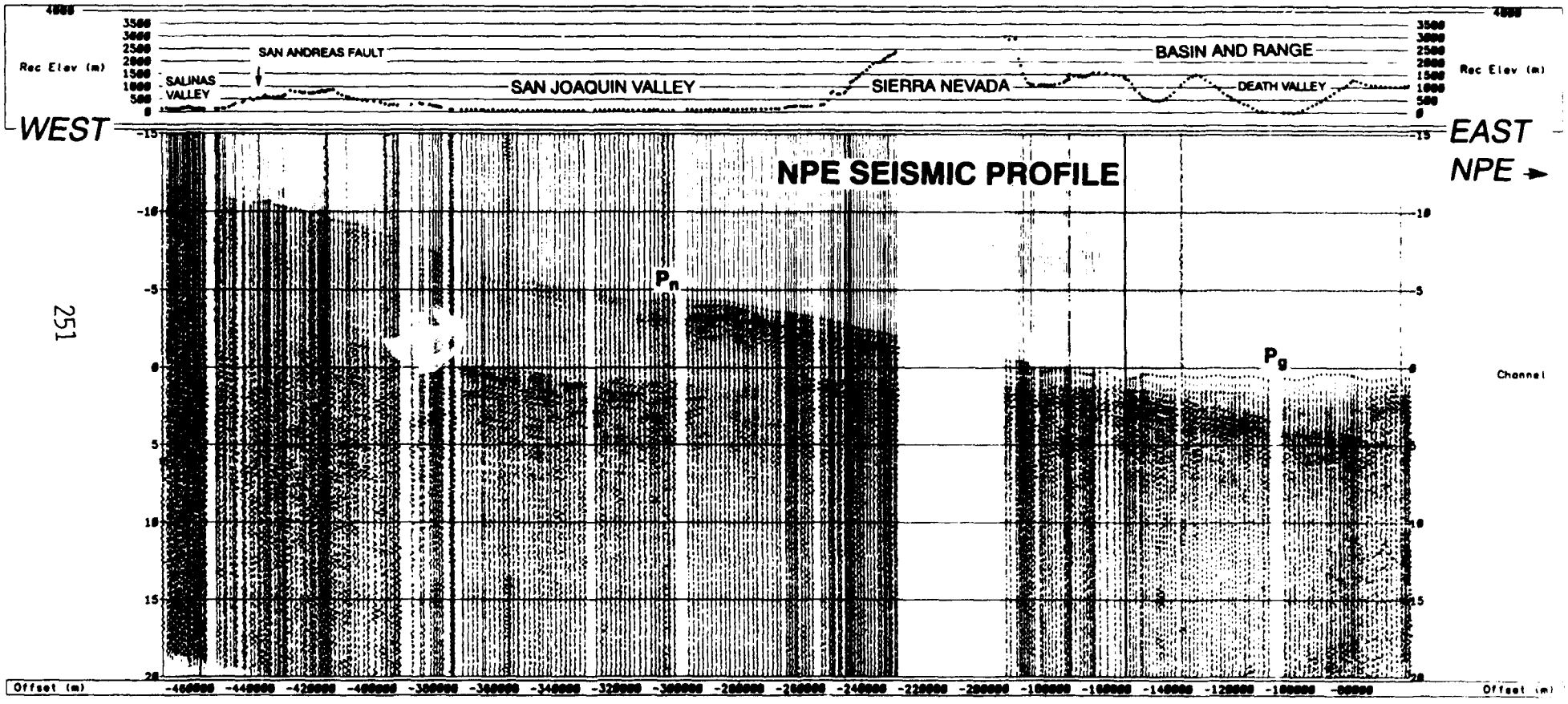


Figure 2. Record section for the NPE seismic profile. A reducing velocity of 8.0 km/sec was employed for display purposes. Reduced travel times in seconds are shown on the vertical axis. Small +'s denote first arrivals which are very clear on enlarged displays of the data.

Studies of Lithospheric Structure in Southwestern North America
Part III: Lithospheric Profiles in the Nevada Test Site Region: The DELTA FORCE experiment

Carlos Montana, G. Randy Keller, Kate Miller, and Julia Whitelaw
Department of Geological Sciences
The University of Texas at El Paso
El Paso, Texas 79968
Contract No: F49620-92-J-0438

Objective

The University of Texas at El Paso conducted a seismic refraction/wide angle reflection survey during May of 1994 with the objective of achieving a better understanding of the nature of the crust and upper mantle in the Basin and Range and Colorado Plateau geologic provinces. Of primary interest was lithospheric structure and wave propagation in the vicinity of NTS. The participants in this experiment were the University of Texas at El Paso, the U.. S. Geological Survey, the California Institute of Technology, and Iris-Passcal support personnel. In addition, networks operated by Sandia and Lawrence Livermore National Laboratories recorded the shots. A Mexican research group, CICESE, based in northwestern Mexico contributed by recording across northern Mexico from the Imperial Valley to the Pacific Ocean.

Research Accomplished

The seismic experiment was conducted in southeasternmost California, southernmost Nevada, and northwestern Arizona. The seismic experiment was designed around four explosive source locations shown on Figure 1 and located in the vicinity of the north rim of the Grand Canyon, Death Valley Junction, NV, Kingman, AZ, and Blythe, CA. A total of 474 recording instruments were deployed in a single deployment along 5 line segments as shown on Figure 1. The instruments deployed were 166 Refteks, 188 Seismic Group Recorders and 120 Seismic Cassette Recorders and were positioned at ~2km spacing. The natural frequencies of the geophones utilized were either 1, 4.5 or 8 Hz. The sources utilized were ammonium nitrate compounds loaded into boreholes ~180 ft. deep in amounts of 8000 lbs with the exception of the Kingman shot which measured 6000 lbs. The

number of people required to conduct this experiment was in excess of 50, and the project took a week to complete.

Preliminary plotting of seismic traces show good quality data for the most part, with prominent phases showing up clearly, ie. Pg, Pn, and PmP. By combining our results with previous studies a clearer picture of the lithosphere in this region should emerge. Our Mexican colleagues were able to record at least the southernmost shot with quality seismograms being obtained out to the continental margin.

Conclusions

The the results of the Delta Force experiment look extremely promising at this point. The number and quality of seismic traces suggests that it will provide significant data that will improve our understanding of the character of the lithosphere in this region. It was only through a significant amount of interagency cooperation that this ambitious project could be completed.

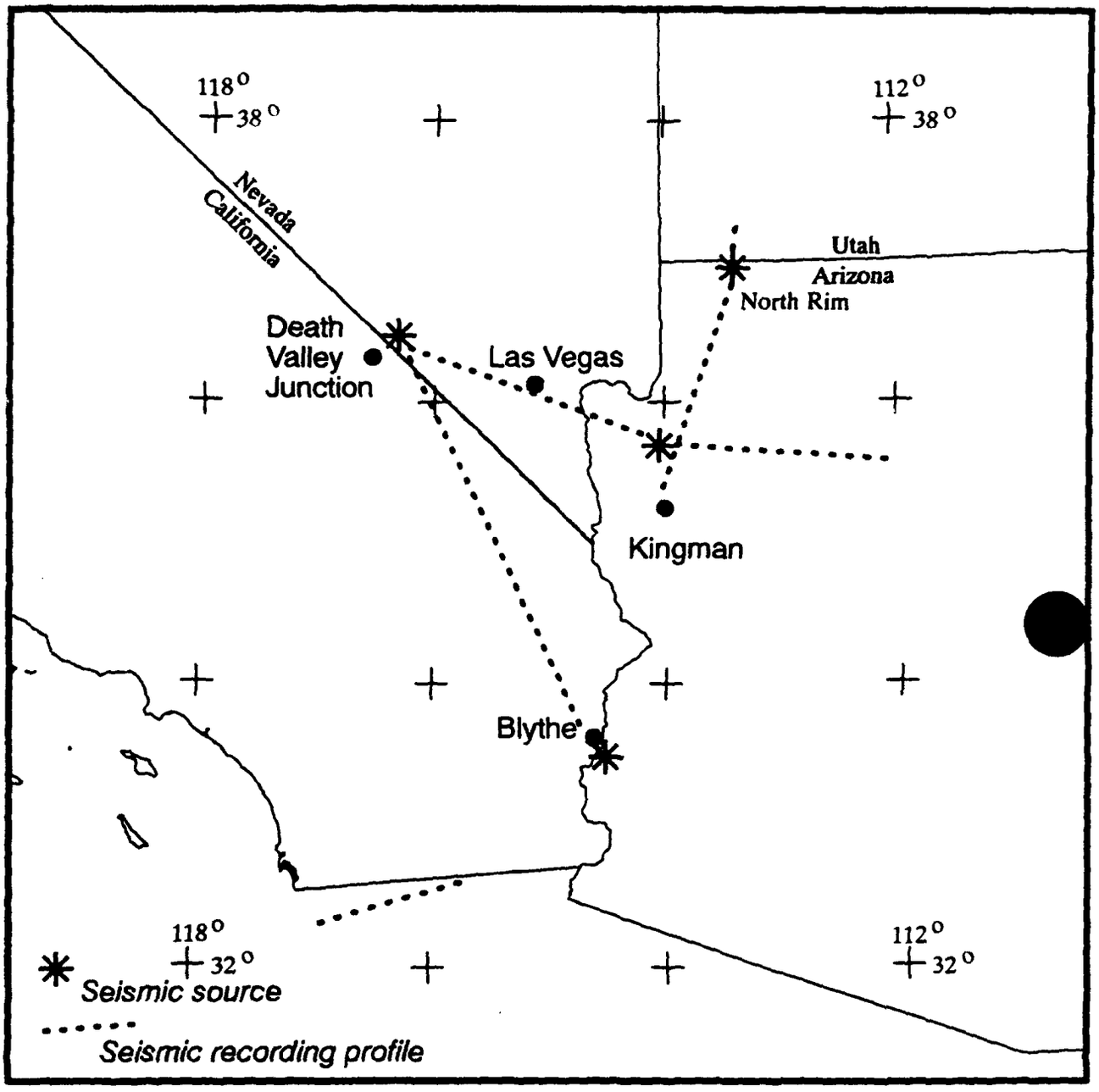


Figure 1: Index map of the Delta Force experiment. Seismic sources are shown as well as the profiles along which the seismic recorders were deployed..

Studies of P_n, S_n and L_g wave propagation across major crustal studies using PNEs

Elena A. Morozova*, Igor B. Morozov*, Scott B. Smithson*, James Shatzman**, Leonid N. Solodilov***

*Department of Geology and Geophysics, University of Wyoming, PO Box 3006, Laramie, WY, 82071.
**Department of Mathematics, University of Wyoming, PO Box 3006, Laramie, WY, 82071.
***Center for Regional Geophysical and Geoecological Research (GEON), Moscow, Russia.

Grant F49620-94-1-0134

OBJECTIVES

University of Wyoming (UW) is currently conducting a research project aimed at digitization and advanced processing of the unique Deep Seismic Sounding (DSS) data acquired in the former USSR during the past 25 years in order to better understand wave propagation through complex lithospheric structure by using long, densely sampled seismic profiles from nuclear and chemical explosions. Under the agreement of scientific cooperation between the University of Wyoming and center GEON (Moscow, Russia; formerly the Special Geophysical Expedition) we obtained a part of the DSS profile "Quartz". The remaining part of the data will be transferred to UW in the near future.

The specific overall objectives of our study are:

1) Digitization of all of the original 3-component analog field records to their full length (up to 600 seconds of seismic data). Recovery of all vital seismic trace header information and storage of the data in a standard (portable) format.
2) Identification and true amplitude recovery of seismic phases (especially, P_n, S_n, L_g and converted phases) along the profile.
3) Inversion of the DSS wavefield for the P- and S-wave velocity structure; modeling of L_g wave propagation across laterally variable geological structures; estimation of the resolution of the crustal velocity structure and its implication for the analysis of L_g wave propagation.
4) Study of the detailed structure of major crustal units such as the Ural Mountains and Pechora Basin.
5) Calibration of regional seismic event discriminants.

RESEARCH ACCOMPLISHED

DSS profiling in the USSR and the "Quartz" profile

The "Quartz" profile is one of the 14 major profiles acquired in the USSR during the fulfillment of an extensive program of deep seismic sounding. The program is unique in the use of "Peaceful Nuclear Explosions" (PNE) combined

with the use of 3-component recorders at offset ranges over 3000 km. Recent descriptions of DSS program are given by Benz et al. (1992a) and Benz et al. (1992b).

The profile "Quartz" (Murmansk-Kizil) completed in 1984-87 extends 3950 km across several major tectonic units of northern Eurasia (Zonenshain et al., 1990; Mechie et al., 1993). Starting at the northwest end of the profile, these units are (Fig. 1):

1) The East European Platform (770 km), including 440 km of the Baltic Shield. The oldest rocks of the East European Platform are early Archean; the last significant event here was the intrusion of rapakivi granites about 1600 Ma ago.
2) The Timan Belt (120 km of the profile), which is a late Precambrian fold belt or a suture between eastern Europe and Barentsia.
3) The Pechora Basin (360 km), which underwent a number of extensional events from early Devonian to late Cretaceous or early Palaeogene.
4) The Uralian Belt (260 km), formed at the end of the Paleozoic and the beginning of the Mesozoic.
5) The West Siberian Basin (1540 km) - a broad extensional basin with very thick Triassic and Holocene sediments.
6) The Altai-Sayan Foldbelt (900 km of the profile) - an active Alpine belt which underwent several phases of deformation from the early to middle Cambrian to the Permian throughout the Paleozoic.

Fig. 2 shows the corresponding crustal velocity structure developed in the center GEON. Recordings were made with about 400 3-component seismographs from 3 PNEs (located at about 1130, 2050 and 2820 km from the northwestern end of the profile) and 42 chemical explosions. The station spacing was generally about 10 km.

Data

The "Taiga" and "Cherepakha" seismographs recorded 2 sets (with different gains) of 3-component seismic records directly onto magnetic tapes. The records were digitized at the center GEON to their full length (nearly 10 minutes) and sent to the University of Wyoming for further processing. To date, we have obtained the northwestern part of the profile including 2 of the 3 PNEs and 28 of 42 chemical explosions. Figures 3 and 4 show the vertical component of the reduced record section for the shotpoints 123 and 213. A correction for different amplitude responses of the instruments and band-pass filtering was applied. The general form of the DSS record is close to that usually observed in earthquake seismology. Therefore, methods developed for the analysis of earthquake data (multiple filtering, polarization analysis, seismic coda analysis) may be applicable to the processing of these unique records, with the advantage of having 200-300 stations lined up along the direction of wave propagation.

Correlation of Seismic Phases

The data from the shotpoint 123 (Fig. 3) show clear first Pg arrivals with apparent velocity about 5.8 km/s at offsets of 0-200 km in the NW and 0-300 km in

the SE directions. Pg is replaced by strong P_n first arrivals with apparent velocities 8.0-8.5 km/s. In the NW part of the profile we distinguish two P_{n1} and P_{n2} events, corresponding to a refraction in a layered mantle. The P_{n1} event has apparent velocities 8.0-8.2 km/s and is seen in the offset range 200-800 km, while P_{n2} with apparent velocity 8.4-8.5 km/s appears at an offset of 600 km, becomes a first arrival at 800 km and is strong to the end of the profile. In the second arrivals, we observe a strong event at offsets 860-1130 km near the NW end of the profile (at approximately 17 sec in Fig. 3). The event may be associated with an upper mantle reflection. Closer to the shotpoint, we see a complicated wave pattern in the second arrivals at the offset range 170-650 km in the NW and 250-700 km in the SE directions. In this section of the shot gather we recognize PmP and apparently a deeper mantle reflection (marked Pm_1P). At later times, S_n (apparent velocity 4.6-4.8 km/s) and L_g (apparent velocity 3.2 km/s) can be traced to the NW end of the profile. The waveforms of the S_n and especially L_g waves become progressively more diffuse with increasing offset. This change in the waveforms must be related to the scattering and the dispersion of the L_g wave. Multiple filtering of transverse components of selected records with the best signal/noise ratio indicates the L_g wave dispersion. To the SE, the L_g phase is not seen and S_n is weak after the Ural Mountains. Unfortunately, the data quality is poor in this part of the profile and the field records are shorter. Finally, at small offsets (0-100 km in the NW direction) we observe short-period Rayleigh wave R_g with apparent velocity about 1.9-2.0 km/s.

The analysis of the shot gather for the shotpoint 213 (the middle PNE, Fig. 4) shows again all the seismic phases described above. A remarkable feature is the disappearance of the L_g phase behind the Ural Mountains. Thus, from the preliminary analysis of the shot gathers we infer evidence for L_g-wave blockage under the Ural Mountains. This conclusion, however, still is to be supported by the study of the third PNE along the same profile, by quantitative analysis of seismic attenuation and by modeling.

Preliminary modeling.

The modeling of seismic wave propagation (especially L_g) across the contacts of different geological structures requires the use of 2- or 3- dimensional velocity models. As a starting model for our preliminary ray tracing we used 2-dimensional crustal P-wave velocity model proposed used in the center GEON (Solodilov, 1994). Adjusting the mantle velocities to achieve a fit of the picked P_n and PmP travel times, we obtained a velocity model, which suggests an upper mantle P-wave velocity discontinuity under the Ural Mountains. Figure 2 shows the P-wave velocity model, rays traced for the shotpoint 123, and corresponding travel time fit.

The use of the velocity model in Fig. 2, however, requires a certain degree of caution. The model was obtained by trial-and-error forward modeling and adjustment of parameters in order to fit break times. Whether the small blocks shown in Fig. 2 can be really resolved independently has not been determined. The detailed velocity structure with an abundance of velocity contrasts will cause difficulties in the modeling of surface wave propagation. Therefore, one of the

immediate purposes of our study now is to obtain a relevant P- and S-wave velocity model and to estimate its resolution. Seismic tomography (e.g., Ammon and Vidale, 1993) provides one of possible means to determine such a model.

CONCLUSIONS AND RECOMMENDATIONS

The identification of a number of seismic phases in the PNE shot gathers, especially L_g and S_n, and observation of the possible L_g blockage at the Ural Mountains will enable us to contribute in the solution of a number of important questions:

1) the characteristics of L_g wave propagation in different tectonic structures and across their contacts;
2) the nature of L_g blockage;
3) the use of L_g/P_n and L_g/S_n as regional discriminants.

After practically all preliminary processing of the data has been done, we plan to proceed with advanced analysis of the data. This analysis will pursue the following general lines:

1) quantitative analysis of the dispersion of L_g waves;
2) the inversion for the P- and S-wave crustal and upper mantle velocity structure using seismic tomography techniques (using the PNEs as well as all chemical shots); analysis of the resolution of the resulting velocity model;
3) the analysis of seismic attenuation along the profile;
4) modeling of L_g wave propagation across the boundaries of the geological structures crossed by the profile.

References

Ammon, C.J. and J Vidale, 1993. Tomography without rays: Bull. Seismol. Soc. Am., 83, 509-528.

Benz, H.M., J.D. Unger and M.S. Leith, 1992a. Deep seismic sounding in northern Eurasia: interpretation of the Murmansk-Kizil ultra-long-range profile. In: Proc. of the 14th PL/DARPA Seismic Research Symposium. (Eds. J.F. Lewkowicz, J.M. McPhetres): 17 Aug. 1992., PL-TR-92-2210, ADA256711.

Benz, H.M., J.D. Unger, M.S. Leith, W.D. Mooney, L. Solodilov, A.V. Egorkin and V.Z. Ryaboy, 1992b. Deep seismic sounding in northern Eurasia: EOS, Trans. Am. Geophys. Union, 73, 297.

Mechie, J., A.V. Egorkin, K. Fuchs, T. Ryberg, L. Solodilov and F. Wenzel, 1993. P-wave mantle velocity structure beneath northern Eurasia from long-range recordings along the profile Quartz: Phys. of the Earth and Plan. Int., 79, 269-286.

Solodilov, L, 1994. Personal communication.

Zonenshain, L.P., M.I. Kuzmin and L.M. Natapov, 1990. Geology of the USSR: A Plate-Tectonic synthesis. In: B.M. Page (Ed.), Am. Geophys. Union Geodynamics Ser., 21; 242 pp.

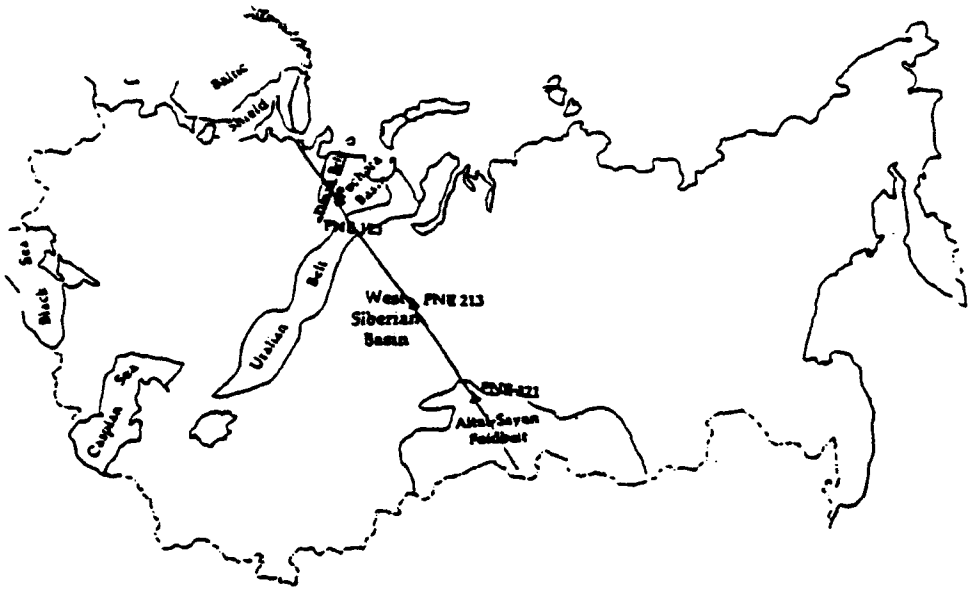


Fig. 1. A simplified geological map of the territory of the former USSR. Major tectonic units crossed by the profile "Quartz" are shown. The triangles denote the locations of the PNEs.

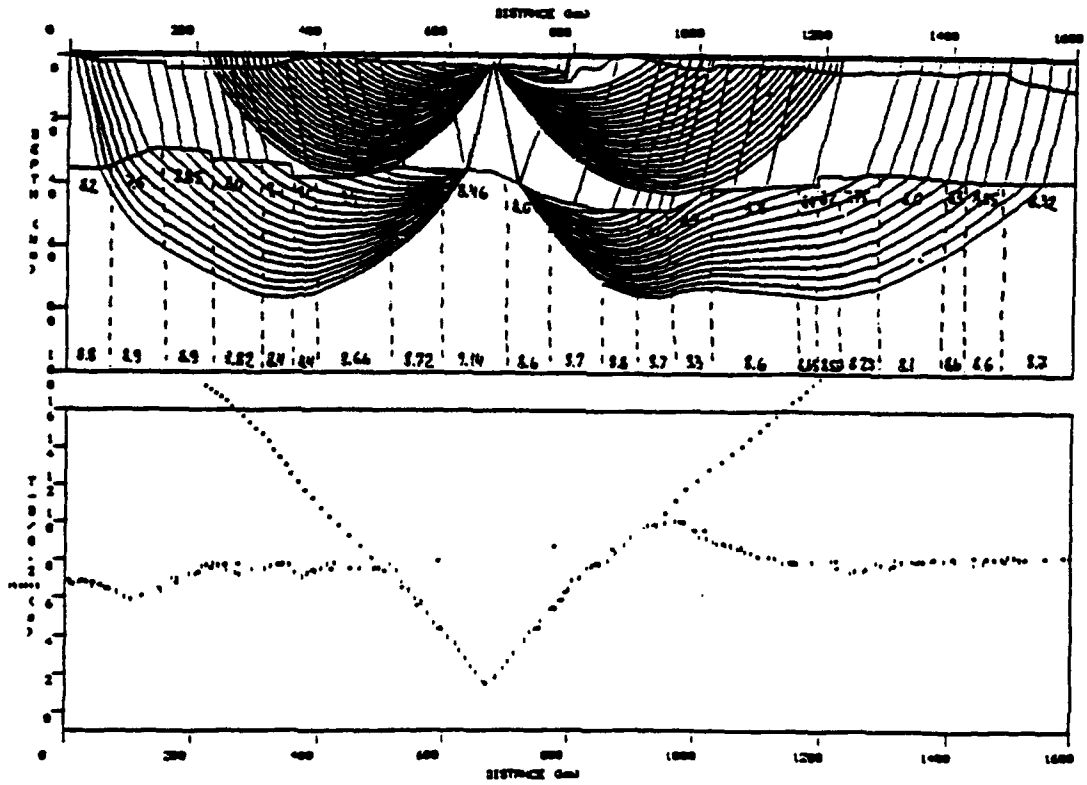


Fig. 2. A preliminary P-wave velocity model for the profile "Quartz" (see the text for the discussion). The detailed velocity structure may require a reevaluation in our study of the propagation of P-, S- and Lg-waves.

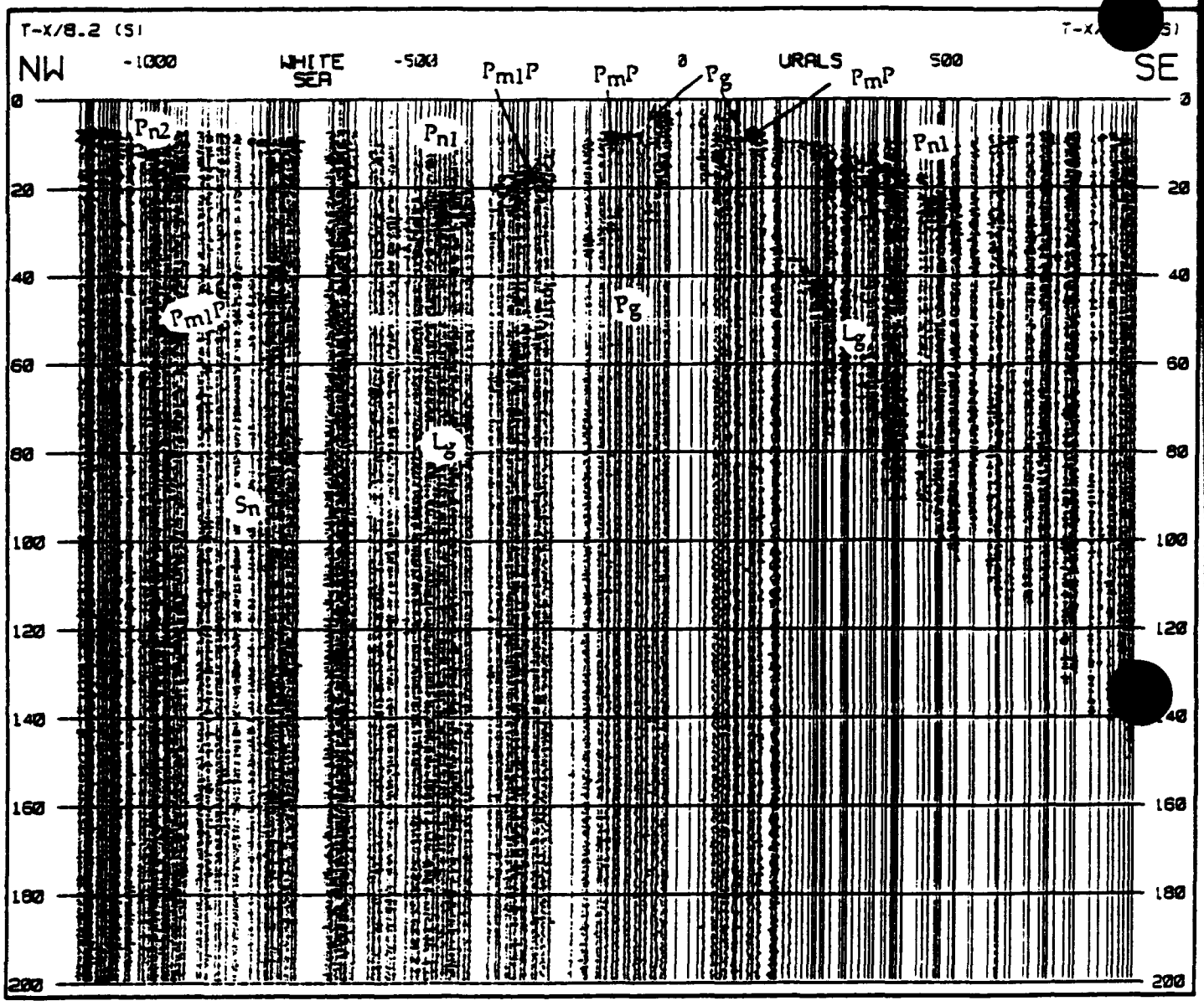


Fig. 3. The first 200 sec. of the reduced vertical component record section for the shotpoint 123 (the northwestern PNE). The reduction velocity is 8.2 km/s. The L_g and S_n arrivals can be traced to the NW end of the profile. In the SE direction the L_g appears to be blocked by the Ural Mountains.

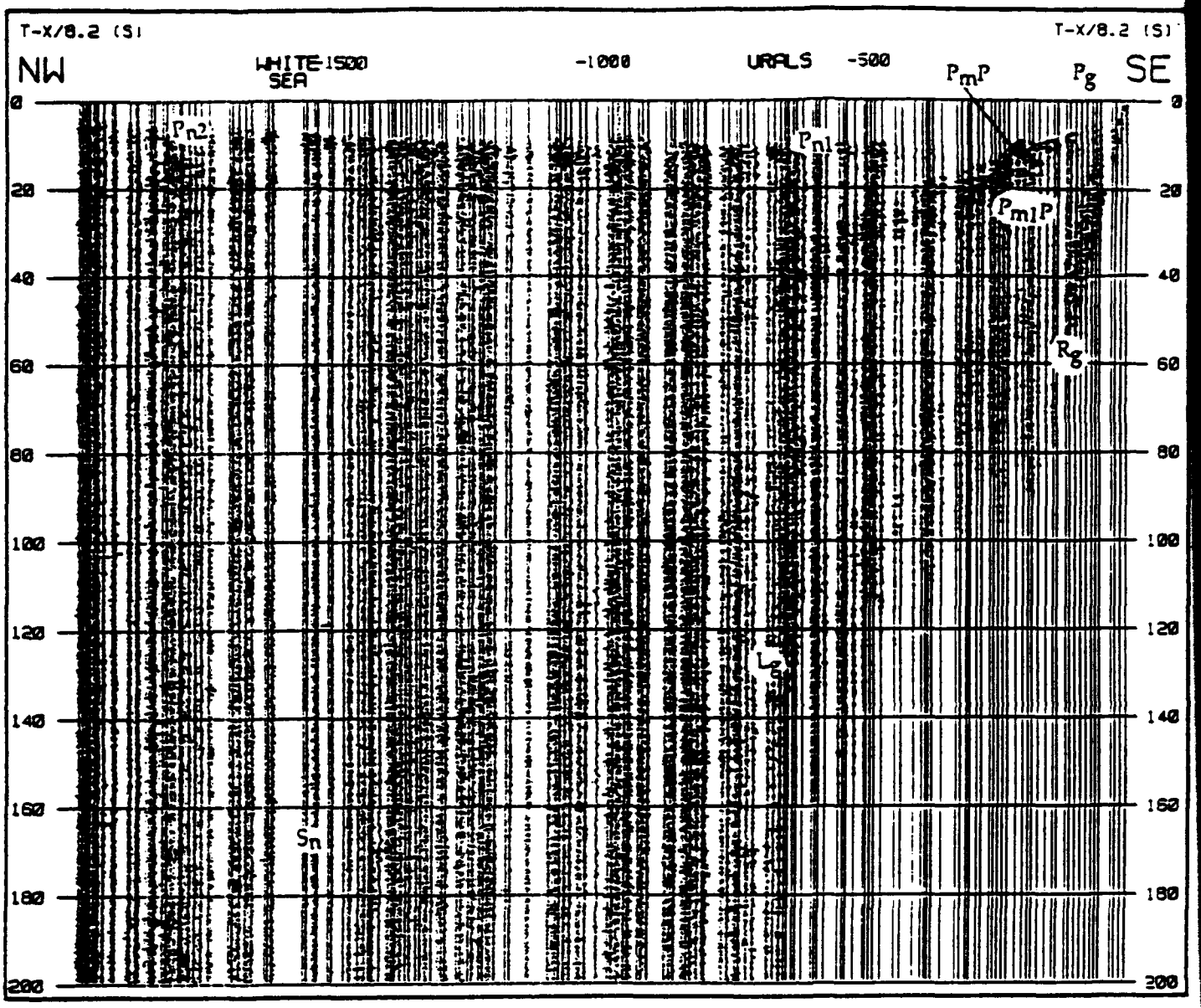


Fig. 4. The first 200 sec. of the reduced vertical component record section for the shotpoint 213 (the middle PNE). The reduction velocity is 8.2 km/s. The L_g arrival becomes indistinguishable after crossing the Ural Mountains. Note the same feature of the L_g arrival in the SE end of the shot gather for the shotpoint 123 (Fig. 3).

Analyses of the Seismic Characteristics of U.S. and Russian Cavity Decoupled Explosions

J. R. Murphy, I. O. Kitov* , J. L. Stevens and D. D. Sultanov*
Maxwell Laboratories, Inc., S-CUBED Division
11800 Sunrise Valley Drive, Suite 1212
Reston, Virginia 22091
Contract Nos. F19628-91-C-0186 and F19628-93-C-0126

Objective

It has long been recognized that the most effective means for evading the detection of a clandestine underground nuclear test is to detonate the explosion in a cavity which is large enough to substantially decouple the radiated seismic signal. In this project we are working with scientists from the Russian Institute for Dynamics of the Geospheres (IDG) to integrate the U.S. and Russian data and modeling experience into a uniform database on cavity decoupling. The objective of the study program is to validate a quantitative prediction capability which can be used by the seismic verification community to evaluate the plausibility of various cavity decoupling evasion scenarios.

Research Accomplished

In this initial phase of the investigation, the research effort has focused on the analysis of data recorded from an extensive series of Russian HE decoupling tests, an evaluation of the importance of radiation diffusion on nuclear cavity decoupling effectiveness and on analyses of seismic data recorded from six Russian nuclear tests conducted in a water-filled cavity at Azgir. The HE decoupling tests consisted of a series of 22 tamped and cavity explosions conducted in a mine in the Tywya Mountains of Kirghizia in the summer of 1960. The tests were conducted in hard, homogeneous limestone in chambers excavated from alcoves constructed off the sides of the main access tunnel to the mine. The decoupled tests were conducted in spherical cavities having diameters ranging from about 3.5 to 10 m, as well as in nonspherical cavities with volumes of about 25 m^3. The approximate locations of these various test chambers with respect to

* Institute for the Dynamics of the Geospheres, Russian Academy of Science

the main access tunnel are shown in Figure 1, where it can be seen that the maximum separation between them is less than 150 m.

The experiments consisted of 10 tamped and 12 decoupled explosions having yields of 0.1, 1.0 and 6.0 tons. The explosives consisted of ammonium nitrate, except for the two 6.0 ton tests which utilized a mix of TNT and ammonium nitrate. For the cavity tests, the explosives were suspended in the chambers and included cases in which the explosives were positioned in the center of the cavity, as well as cases in which they were positioned off-center, near the cavity wall. Seismic data were recorded from these tests at locations in the mine over a distance range extending from about 10 to 250 m. Peak amplitudes of displacement and velocity have been reported for over 250 of these recording locations and these data should provide valuable insight into the dependence of decoupling effectiveness on variables such as cavity volume and shape. For example, the peak displacement data observed from the 1.0 ton decoupled test conducted in a spherical cavity with a radius of 2.88 m are shown in Figure 2 where they are compared with the corresponding peak displacement data observed from the two 1.0 ton tamped tests. It can be seen that these data suggest a peak displacement decoupling factor of about 10 in this case. Spectral analyses of the corresponding digitized waveform data are currently in progress and preliminary results suggest a maximum low frequency decoupling factor of the order of 40 to 50 for this 1.0 ton test.

With regard to the modeling of nuclear explosions in air-filled cavities, Glenn et al. (1994) have recently suggested that the inclusion of radiation diffusion effects can have a significant influence on the computed seismic source function. In order to further investigate this issue, we have carried out a series of coupled radiation/hydrodynamic finite difference simulations of a 380 ton nuclear explosion in a 17 m radius air-filled cavity in salt (i.e., STERLING). The calculations were performed with and without radiation and over a wide range of air opacities, using the ZOOS Lagrangian coupled radiation/hydrodynamics code. Figures 3 and 4 show comparisons of typical pressure and impulse time histories at a range of 25 m from the center of the cavity, computed with and without radiation. The pressure time histories show the reverberations that are characteristic of explosions in air-filled cavities and it can be seen that the principal effect of radiation is a small change in the timing of these reverberations. That is, radiation causes a small amount of salt to be vaporized near the cavity wall, causing dispersion of the shock wave and a slight delay in the timing of the reverberations. As can be seen from Figure 4, this effect also causes a very small reduction in the amplitude of the impulse at this range. In an attempt to bound these radiation effects, calculations were also performed in which the nominal air opacity was reduced by factors of 10, 100 and 1000. It was determined that changes in opacity over this range resulted in a

maximum reduction of less than 3 percent in the computed impulse at the 25 m range. Thus, our results do not support the hypothesis that radiation has a significant influence on the computed decoupling effectiveness of nuclear explosions in air-filled cavities.

During the period 1975 to 1979, the Russians conducted a series of nuclear tests in salt at Azgir in the cavity created by the 25 kt tamped explosion of 7/01/68. The tamped explosion was detonated at a depth of 597 m and produced a roughly spherical cavity with a maximum horizontal radius of 32.5 m. Following the detonation, the cavity filled with water and the six subsequent nuclear tests at that site were conducted in the water-filled cavity. The yields of these tests varied over a range of approximately a factor of 50, up to a maximum yield of about 1 kt. The two largest of these explosions were detected teleseismically and have been assigned m_b values in the 4.5 to 5.0 range. Thus, since a fully tamped 1 kt explosion at Azgir corresponds to an m_b value of 4.5 or less, these tests were not decoupled and, in fact, showed enhanced coupling, at least over some frequency bands. This appears to be due to the response characteristics of the water in the cavity and preliminary theoretical simulation results show a cavity resonance effect which is associated with enhanced coupling in the short-period band with respect to that expected from a fully tamped explosion of the same yield in salt. As part of the testing procedure, the cavity condition was resurveyed after selected tests and the observed configuration after the fourth of the cavity shots is summarized graphically in Figure 5, which also shows a subsurface geologic profile of the site down to source depth. It can be seen that the cavity remained basically intact under the repeated testing in this case, although the depth to the bottom was observed to decrease over time by about 1 m due to spallation of material off the upper cavity walls. As is indicated in Figure 5, motion measurements were made in the borehole for the cavity tests and seismic measurements were made on the surface in the distance range extending from ground zero to approximately 100 km. These data have been digitized at IDG and they are now being analyzed to define the yield and frequency dependence of the seismic response of this cavity.

Conclusions and Recommendations

Over the past year, we have been working with scientists from the Russian Institute for Dynamics of the Geospheres (IDG) in an attempt to integrate the U.S. and Russian data and modeling experience on cavity decoupling. Current research activities focus on the analysis of data recorded from an extensive series of Russian HE decoupling tests, a theoretical evaluation of the importance of radiation diffusion on nuclear cavity decoupling effectiveness and an analysis of seismic data recorded from six Russian nuclear tests conducted in a water-filled

cavity in salt at Azgir. The HE decoupling tests were conducted in a mine in Kirghizia in 1960 and included tests in mined spherical cavities in limestone having diameters ranging from about 3.5 to 10 m, as well as tests in nonspherical cavities of comparable volume. Peak amplitude decoupling factors of about 10 were observed in these tests and preliminary spectral analysis results suggest corresponding maximum low frequency decoupling factors in the 40 to 50 range. A series of coupled radiation/hydrodynamic theoretical simulations of the STERLING test configuration have been conducted in an attempt to assess the effects of radiation on the computed seismic source function. Our results indicate that the inclusion of radiation diffusion effects has a very small influence on the computed decoupling effectiveness of nuclear explosions in air-filled cavities. Finally, preliminary analyses of data recorded from the series of six nuclear tests in the water-filled cavity at Azgir indicate that these tests were not decoupled and, in fact, showed enhanced coupling, at least over some frequency bands.

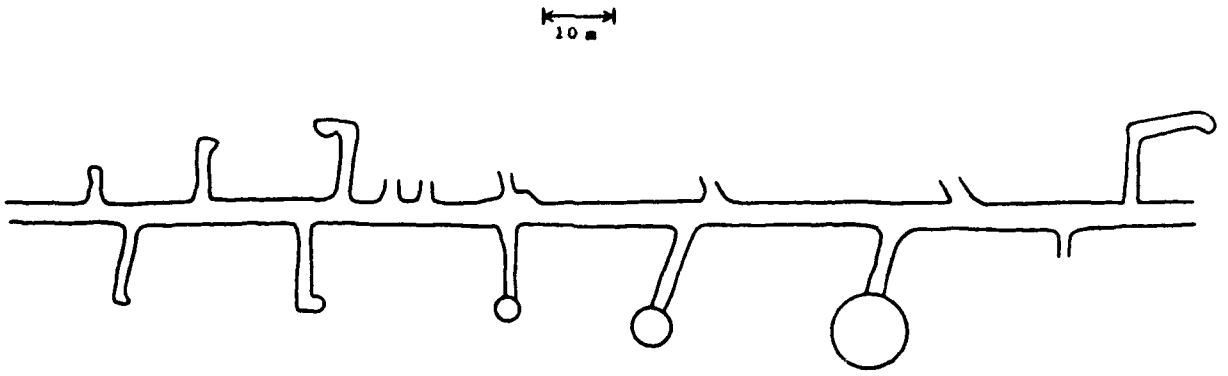


Figure 1. Relative locations and configurations of the various test chambers used for the Kirghizia HE decoupling test series.

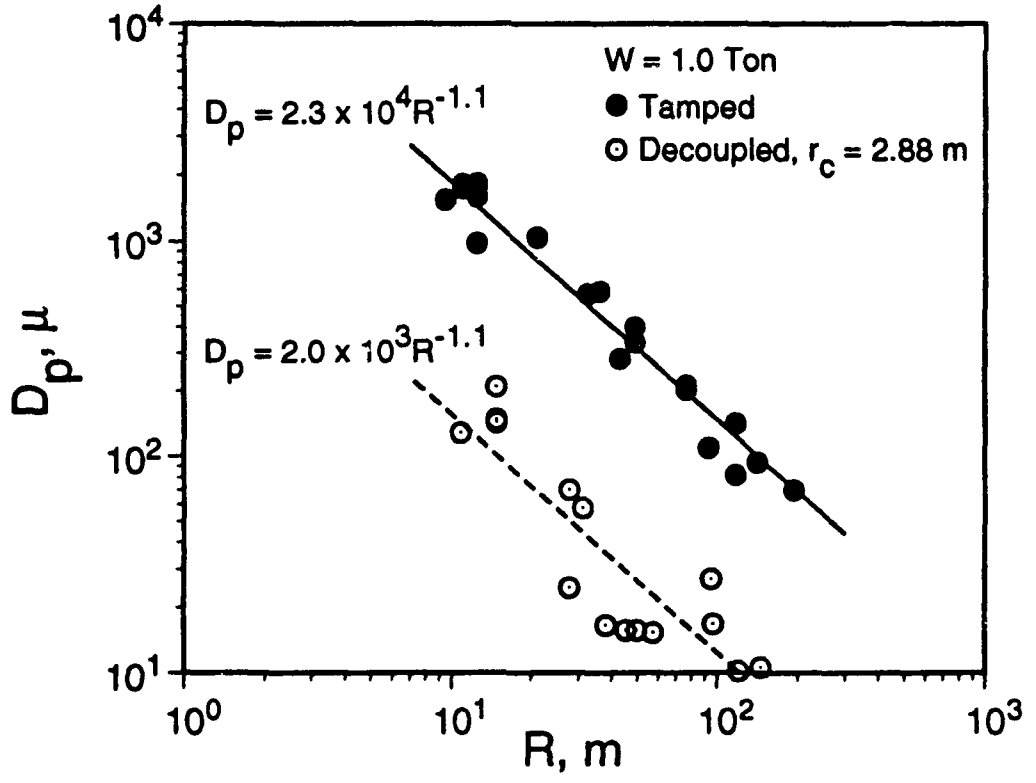


Figure 2. Comparison of peak displacement data observed from 1.0 ton tamped and cavity decoupled HE tests at Kirghizia.

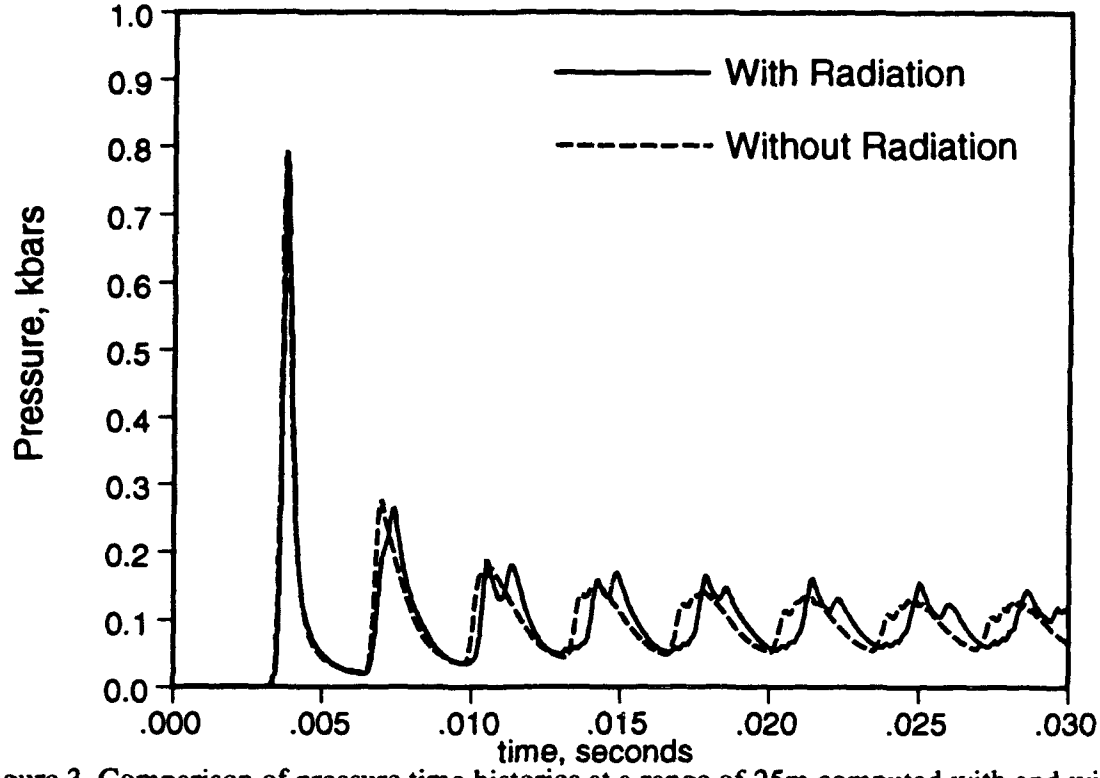


Figure 3. Comparison of pressure time histories at a range of 25m computed with and without radiation effects for a 380 ton nuclear explosion in a 17m radius air-filled cavity.

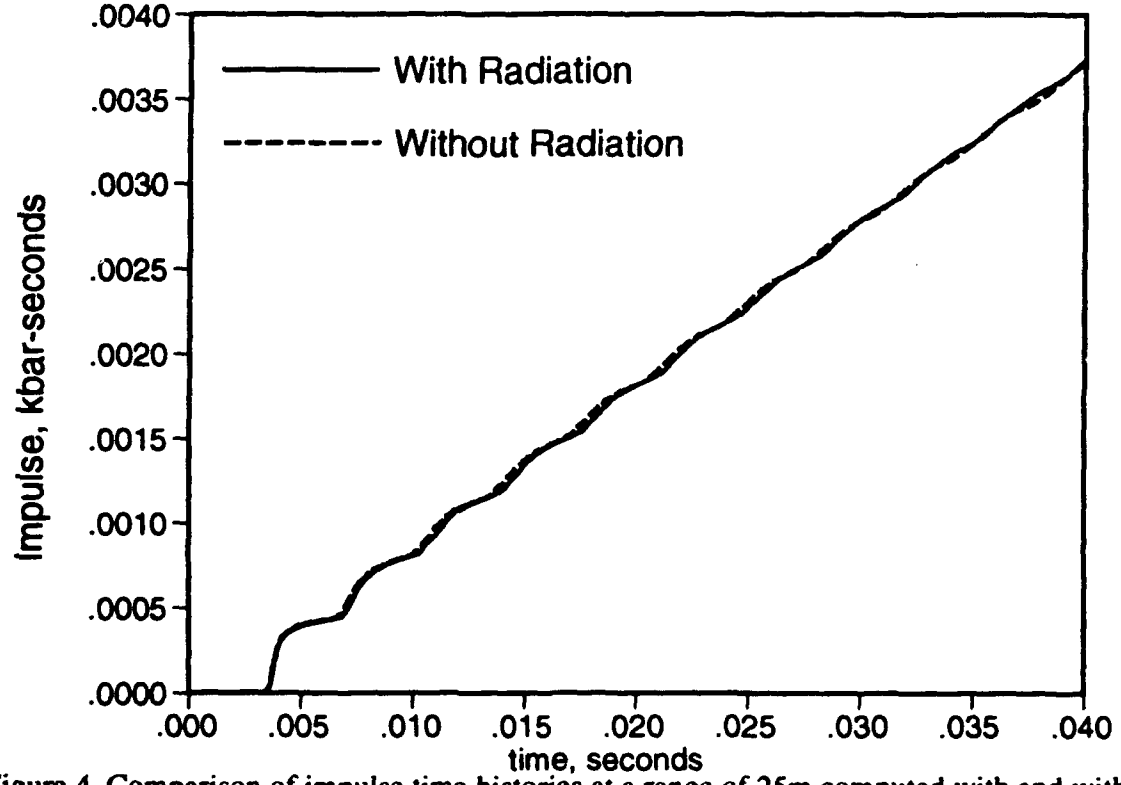


Figure 4. Comparison of impulse time histories at a range of 25m computed with and without radiation effects for a 380 ton nuclear explosion in a 17m radius air-filled cavity.

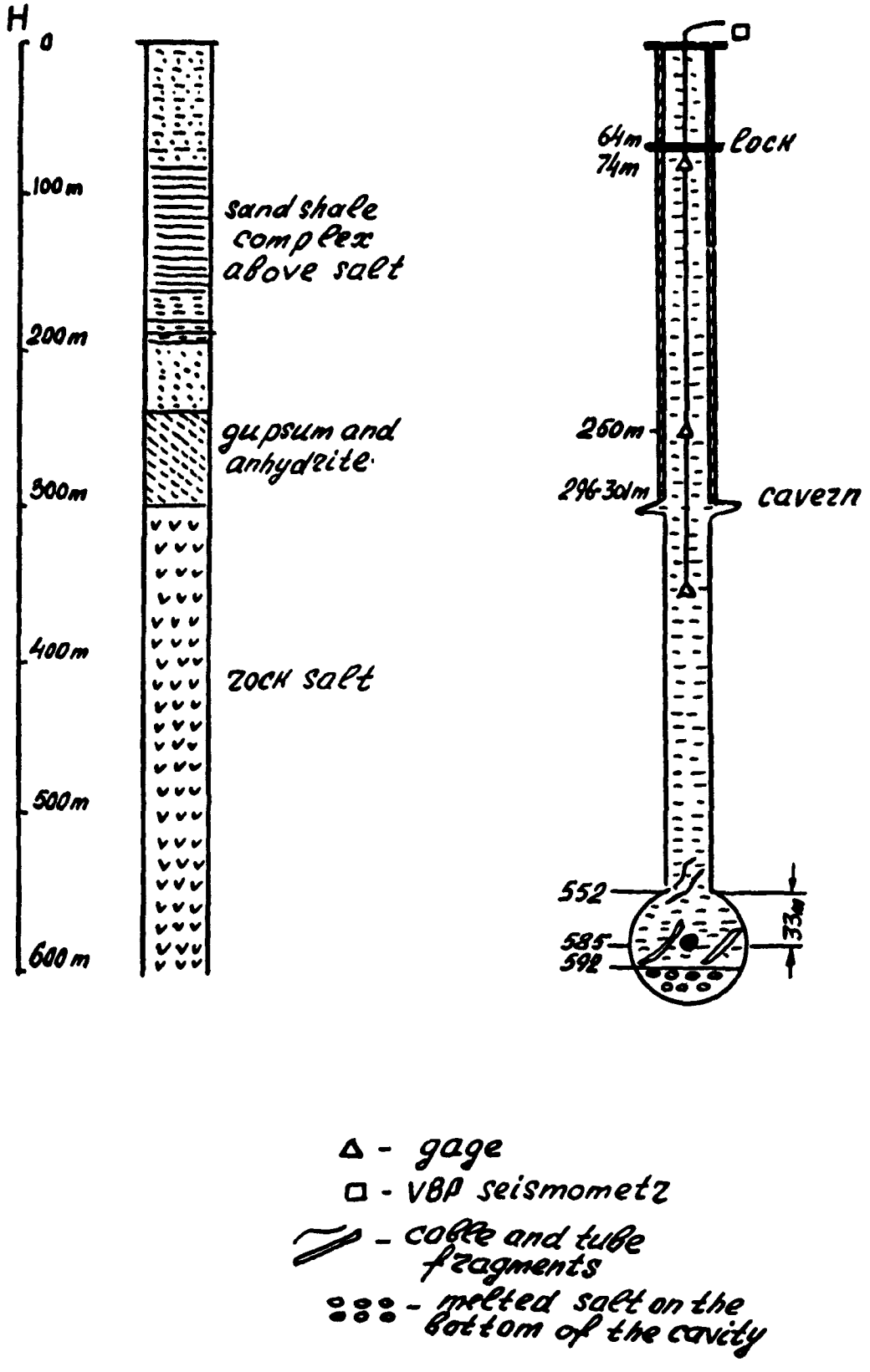


Figure 5. Schematic drawing illustrating the cavity condition following the fourth Soviet nuclear test in the water-filled cavity at Azgir. The section at the left shows the subsurface geologic profile down to shot depth at this site.

Investigation Of Non-Double-Couple Earthquake Sources

Paul A. Nyffenegger,
University Of Texas Department Of Geological Sciences and
University Of Texas Institute For Geophysics,

Lian-She Zhao and Cliff Frohlich
University of Texas Institute For Geophysics
8701 North MoPac, Austin, TX 78759-8397

Contract No. F19628-91-K-0026 ASSERT

OBJECTIVES

In this study we investigate earthquakes with reported source mechanisms that contain a large non-double-couple (NDC) component. Our objectives are to constrain the observational characteristics of naturally occurring earthquakes with NDC source mechanisms, and to determine the nature of systematic errors afflicting moment tensor determination. The fundamental questions motivating this research are: 1) Do earthquakes with NDC mechanisms possess complexity in the source time function not attributable to surface reflections or other propagation effects? 2) To what extent are reported NDC mechanisms due to systematic errors in the source determination process? and 3) How can we distinguish earthquakes with genuine NDC mechanisms from earthquakes with poorly determined or anomalous sources, and from explosions? Although our research currently focuses on seismic events with magnitude M_w ~ 5.5 and larger, we expect that this research ultimately will help to reduce erroneous characterization of natural and manmade seismic events of smaller magnitude.

RESEARCH ACCOMPLISHED

The moment tensors for many earthquakes reported in the Harvard centroid moment tensor (CMT) catalog cannot be explained solely as being due to slip along a simple planar fault. The most likely explanation for such NDC sources is that they are caused when two or more subevents with appropriately different focal mechanisms occur nearly simultaneously. However, systematic errors in the determination of the moment tensor may also cause large apparent NDC components. We organize this investigation into two stages: a) Analysis of source-time complexity for earthquakes with CMT having large NDC components; and b) Comparison of moment tensors determined from regional and teleseismic data.

Source Time Complexity of Earthquakes with Large NDC Components

We examine the nature of NDC sources by investigating earthquakes in groups which possessed at least one event with a well determined NDC component and one or more nearby earthquakes with well-detemined double-couple mechanisms. By jointly studying nearby events is it allows us to identify apparent source complexity attributable to near-source structure. We have identified 35 recent earthquakes in the CMT catalog which possess well determined NDC components and which have double-couple companions occurring within 200 km.

Our approach for each group of earthquakes is to compare geometric ray theory synthetics generated for a simple triangular source time function with broadband displacement waveforms from available IRIS stations (Figure 1). When the comparison reveals a good match the event is "simple," when there are obvious unmatched arrivals the event is "complex." Our intent is to investigate whether NDC events exhibit complexity more often than the nearby double-couple events. In Figure 1 the match between synthetics and obsevations is quite good for both the

NDC event and the first double-couple, although for the NDC at all three stations there is some indication of an unmatched arrival about 5-10 seconds after the initial arrival. However, the second double-couple event clearly is complex, as at least three late arrivals unmodeled by the simple triangular source are evident at all three stations. Note that the observed complexity cannot be attributed to near-station structure, since it is present at all three stations. Also, it is improbable that it is due to near-source structure since it does not occur for the second event, and since the hypocenters of the second and third event are situated only 298 km and 273 km, respectively, from the NDC event.

We are currently processing numerous groups of events using procedures similar to those illustrated in Figure 1. For each event, we bandpass filter the records into long period (0.006-0.02 Hz), mid-period (0.02-1. Hz), and short period (1.-4. Hz) frequency bands for comparison. We make comparisons for as many well-recorded phases as are available, including phases such as ScP and PKP which are often well-recorded at the higher frequencies. From this analysis we will investigate what fraction of NDC and double-couple sources possess identifiable subevents, and how this depends on event magnitude, focal depth, or tectonic setting.

Comparison Of Source Mechanisms Determined From Regional And Teleseismic Data

Our basic approach is to determine moment tensors by comparing synthetic seismograms and observations of events with reported NDC sources using a grid search method to find the moment tensor which best fits the available data. For this study we have separately determined best-fitting mechanisms for three types of data, (1) teleseismic vertical-component data; (2) regionally recorded three-component broadband data; and (3) both teleseismic and regional data combined.

To determine the moment tensor, we first determine the best-fitting double-couple by performing the grid search over the strike, dip and rake of possible focal mechanisms. Then, we determine the NDC component by adding a second double-couple with relative strenth ε having the same three principal axes as the best-fitting double-couple, but with the T and B axes exchanged. We generate both teleseismic and regional synthetics using a reflectivity method. For regional waveform data (Figure 2) we relocate the event prior to final determination of the source parameters by searching for the location most consistent with waveforms from individual stations (Zhao and Helmberger, 1994).

For example, for the northern California earthquake of 26 April 1992, we find that the best-fitting moment tensors determined for teleseismic, regional, and combined data all have approximately the same P and T axes as the CMT reported by Harvard (Figure 3 and Table 1). Furthermore, in each case the size of the NDC component we determine seems statistically well-constrained since the relative error increases by 5-10% as the parameter ε is changed by 0.1. However, there is a significant discrepancy between the value for the NDC component as determined by the various methods, and all three of our determinations differ from the Harvard CMT. Clearly, the shape of the relative error curves is not indicative of the true uncertanties in the size of the NDC components.

We are currently applying these methods to a number of earthquakes for which we have adequate data from both teleseismic and regional stations, including several events in California. Generally our preliminary results find a somewhat smaller NDC component than reported in the Harvard catalog (Table 1). In addition, when we attempt to find the NDC component using data from only a few regional stations the size of the NDC component varies depending on the location chosen for the event.

CONCLUSIONS AND RECOMMENDATIONS

We are currently investigating earthquakes with a large reported NDC component using both teleseismic and regional broadband data. We have demonstrated that the application of a grid-search method for comparing of synthetic data and observations is an efficient scheme for exploring how source mechanisms depend on the available data. Our ongoing research focuses on determining the origin of differences between NDC source components as determined from regional and from teleseismic data. We are currently identifying NDC earthquakes having source-time functions consisting of multiple subevents, as these may require a different explanation than events with "simple" sources.

REFERENCE

Zhao, L.-S., and D. V. Helmberger, Source estimation from broadband regional seismograms, *Bull. Seism. Soc. Am.*, **84**, 91-104, 1994.

Table 1. Comparison of Harvard CMT and results determined in this study for the northern California earthquake of 26 April 1992

P axis		T axis		Moment	NDC parameters			Data
strike	plunge	strike	plunge	(10^{25} dyne-cm)	ε	Γ	f_{clvd}	
348°	5°	80°	16°	5.96	0.47	-0.82	-0.32	Harvard CMT
353°	5°	262°	16°	8.65	-0.08	0.19	0.08	Teleseismic vertical
139°	1°	229°	12°	1.11	-0.19	0.51	0.19	Regional waveforms
140°	8°	233°	18°	7.92	-0.10	0.25	0.10	Combined data

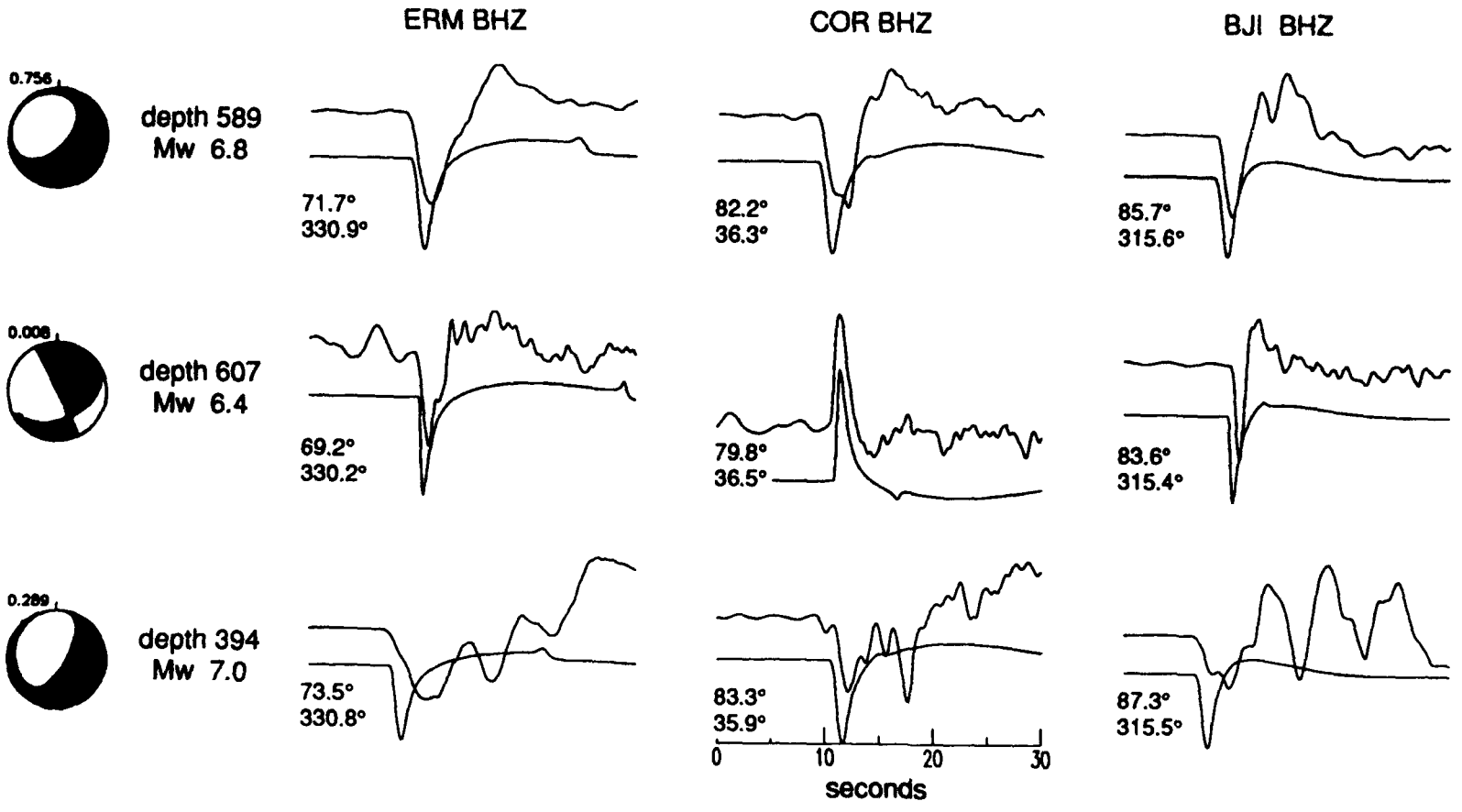


Figure 1. P arrivals and synthetics for three deep earthquakes from the Tonga region. For each event we display geometrical ray theory synthetics (bottom trace) and broadband vertical-component seismograms (top trace) for stations ERM (Erimo, Japan), COR (Corvalis, Oregon), and BJI (Beijing, China); the event-station distance and azimuth are at the lower left of each pair of traces. The mechanisms at left are Harvard CMT, with the value of Γ noted above each mechanism. The synthetics utilized a simple triangular source-time function. The predominantly NDC source (top traces, earthquake of 9/30/91) and the "simple" double-couple source (middle traces; earthquake of 3/21/93) match the synthetics much more closely than does the "complex" double-couple source (bottom traces; 7/11/92).

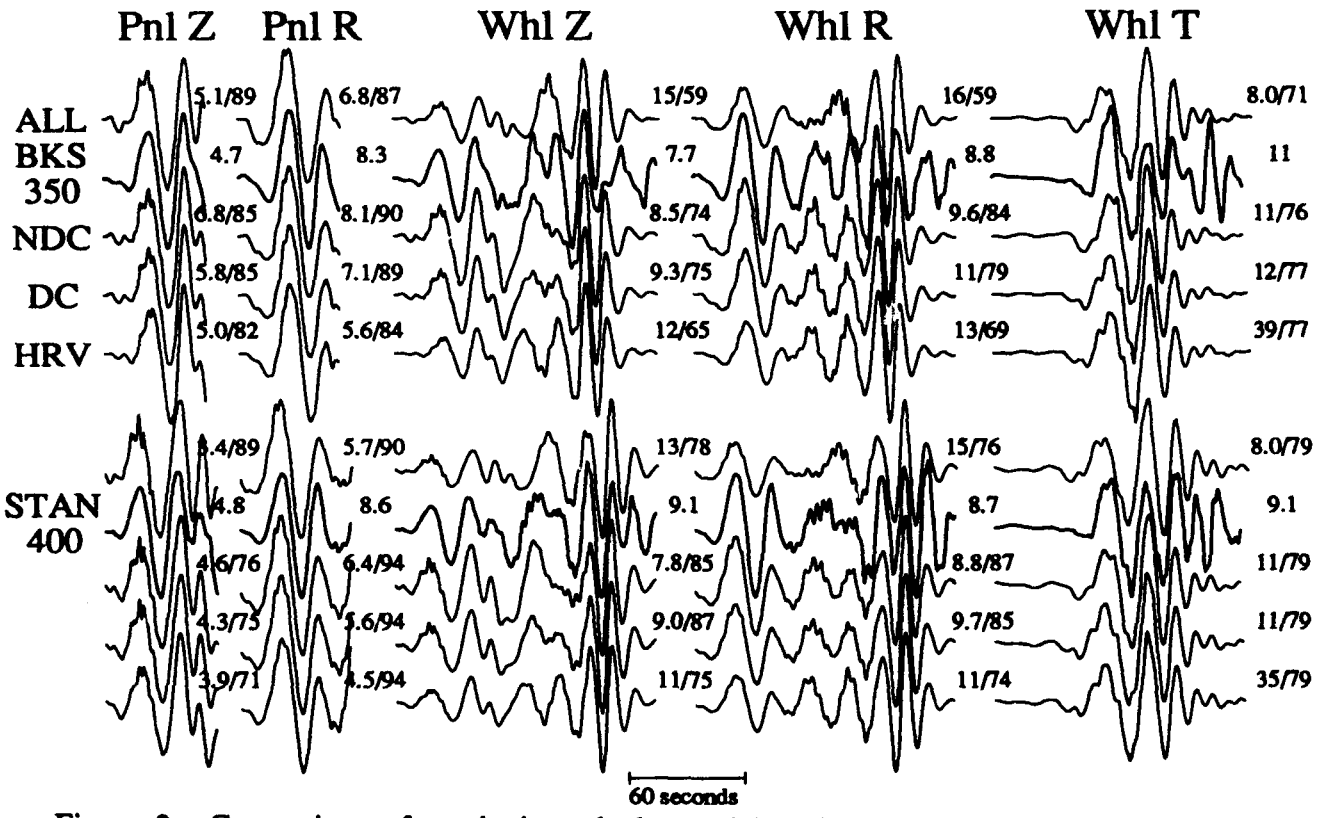


Figure 2. Comparison of synthetic and observed broadband waveforms for the northern California earthquake of 26 April 1992 observed at regional distances. Top group of traces are for station BKS (Berkeley, CA); bottom group is for STAN (Standford, CA); each group of traces includes vertical- and radial-component Pnl phases (Pnl Z and Pnl R) as well as the entire wave train for vertical, radial, and tangential components (Whl Z, Whl R, and Whl T). In each group, the second trace is the observations; the first trace (ALL) presents the synthetic that is the best fit to both teleseismic and regional observations; the third trace (NDC) is the synthetic that is the best NDC fit to regional observations; the fourth trace (DC) is the synthetic that is the best double-couple fit to the regional observations; and the last trace (HRV) is the synthetic generated using the source mechanisms reported by Harvard. The numbers to the right of each trace are the maximum trace amplitude in units of 10^{-2} cm, and 100 times the cross correllation coefficient between the synthetic and the observed waveforms.

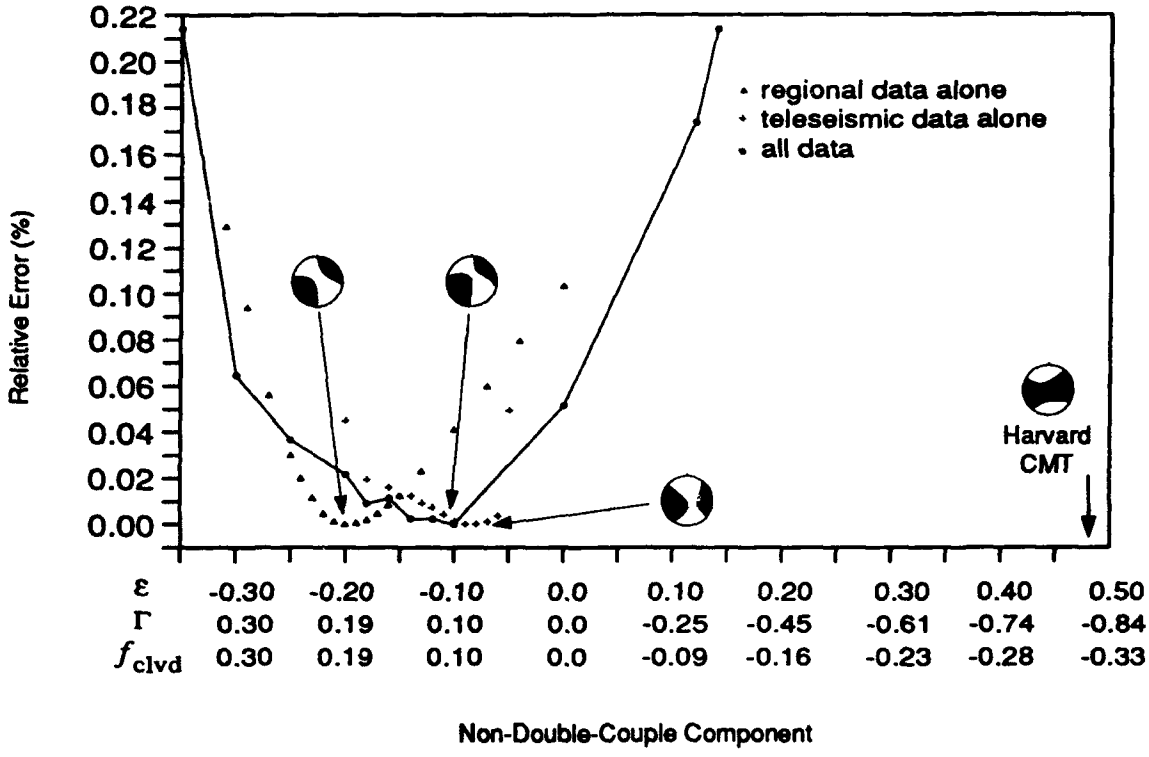


Figure 3. For the northern California earthquake of 26 April 1992, comparison of the size of NDC component determined by Harvard with that determined using regional data alone, teleseismic data alone, and a combined data set. Relative error represents increase in misfit between data and synthetics when NDC component is constrained at value plotted on the horizontal axis. The horizontal axis is the size of the NDC component as measured by three different commonly used parameters; these are: ε - the ratio of the minor and major double couples, where the major double couple.has the strength of the principal moment associated with the T axis; Γ - 2.6 (determinant of the moment tensor M)/(scalar moment of M)$^{3/2}$; $f$clvd - ratio of smallest and largest principal moments of M. Focal mechanisms plotted are for the moment tensor with the smallest relative error. For the teleseismic data we utilized vertical-component data from seven teleseismic stations at distances ranging from 39°to 74°, and having azimuths in the northern half of the focal sphere. For the regional data we used three-component data recorded at two stations, BKS and STAN. Note that the four mechanisms all possess approximately the same P and T axes, but that there are significant differences in the size and polarity of the NDC component.

A Generalized Pseudospectral Method and its Application to Regional 3-D Seismic Wavefield Synthesis

Jeffrey Orrey and Charles Archambeau
Dept. of Physics, TAGG
University of Colorado
Boulder, CO 80309-0583

Contract No. F49620-94-1-0124

Objective

The objective of this study has been the development and application of a new method for numerically modelling seismic wavefields in arbitrarily heterogeneous media in the regional distance range. The emphasis of the method is on the accurate representation of signal types important, or potentially important, for event discrimination. The method is based on the Fourier pseudospectral method in order to minimize the large storage requirements of numerical modelling in 3-D. Our approach has been to extend the regular Fourier method, which intrinsically admits wavefield synthesis in a periodic domain, to produce a generalized Fourier method that is capable of accurately representing wavefields in media with surfaces of discontinuity. Using a general coordinate transformation in the integral formulation, surface topography and irregular material interfaces may be included. By testing the method against known analytical and accurate modal and numerical methods for simple problems, the method's accuracy is evaluated for the important signals in the wavefield. The method may be used in 2- or 3-D to systematically study the energy partitioning between important seismic phases for anelastic earth structures that contain strong lateral heterogeneities and surface topography.

Research Accomplished

The method that has been developed and tested is a generalization of the Fourier pseudospectral method. In this approach, a wavefields's spatial dependence is approximated by a truncated series of harmonic functions and the expansion coefficients are integrated in time as in a finite difference method [5]. In the new method, the expansion set is supplemented by a finite set of functions that are not infinitely differentiable with continuous derivatives like the harmonic functions. This discontinuous set synthesizes the discontinuous or rapidly varying portion of the wavefields's spatial dependence, leaving a smooth, continuous remainder whose Fourier series representation is rapidly convergent. The method is formally expressed as a weighted residuals statement of the weak form of momentum conservation. Using the weak form, the boundary conditions, including a traction-free surface, are explicitly satisfied. The integral statement is evaluated by invoking orthogonality between the basis functions, and the resulting algebraic system is solved at each time step for the expansion coefficients.

Analytical Formulation

The numerical method's governing equations are initiated from an integral statement of momentum conservation with surfaces of discontinuity present. In the following derivation, Greek subscripts denote spatial coordinate directions, and a comma before a subscript indicates a derivative with respect to the coordinate whose label follows the comma. The Einstein summation convention is assumed unless otherwise indicated. Consider the Lagrangian description of momentum conservation in a continuous volume V bounded by a surface of discontinuity S. Boundary conditions exist for any material surface across which the field quantities undergo a discontinuous change [4], [1]. Let the bounding surface S have an outward normal unit vector $\mathbf{n}$. Then a jump in a quantity Q across S is defined as $[\![Q]\!]_S = Q^+ - Q^-$ where Q^+ and Q^- are the values of Q immediately near S on the positive and negative sides of $\mathbf{n}$, respectively. From now on we neglect the subscript S on double brackets, understanding that all jump conditions are taken across surfaces of discontinuity. The equation of momentum conservation for the volume V bounded by S is

$$\int_{V\Theta(V\cap S)} [\rho\,\ddot{u}_\alpha - t_{\alpha\beta,\beta} - f_\alpha]\,dV - \oint_S [\![t_{\alpha\beta}n_\beta]\!]dS = 0 \tag{1}$$

where $\ddot{u}_\alpha$ and f_α are the components of particle acceleration and body force density, respectively, in the α coordinate direction, and $t_{\alpha\beta}$ is the stress tensor. The symbols Θ and $\cap$ denote the set theoretic difference and intersection, respectively (see [1]). In the following, $V-S$ is used to abbreviate $V\Theta(V\cap S)$. Since V is arbitrary and therefore could be chosen to exclude S, the integrals in (1) are zero separately. While the first integral provides the differential equation of momentum equation in the continuum, the second integral provides the boundary conditions: Across S the traction jump condition is $[\![t_{\alpha\beta}\,n_\beta]\!] = 0$. Note that for a solid-liquid interface, tangential components may contain jumps if slip occurs. From an analogous treatment of the energy equation, the jump condition from energy conservation of an adiabatic system is $[\![\dot{u}_\alpha t_{\alpha\beta}\,n_\beta]\!] = 0$. Combined with the traction jump condition this becomes $[\![\dot{u}_\alpha]\!]t_{\alpha\beta}\,n_\beta = 0$, which provides the jump condition on particle velocities.

The spatial dependence of the field variables is approximated by a finite wave number expansion in terms of orthogonal functions that are not generally the eigenfunctions of the problem. For a set of expansion functions $b(\mathbf{k},\mathbf{x})$, each component of displacement is expressed as

$$\begin{aligned} u_\alpha(\mathbf{x},t) &= \sum_{\mathbf{k}} \hat{U}_\alpha(\mathbf{k},t)\,b(\mathbf{k},\mathbf{x}) \\ &\equiv \hat{\mathbf{U}}_\alpha \cdot \mathbf{b} \end{aligned} \tag{2}$$

where $\hat{\mathbf{U}}_\alpha$ is a vector of expansion coefficients whose components are the coefficients for each wave vector $\mathbf{k}$. Throughout the following, the components of all boldface vector functions are components in the wave number domain unless otherwise indicated. For the following analysis we consider a linear constitutive relation $t_{\alpha\beta} = C_{\alpha\beta\gamma\delta}\,\epsilon_{\gamma\delta}$ with strain $\epsilon_{\gamma\delta} = \frac{1}{2}\,(u_{\gamma,\delta} + u_{\delta,\gamma})$, but in general $C_{\alpha\beta\gamma\delta}$ can be an integral operator incorporating relaxation and viscous terms. We denote the strain approximation obtained by using the finite expansion of (2) with the superscript (b):

$$\epsilon^{(b)}_{\gamma\delta} = \frac{1}{2}\left(\hat{\mathbf{U}}_\gamma \cdot \mathbf{b}_{,\delta} + \hat{\mathbf{U}}_\delta \cdot \mathbf{b}_{,\gamma}\right) \tag{3}$$

Similarly, the corresponding stress approximation is $t^{(b)}_{\alpha\beta} = C_{\alpha\beta\gamma\delta}\,\epsilon^{(b)}_{\gamma\delta}$. The momentum of the system with these finite expansions is not the same as the momentum of the continuous system. In other words, the lack of completeness in the expansions produces an error, or residual, in momentum. Therefore, the expansion coefficients of the field variables must be chosen to satisfy momentum in a sufficiently accurate approximate sense. An approximation that makes the momentum residual orthogonal to a specified set of weighting functions is termed a weighted residuals approximation. When the set of weighting functions is the same as the field variables' expansion set, the approximation is referred to as Galerkin's method. In this case, the error is made orthogonal to the expansion set. For the set of orthogonal basis functions $\mathbf{b}$, the Galerkin weighted residuals statement of momentum conservation is

$$\int_{V-S} \mathbf{b}^* \left[\rho\, \mathbf{b} \cdot \left(\frac{\partial^2}{\partial t^2} \hat{\mathbf{U}}_\alpha \right) - t^{(b)}_{\alpha\beta,\beta} - f^{(b)}_\alpha \right] dV - \oint_S \mathbf{b}^* [\![t^{(b)}_{\alpha\beta}\, n_\beta]\!] dS = 0 \tag{4}$$

The jump in tractions across the bounding surface S incorporates the externally applied tractions, since $[\![t^{(b)}_{\alpha\beta}\, n_\beta]\!] = \bar{t}_{\alpha\beta}\, n_\beta - t^{(b)}_{\alpha\beta}\, n_\beta$, where $\bar{t}_{\alpha\beta}\, n_\beta$ is the applied traction on S and $t^{(b)}_{\alpha\beta}\, n_\beta$ is the finite traction expansion on S. Since the jump condition on displacements is an essential boundary condition, it must be satisfied explicitly by the basis functions rather than as an integral quantity. The weak form of momentum conservation is obtained via integration by parts of the second term in (4), and the governing equation for the numerical solution becomes

$$\int_{V-S} \left[\mathbf{b}^*\, \rho\, \mathbf{b} \cdot \left(\frac{\partial^2}{\partial t^2} \hat{\mathbf{U}}_\alpha \right) + \mathbf{b}^*_{,\beta}\, t^{(b)}_{\alpha\beta} - \mathbf{b}^* f_\alpha \right] dV = \oint_S \mathbf{b}^*\, \bar{t}_{\alpha\beta}\, n_\beta\, dS \tag{5}$$

By expanding applied forces and the material modulus and density in the orthogonal basis functions, the integrals may be evaluated analytically by invoking orthogonality. Then the equation may be solved for $\hat{\mathbf{U}}_\alpha$ at discrete time steps by numerically integrating as in a finite difference method. Because the mass matrix $\hat{\mathbf{M}} = \int_V \mathbf{b}^* \rho^{(b)}\, \mathbf{b}\, dV$ must be inverted at each time step, the basis functions must be chosen so that this inversion is rapid. For the case of trigonometric functions, $\hat{\mathbf{M}}$ can be inverted rapidly using the Fast Fourier Transform (FFT), which requires roughly $D \cdot N log N$ operations with N wave numbers for each expansion in D dimensions.

Consider the particular case of trigonometric basis functions. For Cartesian coordinates with directional unit vectors $\mathbf{n}_\alpha$, $\alpha = 1,2,3$, the spatial domain volume is $V_X = \prod_{\alpha=1}^{3} X_\alpha$, and we define the wave vectors $\tilde{\mathbf{k}} = \tilde{k}_\alpha \mathbf{n}_\alpha$ discretized over each coordinate length X_α:

$$\tilde{k}_\alpha = \frac{2\pi k_\alpha}{X_\alpha} \quad ; \quad -\frac{N_\alpha}{2} \le k_\alpha \le \frac{N_\alpha}{2} \tag{6}$$

For each coordinate direction we define a set of Fourier basis functions with the compact notation

$$\mathbf{e}_{(\alpha)} = \left(e^{i \tilde{k}_\alpha x_\alpha} \right)_{\tilde{k}_\alpha} \qquad (\text{no sum on } \alpha) \tag{7}$$

where $(\,)_{\tilde{k}_\alpha}$ denotes the set of functions for all values of $\tilde{k}_\alpha$. For an expansion of the displacement component u_β in the basis functions of (7), we define the expansion coefficient set

$${}^{(a)}\hat{\mathbf{U}}^{(e)}_\beta = \left(\hat{U}^{(e)}_\beta(\tilde{k}_\alpha) \right)_{\tilde{k}_\alpha} \tag{8}$$

so that the Fourier expansion is

$$ {}^{(\alpha)}\hat{\mathbf{U}}_{\beta}^{(e)} \cdot \mathbf{e}_{(\alpha)} = \sum_{\tilde{k}_\alpha} \hat{U}_{\beta}^{(e)}(\tilde{k}_\alpha)\, e^{i\tilde{k}_\alpha x_\alpha} \qquad (\text{ no sum on } \alpha \text{ }) \tag{9} $$

The product of 1-D Fourier terms is combined by defining an unsubscripted Fourier basis vector $\mathbf{e} = \left(e^{i\tilde{\mathbf{k}}\cdot\mathbf{x}}\right)_{\tilde{\mathbf{k}}}$. Then the Fourier series expansion may be written compactly as $u_\beta = \hat{\mathbf{U}}_{\beta}^{(e)} \cdot \mathbf{e}$. If equation (5) were solved for the wave number coefficients $\hat{\mathbf{U}}_\alpha$, then the displacement $u_\alpha(\mathbf{x}, t)$ would be given by the expansion of (2). For a numerical solution, however, $u_\alpha(\mathbf{x}, t)$ is given only at discrete points in space. The continuous space $\mathbf{x} = x_\alpha \mathbf{n}_\alpha$ is discretized into the positions $j_\alpha \Delta x_\alpha \mathbf{n}_\alpha$, with N_α collocation points evenly spaced by a distance Δx_α along the direction α. The coordinate lengths are $X_\alpha = N_\alpha \Delta x_\alpha$ (no sum on α). The solution method maps a set of wave number coefficients $\hat{\mathbf{U}}_\alpha$ into a set of collocation values $\mathbf{U}_\alpha$ whose components are the values of displacement at the collocation points. The expansion coefficients are related to the collocation values by a discrete transform:

$$ \hat{U}_\alpha(\mathbf{k}) = \frac{1}{V_N} \sum_{\mathbf{n}} U_\alpha(\mathbf{n})\, e^{-i\tilde{\mathbf{k}}\cdot\tilde{\mathbf{n}}} \quad ; \quad V_N \equiv \prod_{\gamma=1}^{3} \mathrm{N}_\gamma \tag{10} $$

where $\tilde{n}_\alpha = n_\alpha \Delta x_\alpha$. Consider a collocation representation of the material modulus: $C_{\alpha\beta\gamma\delta}(\mathbf{n}) = C_{\alpha\beta\gamma\delta}(\mathbf{x})\Big|_{\mathbf{n}\cdot\Delta\mathbf{x}}$. If the modulus is expanded in a Fourier series as $C^{(e)}_{\alpha\beta\gamma\delta}(\mathbf{x}) = \hat{\mathbf{C}}^{(e)}_{\alpha\beta\gamma\delta} \cdot \mathbf{e}$, the discrete transform relationship allows the continuous modulus to be represented as the trigonometric interpolation of the nodal quantities:

$$ C^{(e)}_{\alpha\beta\gamma\delta}(\mathbf{x}) = \frac{1}{V_N} \sum_{\mathbf{n}} C_{\alpha\beta\gamma\delta}(\mathbf{n}) \sum_{\mathbf{k}} e^{-i\tilde{\mathbf{k}}\cdot(\tilde{\mathbf{n}}-\mathbf{x})} \tag{11} $$

With an analogous expansion of the material density and applied forces, equation (5) with trigonometric basis functions becomes the particular case of the Fourier pseudospectral method. Derivatives in the governing equation are computed by multiplying the wave number coefficients $\hat{U}_\alpha(\mathbf{k})$ by $i\mathbf{k}$ and performing the discrete inverse transform with an FFT. The collocation values $\mathbf{U}_\alpha$ are obtained at each time step.

A valid numerical approximation to momentum conservation and the boundary conditions converges towards the true solution as the order of the approximation is increased. Even for a convergent approximation, the error that is introduced by replacing the continuous function $u(x)$ with its N-th order truncated Fourier expansion depends upon how rapidly the function's Fourier coefficients decay to zero. By denoting the N-th order truncated Fourier expansion of $u(x)$ as $\mathcal{F}_N[u(x)]$, the error is expressed as

$$ |u(x) - \mathcal{F}_N[u(x)]| \leq \sum_{|k|>N/2} |\hat{U}(k)| \tag{12} $$

The convergence rate, in turn, depends upon the smoothness and continuity properties of the function u. A function whose m-th derivative is discontinuous is referred to as C_{m-1}-continuous. In general, a function that is C_{m-1}-continuous has a Fourier series expansion

equations. Column vectors are denoted with braces, as { } , and matrices are denoted with square brackets, as [ ]. For convenience, we write the weak form of momentum conservation (4) as

$$\hat{\mathbf{M}} \cdot \frac{\partial^2}{\partial t^2} \hat{\mathbf{U}}_\alpha + \hat{\mathbf{K}}_{\alpha\gamma} \cdot \hat{\mathbf{U}}_\gamma = \hat{\mathbf{F}}_\alpha + \hat{\mathbf{T}}_\alpha \tag{16}$$

where

$$\hat{\mathbf{M}} = \int_V \mathbf{b}^* \rho^{(b)} \mathbf{b} \, dV \tag{17}$$

$$\hat{\mathbf{K}}_{\alpha\gamma} = \int_V \mathbf{b}^*_{,\beta} C^{(b)}_{\alpha\beta\gamma\delta} \mathbf{b}_{,\delta} \, dV \tag{18}$$

$$\hat{\mathbf{F}}_\alpha = \int_V \mathbf{b}^* f_\alpha dV \tag{19}$$

$$\hat{\mathbf{T}}_\alpha = \oint_S \mathbf{b}^* \bar{t}_{\alpha\beta} n_\beta \, dS \tag{20}$$

The mass matrix $\hat{\mathbf{M}}$ and stiffness matrix $\hat{\mathbf{K}}_{\alpha\gamma}$ are partitioned as follows:

$$\hat{\mathbf{M}} = \begin{bmatrix} \hat{\mathbf{M}}^{(ee)} & \hat{\mathbf{M}}^{(es)} \\ \hat{\mathbf{M}}^{(se)} & \hat{\mathbf{M}}^{(ss)} \end{bmatrix} \quad ; \quad \hat{\mathbf{K}}_{\alpha\gamma} = \begin{bmatrix} \hat{\mathbf{K}}^{(ee)}_{\alpha\gamma} & \hat{\mathbf{K}}^{(es)}_{\alpha\gamma} \\ \hat{\mathbf{K}}^{(se)}_{\alpha\gamma} & \hat{\mathbf{K}}^{(ss)}_{\alpha\gamma} \end{bmatrix} \tag{21}$$

Body forces and tractions, in general, may be applied with both Fourier and supplementary terms:

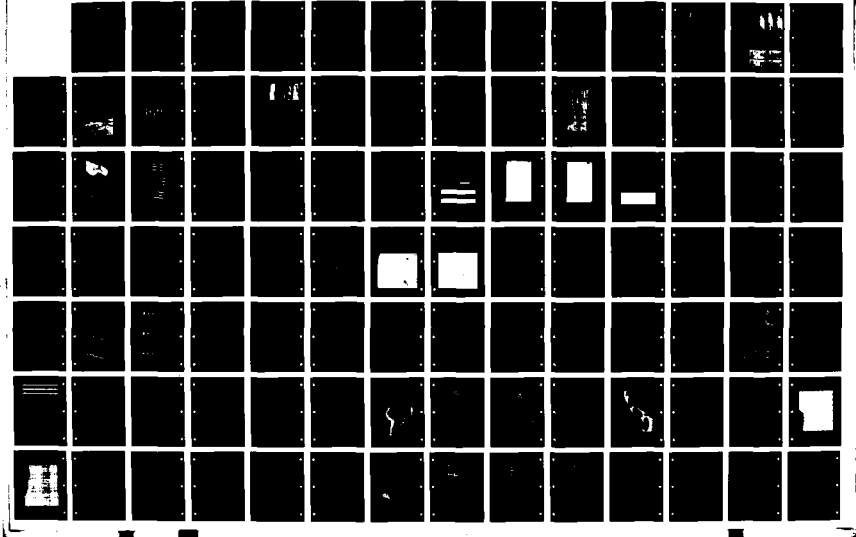
$$\hat{\mathbf{F}}_\alpha = \begin{pmatrix} \hat{\mathbf{F}}^{(e)}_\alpha \\ \hat{\mathbf{F}}^{(s)}_\alpha \end{pmatrix} \quad ; \quad \hat{\mathbf{T}}_\alpha = \begin{pmatrix} \hat{\mathbf{T}}^{(e)}_\alpha \\ \hat{\mathbf{T}}^{(s)}_\alpha \end{pmatrix} \tag{22}$$

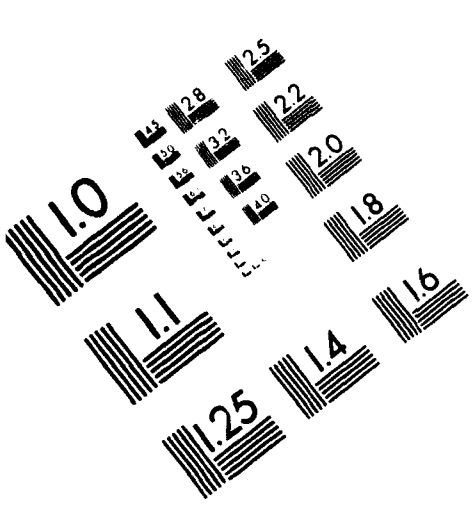
The system of equations (16) is solved for the collocation values $\mathbf{U}^{(e)}_\beta$ and $\mathbf{U}^{(s)}_\beta$ analogously to the system described earlier for the purely Fourier method. Anelastic attenuation may be added to the time-domain formulation as per Emmerich and Korn [3] or Witte and Richards [8].

The performance of the generalized pseudospectral method has been tested for a traction-free surface. Let the surface be oriented with $\mathbf{n} = \mathbf{n}_3$. In this case it is sufficient to use the mixed set of a Fourier expansion plus interface functions in the x_3-direction only; in the other two coordinate directions only a Fourier expansion is used. The supplementary basis function becomes $\mathbf{s} = e_{(1)} e_{(2)} d_{(3)}$. Of course this doesn't preclude the use of interface functions in the other coordinate directions, but doing so at this point unnecessarily complicates the analysis. Indeed, individual cubes (in cartesian 3-D) surrounded by surfaces of discontinuity could be coupled together with the boundary conditions to generate a multi-domain method, as discussed in chapter 13 of [2], and [7]. Combined with a general coordinate transformation, highly irregular material interfaces may be created. Since the Fourier expansion in x_3 is periodic over the coordinate length X_3, the endpoint planes at $x_3 = 0$ and $x_3 = X_3$ are identical in the absence of the interface functions. Decoupling these planes with the interface functions creates two surfaces, one at $x_3 = 0$ and the other at $x_3 = X_3$. One may think of the surfaces after decoupling as existing immediately next to one another but separated by an infinitesimal void. The interface functions must be chosen so that the boundary conditions

AD-A284 667 PROCEEDINGS OF THE ANNUAL SEISMIC RESEARCH SYMPOSIUM (16TH) HELD IN THORNWOOD NEW YORK ON 7-9 SEPTEMBER 1994 (U) PHILLIPS LAB HANSCOM AFB MA J J CIPAR ET AL. 475

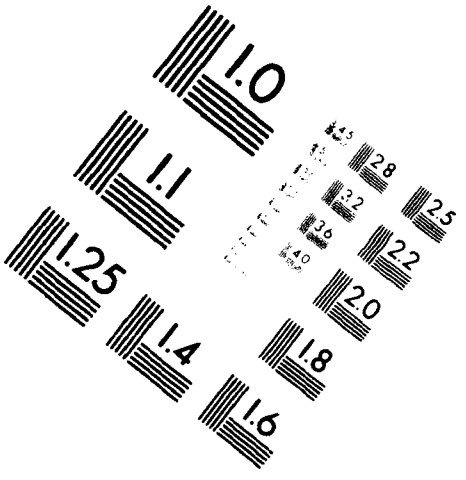
UNCLASSIFIED 8 AUG 94 PL-TR-94-2217 SBI-AD-E202 178 NL

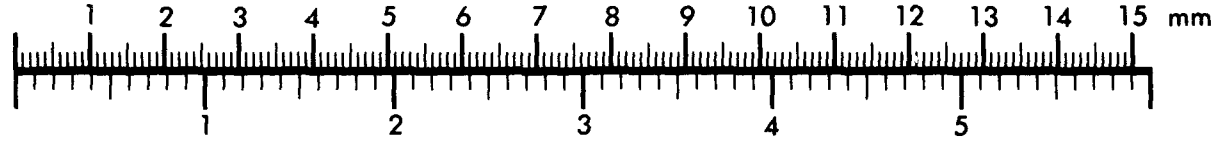


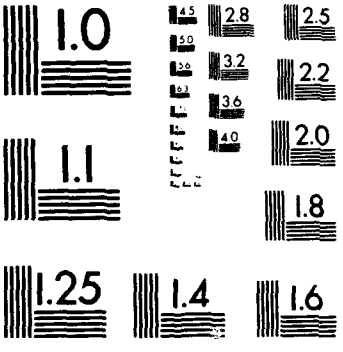


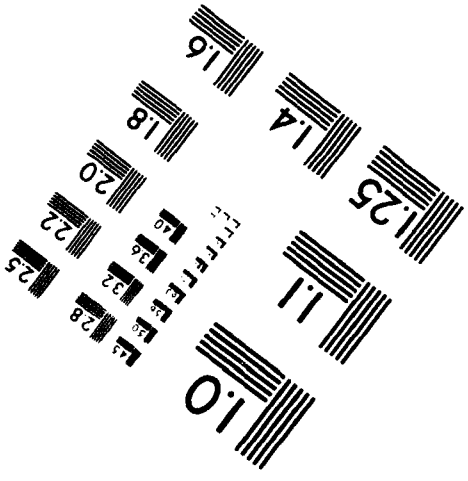


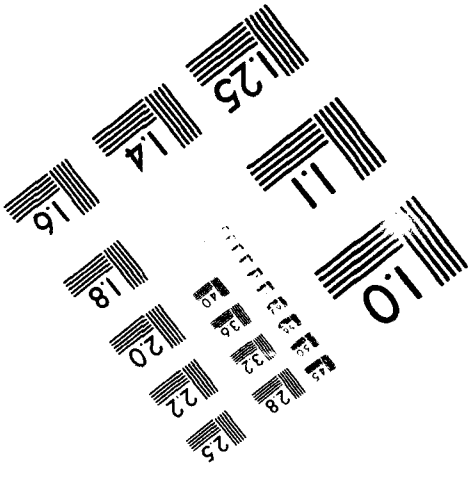
Association for Information and Image Management
1100 Wayne Avenue, Suite 1100
Silver Spring, Maryland 20910
301/587-8202











MANUFACTURED TO AIIM STANDARDS
BY APPLIED IMAGE, INC.

equations. Column vectors are denoted with braces, as ( ) , and matrices are denoted with square brackets, as [ ]. For convenience, we write the weak form of momentum conservation (4) as

$$\hat{\mathbf{M}} \cdot \frac{\partial^2}{\partial t^2} \hat{\mathbf{U}}_\alpha + \hat{\mathbf{K}}_{\alpha\gamma} \cdot \hat{\mathbf{U}}_\gamma = \hat{\mathbf{F}}_\alpha + \hat{\mathbf{T}}_\alpha \tag{16}$$

where

$$\hat{\mathbf{M}} = \int_V \mathbf{b}^* \rho^{(b)} \mathbf{b} \, dV \tag{17}$$

$$\hat{\mathbf{K}}_{\alpha\gamma} = \int_V \mathbf{b}^*_{,\beta} C^{(b)}_{\alpha\beta\gamma\delta} \mathbf{b}_{,\delta} \, dV \tag{18}$$

$$\hat{\mathbf{F}}_\alpha = \int_V \mathbf{b}^* f_\alpha dV \tag{19}$$

$$\hat{\mathbf{T}}_\alpha = \oint_S \mathbf{b}^* \bar{t}_{\alpha\beta} n_\beta \, dS \tag{20}$$

The mass matrix $\hat{\mathbf{M}}$ and stiffness matrix $\hat{\mathbf{K}}_{\alpha\gamma}$ are partitioned as follows:

$$\hat{\mathbf{M}} = \begin{bmatrix} \hat{\mathbf{M}}^{(ee)} & \hat{\mathbf{M}}^{(es)} \\ \hat{\mathbf{M}}^{(se)} & \hat{\mathbf{M}}^{(ss)} \end{bmatrix} \quad ; \quad \hat{\mathbf{K}}_{\alpha\gamma} = \begin{bmatrix} \hat{\mathbf{K}}^{(ee)}_{\alpha\gamma} & \hat{\mathbf{K}}^{(es)}_{\alpha\gamma} \\ \hat{\mathbf{K}}^{(se)}_{\alpha\gamma} & \hat{\mathbf{K}}^{(ss)}_{\alpha\gamma} \end{bmatrix} \tag{21}$$

Body forces and tractions, in general, may be applied with both Fourier and supplementary terms:

$$\hat{\mathbf{F}}_\alpha = \begin{pmatrix} \hat{\mathbf{F}}^{(e)}_\alpha \\ \hat{\mathbf{F}}^{(s)}_\alpha \end{pmatrix} \quad ; \quad \hat{\mathbf{T}}_\alpha = \begin{pmatrix} \hat{\mathbf{T}}^{(e)}_\alpha \\ \hat{\mathbf{T}}^{(s)}_\alpha \end{pmatrix} \tag{22}$$

The system of equations (16) is solved for the collocation values $\mathbf{U}^{(e)}_\beta$ and $\mathbf{U}^{(s)}_\beta$ analogously to the system described earlier for the purely Fourier method. Anelastic attenuation may be added to the time-domain formulation as per Emmerich and Korn [3] or Witte and Richards [8].

The performance of the generalized pseudospectral method has been tested for a traction-free surface. Let the surface be oriented with $\mathbf{n} = \mathbf{n}_3$. In this case it is sufficient to use the mixed set of a Fourier expansion plus interface functions in the x_3-direction only; in the other two coordinate directions only a Fourier expansion is used. The supplementary basis function becomes $\mathbf{s} = e_{(1)} \, e_{(2)} \, d_{(3)}$. Of course this doesn't preclude the use of interface functions in the other coordinate directions, but doing so at this point unnecessarily complicates the analysis. Indeed, individual cubes (in cartesian 3-D) surrounded by surfaces of discontinuity could be coupled together with the boundary conditions to generate a multi-domain method, as discussed in chapter 13 of [2], and [7]. Combined with a general coordinate transformation, highly irregular material interfaces may be created. Since the Fourier expansion in x_3 is periodic over the coordinate length X_3, the endpoint planes at $x_3 = 0$ and $x_3 = X_3$ are identical in the absence of the interface functions. Decoupling these planes with the interface functions creates two surfaces, one at $x_3 = 0$ and the other at $x_3 = X_3$. One may think of the surfaces after decoupling as existing immediately next to one another but separated by an infinitesimal void. The interface functions must be chosen so that the boundary conditions

can be satisfied on both of these surfaces. Since the surfaces are essentially back-to-back (in the sense of having been decoupled), displacement discontinuities must be allowed from one endpoint plane to the other. In addition to the displacement condition, we have boundary conditions on tractions, which in general require discontinuities in derivatives of displacement. Discontinuities could be included in the modulus expansion, but we consider here the simpler case of a continuous modulus represented by a Fourier expansion. The boundary condition is handled solely by discontinuities in the expansion of the strain field. Evidently the boundary conditions require that the interface functions remove the C_{-1}- and C_0-continuous portions of the wavefield. Nevertheless, adding more interface functions to make a smoother remainder inevitably will improve the solution. We find that by including only 2 interface functions, one that is C_{-1}-continuous and the other that is C_0-continuous, very accurate interface waves are generated. The solution can be improved by compressing the computational grid near the interface with a coordinate transformation so that the grid spacing is smaller near the interface.

Using the new method with only a single C_{-1}-continuous function, and moderately compressing the grid near the traction-free interface, we have compared the solution to a normal mode solution [6] for a 1 km deep explosive source in the structure shown in Figure (1). The C_{-1} function is a linear term, or sawtooth. A high-velocity cap layer was included in the structure at a depth of 150 km for the normal mode simulation, and the results were lowpass filtered with a corner frequency of 0.5 Hz. The time series from the two methods at a source-receiver distance of 205 km are overlayed in Figure (2) to compare the surface wave dispersion. Because the normal mode algorithm has cylindrical symmetry and the pseudospectral method is cartesian, the relative body wave to surface wave amplitudes do not match, but the surface waves display very similar dispersion characteristics when scaled for comparison.

Conclusions

We have developed a generalized pseudospectral method that can accurately simulate elastic wavefields in anelastic earth structures that contain sharp material interfaces. Testing the new method against analytic and modal methods for free surface problems shows excellent agreement for body and interface wave phases. The computational requirements of the new method are not significantly more than those of the regular Fourier pseudospectral method. By using a general coordinate transformation and by coupling distinct spatial domains with boundary conditions, wavefields may be generated in the presence of highly irregular topographic surfaces and interfaces.

The generalized pseudospectral method is being applied to demonstrate the effects of strong lateral heterogeneity on the energy partitioning between important seismic phases, such as Pg, Lg, and Rg. In particular, we are examining varying degrees of anelastic losses and scattering due to random inhomogeneities, as well as the effects of strong coherent lateral variations such as those caused by sedimentary basins, faults, or crustal transitions.

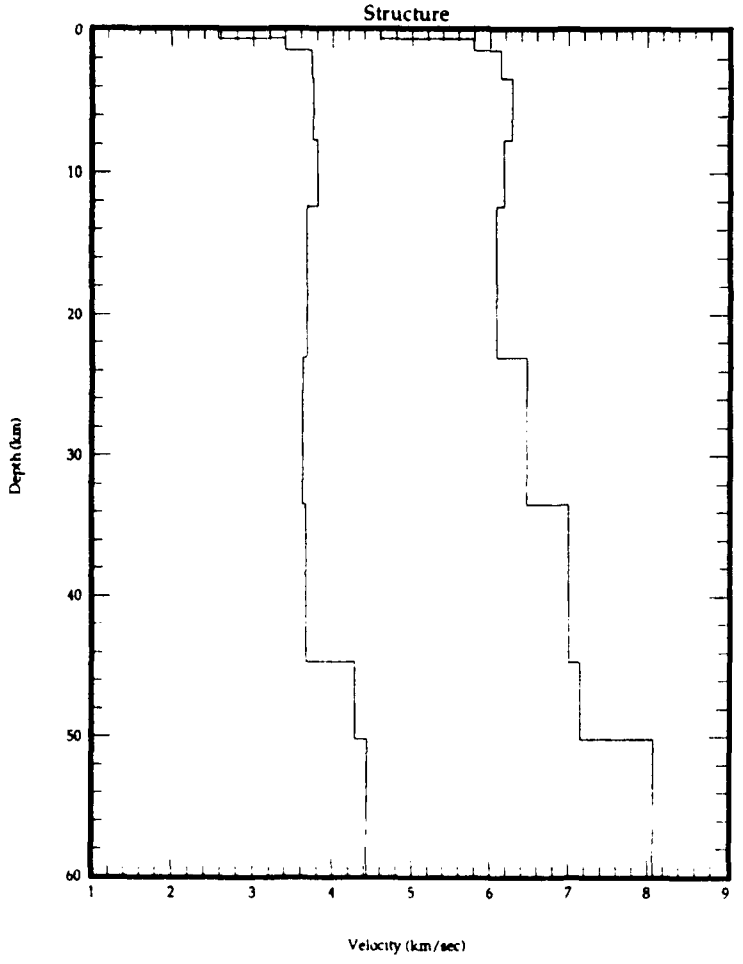


Figure (1). Structure used for Fourier-Sawtooth/Normal Mode comparison.

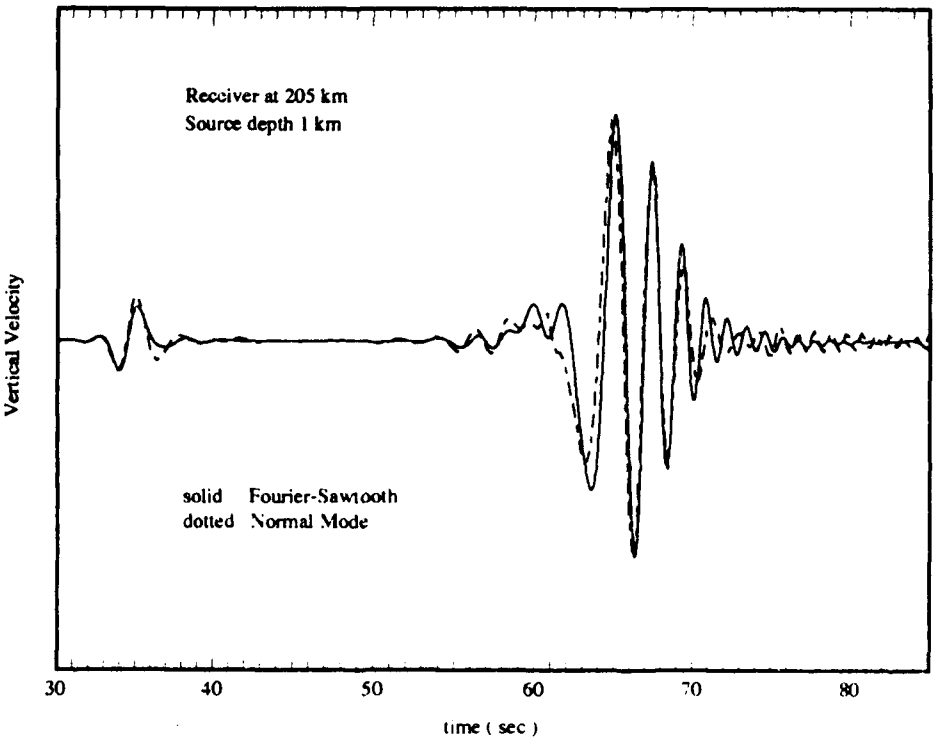


Figure (2). Time series comparison of the Fourier-Sawtooth and Normal Mode methods at a source-receiver distance of 205 km for the structure shown in Figure (1).

References

[1] C. B. Archambeau and J. B. Minster. Dynamics in prestressed media with moving phase boundaries: a continuum theory of failure in solids. *Geophys. J. R. astr. Soc.*, 52:65–96, 1978.

[2] C. Canuto, M. Y. Hussaini, A. Quarteroni, and T. A. Zang. *Spectral Methods in Fluid Dynamics.* Computational Physics. Springer Verlag, New York, 1988.

[3] H. Emmerich and M. Korn. Incorporation of attenuation into time-domain computations of seismic wave fields. *Geophysics*, 52(9):1252–1264, September 1987.

[4] A. C. Eringen. *Mechanics of Continua.* Krieger, New York, 2 edition, 1980.

[5] B. Fornberg. The pseudospectral [illegible] Comparisons with finite differences for the elastic wave equation. *Geophysics*, 52(4): 483–501, April 1987.

[6] D. Harvey. Seismogram synthesis using normal mode superposition: the locked mode approximation. *Geophys. J. R. astr. Soc.*, 66:37–61, 1981.

[7] E. Tessmer, D. Kessler, D. Kosloff, and A. Behle. Multi-domain chebyshev-fourier method for the solution of the equations of motion of dynamic elasticity. *J. Comp. Phys.*, 100:355–363, 1992.

[8] D. C. Witte and P. G. Richards. The pseudospectral method for simulating wave propagation. *Computational Acoustics*, 3, 1990.

TITLE: The Effects of Anisotropy on Regional Seismic Wave Propagation

PRINCIPAL INVESTIGATOR: Jeffrey Park
Co-WORKERS: Yang Yu, Liqiang Su, Jonathan Lilly & Robert Fischer
AFFILIATION: Department of Geology and Geophysics, Box 208109
Yale University, New Haven, CT 06520-8109
AFOSR contract: F49620-94-1-0043

July 23, 1994

OBJECTIVE

We wish to determine the effect of seismic anisotropy, within the crust and uppermost mantle, on surface waves with periods between 10 and 30 seconds. In particular, we wish to characterize the scattering caused by lateral variations in anisotropy in regions of past and present lithospheric deformation. This path-dependent scattering can distort seismic waveforms, and make more difficult the discrimination of explosions from earthquakes. We plan to identify regions of the Earth where scattering associated with lithospheric anisotropy is important. Data from regional networks and arrays located in Eurasia and the US will also be used in experiments to extract 'scattered' waveforms from the principal Love and Rayleigh wavepackets. In addition to standard stacking/beamforming techniques, we will apply a frequency-dependent variant of the MUSIC algorithm to identify coherent surface waves that traverse an array. We plan to test, in selected areas, whether anisotropy inferred from the 'splitting' of 1-20 second shear waves is sufficient to explain observed Love to Rayleigh scattering.

RESEARCH ACCOMPLISHED

We have examined the effect of seismic anisotropy on the scattering of surface waves in continental collision zones, many of which occur in areas of nonproliferation concern. We have approached the problem from three angles, 1) evidence for Love-Rayleigh coupling in seismic data from the Tibetan Plateau and Tien Shan region, 2) theoretical investigation of the effect of crust and upper-mantle anisotropy on crustal resonances, and 3) wavelet-based signal processing methods for estimating the polarization of coherent seismic energy in a noisy background.

The first project demonstrated that Love-Rayleigh coupling associated with elastic

anisotropy in the uppermost mantle, which had been observed in oceanic settings (Park and Yu, 1993; Yu and Park, 1994), is also prevalent in an actively deforming continental region. We investigated surface waves propagating across the Tibetan Plateau, based on the seismic records from a PASSCAL portable array and nearby CDSN stations (Figure 1). Significant long-period quasi-Love waveform anomalies, associated with fundamental Rayleigh-Love coupling, are consistently observed, suggesting that strong lateral gradients in azimuthal anisotropy exist beneath the plateau. More intense surface wave scattering is observed at intermediate periods ($T \sim 50$ s), which suggests that the cause of the long-period quasi-Love waves lies in the upper mantle, not the thickened crust of the plateau. A detailed analysis of the data indicates that the long-period waveform anomalies are generated beneath the central Tibetan Plateau, where the structural trend implies deep deformations induced by continental collision. Figure 2 shows an example of a quasi-Love wave that is generated in the central Plataeu as the Love wave travels sourthard along the PASSCAL array. The absence of quasi-Love anomalies at the westernmost station of the PASSCAL array (XIGA, not shown) suggests the east-west extent of this mantle deformation is limited.

The quasi-Love wave observations are correlated to surface geologic deformation fabrics, and favor an anisotropic upper-mantle compression zone beneath the central-south Plateau. The intense scattering in the crustal surface waves indicate that the structure within the thickened Tibetan crust, whether anisotropic or isotropic, is more complex than, and not simply correlated with, the upper mantle structure. This is probably due to the different ways that the crust and lithosphere accommodate deformation. The lithosphere, though stronger, is thought to experience large-scale bulk deformation, which tends to align anisotropic olivine and orthopyroxene crystals in a coherent way within a large volume of peridotite rock. The upper crust deforms largely through brittle failure, so that anisotropy due to large-scale mineral orientation may be secondary to bulk anisotropy caused by aligned microcracks and a complex pattern of thrust ramps. Recent petrologic work in exhumed deep-crust metamorphic zones (Ague, 1994ab) suggests that such effects could influence seismic velocity structure in the deep crust as well.

Surface deformation features associated with the Tanggula Shan are consistent with the strong quasi-Love observations east of Lhasa. Speculatively, weak quasi-Love wave generation in the western and northern Plateau may be due to the volcanism in that region. Arnaud et al. (1992) investigated the volcanism at the west and north of the Plateau and concluded that the rocks are very similar to island-arc volcanism, which would occur if south-dipping subduction occurs at the northern edge of Tibet. Water released by a subducting slab would lower the melting temperature in the overlying mantle wedge, lower its seismic velocity, and could also inhibit the development of lattice-preferred-orientation (LPO) anisotropy (Karato et al., 1986). Alternatively, temperature-related annealing may retard the development and retention of LPO.

Some, but not all, of the quasi-Love observations are consistent with SKS splitting observations (McNamara et al, 1994). Quasi-Love waveforms are sensitive primarily to the gradient, not the absolute level of anisotropic properties. Both sets of observations

predict a strong gradient in anisotropic properties in central Tibet. However, the quasi-Love waveforms are absent from records collected in the northern plateau for northerly propagation paths, which is not consistent with a gradient at the northern edge of the plateau, as suggested by SKS studies. This discrepancy indicates that the simple models used to interpret both body and surface wave data may be inadequate. Either significant P-wave anisotropy exists under the plateau, the S-wave anisotropy does not possess a uniformly horizontal symmetry axis, or strong east-west gradients in anisotropy bias our data-synthetic comparison.

The second project involved developing computer code for the reflection and transmission of plane waves in layered anisotropic media with a symmetry axis of arbitrary orientation. Our previous work (Su et al, 1993; Su and Park, 1994) had demonstrated that a Born approximation with coupled free oscillations could be used successfully to model the effects of anisotropy on body waves, in particular, to model shear-wave splitting. Although most previous modelling studies in layered media specified either a vertical or a horizontal axis of symmetry for anisotropic structure, we had found (Park, 1993) that a tilted axis of symmetry was associated, in some cases, with enhanced Love-Rayleigh coupling, especially the overtone surface waves which combine to form crustal guided phases. Such anisotropic geometry might be expected in a crust whose detailed velocity structure is dominated by thrust ramps and listric normal faults e.g. an actively deforming region. We have started to convert coupled-mode codes from spherical to plane-layered geometry in order to model such effects in more detail. As a first step, we developed a convenient formulation for reflection/transmission in a stack of anisotropic layers whose axis of symmetry is arbitrary. An eigenvalue problem must be solved in each anisotropic layer for the vertical wavenumber, a complication not encountered in isotropic media. We examined the potential for unusual wave conversions in such media, as a possible explanation e.g., for impulsive arrivals on the transverse component of P-wave coda (Figure 3). We found, in this particular case, only weak P-to-SH conversion for tilted axes of symmetry, unless the P wave arrives at relatively shallow incidence.

The third project addresses a problem in estimating the spectral properties of seismic data as a function of time. Our project objectives include developing methods to detect scattered waves within a seismic array or sparse network using MUSIC or related algorithms. Previous experience in seismic polarization estimation, however, indicated that near-receiver scattering tended to degrade the ability to detect short-period signals unless the time window analysed was also short. Fourier transforms of short time windows, however, distort longer-period signals. The wavelet transform scales the data window with the period of the signal analysed, and so (purportedly) overcomes this conundrum. We therefore developed spectrum analysis and cross-correlation tools using a variant of the wavelet transform, for use in array-processing algorithms.

Using frequency-concentration concepts from multiple-taper spectral analysis, we designed a sequence of mutually orthogonal wavelets with optimal spectral leakage properties. We call these discrete functions "Slepian wavelets." A family of Slepian wavelet sequences of various lengths M is parameterized by the dimensionless time-bandwidth and time-bandcenter products p and p_c, respectively, with $p < p_c$. For time-bandwidth

product p, the associated Slepian wavelet family has approximately $4p-2$ wavelets with good spectral leakage properties. The parameters govern the passband of the wavelets. If $p << p_c$, the wavelets are frequency concentrated. If $p \approx p_c$, the wavelets are time-concentrated. The most sagacious choice of parameters will depend on the data set analysed. The Slepian wavelets are real-valued, and come in pairs of even and odd functions with similar spectral sampling properties. The pairs can be combined into complex-valued wavelets, the even wavelet as the real part, and the odd wavelet as the imaginary part.

Multiwavelet spectral analysis convolves a data series with sets of Slepian wavelets to obtain sets of eigenspectra that integrate spectral information in specified rectangles in the time-frequency plane. Wavelet eigenspectra from different data series can combined into a multiwavelet transform matrix M, from which the spectral density matrix estimator $\hat{\mathbf{S}}(f,t) = \frac{2}{K}\mathbf{M}^H \cdot \mathbf{M}$ can be calulated, where K is the number of real-valued Slepian wavelets used. The singular value decomposition (SVD) of M identifies correlated variance among the data series, e.g., components of seismic data at a single observatory. The first right singular vector of the multiwavelet transform matrix M of three-component seismic motion, identified as the principal polarization, reconstructs the particle motion ellipse as a function of time and frequency. The first left singular vector contains the coefficients of a linear combination of wavelets that reconstruct the particle motion associated with the principal polarization.

We tested the multiwavelet algorithm with data from three earthquakes. In the first example, wavelet polarization analysis captures successfully the polarization and dispersion behavior of Love and Rayleigh waves in data from a shallow earthquake. In data from the 9 June 1994 deep Bolivian earthquake, wavelet spectrum estimates identify a deficiency in the P wave, relative to the pP phase, of spectral energy in the $3 < T < 5$ period range, suggesting either unusual scattering or attenuation effects in the deep slab region, or a Doppler effect associated with a downward-propagating moment release. Multiwavelet spectra of particle motion at ARU (Arti, Russia, $\Delta = 120.8°$) reveals an abrupt increase in transverse-component energy roughly 13 seconds after the peak energy on the vertical component, suggesting intense scattering at least 100 km from the receiver (Figure 3). This signal occurs at ARU in data from several other earthquakes, and could be caused by a reflection from the nearby continental suture associated with the Ural Mountains. In data from the 9 March 1994 deep earthquake beneath the Fiji Islands recorded at FFC (Flin Flon, Northwest Territories, $\Delta = 96.8°$), wavelet polarization analysis detects a progressive increase in ellipticity between the radial and transverse components of the SKS phase, consistent with a fixed time delay associated with shear-wave splitting (Figure 4).

Ague, J. J., 1994. Mass transfer during Barrovian metamorphism of pelites, south-central Connecticut, II: Channelized fluid flow and the growth of staurolite and kyanite, *American J. of Science,* in press.

Ague, J. J., 1994. Deep crustal growth of hydrothermal quartz, kyanite and garnet in a high-porosity open fracture system, *J. of Metamorphic Petrology,* in press.

Arnaud, N.O., Ph. Vidal, P. Tapponnier, Ph. Matte and W.M. Deng, 1992. The high K_2O volcanism of northwestern Tibet: geochemistry and tectonic implications, *Earth Planet. Sci. Lett., 111*, 351-367.

Karato, S., Paterson, M. S., and J. D. F. Gerald, 1986. Rheology of synthetic olivine aggregates: influence of grain-size and water, *J. Geophys. Res., 91*, 8515-8176.

McNamara, D.E., T.J. Owens, P.G. Silver and F.T. Wu, 1994. Shear wave anisotropy beneath the Tibetan Plateau, *J. Geophys. Res., 99*, 13655–13665.

Park, J., 1993. The sensitivity of seismic free oscillations to upper mantle anisotropy I: Zonal symmetry, *J. Geophys. Res., 98*, 19933-19949.

Park, J., and Y. Yu, 1993. Seismic determination of elastic anisotropy and mantle flow, *Science, 261*, 1159-1162.

Su, L., J. Park, and Y. Yu, 1993. Born seismograms using coupled free oscillations: The effects of strong coupling and anisotropy, *Geophys. J. Int., 115*, 849–862.

Su, L., and J. Park, 1994. Anisotropy and the splitting of PS waves, *Physics of the Earth and Planetary Interiors*, in press, 1994.

Yu, Y., and J. Park, 1994. Hunting for azimuthal anisotropy beneath the Pacific Ocean region, *J. Geophys. Res.*, in press.

Manuscripts Supported Thusfar

Yu, Y., J. Park and F. Wu, Mantle anisotropy beneath the Tibetan Plateau: Evidence from long-period surface waves, *Physics of the Earth and Planetary Interiors*, in press, 1994.

Lilly, J., and J. Park, Multiwavelet spectral and polarization analysis of seismic records, *Geophysical Journal International*, submitted, 1994.

CONCLUSIONS AND RECOMMENDATIONS

- Love-to-Rayleigh scattering, caused by lateral gradients in anisotropy, is important in continental collision zones, many of which occur in areas of nonproliferation concern. Further research in this area is warranted.
- Using elastic anisotropy with an arbitrarily-oriented axis of symmetry, but plane-layered media, the conversion of P to SH motion appears weak at steep incidence. Therefore, the rapid growth of transverse-component motion in the teleseismic P coda argues for either side-scattered P waves, P-to-S conversion at dipping interfaces, or anisotropy with weaker symmetry. To investigate the first two hypotheses, we plan to apply wavelet-array analysis to broadband array data.
- Wavelet-based spectral analysis techniques are feasible, offer a detailed picture of seismic body waves in both time and frequency, and have potential as a polarization detector. We are developing wavelet-based array analysis algorithms to investigate scattered waves within sparse networks of seismic stations.

Figure 2. Vertical- and transverse- component seismic motions along the north-south oriented PASSCAL array for the 8/17/91 earthquake off the northern California coast. The data are lowpassed at 10 mHz, and the amplitudes are scaled for easy comparison. In the Love-wave (G1) arrival time window, there is no significant QL wave anomaly at stations TUNL, BUDO, ERDO and WNDO, in the northern-central Plateau. However, significant QL waves (marked by asterisks) appear at station AMDO, SANG and LHSA, in the central-southern Plateau.

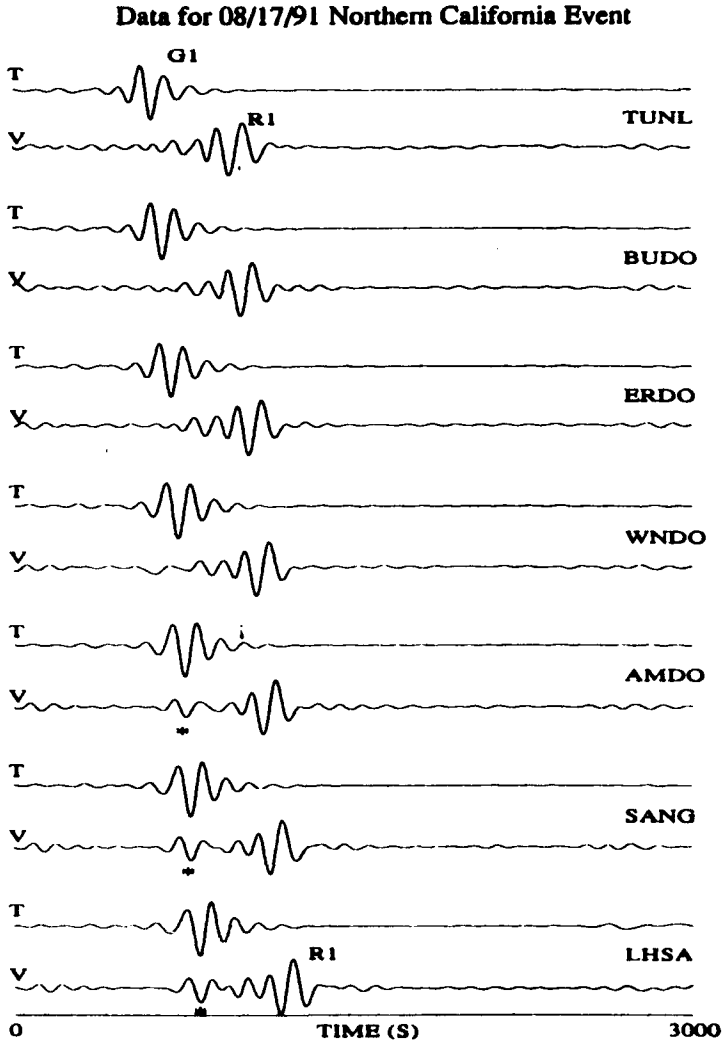


Figure 1. Great circle paths (solid lines) for QL waveform observations within the Tibetan Plateau. Black diamonds and letters mark seismic station locations and names. 3000-m and 4000-m contours of elevation are plotted to outline the Tibetan Plateau. The inset shows the surface wave propagation paths outside Tibet (dark rectangle).

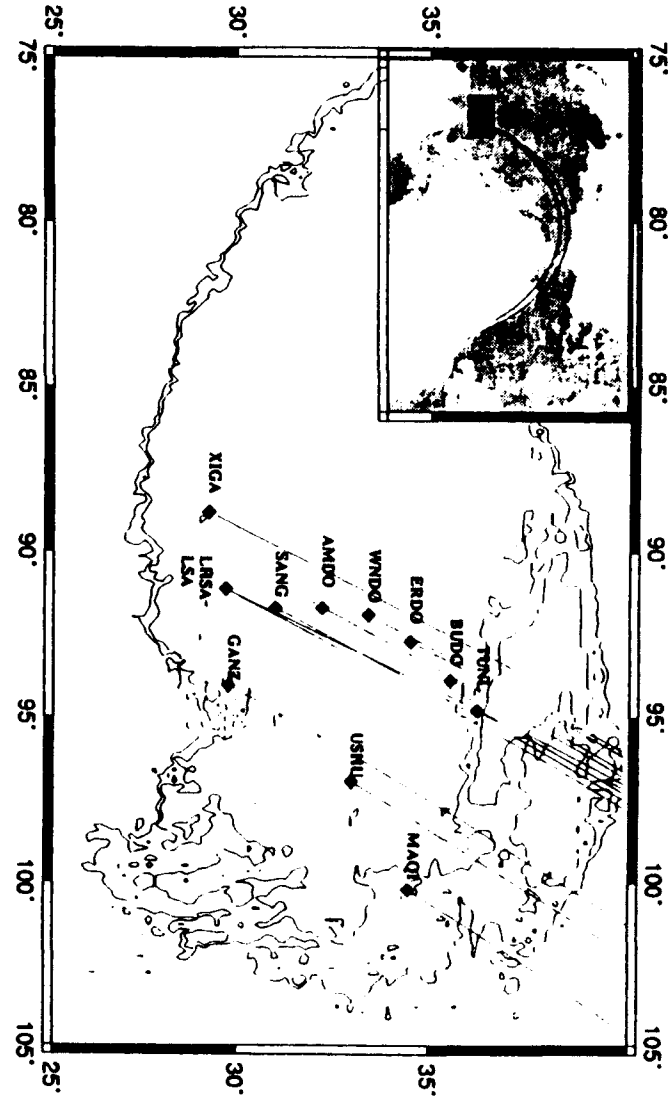


Figure 4. Multiwavelet polarization analysis of the broadband SKS, S and ScS waves of the 9 March 1994 deep Fiji earthquake, recorded at FFC (Flin Flon, Canada, Δ = 96.8°). The upper panel shows the data, with the radial component atop the transverse atop the vertical component. Our analysis uses three complex Slepian wavelets with p = 2.5, p_c = 3.0. In the lower panels the normalized first singular value d_1 of the multiwavelet transform matrix M is shaded where it exceeds 90% confidence for nonrandomness. The center panel shows particle motion in the horizontal plane, with radial component oriented rightward, and the transverse component oriented upward. The lower panel shows particle motion in the radial-vertical plane, with radial component oriented rightward, and the vertical component oriented upward.

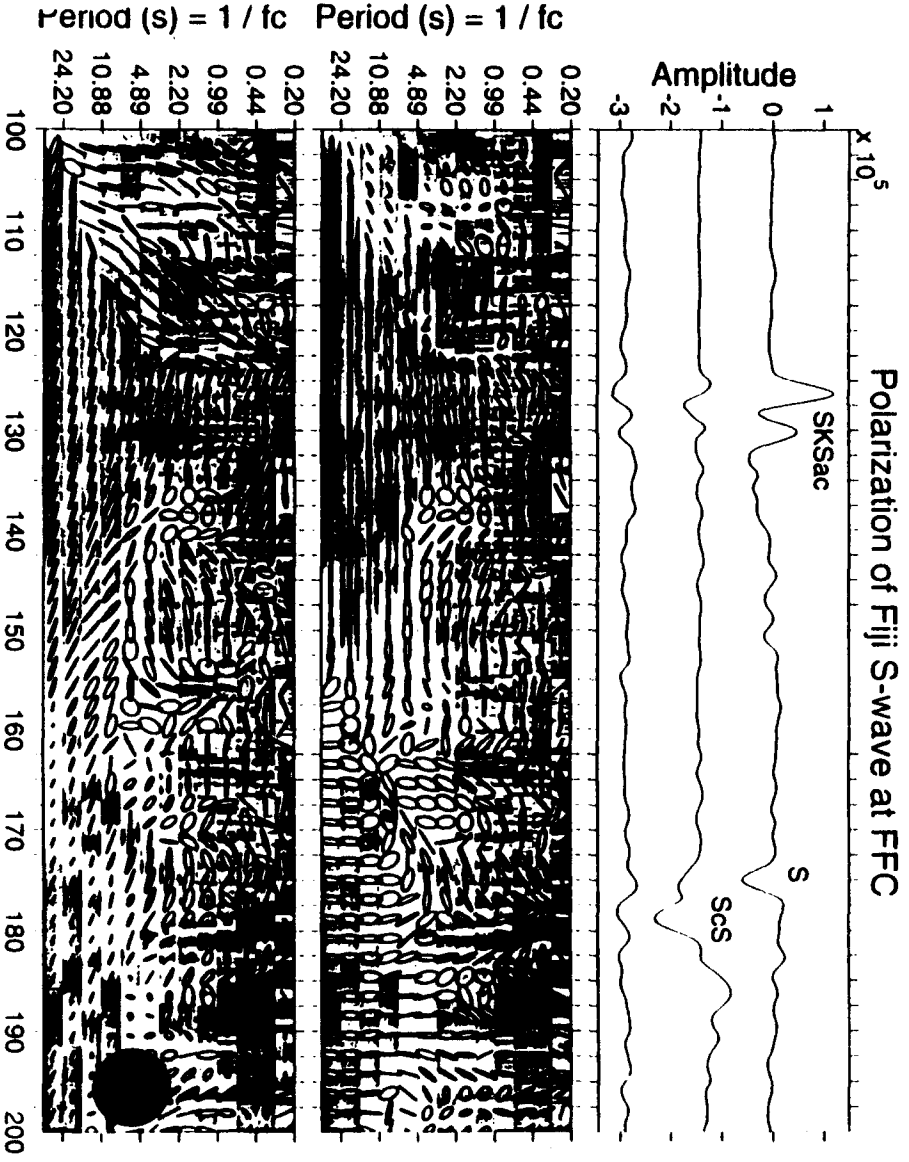
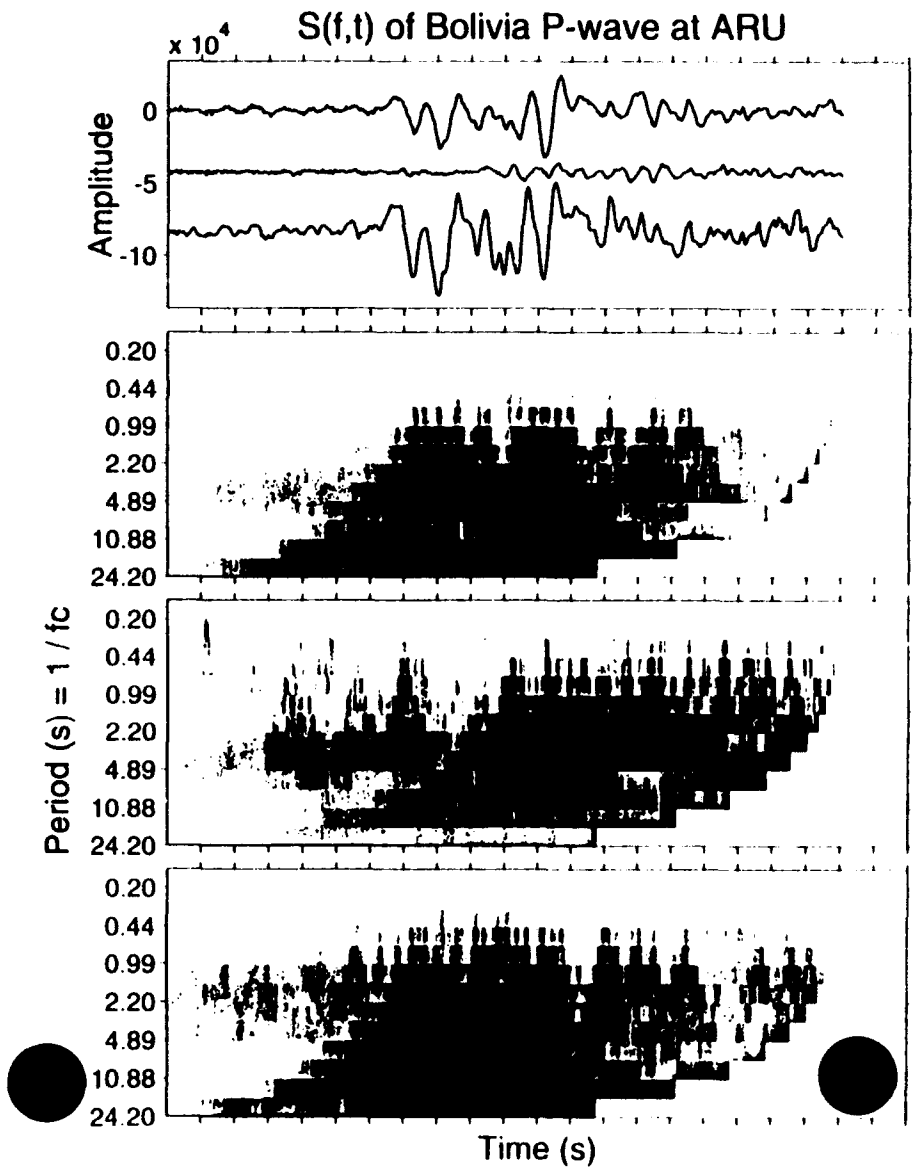


Figure 3. Multiwavelet spectral analysis of the broadband P phase from the 9 June 1994 deep earthquake beneath northern Bolivia (NEIC magnitude m_b = 7.8, location 13.7°S, 67.4°W), recorded at ARU (Arti, Russia, Δ = 120.8°). The upper panel shows the data, with the radial component atop the transverse atop the vertical component. In the same order, the lower panels show the gain ranged wavelet spectrum estimates for each component of motion. Our analysis uses three complex Slepian wavelets with p = 2.5, p_c = 3.0. The scattered wave energy on the transverse component lags the main P energy by roughly 13 seconds.



Surface Wave Propagation in Central Asia: Observations of Scattering and Multipathing with the Krygyz Broadband Array

Gary L. Pavlis and Hanan Mahdi
Indiana University
Frank L. Vernon
University of California, San Diego
F49620-94-1-0037 and F49620-94-0039

Objective

We are working to develop improved methods for utilizing broadband, three-component seismic arrays to improve estimates of surface-wave magnitudes from small events observed at regional distances. Our ultimate objective in this work is to try to improve the reliability of the m_b-M_s discriminant for smaller events by providing stable estimates of M_s under low signal-to-noise conditions that characterize smaller nuclear explosions recorded at regional distances.

Research Accomplished

Introduction

For this study we have utilized data from the IRIS Joint Seismic Program broadband array in Kyrgyzstan, which we will refer to as KNET (Figure 1). KNET is a ten element array that began operation in the summer of 1991 and remains operational as of the date of this report. The aperture of this array is approximately 150 km with nominal station spacings of 20-30 km. It is equipped with STS-2 broadband sensors and utilizes digital telemetry to provide a dynamic range of 120 dB. We have found regional and teleseismic signals recorded by this array can be processed by conventional array processing methods to enhance signals in the 0.01 to 0.2 Hz band. In this report we focus on results from an analysis of surface waves from three regional events: (1) a M_s=5.1 event located near Ashgabad, Turkmenistan (11/27/92); (2) a M_s=5.8 event in south-central Tibet (3/20/93); and (3) the May 21, 1992, nuclear explosion at Lop Nor. The two earthquakes we selected for this initial study were chosen because they were the two best recorded regional events in this data set. Four nuclear explosions from Lop Nor have been recorded by KNET, but the May 1992 event was the largest.

Methods

Our current work merges existing single station surface wave and array processing techniques. For surface wave processing we obtain first-order estimates of group velocity curves using the multiple filter technique of Dziewonski *et al.* (1969). This initial estimate is used as input to a frequency variable filter technique program developed by Russell *et al.* (1988). This analysis method is an improved version of the phase-matched filter technique of Herrin and Goforth (1977). Array processing was limited to simple delay and sum, time domain stacking since the behavior of this algorithm is totally predictable.

We have applied these techniques to both possible permutations of these two rather independent algorithms: (1) we can phase-match filter the data from each station, and then calculate the beam of the phase-match filter estimates of the fundamental mode from each station; or (2) we can estimate a best beam in the vicinity of the back-azimuth to the source, and then phase-match filter the beam signal. The former is likely to be inferior to second for analysis of low signal-to-noise events, but we have tested both permutations here to investigate the overall stability of the results and to appraise how far we can push the approximation of a constant phase velocity stack on a dispersed wavetrain.

RESULTS

Russell *et al.'s* (1988) frequency variable filter technique does an excellent job of isolating fundamental mode Rayleigh wave signals in these regional seismograms. However, the waveforms that the algorithm produces show remarkable variations on distance scales comparable to one wavelength. Seismograms from the Ashgabad event shown in Figures 2 and 3 illustrate this well. Both the raw seismograms (Figure 2) and the frequency variable filter signals (Figure 3) show large waveform variability. The waveforms share nearly identical dispersion characteristics (Figure 6), but the envelope of the packets seen at different stations vary greatly. Given that the highest frequency present in the frequency variable filter signals is 0.1 Hz, KNET is only at most about 4 wavelengths across. This is strong evidence that the actual wavefield crossing this array is strongly modulated by interference patterns set up by scattering and multipathing. As a result, array processing can be expected to significantly stabilize waveform estimates. Figure 3, in fact, illustrates this well. Note that the stack of the frequency variable filter signals and the fundamental mode signal extracted from the KNET beam are nearly identical. The consistency of these results is encouraging and leads us to believe that frequency variable filtering of broadband array beam signals can provide significant improvements in measurements of surface-wave magnitudes by improving the stability of waveform estimates of fundamental mode Rayleigh wave signals. The fundamental reason for this is that stacking reduces the uncertainties in a single station measurement due to scattering and multipathing, while the frequency variable filter can very effectively extract the dispersed waveform buried in the coda of the event. Furthermore, the signal-to-noise gain of the array should allow this approach to be extended to much smaller events. Figure 2 illustrates this capability as the surface wave signal is much clearer in the beam than in any single station.

The Tibetan event shows evidence of much stronger multipathing effects than that seen in the Ashgabad event. Figure 4 compares f-k analysis of the early (lower frequency) part of this signal compared to what we interpret as a strong multipath arrival that becomes dominate at periods around 15 s. The f-k analysis results shown in Figure 4 were constructed from the frequency variable filter signals, but we note that the same result is seen with the raw data although the multipath is not quite as well resolved. This indicates that the frequency variable filter technique does not necessarily remove multipaths as Russell *et al.* (1988) claim, but instead locks onto the largest amplitude signal consistent with the initial estimate of the dispersion curve. This is an inescapable dilemma for a single station technique working with a multipath signal like this one that arrives with only a small time lag from the direct path. Initial results from computer simulations of this event that are in progress suggest multipaths with wide scattering angles can arrive with small time delays at regional distances and reproduce this kind of effect.

In spite of the variability of waveforms seen at different stations (Figures 2 and 3) and multipathing effects like that seen in Figure 4, we have been impressed with the robustness of group velocity measurements. Notice that for the Ashgabad event there is virtually no difference in results from different stations or different techniques (Figure 5a). The situation for the Tibetan event and the Lop Nor explosion shown in Figure 5a and 5b is somewhat different. On the broader perspective of the overall accuracy of group velocity measurements, these results are encouraging. On the other hand, there are significant differences that are noteworthy. In particular, we note that the largest variability of any results are the dispersion curve estimates in the 15-25 s range from the Tibetan event. We suspect this is due to distortions caused by the multipath seen in Figure 4b that is the dominate signal in this period range. We suspect the same problem may cause the scatter in the results in the Lop Nor data. However, we are less certain of this due to the fact that only four stations recorded useable surface wave data for this event, and f-k analysis is not very reliable in this situation. An alternative explanation for the Lop Nor event that cannot be ruled out is that the deviations are signal-to-noise ratio related. (The Rayleigh wave signal-to-noise ratio is about 1/5 compared to about

2 for the Ashgabad event (Figure 2)).

Conclusions and Recommendations

We examined fundamental mode Rayleigh waves in the 0.01 to 0.2 Hz band on pure continental paths in central Asia at regional distances. Our results show strong evidence of scattering and multipathing effects that can seriously distort estimates of the fundamental mode waveforms extracted by frequency variable filtering of a single station record. Array processing in combination with frequency variable filtering of data from a broadband array like KNET, however, shows promise of providing significant improvements in the measurements of M_s from small events at regional distances. We suspect strongly that broadband array processing of this type will provide more stable measurements of M_s of small events than can be achieved with the same number of stations distributed randomly at regional distances because the array stations all see the same basic waveguide. For this reason large aperture, broadband seismic arrays like KNET should be in integral component in a monitoring system for a CTBT.

References

Dziewonski, A. M., S. Bloch, and M. Landisman (1969). A technique for the analysis of transient seismic signals, *Bull. Seism. Soc. Am.*, **59**, 427-444.

Herrin, E. and T. Goforth (1977). Phase-matched filters: application to the study of Rayleigh waves, *Bull. Seism. Soc. Am.*, **67**, 1259-1275.

Russell, D. R., R. B. Herrmann, and H. Hwang (1988). Application of frequency variable filters to surface wave amplitude analysis, *Bull. Seism. Soc. Am.*, **78**, 339-354.

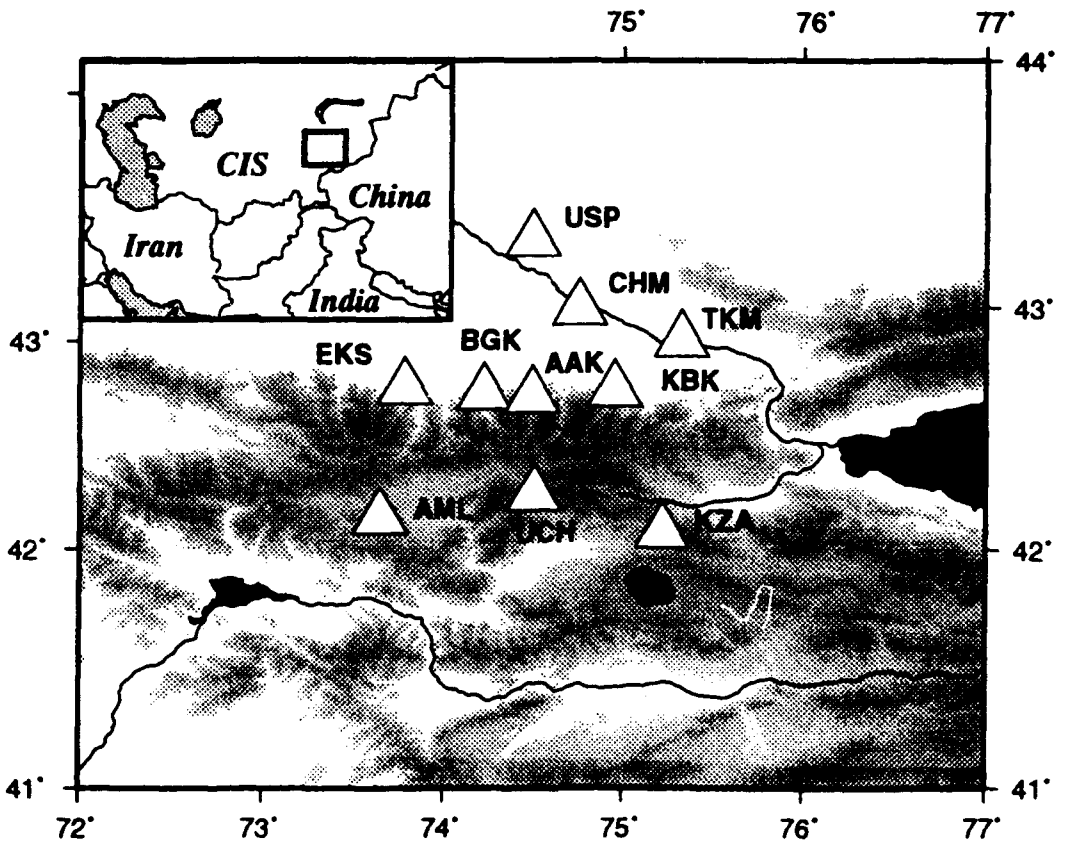


Figure 1. Map of KNET broadband array. Inset map shows location of array in central Asia. Triangles are station locations. Background is a gray scale image scaled to topography.

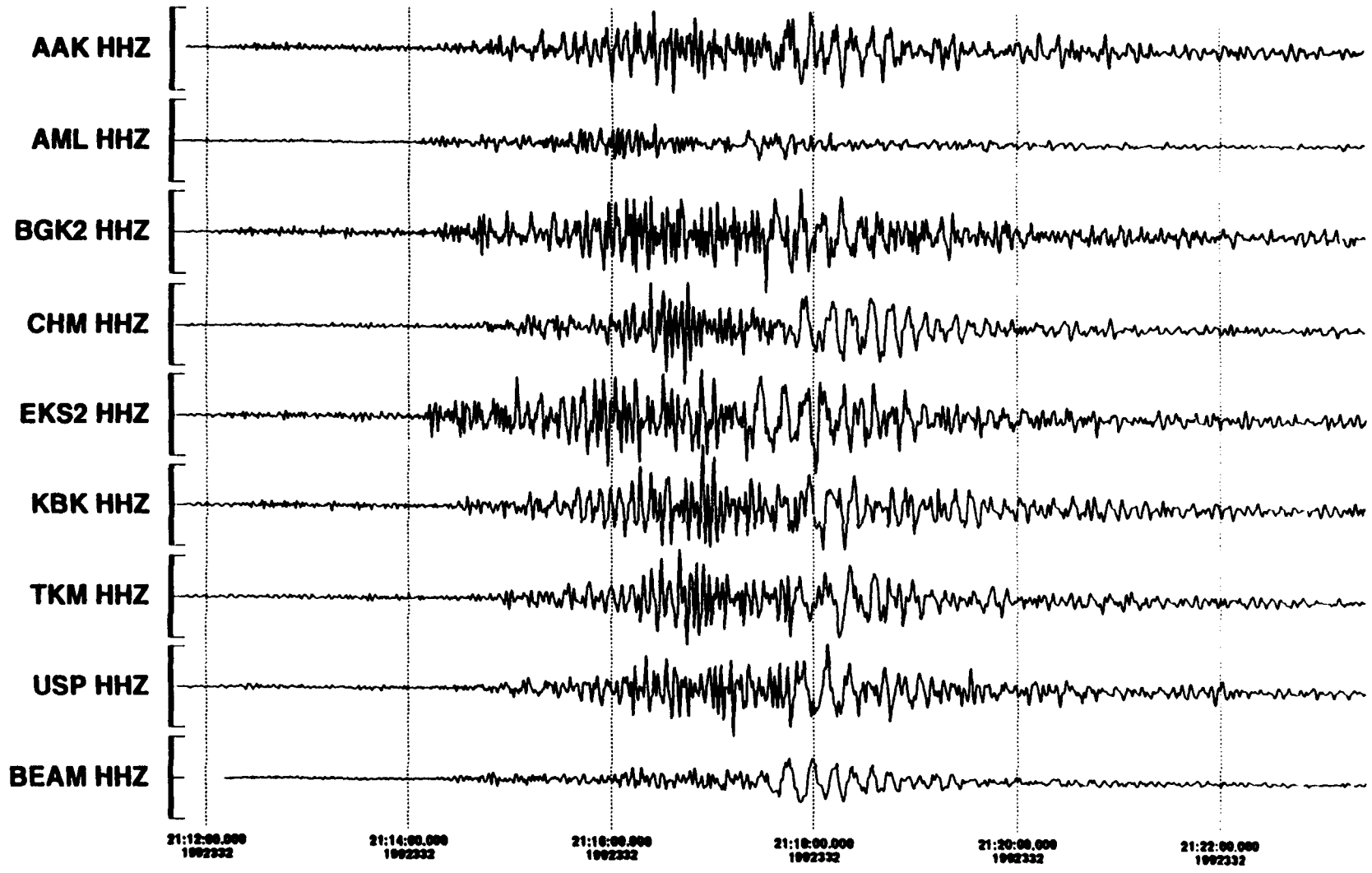


Figure 2. Seismograms showing vertical component records from KNET of the Ashgabad event. Signals have been filtered with a 0.01 to 0.5 Hz bandpass, and scaled to true ground velocity. Station names are shown at the right. The location of each station in the array can be found in Figure 1. The BEAM signal is the array stack along the true back azimuth at 3.3 km/s.

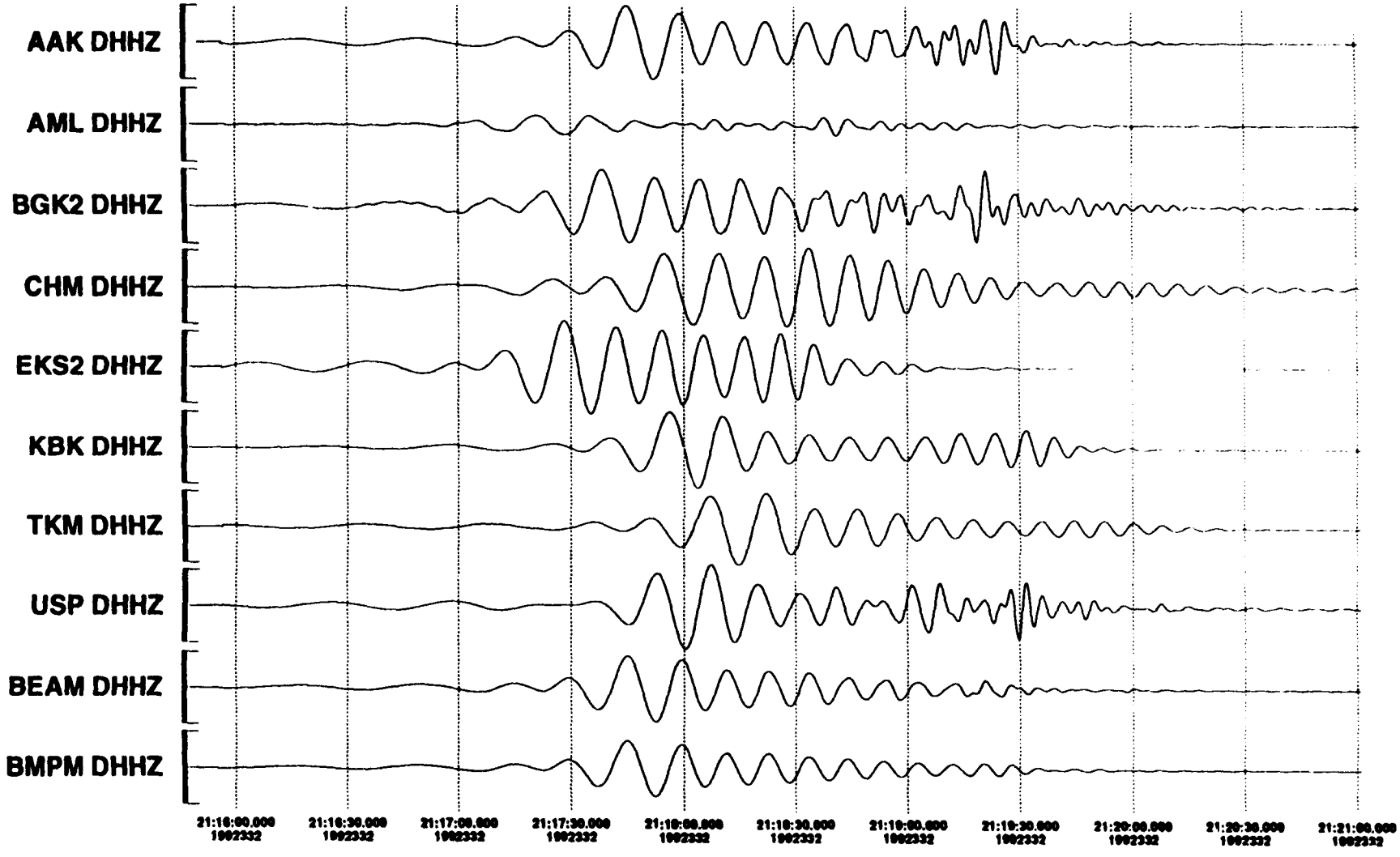


Figure 3. Frequency variable filter estimates of the fundamental mode Rayleigh wave signals from the seismograms shown in Figure 2. Station names are as before. BMPM is the signal produced by running the frequency variable filter algorithm on the BEAM signal shown in Figure 2. BEAM is the stack of the individual station signals shown in this figure. Note the time scale is different from Figure 2, but traces have all again been scaled to true ground velocity.

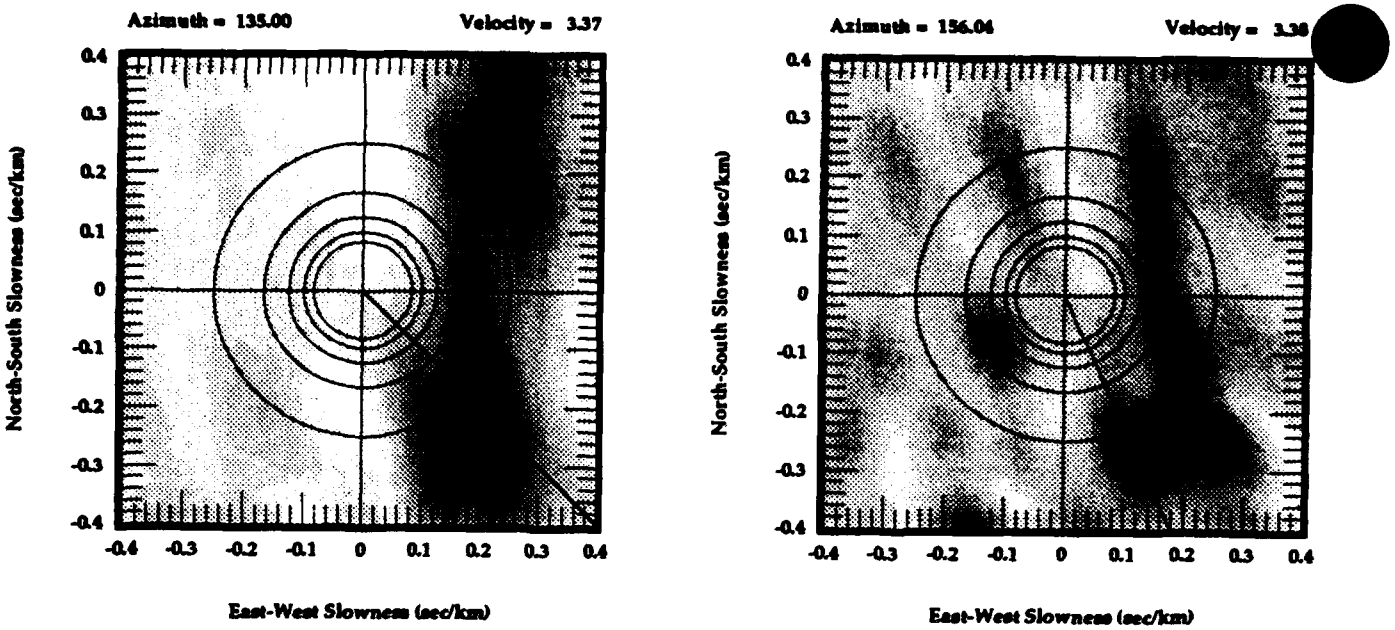


Figure 4. Broadband f-k analysis of Tibet event. The left panel is calculated from a 50 s long analysis window at the beginning of the Rayleigh wave group with dominate periods changing from 50 s to about 20 s across the analysis window. The right panel is a comparable result for a 50 s window translated to 40 s later in time. (i.e. the two windows overlap by 10 s) The dominant energy in this window is in the 25 s to 15 s range. In both cases, the analysis presented is based on a time domain broadband f-k technique were the grey scale is proportional to the total rms signal level in the analysis window when the array is stacked with the slowness vector defined by the axes shown on the figure. Circles are drawn at 12, 10, 8, 6, and 5 km/s. Both figures are scaled separately so that the peak power is black and zero would be white. The velocity and bearing from the peak power estimate are listed at the top of the figure. Note the true back azimuth to this event based on its location estimate from the PDE is 138 degrees.

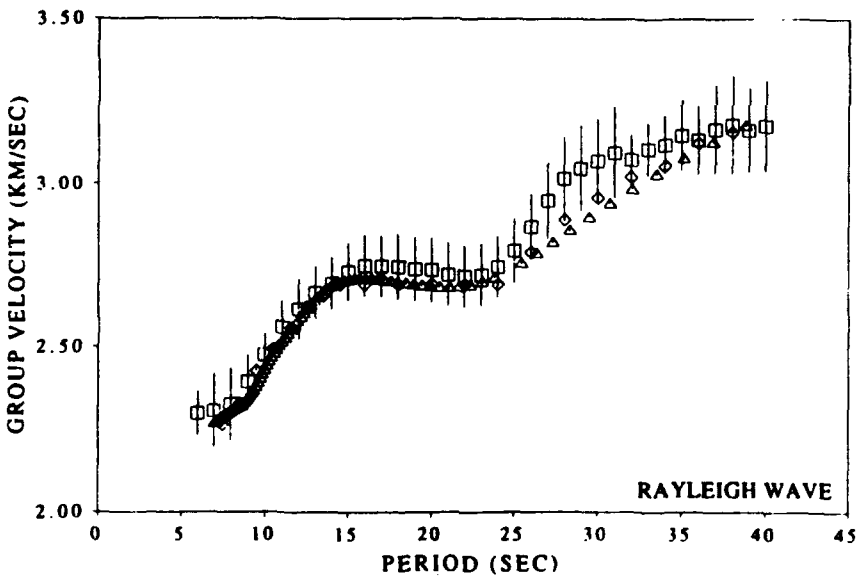
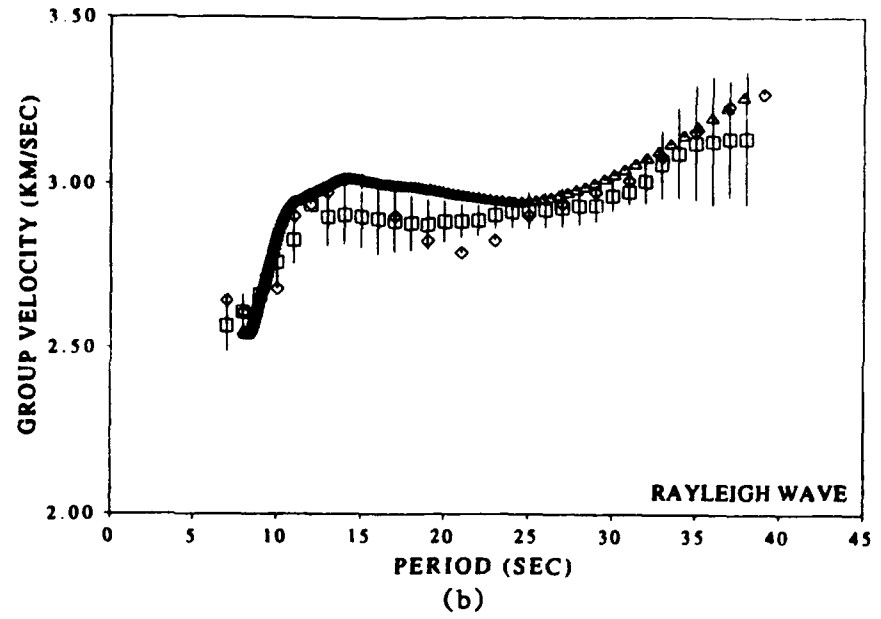
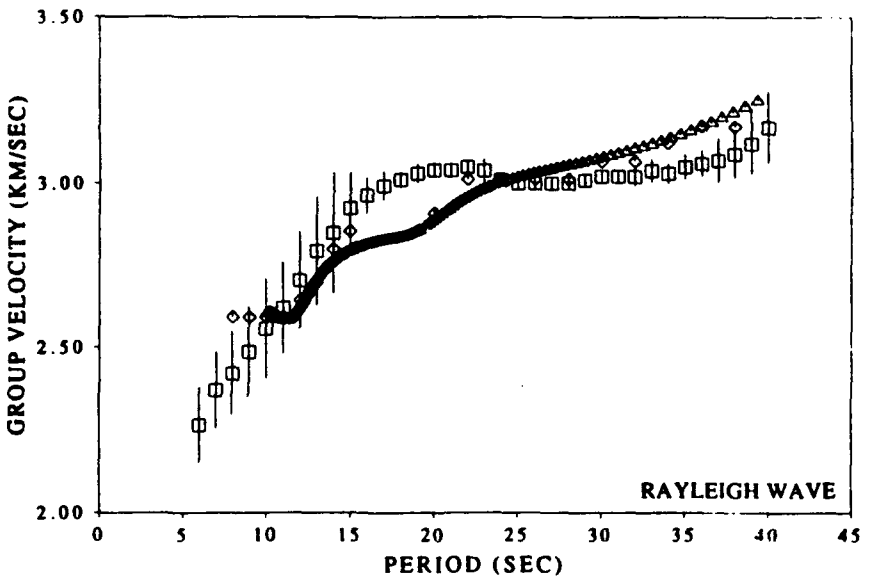


Figure 5a. (caption on following page)



(b)



(c)

Figure 5. Dispersion curves obtained for events analyzed in this study: (a) Ashgabad event, (b) Tibet event, and (c) Lop Nor. In all cases, the squares show the average result from single station measurements made for each array station, and the error bars are the standard deviations of these estimates; the triangles are dispersion measured by applying the frequency variable filter technique to the array beam; and the diamonds are dispersion measured by stacking the frequency variable filter estimates of the fundamental mode and then measuring the dispersion characteristics of that waveform.

Studies of Lithospheric Structure in Southwestern North America
Part I: Lithospheric Structure of West-Central New Mexico Determined from the Minor Uncle Test at White Sands Missile Range

Donald G. Roberts and G. Randy Keller
Department of Geological Sciences
The University of Texas at El Paso
El Paso, Texas 79968
Contract No: F49620-92-J-0438

Objective

As part of the University of Texas at El Paso's ongoing investigations of crustal structure in the Rio Grande rift region, our group has been recording seismic refraction data along a profile extending between the White Sands Missile Range (WSMR), New Mexico, and the Nevada Test Site (NTS). As part of this effort, we deployed a seismic array in June of 1993 to record the Minor Uncle conventional surface explosion at WSMR. Sixty-eight stations were deployed at 1 mile intervals along US Highway 60 beginning four miles west of Socorro, New Mexico, and ending ten miles west of Datil, New Mexico (Figure 1). Each station consisted of a 1 Hz, vertical component seismometer and a USGS Seismic Cassette Recorder (SCR). The Minor Uncle experiment went off as scheduled and 61 SCRs recorded a strong signal. The resultant record section shows excellent signal-to-noise ratios and exhibits a number of prominent arrivals (Figure 2). Taken alone, this unreversed profile would be of limited utility. However, when combined with other seismic data in the region (Figure 1) it provides a useful constraint on crustal structure in the area. In this paper, we present a preliminary interpretation of these new data and update our analysis of regional crustal structure. We hope to gather additional data along this profile over the next few years.

Research Accomplished

Background

A number of previous surveys in the region helped to constrain our seismic model. Sinno et al. (1986) conducted a series of seismic surveys in the southern Rio Grande rift utilizing explosions at WSMR and at the copper mines near Tyrone, New Mexico (Figure 1). Their reversed NE-SW trending profile indicated a relatively flat Moho at a depth of 32 km between Tyrone and the northern portion of WSMR with a slight increase in the depth to the Moho to the southwest.

Jaksha (1982) monitored another WSMR explosion with a widely spaced seismic array extending westward from WSMR to Morenci, Arizona. He reversed his profile by recording blasts from the copper mine at Morenci, and interpreted his results in terms of flat-lying horizontal layers. These data were reinterpreted by Schneider and Keller (1994) who combined the Jaksha (1982) data with their seismic and gravity data gathered along a

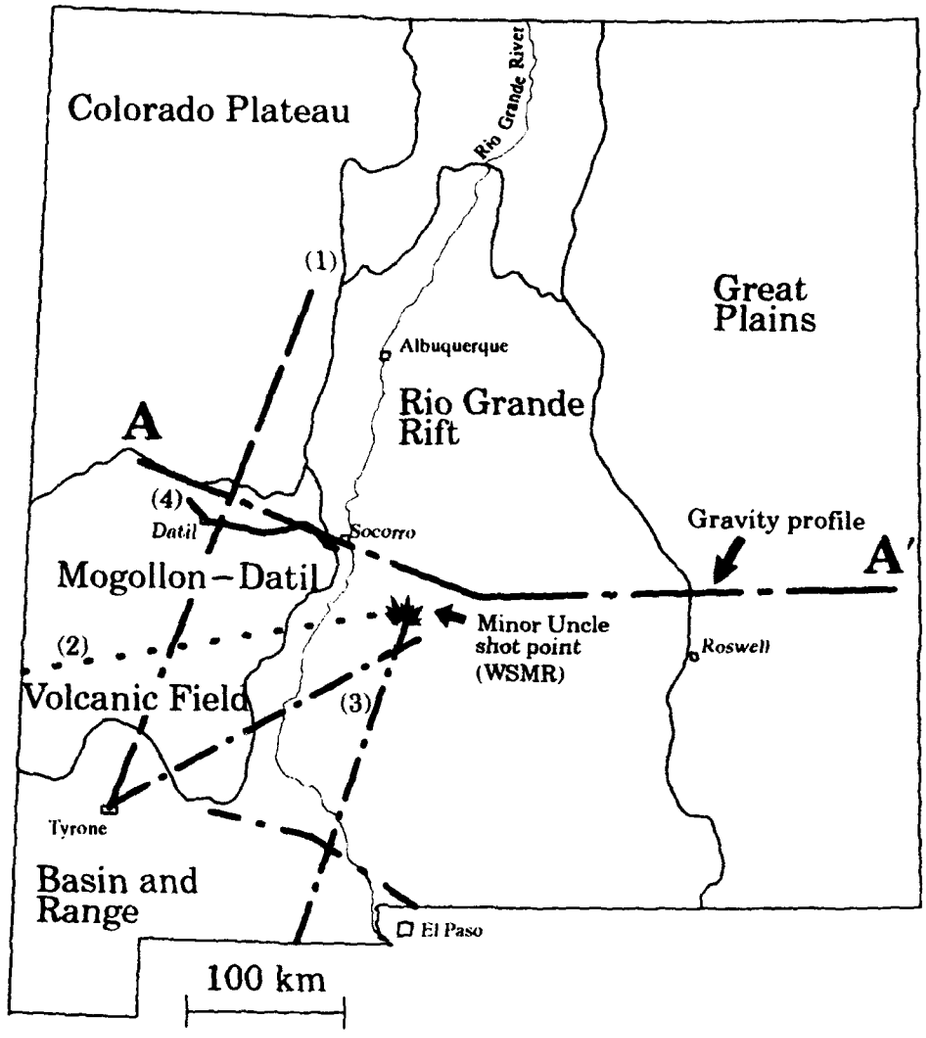


Figure 1: Index map of New Mexico showing locations of seismic profiles and geophysical models. 1 – seismic profile of Schneider and Keller (in press); 2 – seismic profile of Jaksha (1982); 3 – seismic profiles of Sinno et al. (1986); 4 – seismic profile of this study. Shaded area is the zone of transition in crustal structure of Schneider and Keller (in press) as modified in this study. Profile A–A' represents the gravity data modeled to place the seismic results in a regional context.

profile extending from Tyrone to Grants, New Mexico. These two profiles cross in the central portion of the Mogollon-Datil Volcanic Field (Figure 1). They used two-dimensional modeling techniques to interpret the new seismic and gravity data, and to reinterpret Jaksha's data. Their work indicated the presence of an upper crustal intrusive complex beneath the Mogollon-Datil Volcanic Field (MDVF) and under at least part of the San Agustin plains as well as a mostly gradual south to north thickening of the crust. Their analysis suggests a gradual crustal transition between the Colorado Plateau and the Rio Grande Rift which extends under the MDVF (Figure 1).

Adams and Keller (1994) investigated crustal structure in central New Mexico by integrating seismic, gravity, and geologic data. They delineated the general basin structure of the region and found that the transition in crustal structure from the Rio Grande rift to the Colorado plateau across the Datil region was gradual.

Discussion

The data presented here complement the previous studies in the area. The seismic record section (Figure 2) shows clear phase arrivals for P_g (refraction from the upper crust), P_cP (reflection from the middle crust), and P_mP (reflection from the Moho). A P_n (refraction from the upper mantle) arrival is also present on the westernmost traces. Each of these phases were modeled by ray tracing employing the previous work of Sinno et al. (1986) and Schneider and Keller (1990) as independent constraints. A preliminary earth model is shown in Figure 3.

With a maximum source-receiver offset of 155 km, these data do not provide any constraint on the upper mantle velocity structure and contain only a limited amount of information on the structure of the crust/mantle transition. However, these data do suggest that the relatively thin crust ($\sim$32 km) interpreted by Sinno et al. (1986) within the central of the rift extends westward to an offset of at least 70 km in this survey. This is approximately the position of the La Jencia fault (Figure 3). The seismic profile of Schneider and Keller (in press) show that the crustal thickness is about 38km at Datil, and thus requires the westward increase in Moho depth shown in Figure 3.

The shallow crustal features in Figure 3 are noticeably simplistic due to the lack of fine resolution contained in the data. Each of the crustal phases, especially the P_g arrival, are affected by a number of shallow velocity contrasts. The largest contrasts are associated with the transition from thick, central-rift, basin-fill sediments in the east to Tertiary volcanic sequences and thin basin-fills in the west; and the subsidence and sedimentation that form the San Agustin plains. The first transition occurs at a source-receiver offset of approximately 80 km and shows up as a sharp decrease in phase arrival time with increasing offset. This transition is located just east of the Magdelena Mountains at the basin-bounding La Jencia fault. The San Agustin plains show up as a broad travel time delay centered at an offset of 130 km. This anomaly was modeled with approximately 1 km of basin sediments and a slight thickening of the volcanic sequences to the west. No compelling evidence for an upper crustal batholith was found, nor was expected based on the interpreted extent of the Mogollon-Datil batholith presented by Schneider and Keller (1994). Two other regions of the section indicate the presence of shallow crustal features that have not been incorporated into the model at this time. Two subtle phase arrival delays are present between 70 and 80 km (Figures 2 and 3). These are interpreted to be associated with the sediments of the La Jencia basin in the west and the Socorro basin in the east which are separated from each other by the Socorro-Lemitar

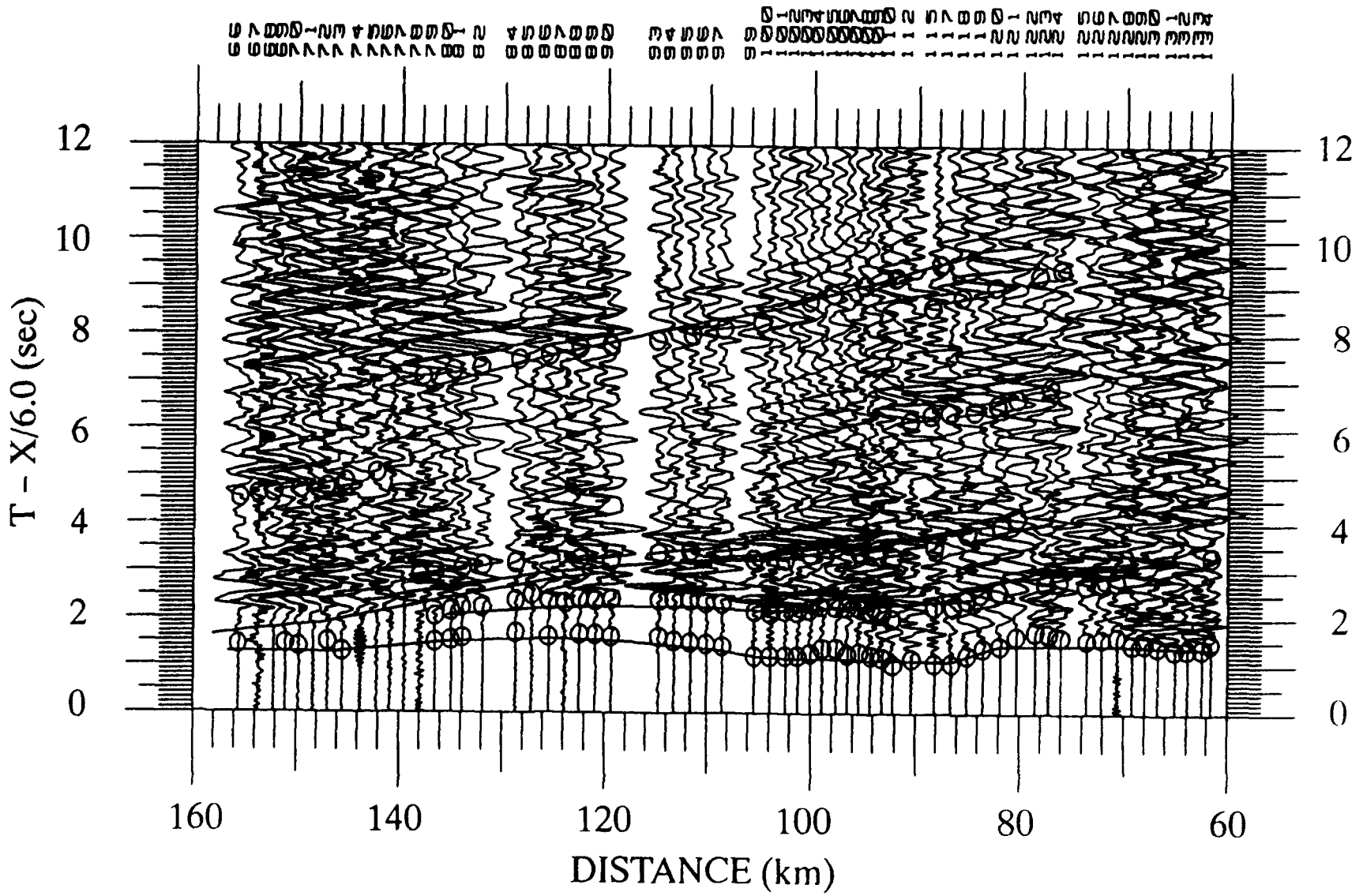


Figure 2. Seismic record section of the Minor Uncle data. The picked arrival times of the main phases modeled are identified by circles and the modeled arrival times are shown as the lines. These arrivals are also shown in Figure 3 and are explained in the text.

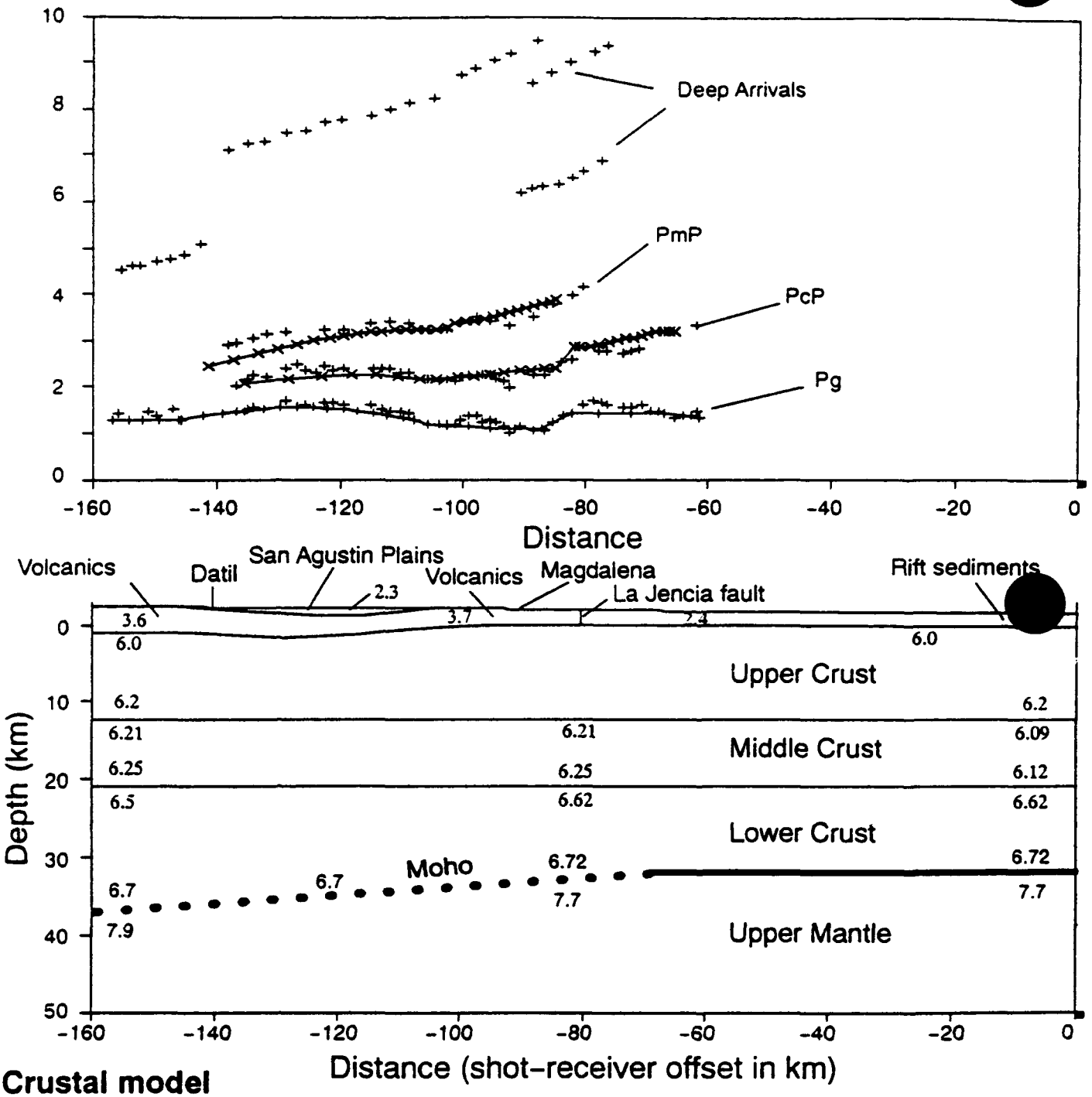


Figure 3: Picked arrival times and preliminary earth model derived from ray tracing the Minor Uncle seismic data. Numbers indicate P-wave velocities in km/s.

Mountains. West of the La Jencia fault (at approximately 100 km offset), a third phase delay is interpreted as the Abbey Springs basin sediments (R. Chamberlain, personal communication).

These data also indicate one and possibly two deep phases arriving significantly later than the crustal phases (Figure 2). The timing of these arrivals is inconsistent with a P_mP crustal multiple or a PmS phase but can be fitted with a west dipping reflector in the upper mantle. The data suggest that there may be at least two such upper mantle reflectors.

In order to place these results in a regional context, a crustal model which crosses the state of New Mexico was constructed by gravity modeling. This model was consistent with the seismic results presented here, and corroborates the conclusions of Schneider and Keller(1994) that the transition in crustal structure between the Rio Grande Rift and the Colorado Plateau occurs over a broad region in western New Mexico. This model also illustrates our interpretation that the eastern (Roberts et al., 1991) and western margins of the rift are quite different with the change in structure across the western margin being more gradual.

Conclusions and Recommendations

The transition zone from the Rio Grande rift to the Colorado plateau in western New Mexico is gradual in terms of crustal structure. However, thin crust associated with the rift extends westward to about the location of Magdalena, New Mexico. The preliminary crustal model shown in Figure 3 is similar to recent results across the transition zone between the Basin and Range province and Colorado plateau in western Arizona (Jill McCarthy, personal communication), but needs further constraints to the west. Our future investigations will focus on a more detailed investigation of the seismic data shown here and on the underlying causes for variations in crustal structure along the margins of the Colorado plateau and Rio Grande rift.

References

Adams, D. C. and Keller, G. R. (in press): Crustal structure and basin geometry in south-central New Mexico; in, Keller, G. R., and Cather, S. M., eds., Basins of the Rio Grande Rift: Structure, Stratigraphy, and Tectonic Setting, Geological Society of America Special Paper 291.

Jaksha, L. H., 1982, Reconnaissance seismic refraction-reflection surveys in southwestern New Mexico: Geological Society of America Bulletin, v. 93, p. 1030-1037.

Roberts, D. G., Adams, D. C. and Keller, G. R., 1991, A geophysical analysis of crustal structure in the Ruidoso area: New Mexico Geological Society, Guidebook, 42 p. 191-197.

Schneider, R. V., and Keller, G. R. (in press), Crustal structure of the western margin of the Rio Grande rift and Mogollon-Datil volcanic field, southwestern New Mexico and southeastern Arizona; in, Keller, G.R., and Cather, S.M., eds., Basins of the Rio Grande Rift: Structure, Stratigraphy, and Tectonic Setting, Geological Society of America Special Paper 291.

Uppermost Mantle Structure in Southern Eurasia from Pn Tomography and Sn Attenuation

Arthur Rodgers, Thomas Hearn and James Ni

New Mexico State University, Department of Physics, Las Cruces, NM, USA

Contract No. F49620-93-1-0429

Objective

The uppermost mantle beneath the Middle East (Iran, Iraq, Syria and Turkey) exhibits extremely low Pn velocities that suggest the presence of partial melt. The region of low Pn velocity coincides with the high elevations of Turkish-Iranian Plateau and is linked to recent episodes of subduction and the presence of partial melt. The objective of our research is to investigate this low-velocity mantle and its effect on regional seismic wave propagation. To this end, we have inverted Pn traveltime data for uppermost mantle P-wave velocity structure and mapped Sn attenuation. Results generally indicate that the uppermost mantle beneath a large region of the Turkish-Iranian Plateau must be underlain by a partially melted mantle that causes both low velocity and high attenuation. However, some regions of low uppermost mantle P-wave velocity reveal intermediate Sn attenuation. High attenuation will lead to underestimation of seismic event magnitudes/yields for regional events and will adversely affect many monitoring discriminants that are based on amplitude and frequency measurements.

Research Accomplished

Uppermost mantle P-wave velocity structure was obtained by inversion of Pn traveltimes reported to the International Seismological Centre (ISC) (Figure 1). On average, uppermost mantle P-wave velocity beneath the Turkish-Iranian Plateau is considerably slower than beneath continental shield regions. While normal Pn velocities (8.0-8.2 km/sec) were inferred under the Black Sea and Southern Caspian Sea, a region of anomalously low Pn velocities (<7.7 km/sec) exists beneath the high elevations of the Turkish-Iranian Plateau. This region coincides with a region of previously observed high Sn attenuation (Kadinsky-Cade, et. al., 1981) and extensive Neogene volcanism. Teleseismic studies show that the low velocities extend at least 100 km into the upper mantle (Spakman, 1991). These structural features suggest that near solidus conditions exist within the uppermost mantle beneath the Turkish-Iranian Plateau. The Pn velocity tomography study was reported by Hearn and Ni (1994).

In order to image details of velocity structures and propagation characteristics in this region, we have read Pn traveltimes and mapped Sn attenuation using digital waveform data. The majority of the waveform data used in this study were recorded by the Iranian Long-Period Array (ILPA). This array operated in the late 1970's, approximately 60 km southeast of Tehran. Stations were arranged in a hexagonal configuration with an aperture of approximately 80 kilometers. Of the seven stations in the array, five recorded short-period vertical motions and two stations recorded short-period three-component motions. Data were also obtained from the IRIS-DMS for the GSN stations ABKT, ANTO, GNI and KIV. Unfortunately, much fewer data were obtained for these stations. Pn traveltimes were read from the vertical component instruments and Sn propagation efficiencies were read on the horizontal components.

Reduced traveltimes of Pn read from the ILPA waveforms are plotted in Figure 2. A robust velocity estimate yields an uppermost mantle P-wave velocity of 8.0 km/sec for these data. This velocity is consistent with the Pn velocities inferred from the ISC data (Figure 1). Some Pn residuals are quite large, in many cases larger than the measured uncertainty. This is probably due to large location errors in many small magnitude events (m_b < 4.5) in the PDE catalog. Hypocenters of larger events relocated by Bob Engdahl from teleseismic ISC observations were used whenever possible.

Sn attenuation was inferred by measuring the propagation efficiency. We ranked Sn propagation efficiency based on the amplitude of Sn relative to Pn and Lg (when present) in three categories: A for efficient Sn propagation, B for inefficient and C for Sn not observed. Figures 3a-c show representative waveforms we ranked with A, B and C Sn propagation efficiencies, respectively. Also shown on the seismograms are Pn and Lg arrivals. The data in Figure 3a approach ILPA from a northern azimuth from an event in the Caspian Sea 12.5° away. Sn propagates efficiently (SnA) from this event; however, no Lg phase is observed from this event, possibly because of crustal thickness variations associated with the oceanic crust of the southern Caspian Sea. The data shown in Figure 3b show inefficient Sn propagation (SnB) from the Lesser Caucasus (azimuth of 320°) and show efficient Lg propagation. Figure 3c shows a waveform propagating from the east which has Pn and Lg propagating clearly; however, Sn is not observed. This waveform is typical of those propagating from eastern, southern and some western azimuths. Generally, Lg phases are present on all seismograms with poor Sn, and Lg is not observed when Sn is present.

A map of 144 Sn propagation efficiency measurements observed at ILPA is shown in Figure 4. Efficient Sn propagation is observed from northern azimuths (Caspian Sea), but tends to inefficient propagation from the northwest and northeast. Generally, paths with unobserved Sn propagation (SnC) correspond to paths intersecting low Pn velocity regions inferred from the ISC data (Figure 1) and paths showing efficient (SnA) or inefficient (SnB) propagation correspond to normal Pn velocity paths of Figure 1. One important exception is ray paths that propagate through the Lesser Caucasus; these paths show poor but visible Sn propagation despite very low Pn velocities (<7.7 km/s). This indicates that factors other than partial melt may influence Sn amplitudes. Possible factors impacting Sn amplitudes are crustal thickness variations, mantle lid gradients and conversions from other phases.

Sn propagation efficiencies read from GSN stations ABKT, ANTO, GNI and KIV complemented the results obtained from ILPA data. That is, poor Sn propagation efficiency was observed for paths intersecting the (low-velocity) Turkish-Iranian Plateau. Efficient Sn propagation was observed for paths through the Black and Caspian Seas. Zones of no Sn propagation mapped by Kadinsky-Cade, et. al. (1981, Figure 20) agree with most of our Sn results; however our results indicate good Sn propagation through the Caucasus and along the southernmost coast of the Caspian Sea where they indicate that Sn does not propagate. Paths traversing eastern Turkey, westernmost Iran,and eastern Iran never show Sn and always have Pn velocities less than 7.9 km/s. We believe that partial melt contributes to both low Pn velocities and Sn blockage.

Conclusions and Recommendations

Beneath the Turkish-Iranian Plateau regions of low Pn velocity correspond to regions of high Sn attenuation. This is probably due to high mantle temperature and partial melt. There are some exceptions to this correspondence that suggest other factors also influence Sn propagation. This could be due crustal thickness variations, mantle lid gradients and/or phase conversions. We are continuing to map Sn wave-propagation and improve our Pn velocity model for the region by analyzing data from the Caucasus Network (CNET) in southern Russian and the Geyosha Array in

Turkmenistan.

The attenuation structure beneath the Turkish-Iranian Plateau has clear implications for many nuclear monitoring discriminants. For instance, discriminants based on Sn or Lg cannot be applied since many paths do not propagate these phases. Furthermore, attenuation of mantle phases may cause significant underestimates of M_S and m_b and make nuclear monitoring and discrimination difficult. Common discriminants, such as m_b/M_S, P/Lg, and Sn/Lg, should be recalibrated for this region.

Acknowledgments

We would like to thank Barbara Rueben of CSS for providing us with the raw ILPA data. The ILPA data was processed into CSS format event volume databases at the Joint Seismic Program Center of the University of Colorado, using codes written by Danny Harvey, Dan Quinlan and Michael Ritzwoller, to whom we are indebted. We thank Bob Engdahl for providing some event locations and origin times inferred from ISC data. Figures 1,2 and 4 were made using GMT (Wessel and Smith, 1991).

References

Hearn, T., and Ni, J., 1994. Pn velocities beneath continental collision zones: the Turkish-Iranian Plateau, *Geophys. J. Int.*, **117**, 273-283.

Kadinsky-Cade, K., Barazangi, M., Oliver, J. and Isacks, B., 1981. Lateral variations in high-frequency seismic wave propagation at regional distances across the Turkish and Iranian Plateaus, *J. Geophys. Res.*, **86**, 9377-9396.

Spakman, W., 1991. Delay-time tomography of the upper mantle below Europe, the Mediterranean and Asia Minor, *Geophys. J. Int.*, **107**, 309-332.

Wessel, P. and Smith, W., 1991. Free software helps display data, *EOS Trans. Amer. Geophys. U.* **72**, 441, 445-446.

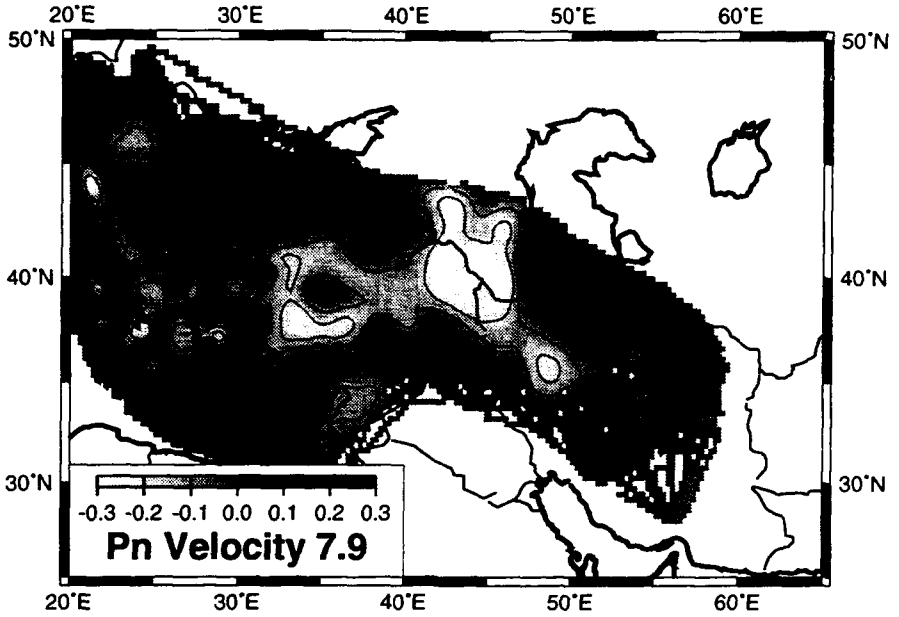


Figure 1. Pn velocity model estimated from ISC traveltime data.

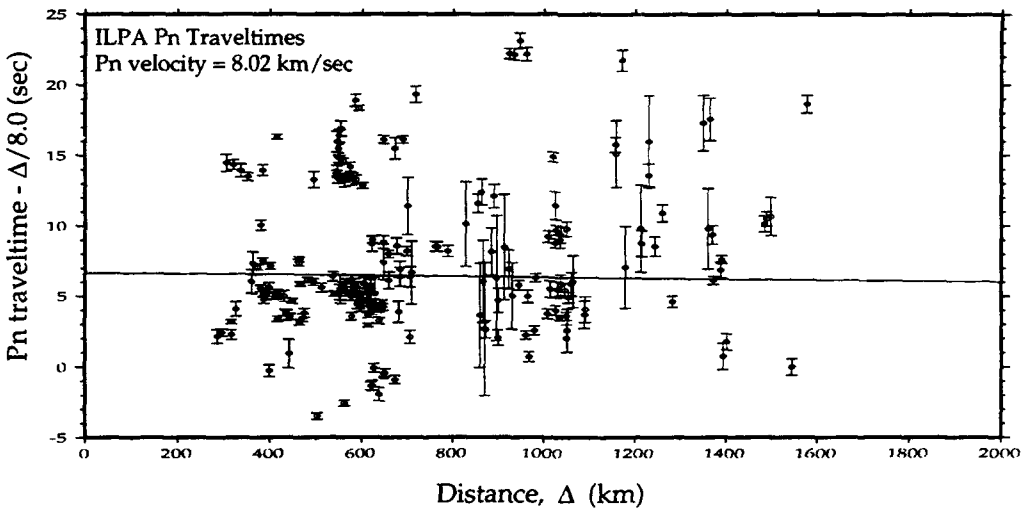


Figure 2. ILPA read Pn reduced traveltimes. The best fitting Pn velocity is 8.02 km/sec.

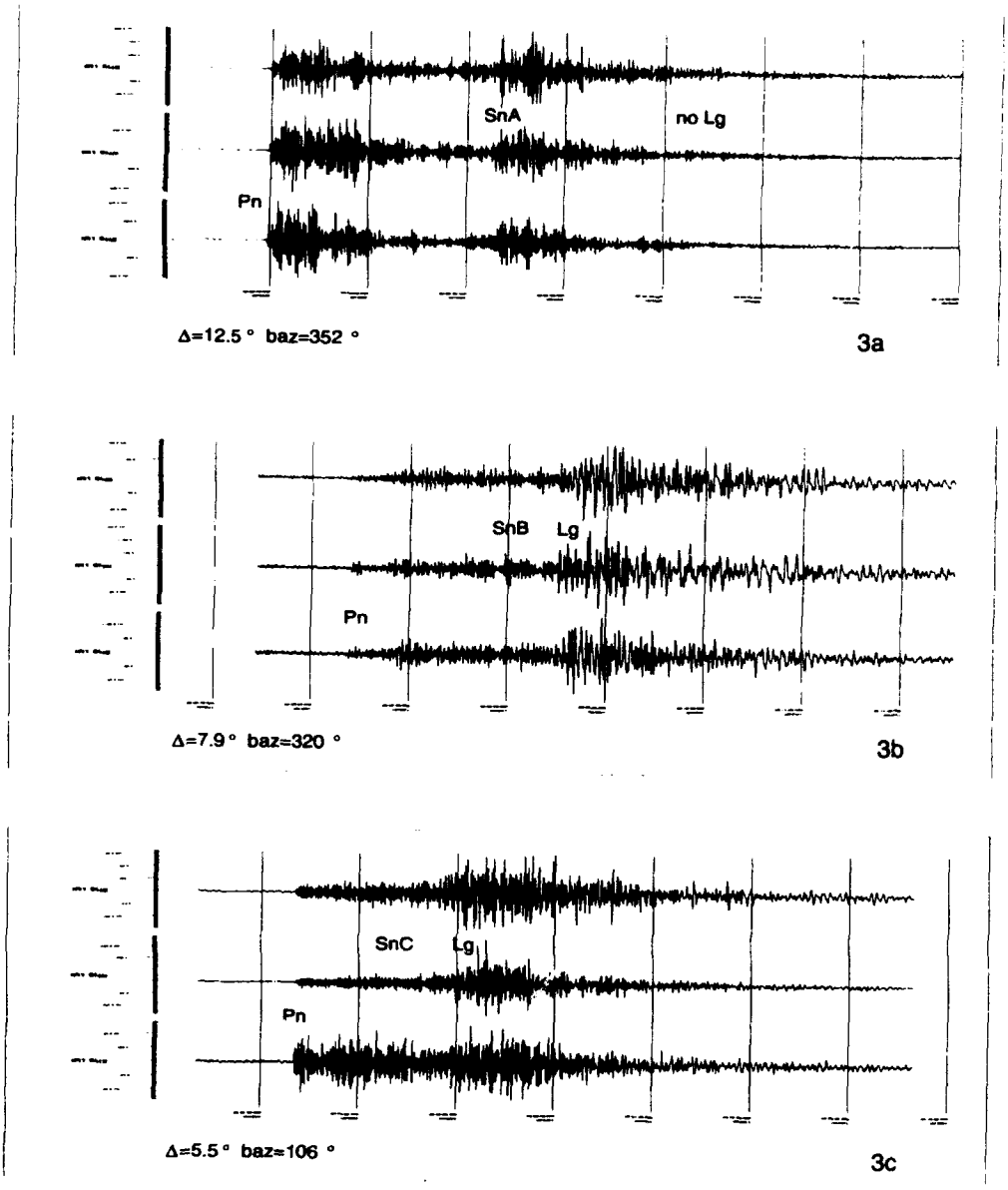


Figure 3. Representative seismograms recorded at ILPA station IR1. Top panel (a) shows efficient Sn propagation, SnA, center panel (b) shows inefficient Sn propagation, SnB, lower panel (c) shows SnC, not observed.

Sn Propagation Efficiency
ILPA
144 total observations

7	•	A efficient Sn propagation
33	▪	B inefficient Sn propagation
104	○	C no Sn propagation

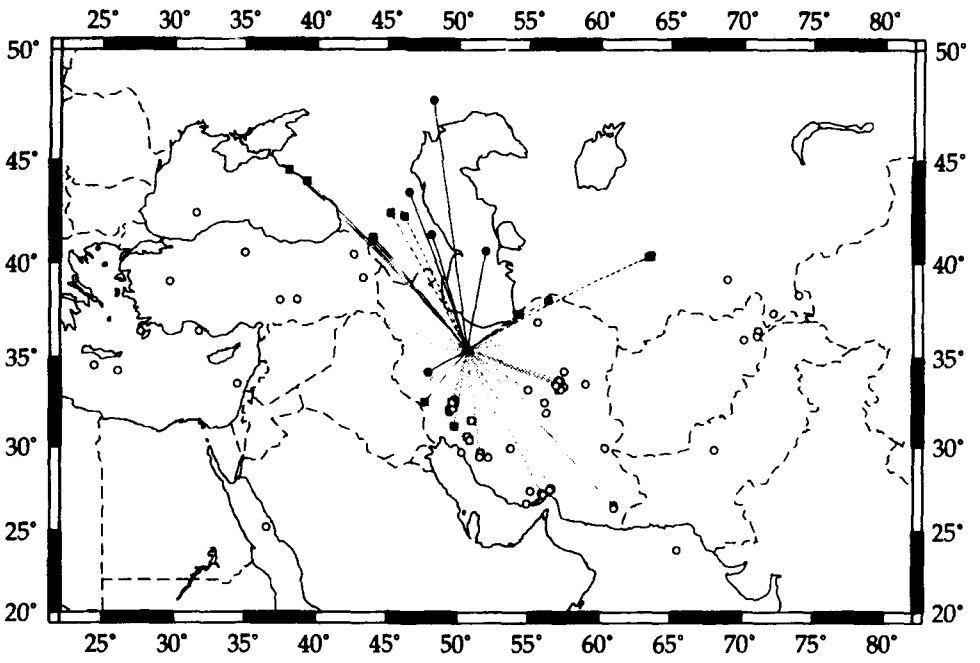


Figure 4. Sn propagation efficiency observed at ILPA.

2D Finite Difference Modeling of Seismic Wave Propagation in Complex Crust – Upper Mantle Media

B.O. Ruud[1,2] and E.S. Husebye[2]

[1] Faculty of Sciences, University of Oslo, Norway
[2] Institute of Solid Earth Physics, University of Bergen, Norway

Grant: AFOSR F49620-92-J-0510

Objective

The aim of the research under this grant is to improve our understanding of seismic phases and coda waves generated from local and regional events and how they propagate in the crustal wave guide and upper mantle. The motivation for this lays in the event identification problem. Most methods that have been proposed for identifying small events, utilize spectral amplitude ratios between various phases and coda waves observed at local and regional distances (Su et al, 1991, Pulli and Dysart, 1992; Blandford, 1993). In the case that a suspicious event takes place in an area where suitable reference events are lacking, the ability to synthesize seismic wave propagation in realistic geological models will be essential.

Our approach to achieve this have been to carry out extensive 2D finite difference modeling experiments in models of variable complexity. Our recent research efforts have concentrated on visualization of the results. For this purpose several video sequences have been produced and will be shown at the poster.

Research accomplished

Implementation of the 2D finite difference algorithm: The modeling technique used is a high order velocity-stress formulation on a staggered grid. A free surface boundary condition is used at the top and absorbing boundaries are used at the other margins of the model. The FD schemes used here is based on the method of Sguazerro et al (1989) and have been described by Husebye and Ruud (1991) and Hestholm et al (1994). The incorporation of 2D free surface topography is detailed by Hestholm and Ruud (1993).

Model generation and representation: The generation of gridded velocity models for use in FD simulations, like the one in Fig. 1a consisting several block of arbitrary shape, is not a trivial task. First a xerox copy of the published model figure is scanned into the computer through an optical scanner. Then the relevant interfaces are digitized from

the screen while leaving out other information from the figure. An automatic procedure have been devised which finds all closed curves from the digitized line segments. An identification number which is common for all points within a particular structural element, and unique for this element, can now be computed for every point in the model. Physical properties like P- and S-velocities are interactively assigned to each structural element by clicking on them with the mouse. Velocity gradients can optionally be used. The matrices of material properties necessary for the FD runs are then easily computed.

The model used for generating the video sequences is 70 km deep and 500 km long. An explosion source near the surface and 100 km from the left edge of the model generates frequencies up to 5 Hz. The first and simplest model used have constant velocities both in the crust and mantle and a gently undulating Moho. In the next model the crust have been divided into several homogeneous blocks/layers with smooth interfaces and velocities in the range 6.0 to 7.1 km/s, see Fig 1a. This model is derived from result tied to deep seismic sounding profiles in the Kola Peninsula. The last video sequence displays the propagating wavefield for a lithosphere model where random velocity perturbations have been added to the Kola model, Fig. 1b. The perturbations have a von Kármán correlation function of order 0.3, correlation distances of 10 and 2.5 km in the horizontal and vertical directions respectively, and an RMS of 1.5 per cent. P- and S-velocities are related through the Poisson's ratio of 0.25, and model densities are calculated from the P-velocities via Birch's law.

Visualization of the seismic wavefield: Since the length of the model is more than seven times its depth and we want to retain the same scaling in the horizontal and vertical directions, it is impractical to keep the entire model within the screen. Instead we use a screen image covering 150 km horizontally of the model and let the image follow the P wavefront until it reach the right edge of the model. This section is then kept fixed until the S/Lg waves arrive. The total simulation time of each sequence is 75 sec and consists of more than 3000 images. The physical quantity displayed is the square root of the length of the vertical particle velocity vector. This is shown in colors in the foreground while the background is the velocity model shown in greytones (the background appears when the particle velocity is less than a certain minimum value).

Modeling results: Conventional seismic sections obtained for the two models in Fig. 1 are shown in Fig. 2. The seismograms are plotted in reduced time and with the same fixed scaling so that amplitudes are directly comparable. Even for the unperturbed model the recorded wavefield is quite complicated (Fig. 1a). The Rg surface wave is very strong and dominating because there is no attenuation in the model. Scattering from P to Rg is seen at points of strong heterogeneities near the surface (e.g., at x = 260 km). The Pn wave (and its coda) is seen to be much stronger in the perturbed model (Fig. 2b) compared to the unperturbed (Fig. 2a). This is further illustrated in Fig. 3 where synthetics for a model with 3.0 per cent perturbations also is included. The anomalous strong Pn is attributed to scattering from sub-Moho heterogeneities

(Hestholm et al, 1994). A large number of multiply reflected and converted waves seen in Fig. 2 is difficult to identify unless one can follow their development through video sequences or a large number of snapshots. In the video one can also see some interesting wave propagation phenomena tied to the low velocity layer just above Moho. Energy is seen to concentrate and this layer and leaks out when passing over points of lateral heterogeneities. One can also see how energy from the Lg wave leaks down into the mantle at points of crustal thinning.

Conclusions and recommendations

Finite difference modeling represent the only useful method for computing synthetic seismograms in arbitrary complex 2D structures. The ability to study the continuous development of local and regional seismic phases is a unique property of the finite difference approach. In order to make this a practical tool in a seismic monitoring context, the generation of models and the visualization of the results should be automated as much as possible. When all types of wave conversions and scattering are included in the computations, as is the case for full elastic finite difference modeling experiments, surprisingly complicated seismograms are generated even for reasonably simple models at a few hundred kms distance. It is therefore likely that many of the models derived from wide-angle reflection and refraction profiles represents over-interpretation of the data and should be treated with some caution.

References

Blandford, R.R., 1993. Discrimination of earthquakes and explosions at regional distances using complexity. Tech. Rep., AFTAC-TR-93-044, AFTAC Headquarters, Patrick AFB, Fl.

Hestholm, S.O., Husebye, E.S., and Ruud, B.O., 1994. Seismic wave propagation in complex crust - upper mantle media using 2D finite difference synthetics. *Geophys. J. Int.*, in press.

Hestholm, S.O. and Ruud, B.O., 1994. 2D finite difference elastic wave modeling including surface topography. *Geophysical Prospecting*, in press

Husebye, E.S. and Ruud, B.O., 1991. Finite Difference Wavefield Synthetics - Understanding Seismic Source Discrimination Features. In *Proceedings of the 13th annual PL/DARPA Seismic Research Symposium*, 8-10 October, 1991, Keystone, Colorado, pp. 268-274, PL-TR-91-2208, ADA241325.

Pulli, J. and Dysart, P., 1992. Analysis and testing of high-frequency regional seismic discriminants. Phillips Laboratory Report PL-TR-92-2125.

Ruud, B.O., Husebye, E.S. & Hestholm, S.O., 1993. Rg observations from four continents: inverse and forward modelling experiments. *Geophys. J. Int.*, **114**, 465-472.

Sguazzero, P., Kindelan, M. & Kamel, A., 1989. Dispersion-bounded numerical integration of the elastodynamic equations. In *Proceedings of the ICOSAHOM Conference*, Como, Italy, June, 1989, pp. 165-172, N. Holland Publ. Co., The Netherlands.

Su, F., Aki, K. & Biswas, N.N., 1991. Discriminating quarry blasts from earthquakes using coda waves. *Bull. Seism. Soc. Am.*, **81**, 162-178.

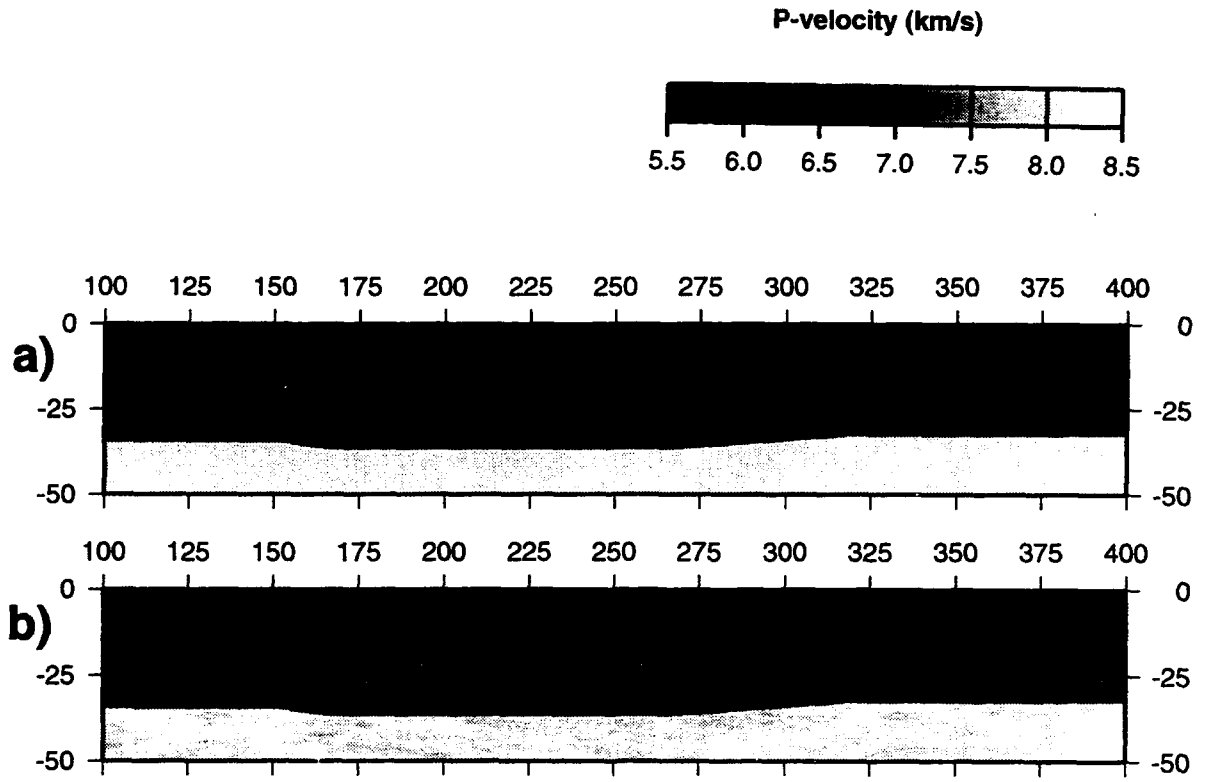


Fig. 1. Two of the P-wave velocity models used for generating the video sequences. a) and b) show the perturbed and unperturbed Kola model respectively.



Fig. 2a. The seismic section obtained from the model in Fig. 1a. The seismograms are vertical components of the paricle velocity recorded at the free surface. Intersensor spacing is 0.8 km. The section is plotted in reduced traveltime with a reduction velocity of 8.0 km/s.

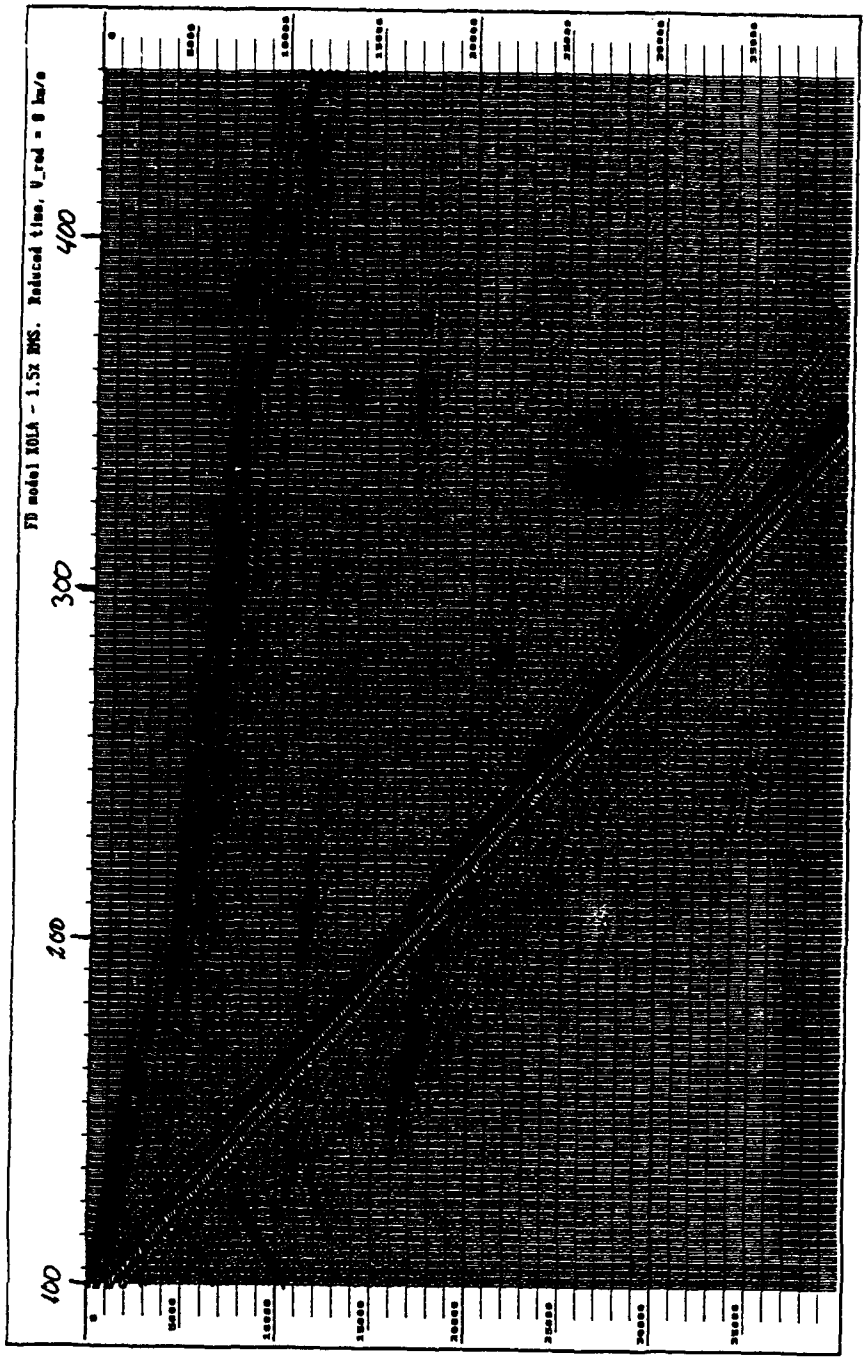


Fig. 2b. The seismic section obtained from the model in Fig. 1b. The seismograms are vertical components of the paricle velocity recorded at the free surface. Intersensor spacing is 0.8 km. The section is plotted in reduced traveltime with a reduction velocity of 8.0 km/s.

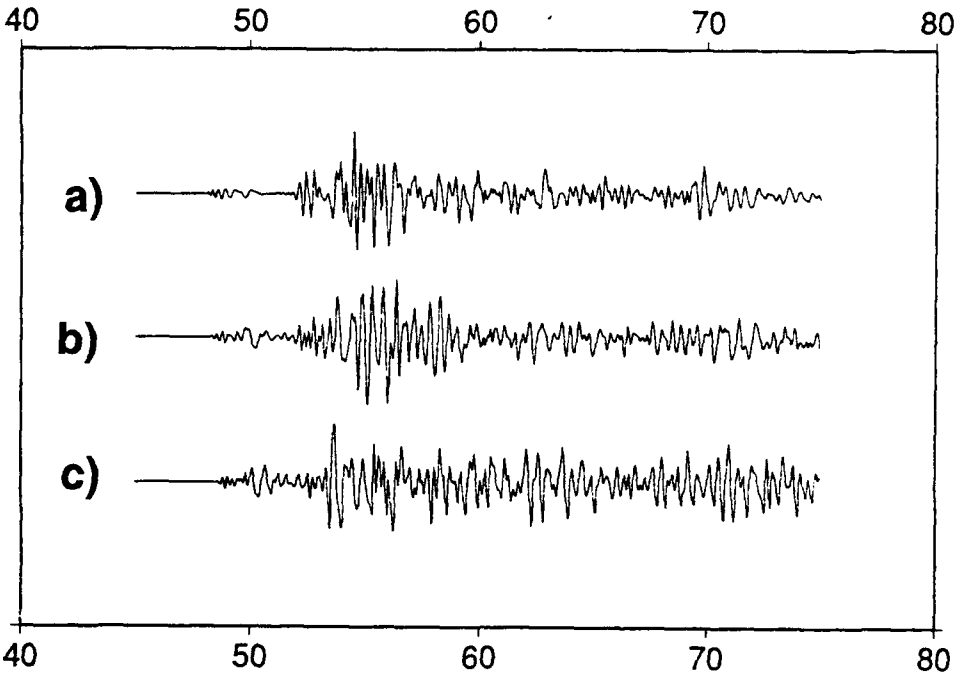


Fig. 3. Synthetic seismograms calculated for three models of variable complexity. a) is for the model in Fig. 1a (unperturbed - 0.0% RMS), b) is for the model in Fig. 1b (1.5% RMS), and c) is for a model similar to that in Fig. 1b but for 3.0% RMS. The distance from the source is 350 km in all cases and the amplitude scaling is the same. Pn is the first arrival and Pg starts about 4 sec later. The late Pn amplitude is seen to be very dependent on the degree of random variations. The Pg amplitude is less affected.

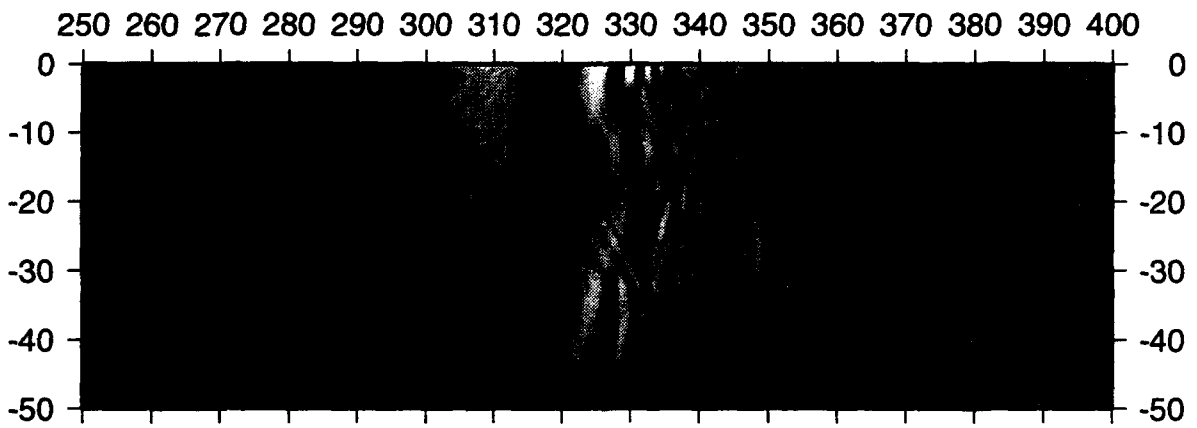


Fig. 4. A snapshot of the vertical component of the particle velocity wavefield at 65 sec in the unperturbed model (Fig. 1a). Energy from the Lg wave (around x = 330 km) is seen to leak down through the Moho after passing the crustal thinning in the x-range 270 to 320 km.

MODELING THE DAMAGE REGIME IN NONLINEAR EXPLOSION SOURCE SIMULATIONS

Charles G. Sammis
Department of Geological Sciences
University of Southern California
Los Angeles, CA 90089-0740

Contract # F49620-93-1-0284

OBJECTIVE

The overall objective of this line of research has been to develop a damage mechanics for the compressive failure of rock which can be used as the constitutive relation in the numerical codes which simulate underground explosions. This work is motivated by the observation that elastic nonlinearities associated with the active fracture of rock in the source region of underground explosions can affect the seismic waveform. Toward this end, Ashby and Sammis (1990) modeled the growth and interaction of fractures which nucleate at preexisting cracks within the rock, and have used these results to formulate a damage mechanics for the compressive failure of low-porosity rock (like granite). There are several advantages to this type of micromechanically based damage mechanics. It accounts for the size of the preexisting fractures in a physical way thus facilitating the scaling of laboratory strength data to the field and it also allows the effects of water saturation to be included.

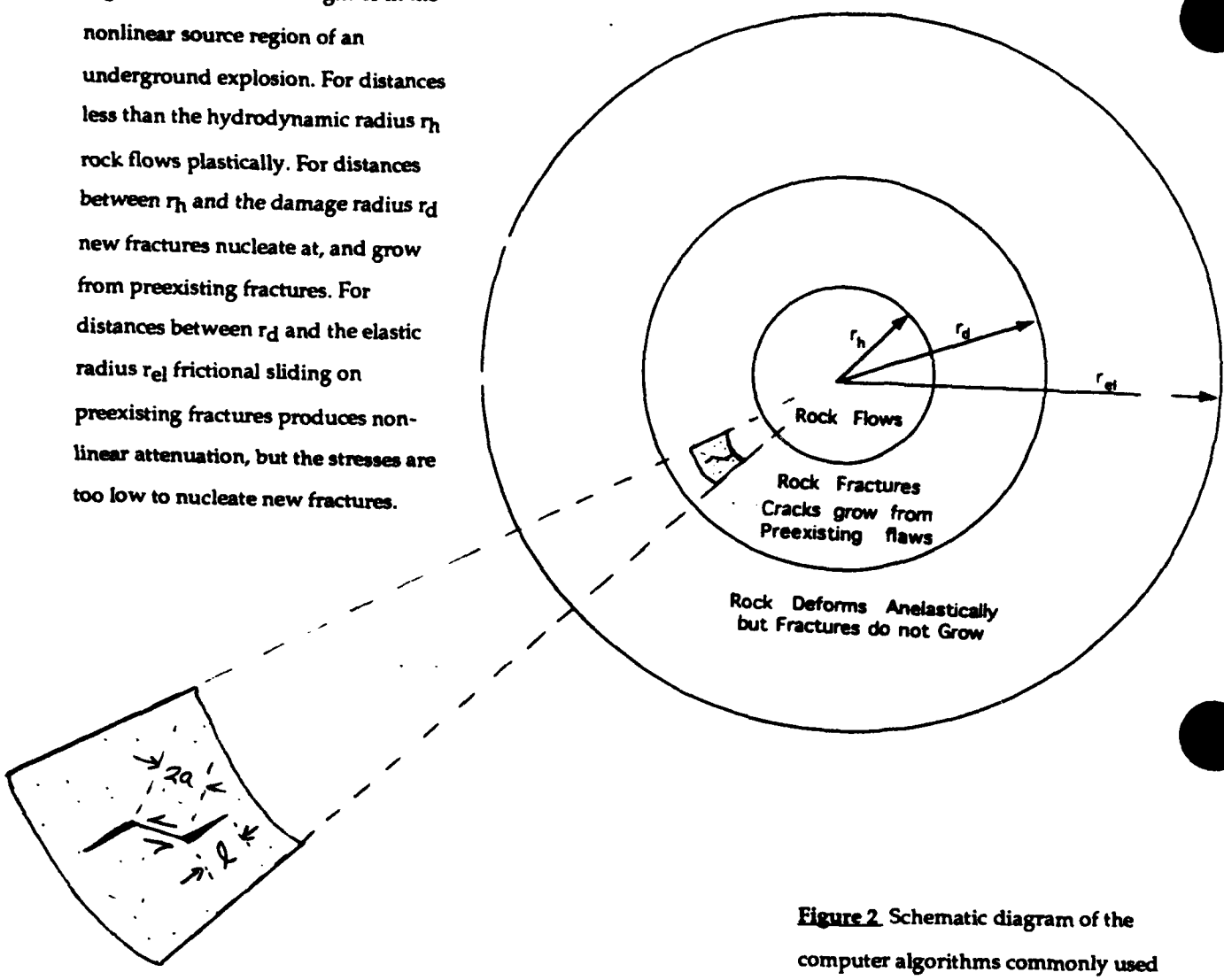
Last year we developed an algorithm by which the damage mechanics rheology may be implemented in the computer programs currently used to simulate underground explosions and calculate the resultant seismic radiation field at the elastic radius (beyond which wave propagation is assumed to be linear elastic). The objective of this years program has been to develop the FORTRAN subroutines necessary to implement this algorithm. We report here on the structure of this programming.

RESEARCH ACCOMPLISHED

Nonlinear source regimes

The nonlinear source region of an underground explosion can be divided into three regimes based on the physics of the deformation as illustrated in Figure 1. Closest to the working point is the hydrodynamic regime in which stresses and temperatures are high enough that the rock flows. At very small radius this is because the rock vaporizes or melts, but at greater distances the rock still flows plastically because stresses are above the yield stress for flow accommodated by dislocation glide. The stresses at which this flow ceases and fracture begins is given by the yield stress, σ_y, where

Figure 1 Deformation regimes in the nonlinear source region of an underground explosion. For distances less than the hydrodynamic radius r_h rock flows plastically. For distances between r_h and the damage radius r_d new fractures nucleate at, and grow from preexisting fractures. For distances between r_d and the elastic radius r_{el} frictional sliding on preexisting fractures produces non-linear attenuation, but the stresses are too low to nucleate new fractures.



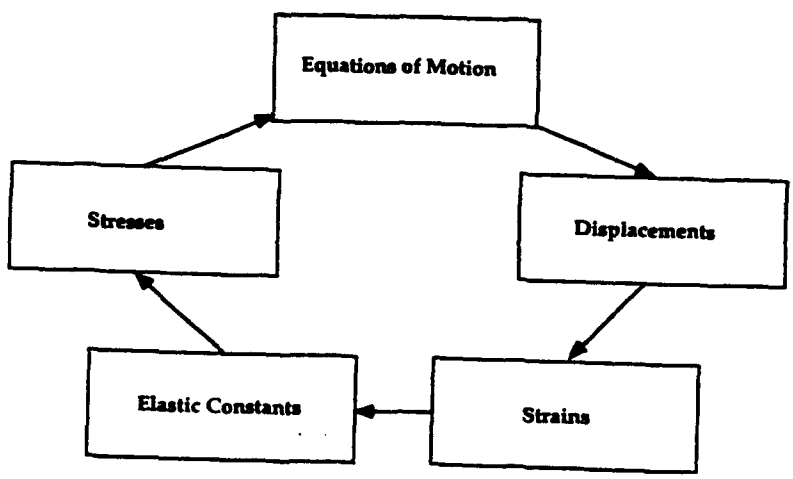


Figure 2 Schematic diagram of the computer algorithms commonly used to model the explosive source. These algorithms must be modified to account for the lowering of the effective elastic constants associated with new crack growth in the damage regime. As discussed in the text, this is done by introducing a new variable, damage, which keeps track of the current crack density. The elastic constants are a function of the damage, and the damage is a function of the stress. The new algorithm which we have programmed is shown in Figure 4.

$$\sigma_y^2 = \frac{1}{2}\left[(\sigma_1-\sigma_2)^2+(\sigma_2-\sigma_3)^2+(\sigma_3-\sigma_1)^2\right]$$

$$=(\sigma_1-\sigma_3)^2 \quad \text{when} \quad \sigma_2=\sigma_3 \tag{1}$$

The yield strength σ_y can be derived from indentation hardness (H) data since

$$\sigma_y = H/3 \tag{2}$$

Equation (2) can thus be used to define the boundary between the hydrodynamic flow regime and the second closest deformation regime which we call the "damage regime". In the damage regime, new fractures nucleate at, and grow from, preexisting fractures. The net result of this crack growth is a softening of the effective elasticity during the active fracturing and behind the advancing stress front. It is this regime which we are working toward modeling in the simulation codes for underground explosions. The damage regime extends out to a distance at which the stresses are no longer high enough to nucleate new fractures. The damage mechanics of Ashby and Sammis (1990) provides an explicit expression for the stresses necessary to nucleate crack growth from a preexisting fracture of length 2a which can be used to define the damage radius, r_d. At r_d the following relationship holds between the dimensionless shear stress τ and the dimensionless pressure p

$$\tau = \frac{3}{2(c_1+2)}\left[(c_1-1)p+s_0\right] \tag{3}$$

where

$$c_1 = \frac{\left(1+\mu^2\right)^{1/2}+\mu}{\left(1+\mu^2\right)^{1/2}-\mu}$$

and

$$s_0 = \frac{\sqrt{3}}{\left(1+\mu^2\right)^{1/2}-\mu}$$

The dimensionless pressure is defined as

$$p = \frac{1}{3}(s_{11} + s_{22} + s_{33})$$

$$= \frac{1}{3}(s_{11} + 2s_{33}) \quad \text{when} \quad s_{22} = s_{33} \tag{4}$$

and the dimensionless maximum shear stress is defined as

$$\tau = \frac{1}{2}(s_{11} - s_{33}) \tag{5}$$

where in both eqns. (4) and (5) the dimensionless stress components are defined as

$$s_{ij} = \frac{\sigma_{ij}\sqrt{\pi a}}{K_{IC}} \tag{6}$$

where σ_{ij} are the stresses, a is the half-length of the preexisting fractures, and K_{IC} is the critical stress intensity factor, a material property of the rock. It is thus apparent that the damage radius depends on the size of the initial fractures, and that damage occurs at lower stress levels in the field than it does in laboratory specimens because of the larger crack lengths in the field.

At distances greater than r_d the wave propagation is still non-linear because frictional sliding on the preexisting fractures produces amplitude dependent attenuation, but no new fractures are nucleated and the medium is not fundamentally altered by the passage of the stress front.

Rheology in the damage regime

The Lagrangian regimes used to model explosion sources usually follow the algorithm diagrammed in Figure 2. Beginning with a specified state of stress σ_i^j in each material element i at time j, the equations of motion are used to find the displacements u_i^j. This displacement field is then used to find the strain ϵ_i^j at each material position. These strains are then used with the elastic constants in each element to find the new stresses σ_i^{j+1}, and the cycle repeats. The incorporation of damage mechanics into these algorithms requires the introduction of a new variable, the damage D_i^j. Damage is a measure of the fracture density in each element which, for a spherically symmetric source, may be written as

$$D_i^j = \frac{4}{3}\pi(\ell + \alpha a)^3 N_V \tag{7}$$

where N_V is the number of initial fractures of length 2a, ℓ is the length of the new fractures which have nucleated from the preexisting ones as illustrated in Figure 1, and α is a geometrical constant near 1. The extended fracture thus has an effective length of $(\ell + \alpha a)$. At the beginning of a simulation, before any crack growth has occurred, all elements have the same initial damage D_0 defined as

$$D_i^j = D_0 = \frac{4}{3}\pi(\alpha a)^3 N_V \tag{8}$$

For each state of dimensionless stress, (p,τ), there exists an equilibrium damage $D(p,\tau)$ which can be calculated explicitly using closed form expressions given be Ashby and Sammis (1990). If (p,τ) lies below the nucleation surface given by (3), then D remains at D_0. If (p,τ) lies above the yield surface (1) and (2), the damage is not changed and the strain is calculated using a dislocation glide flow-law. For all stress states in between, a new equilibrium damage is calculated for each element. In the FORTRAN subroutine we have developed, this is done by interpolation on a table calculated using the expressions in Ashby and Sammis (1990).

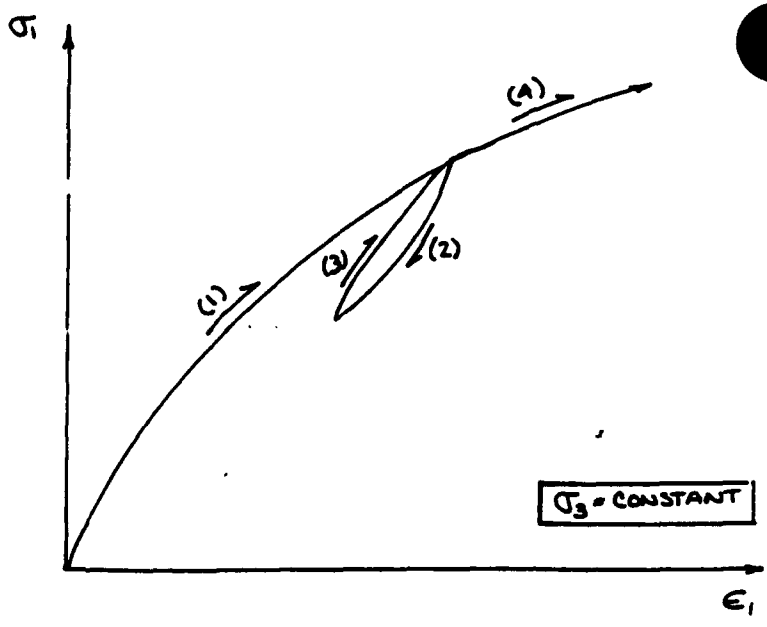
The elastic constants in each element depend explicitly on the damage in that element. The results of Budianski and O'Connell (1976) can be used to relate the Young's modulus E and Poison's ratio ν to the damage as

$$E_i^j = E_0(1 - 0.425)D_i^j$$

$$\nu_i^j = \nu_0 - 0.10D_i^j \tag{9}$$

Where E_0 and ν_0 are the moduli of the uncracked solid. It thus seems rather simple to include the damage mechanics. At each time step simply use the elastic constants appropriate to the old damage D_i^j to calculate the new stresses $(p,\tau)_i^{j+1}$, then use the look-up table to find the new equilibrium damage D_i^{j+1} for the next time step. The problem is that the effective elastic constants are lower than the values given by (9) if damage is increased during a time step. This is apparent in the stress-strain curve shown in Figure 3 where the effective elastic constant (the slope) is less along path 1 where damage is accumulating than it is along either paths 2 or 3 where the damage is constant. As discussed in last year's report (Sammis, 1993a,b), we have developed a way to deal with this problem which abandons the use of elastic constants and reverts to the basic physics of crack propagation. We use the Budianski and O'Connell elastic constants appropriate to the old damage, but if the new equilibrium damage is

Figure 3 Schematic stress-strain curve showing the lower effective elastic modulus over paths (1) and (4) where crack growth is increasing the damage than over paths (2) and (3) where the damage is a constant. We deal with this problem by dropping the concept of an elastic constant and using the Griffith criterion that the change in elastic energy balance the energy required to create the new damage. Figure 4 shows how this is implemented in the programming.



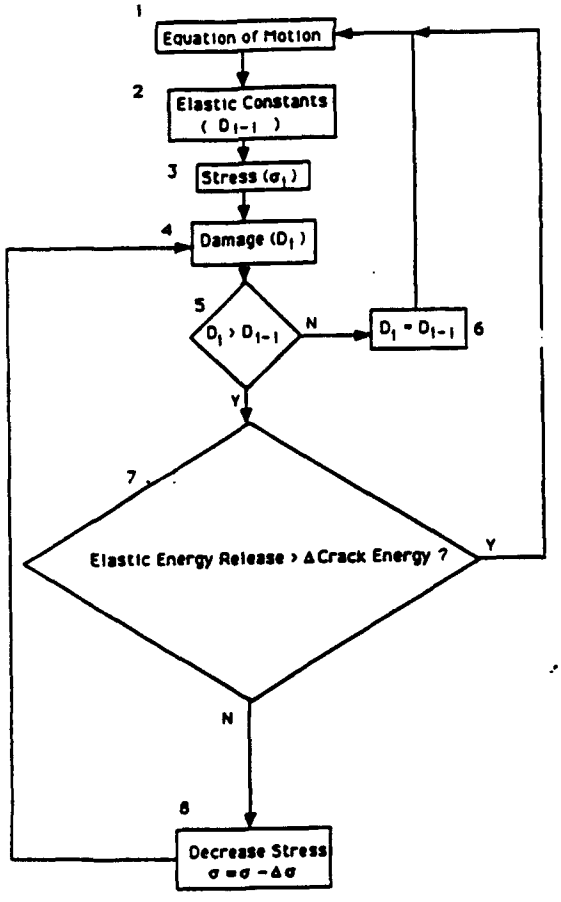


Figure 4 Schematic diagram of the subroutine we have developed to introduce damage rheology into the source simulation models diagrammed in Figure 2.

greater than the old, then we relax the stress along a radial return path until the elastic energy released in an element equals the energy required to increase the damage. This procedure is illustrated in Figure 4. The past year has been spent developing the FORTRAN subroutine required to implement this energy balance. We are now ready to implement these subroutines in a source simulation program.

CONCLUSIONS AND RECOMMENDATIONS

In developing the requisite subroutines we have worked with Livermore Labs who supplied a copy of their KDYNA program with documentation and Los Alamos who provided a copy of HYDROX with documentation. However, it seems more efficient to work directly with a group who are familiar with this type of code to implement my subroutines than to try the simulations ourselves. We are currently negotiating with Jeff Stevens at S^3 to attempt a first spherically symmetric simulation.

REFERENCES

Ashby, M.F., and C.G. Sammis, The damage mechanics of solids in compression, PAGEOPH, 133, 489-521, 1990.

Budianski, B., and R.J. O'Connell, Elastic moduli of a cracked solid, Int. J. Solids struct., 12, 81-97, 1976.

Sammis, C.G., Incorporating damage mechanics into explosion source models, Proceedings 15th annual seismic research symposium, Vail, Colorado, 349-355, 1993a, PL-TR-93-2160, ADA271458.

Sammis, C.G., Incorporating damage mechanics into a spherically symmetric source simulation, Proceedings of the Numerical Modeling for Underground Nuclear Test Monitoring Symposium, Durango Colorado, edited by S.R. Taylor and J.R. Kamm, 65-92, 1993b.

DEALING WITH DECOUPLED NUCLEAR EXPLOSIONS UNDER A COMPREHENSIVE TEST BAN TREATY

Lynn R. Sykes

Lamont-Doherty Earth Observatory, Columbia University, Palisades NY 10964

CONTRACT NO. F19628-90-K-0059

Objectives

The detonation of nuclear explosions in large underground cavities--decoupled testing--constitutes the greatest challenge to verification efforts under a comprehensive test ban treaty (CTBT). This evasion scenario sets the limit on how low a yield can be effectively verified. The United States working paper for the Committee of Disarmament of May 1994 states that the international monitoring system for a CTBT should be capable of detection and identification of nuclear explosions down to a few kilotons (kt) yield or less, even when evasively conducted. The results of our work are described below in the context of identification at the few kiloton level both for countries that have considerable underground testing experience, like the former Soviet Union (FSU), and countries that might attempt to test nuclear devices clandestinely for the first time.

Our work for the past few years has addressed a number of aspects of the problem of clandestine nuclear testing in large cavities in salt domes, bedded salt and hard rock. We are assessing what types of evasion scenarios are plausible based on geological and engineering constraints, seismic identification levels, the need to insure containment, have high confidence that no bomb-produced fission products reach the surface, and on the need of a country attempting to test clandestinely to have a high level of confidence that it can do so without being caught cheating.

In previous work we examined nuclear explosions at Azgir in western Kazakhstan (Fig. 1) using a combination of seismic data and satellite images made by SPOT satellites. Tamped explosions, a partially decoupled event, and six small nuclear devices detonated in a water-filled cavity were conducted at that site from 1966 to 1979. We obtain a decoupling factor, DF, of about 12 from seismic data at teleseismic distances for the partially decoupled explosion of March 1976, by far the largest nuclear explosion set off in a decoupled mode.

Research Accomplished

This report examines three topics--1) an examination of SPOT and Landsat satellite images for two sites of repeated Soviet peaceful nuclear explosions (PNEs) in salt, 2) a re-examination of the yield of the 1976 Azgir event and 3) what modes of clandestine decoupled nuclear testing are possible for either countries that already have considerable experience with underground testing and its containment or other countries that lack such experience.

Repeated Nuclear Testing in Salt at Astrakhan and Karachaganak

The USSR conducted 15 nuclear explosions at a site to the north of Astrakhan from 1980 to 1984 and 6 at Karachaganak in 1983 and 1984 (Fig. 1). Sultanov et al. (1993) identify all of those events as having been detonated in salt and give locations and depths for the 6 events at Karachaganak and for 6 of the 15 shots at Astrakhan. Marshall et al. (1991) obtained epicentral locations for all of the events at the two sites using the JED technique. The locations of the 6 events at Astrakhan reported by Sultanov et al. are situated about 4 km to the ESE of those of Marshall et al., which we interpret as a bias in the teleseismic locations of the latter. The locations of Sultanov et al. are then used to correct the locations of the remaining 9 events at Astrakhan obtained by Marshall et al.

Figs. 2 and 3 are portions of a SPOT image made in 1990 of the sites of the Astrakhan explosions. The revised locations of the 15 events are shown in the more detailed view, Fig. 3. All 15 events are located within the large Astrakhan gas complex. That industrial complex has

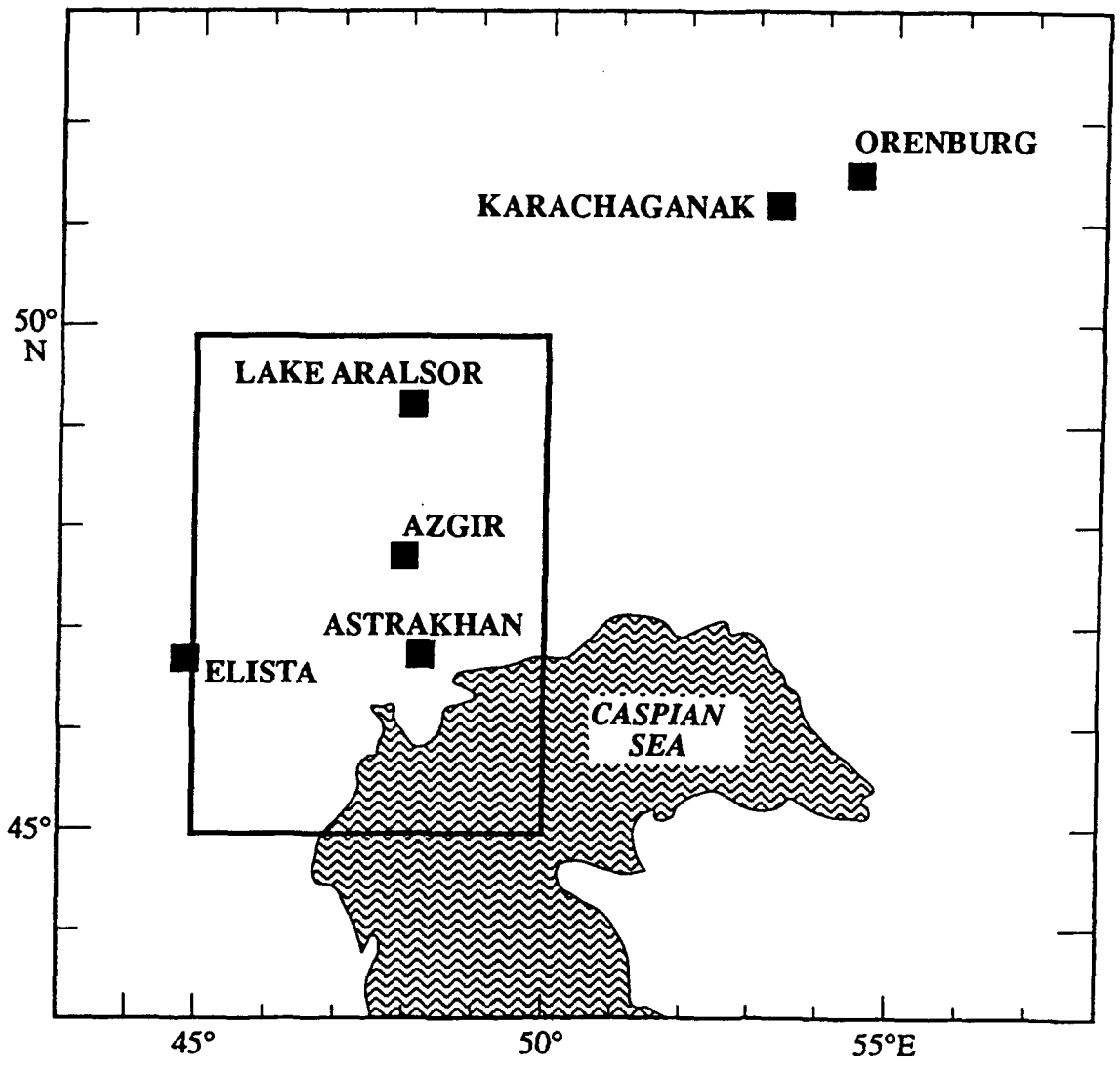


Fig. 1. North Caspian Region showing sites of nuclear explosions in and near thick salt deposits (squares) in Pre-Caspian Depression. Boxed region denotes area of previous special study of small seismic events.

Fig. 2. Processed SPOT satellite image taken in 1990 of Astrakhan gas complex. North is up on figure. Dimension of bottom of figure is about 31 km.

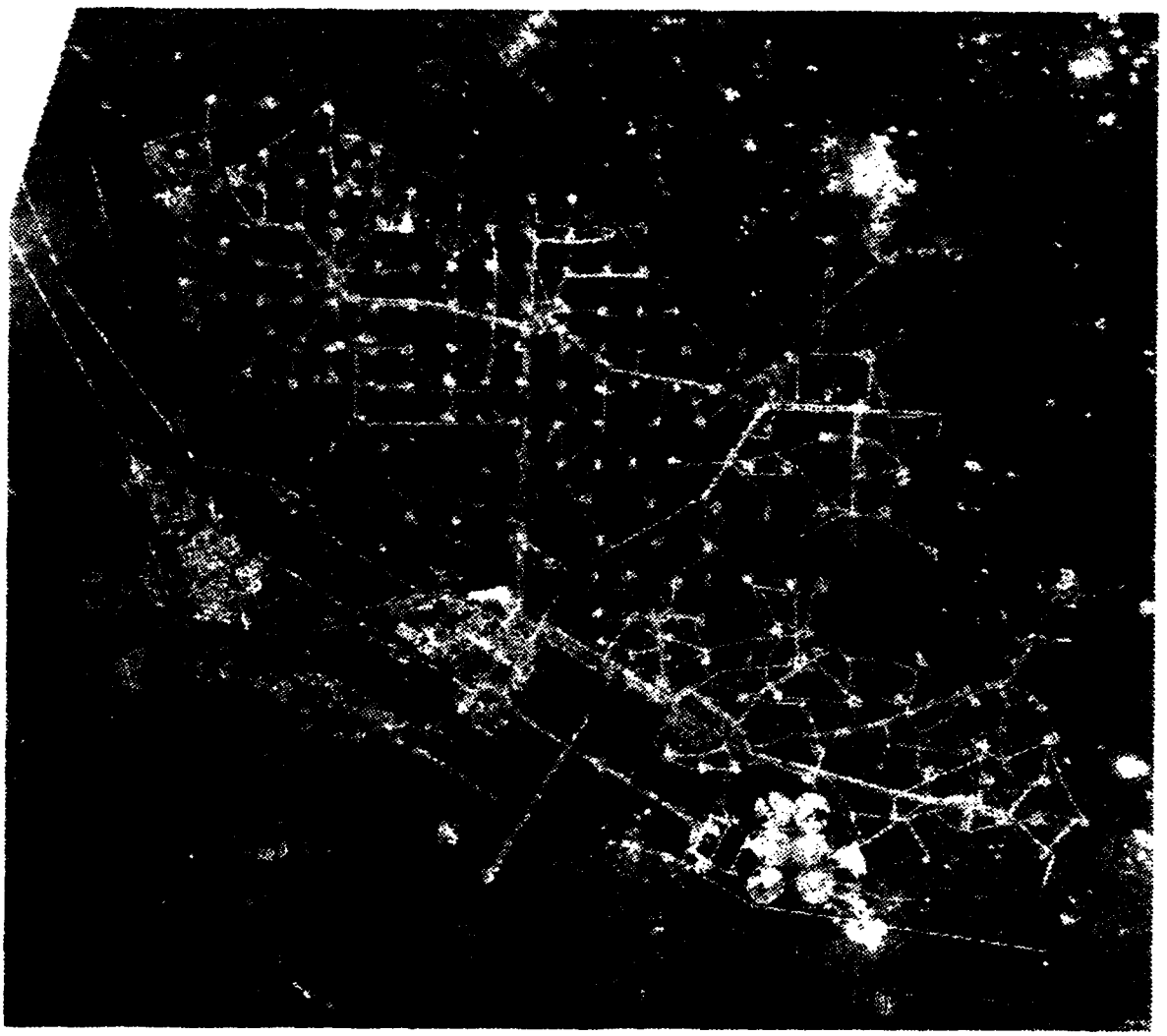
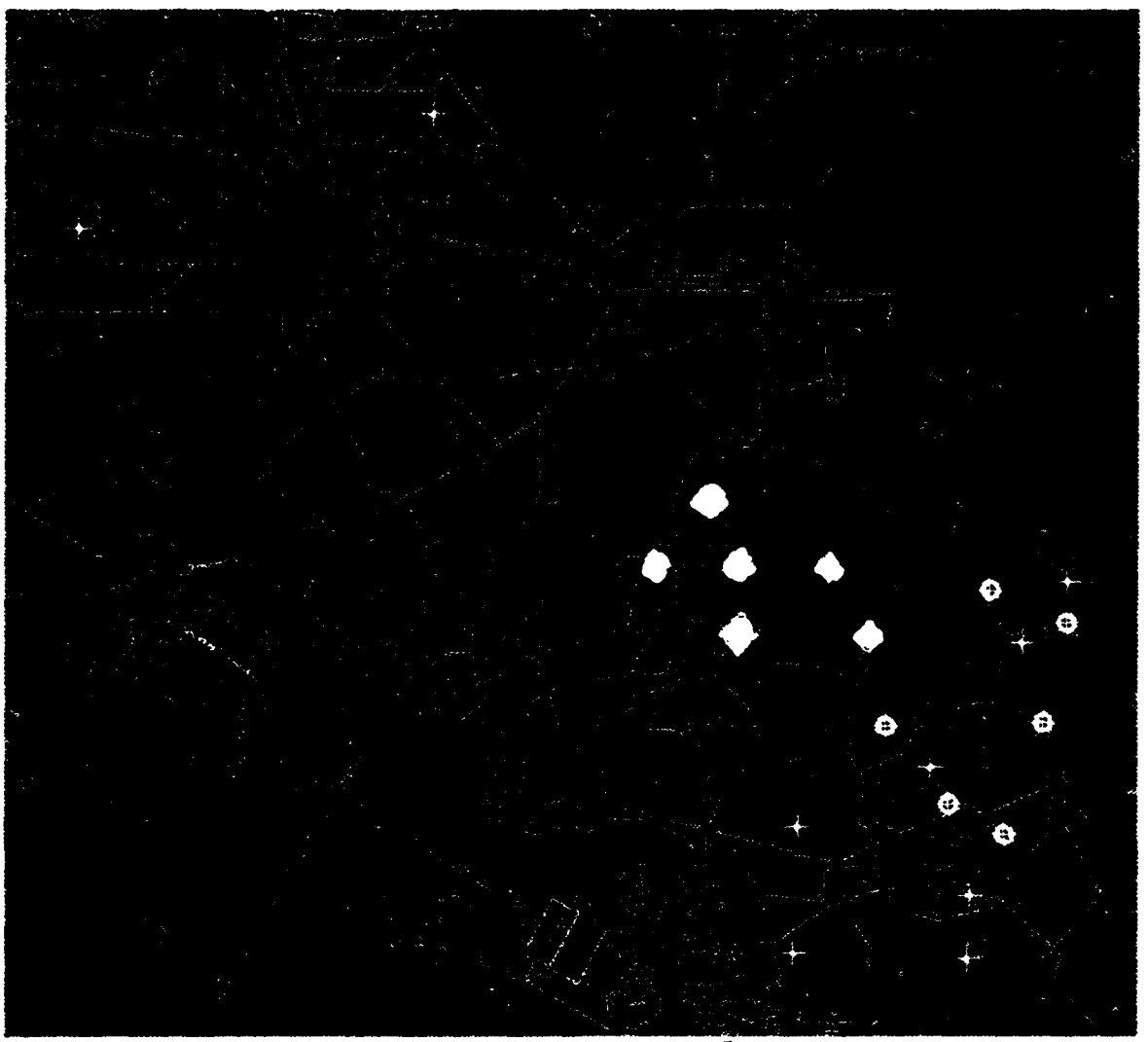


Fig. 3. Detailed view of Fig. 2 showing locations of 6 nuclear explosions on 24 Sept. 1983 reported by Marshall et al. (1991), diamonds, and Sultanov et al. (1993), circles. The locations of the latter were used as master events to correct the epicenters of 9 additional events (pluses) located by Marshall et al. Dimension of bottom of figure is about 20.4 km; north is up. Note two explosions in 1984 near upper-left corner.



clearly grown since the last nuclear explosions in 1984 as evidenced by its extent in a Landsat image made in 1986 and the SPOT image in 1990. Borg (1982) describes the early development of the gas condensate field.

A recent film "Volga, the Soul of Russia" by National Geographic Explorer mentions that 13 of the 15 cavities formed by nuclear explosions near Astrakhan are no longer usable [for their original purpose, storage of gas condensates]. A Russian geophysicist confirmed to Sykes that many cavities created in salt by the Soviet PNE program either collapsed or are no longer usable. The depths of 6 of the cavities given by Sultanov et al. (1993) is 920 to 1100 m. Cavities created in salt by the 1971 explosions at Azgir and Orenburg at depths of 987 and 1140 m (Sykes, 1993), however, did not collapse.

Berest and Minh (1981) give criteria for stability of industrial cavities created in salt. They find that the maximum depth of a stable brine-filled cavity created by solution mining is about 2 km. That depth is not applicable to the conduct of a decoupled nuclear test since brine in a cavity (or product replacing it like oil or gas under pressure) provides considerable support for the cavity. Using the criteria of Berest and Minh, the maximum depth of an air-filled cavity at atmospheric pressure is calculated to be about 900 m. From that calculation and the experience of cavity failure in the FSU and elsewhere, the maximum depth of a stable air-filled cavity in salt ranges from about 900 to 1200 m and depends on the thermal gradient, water content, mineralogy, and proximity to surrounding brittle rocks. Thus, the range of depths possible for clandestine nuclear testing in salt for yields of a few kilotons and larger is very limited since a minimum depth of about 200 m is necessary to insure containment. At Astrakhan and Karachaganak the minimum depth is greater since the cap rock above salt extends to depths of about 730 and 330 m (Sultanov et al., 1993).

Decoupling Factor for Azgir Event of 1976: Implications for Partial Decoupling

Adushkin et al. (1993) describe a partially decoupled nuclear explosion at Azgir in March 1976 with a yield of 8 kt. Goldstein and Glen (1993) and Glen and Goldstein report a 1993 personal communication with V. B. Adamski who gave the yield as 11.5 kt based on radiochemical analysis. Sultanov (personal communication, 1993) described the device used in the 1976 experiment as a standard one whose yield was determined by hydrodynamic methods. Glen and Goldstein (1994) use the larger yield stating that the hydrodynamic method would not be as accurate for an explosion in a large cavity. What is not clear is whether the hydrodynamic method was, in fact, used for the actual device detonated in 1976 or instead was employed earlier in the development of the standard nuclear explosive in a conventional tamped testing mode. This uncertainty is likely to remain until more information becomes available from Russian scientists.

One support for an 8 kt yield comes from estimated yields of several of the Astrakhan explosions, which are close to 8 kt, indicating that they may be the same standard device used in applications of PNEs that was used at Azgir in 1976. Fig. I.2 of Sultanov et al. (1993) gives scaled [relative] yields of Soviet underground nuclear explosions in salt as a function of ISC magnitude. Six events cluster near the same yield on their figure. Calibration of their scale using events in salt of announced yield indicates that those 6 events also had a yield about 7 kt. They also state that 5 of the 6 explosions they describe at Astrakhan and 3 PNEs conducted in granite had the same yield. The average yield of those 5 Astrakhan explosions as determined by Sykes (1993) is 8.8 kt. Thus, there are grounds for thinking the 1976 event at Azgir, in fact, had a yield close to 8 kt. If that is correct, most code calculations of the decoupling factor for the partially-decoupled conditions of the 1976 event are much greater than those calculated from seismic data.

Plausibility of Decoupled Testing under a CTBT for Different Geologic Media

The following addresses full decoupling or nearly full decoupling (taken to be the conditions of the Sterling explosion) at the few kiloton level and above. The results of the Soviet 8 kt experiment at Azgir indicate that the decoupling factor drops of rapidly for cavities overdriven with respect to Sterling conditions, i.e. for long-term cavity pressures greater than about 1.5 times the lithostatic (overburden stress). The following applies to countries with considerable underground

testing and containment experience; countries lacking that experience take a great risk in attempting to test for the first time in this yield range and to have high confidence that containment and secrecy will be assured and that the nuclear test will not be identified by outside parties to a CTBT. Most of the countries considered to be likely potential proliferators are small relative to the FSU, the U.S. and China, and hence would be easier to monitor from adjacent countries.

Salt Domes and Bedded Salt. Significant decoupled testing in cavities created by previous large nuclear explosions is only possible for the Azgir area in Kazakhstan (Sykes, 1993). For Russia itself, the largest cavities created in this manner are located at Astrakhan and Karachaganak but none are of a size that could be used for fully decoupled tests larger than 0.5 to 1 kt. The few nuclear explosions in salt by the U.S. were small enough that they could only be used for testing at the fraction of a kiloton level. No other countries are known to have tested in salt.

The use of cavities created in salt domes by solution mining for decoupled testing constitutes the greatest challenge to the verification of a CTBT. Most of the salt dome areas of the nuclear powers are characterized by low natural seismicity and efficient propagation of seismic waves. The sizes of chemical explosions used in mining of salt are small to negligible. Monitoring salt domes in areas of natural seismicity and low Q, as in Tadzhikistan, would require special verification measures such a local seismic array. While very large cavities have been created by solution mining, most of these cavities are filled with brine or stored products, either of which must be removed to permit significant decoupled testing. Cavity construction in areas of bedded salt is more limited since salt is typically interbedded with other rocks. The FSU conducted a single small nuclear explosion in salt in the large area of bedded salt to the northwest of Lake Baikal (Sultanov et al., 1993). Its yield, about 2.5 kt, was small enough that it could not be used for significant decoupled testing.

Hard Rock. A major issue that has received little debate in the U.S. is what is the maximum size cavity that could be constructed and used for clandestine, fully-decoupled testing of a given yield? Patterson (1966a,b) estimated scaled cavity radii for granite and salt for nearly full decoupling at depths of about 1000 m as 20 and 30 m. The Latter criterion gives 28 m for the Salmon cavity, a scaled radius most workers would accept for salt. The 20 m value for granite, which continues to be widely quoted, however, is based on free-field measurements for early U.S. explosions in granite that were thought then to be in the elastic regime but are now widely regarded as being in an inelastic regime. Heuzé (1983) and Heuzé et al. (1982, 1991) emphasize that hard rock masses are seldom monolithic but are penetrated by numerous joints and other discontinuities. Heuzé et al. (1991) state that traditional continuum codes are not sufficient for simulating multiple dynamic block motion processes for underground nuclear explosions in such media. Neither the U.S. nor any other country is known to have conducted a nuclear explosion in hard rock with a significant decoupling factor. The tiny Millyard nuclear explosion was a decoupled event conducted in softer rock--dry tuff--in a hemispherical cavity in Nevada at a depth of 375 m. Scaling either its volume or radius to 1 kt gives either 32 or 40 m. On a scale of tens of meters, hard rock *in situ* may well have a scaled cavity radius for decoupling more like that of salt.

Leith and Glover (1993) list 10 unsupported cavities mined in hard rock with volumes greater than 280,000 m^3. The depths of at least 5 are too shallow for containment of even a 1 kt explosion. The smallest dimension (width) of the deepest, 351m, is only 28 m. The line of argument that such cavities can, in fact, be constructed at depth and used for decoupled testing at yields well in excess of 1 kt depends on two untested assumptions for hard rock: 1) volume, not the width, is the critical dimensional factor and 2) the radius of a sphere of equivalent volume is 20 m x $(\text{yield})^{1/3}$ for nearly full decoupling. Use of scaled radii of 25 to 30 m for hard rock leads to a reduction in the maximum fully decoupled yield by a factor of about 2.0 to 3.4. Calculations for ellipsoidal cavities in hard rock are likely to be even more uncertain than they are for salt given the presence of joints and large differences in principal stresses. Overdriven decoupled testing in hard rock is more likely to result in leakage from the cavity than one in salt.

Conclusions and Recommendations

Now that a CTBT is under negotiation many issues involving verification that have largely lay dormant for many years are surfacing. Several aspects of decoupled nuclear testing are among the prime issues. For a country to believe that it can cheat on a CTBT with high confidence by testing in a decoupled mode at the few kiloton level, it must be prepared to pass a series of verification challenges: clandestine construction and evacuation of a large cavity at depth, insure containment, and not be identified by seismic or other means. Monitoring salt dome areas of the nuclear powers should be a high priority so as to deal with decoupled testing in cavities constructed by solution mining. A country wishing to test clandestinely in a large cavity in hard rock, however, must contend with greater uncertainties in rock properties (such as the presence of joints and other discontinuities) as they affect cavity stability and containment, a scaled radius for full decoupling that may well be considerably larger than 20 m, and differences in principal stresses that generally increase with depth. Resolving the feasibility of decoupled testing at the few kiloton level for hard rock is critical since hard rock is present in many more areas than salt domes.

References

Adushkin, V. V., I. O. Kitov, O. P. Kuznetsov and D. D. Sultanov (1993). Seismic efficiency of decoupled nuclear explosions, *Geophys. Res. Lett.*, 20, 1695-1698.

Berest, P. and D. N. Minh (1981). Stability of cavities in rocksalt, *Proc. Intern. Symposium on Weak Rock*, (Tokyo, 21-24 Sept.), 473-478.

Borg, I. Y. (1982). The underground nuclear explosions at Astrakhan, U.S.S.R., Lawrence Livermore Laboratory, Univ. of California, Rept. UCID-19543, 1-16.

Glen, L. A. and P. Goldstein (1994). Seismic decoupling with chemical and nuclear explosions in salt, *J. Geophys. Res.*, 99, 11,723-11,730.

Goldstein, P. and L. A. Glen (1993). Modelling of tamped and decoupled explosions in salt (Simulation is easy. Prediction is Difficult!), in *Proc. Numerical Modeling for Underground Nuclear Test Monitoring Symposium*, ed. by S. R. Taylor and J. R. Kamm, Los Alamos Nat. Lab. Rept. LA-UR-93-3839, 341-348.

Heuzé, F. E. et al. (1982). Rock mechanics studies of mining in the Climax granite, *Int. J. Rock Mech. Min. Sci. & Geomech. Abstr.*, 19, 167-183.

Heuzé, F. E. (1983). A review of geomechanics data from French nuclear explosions in the Hoggar granite, with some comparisons to tests in U.S. granite, Lawrence Livermore Laboratory, Univ. of California, Rept. UCID-19812, 1-28.

Heuzé, F. E. et al. (1991). Explosion phenomenology in jointed rocks: new insights, *Geophys. Monog.*, 65, (Amer. Geophys. Union), 253-260.

Leith, W. and D. Glover (1993). Underground construction achievements and decoupling opportunities, worldwide, unpublished manuscript of poster presentation at 15th Annual ARPA/AFPL Seismic Research Symposium, Vail CO, 8-10 Sept., 9 pp, PL-TR-93-2160, ADA271458.

Marshall, P. D., R. C. Lilwall, R. C. Stewart and I. Marsden (1991). Seismometer array recordings of P waves from explosions in the North Caspian USSR area, Atomic Weapons Establishment, AWE Report No. O 4/91, 1-95.

Patterson, D. W. (1966a). Nuclear coupling, full and partial, *J. Geophys. Res.*, 71, 3427-3436.

Patterson, D. W. (1966b). The calculational sensitivity of a model describing the response of a nuclear formed cavity, Lawrence Livermore Laboratory, Univ. of California, Rept. UCID-5125.

Sultanov, D. D. et al. (1993). Investigation of seismic efficiency of Soviet peaceful nuclear explosions conducted in various geological conditions, Rept. submitted to ARPA, 1-220.

Sykes, L. R. (1993). Underground nuclear explosions at Azgir, Kazakhstan, and implications for identifying decoupled nuclear testing in salt, PL-TR-93-2155, 118 pp. Phillips Laboratory, Hanscom Air Force Base, MA. ADA276728.

THE EFFECT OF SEDIMENTS ON ATTENUATION, SCATTERING, AND BLOCKAGE OF Lg WAVE PROPAGATION

Yu-Chiung Teng and John T. Kuo
Aldridge Laboratory of Applied Geophysics
Henry Krumb School of Mines
Columbia University, New York, New York 10027

CONTRACT NO: F49620-93-0073

OBJECTIVE

The objective of this paper is to investigate the effects of sediments on the attenuation, scattering, and blockage of Lg wave propagation, by means of finite-element modeling. The numerical models are particularly focused on the Lg propagation from presumed explosions at test sites of Novaya Zemlya across the Barents Sea to ARCESS and Graefenbury.

RESEARCH ACCOMPLISHED

In our previous studies(Teng and Kuo, 1993; Teng and Kuo 1994), the problem of Lg wave propagation in a complex, laterally inhomogeneous wave guide, such as in the present case of simulating the propagation path from Novaya Zemlya through the Barents Sea, can be accomplished by multi-steps in finite element modeling. This multi-step methodology promises to handle models of large dimensions, without degrading the accuracy of numerical results. Figure 1-(a) simulates the geological structure along the path from former USSR nuclear test sites Novya Zemlya to the Barents Sea, which is represented by a sedimentary basin. The multi-step calculations in the model as shown in Figure 1-(a) are:

(i) an impulsive source be placed in the Island Margin Model to obtain the seismic response everywhere in the model (Figure 1-(b));

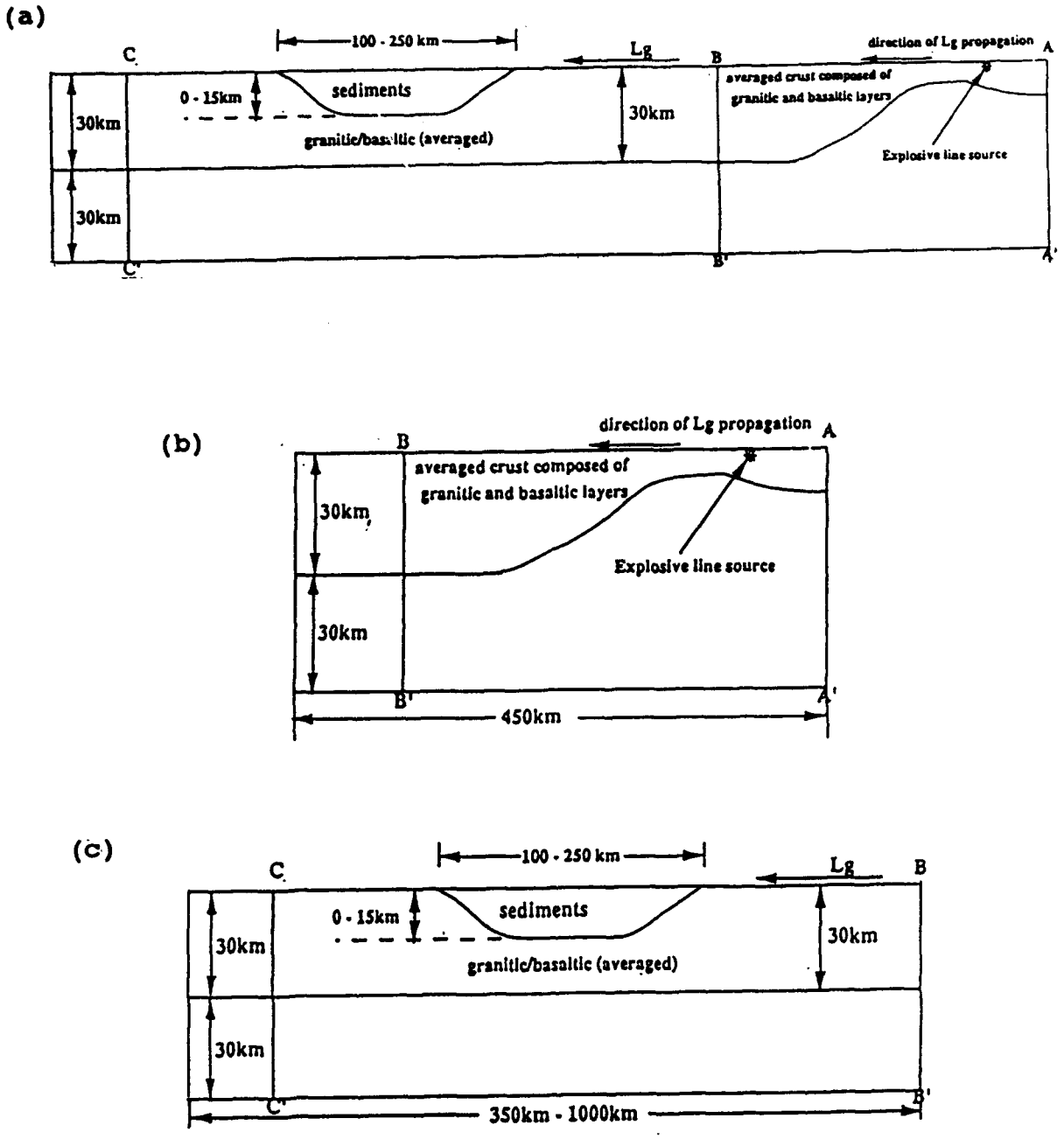


Figure 1. (a) The geological structure along the path from the nuclear test sites Novya Zemlya to the Barents Sea, which is represented by a sedimentary basin; (b) The Island Margin Model; (c) The Basin Model.

(ii) the output of the seismic response, in our case we choose BB′, be used as an input source to drive the Basin Model, and the Basin and Crust Pinch Model (Figure 1-(c)).

From our previously constructed models, we have concluded that the velocity contrast between the sediments in the basin and the surrounding granitic/basaltic crust plays a vital role in determining the characteristics of Lg waves. For a high velocity contrast, the Lg waves are delayed, scattered and therefore blocked. All the previous studies have been emphasized on the elastodynamic problems without considering the effects of sediments on attenuation for the cases of an anti-plane strain approximation. Chan and Mitchell (1985), and Mitchell and Hwang (1987) suggested that the reduction of Lg amplitude might be caused by the attenuation of the thick low-Q sediments as the Lg waves travel crossing the Barents Sea.

In our present study, a line source with the first derivative of Gaussian type of forcing function with center frequency of 0.334 Hz, is located on the island side of the Island Margin Model (Figure 1-(b)). The S wave velocities of the granitic/basaltic (averaged) layer and the upper mantle are assumed to be 3.51 km/sec and 4.7 km/sec, respectively. The seismic waves, as shown in Figure 2, observed along the left termination boundary BB′ have been used as the input waves at BB′ in Figure 1-(c). We consider a series of basin models with different attenuation values of quality factors, Qs = ∞, 150, 100, 50, 25, 10, with a fixed basin velocity of 2.2 km/sec, and a fixed basin width of 250 km. Figures 3-(a), 3-(b), and 3-(c) are the synthetic seismograms obtained from the basin models by using Qs = ∞, 150, and 50 for the basin, respectively. These seismograms are observed along the free surface at the locations of 20 to 400 km from the input waves. In Figure 3, it is clearly shown that the Lg waves are attenuated at the locations after the presence of the basin for the cases of Qs =150 and 50. Figures 4 gives the comparison of seismic waves (Lg and all other waves) at the same locations of observation for cases with different Qs values. Trace 1 to Trace 6 in the figures correspond to the cases of Qs = ∞, Qs = 150, 100, 50, 25, 10 respectively. In Figure 4, comparisons of seismic waves at the distances of 250 km, 350 km and 400 km from the source is given in 4-(a), 4-(b), and 4-(c) respectively. Figure 4 shows that the Lg amplitude is highly attenuated from Trace 1 (Qs = ∞) to

Trace 6 (Qs = 10). The presence of the low-Q basin ,as expected, affects very little on the amplitude of the Sn waves, as the waves are propagated through through mostly the upper mantle.

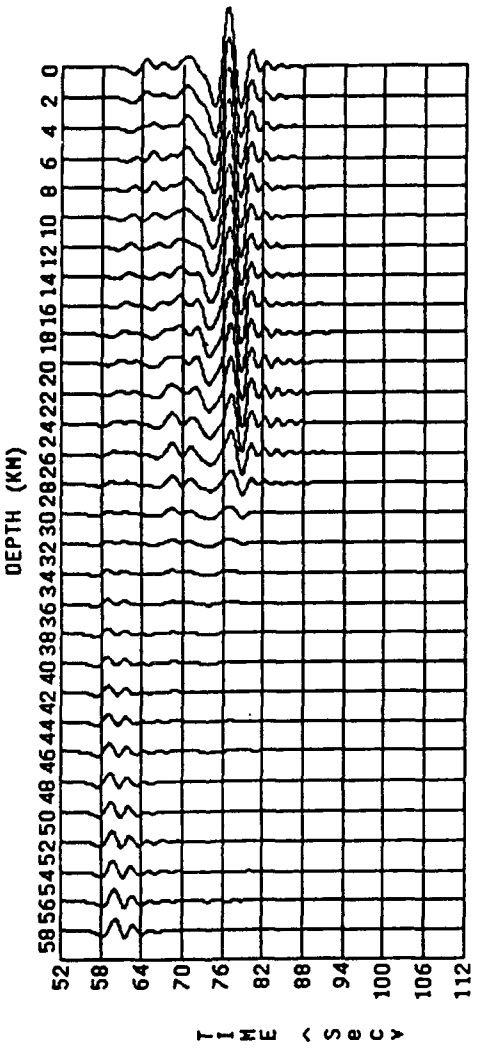


Figure 2. Seismic reponses observed along BB' in Figure 1-(b), which are used to exite the basin model Figure 1-(c).

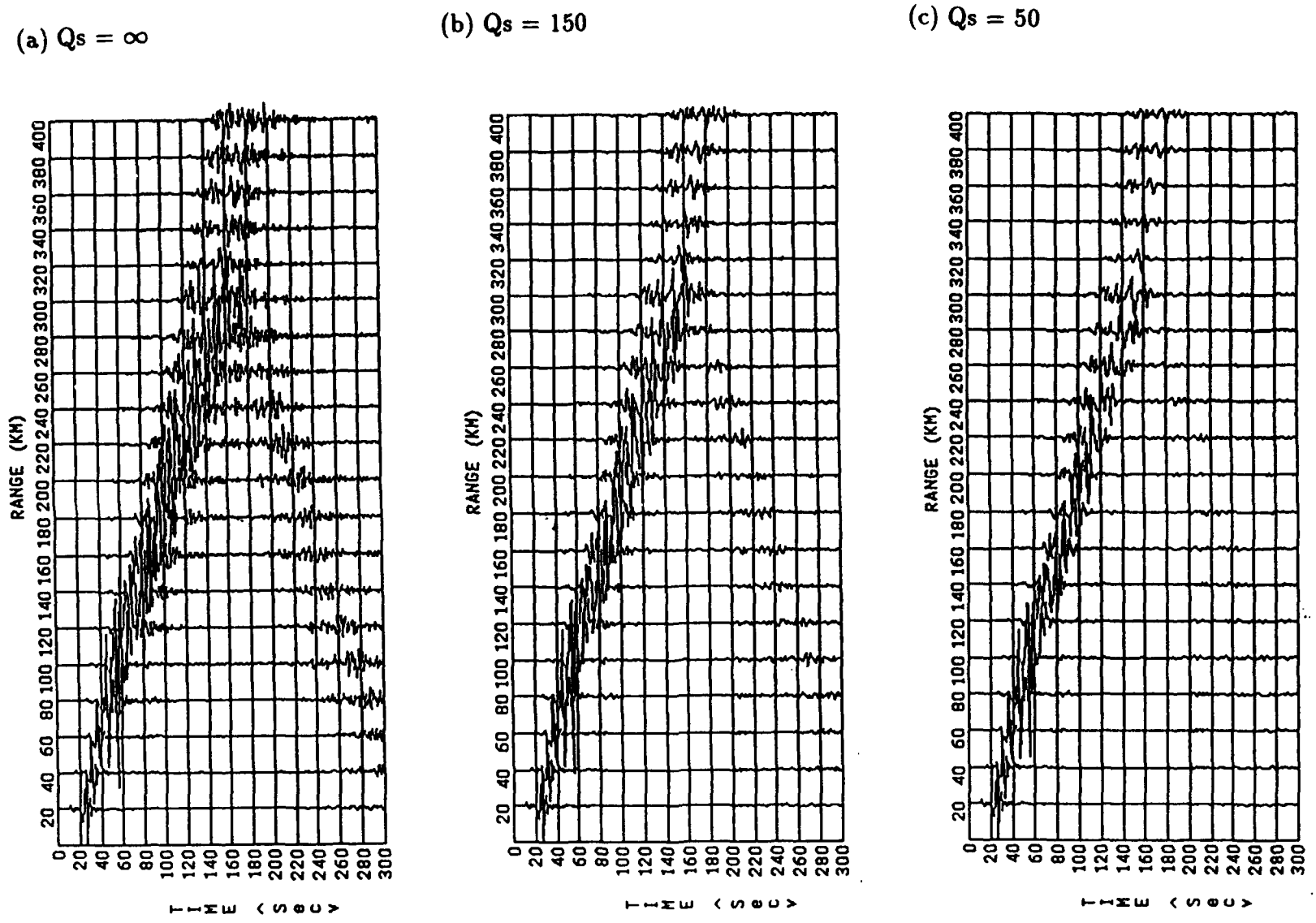


Figure 3. The finite-element synthetic seismograms for the basin models of Figure 1-(c), with the basin velocity of 2.2 km/sec and different Qs values, as observed at distances of 20 km to 400 km from the source.

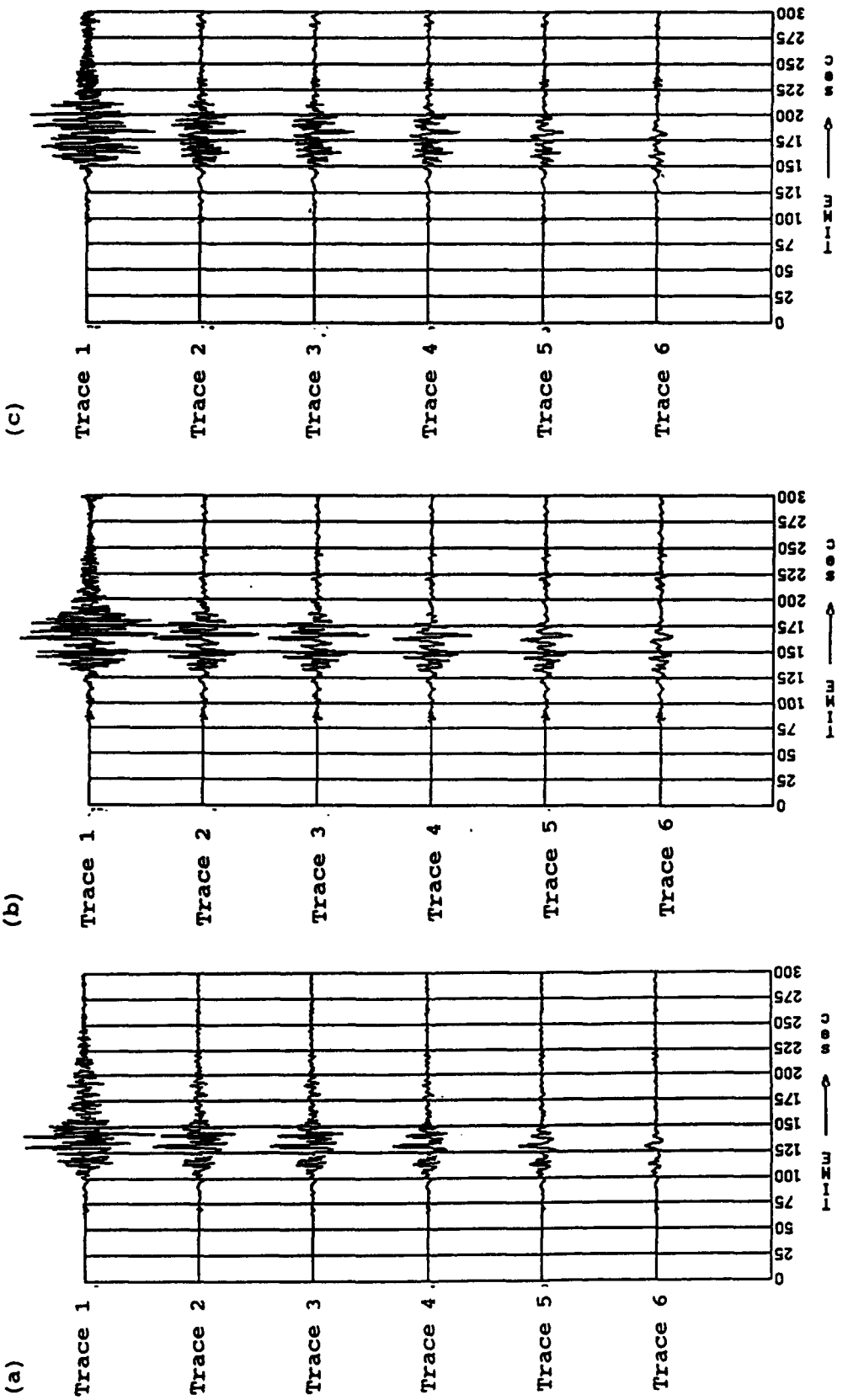


Figure 4. The comparison of seismic waves at the same locations of observation at distacnce of: (a) 200 km; (b) 350 km; and (c) 400 km from the source for cases with different Qs values. Trace 1 to Trace 6 in the figures correspond to the cases of Qs = ∞ , 150, 100, 50, 10, respectively.

CONCLUSIONS AND RECOMMENDATIONS

Numerical results of the present models studied show that thick low-Q sediments do cause the attenuation of the reduction of Lg amplitudes, but do not delay the Lg propagation.

In the future, we suggest more realistic models including the following be studied:

(i) plane strain (P-SV) modeling in elastodynamics, and visco-elastodynamics;

(ii) effects of an ocean on the blockage and scattering of Lg waves, by considering the fluid/solid interaction in finite element modeling;

(iii) three-dimensional modeling in elastodynamics, and visco-elastodynamics;

so that the whole spectrum of the mechanism of Lg wave propagation be better understood.

REFERENCES

1. Baumgardt, D.R., (1990a). Investigation of teleseismic Lg blockage and scattering using regional arrays, Bull. Seism. Soc. Am., **80**, 2261-2281.
2. Baumgardt, D.R., (1990b). Causes of Lg amplitude variations and scattering in the Eurasian continental craton, Proceedings of the 12th Annual DARPA/AFGL Seismic Research Symposium, 18 - 20 Sept., 1990, 224-233, GL-TR-90,0212, ADA226635.
3. Chan, W.W. and B. J. Mitchell (1985). Surface wave dispersion, crustal structure, and sediment thickness variations across the Barents shelf, Geophys. J. R. Astron. Soc., **80**, 329-344.
4. Clarke, J.W. and J. Rachlin (1990). Geology of the Barents Sea Structural Basin. U.S. Geological Survey, Military Geology Project, Open-File Report, July, 1990.
5. Fan, Z.X. and Y.C. Teng (1989). The application of simulation modeling of seismic wave in the transversly isotropic and viscoelastic media, Bull. of Chinese Geophys. Soc., Applied Geophys., **1**, 37-56.
6. Gramberg,I.S.,(1988). The Barents Shelf Plate (in Russian), Volume 196, Nedra, Leningrad.
7. Mitchell, B.J. and H.J. Hwang (1987). Effect of low-Q sediments and crustal Q on Lg attenuation in the United States. Bull. Seism. Soc. Am., **77**, 1197.
8. Teng, Y.C., and J. T. Kuo, (1993), Finit-element modeling of the blockage and scattering of Lg wave propagation., Proceedings, 15th Annual Seismic Research Symposum, 391-397, PL-TR-93-2160, ADA271458.
9. Teng, Y.C., and J. T. Kuo, (1994), Annual Report to the Air Force Office of of Scientific Research, Numerical Modeling of the Blockage and Scattering of Lg Wave Propagation., CONTRACT NO: F49620-93-0073.

Regional Wave Propagation in Central and Southern Africa

Kristin S. Vogfjord[+], Andrew A. Nyblade, and Charles A. Langston
Department of Geosciences, Pennsylvania State University, University Park, PA 16803

[+] now at: Department of Geological and Geophysical Sciences, Princeton University, Princeton, NJ

Grant no. F49620-94-1-0031

Objective

The issue of nonproliferation of nuclear weapons requires that the nature of seismic sources and the nature of wave propagation in largely unexplored continental regions be known to address fundamental problems of event detection, location, source mechanism, and discrimination. In particular, knowledge of structure is essential to the understanding of regional seismograms written by natural and explosive sources. In this study, we investigate crustal and upper mantle structure beneath central and southern Africa using earthquake sources recorded at regional and teleseismic seismic stations. We combine the regional analysis of digital and analog seismograms within Africa with proven teleseismic analysis techniques for the same sources to constrain source parameters. After obtaining constraints on focal mechanism and source depth, we model regional seismograms using synthetic seismograms to determine details of lithospheric structure.

Research Accomplished

Regional waveforms from two earthquakes in central and southern Africa have been modeled to determine characteristics of crustal and upper mantle structure. The first event (Figure 1) occurred in the western branch of the east African rift system and was recorded 1620 kms to the northwest at station BCAO in the Central African Republic. The source-receiver path for this event crosses the Congo Basin, a Paleozoic-Mesozoic sedimentary basin underlain by Precambrian crust and lithospheric mantle. The source-receiver path for this event also lies west of the African superswell, an extensive region of high topography in eastern and southern Africa (Nyblade and Robinson, 1994). Examination of regional wave propagation along this path provides information about crustal structure within and beneath the Congo Basin, as well as upper mantle structure away from the African superswell. The second event (Figure 1) occurred in southern South Africa and was recorded 1170 km to the northeast at station PRE and 1190 km to the northwest at station WIN. The source-receiver paths for this event cross Proterozoic and Archean crust and lie entirely within the African superswell. Modeling of regional wave propagation along the source-receiver paths for the second event provides information on Precambrian crustal structure within southern Africa, in addition to upper mantle structure beneath the African superswell.

Source parameters for the two events are listed in Table 1. Focal mechanism and depth for event 1 have been obtained using both short- and long-period data from the SRO stations NWAO, CHTO, GRFO, the ASRO station KONO, and the NRSA station NRAO. Short-period records from GRFO, KONO, NRAO, and CHTO provide important constraints on focal depth and source duration. First arrivals on the short-period record from CHTO are obvious (Figure 2a), but the first *P*-arrivals at stations GRFO, KONO, and NRAO are near-nodal and thus harder to detect. However, because all three stations

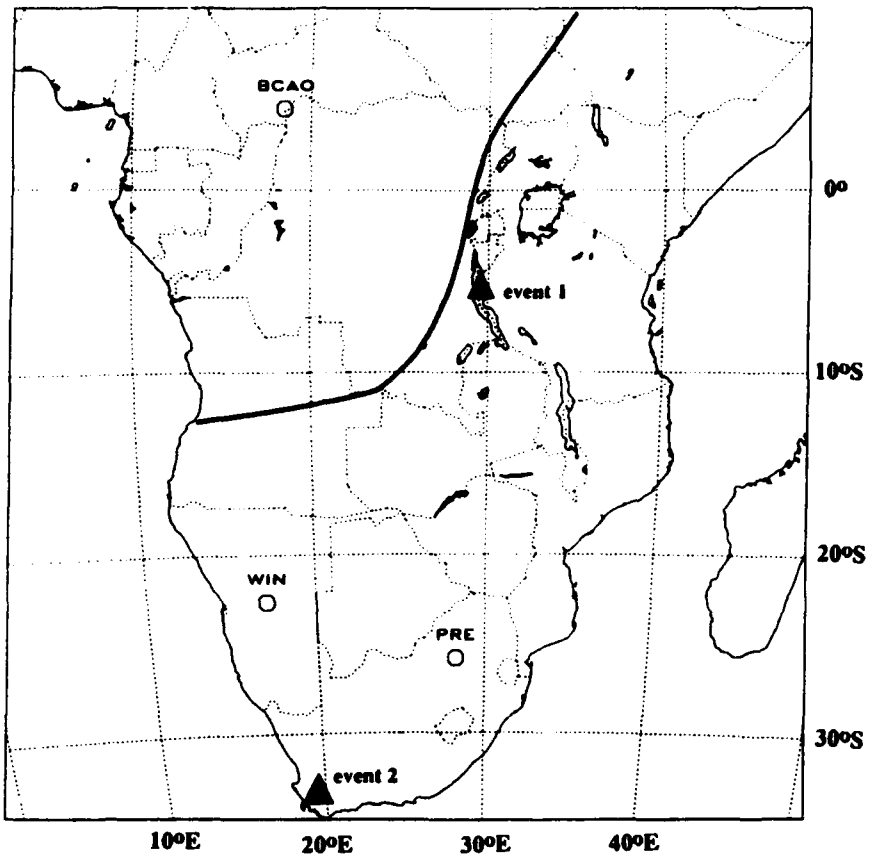


Figure 1. Map of the southern African subcontinent showing earthquake (solid triangles) and station (labeled ovals) locations. The northern margin of the African superswell is delin ted by the solid, bold line.

Table 1. Source Parameters

Event	Date	Lat.	Lon.	m_b	depth	strike	dip	rake
1	6/29/86	5.20 S	29.59 E	5.0	36 km	191.4	81.1	-72.0
2	9/29/69	33.09 S	19.52 E	5.6	4 km	123.5	89.5	-0.54

have similar azimuths (346-351°) and are at similar distances from the source (57-67°), rays to these stations leave the focal sphere at nearly the same location, enabling the waveforms, after correction for instrument responses, to be beamformed to one location to produce a single trace with an improved signal/noise ratio. Source depth for this earthquake can be estimated by convolving the beam with the short-period instrument response from CHTO and comparing it to the record from CHTO (Figure 2a). There is clear correspondence between the two traces, and the arrival times of *P*, *pP*, and *sP* are readily determined, as illustrated in Figure 2b. The *pP-P* and *sP-P* times yield a source depth of 36.5 km, and the time duration of the direct-*P* arrival on the CHTO record indicates a source duration of ~5 seconds.

A focal mechanism for event 1 was obtained by inverting *P*- and *SH*-waves on the long-period records at stations NWAO, CHTO, GRFO, KONO, and NRAO for moment tensor using an iterative, generalized inversion algorithm (Langston et al., 1982). Based on the duration of the direct-*P* arrival on the short-period record at CHTO, a 5 sec source time function was employed in the inversion with a rise-time of 2 sec and a 3 sec fall-off. Inversion was performed for a specified source depth, and focal parameters were then calculated from the moment tensor by representing the source as a point double-couple.

To determine if this approach would yield a source depth consistent with the depth determination from the short-period records (Figure 2), inversions were performed for sources between depths of 22 and 40 kms. The focal depth was then taken as the source depth which yielded the best fit between the data and the synthetic waveforms. When the source depth increased beyond 36 km depth, two cases were considered; (a) a source at various depths in the mantle with a Moho fixed at 36 km depth, and (b) a source in the crust with the Moho depth adjusted so that the Moho was always just beneath the source. For estimating the quality of fit between the synthetics and the data, three different statistical measures of the difference between the data and synthetics were monitored; (1) the least-squares error (lse), (2) the root-mean-square error (rms), and (3) the percentage of compensated linear vector dipole (clvd). These parameters are plotted in Figure 3, and although there is no clear minimum in the rms curve, the lse curve has a broad minimum at 36 km depth, and the clvd term has minima at depths of 32 and 38 km. This result is consistent with the source depth estimate of 36.5 km from the short-period records.

The results of the inversion for a 36 km deep source are shown in Figure 4. The fault plane solution shows normal faulting with primarily northeast-southwest extension. The source mechanism was stable over a wide depth range, lending validity to the mechanism. The mechanism is also similar to the one reported in the Harvard CMT catalog, although our source depth is deeper by 16 km.

Source parameters for event 2 come from a detailed study by Wagner and Langston (1988), where the focal mechanism was obtained by inverting 12 *P*- and 7 *SH*-waves recorded at WWSSN stations for moment tensor and source time function. Inversion yielded a nearly pure sinistral strike-slip fault and a focal depth of 4 km. A source depth of 4 km was also obtained from *sP-P* times on several short-period records.

To examine crustal and upper mantle structure, we have modeled the *Pnl* waves generated by these two events and recorded at stations BCAO, PRE and WIN. We use a wave number integration algorithm to generate our synthetic seismograms, assuming plane-layered structures and dislocation sources. A number of synthetic waveforms have been generated to determine how variations in crustal and upper mantle structure affect the *Pn* and *PL* portions of the waveforms. Variations in model parameters that have so far been examined include; (1) crustal thicknesses of 36, 40, 45 and 50 km, (2) positive *P*-wave velocity gradients in the mantle between 0.0007 and 0.0066 s^{-1}, and (3) 40, 60 and

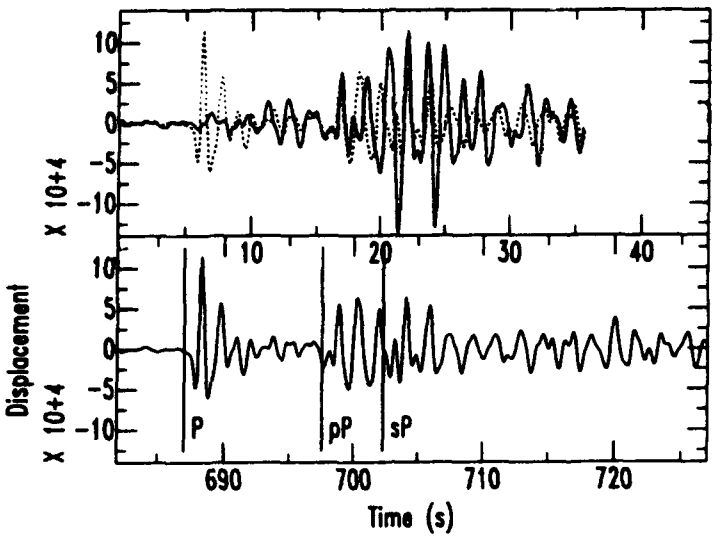


Figure 2. Short-period vertical records. (a) Trace from CHTO (dashed line) and the beamformed trace at GRFO (solid line with reversed polarity to facilitate comparison with record from CHTO). (b) Trace from CHTO showing P, pP, and sP arrivals.

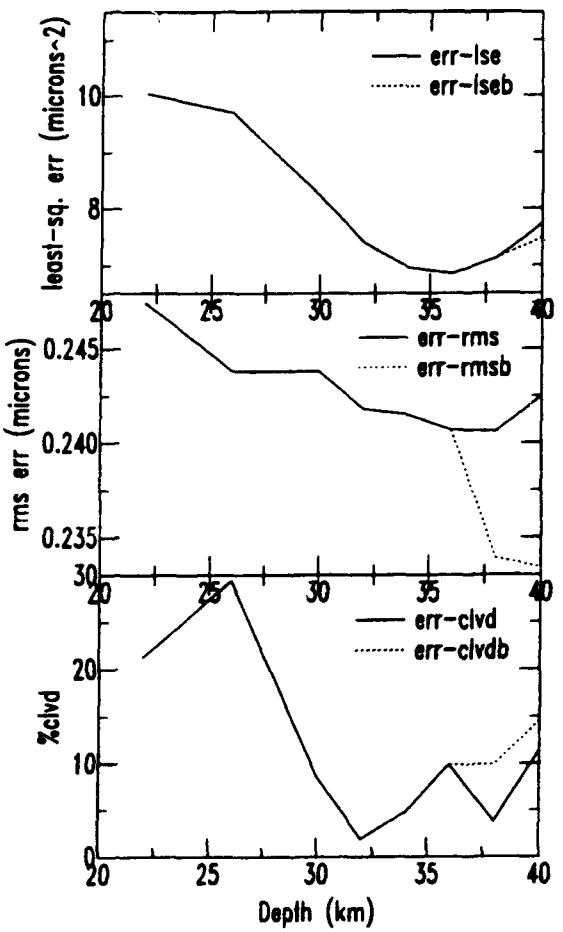


Figure 3. Moment tensor inversion errors for event 1. See text for discussion; solid and dotted lines show results for case a and b, respectively.

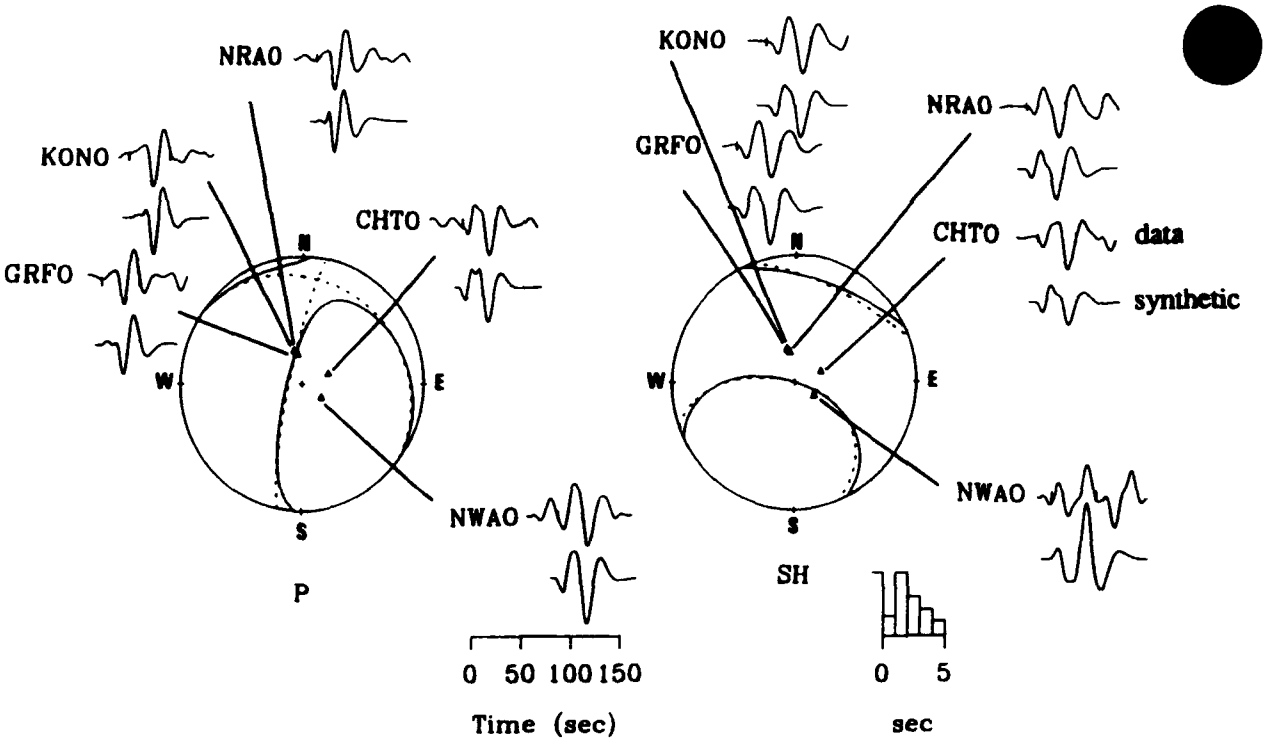


Figure 4. Focal mechanism (lower hemisphere projection) for event 1. For each station, the upper trace is the data and the lower trace is the synthetic waveform. Waveforms are normalized to their maximum amplitude. Tic marks on the upper traces bracket the time window used in the inversion. The source time function is shown in the lower right corner.

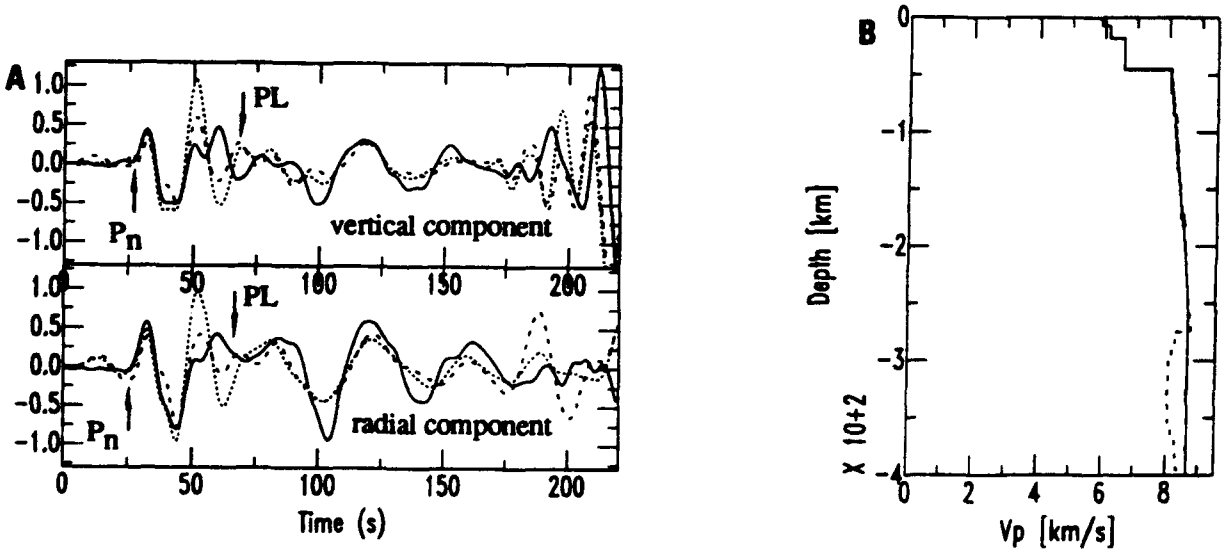


Figure 5. (a) P_{nl} waveform from BCAO (solid line) and synthetic waveforms for models with (1) a 60 km thick low velocity zone beginning at 275 km depth (dashed line) and (2) no low velocity zone in the upper mantle (dotted line). Both models have a 45 km thick crust and upper mantle velocity gradients of 0.003 s^{-1}. Further details of the velocity models are shown in (b).

100 km thick upper mantle low velocity zones (LVZ) beginning at depths of 125, 175, 225 and 275 kms.

The results of the best fit between the *Pnl* waveform recorded at BCAO from event 1 and the synthetic waveforms are shown in Figure 5a. The best fitting synthetic waveform was generated from a model with a crustal thickness of 45 km, a mantle velocity gradient of 0.003 s^{-1}, and a 60 km thick LVZ beginning at a depth of 275 km (Figure 5b). Amplitude and period of the *PL* wave are matched fairly well (except for the large downswing at 105 s), suggesting that the first-order crustal structure in this model is correct. In the *Pn* portion of the waveform, the amplitude and timing of the first arrival is well matched for an upper mantle LVZ beginning at 275 km depth, but this model also produces a second upswing not observed in the data at ~ 50 sec. Clearly, upper mantle structure in the model needs further refinement in order to explain fully the *Pn* portion of the waveform, but nonetheless our preliminary results suggest that the average crustal thickness across the Congo Basin is ~45 km, and that the upper mantle is characterized by a positive velocity gradient of ~ 0.003 s^{-1} above the LVZ. The synthetic waveform for a model with no LVZ is shown for comparison in Figure 5a, and it is obvious that such a model does not reproduce the main features of *Pn* very well.

Of the models tested so far, the synthetic waveforms which provide the overall best match to the *Pnl* waveforms recorded at PRE and WIN from event 2 are shown in Figure 6. The *PL* portion of the waveform at PRE is fit well but not at WIN, where there are differences in both amplitude and period, suggesting that average crustal thickness in the area between event 2 and WIN is less than 45 km. The *Pn* portions of the waveforms at both PRE and WIN are fairly well matched, although in each record the amplitude of the first arrival in the synthetic is somewhat larger than in the data, perhaps because the upper mantle velocity gradient is lower than 0.003 s^{-1}, and/or the LVZ has a stronger effect on *Pn* than in any of our models.

Conclusions

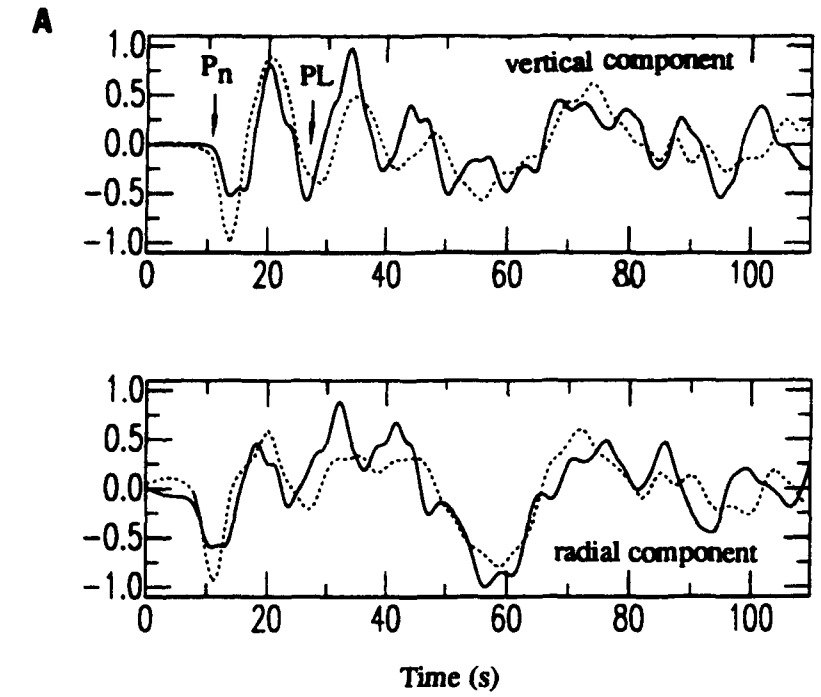
Our preliminary results suggest that the lithosphere beneath central and southern Africa has similar structure characterized by 40-45 km thick crust and small, positive velocity gradients in the upper mantle. If this finding can be corroborated by additional modeling, it would indicate that wave propagation through the African superswell, a region with elevated heat flow and fractured by Mesozoic and Cenozoic rifts, may not be any less efficient than in other shield areas of Africa. Future work will concentrate on refining models of crustal and upper mantle structure for the source-receiver paths described above, with particular emphasis placed on understanding the nature of the low velocity zones within the upper mantle, or the lack thereof. In addition, we plan to model other source-receiver paths both within and outside the African superswell, focusing on waveforms recorded at a variety of regional distances.

References

Langston, C.A., J.S. Barker, and G.B. Pavlin, Point-source inversion techniques, *Phys. Earth Planet. Int., 30,* 228-241, 1982.

Nyblade, A.A., and S.W. Robinson, The African Superswell, *Geophys. Res. Lett., 21,* 765-768, 1994.

Wagner. G.S., and C. A. Langston, East African earthquake body wave inversion with implications for continental structure and deformation, *Geophys. J., 94,* 503-518, 1988.



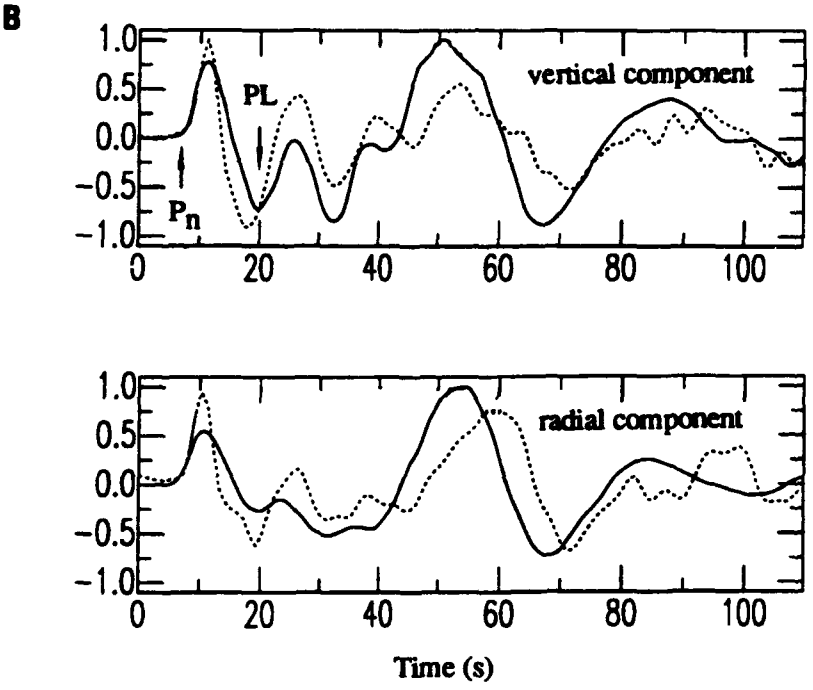


Figure 6. P_{nl} waveforms from (a) PRE and (b) WIN (solid lines) and synthetic waveforms (dotted line) for the velocity model in Figure 5b without at LVZ.

Waveform Estimates from Multi-Channel Seismic Data

Gregory S. Wagner & Thomas J. Owens
Department of Geological Sciences
University of South Carolina
Columbia, SC 29208

Contract No. F49620-94-1-0066

Objective

The primary role seismology plays in monitoring nuclear test ban treaties is in the detection, location, and discrimination of clandestine underground tests. This role has changed somewhat in recent years as we are now faced with the task of monitoring much of the globe for smaller events indicative of countries attempting to develop nuclear weapons. To aid in the continued effort to improve our ability to detect, locate and discriminate between small earthquakes, industrial explosions, and nuclear tests, we have focused our research on two areas: (1) the use of broadband three-component array data to aid in event detection and location, particularly in regions with little or no coverage, and (2) the characterization of lithospheric heterogeneities with the main objective being to answer questions regarding regional wave propagation through laterally heterogeneous media which will in turn prove useful in waveform modeling to distinguish between chemical, nuclear and natural sources.

Research Accomplished

In the following sections we will demonstrate an eigen-analysis signal detection and waveform estimation approach using data from an IRIS Joint Seismic Program array operated near Ashkhabad, Turkmenistan (Pavlis *et al.*, 1993). The array geometry and instrumentation were employed to help investigate some of the fundamental questions about high-frequency regional wave propagation and the use of high-frequency energy to help discriminate between natural and explosive sources. The site is located at regional distance from areas of current and not too distant historical interest. Figure 1 shows the Geyöcha array geometry and broadband three-component data from a m_b 4.0 event that occurred in Iran approximately 10.1° SSW of the array. The data used in this paper are the continuous, 20 sample/sec streams from the 9 Streckeisen STS-2 broadband sensors.

Multi-Channel Data Analysis

Multi-channel seismic data plays an important role in monitoring nuclear test ban treaties. With multi-channel data, we can estimate a signal's propagation direction, velocity, and polarization characteristics by finding the location in the multi-dimensional space where the data exhibits the greatest variance. This information can be used to locate the source and to improve the S/N to aid in waveform modeling for source parameters.

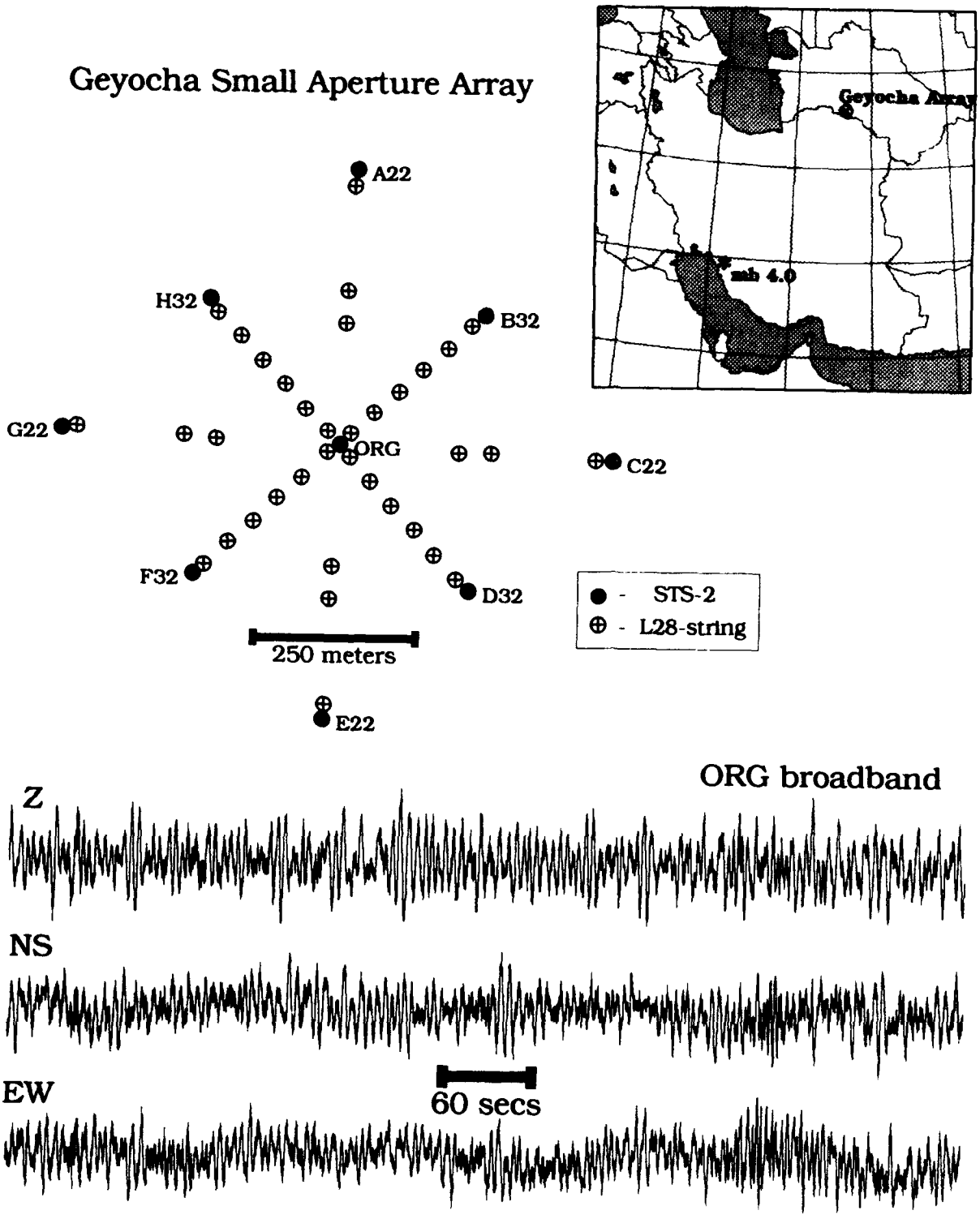


Figure 1: Map of the Iran–Turkmenistan region showing the locations of the array and the m_b 4.0 event, the Geyöcha array geometry, and 645 secs of broadband three-component data from the array's center site.

The magnitude of the data variance in an arbitrary location x in the multi-dimensional space is given by the Hermitian form

$$\mathbf{x}^* \mathbf{R} \mathbf{x} = R(\mathbf{x}) \tag{1}$$

where * denotes conjugate transpose and **R** is the sample covariance matrix. In multi-dimensional analysis, the covariance matrix plays a role analogous to that of the autocovariance function in one-dimensional time series analysis. Element R_{ij} of the covariance matrix is the inner product of the data vectors from channels i and j. The diagonal elements ($i=j$) are the variances and the off-diagonal elements ($i \neq j$) the covariances. The covariances provide a measure of the linear dependence between the data channels.

With array data, we can map the magnitude of the data variance in the multi-dimensional space by forming beams. In beamforming, the x parameterize the channel-wise amplitude and phase variations across the array for an assumed signal model. The assumed signal's amplitude and phase variations are functions of the array geometry, the shape of the wavefront, the signal's propagation direction, apparent propagation velocity and frequency content, and for three-component array data, the signal's polarization. The x are, therefore, functions of up to 5 variables. The models used to search for the maximum variance are usually restricted to plane waves with a few selected bearings, velocities and frequencies. This speeds the computations but also provides biased results. Using multi-component array data implies a search that is either very limited or very time consuming.

An alternative approach to the search for the maximum variance is provided by asking for **R**'s eigenvalues (λ_i) and eigenvectors ($\mathbf{v}_i$). The eigenvalues and eigenvectors can be obtained by asking for the principal axes of the surface defined by Equation 1 subject to the geometric constraint $\mathbf{x}^*\mathbf{x}=1$. The principal axes intersect this quadric surface at its stationary points (maxima and minima) which occur at those points where the surface normals coincide with the radius vectors; in other words, at those points where $\mathbf{R}\mathbf{x}=\lambda\mathbf{x}$. This is the fundamental equation of eigenvalue analysis. The principal axes of the representation quadric are identical to those of **R**'s quadratic form, but because of the geometric constraint, the lengths of quadric's principal axis are inversely proportional to the magnitude of the data variance in those directions.

The eigenvectors define a basis that is the data's preferred frame of reference. The approaches discussed in this paper simply involve examining the data from this natural reference system. Changing to this reference frame greatly simplifies analysis. One advantage of this approach is that we need not assume a signal model; the model is provided by the data itself. This is particularly important when dealing with high-frequency data because of their sensitivity to small scale lateral heterogeneities that commonly results in arbitrary polarization, amplitude, and phase variations that cause the signal to depart from the idealized models used in most analysis approaches.

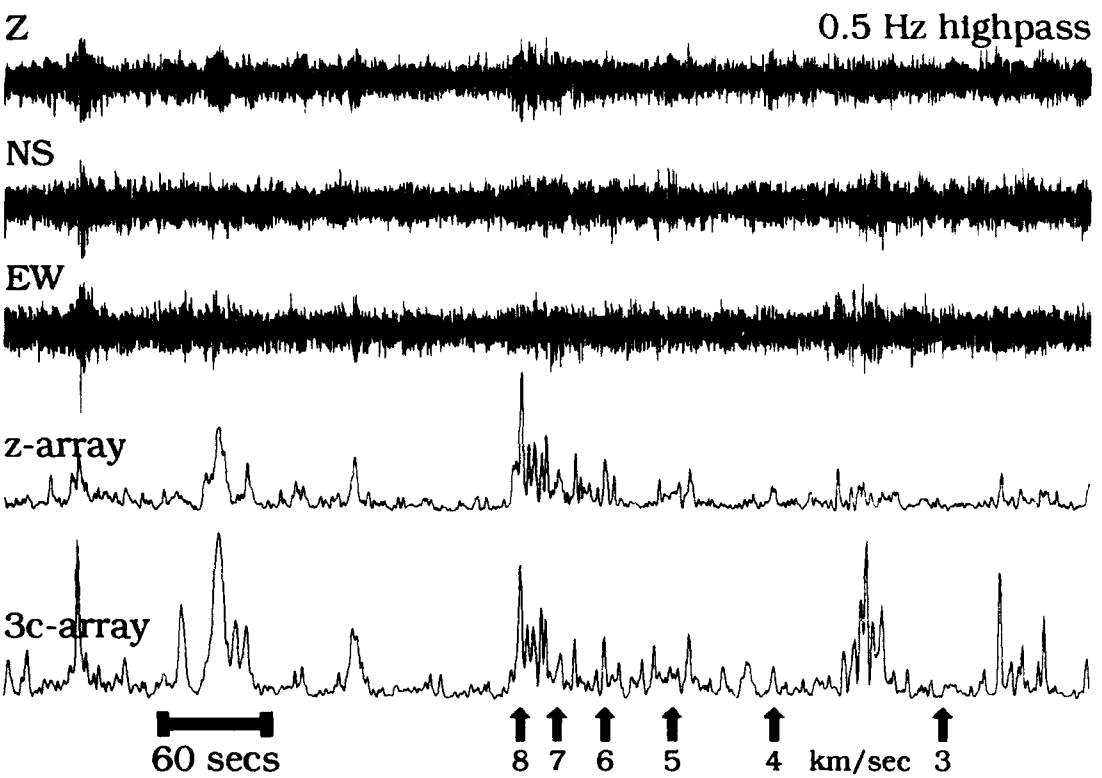


Figure 2: Highpass filtered data and the corresponding broadband, 0.5-10 Hz, $\lambda_1(t)$ computed for the single (z) and three-component (3c) array data using a sliding, 4 sec data window. The approximate phase velocities appropriate for the m_b 4.0 event are also shown.

Signal Detection

The principal component eigenvector defines the model that accounts for the greatest data variance (*i.e.* minimizes the residual-variance between the model and observations). The principal component eigenvalue provides a measure of the variance accounted for by the principal component eigenvector. Beamforming-like signal detection can, therefore, be accomplished without forming a single beam. An eigenstructure detection algorithm can be used with three-component, single-component array, or multi-component array data with absolutely no modifications. Figure 2 shows the highpass filtered data from Figure 1 and the magnitude of the principal component eigenvalue as a function of time. This statistic simply provides a measure of largest component of channel-wise coherent energy a function of time. Both the m_b 4.0 and several local events are easily detected.

Advantages of this approach include: (1) because we need only the largest eigenvalue and none of the eigenvectors, it is very fast; (2) it allows us to easily incorporate three-component array data which, as illustrated in Figure 2, enables us to detect shear arrivals that are missed by a vertical component array; (3) it prevents us from missing signals that do not conform to our biased, and more often than not, overly idealized signal models; (4) because $\mathbf{R}$ is reduced to its canonical form, spatial filtering implies only the inner product of vectors.

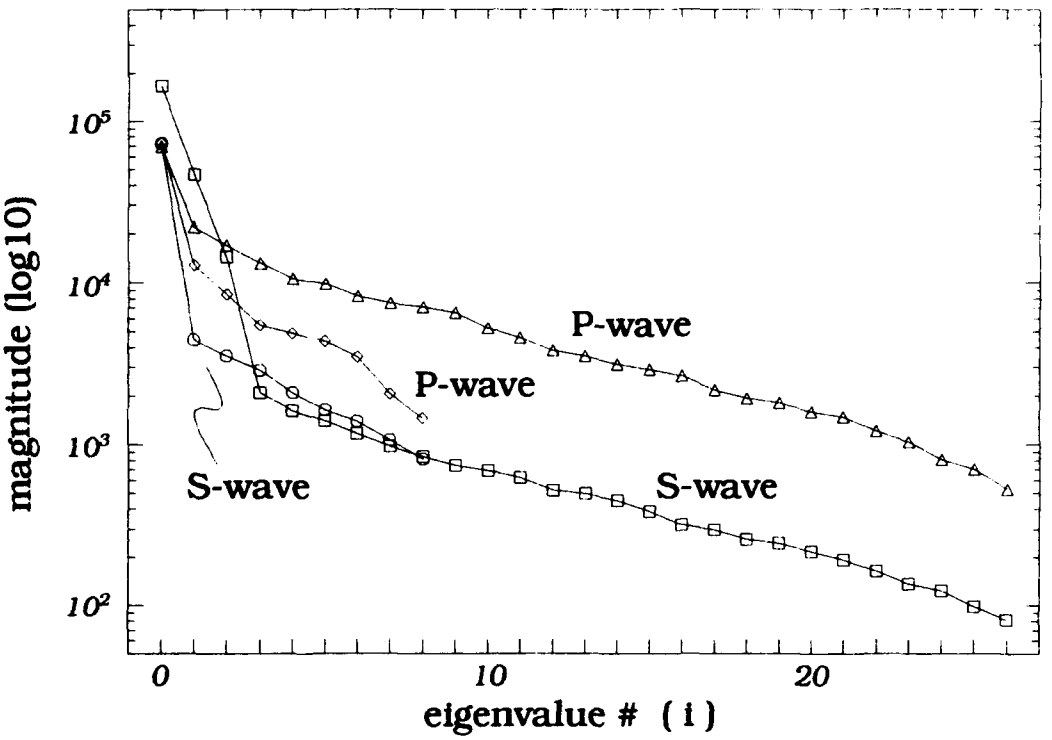


Figure 3: Broadband P_n (≈8.1 km/sec, 0.5–10 Hz) and S (≈3.5 km/sec, 0.25–10 Hz) λ_i magnitudes computed using single (9 channels) and three-component (27 channels) array data.

Waveform Estimation

In an ideal situation, the multi-dimensional data space can be partitioned into signal and noise subspaces based on the magnitude of the eigenvalues (Schmidt, 1979). In an ideal situation noise is channel-wise incoherent. If we have N sensors, M signals and ideal noise, the $(N–M)^{\text{th}}$ eigenvalue will be equal to the noise variance and have multiplicity $N–M$. The significance of multiple eigenvalues is that the associated eigenvectors are not uniquely determined. Unfortunately, seismic noise does not exhibit this feature. Figure 3 shows the magnitude of the eigenvalues for P_n (≈8.1 km/sec) and shear arrivals (≈3.5 km/sec) which have presumably traveled through the crustal wave guide, for the single and three-component array cases. While some eigenvalues are significantly greater than others, the smaller eigenvalues are far from equal. Figure 4 shows the waveforms computed by projecting the observed data $\mathbf{f}(\omega)$ onto the subspaces defined by $\mathbf{v}_i(\omega)$, i=1,2,3,4, separately, for the P and S waves using single and three-component array data. In other words, computing the inner product of the data $\mathbf{f}(\omega)$ and eigenvectors $\mathbf{v}_i(\omega)$ (Gething, 1971). In some instances, these waveform estimates should include several $\mathbf{v}_i(\omega)$, while in others maximum S/N gain can be realized by using none. Figure 3 provides some insight into the the difficulty in determining how to truncate the eigenspace. We should note that in cases where there are superimposed signals, individual eigenvectors will parameterize individual signals only if the signals' mode vectors are in fact orthogonal.

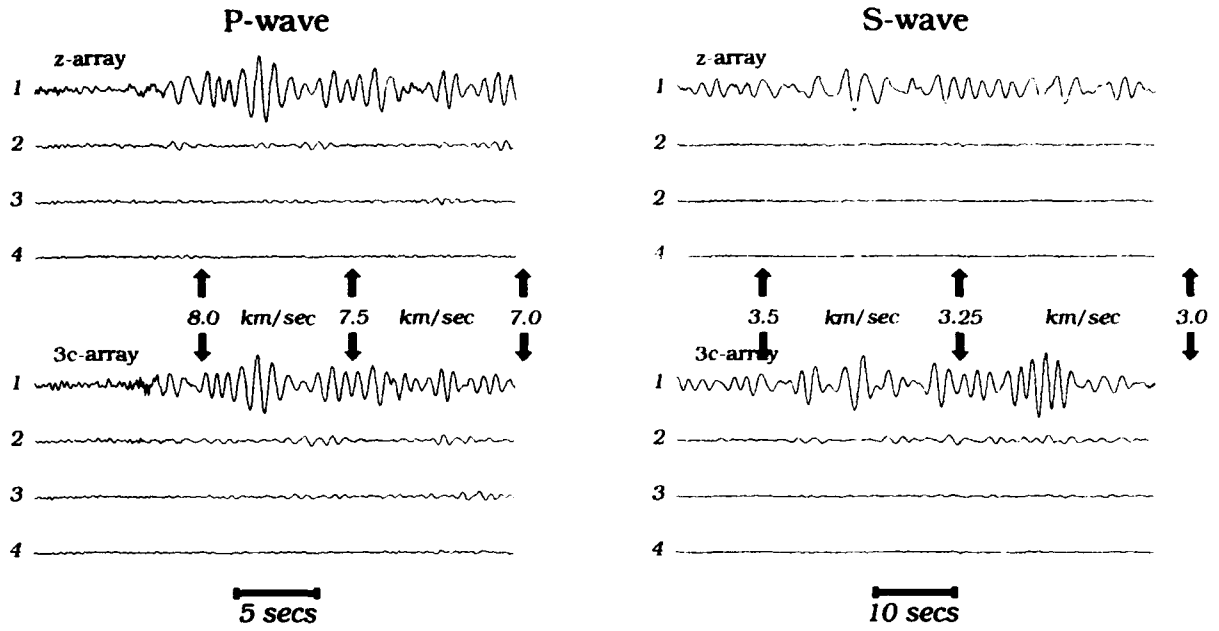


Figure 4: P and S waveform estimates computed using, separately, the single and three-component array $v_i(\omega)$, i=1,2,3,4. The appropriate approximate phase velocities are also shown (see Figure 2). The P and S estimates were computed using the 0.5–10 Hz and 0.25–10 Hz bands, respectively.

Differences between the P and S waveform estimates provided by the single and three-component array data illustrate two important features. First, a comparison of the S wave estimates shows that a considerable amount of information is lost with single-component array data. Second, three-component array data is capable of providing improved S/N gains only if the signal is partitioned between all three-components. A comparison of the P wave estimates reveals that the single-component estimate has a higher S/N than the three-component estimate. This is simply due to the fact that the thick, low velocity sediments underlying the Geyöcha site turn incoming rays sharply upward, resulting in P arrivals that are almost completely vertically polarized. In this case, the horizontal components add only noise, resulting in a lower S/N because the noise at this site is far from random.

Conclusions & Recommendations

Principal component analysis has been a popular tool for multivariate data analysis for more than 60 years (*cf.* Hotelling, 1933). The explicit use of the eigenvalues and eigenvectors in multi-dimensional signal analysis was introduced by Pisarenko (1973). Despite the fact that seismic noise is not ideal noise, principal component analysis provides a powerful data reduction approach that allows us to eliminate those features in the data that are either insignificant and/or poorly constrained.

Both the signal detection statistics and waveform estimates obtained using this approach are surprisingly good considering the relative simplicity and speed of the computations involved. Figures 2, 3 and 4 illustrate that considerable work is needed to

obtain optimal estimates. In particular, further work is needed to find the best way to truncate the eigenspace for cases where the noise is not a white, zero mean, Gaussian process. The single-component array's superior P wave S/N gain suggests that further improvements can be realized by adopting alternative approaches for multi-component array data (Wagner & Owens, 1993a,b).

Finally, this paper helps illustrate the advantages of broadband three-component array data. High-frequency, single-component arrays are oblivious to a wealth of information that is crucial for monitoring nuclear test ban treaties. A prime example is discriminants that use a mixture of vector wave types, such as L_g/P ratios.

References

Gething, P.J.D., Analysis of multicomponent wavefields, *Proc. IEE*, **118**(10), 1333–1338, 1971.

Hotelling, H. Analysis of a complex of statistical variables into principal components, *J. Edu. Psych.*, **24**, 417–441, 1933.

Pavlis, G.L., H. Al-Shukri, D. Repin, F.L. Vernon, J. Hanson, G.S. Wagner, A. Lerner-Lam, G. Abers, D.J. Harvey, S.W. Roecker, and I. Dricker, Preliminary results from the broadband frequency-wavenumber array experiment, Alibek, Turkmenistan (abstract), *EOS Trans. AGU*, **74**(43), Fall Meeting Suppl., 450, 1993.

Pisarenko, V.F., On the estimation of spectra by means of non-linear functions of the covariance matrix, *Geophys, J.R. astr. Soc.*, **28**, 511–531, 1973.

Schmidt, R.O., Multiple emitter location and signal parameter estimation, *Proc. of the RADC Spectrum Estimation Workshop*, 243–258, 1979.

Wagner, G.S. & T.J. Owens, Broadband bearing-time records of three-component seismic array data and their application to the study of local earthquake coda, *Geophys. Res. Letters*, **20**(17), 1823–1826, 1993a.

Wagner, G.S. & T.J. Owens, Improving event detection and parameter estimation using three-component array data (abstract), *EOS Trans. AGU*, **74**(43), Fall Meeting Suppl., 448, 1993b.

Characterization of broadband, regional distance seismograms in Eurasia and other regions of potential underground testing: Path effects in South America

Terry C. Wallace
Susan L. Beck

Department of Geosciences
University of Arizona
Tucson, AZ 85721

Contract F49601-92-J-0416

Objective:

The role of seismology in monitoring compliance with nuclear non-proliferation on comprehensive test ban treaties is one of detection and discrimination of low-yield devices in uncalibrated geologic environments. The low-yield condition requires that the backbone of the monitoring effort be at regional distances, where broadband seismic signals are a complex combination of both propagation and source effects. Thus, is is essential to "calibrate" regions of interest by studying the propagation characteristics of earthquakes and mining seismicity (mining explosions and rock bursts). Further, it is likely that a "suspect event" will be recorded by a limited number of regional distance stations, so it is important to develop a full range of algorithms to detect, locate, and discriminate seismic events at a single broadband seismic station.

In this project we have investigated a number of regions; in this final stage of research we have concentrated on western South America.

Research Accomplished:

In the recent past several countries of South America were suspected of having programs to develop nuclear weapons. The crustal structure of South America is poorly characterized in terms of seismic wave propagation efficiency. However, it is known that there are many anomalous path effects. Some paths exhibit extraordinary attenuation; others show preferential blockage of certain regional phases such as *Pn* and *Pg*. This fact, coupled with a relative high level of shallow seismicity, numerous large mines, and large historical mining rock bursts, makes South America an important target for further characterization.

Figure 1 shows the location of several shallow earthquakes (21 events) and recording stations in western South America. Using this data base we determined the gross crustal structure for the Altiplano, the Peruvian Andes, and northern Chile. We modeled the entire regional waveform using the reflectivity method in the pass band of 20 to 100 seconds. The observed and synthetic waveforms are correlated; we use a grid search to maximize the correlation in terms of average crustal thickness, crustal velocity, and lid structure. There are trade-offs between the various model parameters, so we investigated the resolution by a series of synthetic tests. In particular, we investigated the effects of lateral variations in structure, the effect of event mislocation, the sensitivity of waveform fit to attenuation, the effects of uncertainty in the crustal V_P/V_S ratio, and the signature of the mantle lid thickness. We developed error bounds on the basis of these experiments.

We have grouped seismic events based on similar event–station paths. Ideally, similar event–station paths should sample a "similar" structural column. Three regions were generalized:

(1) the Peruvian Andes north of the IDA/IRIS station NNA, (2) paths which crossed the Altiplano, and (3) a transition zone from the Peruvian Andes to the Altiplano. Figure 2a shows five event–station paths used to characterize the Peruvian Andes. These events are all located within 3° of each other, and they sample similar paths. A wide range of crustal thicknesses and velocities were tested in order to determine a best fit between the data and synthetics. A two-layered crust, a mantle lid, and a high-velocity subducting slab (approximately flat layering) were used to model the events. Figure 2b shows examples of the grid searches where the highest correlation coefficient indicates the best fit. The "best" average gross structure parameters are an average crustal thickness of 48 km and an average crustal velocity of 6.18 km/s. There is no asthenospheric wedge for this area (due to the flat subduction from 8° to 13°S [Cahill and Isacks, 1992]). Therefore we modeled the mantle with a 40-km-thick layer underlain by a high-velocity zone (representing the slab). The data do not appear to be sensitive to the upper mantle structure (although a wide range of parameters was tested).

Figure 3a shows the travel paths used to constrain the structure of the Altiplano. For these events a three-layered crust was used, with a 10-km-thick sedimentary cover with a *P*-wave velocity of 5.0 km/s. The average results are a crustal thickness of 75 km and a *P*-wave velocity of 5.95 km/s. There was considerable variation in the results from individual travel paths. In particular, events which had paths mainly confined to the Altiplano typically require very thick crustal columns (>80 km). However, paths which traverse the coastal range require a thinner crust (60–65 km).

Figure 4 shows three events south of NNA and four events north of ZOBO. These paths were in the transition zone between the Andes and Altiplano. The individual paths showed variations in crustal thickness of between 55 and 70 km with an average of 62 km. The crust *P*-wave velocity was also transitional between the relative high velocities of the Peruvian Andes and the Altiplano.

The rapid variations of crustal thickness strongly suggest a causative phenomenology for the observed variations in regional seismic phases. As an additional constraint and a first-order check on the modeling results, we determined the teleseismic receiver function beneath the GTSN station LPAZ, which was recently installed northeast of La Paz in the Eastern Cordillera. We computed two receiver function stacks using two teleseismic seismograms from a NW azimuth (the events were located near Guerrero, Mexico) and two events from the NE (the events were located near the Mid-Atlantic Ridge. Although the crustal column sampled by these teleseismic events is not exactly the same as that sampled by the regional waveforms, these events provide a good estimate of the crustal structure of the Eastern Cordillera. Figure 5 shows a comparison of two stacks (NW and NE azimuths) with synthetics from layered models. For the NW stack there is a large *Ps* conversion 7.6 s after the crustal *P* arrival; this *Ps* conversion is observed 7.3 s after the *P* wave. These large second arrivals are the *P* to *S* conversion at the base of the crust. The NW stack is best modeled with a 54-km-thick crust and an average crustal velocity of 6.1 km/s, while the NE stack is best modeled with a three-layered crust, 56 km thick and having an average crustal velocity of 6.18 km/s. These results contrast with the the crustal structure derived for the Altiplano. This suggests that the Eastern Cordillera crust is much thinner than that beneath the Altiplano and that the crustal thickness must change dramatically over relatively small distances.

Figure 6 summarizes the crustal thicknesses and velocities for western South America. There are distinct differences between the Peruvian Andes, the Altiplano, and the Eastern Cordillera. The paths for the Peruvian Andes generally show a crustal thickness between 40 and 50 km. The paths for the Altiplano show crustal thickness ranging from 65 to 80 km. The crustal thicknesses for the transition paths indicate a crustal thickening from north to south. The region between stations NNA and ZOBO, transitional between the Andes and the Altiplano, has a crustal thickness ranging between 60 and 70 km.

Conclusions and Recommendations:

The western margin of South America has one of the most rapidly varying crustal columns in the world. We have developed gross crustal models to account for the variations. It remains to be tested whether our parameterization can explain observed variations in *short-period* propagation. Most spectral discriminants are based on two things: (1) given the same zero frequency moment, an earthquake will be enriched in high frequencies as compared to an explosion, and (2) earthquakes will excite more *S*-wave-type energy than explosions. Typical spectral discriminants ratio the amplitude of a particular regional distance phase in narrow bands. Various phase-pair ratios, such as *Pg/PL* and *Pn/Lg*, show good separation of earthquakes and explosion populations. It is essential to empirically map the "base-line" trend of these discriminants, and that can only be done with regional characterization.

References:

Cahill, T. and Isacks, B. (1992). Seismicity and shape of the subducted Nazca Plate, *J. Geophys. Res.*, *97*, 17,503–17,529.

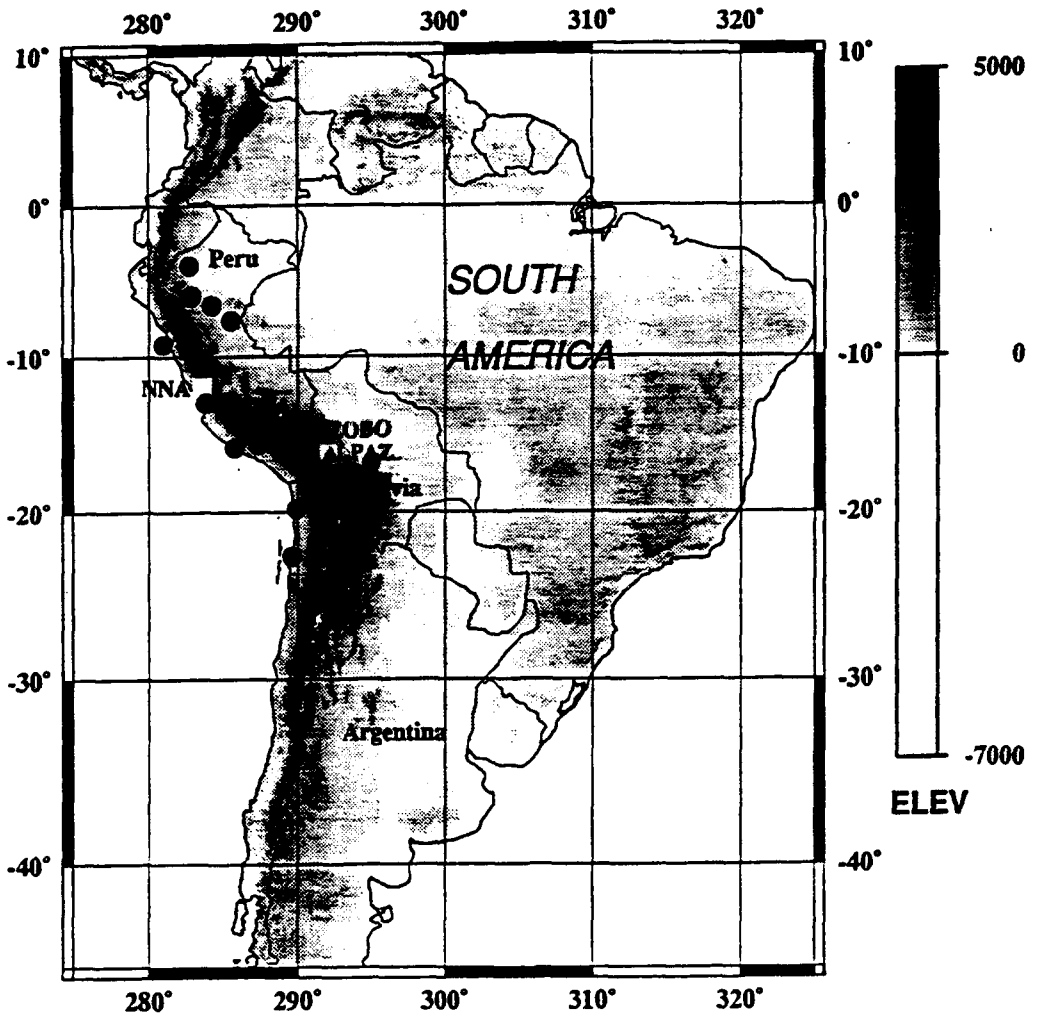
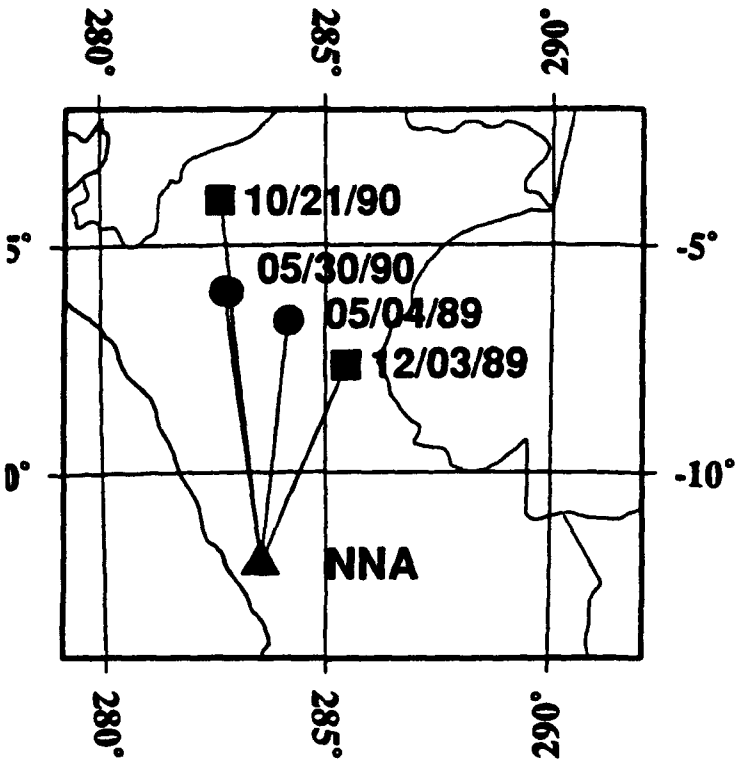


Figure 1: Study region, the western margin of South America. The Altiplano–Puna Plateau from 14° to 30°S has a mean elevation of 4 km. The black dots represent the locations of the events used in this study, while the stations are shown with triangles or squares.



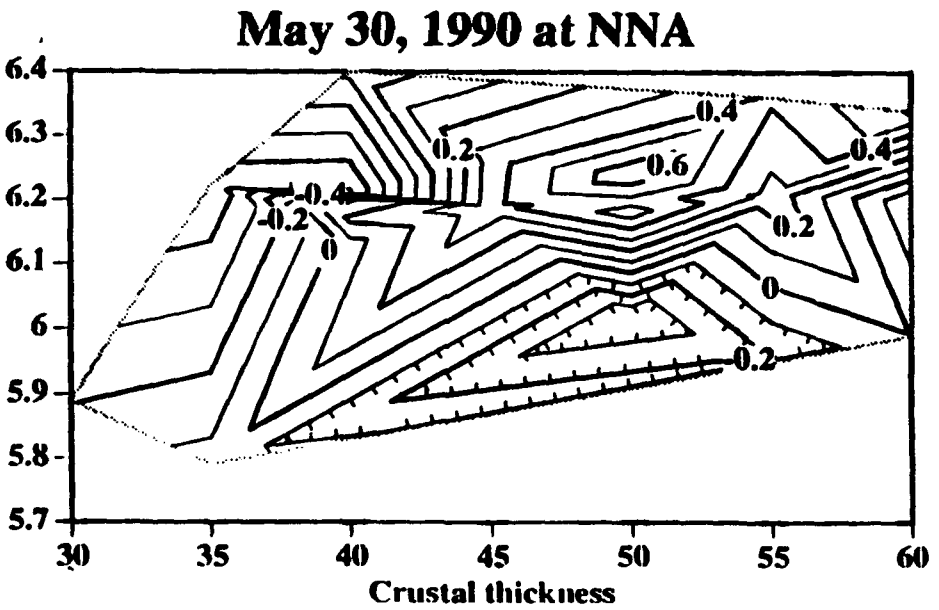


Figure 2: (a) Location of the travel paths used in the study of the Peruvian Andes.
(b) Correlation coefficient comparisons for some of the events used in the Peruvian Andes study. The correlation coefficient is contoured as a function of average crustal thickness and average crustal velocity.

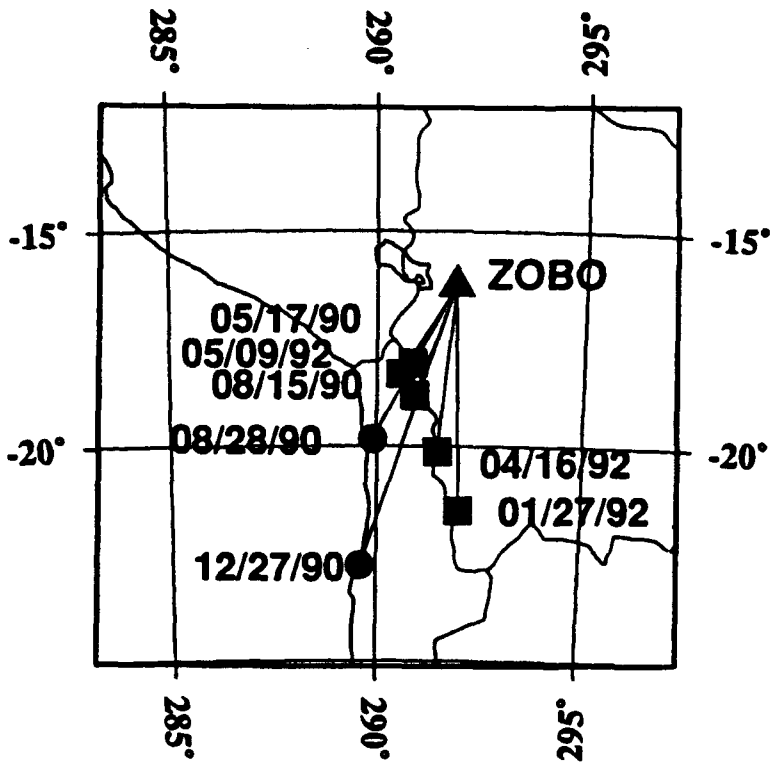


Figure 3: Travel paths used for the Altiplano study.

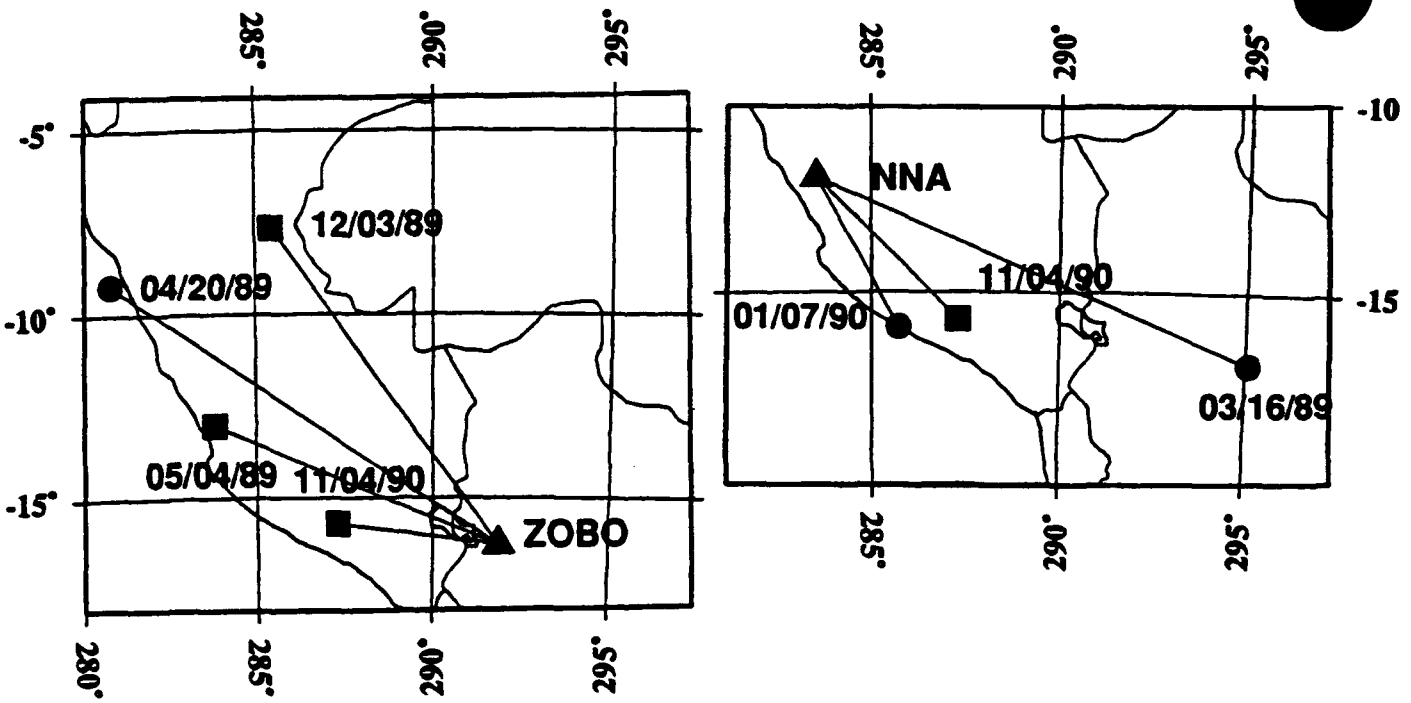


Figure 4: Travel paths used for the transition zone study.

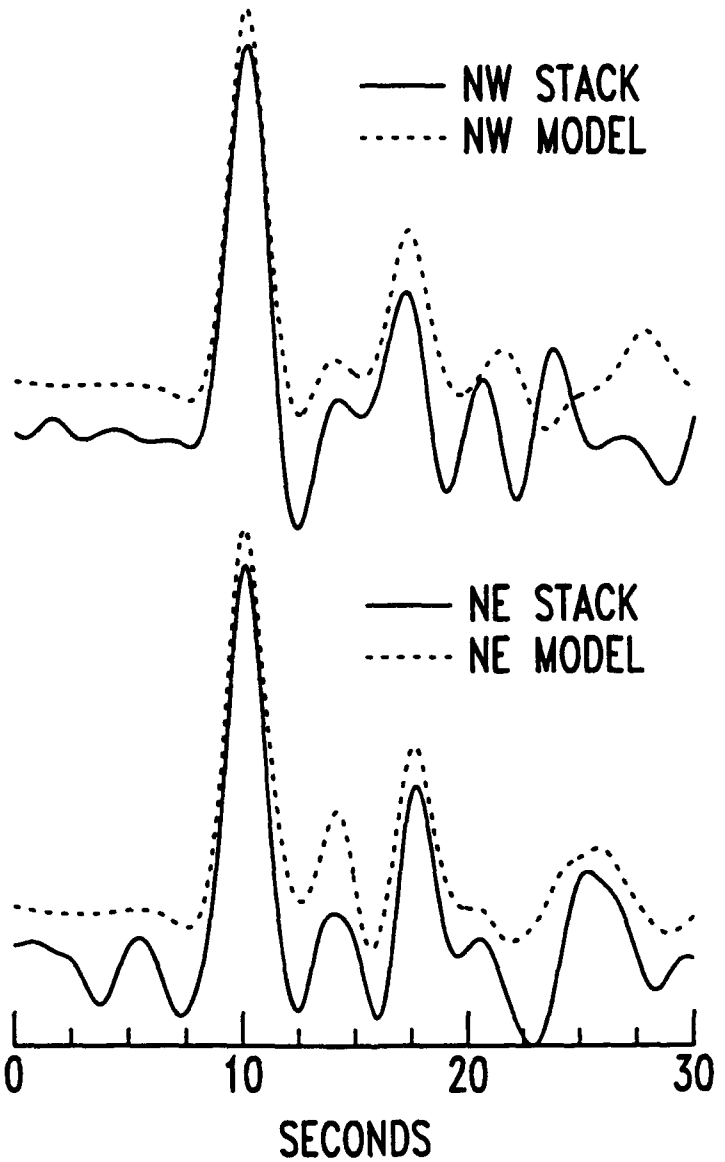


Figure 5: (a) Comparison of the receiver function data stack and the synthetics from events to the northwest. Note the *P*-to-*S* conversion 7.6 seconds after the *P*-wave arrival.
(b) Comparison of the receiver function data stack and the synthetics for events NE of the recording station LPAZ.

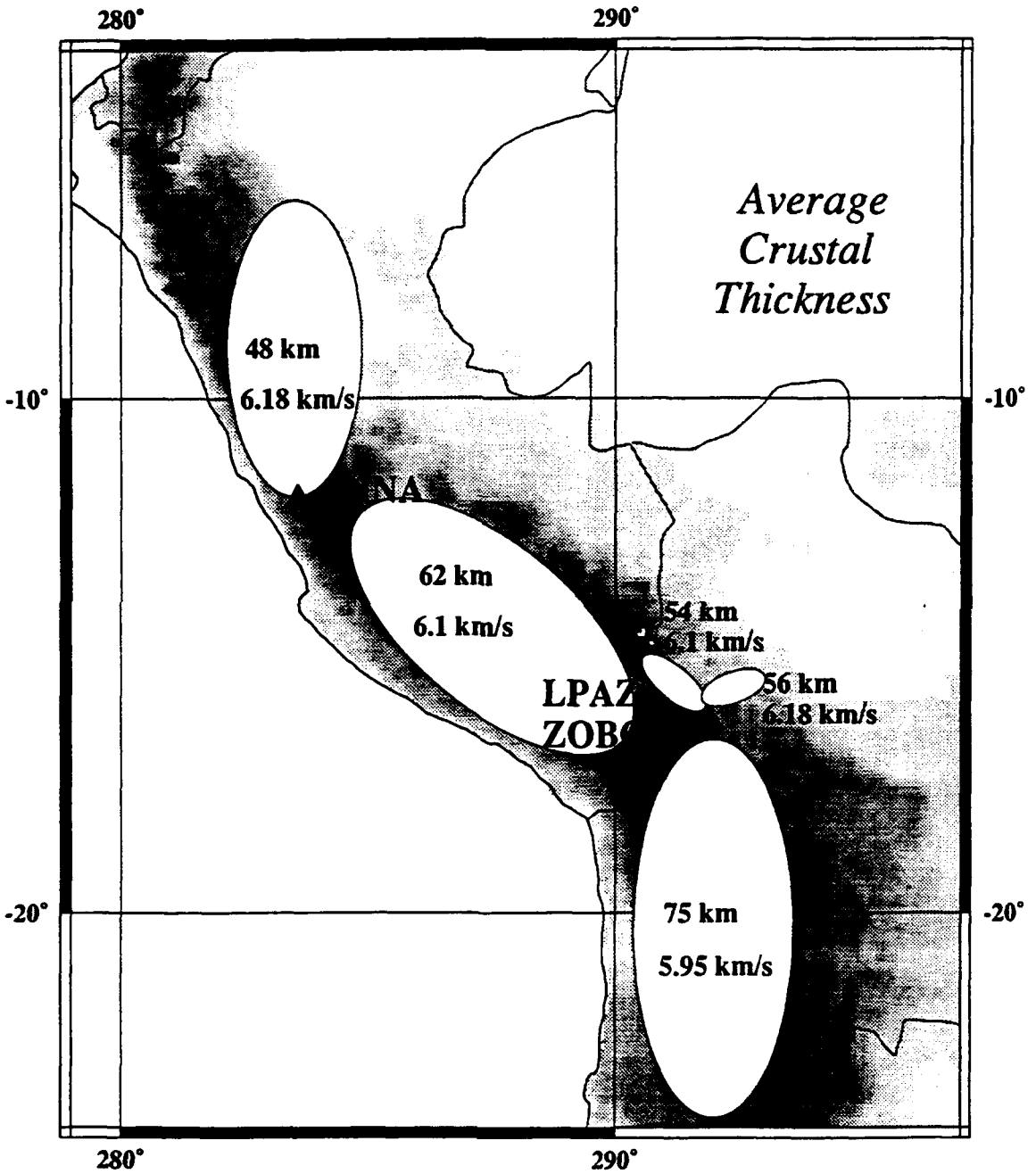


Figure 6: Composite crustal thickness estimates and corresponding average crustal velocities for the Peruvian Andes, the transition zone, and the Altiplano. Also shown is the average crustal thickness and velocities for the receiver function analysis done for LPAZ.

Discrimination at regional distances: Seismic characterization of South America and Korea

Terry C. Wallace
Susan L. Beck

Department of Geosciences
University of Arizona
Tucson, AZ 85721

Contract F49620-94-0147

Objective:

It is essential to develop a detailed understanding of the broadband seismic phases from nuclear explosions, chemical explosions, and earthquakes for accurate discrimination techniques. This will require development of both empirical and analytical models. Much work has been done on the detection/discrimination problem in the western U.S. (NTS) and for the former Soviet Union (Novalya Zemlya, Kazakhstan), and some promising regional distance discriminants such as spectral ratios, spectral scalloping, and M_0/M_L have been developed. Unfortunately, the character of regional phases is extremely sensitive to differences in propagation paths. This casts doubt on the transportability of the present suite of discriminants to regions in which there is no experience in characterizing regional wave propagation. In this contract we are targeting two regions of monitoring interest (the Korean Peninsula and South America) and developing data bases for seismic propagation characterization.

Research Accomplished:

We have begun to develop data bases of regional waveforms for earthquakes, chemical explosions, and rock bursts in the Korean Peninsula and South America (principally Argentina and Chile). Our objective is fairly straightforward: develop an observational catalogue, then attempt to characterize the propagation effects and calibrate the source effects.

Until recently both Brazil and Argentina were considered potential nuclear powers, although both countries have now endorsed the NPT. However, South America remains one of the most poorly characterized continental regions in terms of seismic wave propagation. This is principally due to inadequate coverage of the continent with high-quality seismic stations. Recently a temporary array of broadband seismic instruments has been deployed in the Central Andean Cordillera of Bolivia and northern Chile. This deployment, an international experiment with participants from the University of Arizona, the Carnegie Institution of Washington, and Lawrence Livermore National Laboratory in the USA, has two transects: an east-west transect called BANJO (Broadband ANdean JOint experiment) and a north-south transect called SEDA (Seismic Exploration of the Deep Altiplano experiment) The combined array provided an excellent platform to collect waveforms from a number of sources. Figure 1 shows the location of the seismic stations.

Figure 2 shows the locations of large mines in northern Chile. A cooperative effort with the University of Chile (Dr. Sergio Barrientos) will allow us to construct an expansive data base of man-made seismicity. These mines routinely have explosions in excess of 100 tons, and occasional events in excess of 400 tons. In addition, there are several mines which are in excess of 3 km depth. Within these mines there have been some large rock bursts.

We have just begun assembling a data base for the Korean Peninsula. Historically, the Peninsula has shown a relatively low level of seismicity. Figure 3 shows the location of earthquake sources within, or near, the Peninsula during the time interval of 1962–1993 as reported in the ISC and PPE catalogues (magnitude greater than $m_b = 3.0$). Although the catalogue is not complete at low magnitudes, it is reasonable to assume that there are only 1–2 shallow earthquakes per year which are within regional distances of seismic stations operating in South Korea. On the other hand, there appear to be a significant number of man-made seismic sources on the Peninsula.

Conclusions and Recommendations

We have just started this contract and are in the beginning stages in developing the data bases for future research. We are taking advantage of an extensive array in the central Altiplano in South America. In Korea we have begun collecting data from a broadband POSEIDON station. In the next few months there will be an IRIS GSN station in northern Korea.

BANJO and SEDA Seismic Deployment

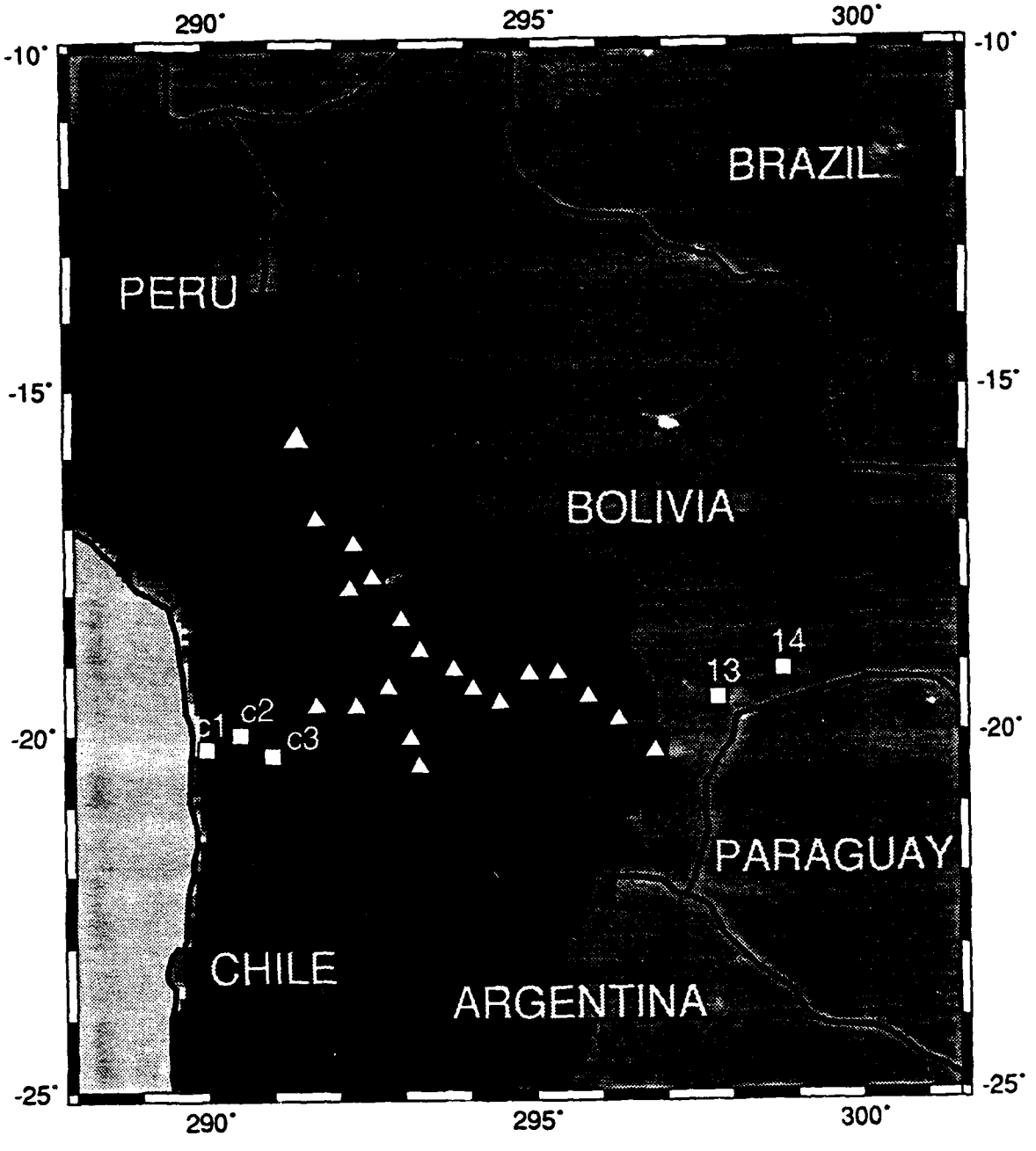


Figure 1: Map of BANJO and SEDA broadband seismic stations. The stations are shown with triangles (presently operational) and squares (to be installed in the fall of 1994).

University of Chile Seismic Network

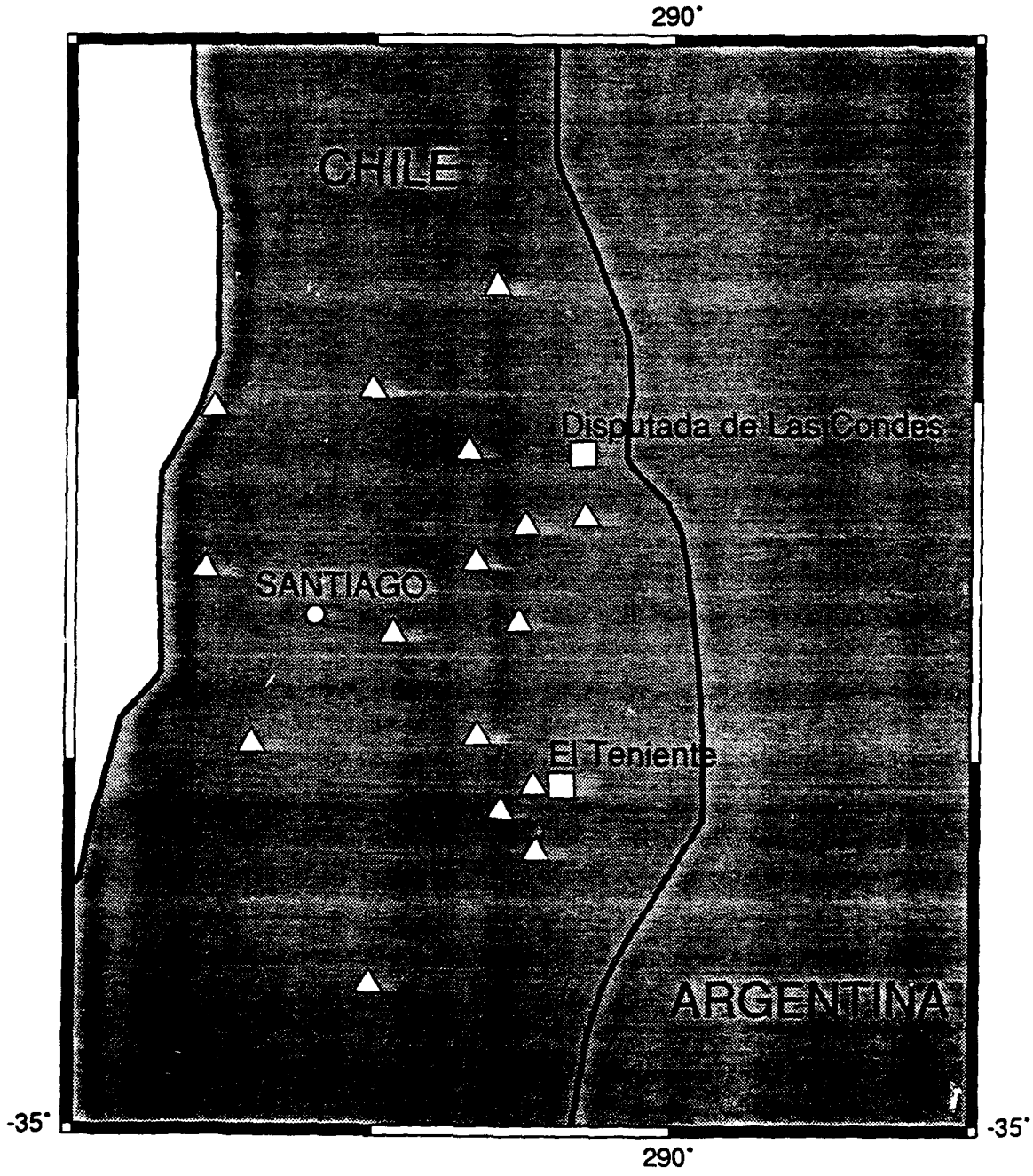


Figure 2: Location of two large mines in northern Chile (squares) and the stations in a short-period network operated by the University of Chile (triangles).

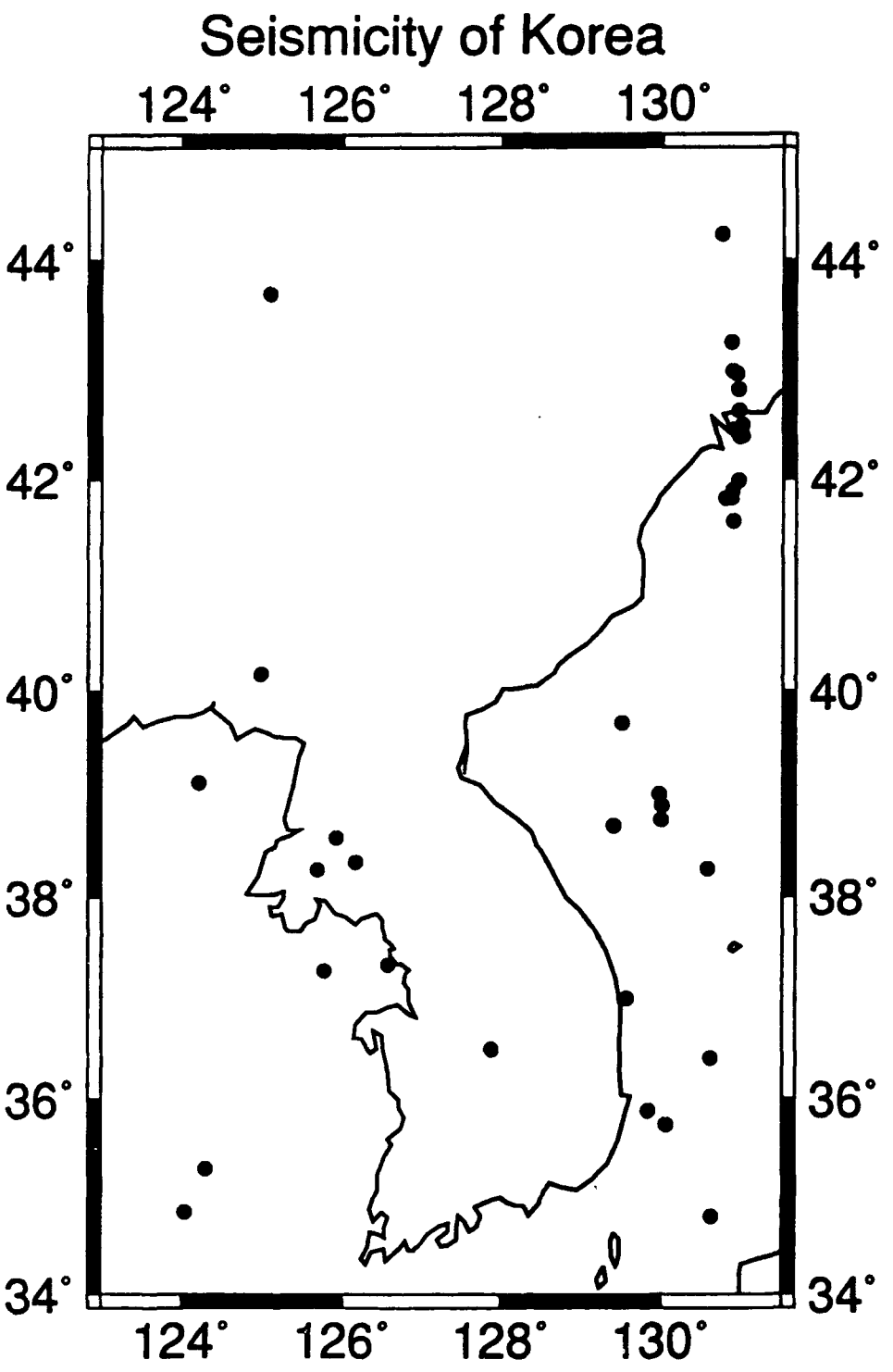


Figure 3: Seismicity of Korea as reported in the PPE and ISC catalogues. These catalogues are only complete down to magnitude 4.4.

A Comparison of Regional Explosion and Earthquake Waveforms in North America and Eurasia with Application to Event Discrimination

Bradley B. Woods and Chandan K. Saikia

Woodward-Clyde Federal Services, Pasadena, CA
Pasadena, CA

AFOSR Contract No. F49620-94-C-0046

OBJECTIVE:

We are investigating the applicability/portability of four regional seismic discriminants, developed from southwestern U.S. earthquake and NTS explosion data, to data sets in other tectonically active regions. Some of these discriminants are empirical in nature, while other deterministic ones involve waveform inversion, which in turn requires reasonably accurate crustal models. Events to be studied are the U.S. PNE's and earthquakes in the Colorado Plateau/Rockies region, explosions at the Kazakh (CIS) and Lop Nor (PRC) test sites, as well as earthquakes in the same region. The discriminants being used here are the ratio of integrated short-period P-wave to long-period energy (predominantly surface wave) summed over the three components (sp_z-P/lp_3) (Woods and Helmberger, 1994), the ratio of integrated short-period vertical component energy between the P and S wavetrains (sp_z-P/sp_z-S), the ratio of M_L to scalar seismic moment (M_0) (Woods *et al*, 1993), and the ratio of the broadband energy (M_E), integrated along the entire wavetrain, to the broadband moment (M_B) (Zhao and Helmberger, 1994).

Besides determining whether or not these discriminants are effective in the various locations, it will be possible to calibrate the effective discriminant parameters for these different regions, so that an event from any such area can be incorporated into a unified database. Once the crustal structures are established for the Kazakh/Lop Nor region, the earth structure modeling will be continued to the west into Pakistan and eastern Iran. Parameters for the above successful discriminants will be determined for a large earthquake data set for this region in order to calibrate the discriminants, thus establishing criteria to detect a "first-blast" for the area. The crustal structures which come out of this study will also be of use for calibrating other discriminants which make use of regional seismic phases, such as P_n, P_g and L_g.

RESEARCH ACCOMPLISHED:

Although we are still involved in an exhaustive data search for the study regions, we do have some preliminary results for the Kazakh/Lop Nor region, shown in figure 1. In order to gain insight into the differences and/or similarities of the discrimination parameters between regions, it is necessary to compare waveforms as well. Figure 2 shows vertical component displacements for explosions from Lop Nor, Kazakh, and the three distinct NTS sub-areas. All records are at distances between 210 and 255 km. The BAY recording of the Kazakh event is from an intermediate-period instrument, thus enhancing the surface wave and surface

wave coda relative to the short-period body-waves. One of the most striking features is that the Lop Nor (particularly) and Kazakh wavetrains show significantly less energy in scattered phases and coda than do the NTS events. In other words the central Asian explosion waveforms appear to be more deterministic than those from NTS. The Asian explosions also appear to be richer in high-frequency; whether this is attributable to the source or a higher crustal and upper-mantle Q is not clear. As the data set expands, more comprehensive comparisons will be made.

We have applied the empirical discriminants to the central Asian data. Figure 3a plots the sp_z-P/lp_3 integrated energy ratio vs. distance. Explosions are circles and earthquakes are crosses, and each datum point represents one station - event pair. This method yields good separation of the two populations. Obviously more data is necessary to establish any firm conclusions. We compare these results to our previous North American results in figure 3b and find that earthquakes and explosions demonstrate the same trends in Asia as they do in North America, although several Asian earthquakes near 500 km have relatively high sp_z-P/lp_3 ratios. The Asian explosions also plot fairly high, suggesting the the regional crustal structure and Q may be responsible for these differences.

Another promising empirical discriminant is the ratio of integrated sp_z-P/sp_z-S. Figure 4a shows an example of WMQ recordings of a Lop Nor explosion and a nearby earthquake (an "X" in figure 1). These two events are recorded at the same distance (d=238.5 km). These vertical component seismograms have been bandpass filtered between 3 - 8 Hz. It is in this frequency band that the relative shear-wave energy is least for observed explosions. In this case, the difference in the P to S integrated energy ratio between events is more than a factor of 160. These two events are recorded at the same distance. Figure 4b plots this ratio vs. distance for Asian events. Each datum point represents one station - event pair. The populations are well separated, although, again the data sets are too small to make any firm conclusions. A similar discriminant had been applied to regional TERRAscope data, with poorer results, however the seismograms had not been narrow-band filtered. It is believed that this step significantly enhances the separation of source types.

Path modeling of regional broadband records is progressing. Figure 5a shows the data and synthetic, convolved with a Press-Ewing 30-90 (PE30-90)instrument, for the Soviet JVE explosion recorded at BAY (see figure 1). The waveform fit is good, although the relative timing of the P-wave and Rayleigh wave can be improved. With our "cut and paste" inversion method, where the inverted phases can be shifted in time individually, such timing differences do not affect the determination of the source parameters. A Lop Nor blast recorded at WMQ and played-out with a PE30-90 response is shown along with its corresponding synthetic seismograms in figure 5b. The waveform fit is good, but again the P-wave and Rayleigh wave are mis-aligned. The relative amplitudes of these phases are in good agreement. It should be noted that for this path, cross-over distance is very near to the travel distance, that is why the P_n and direct P are combined into one pulse in the data, whereas for the synthetic the two phases come in separately (but close together). Fine tuning of the model should correct for this. Adding thin, low velocity and low Q layers at the top of the crust should remove the ringing surface waves seen in the synthetics.

We have used these preliminary path modeling results to generate Green's functions for use in inverting regional waveforms to obtain source parameters, in particular seismic mo-

ment, M_0. Zhao and Helmberger (1994) found that changes in the path model do not significantly change the scalar moment, so that we have used our initial moment estimates for discriminants using this parameter, *i.e.* the M_L:M_0 and M_E:M_B ratios. Figure 6 plots M_L vs. M_0, circles are explosions, and triangles and crosses are earthquakes. The earthquake data for $M_L < 4$ events was taken from Bakun *et al* (1985) in a study of Yunnan, China. Separation of the two source types is good, in general, but the Lop Nor explosion plots close to the earthquake population. Energy and broadband moments determined for the Lop Nor explosion and nearby earthquake were found to discriminate the two events with respect to the M_E/M_B vs. M_0 criterion.

CONCLUSIONS AND RECOMMENDATIONS:

The discriminants discussed above all show promise with the initial Asian data set. The success of the narrow-band sp_z-P/sp_z-S ratio suggests that narrower-band measurements for any empirical discriminants may be in order. This passband will be applied to North American sp_z-P/sp_z-S data to compare with that for Asia. We will continue acquiring regional Eurasian seismograms to fill-out our data set in order to make more comprehensive conclusions concerning these discriminants. From observations and waveform modeling experience, it appears that the Eurasian explosions have more deterministic waveforms.

REFERENCES:

Bakun, W. H., Yizheng, L., Fischer, F. G. and Yafu, J, 1985. **Magnitude and Seismic Moment Scales in Western Yunnan, Peoples Republic of China,** *Bull. Seism. Soc. Am.*, vol 83, pp.1599-1612.

Saikia, C. K. and Helmberger, D. V., 1994. **Modeling of Regional Seismograms in the CIS - Implication Towards Event Discrimination**, submitted to *Geophys. J. Int.*

Woods, B. B., Kedar, S., and Helmberger, D. V., 1993. M_L:M_0 as a Regional Seismic Discriminant, *Bull. Seism. Soc. Am.*, vol 83, pp.1167-1183.

Woods, B. B. and Helmberger, D. V., 1994. **Regional Seismic Discriminants Using Wavetrain Energy Ratios**, printed elsewhere in these proceedings.

Zhao, L. Z. and Helmberger, D. V., 1994. **Regional Moments, Energy Levels and a New Discriminant**, submitted to *J. Geophys. Res.*

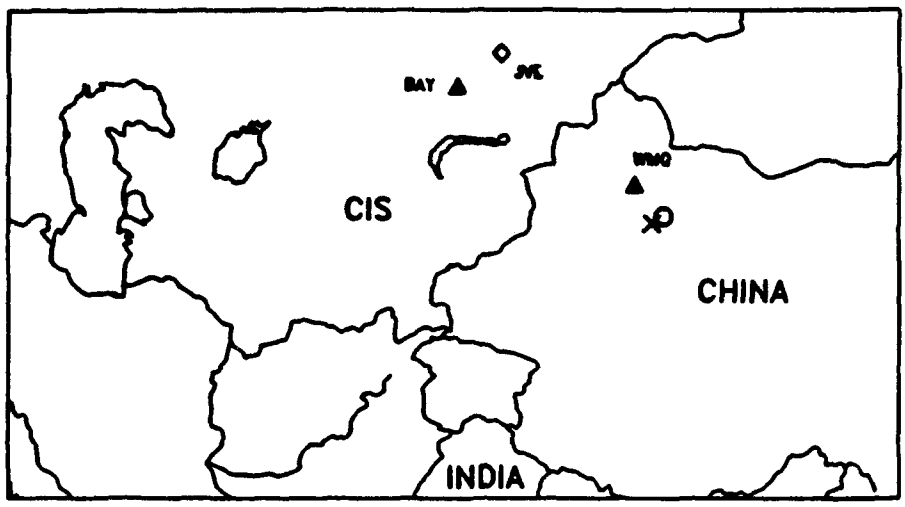


Figure 1. Map showing the geographic locations of BAY (Bayunal) and WMQ stations and epicenteral locations of the Soviet JVE (JVE) and Lop Nor explosion (open circle), and an earthquake near Lop Nor (cross).

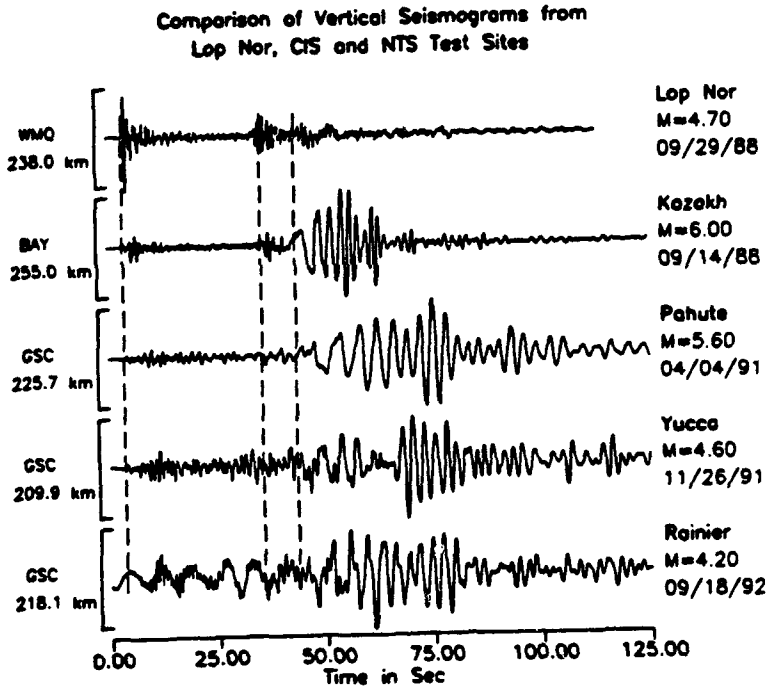
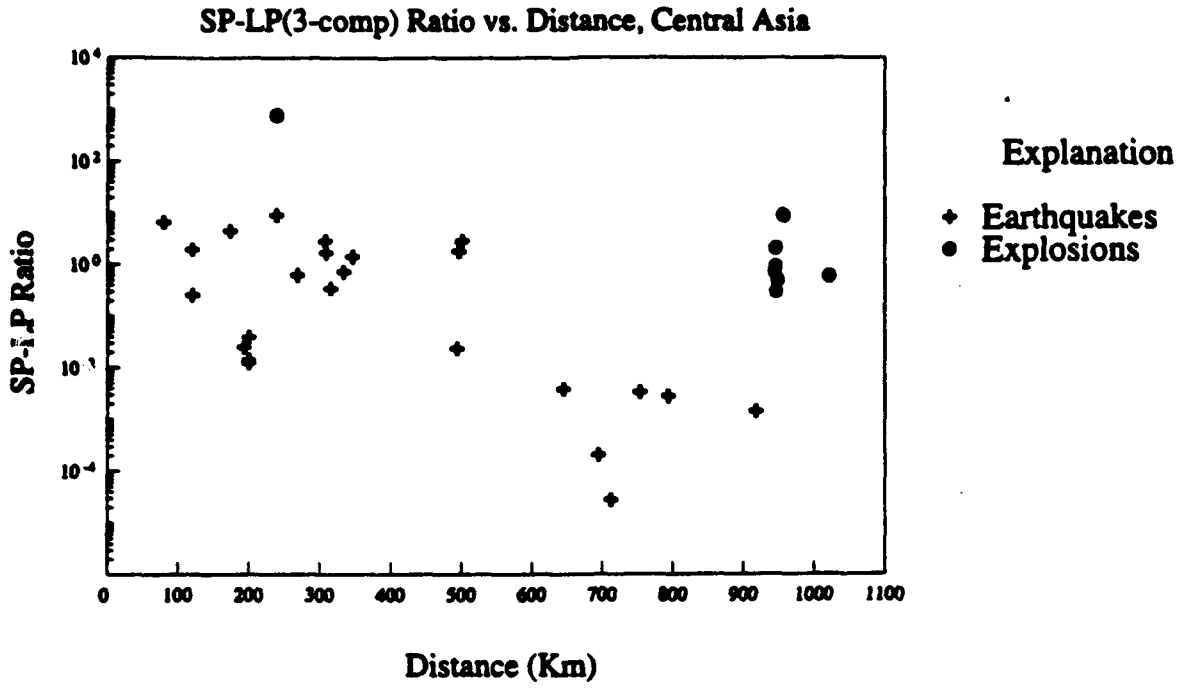


Figure 2. Figure showing the waveform variation recorded at various nuclear test sites. The seismograms are aligned according to the onset arrival marked by the first dotted line. The second dotted line shows arrival of pSmS followed by the Rayleigh waves. The most variation is observed in the Rayleigh wave. Clearly, NTS events show the largest amount of scatter in the Rayleigh waves and coda.



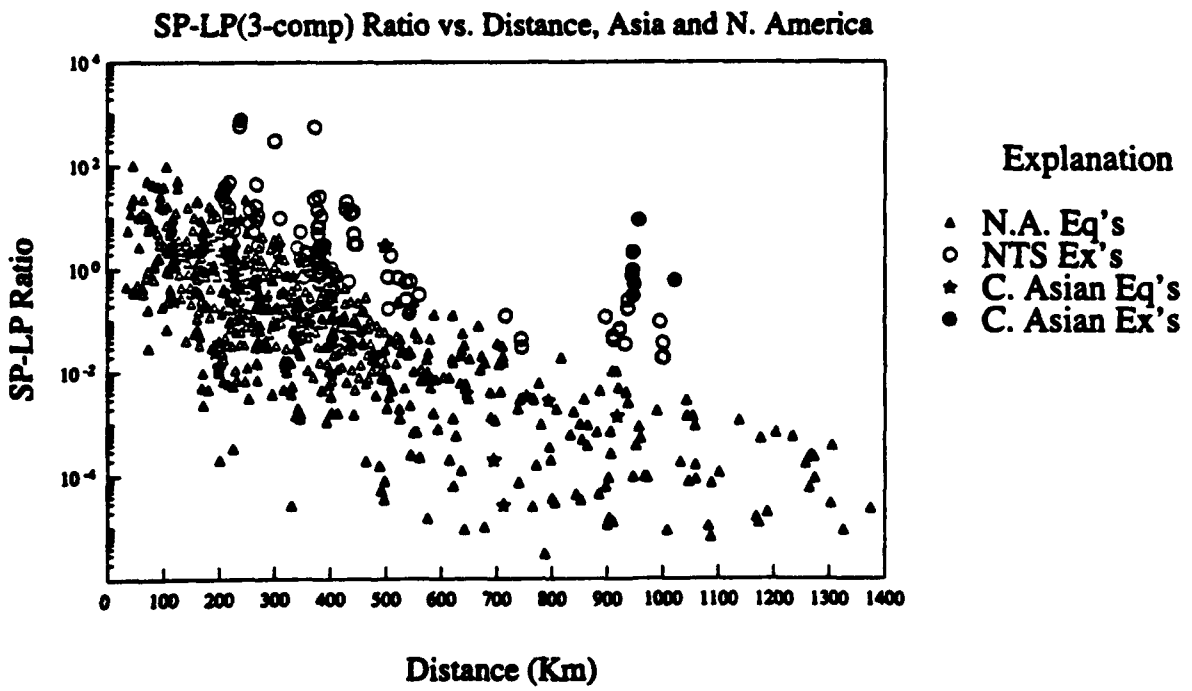


Figure 3. sp_z-P/lp_3 integrated energy ratios vs. distance for (a) central Asian events and (b) combined with North American events studied previously.

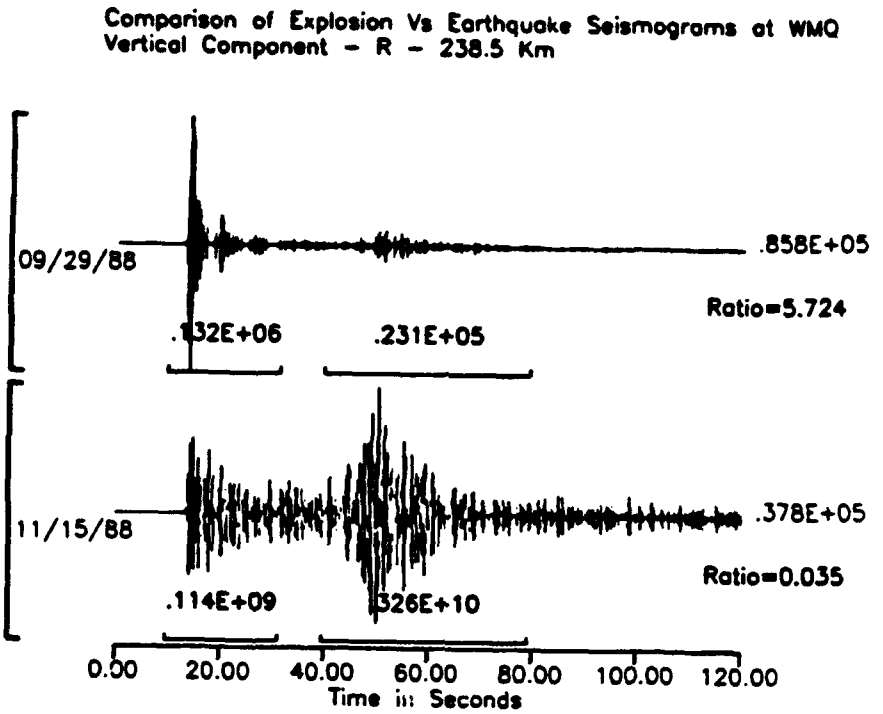


Figure 4a. Comparison of explosion and earthquake seismograms (both located approximately 240 km from WMQ) in the frequency band of 3 - 8 Hz. Note the relative richness of P-wave vs. S-wave on the explosion seismogram compared to that in the earthquake seismogram. The bracketed lines shows the window lengths used to estimate the energy contained within these two wave groups.

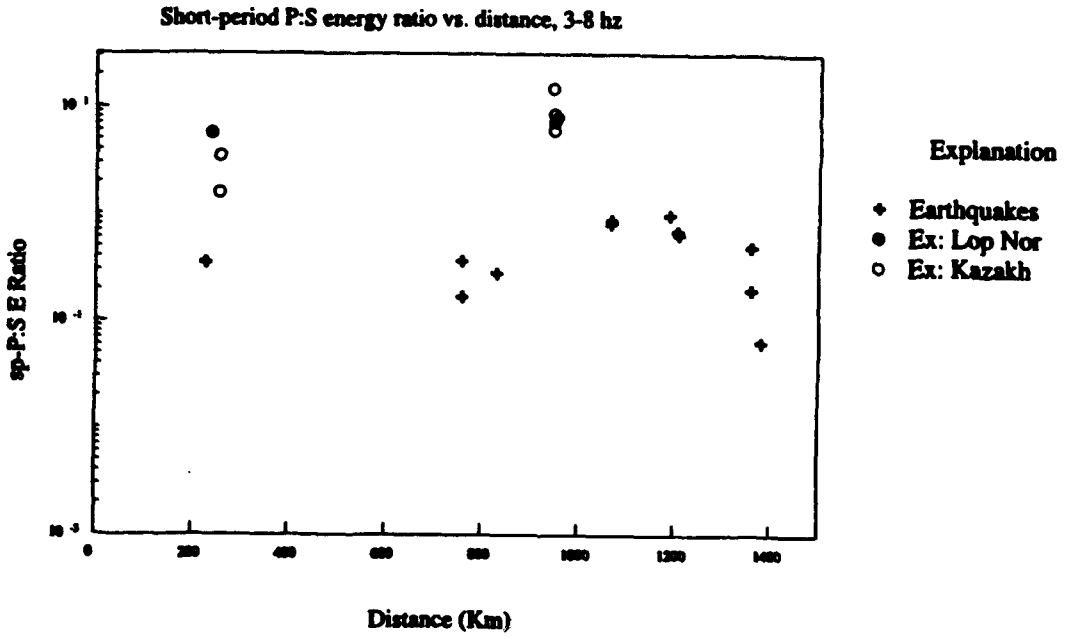


Figure 4b. sp_z-P/sp_z-S energy ratio vs distance for the Lop Nor and Kazakh explosions and earthquakes recorded at WMQ stations. Clearly, the explosions are well separated from the earthquakes.

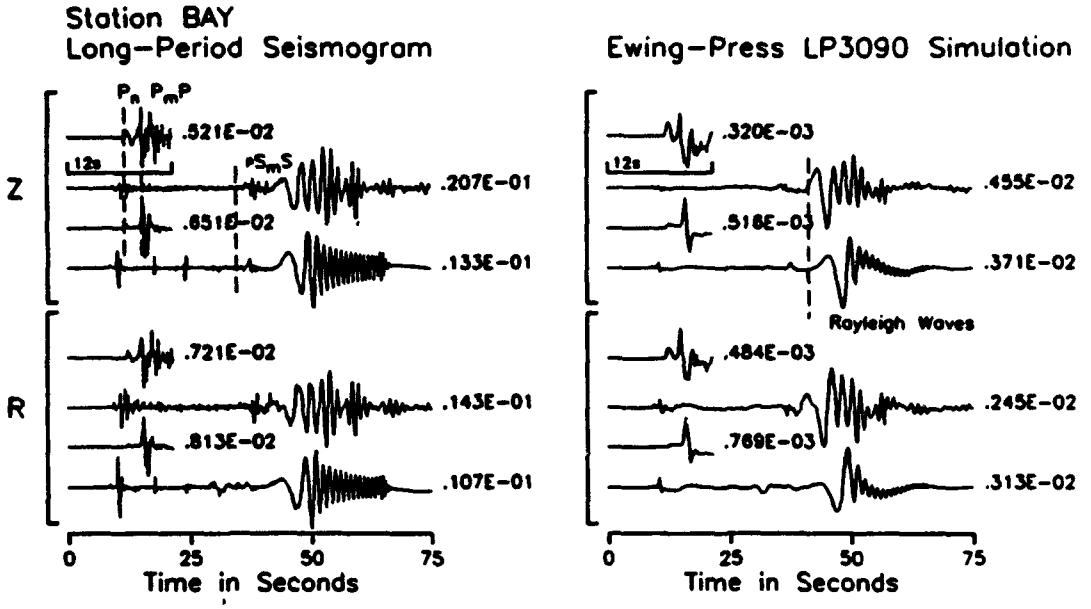


Figure 5a. Figure shows the vertical and radial seismograms recorded at BAY station from the September 14, 1988 Soviet JVE explosion (upper seismograms). Also shown are the synthetic seismograms plotted beneath each observed seismogram and were obtained using a source RDP of ψ_∞=2.0, B=1 and K=16 (Taken from Saikia and Helmberger, 1994). We also show the agreement observed in the L3090 seismograms on the right.

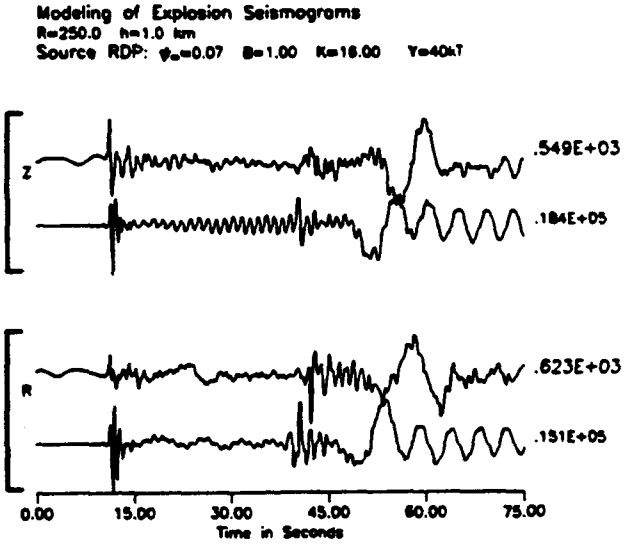


Figure 5b. A preliminary comparison between the data recorded at WMQ station from the Lop Nor explosion (upper seismograms) and the synthetic seismograms computed using the frequency-wavenumber integration code (bottom seismograms). The ψ_∞ is obtained using Murphy's relation for M_s=4.7, B is set equal to unity and K is derived iteratively. While the agreement between data and synthetic is reasonable, the model still needs further modification to produce a better fit in the travel time of various phases.

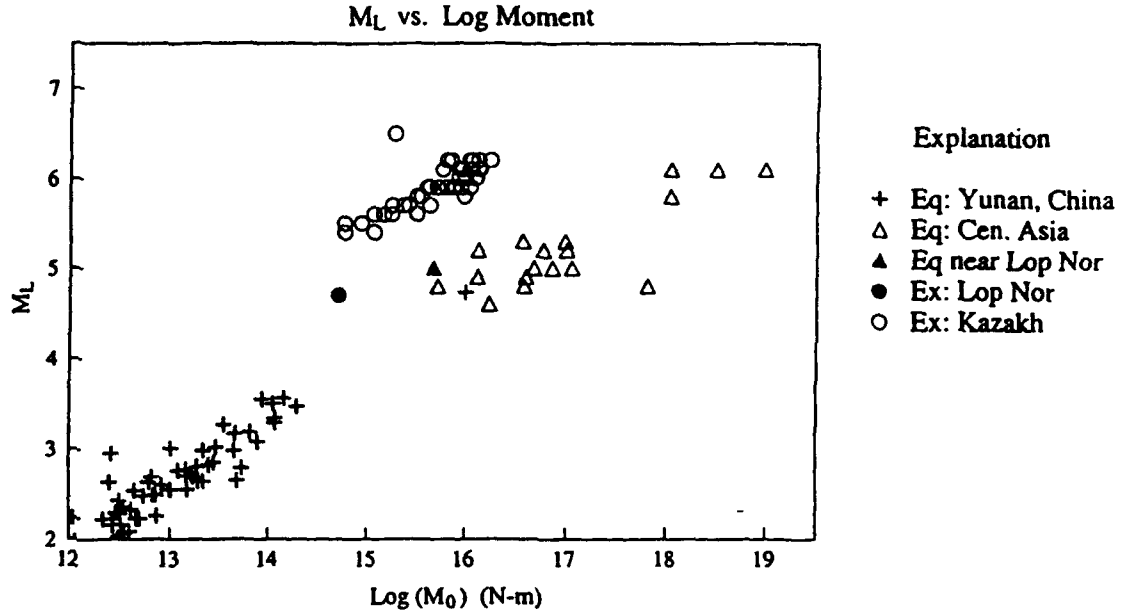


Figure 6. M_L vs. M_0 for Eurasian events.

REGIONAL SEISMIC DISCRIMINANTS USING WAVETRAIN ENERGY RATIOS

Bradley B. Woods and Donald V. Helmberger
California Institute of Technology
F49620-93-1-0221

OBJECTIVE

We have examined broadband regional waveforms from 32 NTS underground shots and 131 recent (1988+) earthquakes throughout the Southwestern U. S. and Mexico in order to characterize seismic sources and regional propagation effects. In general, explosions were found to be richer in coda energy than earthquakes. We interpret such phases to be energy trapped in the upper crust. These coda phases are consistent between explosions at the same test site (Pahute Mesa, Yucca Flat, or Rainier Mesa), implying that this late arriving energy is generated in the source region. Most earthquakes show little relatively long-period ($T > 6$ seconds) coda energy, which we attribute to their deeper source depths. As expected, earthquakes also tend to be richer in long-period and shear-wave energy than explosions. Our objective based on these results is to establish a set of seismic discriminants that can be routinely used in other tectonic regions. Since we are concerned about transportability, we have chosen measures that are related to quantities that can be modeled for the larger earthquakes, $M_L > 5$. This allows the regional calibrations to be established from earthquakes and is tailor-made to recognize the first test in a region. We have developed several seismic discriminants based on these considerations.

RESEARCH ACCOMPLISHED

The most promising discriminant is the ratio of short-period (1 Hz), vertical component, *Pnl* wavetrain energy to intermediate-period (0.05 to 0.16 Hz), three component, surface wave energy, for which explosions tend to have a higher value ratio than earthquakes. This discriminant works on the same premise as the teleseismic M_S:m_b ratio, for which earthquakes are richer in long-period surface wave energy relative to explosions with the same body wave magnitude. This effect is believed to be due to the more distributed nature of earthquake sources (both spatially and temporally) relative to explosions. Using reasonable assumptions for seismic sources and a regionalized earth model, theoretical seismograms produce similar energy ratio results. These discriminant criteria are useful in that they are simple and fast to calculate, and the SNR of the long-period surface wave can be very low, so long as the predominant Airy phase is visible, for this method to work. Using regional stations for sources 300 to 1300 km away, the magnitude threshold for these discriminants is roughly $M_L >= 3.5$ for earthquakes and $M_L >= 4.0$ for explosions.

Recent studies of regional seismic data (Woods *et al*, 1993; Walter and Patton, 1993) support teleseismic observations that explosive sources tend to be significantly richer in short-period energy than earthquakes, relative to their long-period energy, as manifested by the m_b:M_S discriminant (Basham, 1969); Liebermann and Pomeroy, 1969); Marshall *et al*, 1971; Stevens and Day, 1985). Extending such a short-period:long-period measure to regional distances would lower the effective discrimination magnitude threshold, as it makes it possible to observe surface wavetrains from smaller events as attenuation and geometrical spreading effects are less than for teleseismic distances, thus making this type of discriminant more useful.

In order to better appreciate the robustness of these energy measurements and their application to particularly small events, we will show a suite of regional waveforms and their associated integrated energy curves, for small explosions from the three NTS subsites and for earthquakes near NTS.

Figure 1 displays vertical component records of NTS shots recorded at GSC (first four rows) and ISA (bottom four rows). The first column is the broadband displacement, followed by convolutions with PE and WA instruments, respectively. The test site or name of the event is to the left of each row. At both these stations, long-period fundamental-mode Raleigh wave energy

is evident for all four events, with $T > 8$ sec. dispersed coda waves having the largest amplitudes. In making comparisons between events, it should be noted that the Pahute shot is larger than the others, so that it has a much better SNR. On the BB and PE recordings there are no distinguishing waveform characteristics between the three test sites or for the 1 kt chemical explosion. This holds true for all TERRAscope records gathered to data. On inspection of the WA records, certain patterns emerge. Recordings of the Pahute shot have a strong, prominent P-wavetrain followed by relatively small Short-period coda compared to the other test-site shots. The Yucca shot sports a great deal of what appears to be scattered shear-wave energy at both stations, which equals or exceeds the peak P-wave amplitude. The Rainier shots seem to be an intermediate case, for which the shear-wave energy may nearly rival, but not exceed the peak P-wave amplitudes. In all cases the shear-wavetrain does not have a sharp onset, but rather is a dispersive wavetrain.

These recordings are at fairly near distances ($200 < D < 280$ km), so that propagation effects are minimized. However, these characteristics persist to larger ranges, Woods and Helmberger (1994). These waveform characteristics come out in the integrated energy curves, too.

Figure 2a displays the short-period, vertical component, integrated energy curves vs. time for explosions recorded at the four TERRAscope stations; the time scale is the same as for the seismograms. All curves are normalized to unity, with the actual integrated energy value given to the right in the legend. For records with a prominent P-wavetrain arrival, the curves resemble step functions. This is particularly true of the Pahute shot. For the Yucca shot, on the other hand, the P-wavetrain energy comprises less than half of the short-period energy. The Rainier nuclear explosion and chemical blast are intermediate in shape to the Pahute and Yucca energy curves. At the more distant stations (PAS and PFO), the Rainier energy curves more closely resemble those of Yucca than Pahute, whereas at the closer stations, particularly ISA, the opposite is true.

Figure 2b is an analogous plot of integrated energy curves for earthquakes from the Little Skull Mountain sequence. Here the onset of the S-wave energy is pronounced and sharp. For explosions, in general, the S-wave onset is much more gradual, with the exception of the Yucca event recorded at PFO, which looks very much like the earthquake energy curves. It is not clear whether these differences are due to near-source or propagation effects. In the case of Yucca Flat for which the energy curve at each station deviates significantly from the "cleaner" Pahute curve, it seems likely that shallow structure in the source region is at least partly responsible for the large amount of scattered energy in the waveforms.

The contrast in these curves can be understood from their GSC seismograms as displayed in Figure 3. The top panel contains the explosion data and the bottom panel the earthquake data (A.S#1). The upper traces are the data and the lower corresponding synthetic traces are from a source estimation code where all events are assumed to be a double-couple (see Zhao and Helmberger (1994a and 1994b). Note that the P_{nl}-portions are separated and weighted in this approach. Since the synthetics and earthquake data have strong P-waves and S-waves, they have similar energy curves. However, the observed explosion has many complexities which produces extra energy.

Figure 4 (upper panel) shows their results for NTS explosions and southwestern U. S. earthquakes. Each datum point represents one event. The chemical KT explosion also has been added to the data set. This event and the normal Rainier shot (denoted with an "R") lie at the lower limit of the explosion population, but they are still separated from the earthquake population.

A more empirical approach is to use the short-period:long-period (SP:LP) ratio. The source properties that we want to quantify are the short-period (1 Hz) P-wave and long -period (0.14 to 0.05 Hz) surface wave energy levels, the ratio of which is used as the discrimination criterion. The short-period bandpass is the same used to measure teleseismic P-wave amplitudes for the m_b:M_S discriminant. The long-period bandpass represents the predominant frequency

range of the fundamental-mode Airy Phase at regional distances (Alewine, 1972). This short-period vs. long-period energy ratio ($E_{SP:LP}$) is defined as:

$$E_{SP:LP} = \frac{\int_{t_{Pn}}^{t_{Sn}} v_{sp}(t)^2 dt}{\sum_{i=1}^{3} \int_{t_1}^{t_2} v_{lp}(t)^2 dt},$$

with the summation being for the three components and t_i representing the windowing times determined from travel path length and the wave train of interest; t_{Pn} corresponds to the time before the onset of the P-wave and t_{Sn} the time prior to the S-wave onset time, and t_1 and t_2 bracket the time window of the fundamental Raleigh and Love waves. v_{SP} and v_{lp} are the short-period and long-period ground bandpass velocities, respectively. v_{SP} is obtained by convolving the broadband velocity record convolved with a Wood-Anderson (WA) short-period instrument and v_{lp} is the broadband velocity record convolved with a Press-Ewing long-period instrument (PE). The velocities are squared in order to obtain units of energy; the factor of $m/2$ in the numerator and denominator, where m is the unit mass of the particle of motion, cancel out.

Figure 4 (lower panel) plots the log SP:LP integrated energy ratio vs. distance for all data; each data point represents one event-station pair. Crosses represent earthquakes, circles signify nuclear explosions, and stars are data points for the chemical kt test. The explosions tend to have higher SP:LP integrated energy ratios than do the earthquakes at all distance ranges. Although there isn't complete separation of the two populations, the portion of the earthquake population which overlaps with the explosion population is small (approximately 10 percent).

It appears that separation is greatest at longer distances ($D \geq 900$ km) and least at distances less than 400 km. This effect may have to do to the population sample, however. Data points at larger distances are usually from larger events ($M_L \geq 5.0$), for which the difference in relative short-period to long-period energy levels between earthquakes and explosions is already firmly established.

RECOMMENDATION

Because the parameters used in these discrimination methods can be obtained from a sparse broadband network, these discriminants can be applied throughout the world as more broadband stations similar to those of the IRIS network come on line. For an active tectonic region, the threshold for this discriminant is $M_L = 3.1$ for earthquakes and $M_L = 3.6$ for explosions for epicentral distances up to 600 km.

REFERENCES

Basham, P. W. (1969). Canadian Magnitudes of Earthquakes and Nuclear Explosions in Southwestern North America, *Geophys. J. R. Astr. Soc.*, **17**, 1-13.

Liebermann, C. R. and P. W. Pomeroy (1969). Relative Excitation of Surface Waves by Earthquakes and Underground Explosions, *J. Geophys. Res.*, **74**, 1575-1590.

Marshall, P. D., A. Douglas, J. A. Hudson (1971). Surface waves from Underground Nuclear Explosions, *Nature*, **234**, 8-9.

Stevens, J. L. and S. M. Day (1985). The Physical Basis of m_b:M_S and Variable Frequency Magnitude Methods for Earthquake/Explosion Discrimination, *J. Geophys. Res.*, **90**, 3009-3020.

Walter, W. R. and H. J. Patton (1994). Regional Moment: moment relations for earthquakes and explosions, *Geophys. Res. Lett.* (in press).

Woods, B. B., S. Kedar, and D. V. Helmberger (1993). ML:MO as a Regional Seismic Discriminant, *Bull. Seism. Soc. Am.*, **83**, 11677-11683.

Zhao, L. S. and D. V. Helmberger (1994a). Source Estimation from Broadband Regional Seismograms, *Bull. Seism. Soc. Am.*, **84**, 91-104.

Zhao, L. S. and D. V. Helmberger (1994b). Regional Moments, energy levels, and a new discriminant, submitted to *Bull. Seism. Soc. Am.*

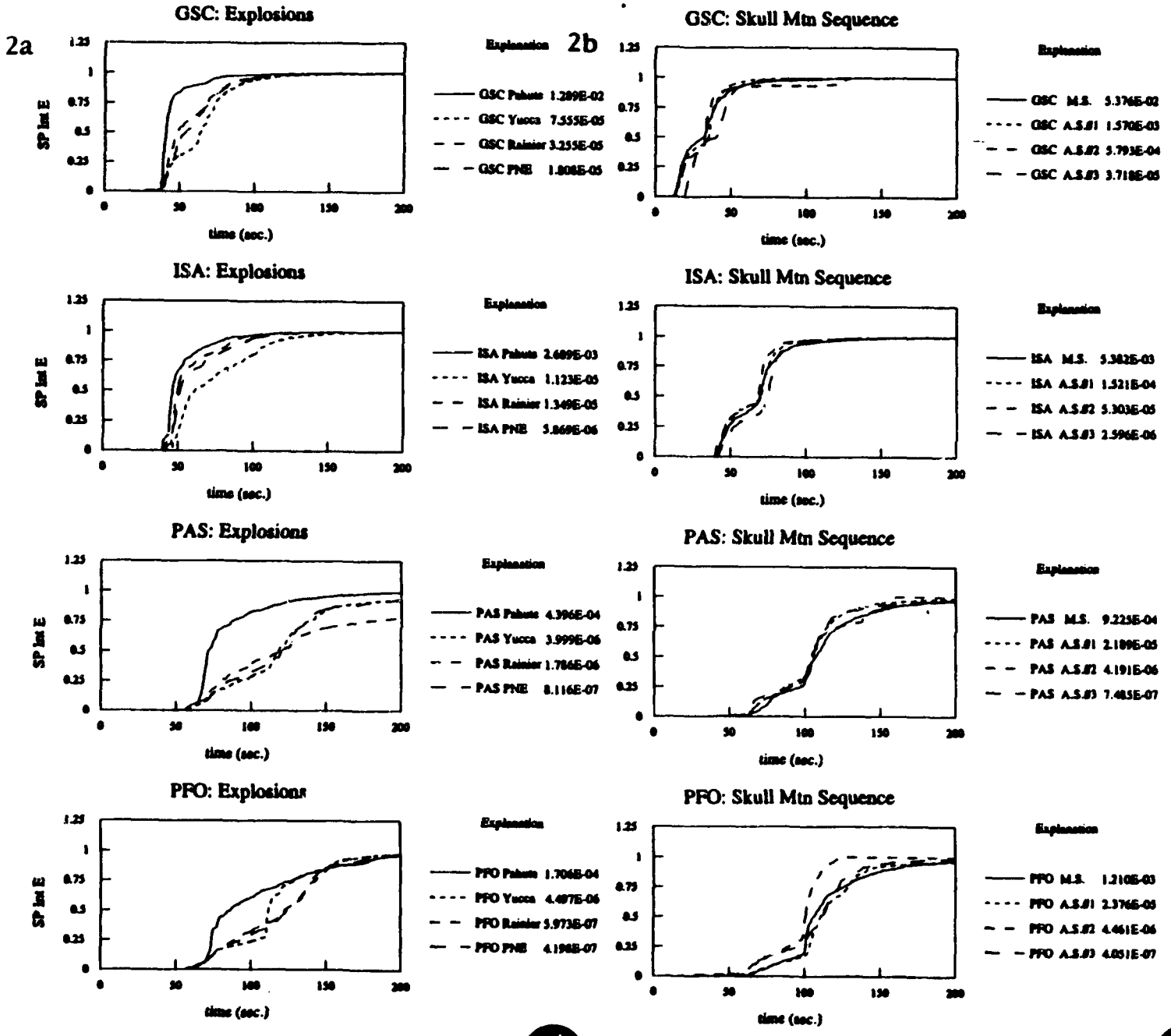


Figure 2. Comparison of short-period curves of explosions and earthquakes (Skull MTN) at the various stations.

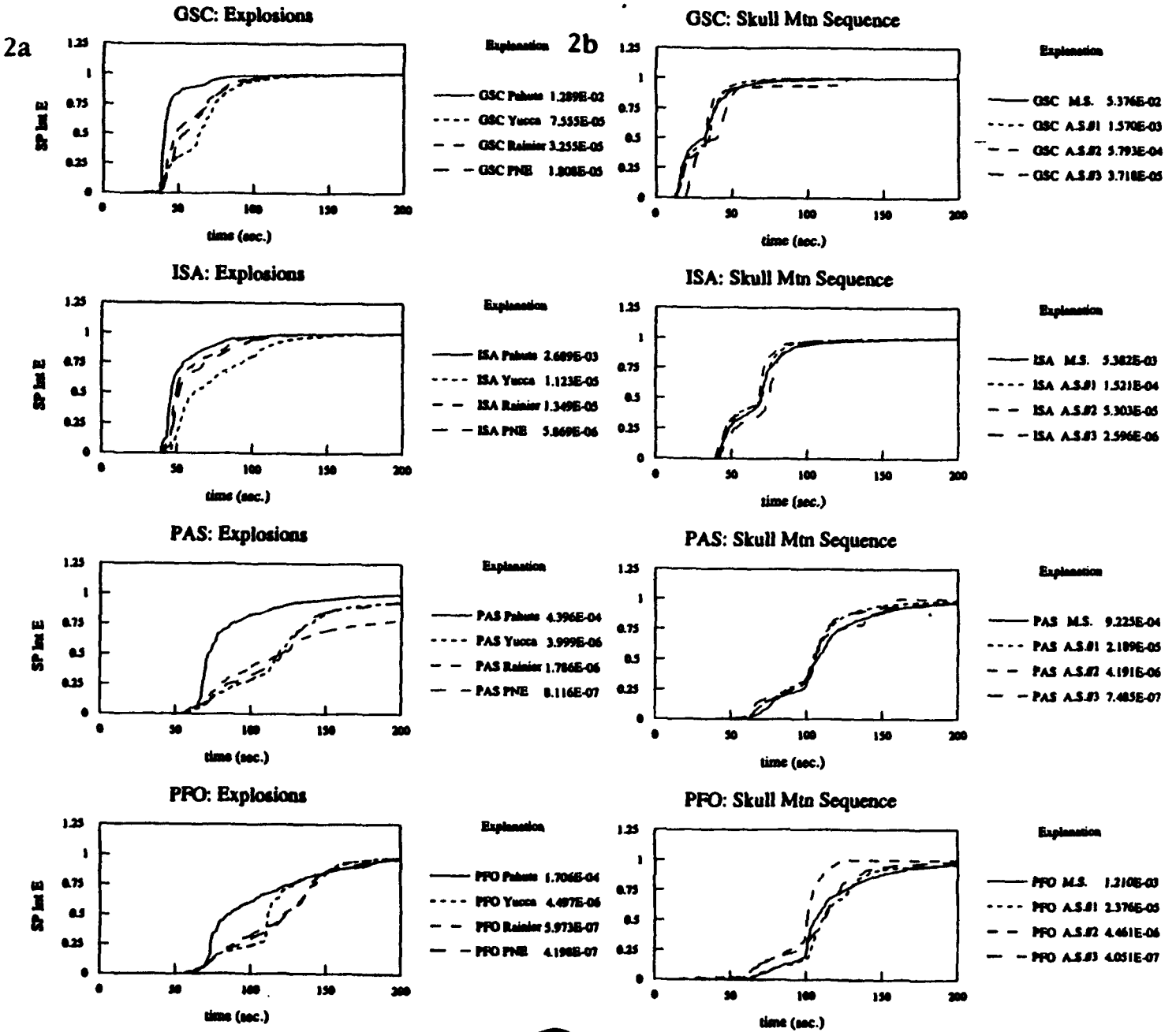


Figure 2. Comparison of short-period e curves of explosions and earthquakes (Skull MTN) at the various stations.

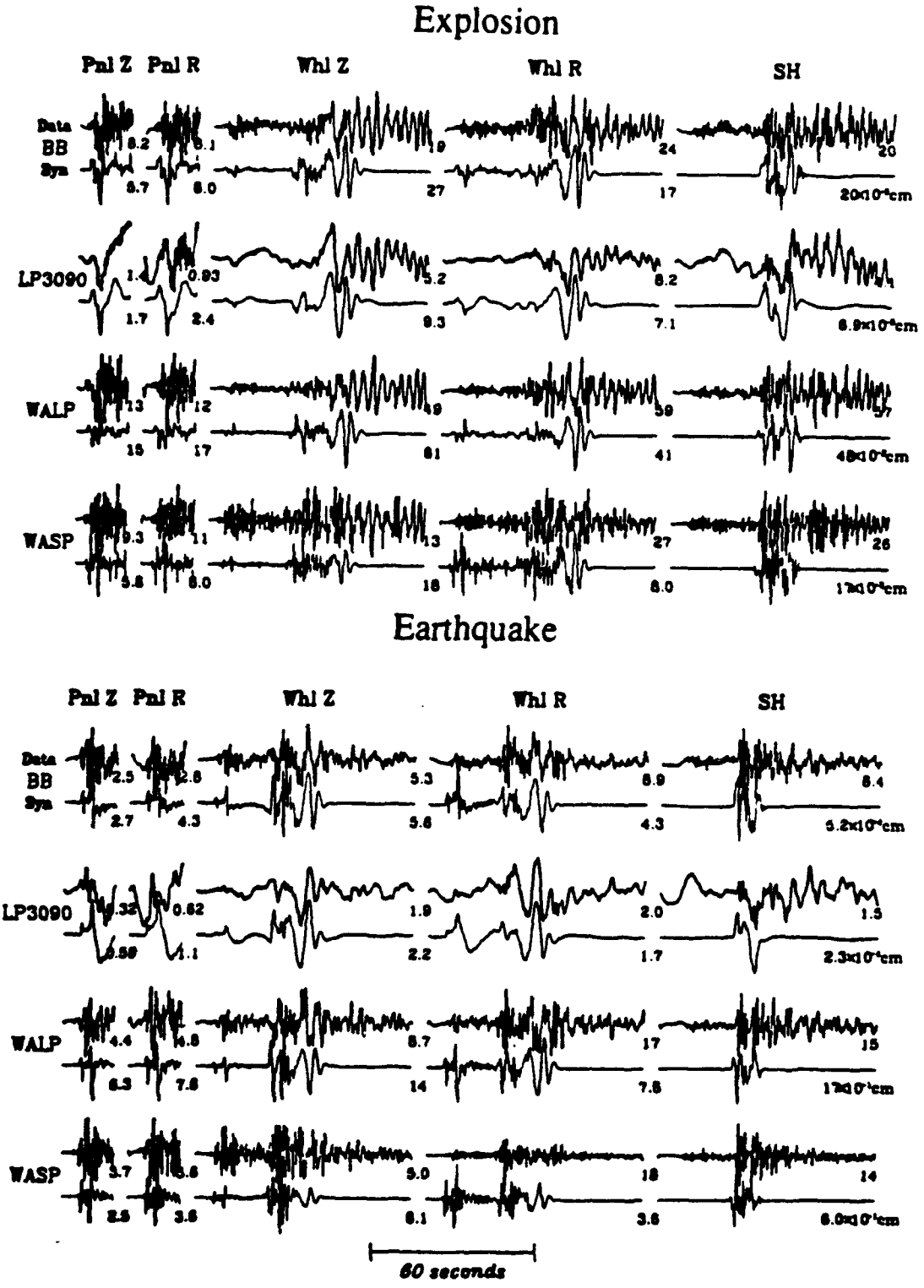
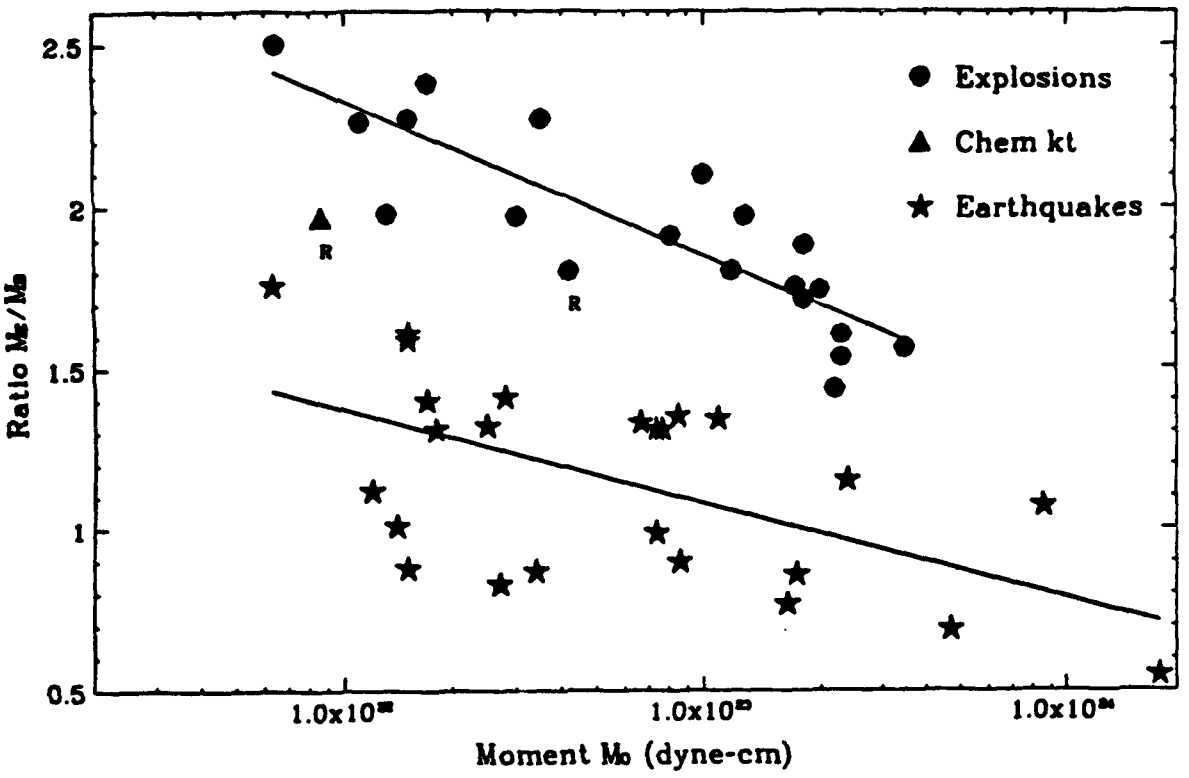


Figure 3. Comparison of an NTS explosion (Δ = 312 km, M_L = 4.1) with a Skull MTN aftershock (A. S. #1) of comparable magnitude. The bottom set of traces are synthetics found by the best fitting double-couple solutions. Note that the seismograms of the explosion contains more scattered energy than does the earthquake records. Explosions from Pahute, also, discriminate because of the extremely strong short-period P-waves, see figure 4 (upper panel).



SP-LP(3-comp) Ratio vs. Distance, M=3.5+

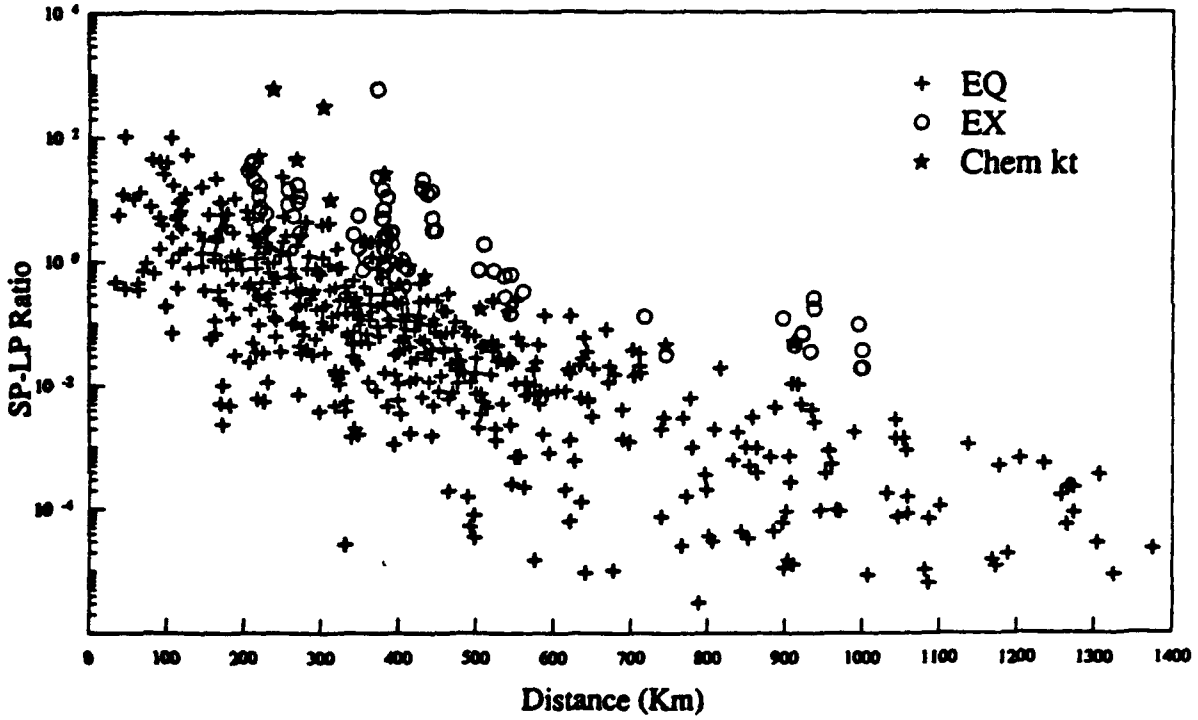


Figure 4. Upper panel displays a discriminant based on energy moment vs. moment where all events are assumed to be earthquakes, see Zhao and Helmberger (1994b). The lower panel displays a short period-long period energy discriminant, Woods and Helmberger (1994).

Modeling Elastic Wave Propagation in 3D Heterogeneous Media By Elastic Complex-Screen (ECS) Method

Ru-Shan Wu and Thorne Lay
University of California, Santa Cruz

Contract No. F49620-92-J-0461

Objective

This research is directed at development and application of a new three-dimensional wave propagation methodology in the context of improving our understanding of regional phase propagation in three-dimensional complex structure with random heterogeneities. A new methodology, involving an Elastic Raleigh Integral-Elastic Born Scattering iterative formalism has been adopted and a new theory/method on elastic wave wide-angle one-way propagation has been successfully developed during the first year's effort. The elastic complex-screen (ECS) method uses dual domain implementation (shuttling between the space and wavenumber domains by FFT) and is much faster than the full wave finite difference program. For a medium size 3D problem, the time saving is more than 2-3 orders of magnitude. Because it needs to store the medium parameters for only one grid-plane for each step, the tremendous computer memory saving makes it capable of handling large 3D problems prohibitive to other methods. We further enhance the capability of the method and algorithm by introducing anelasticity, oblique incidence, point source excitation with different moment tensors, and the capacity of dealing with wave propagation problems in 3D random media. Our effort will be aimed to the problem of accurately synthesizing regional phases for three-dimensional earth models appropriate for the wide variety of Eurasian paths of interest. A large data set of Eurasian recordings for nuclear tests, moderate size earthquakes, and large quarry explosions is being analyzed under a parallel AFOSR-funded effort. The combined theoretical and observational effort should enhance our ability to extract quantitative information from regional phases, and to place regional discrimination and yield-estimation applications on a sound physical basis.

Research Accomplished:

I. Seismic wave propagation and diffraction by large-scale complex visco-elastic structure.

After the success in developing the theory of elastic complex-screen for wide-angle one-way elastic wave propagation (Wu, 1994) and the corresponding method and algorithm (Wu and Xie, 1993; Lay and Wu, 1993) in the first year's effort, we further improved the method and enhanced its range of application by introducing anelasticity (absorption), oblique plane wave incidence, and point source excitation into the method and programs (Wu and Xie, 1994).

We test and apply our ECS program to the teleseismic response of a complex large-scale structure as shown in Fig. 1. The model is represented by three low-velocity, low-Q zones (LVLQZ) buried in a homogeneous background velocity field. In order to simplify the model input procedure, we use axis-symmetric (with respect to Z-axis) LVLQZ structures. The first two LVLQZs are two discs with radius of 17 km and 8 km, and same thickness of 2 km. They are located near the surface and served to simulate the low velocity sedimentary structure. The third LVLQZ is a tri-axial ellipsoid located at the 10 km depth with its half-horizontal axis of 7 km and half-vertical axis of 4 km. This is used to simulate the magma chamber, fracture zone or other low-Q low-velocity inclusion. The model parameters for homogeneous background are $V_p = 5.8km/s$, $V_s = 3.3km/s$,

$\rho = 2.4g/cm^3$, $Q_p = Q_p = \infty$. The velocities and shear modulus perturbations for three LVLQZs are $\delta V_p/V_p = -0.25$, $\delta V_s/V_s = -0.25$, $\delta\mu/\mu = -0.25$ and $Q_p = Q_s = 30$. The dimensions of the model are 128 km x 64 km x 20 km, with a grid size of 1 km x 1 km x 0.5 km. Three incident angles, 0, 10 and 20 degree, are used to simulate teleseismic incidence.

In Fig. 1, the geometry of the structure is shown in the upper part; Snap shots of the wave field are shown in the lower part. The LVLQZ's are also outlined in the snap shots for reference. A plane P-wave is incident upon the bottom of the model obliquely with 10^o to the z-axis. The interactions between the wave front and the LVLQZs, focusing/defocusing, P-S conversion, time delay and attenuation etc., are clearly seen in the figure. Also seen is how the interface waves (creeping waves) are formed and propagate as well as how diffracted waves are interfering with transmitted waves. The simulation demonstrated the important influence of a low-V, low-Q body under a sedimentary structure to the observed wave field distribution on the surface.

II. The influence of small-scale random heterogeneities to seismic wave propagation

Small-scale random heterogeneities can produce long codas, reduce the spatial and frequency coherencies of the major arrivals and cause complicated apparent attenuation and dispersion. It can scatter the guided waves out of the crustal waveguide and influence the apparent attenuation and wave field characteristics of regional waves. Therefore it is important to study the influence of such random heterogeneities by forward modeling. Using our ECS program, we can study numerically the forward scattering by random heterogeneities. We have combined a 3D random medium model builder into our main code. In the model builder, the power spectrum of the random medium is specified in the 3D spectral domain. The random medium in space-domain is obtained by 3D FFT of the random spectrum.

Fig. 2a. shows a three-dimensional velocity model of a random elastic slab. The 3D random slab of thickness 8 km is buried in a constant velocity background. The P- and S-wave velocity random perturbations have a relative rms value of 10% and an exponential correlation function with horizontal and vertical correlation lengths of 5 km and 3 km, respectively. In Fig. 2b. are the snap shots of the wave field. The random slab is indicated by light lines. A plane P-wave is vertically incident on the bottom of the model. When passing through the random slab, the plane wave front is progressively distorted. The focusing/defocusing effects and the formation of coda can be seen clearly. The loss of coherency can be seen from synthetic seismograms. Because of the interference between scattered waves some features in the synthetic seismograms or snap shots bear strong similarities to that of large scale structure and might be mistakenly interpreted as signatures from large-scale structures. Quantitative analysis of the influence of random heterogeneities when large structures are present is underway.

III. Excitation by Point Sources With Different Moment Tensors:

In order to use the ECS algorithm for more practical applications to local and regional seismogram synthetics, the excitation by point sources with different moment tensors should be incorporated into the program. Since the wave field from a point source has strong large-angle components, the influence of the periodical boundary effects inherent to the FFT methods appears to be severe. We tested both boundary tapering and wavenumber filtering methods to reduce the boundary influence. It is found that proper combination of the two methods gives the best results. This hybrid method of eliminating boundary effects is used in all the following examples,

Fig. 3 shows examples of synthetic seismograms of point sources in constant elastic media. The types of point source are A) explosion source, B) single force, C) double-couple forces along x- and z-axes. They agree with the theoretical predictions. Fig. 4 presents the snap shots (Fig. 4a) and synthetic seismograms (Fig. 4b) of a point explosion source propagating its wave through a inhomogeneous background composed by a low velocity sphere immersed in a constant medium. The size of the model space is 3.2 x 3.2 x 2.1 km^3. Only results within a 2.0 x 2.0 x 2.1 km^3

volume are shown here. The elastic parameters for the background medium are $V_P = 3.2km/s$, $V_S = 1.85km/s$ and $\rho = 2.20g/cm^3$. The solid sphere has a P-wave velocity 15% lower than the background velocity. The radius of the sphere is 0.3 km. We use a 128 x 128 grid phase screen with a grid interval 0.025 km. The interval between screens is 0.1 km. A total of 65 frequencies are calculated with the Nyquist frequency of 50 Hz. The calculated time length is 1.28 seconds. This three-dimensional elastic wave example is calculated on a SUN SPARC-10 workstation with 2.5 hours of CPU time.

Conclusions and Recommendations:

Our wide-angle one-way elastic wave propagation algorithm ECS (elastic complex-screen) has been enhanced and improved by introducing anelasticity, oblique incidence, point source excitation with different moment tensors, and by incorporating the capability of wave propagation in 3D random media. The influence of the periodic boundary effects is substantially reduced by a hybrid method of boundary tapering and wavenumber filtering. The elastic complex-screen (ECS) method developed during this project uses dual domain implementation (shuttling between the space and wavenumber domains by FFT) and is much faster than the full wave finite difference program. The tremendous saving in CPU time and computer memory makes it capable of handling large 3D problem prohibitive to other methods. Under continuing AFOSR support we will further improve the 3D elastic wave algorithm and expand its capability of simulating elastic wave propagation im more realistic geophysical situations. At the same time the 2D SH program (Liu and Wu) will be further developed and adapted for regional wave propagation and applied to the simulation of Lg and Lg-coda generation in complex crustal structures. The results will be compared with the Eurasia data sets of nuclear explosions. We plan to solve the free surface and Moho boundary problems for the full elastic wave complex screen method in the continuation of the current project.

Acknowledgement:

We appreciate the help and contribution of Dr. X.B. Xie to this project.

References

Lay, T. and R.S. Wu, 1993, Analysis of 3D complex structure and heterogeneity effects on formation and propagation of regional phases in Eurasia. *Proc. 15th Annual Seismic Research Symposium*, PL/AFOSR/ARPA, 241-247, PL-TR-93-2160, ADA271458.

Liu, Y.B. and R.S. Wu, 1994, A comparison between phase-screen, finite difference and eigenfunction expansion calculations for scalar waves in inhomogeneous media, *Bull. Seis. Soc. Am.*, in press.

Wu, R.S., 1994, Wide-angle elastic wave one-way propagation in heterogeneous media and an elastic wave complex-screen method, *J. Geophys. Res., 99,* 751-766.

Wu, R.S. and X.B. Xie, 1993, A complex-screen method for elastic wave one-way propagation in heterogeneous media, *Expanded Abstracts of the 3rd international congress of the Brazilian Geophysical Society.*

Wu, R.S. and X.B. Xie, 1994, Multi-screen backpropagator for fast 3D elastic prestack migration, submitted to *Proceedings of SPIE annual meeting on Mathematical Methods in Geophysical Imaging II.*, San Diego, California, July 25-26, 1994.

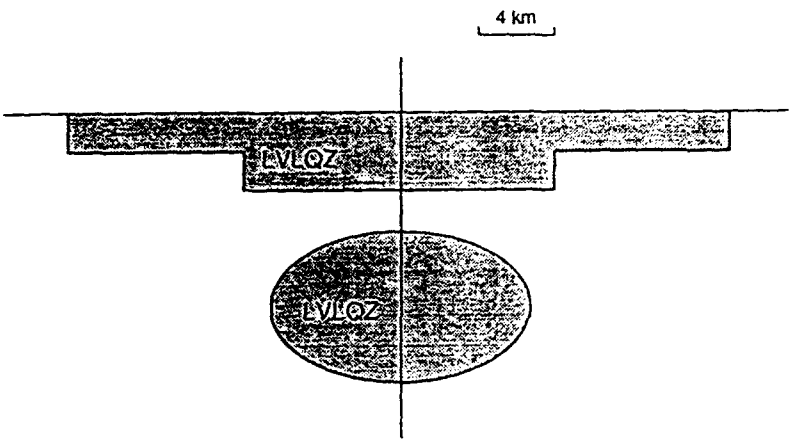


Fig. 1a. The model, composed by two low-velocity low-Q zones immersed in a constant elastic medium.

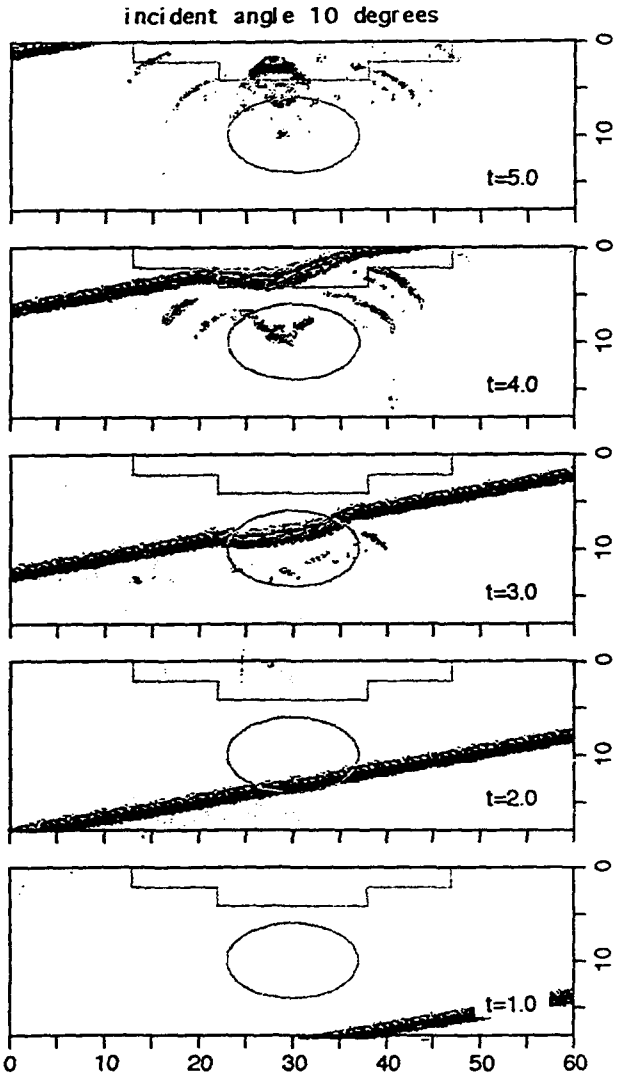
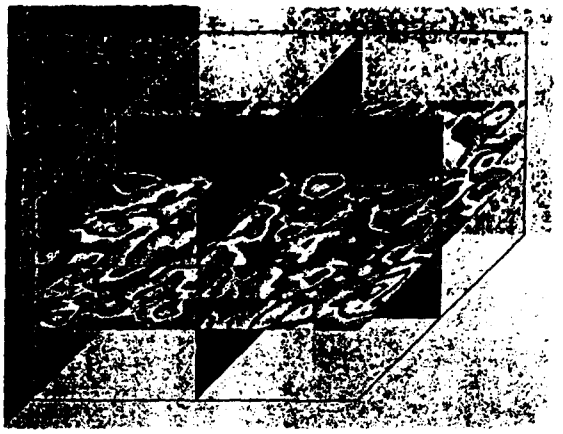


Fig. 1b. Snap shots of the wave field. The structures are indicated by light lines. A plane P-wave is incident with 10° to z-axis upon the bottom of the model. The interactions between the wave front and the LVLQZs, focusing/defocusing, P-S conversion, time delay and attenuation are clearly shown in the figure.



3-D velocity model

Fig. 2a. Three-dimensional velocity model with a 3D random slab. In the figure, three horizontal cross-sections of the random slab are shown.

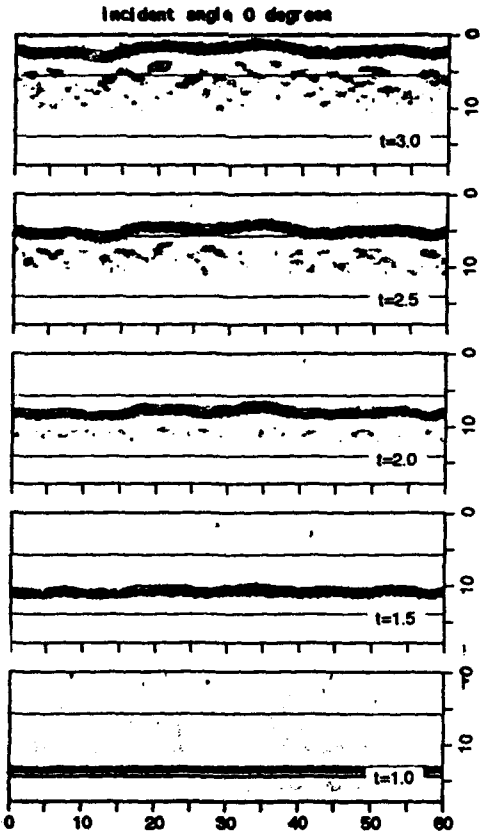


Fig. 2b. Snap shots on the vertical cross-section showing wave front distortion and coda genration when passing through the random slab. The random slab is indicated by by the two parallel lines.

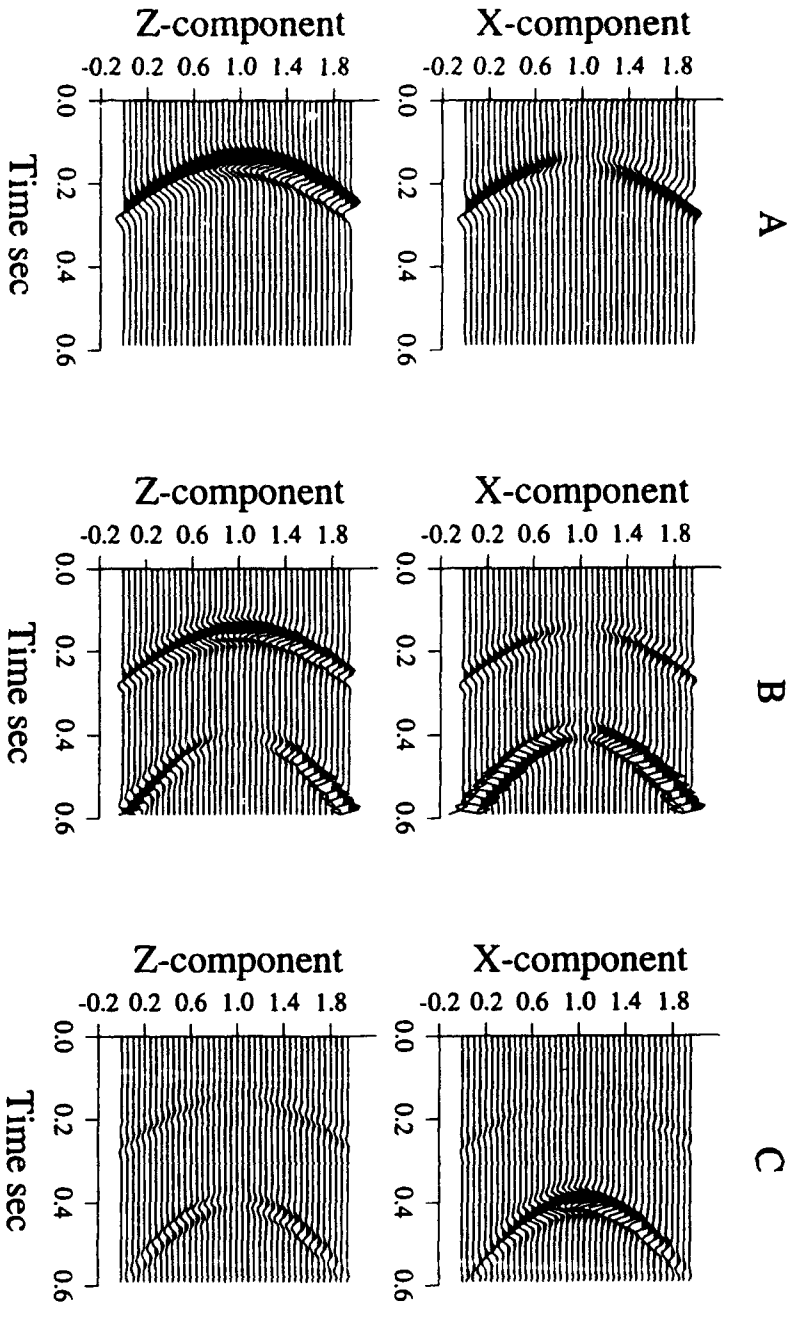


Figure 3. Synthetic seismograms for point sources with different moment tensors: A. explosion source; B. single force in z-direction; C. double-couple along x- and z-axes.

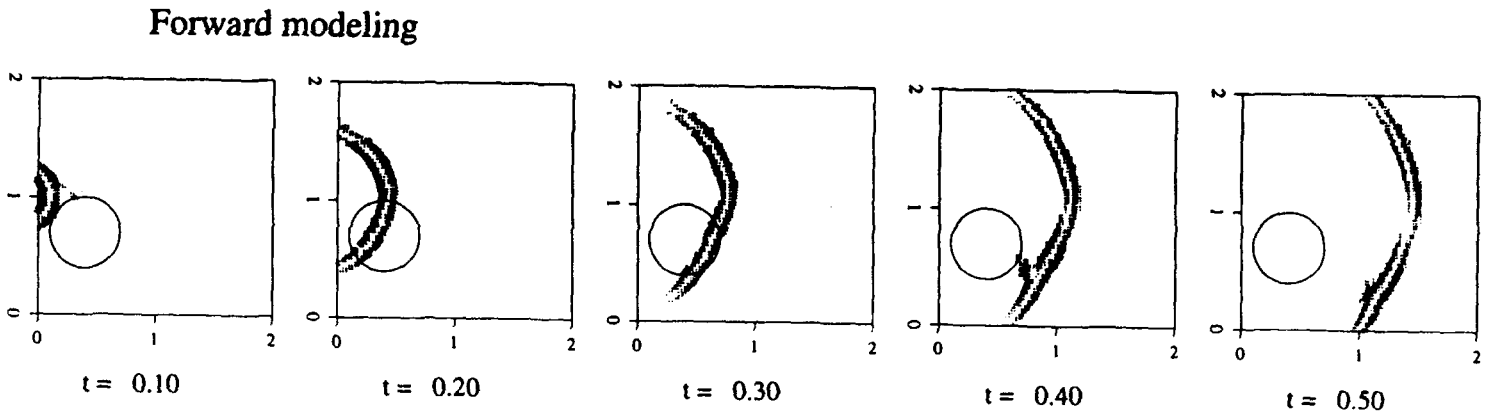


Fig. 4a. Snap shots of wave propagation in an inhomogeneous medium composed by an elastic sphere immersed in a constant background. The vector displacement field above certain threshold is displayed by arrows whose lengths represent the magnitudes.

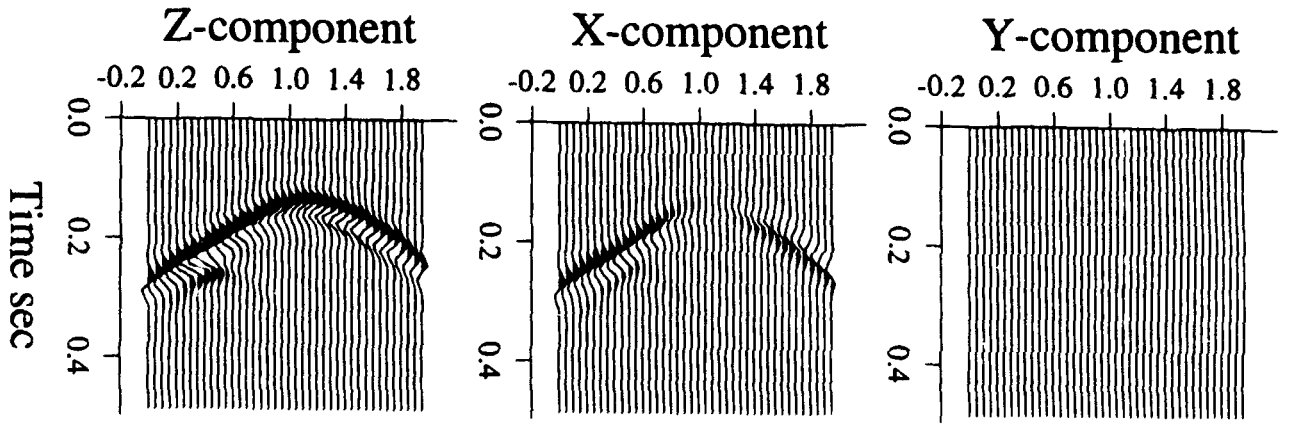


Fig. 4b. Synthetic seismograms at distance z=1 km.

SOURCE SCALING AND DEPTH DETERMINATION FROM Lg SPECTRA

Jiakang Xie, Lianli Cong, Jiang Chuan Ni and B.J. Mitchell
Department of Earth and Atmospheric Sciences, St. Louis University
3507 Laclede Ave., St. Louis, MO 63103

Contract No. F49620-94-1-0025

Objective

There are three objectives of this research. First, we want to determine Lg source spectral parameters, including seismic moments (M_0) and corner frequencies (f_c) for explosive and earthquake sources in Central Asia and China, and to find scaling relationships between M_0 and f_c values for both types of sources. Second, we want to determine path-variable Q at 1 hz and its frequency dependence from the *direct* Lg phase, rather than from Lg coda, and compare Q_{Lg} values with the tomographic Q map derived from Lg coda (Xie & Mitchell, 1991; Pan *et al.*, 1992). The third objective of this research is to develop a depth discriminant based on the synthetic Lg spectra computed for events with varying depths. In previous studies using higher-mode surface waves to determine crustal Q, we noticed that the spectra of higher-mode surface waves were strongly influenced by the depth of the events which were used in the studies (Cheng and Mitchell, 1981; Kijko and Mitchell, 1983) and it appeared that these spectra might prove to be useful for determining the depths of shallow events at regional distances.

Research Accomplished

To study source spectral parameters and path-variable Q using real data, we have applied the non-linear spectral inverse method of Xie (1993) to broad-band Lg spectra from many Balapan and Lop Nor explosions in Central Asia and China. Several interesting findings have been made:

(1) *Performance of the inverse method*: The method of Xie (1993) for the simultaneous inversion of M_0, f_c and path-variable Q_{Lg} values appears to work well when high quality Lg waveforms from three or more stations, with relatively short (<2,000 km) distances, are available. It appears that when the condition in (1) is not met, *a priori* knowledge on Q_{Lg} is required to constrain the inversion of M_0 and f_c values. The need of *a priori* knowledge, however, is fundamental and is due to the insufficient information contained in data, as well as the stochastic nature of the ω-square source model.

(2) *Agreement between Lg Q and Lg coda Q*: The path-variable Lg Q at 1 hz obtained in this study agrees well with the tomographic Lg coda Q map obtained earlier (Figures 1 and 2).

(3) *Stability of Lg propagation in central Asia as compared to regional P*: An interesting discovery was made on the relative stability of Lg, as compared to regional P waves, for paths between the Lop Nor Test Site and the Kyrghizstan Seismic Network (KNET). Figure 3 presents broad band seismograms from the Lop Nor explosion of October 19, 1993, collected from six KNET stations. Despite the small aperture of the KNET and the stability of the amplitudes of Lg (Figure 4), the Pn wave amplitudes vary by an order of magnitude across the array. Correction of path effects for the Pn phase in this case would be considerably more difficult than for the Lg phase.

(4) *Scaling between* M_0 *and* f_c *values for explosions*: Figure 5 shows the M_0 versus f_c values for some Balapan and Lop Nor explosions, obtained by inverting the Lg spectra using an *earthquake source model* (*cf.*, Xie 1993). Figure 6 shows the M_0 versus f_c values for the same Balapan and Lop Nor explosions, obtained by inverting the Lg spectra using an *explosion source model* with an overshoot, β, of 0.75 (Sereno *et al.*, 1989; Xie, 1993). In both Figures 5 and 6, f_c values increase more slowly with decreasing M_0 values than predicted by the $M_0 \sim f_c^{-3}$ law. These slow rates of f_c increments, if combined with scalings between f_c versus M_0 for earthquake sources yet to be obtained, may form a basis for discrimination of explosions.

In the synthetic study for Lg as a depth discriminant for regional events, theoretical amplitude spectra were computed for a central United States velocity model (Mitchell and Herrman, 1979) combined with either a low-Q or a high-Q crustal model of anelasticity. Figure 7 presents a theoretical spectrum generated by a strike-slip fault at a depth of 0.3 km for ground motion recorded at a distance of 300 km from the source and Figure 8 shows a spectrum at the same distance for the same type of event, but at a depth of 5.0 km. Both computations were done for a low-Q model in which the average shear-wave Q in the upper crust to depths of 15 km is about 80 and the lower crust is about 1000. Spectral levels are the same for the events at frequencies above about 1 Hz. At lower frequencies (0.2-0.8 Hz), however, spectral levels of the shallower event are lower than those for the deeper event by a factor of between two and three. This indicates that we should be able to align observed spectra and theoretical spectra at frequencies greater than 2 or 3 Hz and compare spectral levels at frequencies between 0.2 and 0.8 Hz to estimate source depth.

Similar results were found for a high-Q model in which shear-wave Q in the upper 15 km of the crust is 500 rather than 80. Additional studies showed that we can expect to obtain robust depth estimates from Lg spectra even when significant seismic noise is present.

Conclusions and Recommendations

In central Asia and China, when Lg is recorded by multiple stations, the source spectral parameters and path Q can be obtained on single event

and real time basis. Lg spectra appear to be stable measurements of source properties, although the transfer function between S wave and Lg is not necessarily flat. Toward the understanding of Lg excitation and the discrimination of explosions using Lg, analyses of more Lg spectra from explosions, as well as that from earthquakes in the same area, are necessary.

In central Asia, path effects on regional P wave amplitudes can be unstable, and should be more difficult to correct than in the Lg study. Understanding those effects remains a major challenge in utilizing regional waves in seismic studies.

In areas where Q and velocity structure are poorly known (such as in Mideast), the inverse method of Xie (1993) can be applied on single event basis to study Q and source spectra using Lg when multiple station records are available. Extension of the method into other phases, such as Pn, is possible and is recommeded.

Our synthetic study on Lg spectral amplitudes as a depth discriminant, to date, has been very promising. It indicates that those spectra should easily be able to distinguish between possible explosive events which occur a depth of 0.3 km or less and earthquakes which occur a depth of 5 km. In addition, computations of spectra for synthetic seismograms which include a realistic level of noise, suggest we should be able to accurately determine depths of seismic events from those spectra.

References

Cheng, C.C., and B.J. Mitchell, 1981. Crustal Q structure in the United States from multimode surface waves, *Bull. Seism. Soc. Am.*, **71**, 161-181.

Kijko, A., and B.J. Mitchell, 1983. Multimode Rayleigh wave attenuation and Qb in the crust of the Barents shelf, *J. Geophys. Res.*, **88**, 3315-3328.

Mitchell, B.J., and R.B. Herrmann, 1979. Shear velocity structure in the eastern United States from the inversion of surface-wave group and phase velocities, *Bull. Seism. Soc. Am.*, **69**, 1133-1148.

Pan, Y., Mitchell, B.J. & Xie, J., 1992. Lg coda Q across Northern Eurasia, paper presented at the 14th annual PL/DARPA research symposium, September 1992. PL-TR-92-2210, ADA256711.

Sereno, T.J., S.R. Bratt and T.C. Bache, 1988. Simultaneous inversion of regional wave spectra for attenuation and seismic moment in Scandinavia, *J. Geophys. Res.*, **93**, 2019-2036.

Xie, J. and B.J. Mitchell B.J. 1991. Lg coda Q across Eurasia, in *Yield and discrimination studies in stable continental regions*, B.J. Mitchell (ed). Report PL-TR-91-2286, Phillips Laboratory, Hanscom Air Force Base, MA, 77-91, ADA251590.

Xie, J. (1993). Simultaneous inversion of source spectra and path Q using Lg with applications to three Semipalatisk explosions, *Bull. Seism. Soc. Am.*, **83**, 1547-1562.

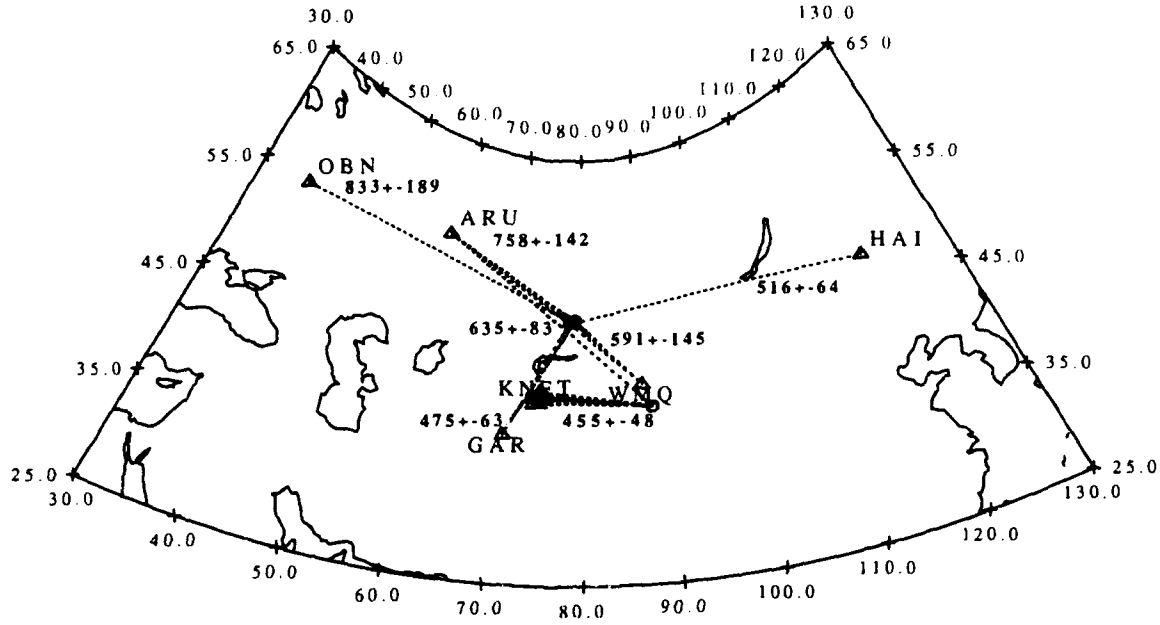


Fig. 1. Great circle paths from the Balapan and Lop Nor nuclear explosions to the IRIS/CDSN stations used in this study. Numbers near the paths are the Q_0 values obtained for the path, with the estimated uncertainties.

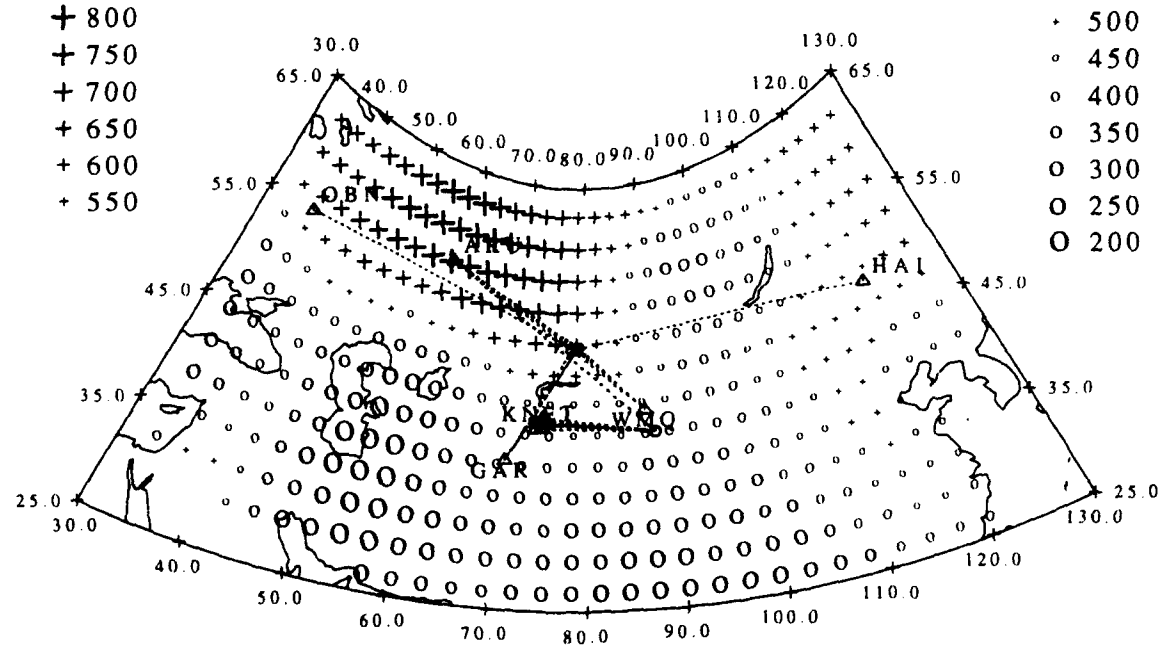


Fig. 2. Tomographic map of laterally varying Lg coda Q_0 in the area under study, adapted from Xie and Mitchell (1991). The paths used in this study are superposed for comparison.

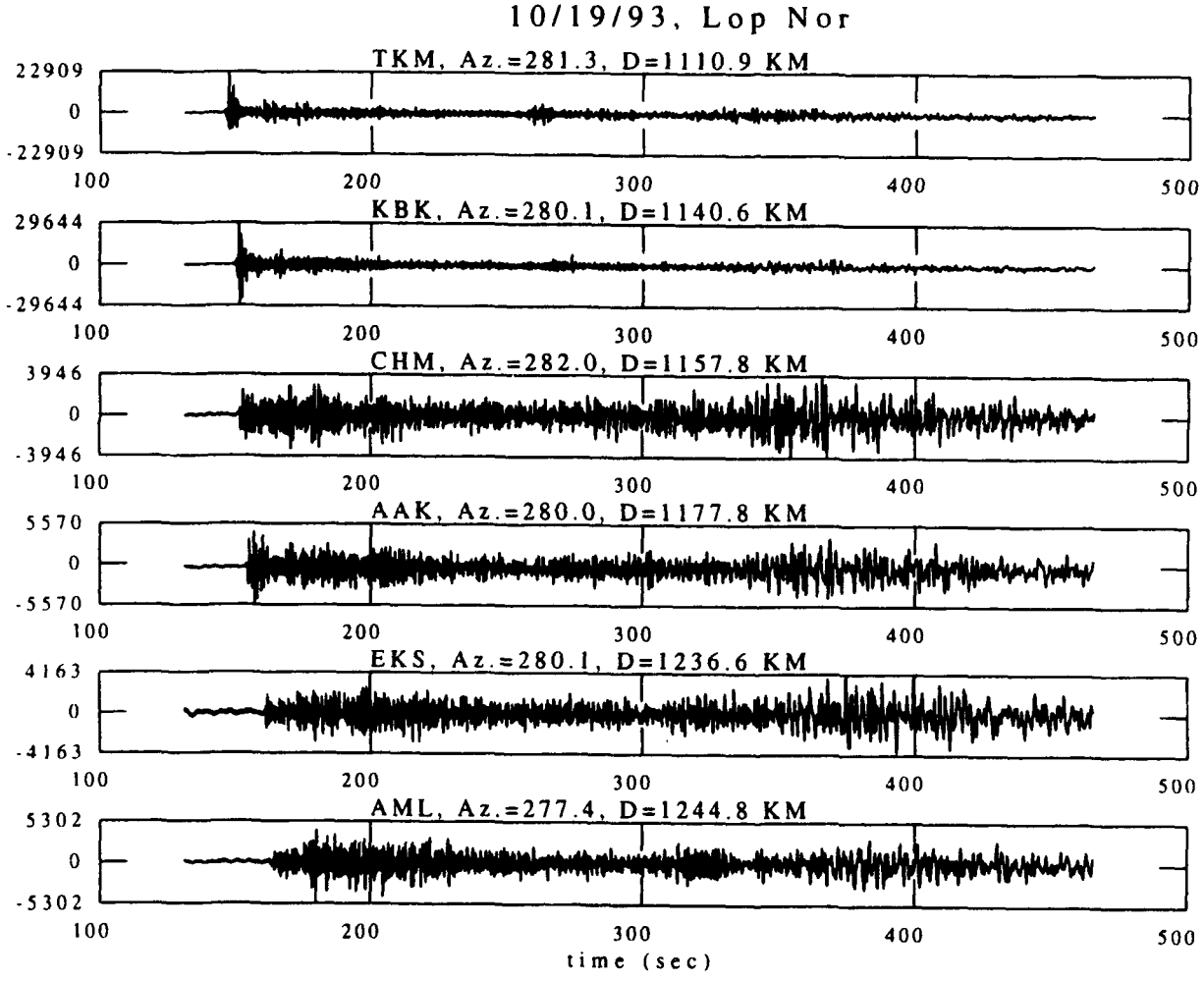


Fig. 3. Broad-band seismograms from six Kyrghiztan Network (KNET) stations recording the October 19,1993 Lop Nor explosion. The gains are normalized for all traces. Note the similarity in event azimuths and epicentral distances marked on top of the seismograms, and the drastic variation in P amplitudes across the KNET.

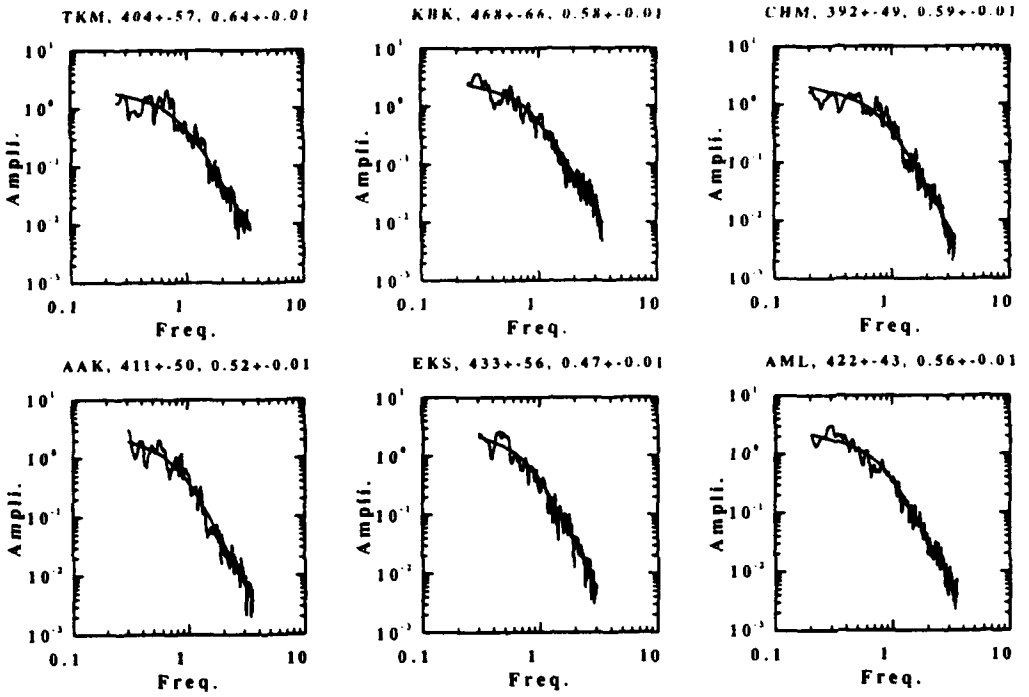


Fig. 4. Synthetic Lg spectra for all of the six KNET stations recording the October 19,1993 Lop Nor explosion, versus the observed. The spectra are normalized to source (*cf.*, Xie, 1993, Fig. 4). The synthetic spectra are calculated using optimal source spectral parameters (M_0 = 7.9×10^{22} dyne-cm, fc=0.68 hz) obtained in the inversion of the spectra at KNET stations, as well at IRIS station ARU. The Q_0 and η values for all stations are marked on the top of the panels and are close to one another, indicating similar Lg spectral amplitudes at all of the stations.

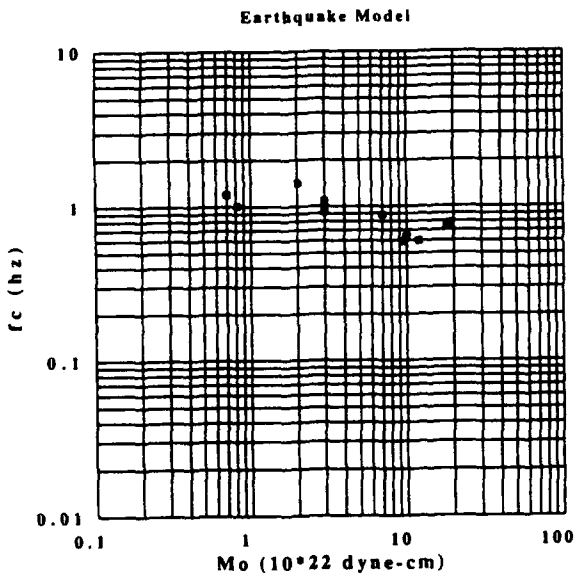


Fig. 5. M_0 versus f_c values for some Balapan and Lop Nor explosions, obtained by inverting the Lg spectra using an *earthquake source model* (*ie.*, no overshooting).

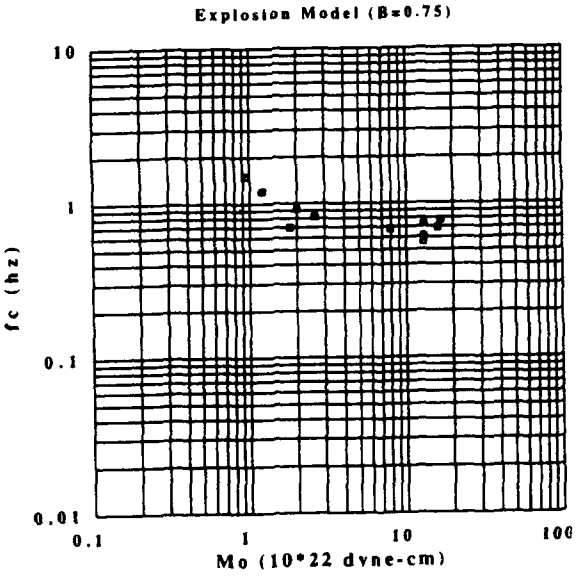


Fig. 6. M_0 versus f_c values for some Balapan and Lop Nor explosions, obtained by inverting the Lg spectra using an *explosion source model* (overshooting β = 0.75)

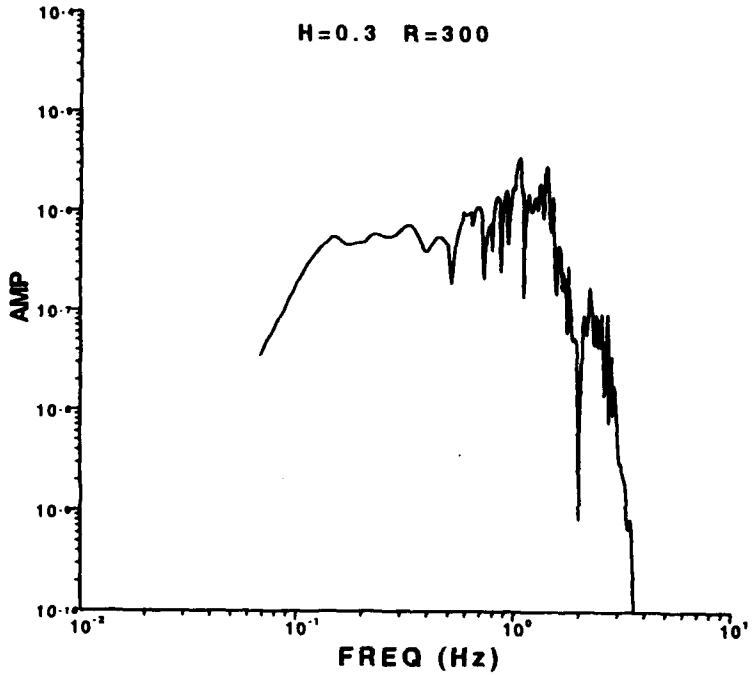


Fig. 7. Synthetic Lg amplitude spectrum generated for a strike-slip source at a depth of 0.3 km. The epicental distance is 300 km. A low-Q model is used.

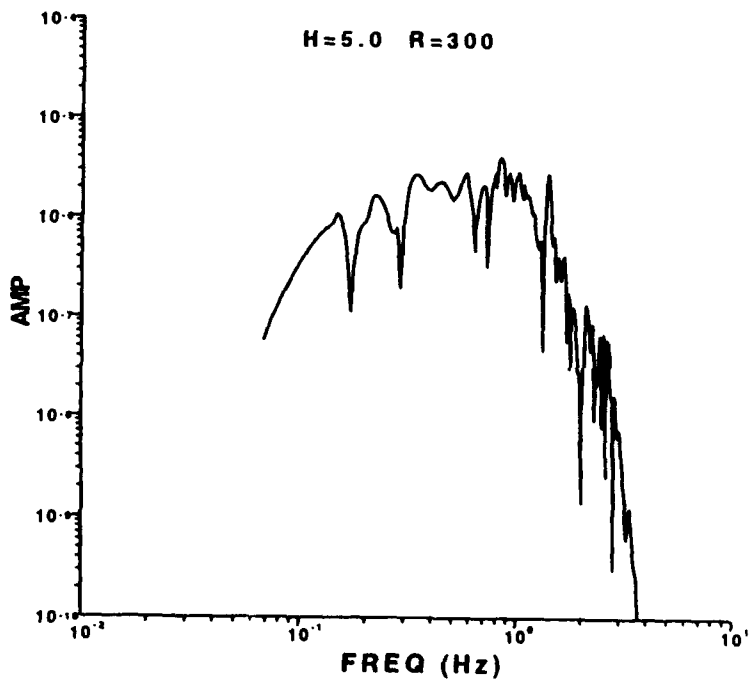


Fig. 8. Same as Figure 7, except that the source depth is 5.0 km.

Polarization Characteristics of Seismic Waves From the May 21, 1992 Lop Nor Nuclear Explosion Using IRIS/GSN Broadband Data

AUTHOR & AFFILIATION: J Zhang (Institute of Tectonics, University of California, Santa Cruz)

GRANT NO: 94-0315

OBJECTIVE: To use broadband seismic data recorded by IRIS/GSN stations to study the characteristics of seismic waves and the source of the May 21, 1992 Lop Nor, China, underground nuclear explosion. The emphasis will be on identification and analysis of individual surface wave phases of periods between 10 and 80 s, with the long term objective being to understand the excitation and propagation of surface waves from explosion and earthquake sources in Southern Asia. Several techniques for analysis of wave excitation and propagation will be used. These techniques include first, the newly developed method of polarization analysis for the determination of azimuthal anomalies of surface waves propagating along various geological provinces; second, the empirical Green's function method to determine any non-isotropic seismic radiation in the period range of 10 to 20 s from the May 21, 1992 (m_b=6.5) explosion using surface waves recorded for smaller Lop Nor nuclear explosions (August 16, 1990, m_b=6.2; October 5, 1993 m_b=5.9) as empirical Green's functions; and third, the centroid moment tensor method for source inversions to investigate seismic wave excitations by the nuclear explosion source at Lop Nor for seismic waves with periods of 30 s and longer using recently developed high resolution Earth models.

RESEARCH ACCOMPLISHED: We have obtained broadband data recorded at IRIS/GSN stations for three recent Lop Nor nuclear explosions, including the tests of the May 21, 1992, Augest 16, 1990, and October 5, 1993. The data for the May 21, 1992 explosion are deconvolved for instrument response, filtered at various frequency passbands, and compared with theoretical travel times for various body and surface waves for phase identification. We have obtained instantaneous envelopes and polarization state vectors for seismograms at several stations within distances less than 42° from the test site, which include CHTO, TATO, MAJO, and KEV.

CONCLUSIONS AND RECOMMENDATIONS: The May 21, 1992 Lop Nor, China, underground nuclear explosion was well recorded by broadband instruments from IRIS/GSN stations. There are about 25 IRIS/GSN stations, which are located in regional and teleseismic distances from Lop Nor. The data from these stations provide complete, three component recordings of P, S, and surface wave phases for each event. There are four stations, CHTO, TATO, MAJO, and KEV, within distances less than 42° from the test site, with the broadband recordings showing clear arrivals of various body and surface wave phases. The ray paths for these stations traverse high mountain systems in Central Asia, where the crust and mantle structure are very complex. The instantaneous envelopes and polarization state vectors for seismograms recorded at these stations show strong dependence in shape and arrival times of various surface wave phases, indicating large effects of the Earth's lateral heterogeneity beneath ray paths.

We will extend the data set by including recordings available from other global and regional seismic networks, including worldwide IRIS/IDA and GEOSCOPE and regional POSEIDON in Japan. In particular, we will collect and analyze data from several broadband stations of IRIS/IDA at close distances from the test site, which include AAK (Ala Archa, Δ=11°), GAR (Garm, Δ=14°), NVS (Novosibirsk, Δ=14°), TLY (Talaya, Δ=14°), ARU (Arti, Δ=24°), KIV (Kislovodsk, Δ=34°), and OBN (Obninsk, Δ=36°). We will compare data recorded at the same station for different

explosions at the Lop Nor test site to identify signals pertinent to the source and propagation path for each station. The polarization characteristics of these signals will be analyzed.

INTRODUCTION

The May 21, 1992 Lop Nor, China, nuclear explosion is the largest underground nuclear test in China, which has a m_b magnitude of 6.5. This explosion is in the proximity of several recent nuclear tests at Lop Nor, which include the explosions of Augest 16, 1990 (m_b=6.2) and October 5, 1993 (m_b=5.9). These explosions were well recorded by broadband instruments from the IRIS/GSN and several other global and regional seismic networks.

Recent investigations of the explosion spectrum using body waves and surface waves with periods of a few seconds and longer indicate that although surface-wave data offer extensive evidence for the effects of non-isotropic sources, they do not place an important bound on the source mechanisms responsible for their excitation [Wallace, 1991; Patton, 1991]. With the exception of the non-uniqueness in the determination of a combined explosion and tectonic release source model when the source depth is not known [Aki and Tsai, 1972], the ambiguity in interpretations of surface wave data with a definitive source model is perhaps largely due to the poorly known effects of Earth's lateral heterogeneities on surface wave propagation in teleseismic and regional distances.

The complexities of the crust and upper mantle structure in various distances from Lop Nor are perhaps among the most prevalent ones in the Earth. The Lop Nor test site is located between Bosten Hu and the Lop Nor lake, which lie in the northern part of the Tarim Basin, the largest inland basin in China. The Tarim Basin is located in the innermost part of Eurasia, the world's largest continent, within the vast territory that encompasses the high mountain systems of Central Asia. The regions to the north and west of the Tarim Basin include the mountain massifs of Tien Shan, Pamir, and Hindu Kush. The region to the south includes Karakoram, Kunlun, and Tibetan Plateau. These regions are the most spectacular consequences of the collision of the Indian subcontinents with the rest of Eurasia in Cenozoic time.

Various geophysical and geological data indicate that there are large lateral heterogeneities in the crust and upper mantle beneath the high mountain systems in Central Asia. Large variations in crustal thickness and surface wave dispersion characteristics are observed for regions under Tien Shan and Pamir. Wu and Levshin [1992] used data recorded by Chinese Digital Seismic Network (CDSN) stations in the determination of surface wave group velocities in China. The group velocity gradients on the eastern and northern sides of the Tibetan plateau are quite high, reflecting the sudden change in crustal thickness in these regions [Wu and Levshin, 1992]. For these reasons, surface waves propagating in regions near the high mountain systems in Central Asia, in particular the margin of the Tibetan plateau, are expected to show strong variations of amplitude, phase, and polarization anomalies.

Recent advances in understanding the effects of the laterally heterogeneous and anisotropic structure of the Earth on seismic wave propagation have resulted in renewed attention to the polarization pattern of seismic waves. In the laterally homogeneous structure the particle motion of principal wave types (i.e., P, S, Rayleigh, and Love waves) are linearly or elliptically polarized, represented by a pure state process defined by Samson [1983]. The effects of heterogeneous structure involve interferences of direct, refracted, reflected, and scattered body and surface waves, which are characterized by unstable polarization patterns in both the time and frequency domains.

The nature of seismic recordings is usually much more complex than a pure state process, as an event is followed by subsequent phases, resulting in the shape and orientation of the polarization ellipse varying with time; and only for a short time interval the

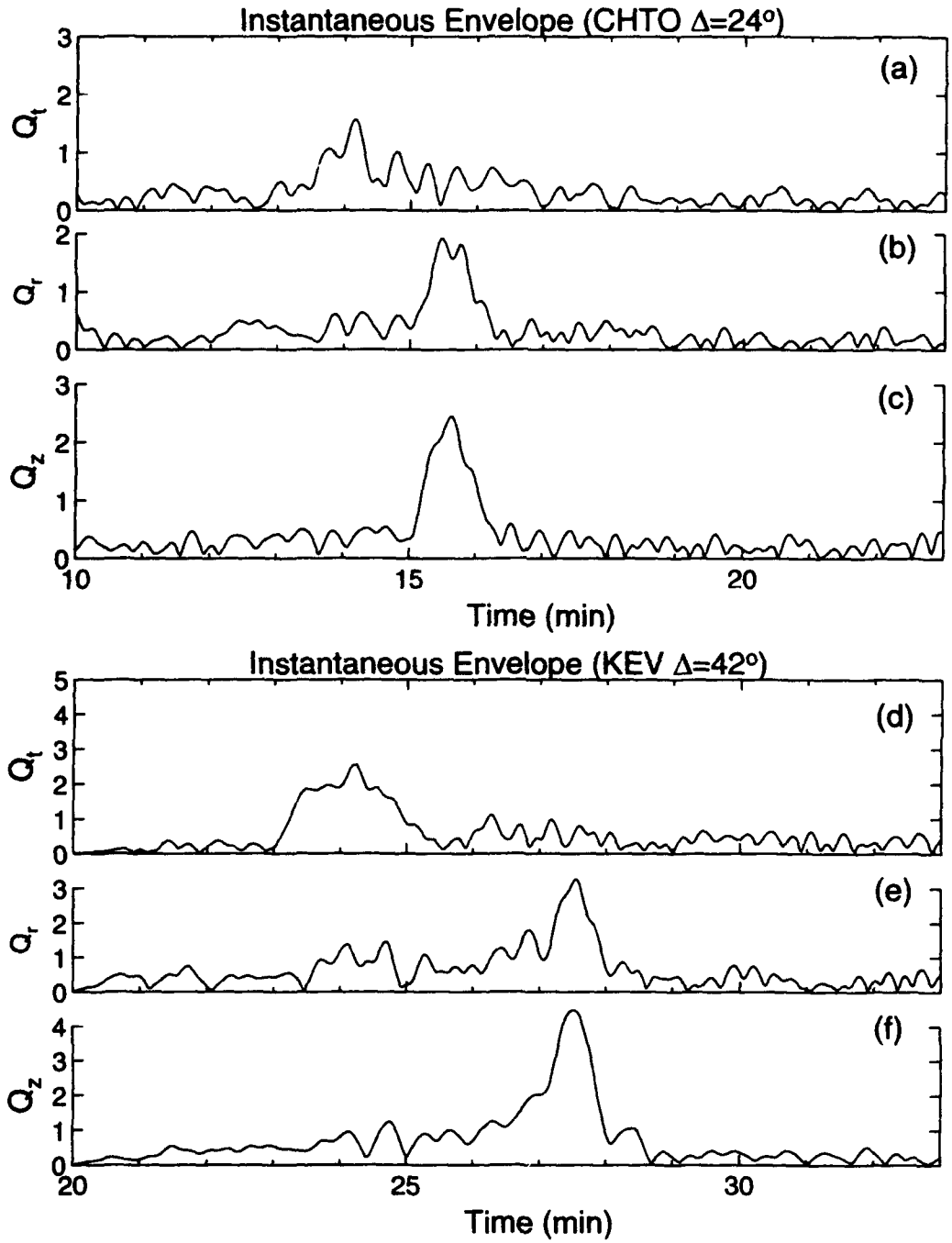


Fig. 1. The instantaneous envelopes (units in microns) of the ground displacement seismograms bandpass filtered between 3 and 100 mHz from the May 21, 1992 Lop Nor, China, nuclear explosion for stations CHTO (distance Δ=24°, azimuth ϕ=156°) and KEV (Δ=42°, ϕ=333°) for transverse (a,d), radial (b,e), and vertical components (c,f), respectively. Time is relative to the origin time reported by the NEIC.

recorded motion is in the pure state. However, the formulas given by Samson [1983] for the pure state process are useful for the determination of the instantaneous ellipticity and polarization orientation of the ground motion for any given time. The polarization parameters calculated using these formulas are consistent with that using the method of Vidale [1986].

In this study we analyze polarization anomalies of surface waves to investigate the effects of Earth's lateral heterogeneities beneath ray paths on the propagation of seismic waves from the May 21, 1992 Lop Nor explosion. We use the newly developed method of polarization analysis, retrieving instantaneous envelopes and polarization state vectors for waves in the period range of 10 to 80 s.

ANALYSES

In the following we include a brief illustration of the polarization analysis using data recorded at four IRIS/GSN stations, CHTO (Chiang Mai), MAJO (Matsushiro), TATO (Taipei), and KEV (Kevo), from the May 21, 1992 explosion. Figures 1(a-c) show the instantaneous envelopes of ground displacements with 20-s cut-off period at station CHTO. The envelopes are given by

$$Q_t = \left[u_t^2 + \hat{u}_t^2\right]^{1/2}, \; Q_r = \left[u_r^2 + \hat{u}_r^2\right]^{1/2}, \; Q_z = \left[u_z^2 + \hat{u}_z^2\right]^{1/2}$$

where $\hat{u}_t(t)$, $\hat{u}_r(t)$, and $\hat{u}_z(t)$ denote the Hilbert transform of the transverse (clockwise) $u_t(t)$, radial (outward) $u_r(t)$, and vertical (upward) $u_z(t)$ components of the seismic signals, respectively.

Figure 1a shows the transverse component of the instantaneous envelope. The Love waves start with an emergent onset, with a group velocity about 3.4 km/s. The Love wave energy reaches its maximum with a group velocity of 3.2 km/s, reflecting slower than average velocity for continental Love waves. The Rayleigh wave arrival corresponds to a relatively sharp onset on radial and vertical components (Figures 1b and 1c) with a group velocity of 3.0 km/s and reaches the maximum with a group velocity of 2.9 km/s, also slower than average velocity for continental Rayleigh waves. The Rayleigh waves appear mainly on vertical and radial components, with relatively weak energy on the transverse component.

Figures 1(d-f) show the envelopes for station KEV, which have a relatively sharp onset of Love waves on the transverse component with a velocity of 3.4 km/s and an emergent onset of Rayleigh waves with a velocity between 2.9 and 3.0 km/s. The energy of Love waves and Rayleigh waves reach the maximum with a velocity of 3.2 km/s and 2.8 km/s, respectively.

In contrast to the instantaneous envelopes for stations CHTO and KEV, the envelopes for stations MAJO and TATO show quite different characteristics. For station MAJO, while the arrivals of P and S waves (not shown in the figure) can be clearly identified on the envelopes with distinct, isolated pulses, the arrivals of surface waves are somewhat ambiguous. The energy on the vertical component starts with a sharp onset with a group velocity about 3.9 km/s and peaks at a velocity of 3.7 km/s; while on the transverse component it starts with a group velocity about 4.4 km/s, corresponding to the predicted arrival time of the SS wave for standard earth models. The multiple, irregular pulses on the radial component are followed by high amplitude noise for at least an hour (not shown in the figure), with the maxima arriving about every 18 minutes. These pulses appear also on the transverse component but with smaller amplitudes. The pulses that appear on all the three components with an onset at about 21 min perhaps were caused by sources of the same origin as those later pulses on radial and transverse components.

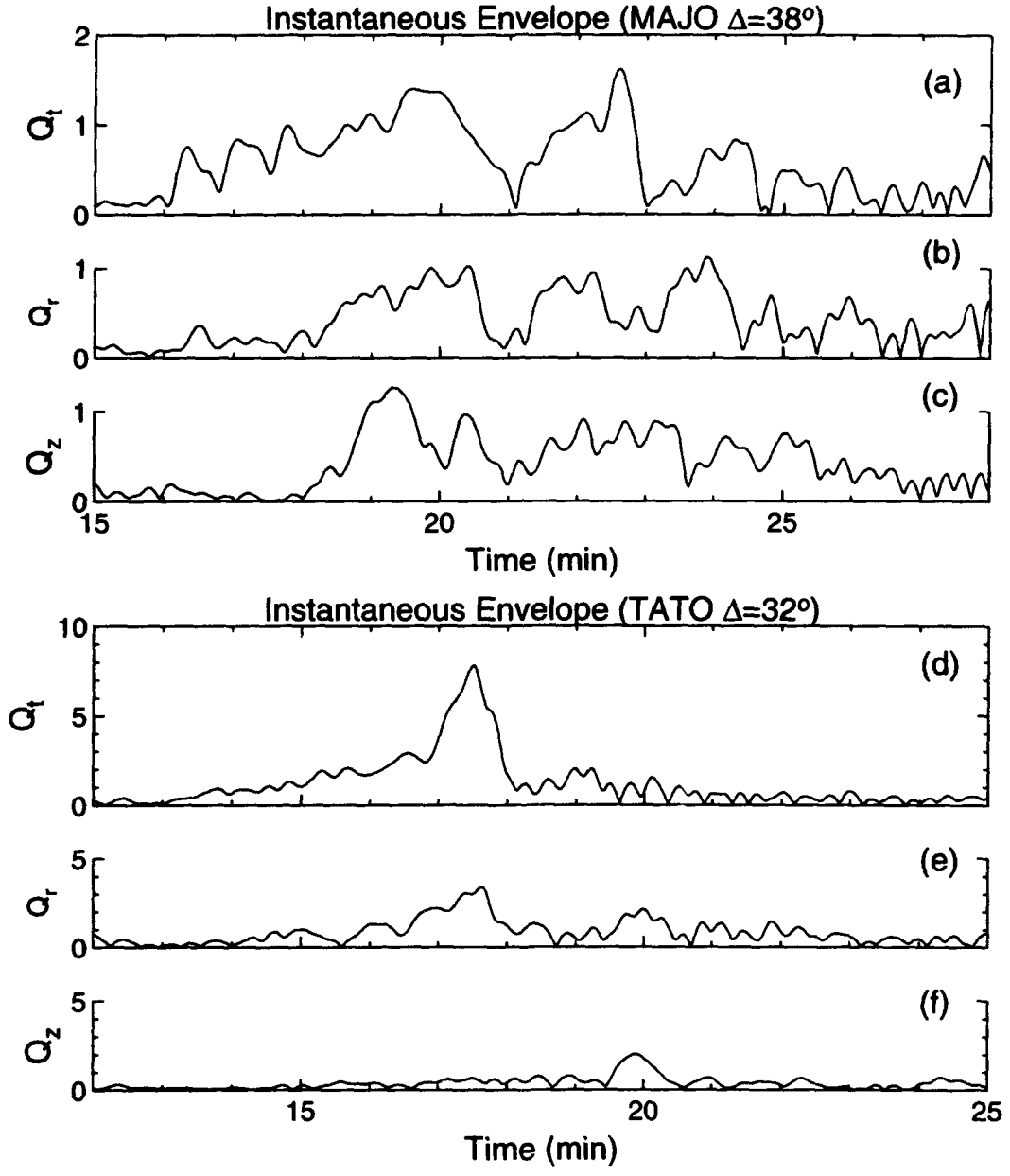


Fig. 2. The instantaneous envelopes of the ground displacements from the May 21, 1992 Lop Nor, China, nuclear explosion for stations MAJO (Δ=38°, ϕ=81°) and TATO (Δ=32°, ϕ=111°).

The envelopes of transverse and radial components for station TATO are dominated by a large pulse with a group velocity of about 3.4 km/s, which is followed by two broad, yet distinct pulses commencing every 25 minutes (not shown in the figure). We would consider these pulses are caused by a noise source of unknown origin. It is interesting, still, that the noise appears mainly on transverse and radial components for stations MAJO and TATO.

For a comparison, in Figure 3 we show the envelopes of the ground displacement recorded at station PAS for the September 4, 1989 earthquake in South of Alaska (m_b=6.5). The first pulse of relative small amplitude on each component corresponds to the S wave. The Love waves reach the maximum with a group velocity of 4.2 km/s, typical for oceanic paths. The Rayleigh waves arise sharply on the vertical component with a group velocity of 4.0 km/s and reach the maximum with a group velocity of 3.7 km/s, typical for oceanic paths.

Figure 4 shows the polarization state vectors [Samson, 1983] for station CHTO. r_{11}, r_{12}, and r_{13} denote the transverse, radial, and vertical components of the major polarization vector r_1, respectively; similarly, r_{21}, r_{22}, and r_{23} are for the minor polarization vector r_2. r_1 and r_2 together form a polarization ellipse. r_{31}, r_{32}, and r_{33} are for the ellipticity vector r_3, which is the cross product of r_1 and r_2.

The P and S waves correspond to pulses of the state vectors arriving at 5 and 10 min from the origin time, respectively. The Love waves start with an emergent onset and reach the maximum on r_{11} with a group velocity of 3.7 km/s with weak amplitudes on r_2 and r_3, indicating predominantly linearized polarization on the transverse component. The Rayleigh waves correspond to a sharp onset on r_{31}, indicating an elliptical polarization on vertical and radial components. There is some energy on r_{32}, demonstrating off great circle propagation of Rayleigh waves.

REFERENCES

Aki, K., and Y. B. Tsai, Mechanism of Love wave excitation by explosion sources, *J. Geophys. Res., 77*, 1452-1475, 1972.

Patton, H. J., Seismic moment estimation and the scaling of the long-period explosion source spectrum, in *Explosion Source Phenomenology*, edited by S. R. Taylor, H. J. Patton, and P. G. Richards; pp. 171-183, Geophysical Monograph 65, American Geophysical Union, 1991.

Samson, J. C., Pure states, polarized waves, and principal components in the spectra of multiple, geophysical time-series, *Geophys. J. R. astr. Soc., 72*, 647-664, 1983.

Vidale, J. E., Complex polarization analysis of particle motion, *Bull. Seism. Soc. Am., 76*, 1393-1405, 1986.

Wallace, T. C., Body wave observations of tectonic release, in *Explosion Source Phenomenology*, edited by S. R. Taylor, H. J. Patton, and P. G. Richards; pp 161-170, Geophysical Monograph 65, American Geophysical Union, 1991.

Wu, F. T., and A. Levshin, Tomography of China using surface waves from CDSN, *Proceedings of the 14th Annual PL/DARPA Seismic Res. Symposium*, 470-477, 1992. PL-TR-92-2210, ADA256711.

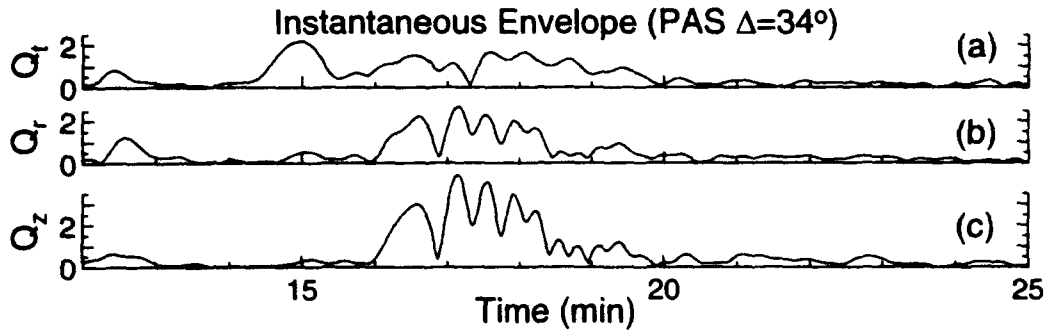


Fig. 3. The instantaneous envelopes of the ground displacements filtered between 0.3 and 100 mHz from the September 4, 1989 South of Alaska earthquake (m_b=6.5) recorded at PAS (Δ=34°, ϕ=113°).

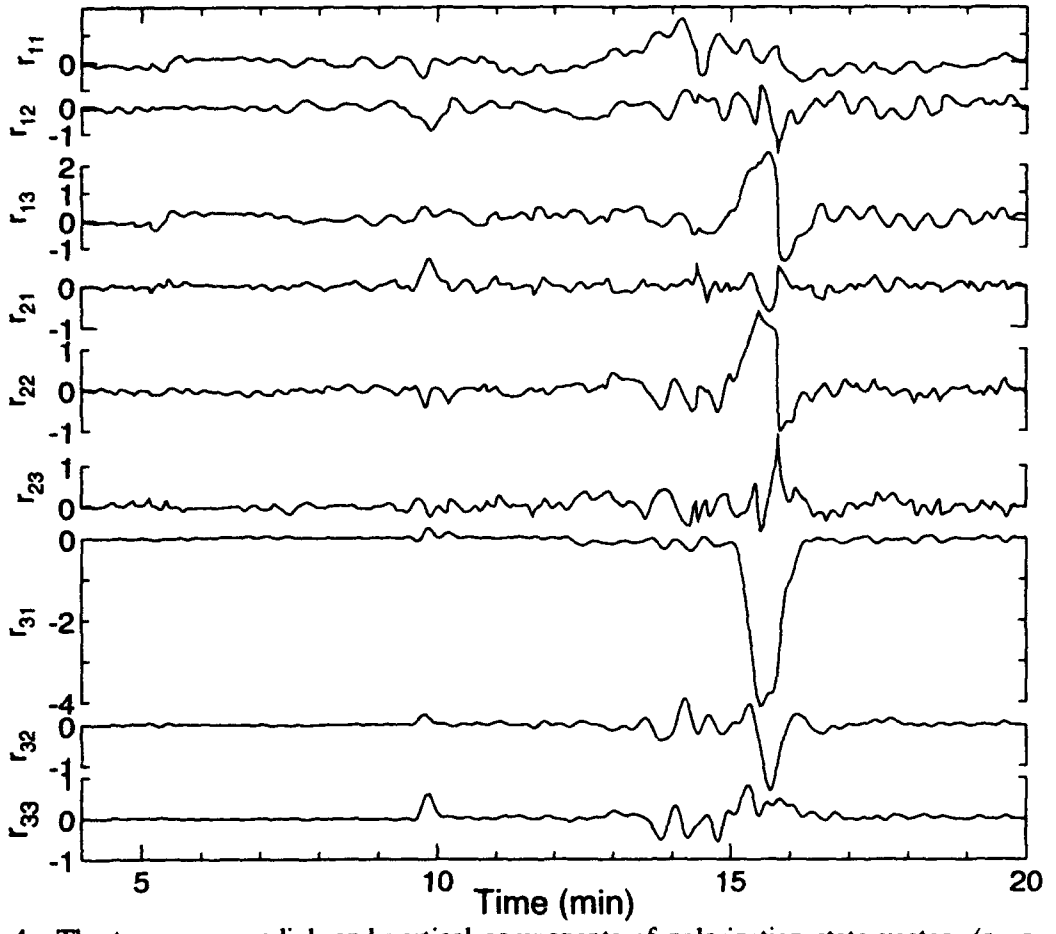


Fig. 4. The transverse, radial, and vertical components of polarization state vectors (r_1, r_2, r_3) for the ground displacement seismograms recorded at CHTO from the May 21, 1992 Lop Nor nuclear explosion. The units are in microns.

Crustal and Upper Mantle Velocity Structure Beneath Seismic Stations from Modeling Teleseismic Waveforms

Lian-She Zhao and Cliff Frohlich
Institute for Geophysics
The University of Texas at Austin
8701 North MoPac
Austin, TX 78759-8397

Contract No. F49620-94-1-0287

OBJECTIVES

In this study, we develop a method for investigating the crustal and uppermost mantle velocity structure beneath three-component seismic stations. The structure so found will allow us to construct improved synthetic seismograms and thus determine better locations and magnitudes for smaller seismic events.

RESEARCH ACCOMPLISHED

We have implemented a grid search scheme to determine the crustal and uppermost mantle velocity structures beneath seismic stations using teleseismic P waveforms. We use the vertical component record to approximate the signal arriving at the base of the crust near the receiver. Then, for any particular layered crustal structure, we calculate a synthetic radial-component waveform using a second order approximation which should be accurate to within a few percent at teleseismic distances. We then compare the synthetic radial component with the recorded radial component directly in the time domain, using a linear combination of L1 and L2 error norms to measure the mitsfit. To find the optimum structure we find the smallest data misfit by performing the grid search over a range of P velocities, S velocities, and layer thickness for structures having from one to five layers.

Theoretical Background

Suppose that the P signal arriving at the base of the crust from a teleseismic event is $S(t)$, which includes both the source signal and complexity caused by near-source. Then, the observed vertical-component seismogram $Z(t)$ and radial-component seismogram $H(t)$ are:

$$(1) \qquad Z(t) = z_0 S(t) + \sum_i z_i S(t - t_i)$$

and

$$(2) \qquad H(t) = r_0 S(t) + \sum_i r_i S(t - t_i)$$

where z_i and r_i are the appropriate products of transmission and reflection coefficients from the Moho to the free surface along the ray path and receiver responses R_{pz}, R_{pr}, R_{sz}, and R_{sr} are vertical- and radial-component receiver responses for P and S waves incident at the station. The t_i are the time delays for reflected and converted rays in the crust.

We normalize both the vertical component $Z(t)$ and the radial component $H(t)$ to unit maximum amplitudes and rewrite Eqs.(1) and (2) as:

$$(3) \qquad Z_n(t) = S(t) * (1 + \sum_i \frac{z_i}{z_0} \delta(t - t_i))$$

and

$$(4) \qquad H_n(t) = S(t) * (1 + \sum_i \frac{r_i}{r_0} \delta(t - t_i)).$$

We then Fourier transform Eqs. (3) and (4), writing $\delta_{t_i}(\omega)$ as the transform of $\delta(t - t_i)$, and expand to second order in z_i and r_i to obtain:

$$(5) \qquad Z_n(\omega) = S(\omega)(1 + \sum_i \frac{z_i}{z_0} \delta_{t_i}(\omega))$$

and

$$(6) \qquad H_n(\omega) = S(\omega)(1 + \sum_i \frac{r_i}{r_0} \delta_{t_i}(\omega)). = \frac{Z_n(\omega)(1 + \sum_i \frac{r_i}{r_0} \delta_{t_i}(\omega))}{1 + \sum_i \frac{z_i}{z_0} \delta_{t_i}(\omega)}$$

$$= Z_n(\omega)(1 + \sum_i \frac{r_i}{r_0} \delta_{t_i}(\omega)) \qquad \text{(0th order)}$$

$$= Z_n(\omega)(1 + \sum_i (\frac{r_i}{r_0} - \frac{z_i}{z_0}) \delta_{t_i}(\omega)) \qquad \text{(1st order)}$$

$$= Z_n(\omega)(1 + \sum_i (\frac{r_i}{r_0} - \frac{z_i}{z_0}) \delta_{t_i}(\omega)(1 - \sum_j \frac{z_j}{z_0} \delta_{t_j}(\omega)) \qquad \text{(2nd order)}$$

In the time domain, these expressions for the normalized radial component are:

$$(7) \qquad H_n(t) = Z_n(t) + \sum_i \frac{r_i}{r_0} Z_n(t - t_i) \qquad \text{(0th order)}$$

$$= Z_n(t) + \sum_i (\frac{r_i}{r_0} - \frac{z_i}{z_0}) Z_n(t - t_i) \qquad \text{(1st order)}$$

$$= Z_n(t) + \sum_i (\frac{r_i}{r_0} - \frac{z_i}{z_0})(Z_n(t - t_i) - Y(t - t_i)) \qquad \text{(2nd order)}$$

where

$$Y(t) = \sum_i \frac{z_i}{z_0} Z_n(t - t_i).$$

The zero order approximation is simply Eq. (2) with normalized amplitude and $Z(t)$ instead of $S(t)$. In the first order expression, it is clear that converted and reflected rays arriving at the receiver as a P phase do not contribute to the response. However, in the second order expression, P arrivals do have an effect expressed in the $Y(t)$ term, although their contribution is smaller than that of the S arrivals.

Synthetics and Comparisons

Computer implementation of the above theory is not difficult, as explicit formulas for the r_i, z_i, and t_i are available (e.g., Helmberger, 1968; 1980). For this method to be valid it is crucial that Eqs. (1) and (2) give correct synthetics. To test this, we determine synthetics (Figure 1) for a two-layer crustal model, using both Eq. (7) as well as the reflectivity method of Fuchs and Müller (1976). It is evident in Figure 1 that the waveforms predicted by the two methods are in excellent agreement.

To illustrate the effect on the synthetics of each term in the expansion (Eq. 7 above), we use a layer-over-half space model (Figure 2). While the difference between the exact calculation (the "Real" trace) and the "0 order" trace is as much as 15.8% of the maximum trace amplitude, this difference is reduced to only 1.5% when we use the second order approximation. For all our remaining applications we used the second order approximation; at teleseismic distances this introduces an error in the amplitude that is no more than a few percent (Figure 2).

Grid Search Scheme

To determine crustal structure using the grid search scheme, we allow P velocity, S velocity, and layer thickness to be free parameters, while assuming a density corresponding to the S velocity as determined from the Nafe table. Our present computer code performs grid searches for models with as many as six layers (17 free parameters). To determine the velocity structure beneath any particular station, we find the velocity model which provides the closest fit to either a single seismogram or (if available) a suite of seismograms available for that station. The scheme is fast; on a SPARC 10 machine, it takes one second to search about 200 four-layer models and fit seismograms with 800 points.

Applications

As a preliminary test of this method we have determined the velocity structure beneath several IRIS and Chinese digital stations. Generally we begin the search using a velocity structure with a single crustal layer, where there are five free parameters (Figure 3a, model "syn 1"). If we are fitting data from only one seismic event the program requires only a few minutes to search over all reasonable models.

Evaluation of the error distribution of the five parameters for the one-layer model (Figure 3b) gives us much information about what we can expect to extract from the available data, i.e. the sensitivity. Then we limit the range of the free parameters as we proceed to investigate data fits for crustal structures with more layers (Figure 3a, models "syn 2" and "syn 3", Table 1). For the Chinese station LZH, the sensitivity analysis (Figure 3b) demonstrates clearly that the data place the strongest constraint on the crustal S velocity, crustal thickness, and mantle S velocity, while crustal P velocity is less well determined, and mantle P velocity is not contrained at all. Thus, on the following searches, we do not need to vary the mantle P velocity, which we can choose to fit Nafe table and the corresponding mantle S velocity.

For LZH, the error reduction is 3% as we proceed from a one-layer crust to a two-layer crust, and 8% as we proceed from a two-layer crust to a three-layer crust. Figure 3a demonstrates that the waveform fit does improve as we increase the number of crustal layers.

We evaluated the crustal structure beneath the station CHTO using data from nine different earthquakes (Figure 4). By finding the best-fitting crustal structure using data from a suite of

earthquakes, individual waveform peculiarities caused by recording errors or near-source structure are unlikely have any effect on the grid search process.

CONCLUSIONS AND RECOMMENDATIONS

The grid search scheme introduced in this study is an efficient, practical method for determining the crustal and uppermost mantle velocity structure beneath seismic stations. This provides essential information about regional velocity structure, and for undertaking single-station relocations of smaller earthquakes and explosions. We plan to apply this method to determine best-fitting layered velocity structures for numerous stations in Asia, the Middle East, and Northern Africa.

A possible problem is that the velocity structure beneath some stations may not consist of flat layers. It may be possible to investigate this by deterining different structures for data in various azimuth windows, or, by comparing data with synthetics determined for dipping or even non-planar boundaries.

References:

Fuchs, K., and G. Müller, Comparison of synthetic seismograms with the reflectivity method and comparison of observations, *Geophys. J. Roy. astro. Soc.* **23**, 417-433. 1976

Helmberger, D. V., The crust-mantle transition in the Bering Sea, *Bull. Seism. Soc. Am.* **58**, 179-214, 1968.

Helmberger, D. V., Theory and applications of synthetic seismograms, in *Proceedings of the International School of Physics «Enrico Fermi», Course LXXXV, Earthquakes: Observation and Interpretation*, pp. 174-222, eds: Kanamori, H. and Boshi, E., North-Holland, 1980.

Table 1. Models for stations LZH and CHTO

crustal layers									mantle		label
α_1	β_1	th_1	α_2	β_2	th_2	α_3	β_3	th_3	α_m	β_m	
LZH											
6.2	3.75	51							7.7	4.4	syn 1
6.3	3.6	35	6.4	3.85	30				8.1	4.5	syn 2
5.0	2.8	2	6.3	3.6	28	6.6	3.85	20	7.9	4.4	syn 3
CHTO											
5.6	3.0	4	5.3	3.2	9	6.9	3.8	17	7.1	4.0	

units are: km/sec for α_i, β_i and km for th_i

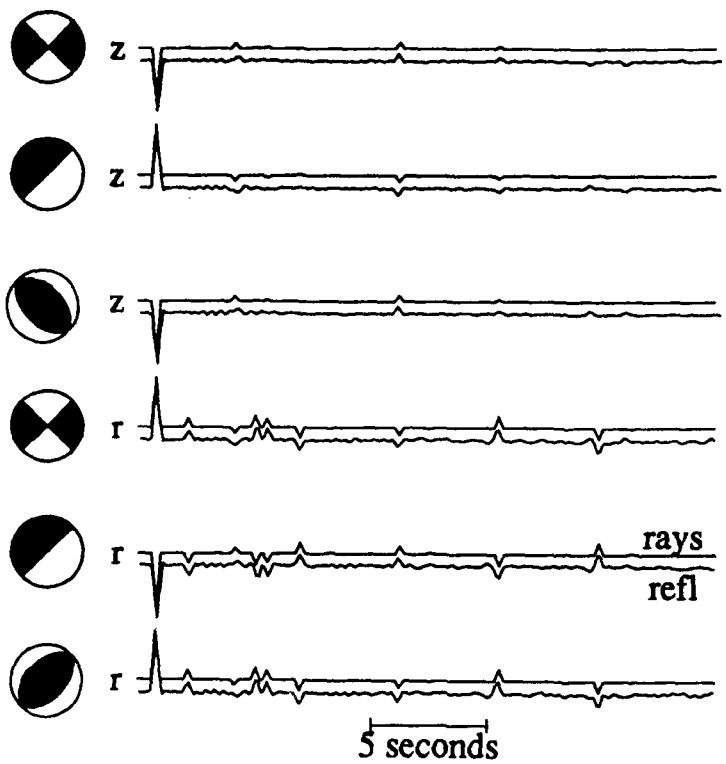


Figure 1. Comparison of synthetic waveforms constructed using ray theory (Eqs. 1 and 2) and with the reflectivity method of Fuchs and Müller (1976). The synthetic vertical (labeled "z") and radial (labeled "r") waveforms are determined for an event at 70° distance and an azimuth 90°. The source mechanisms are shown by the icons at the left of the traces. For the reflectivity calculations we used a source at 550 km depth, and a PREM model with a two layer crust with P velocity, S velocity, density and thickness of 5.6 km/s, 3.2 km/s, 2.6 gm/cm^3, and 10 km for first layer, 6.7 km/s, 3.8 km/s, 2.9 gm/cm^3, 25 km for the second layer, and 8.1 km/s, 4.5 km/s, and 3.3 gm/cm^3 for the mantle. For the ray theory synthetics we used 16 rays, including all the strongest transmitted and reflected crustal reverberations.

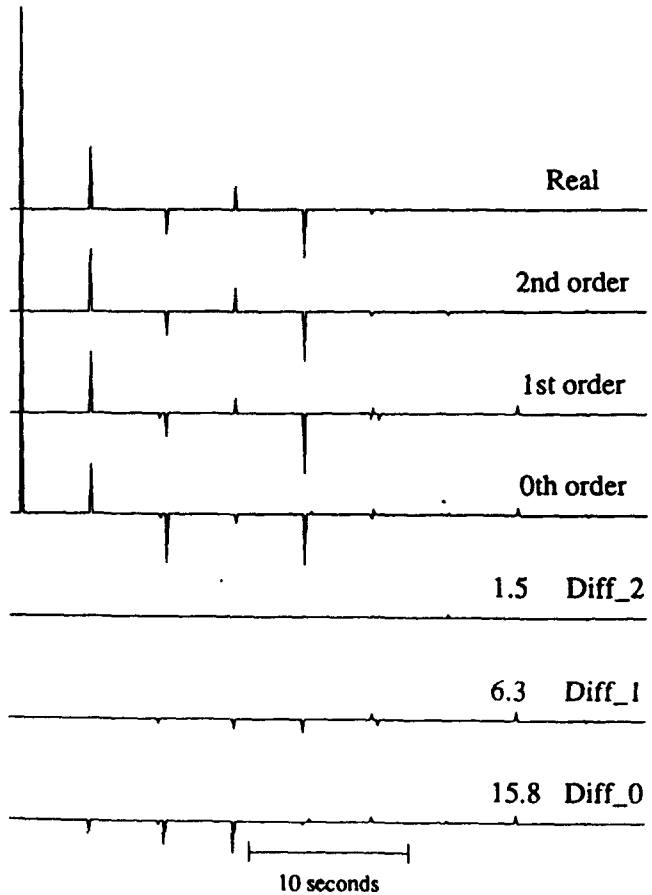


Figure 2. Error introduced from approximations of different order. "Real" is the synthetic radial component (Eq. 2) for a simple layer-over-half space model (crust: P, S velocities: 6.2 km/s, 3.5 km/s, density 2.7 gm/cm^3, thickness 32 km; mantle: 8.2 km/s, 4.5 km/s, 3.3 gm/cm^3). "Real" is determined using 10 rays-- the direct P ray and all P or S reflected or converted rays that bounce once at the Moho. The traces marked "Diff_*i*"s are the difference between the "Real" trace and those determined using the approximate expansion up to order *i* (Eq. 7). The numbers on the left of "Diff_*i*" are the maximum amplitude expressed as a percent of the maximum amplitude of the "Real" trace. Synthetics are determined for a source at a distance of 70°.

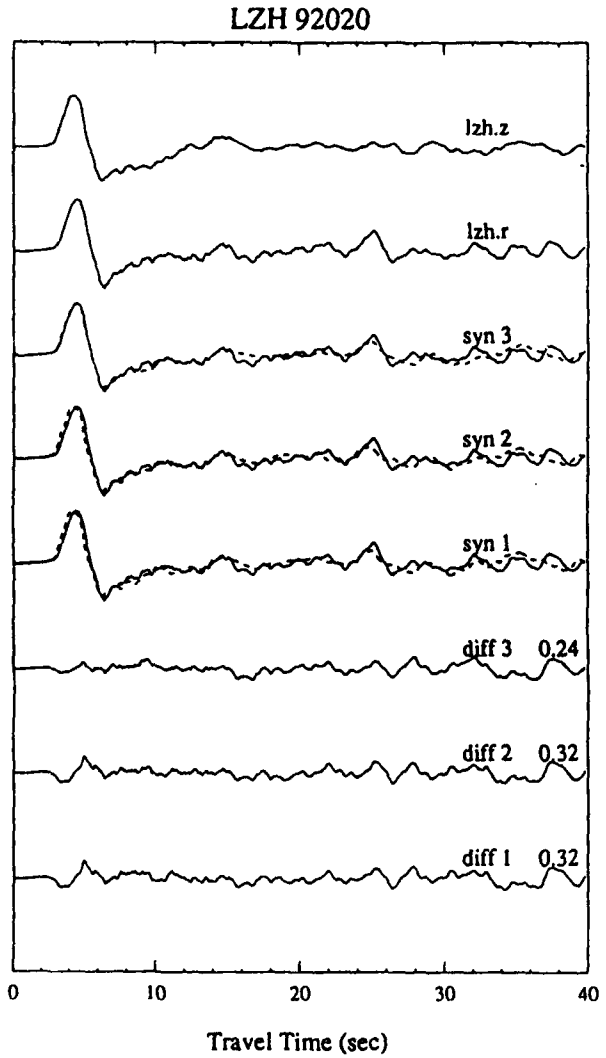


Figure 3a) Comparison of vertical- and radial-component data (labeled "lzh.z" and lzh.r" from the Chinese station LZH with radial-component synthetics for three different models (labeled "syn 1", etc., see Table 1) for the 20 Jan. 1992 Bonin earthquake (m_b = 5, depth 510 km). The traces labeled "diff 1", etc. are the difference between the observations and the synthetics; the numbers at right are the maximum difference expressed as a fraction of the maximum of the "lzh.r" trace. The models are given in Table 1).

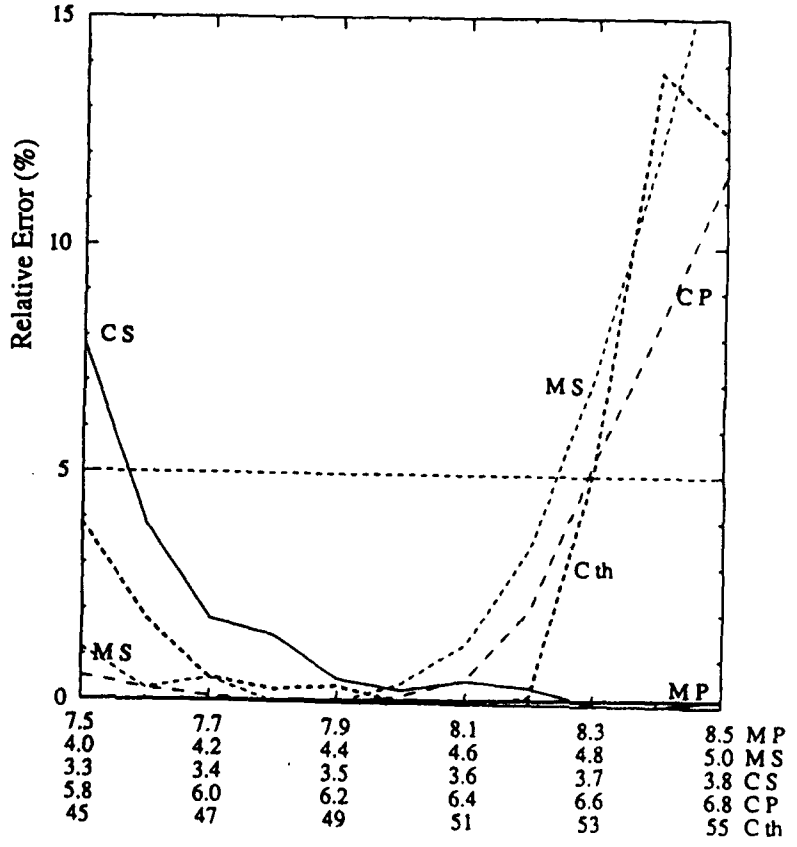


Figure 3b) Effect of variation of model parameters for model "syn 1" on fit to trace "lzh.r" at station LZH. Relative error is the difference between the misfit and the global minimum misfit, divided by the global minimum misfit. Parameters are: "C S" crustal S velocity, "C P" crustal P velocity, "M S" mantle S velocity, "M P" mantle P velocity, and " C th" crustal thickness. The horizontal axis gives the range of each of these parameters.

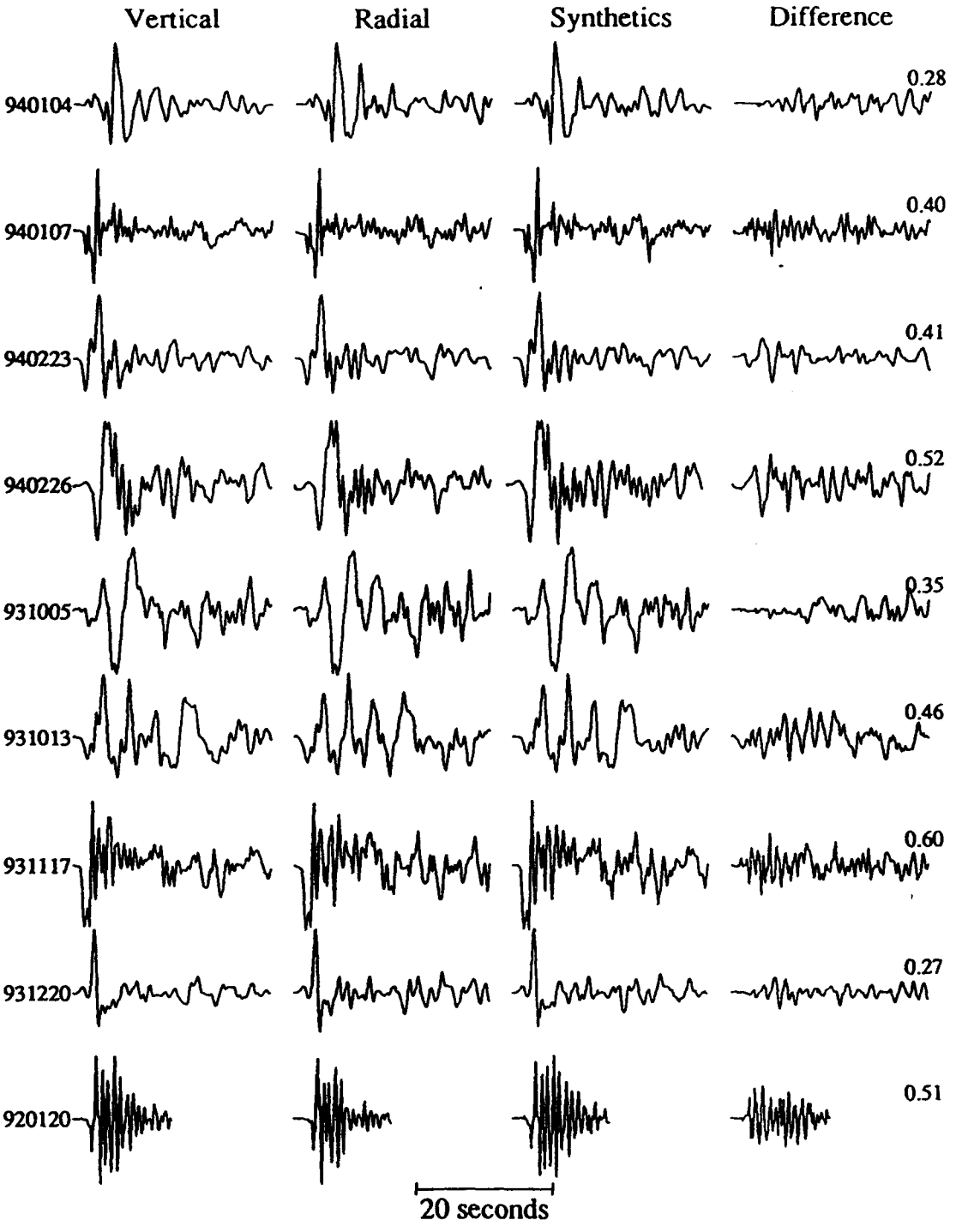


Figure 4. Comparison of vertical- and radial-component observations and radial-component synthetics for nine earthquakes recorded at station CHTO. The synthetics were calculated using the best-fitting three-layer model (Table 1). The numbers at the left of each trace are the year, month and day of each event; the numbers at the right of the difference trace are the maximum difference between observation and synthetic, expressed as a fraction of maximum observed amplitude.

Regional Earthquake Waveform Modeling on the Tibetan Plateau

L. Zhu and D. V. Helmberger

California Institute of Technology
Contract No. F49620-92-J-0470

OBJECTIVE

Broadband records of regional earthquakes can help to constrain the source mechanisms and crustal structure. The objective of this report is to study the crustal structure and source mechanisms by using regional earthquake waveform data obtained during the 1991-1992 passive recording experiment on the Tibetan Plateau (Owens et al., 1993). The data also provide an opportunity to test the ability of determining source mechanisms of regional events by broadband waveform modeling in an area where only limited number of stations are available and the structure is not well known.

RESEARCH ACCOMPLISHED

Introduction

The Tibet Plateau, produced by collision of two continental plates, India and Eurasia, has been a challenge in Earth science for a long time. Several models of collision and formation of the plateau have been proposed. But none of them can give a satisfactory explanation.

Seismic velocity structure of the crust and upper mantle can provide us information on the present state deep in the plateau, which is crucial to understanding the process of plateau formation. Due to the difficulties of accessing this area, previous seismic studies had to rely on the data recorded at stations outside the plateau. Most studies were done by using long-period surface wave, short-period travel time analysis, or waveform modeling (S, SS etc), see Zhao et al (1991). In 1991-1992, a passive source seismic recording experiment was conducted on the Tibet Plateau by Sino-US seismologists. For the first time, 11 digital broadband seismic stations were deployed on the plateau (Figure 1). Large amount of data was obtained from teleseismic and regional events.

In this report, we will use the data from several regional events to study the source mechanisms and the crustal structure. Two previous velocity models are examined and a new model is formed from the waveform modeling. We will also test the ability of of constraining the source mechanisms of regional events by one or few broadband stations.

Relocation of events and Pn, Sn velocities

More than 50 regional events with reasonable signal/noise ratio have been recorded during the one year experiment. We selected 5 events with 4 of them located within the array (Figure 1). Due to lack of reports of regional seismic stations and the difference of Tibet crust structure from standard earth model, the source location parameters of the events in Tibet give by PDE are not satisfactory. Thus, we first relocate the events by their first arrivals. The velocity model for relocation is a two-layer crust model simplified from previous teleseismic receiver function study (Zhu, 1993). It has a 3 km top layer with P velocity 4.5 km/s and 62 km layer with P velocity of 6.2 km/s, the uppermost mantle velocity is 8.1 km/s. Since most earthquakes in Tibet occur at depths between 5 to 20 km (Molnar and Chen, 1983; Zhao and Helmberger 1991), we fix the source depth at 10 km. The relocation results are listed in Table 1. It is shown that PDE tends to give later origin times for events in Tibet plateau because the

crust thickness used by PDE is much less than 65 km average thickness of Tibet crust.

Table 1 Event list and relocation results

Event	PDE origin time yr-mo-da hr mi t0	lat. °	long. °	h km	Mb	rms s	Relocation t0 s	lat. °	long. °	rms s	Δt0 s	Δx km
222	91-08-10 20 21 51.7	33.91	92.16	10	4.7	1.2	52.1	33.92	92.28	0.9	0.4	11
323	91-11-19 01 04 18.0	32.48	93.59	33	4.9	3.0	15.9	32.55	93.82	0.8	-2.1	23
330	91-11-26 21 15 59.9	34.07	94.25	33	4.3	2.5	57.6	34.09	94.23	0.8	-2.3	3
336	91-12-02 19 45 36.6	32.09	94.69	*	4.4	4.0	33.6	32.17	94.62	0.7	-3.0	11
348	91-12-14 08 20 23.8	33.98	88.84	33	5.1	5.4	20.8	33.93	89.06	0.3	-3.0	20

Event 222 was recorded by all the 11 stations in epicentral distance range of 80-800 km. In addition, it occurred in the middle of the north-south station line, forming a nature seismic profile. Figure 2 is a record section of this event. By identifying the Pn and Sn arrivals and using least-square fitting, we obtain the following travel time relations:

$$Pn = 12.39 + \Delta/8.11 \quad (sec)$$

$$Sn = 23.90 + \Delta/4.71 \quad (sec)$$

Our 8.11 km/s and 4.71 km/s for P and S velocities in uppermost mantle are very consistent with previous results (Chen and Molnar, 1981) The average crust P and S velocities estimated from intercept time are 3.46 km/s and 6.24 km/s, assuming the source depth of 10 km and crust thickness of 65 km. All these velocity analyses, combined with results of previous work, provide initial models for our next step involving waveform modeling.

Waveform modeling

To estimate the source mechanisms, we used a procedure developed by Zhao and Helmberger (1994). It uses a direct grid search in the strike, dip, rake and source depth parameter space for the minimum L1 and L2 norms of the difference between waveforms and synthetics. The method desensitizes the timing between principal crustal arrivals by fitting portions of the waveforms independently, allowing some time shifts between the observation and synthetics. We find that introducing one more parameter, the scalar moment, in the search process and using the same moment for all stations and components increases the resolution.

Two previous velocity models of Tibet plateau have been examined. Model M45 was derived from pure path phase velocity dispersions of long-period surface wave (Romanowicz, 1982). Another model, TIB, was from waveform modeling of regional long-period Love wave (Zhao et al., 1991). Figure 3 shows these two models. Both models give reasonably good waveform fits of the Love waves. But it turns out that TIB yields SmS arrivals that are too fast relative to the observed SmS (Figure 4). M45's prediction of SmS arrival times is better than TIB's. By comparing these two model, we conclude that TIB has mid-lower crustal velocities that are too high. This conclusion is also consistent with previous receiver function study (Zhu, 1993).

We start with a simple initial model: a low velocity top layer on a uniform crustal layer of 50 km thick with a transition zone above moho. By adjusting the thickness and velocities of each layer, we try to model the observed waveforms of both Pnl and surface wave. Generally, the Love wave provides constraint on the velocity structure of upper crust and Pnl, SmS provide constraint on the lower crust. Our final model is given in Figure 3 labeled T91: the top layer thickness is 3 km with a S velocity of 2.50 km/s and a P velocity of 4.45 km/s followed by a 50 km main crust with a S velocity of 3.45 km/s and a P velocity of 6.2 km/s. Moho is at a depth of 68 km with a 15 km transition zone above it. Figure 5 is the waveform fit by this model for event 222. For all 5 events, this model produces good fits between observations and synthetics, especially the SH components. The obtained source mechanisms are listed in Table 2. The two northern events are strike-slip type. The other 3 are normal fault type (Figure 1).

Table 2 Source mechanisms from waveform modeling

ent	whole array						one station (AMDO)					
	strike	dip	rake	10^{22} M0 dyn cm	depth km	error	strike	dip	rake	10^{22} M0 dyn cm	depth km	error
222	340	70	170	20.0	10	3.7	340	80	170	21.0	10	3.2
323	190	50	260	1.5	10	4.0	170	50	220	1.8	10	3.1
330	30	60	210	7.3	10	4.2	30	80	240	8.8	10	3.4
336	170	30	220	2.6	10	4.1	210	30	260	2.3	10	3.3
348	0	60	240	19.0	5	4.0	190	70	220	20.0	10	3.3

CONCLUSION AND RECOMMENDATIONS

The result of regional earthquake waveform modeling shows that the crust of Tibet plateau is roughly vertically uniform and has a very low average velocity, especially the shear velocity. It suggests that the temperature in the mid-lower crust is high which might be caused by the concentration of continental crust materials or high heat flow from the upper mantle. Our results are consistent with previous surface wave and teleseismic receiver function studies. Two types of source mechanisms have been obtained for 5 regional events: strike-slip with one EW-striking fault plane and normal fault with EW T-axes. The source mechanisms and their indicated stress states support the proposed EW extrusion and extension of the crust in the high plateau under the indentation of India subcontinent (Molar and Layon-Caen, 1989).

To test the ability of constraining source mechanism of regional events by one or few broadband stations, we select one station (AMDO) and only use its recordings to search for the source mechanisms. The solutions are also listed in Table 2 with solutions from the whole array. The result is encouraging. Under the circumstance that we have good Pnl and surface wave recordings and suitable velocity model, the source mechanisms can be obtained by one station, as found in California (Dreger and Helmberger, 1993). We believe such kind of test is very helpful for further broadband waveform modeling in area as Tibet where only few stations are available. For example, beginning from 1992 CDSN has one more permanent broadband station operating at Lhasa. More regional earthquake data can be accumulated in recent future.

References

Dreger, D. S. and D. V. Helmberger, 1993, Determination of source parameters at regional distances with three-component sparse network data, *J. Geophys. Res.* 98, 8107-8125.

Molnar P. and W. Chen, 1983, Focal depths and fault plane solution of earthquakes under the Tibetan Plateau. *J. Geophys. Res.* 88, 1180-1196.

Owens, T. J., G. E. Randall, F. T. Wu and R. S. Zeng, 1993, PASSCAL instrument performance during the Tibetan plateau passive seismic experiment, *Bull. Seism. Soc. Am. 83, 1959-1970.*

Romanowicz, B. A., 1982, Constraints on the structure of the Tibet Plateau from pure path phase velocities of Love and Rayleigh waves, *J. Geophys. Res.* 87, 6865-6883.

Zhao, L. and D. V. Helmberger, 1991, Geophysical implication from relocation of Tibetan earthquakes - hot lithosphere, *Geophys. Res. Lett.*, 18, 2205-2208.

Zhao, L., D. V. Helmberger, and D. G. Harkrider, 1991, Shear-velocity structure of the crust and upper mantle beneath the Tibetan and southeastern China, *Geophys. J. Int.* 105, 713-730.

Zhao, L. and D. V. Helmberger, 1994, Source estimation from broadband regional seismograms, *BSSA* 84, 91-104.

Zhu, L., R. S. Zeng, F. T. Wu, T. J. Owens, and G. E. Randall, 1993, Preliminary study of crust-upper mantle structure of the Tibetan Plateau by using broadband teleseismic body waveforms, *Acta Seism. Sinica* 6, 305-315.

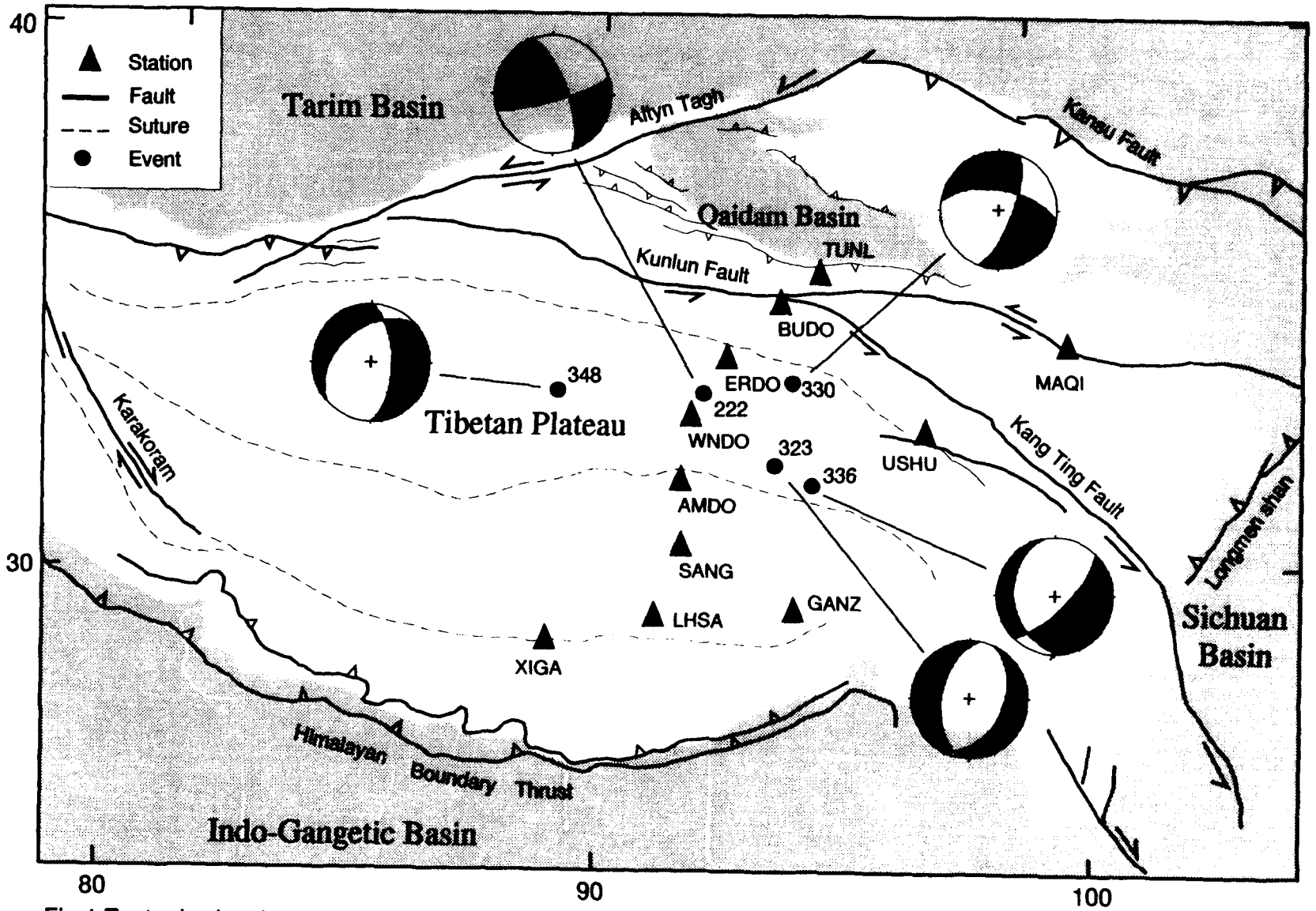


Fig.1 Tectonic sketch map of Tibet plateau (modified from Dewey et al., 1988), gray areas are below 3 km elevati
Blacken dots are 5 events with their source mec ms from waveform modeling

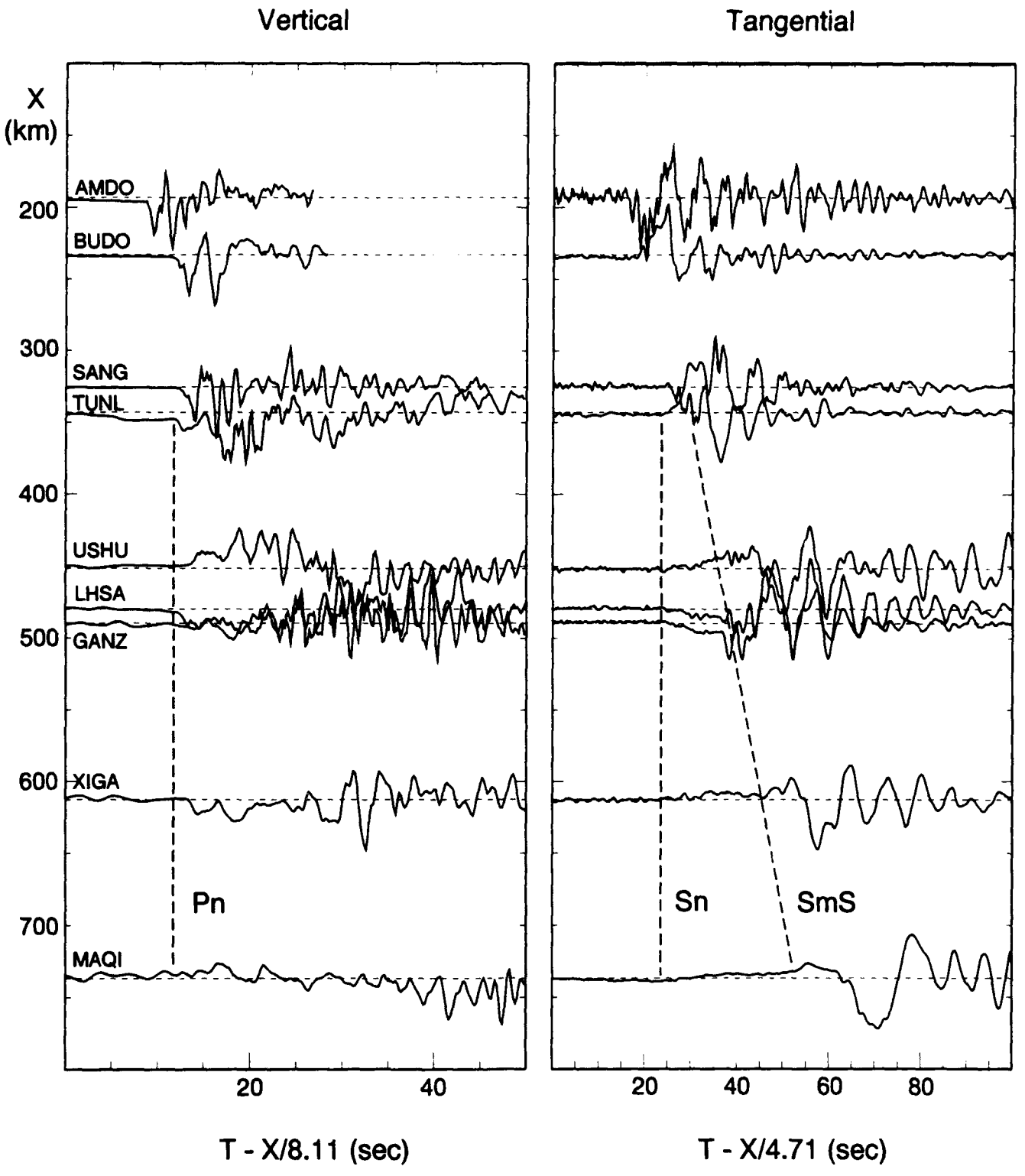


Fig. 2 Recording section of event 222, dashed lines show the Pn, Sn and SmS.

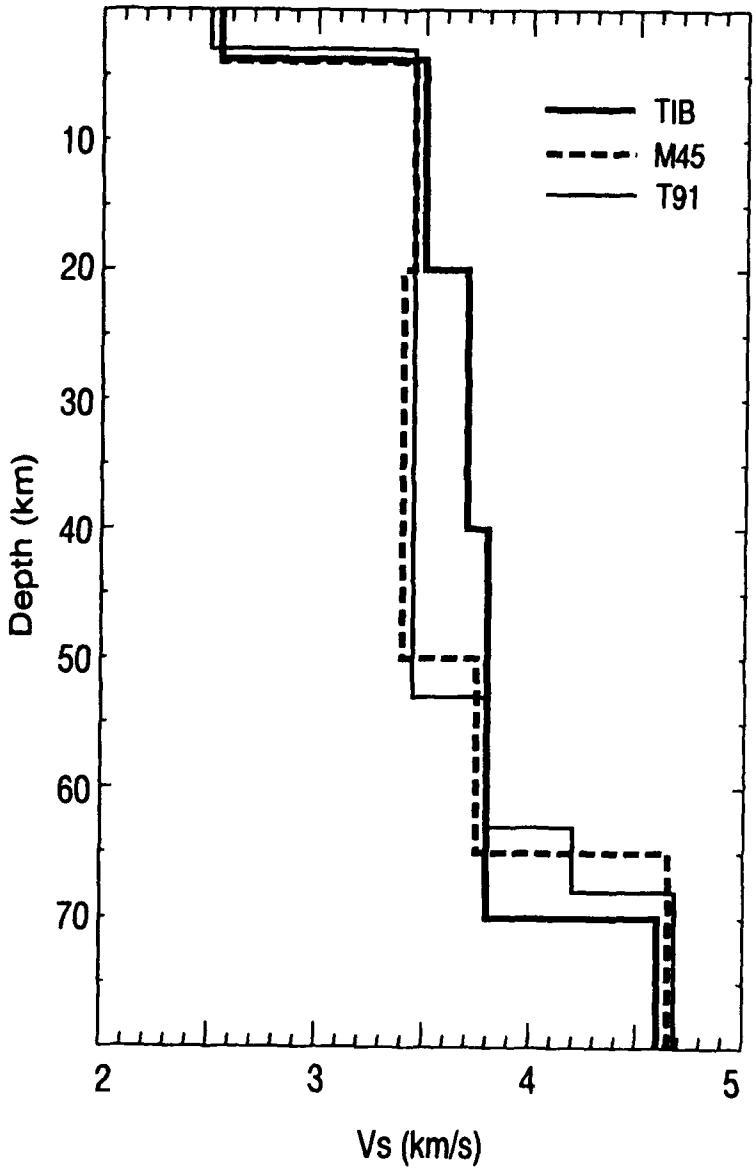


Fig.3 Model M45, TIB and T91 (see paper)

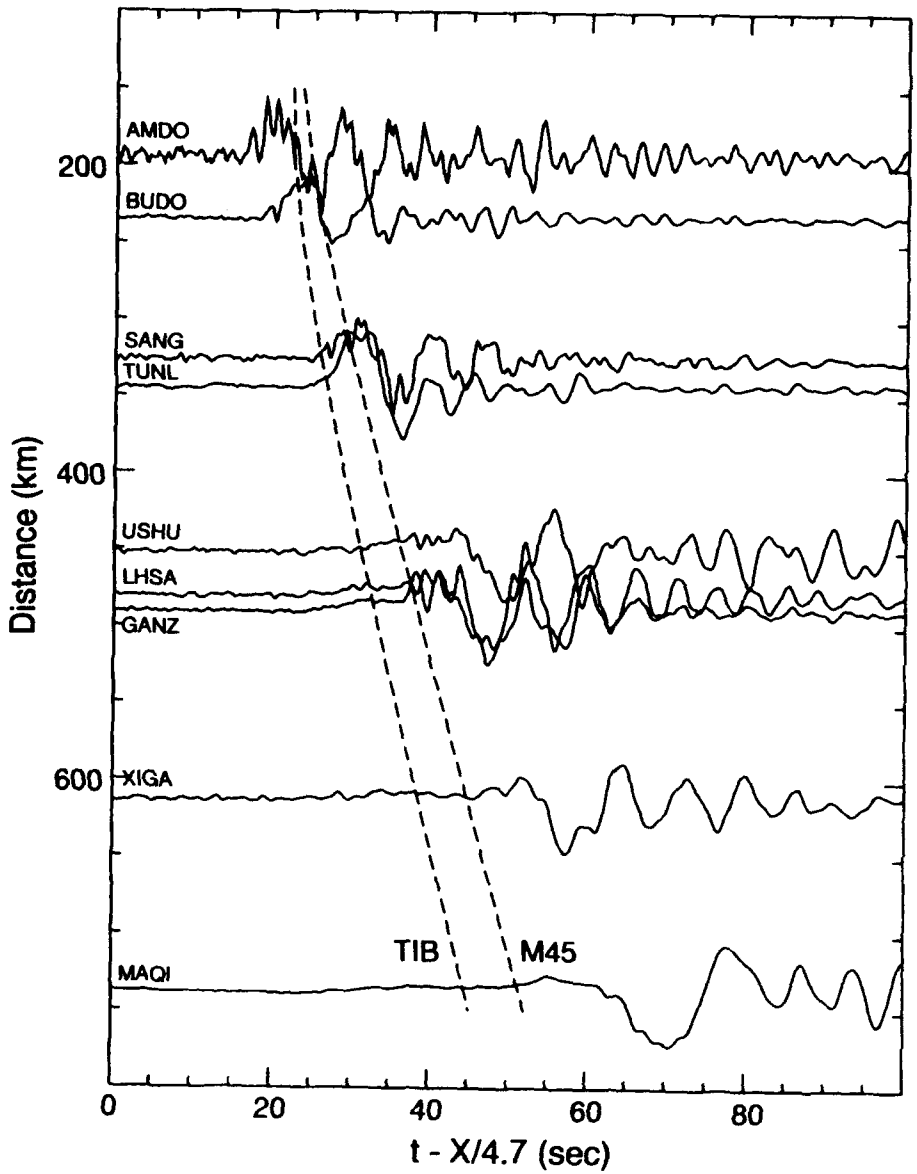


Fig.4 Polarity-corrected SH component record section of Event 222 and SmS arrival times predicted by model TIB and M45

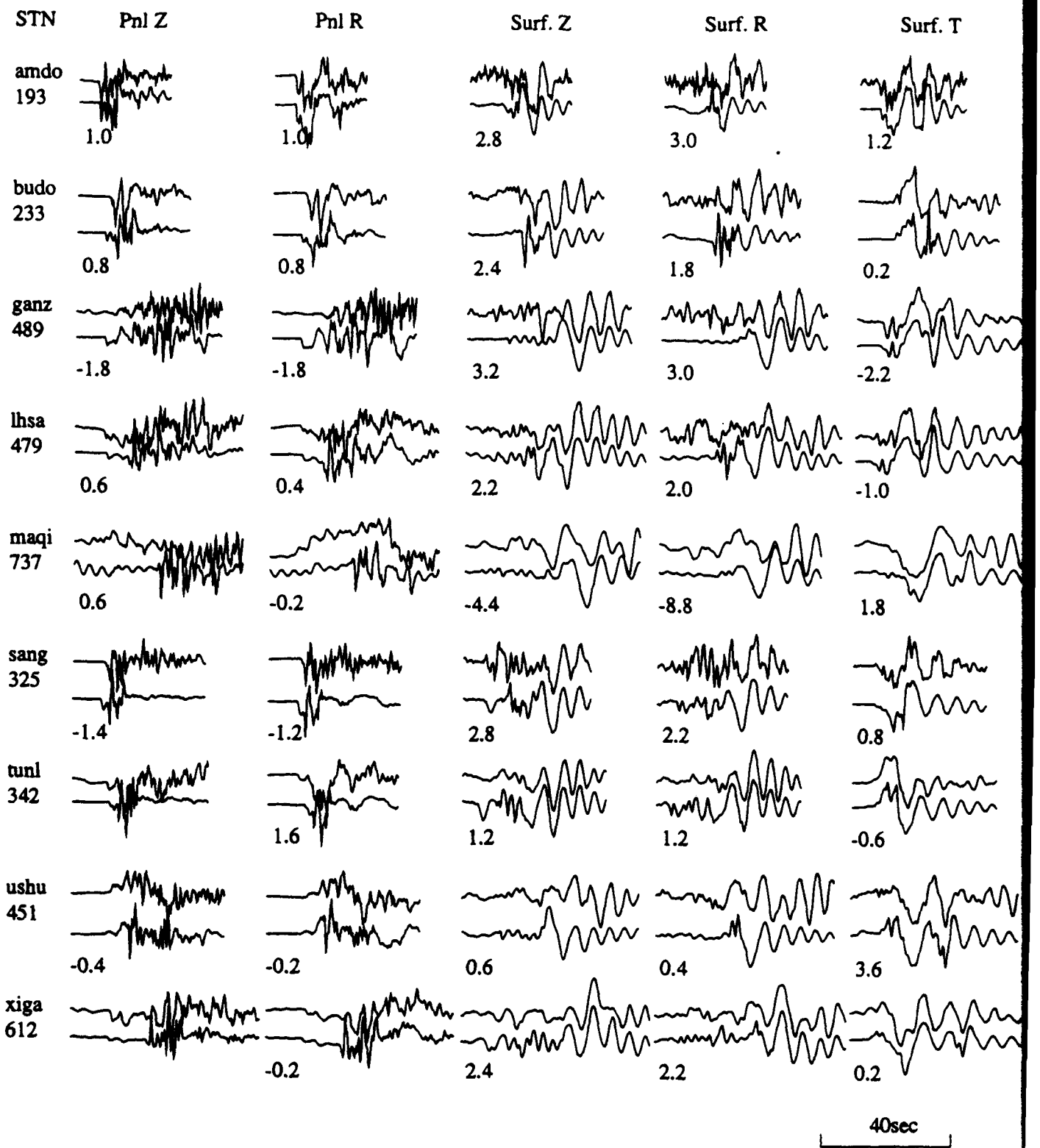


Fig. 5 Waveform modeling of Event 222, upper traces are observation and lower traces are synthetics with time shifts in sec (positive number means synthetic is shifted back). Numbers below station names are distances in km. Model used is T91 with source at depth of 10 km. Source mechanism from modeling is strike 340, dip 70 rake 170 and M0 2.0e+23 dyn cm